

*Electrochemistry of Silicon: Instrumentation, Science, Materials and Applications.*  
Volker Lehmann  
Copyright © 2002 Wiley-VCH Verlag GmbH  
ISBNs: 3-527-29321-3 (Hardcover); 3-527-60027-2 (Electronic)

*Volker Lehmann*  
**Electrochemistry of Silicon**

### Cover illustrations

Upper left: Electrolytic double cell for diffusion length mapping of 200 mm silicon wafers using the ELYMAT technique, as discussed in Section 10.3. After [21].

Upper right: Electroluminescence from a micro PS film anodized in an O-ring cell viewed from the top (10% acetic acid,  $10 \text{ mA cm}^{-2}$ ,  $2.6 \text{ cm}^2$  active area). Note that the luminescence appears orange in the center line, where the film has been formed under high current density (in 1:1 ethanoic HF at  $200 \text{ mA cm}^{-2}$ ), while it appears red for low formation current density ( $10 \text{ mA cm}^{-2}$ ). After [Le3].

Lower left: Free-standing porous silicon samples mounted on top of a  $20 \mu\text{m}$  thick bulk silicon grid (with grid bars of  $7 \mu\text{m}$  width) and illuminated with white light from the back. Upper left square:  $70 \mu\text{m}$  micro PS of 69% porosity (50 min at  $30 \text{ mA cm}^{-2}$  in 1:1 ethanoic HF,  $1 \Omega \text{ cm p-type}$ ), upper right square:  $32 \mu\text{m}$  meso PS of 39% porosity (16 min at  $30 \text{ mA cm}^{-2}$  in 1:1 ethanoic HF,  $0.03 \Omega \text{ cm p-type}$ ), lower left square:  $69 \mu\text{m}$  macro PS of 72% porosity ( $1.85 \mu\text{m}$  diameter pores in  $2.3 \mu\text{m}$  trigonal pitch parallel to the light beam) and lower right square  $7 \mu\text{m}$  bulk silicon. Note that porosity and thickness of all porous samples has been selected to correspond to  $20 \mu\text{m}$  thick bulk silicon. After [Le27].

Lower right: First macroporous silicon-based chip capacitor ( $100 \text{ nF}$ ,  $10 \text{ V}$ ) on a match for size comparison.

*Electrochemistry of Silicon: Instrumentation, Science, Materials and Applications.*

Volker Lehmann

Copyright © 2002 Wiley-VCH Verlag GmbH

ISBNs: 3-527-29321-3 (Hardcover); 3-527-60027-2 (Electronic)

*Volker Lehmann*

## **Electrochemistry of Silicon**

Instrumentation, Science,  
Materials and Applications

**Author**

**Dr. Volker Lehmann**

Infineon Technologies AG  
Corporate Research  
Otto-Hahn-Ring 6  
81739 München  
Germany

■ This book was carefully produced. Nevertheless, authors, editors and publisher do not warrant the information contained therein to be free of errors. Readers are advised to keep in mind that statements, data, illustrations, procedural details or other items may inadvertently be inaccurate.

**Library of Congress Card No. applied for**

**British Library Cataloguing-in-Publication Data:**

A catalogue record for this book is available from the British Library.

**Die Deutsche Bibliothek –**

CIP-Cataloguing-in-Publication Data

A catalogue record for this book is available from Die Deutsche Bibliothek

© WILEY-VCH Verlag GmbH

D-69469 Weinheim, 2002

All rights reserved (including those of translation in other languages). No part of this book may be reproduced in any form – by photoprinting, microfilm, or any other means – nor transmitted or translated into machine language without written permission from the publishers. Registered names, trademarks, etc. used in this book, even when not specifically marked as such, are not to be considered unprotected by law.

printed in the Federal Republic of Germany

printed on acid-free paper

**Composition** K+V Fotosatz GmbH, Beerfelden

**Printing** Strauss Offsetdruck GmbH,  
Mörlenbach

**Bookbinding** Großbuchbinderei J. Schäffer  
GmbH & Co. KG, Grünstadt

**ISBN** 3-527-29321-3

*Electrochemistry of Silicon: Instrumentation, Science, Materials and Applications.*

Volker Lehmann

Copyright © 2002 Wiley-VCH Verlag GmbH

ISBNs: 3-527-29321-3 (Hardcover); 3-527-60027-2 (Electronic)

Dedicated to Hadley and other colleagues,  
with thanks for good advice

## Preface

Silicon has been and will most probably continue to be the dominant material in semiconductor technology. Although the defect-free silicon single crystal is one of the best understood systems in materials science, its electrochemistry to many people is still a matter of alchemy. This view is partly a result of the interdisciplinary aspects of the topic: Physics meets chemistry at the silicon-electrolyte interface.

So far, researchers interested in this topic have had to choose either monographs that deal with the electrochemistry of semiconductors in general or recent editions that deal with special topics such as, for example, the luminescent properties of microporous silicon. The lack of a book that specializes on silicon but which gives the whole spectrum of its electrochemical aspects was my motivation to write the *Electrochemistry of Silicon*.

With this book I hope to address different groups in the scientific community. For beginners in the field a comprehensive overview of the topic is given in ten chapters, including a brief historical review and safety tips. The practitioner will find inspiration for instrumentation as well as examples of applications ranging from photonic crystals to biochips. For experts the book may serve as a quick reference with more than 150 technical tables, diagrams and micrographs, as well as ca. 1000 references cited for easy access to in-depth information.

I did my best to eliminate mistakes and unclear descriptions, but I suspect that even writing is governed by the laws of thermodynamics. So, I welcome comments from readers and will attempt to correct any mistakes that they find.

## Contents

### Preface VII

<b>1</b>	<b>Introduction, Safety and Instrumentation</b>	<b>1</b>
1.1	Early Studies of the Electrochemistry of Silicon	1
1.2	Safety First	3
1.3	The Basic Properties of Silicon	5
1.4	Common Electrolytes	7
1.5	The Electrodes	11
1.6	Cell Designs	15
<b>2</b>	<b>The Chemical Dissolution of Silicon</b>	<b>23</b>
2.1	The Basics of Wet Processing of Silicon	23
2.2	Silicon Surface Conditions and Cleaning Procedures	24
2.3	Chemical Etching in Alkaline Solutions	27
2.4	Chemical Etching in Acidic Solutions	30
2.5	Defect and Junction Delineation	33
2.6	Selective Etching of Common Thin Film Materials	36
<b>3</b>	<b>The Semiconductor-Electrolyte Junction</b>	<b>39</b>
3.1	Basics of the Semiconductor-Electrolyte Contact	39
3.2	The I–V Characteristics of Silicon Electrodes in Acidic Electrolytes	42
3.3	The I–V Characteristics of Silicon Electrodes in Alkaline Electrolytes	49
<b>4</b>	<b>The Electrochemical Dissolution of Silicon</b>	<b>51</b>
4.1	Electrochemical Reactions	51
4.2	The Dissolution Valence	57
4.3	The Characteristic Anodic Currents in HF	59
4.4	Reverse Currents, Electron and Hole Injection	63
4.5	Electrochemical Etch Stops	68
4.6	Photoelectrochemical Etching	72

<b>5</b>	<b>Anodic Oxidation</b>	77
5.1	Silicon Oxidation Techniques	77
5.2	Native and Chemical Oxides	78
5.3	Anodic Oxide Formation and Ionic Transport	79
5.4	Oxide Morphology, Chemical Composition and Electrical Properties	82
5.5	Electrochemical Oscillations	89
5.6	Electropolishing	94
<b>6</b>	<b>Electrochemical Pore Formation</b>	97
6.1	Basics of Pore Formation	97
6.2	Porous Silicon Formation Models	99
6.3	Pore Size Regimes and Pore Growth Rates	104
6.4	Porosity, Pore Density and Specific Surface Area	108
6.5	Mechanical Properties and Drying Methods	114
6.6	Chemical Composition and Ageing Effects	117
6.7	Electrical Properties of Porous Silicon	120
<b>7</b>	<b>Microporous Silicon</b>	127
7.1	Micropore Formation Mechanism	127
7.2	Morphology of Microporous Silicon	128
7.3	Absorption, Reflection and Nonlinear Optical Effects	133
7.4	Luminescence Properties	138
7.5	Quantum Confinement and Models of the Luminescence Process	150
7.6	Oxidized Porous Silicon	159
7.7	Related Materials	162
<b>8</b>	<b>Mesoporous Silicon</b>	167
8.1	Mesopore Formation Mechanisms	167
8.2	Mesopores in Highly Doped p-Type Silicon	171
8.3	Mesopores in Highly Doped n-Type Silicon	174
8.4	Mesopore Formation and Spiking in Low-Doped n-Type Silicon	177
8.5	Etch Pit Formation by Avalanche Breakdown in Low-Doped n-Type Silicon	180
<b>9</b>	<b>Macroporous Silicon</b>	183
9.1	Macropore Formation Mechanisms	183
9.2	Macropores in p-Type Silicon	187
9.3	The Phenomenon of Macropore Formation in n-Type Silicon	190
9.4	Calculating Macropore Growth and Mass Transport	198
9.5	Design Rules and Limits of Macropore Array Fabrication	202



<b>10</b>	<b>Applications</b>	207
10.1	Overview	207
10.2	AC Properties of Silicon Electrodes and Carrier Concentration Profiling	208
10.3	Diffusion Length and Defect Mapping	211
10.4	Sensors and Biochips	219
10.5	Passive and Active Optical Devices	225
10.6	Porous Silicon-Based Electronic Devices	232
10.7	Sacrificial Layer Applications	236
	<b>Appendices</b>	243
	<b>Supplier References</b>	249
	<b>References</b>	251
	<b>Subject Index</b>	273

## Subject Index

- absorption
  - chemical 220
  - cross-section 137
  - coefficient 136, 212
  - optical 133, 145, 212
- acceptor compensation 52
- accumulation 39, 44
- acidic etching 30
- activation energy 11, 29, 61
- active state 97, 186
- aging 29, 117
- alkaline etching 27, 49, 53, 193
- alternating current properties 126, 208
- ambipolar diffusion 124
- amorphous silicon 131, 164
- anisotropic etching 27, 50–54
- annealing 88, 117
- anodic oxide 77–96, 101, 149
  - chemical composition 86
  - defects 86, 87
  - density 78, 85
  - dissolution 67
  - electrical properties 88
  - etchrate 69, 83, 92
  - formation mechanisms 52, 56, 79
  - growth rate 81
  - morphology 83, 92
  - porous 90
  - refractive index 86
- anodic regimes 44–49
- anti-reflective coating 227
- anti-scatter grid 239
- applications 207–241
- atomic force microscopy 85
- attenuated total reflection 20
- Auger recombination 6, 136, 145, 156
- autocatalytic 33, 163
- avalanche breakdown 103, 180
- backside photo current 212
- band-structure 139, 144, 151, 229
- bifluoride 55
- biochips 223
- Bragg-filter 130, 222, 226
- breakdown electrical 88, 103, 168
- breakdown passivity 101
- Brunauer-Emmet-Teller method 112
- buffered oxide etch 36
- capacitance-voltage curve 209
- capillary forces 115
- carrier concentration profiling 208
- cathodic regime 45, 51
- cell designs 15–22, 214
  - double 19, 214
  - electrolyte circulation 21
  - immersion 17
  - internal 72, 75
  - materials 15
  - o-ring 16, 18
  - windows 16
- chemical
  - dissolution 23–38, 53
  - oxide 78
  - polishing 31
  - reactions 51–57
  - vapor deposition 234
- chemomechanical polishing 24, 64, 96
- cleaning 24, 57
- cleaving 4, 14, 17
- cold cathode 232
- collimator 239
- colloidal silica 24
- concentration 7, 201
- conduction band 39–50, 128, 144
- contact 14, 39, 120
- contact angle 24

- Coulomb-blockade 122
- cracking 86, 115
- current
  - characteristic 59–63, 90
  - critical 60
  - efficiency 83
  - multiplication 45, 54, 66
  - pore tip 59, 195
  - reverse 63–68
  - transient 64
- current-voltage characteristic 41–50
  - acidic 42–49, 65, 80
  - alkaline 41, 49, 50
  - basics 39
  - hydrofluoric acid 42–49, 60–68, 178, 196
- dangling bond 121
- dark current 65, 217
- Debye length 100
- deep level transient spectroscopy 211
- defect
  - delineation 33, 70, 217
  - etch 35, 178
  - mapping 211
- density of states 121, 145, 150
- deoxyribonucleic acid 113, 223
- depletion 39, 44
- deuterium 52, 120, 142
- diffusion
  - coefficient 7, 107, 125, 200, 212
  - current 184
  - doping 114, 123, 234
  - length 6, 100, 191
  - length mapping 211
  - limited aggregation 100
- dielectric 154, 234, 226
- dislocation 1,34
- dissolution
  - chemical 23–38, 110
  - electrochemical 11, 51–75
  - hierarchy 71
  - oxide 27, 36, 67
  - valence 54, 57, 94, 111, 189, 200
- dissolved oxygen concentration 26, 54, 63
- divalent dissolution 46, 54, 57
- double-sided electrolytic contact 214
- early studies 1
- Eden model 100
- effective medium 125, 134
- electrical serial resistance 208, 236
- electrochemical dissolution 51–75
- electrochemical photocapacitance spectroscopy 211
- electrode 11–15, 98
  - counter 12
  - geometry 85
  - reference 12
  - rotating disk 11, 21, 59, 62
- electroluminescence 93, 148, 230
- electrolyte 7–11
  - acidic 39, 42–49, 52
  - alkaline 39, 49, 52, 81
  - circulation 21, 33
  - convection 52, 107, 200
  - organic 56, 187
- electrolytic metal tracer 72, 214
- electron injection 46, 49, 54, 63–68, 91
- electron spin resonance 160
- electronic devices 232
- electropolishing 56, 74, 93, 203, 221
- ellipsometry 49,9 1
- epitaxial layer transfer 239
- epoxy 21, 28, 241
- equivalent circuit 208
- etchpit 34, 97, 180
- etchrate
  - aluminum 37
  - defects 33
  - nitride 36
  - oxide 27, 36, 67, 88
  - porous silicon 106–111
  - silicon 24–38, 94
- etchstop 50, 68–72
- exchange splitting 143, 155, 158
- exciton 138–159
- Fabry-Perot filter 228
- Fick's first law 200
- field current 184
- filters 72
  - interference 222, 226
  - short-pass 72, 225
- first aid 4
- flat-band potential 48, 201
- fluorine-termination 54
- front side photocurrent 212
- full isolation by porous oxidized silicon 237
- gallium-indium 14
- galvanostat 12
- galvanostatic characteristic 79, 82, 90
- gas sensors 220
- generation rate 213

- Gouy-Chapman model 40  
gravimetric measurements 31, 57, 85, 108
- hardness 114  
haze 35, 85, 218  
Helmholtz layer 39, 89, 208  
hexafluorosilicate 32, 36, 55, 118  
high-frequency-resistometry 43, 209  
hillocks 29, 94  
hole, definition 40, 97  
hole burning spectroscopy 158  
hole injection 32, 49, 64, 163, 190  
hydrocarbons 25, 87, 117, 119  
hydrofluoric acid  
– properties 7–11  
– safety 3, 219  
– sensor 219  
– toxic effects 4  
hydrogen  
– bubbles 29, 34, 107, 163, 204, 217  
– desorption 136  
– formation 28, 32, 51, 55, 91  
– overpotential 52  
– termination 25, 53, 78, 118, 142, 155  
hydrophilic 26, 53, 78  
hydrophobic 25, 53, 78, 117
- illumination 65, 72, 128, 190  
– backside 191  
– current-voltage characteristic 41–44, 68, 196  
– inhomogeneous 72, 215  
– sources 22, 72  
image etching 74  
indirect bandgap 138  
induction period 33  
infrared spectroscopy 20, 54, 84, 91, 118  
initial state 98  
injection level spectroscopy 215  
instrumentation 1–23  
interference filter 221  
internal surface 104  
inversion 39, 44  
ionic transport 79
- junction  
– delineation 33  
– electrolyte-semiconductor 39–50  
– pn 36, 69, 75
- kinetics 51, 59
- lattice expansion 114  
Levich equation 59
- lifetime 145, 155, 212, 231  
light emitting diode 72, 215, 230  
lithography 22, 193, 220–241  
linear stability analyses 99  
luminescent microstructures 165  
luminescent silicon 138–158, 230
- macropores 183–205  
– applications 188, 223–239  
– arrays 192–205  
– calculations 198  
– conductivity 121  
– degradation 203  
– design rules 202  
– formation mechanisms 97, 183–187  
– growth rate 200  
– n-type substrates 190–205  
– phenomenology 190  
– p-type substrates 187  
– through-pores 203, 223  
masking 22, 33, 37, 108, 236  
mass transport 79, 198, 204  
mesopores 167–181  
– applications 226, 238  
– conductivity 121  
– formation mechanisms 97, 167–171  
– highly doped n-type substrates 174  
– highly doped p-type substrates 171  
– low doped n-type substrates 177–181  
– morphology 171  
metal insulator semiconductor 41, 46, 89, 120  
metal plating 35, 51, 75, 217  
microelectromechanical systems 23, 219–241  
micromachining 12, 27, 30, 222–241  
micropores 127–166, 236  
– applications 220, 226, 230, 232, 236  
– conductivity 122  
– formation mechanisms 97, 127  
– morphology 128  
microscopy  
– atomic force 84  
– optical 105, 178, 188  
– scanning electron 171–181  
– scanning tunneling 95  
– transmission electron 34, 129, 170  
minority carrier density 213  
minority carrier lifetime 211  
mobility 40, 122  
molecular recombination model 157  
Mott-Schottky relation 210

- nanoporous 104
- native oxide 26, 78, 113, 119
- neutrality 186
- nitridized porous silicon 161
- non-linear optical effects 133
- normal hydrogen electrode 13
- nucleophilic 53
  
- Ohmic contact 214
- Onsager model 124
- optical devices 225
- optical microbench 21
- open circuit potential 42, 46, 49, 209
- orientation dependent etching 27, 50–54
- oscillations 48, 60, 80, 89
- Ostwald ripening 192
- overall reactions 51
- oxide replica 178, 195
- oxidized porous silicon 119, 155, 159, 232, 237
- oxidizing agents 27, 31
- oxygen evolution 83
  
- passivation potential 49, 53, 69
- passive state 28, 69, 97
- passivity breakdown 100
- persulphate 150
- photo conductive decay 215
- photoconductivity 124
- photoelectrochemistry 72, 128, 140
- photoluminescence 123, 138–158
  - Auger recombination 145
  - decay 146
  - dependence on chemical environment 141
  - dependence on formation current 139
  - dependence on hydrostatic pressure 141
  - dependence on illumination 140
  - dependence on magnetic field 141, 176
  - dependence on temperature 146, 160
  - excitation spectroscopy 142
  - green-blue band 147
  - infrared band 148
  - models 157
  - oxidized porous silicon 160
  - polarisation 140
  - quenching 123, 147
  - red band 139
  - silicon compounds 166
  - silicon microstructures 165
  - stability 161, 231
  - thermostimulation 145
- photonic crystals 229
- pirhanja-clean 26
- pitch 109, 192, 199
- Poisson ratio 115
- polysilicon 13, 31, 37, 164, 232
- pore
  - arrays 192–205, 223–239
  - bottleneck 192, 200, 203
  - branching 120, 189, 192
  - definition 97
  - degradation 174, 203
  - density 108–113
  - dying 192
  - facetting 195
  - filling, liquid 123, 141, 154
  - filling, solid 189, 235, 238, 240
  - geometry 98, 167, 195
  - initiation, nucleation 98, 171, 187
  - orientation dependence 105, 176–180, 197
  - position 99
  - spiking 178, 195
  - tip 168, 185, 195, 201
  - wall 99, 168, 189, 192
- porous oxide 85, 90, 159
- porous semiconductors 164
- porous silicon 2, 46, 97–205
  - aging effects 117
  - biocompatibility 223
  - carrier mobility 125
  - chemical composition 112, 113, 117
  - conductivity 121–125
  - critical thickness 115
  - dielectric constant 125, 154
  - doping dependence 141
  - drying 109, 114
  - electrical properties 120
  - formation models 97, 99–104
  - growth rates 17, 104, 108
  - mechanical properties 114
  - morphology 128, 171, 188, 196
  - orientation dependence 105, 170, 178, 180, 195
  - oxidation 119, 155, 159, 232, 237
  - photoconductivity 124
  - size regimes 104, 113
  - specific surface 108–113
- porosity 108, 113, 198
- potential-charge curve 80
- potentiostat 12
- potentiostatic characteristic 41, 50, 60, 80
- precipitates 215
- probability analyses 100
- pseudo-reference 13, 21, 195

- pumps 21
- punch-through 170
- quantum
  - confinement 102, 127, 150–161
  - dot, wire, well 151, 165
  - efficiency 65, 148, 165, 228, 231
  - recombination model 157
- radiative recombination 138–158
- Raman spectroscopy 130, 141
- rapid thermal annealing 77
- reflection 133, 227
- refractive index 126, 134, 227
- related materials 162
- roughness 25, 30, 84, 95, 107
- sacrificial layer 236
- safety 3, 219
- saturated calomel electrode 13
- scanning tunneling microscopy 54, 95
- Schottky contact, junction 41, 46, 169, 215
- selectivity 36, 68, 70
- semiconductors-electrolyte junction 39–50
- sensors 219
- silanol 26, 53, 78, 148
- silicon
  - capacitor 233
  - fluorides 55, 118
  - nitride 36, 159, 234
  - on insulator 238
  - phase transitions 141
  - properties 5
  - surface conditions 24
  - wafer 13, 16, 72, 216
- siloxene 157
- size regimes 104
- small angle x-ray scattering 133
- spin 144
- Stern model 40
- surface
  - photovoltage spectroscopy 215
  - recombination 46, 94, 154, 191, 214
  - states 94, 123, 157, 208
  - tension 115
- surfactant 11, 117, 188, 201
- space charge capacitance 210
- space charge region 6, 101, 168, 215
- spiking 170,
- stain film 31, 75, 162
- Stokes shift 142, 153, 156, 166
- stress 114, 131, 159
- striations 107
- surfactant 117
- susceptibility 137
- Tafel plot 46
- tetravalent dissolution 32, 48, 56, 57
- thermal
  - conductivity 115
  - desorption spectroscopy 87, 114, 120
  - expansion coefficient 114
  - oxidation 77
- thermionic emission 185
- thin films 36
- through-pores 224
- transient currents 42, 68, 80, 178
- transistor 1, 43, 70
- transmission 136, 226, 229
- tunneling 81, 103, 167–180
- valence band 39–50, 128, 144
- Van der Waals forces 117
- viscosity 11, 31, 96
- voltammogram 59
- waveguide 227, 230
- wet processing 23
- x-ray diffraction 131
- x-ray absorption finestructure 133, 152
- x-ray photoelectron spectroscopy 78
- Youngs modulus 114
- Zeeman splitting 141

# 1

## Introduction, Safety and Instrumentation

### 1.1

#### Early Studies of the Electrochemistry of Silicon

This section briefly surveys the history of the electrochemistry of silicon. Electrochemistry is a much older science than the solid-state physics of semiconductors. Batteries had already been built, by Volta in 1799, when Berzelius first prepared elementary silicon in 1823 by reducing  $\text{SiF}_4$  with potassium. In 1854 Deville prepared silicon by electrochemical methods. Faraday, who found the exchanged charge and the deposited matter at electrodes to be proportional, also observed that the resistivity of certain materials decreased with increasing temperature. However, it took another century for a deeper understanding of the semiconducting state to be developed, based on the pioneering work of Bethe, Bloch, Braun, Lark-Horovitz, Mott, Pohl, Schottky, Wilson and many others between 1930 and 1940. Their results finally led to the invention of the transistor by Bardeen, Brattain and Shockley in 1947. In one of the first papers about the semiconductor-electrolyte junction, by Brattain and Garrett [Br2], it was already realized that holes control anodic oxidation and that current multiplication effects at illuminated n-type electrodes are caused by electron injection during the electrochemical dissolution process. The first transistor, however, was made from germanium, because silicon single crystals were not grown until 1950, by crucible pulling. Two years later the float-zone (FZ) method was invented and the first silicon-based transistor was presented in 1954 by Teal. Since 1961, the preparation of silicon has involved its transformation into silane, which is then purified by distillation and adsorption and finally retransformed to elemental silicon by chemical vapor deposition (CVD). The availability of dislocation-free silicon single crystals and the idea of an integrated silicon circuit, developed by Kilby in 1958, were the beginnings of what today is known as 'the silicon age'.

Silicon has long been the subject of numerous electrochemical investigations. Early electrochemical studies on silicon dealt mainly with problems of anodic oxidation, electropolishing and chemical etching. The first experiments attempting to grow anodic oxides on silicon were performed by Guenther-Schulze and Betz as early as 1937 [Gu1]. Schmidt and Michel carried out a more detailed study in 1957 [Sc1], leading to a method of local anodic oxidation by the projection of light patterns onto n-type silicon electrodes [Sc3]. At this time the first etchants for defect delineation

[Da1, Si1] or chemical polishing (CP) [La1] were also developed. Alkaline etching in sodium hydroxide solution was studied by Seipt [Se1], who observed passivation under anodic bias, and he interpreted this in terms of an insoluble oxide film. Seipt and others [Bo1, Ef1, Hu1] reported that bias-dependent variations in the capacitance of a silicon-electrolyte junction could be used to verify the existence of a depletion layer in the electrode. Pleskov [Pl1] was the first to apply independent electrolyte contacts to both sides of an n-type germanium disk. He reported hole injection when the electrode reaction involved the cathodic reduction of an oxidizing agent and pointed out that the amount of collected holes depends on the diffusion length of these holes as well as on the thickness of the germanium disk. An extension of this method was used by Harvey [Ha1] to measure the surface recombination velocity of the electrode. A detailed study of the anodic dissolution mechanism of germanium and silicon was carried out by Beck and Gerischer [Be1, Ge1].

The first report of porous silicon (PS) dates back to 1956. In this study, which dealt mainly with electrolytic shaping of germanium, Uhlir found matte black, brown or red deposits on anodized silicon samples and tentatively supposed them to be a suboxide of silicon. He found that smooth etching occurred for higher current densities and a dissolution valence of four while at lower current densities the dissolution occurred under hydrogen evolution at a valence of about two [Uh1]. Shortly after, Fuller and Ditzenberger reported similar films, which developed without any applied bias in HF/HNO<sub>3</sub> solutions [Fu3]. Anodically formed films were studied in more detail by Turner and by Schmidt and Keiper [Tu1, Sc2], while chemically formed films were investigated by Archer [Ar1]. Turner found electropolishing to occur above a critical current density, which increased with HF concentration and temperature, but decreased with viscosity. He interpreted this critical value to be a result of mass transfer in the electrolyte. Below the critical current density he observed a thick film with an orange-red color and a glassy appearance and speculated that it was a silicon subfluoride. Turner assumed SiO<sub>2</sub> to be present during electropolishing, and observed oscillations of cell current and potential for current densities above the critical value [Tu2]. In 1960, Gee [Ge2] observed anodic electroluminescence (EL) in different electrolytes from stain films grown chemically or electrochemically on silicon electrodes. An excellent review of these early studies is given by Turner [Tu2].

In 1965 Beckmann [Be2] investigated stain films on silicon by means of infrared (IR) spectroscopy. He found the chemical composition of electrochemically formed films to be between SiH and SiH<sub>2</sub>, and interpreted this as polymerized silicon hybrids. In contrast to these findings, films grown chemically in mixtures of HF and HNO<sub>3</sub> showed high amounts of oxygen. In 1966, Memming and Schwandt [Me11] presented a dissolution mechanism for silicon electrodes in HF and proposed the resulting films to be a result of redeposition of silicon from SiF<sub>2</sub>. Macropores on n-type substrates and their dependence on crystal orientation were first reported by Theunissen and co-workers in 1970 [Th1]. In that same year, the first studies on electrochemical etch-stop techniques [Di1] and photoelectrochemical etching [Da2] of n-type silicon were published. In 1971, Watanabe and Sakai first reported the porous nature of electrochemically formed films on silicon electrodes [Wa7].



The number of publications dealing with the electrochemistry of silicon and PS has increased rapidly since 1971. The first model for pore formation in n-type silicon electrodes, based on a breakdown of the depletion layer, was proposed by Theunissen in 1972 [Th2]. In 1988, it was shown that macropores could be etched in arbitrary patterns using a pre-structured n-type silicon electrode [Le11]. Using electron diffraction, Arita and Sunohara proved in 1977 [Ar2] that PS on silicon electrodes, independent of their doping, is single crystalline with the same orientation as the substrate. This allowed them to conclude that localized dissolution generates pores in the electrode and the remaining substrate forms the PS. Bomchil et al. demonstrated in 1983 [Bo2] using gas absorption that the pore diameters in PS may be as small as 2 nm.

The conversion of PS to SiO<sub>2</sub> by thermal oxidation was reported in 1971 by Watanabe and Sakai [Wa7]. Arita in 1978 [Ar3] and Unagami in 1980 [Un1] performed thermal oxidation experiments on PS, which a few years later led to an silicon-on-insulator (SOI) technology based on oxidized PS [Ho1, Im1]. Another approach to manufacturing SOI structures was developed in 1986 by Lin and co-workers [Li1], by growing a Si molecular beam epitaxy (MBE) film on PS and subsequent oxidation. However, a major drawback of PS-based SOI technologies is the need for windows in the Si film to carry out the oxidation of the underlying PS.

Pickering and co-workers observed visible photoluminescence (PL) from PS at 4.2 K in 1984 [Pi1], which they interpreted as due to a complex mixture of amorphous phases. The questions of why PS is transparent for visible light and why it is photoluminescent remained unanswered until 1990–91 when a quantum size effect was proposed as an explanation [Ca1, Le1]. Two years later PL was also found for oxidized PS [Le15, It2]. These astonishing optical properties of PS initiated vigorous research and resulted in more than a thousand publications, as well as several books and reviews [Cu2, Th7].

## 1.2

### Safety First

It is very important to first consider the safety aspects of electrochemical experiments with silicon. The single most dangerous compound, which cannot be avoided in the electrochemistry of silicon, is hydrofluoric acid (HF). HF in its anhydrous form and in concentrated aqueous solutions is highly corrosive towards living tissue. Inhalation, ingestion or skin contact with HF are all extremely hazardous.

For aqueous HF of high concentrations (> 10%) or for elevated temperatures (above room temperature, RT), HF is in its most dangerous phase, the vapor phase. The liquid solution generates considerable amounts of HF vapor. HF has a stinging smell not unlike hydrochloric acid, and its smell is detectable at levels above 0.04 ppm. The permissible exposure limits in industrial countries vary from 0.5 to 2 mg m<sup>-3</sup> (0.62–2.50 ppm). At 30 ppm, HF is immediately dangerous to life and health. An exposure to 50 ppm for 30 min can be lethal. It is self-evident that

HF should only be handled under a hood with proper ventilation. However, even if all safety regulations are obeyed the risk of accidents cannot be totally eliminated. In case of large spills, the contaminated laboratory area should be evacuated immediately because of the danger of inhalation.

If HF vapor is inhaled, a corticosteroid aerosol and inhalation of pure oxygen are recommended as first aid, because they relieve inflammatory reactions such as pulmonary edema or hypersecretion of mucus in bronchial tubes and help to prevent bronchospasm. A  $\beta$ -mimetic aerosol can be given to control apparent bronchospasm.

For concentrations below 10%, the evaporation of HF is reduced and direct contact with the liquid becomes the greatest risk. If HF is swallowed, it is advisable to drink lots of water, if possible with activated carbon added, in order to dilute the acid. Small amounts in the eye can cause intense irritation of the eyelids and slow ulceration of the conjunctivae. Large amounts in the eye cause immediate blindness. As first aid treatment the eyes should be irrigated immediately and copiously with clean water for a minimum of 15 min. Immediate medical care is mandatory after all the accidents mentioned above, even if no symptoms are apparent, because respiratory problems or other symptoms of poisoning can be delayed for hours after the incident has occurred.

In contact with skin, HF causes burns that show a progressive necrosis, often resulting in permanent tissue loss. The dissociation of HF yields  $H^+$  ions, which exhaust the buffering capacity of the tissue, and  $F^-$  ions, which remove calcium ions from the tissue. This mechanism has been invoked to account for the prolonged inflammation and delayed wound healing. If skin contact is noticed immediately, first-aid treatment should include the removal of contaminated cloth and the exposed skin should be rinsed thoroughly with water. Next, a bandage with polyethylene glycol or calcium gluconate gel is recommended [1]. If there is a time delay of more than a few seconds or if larger areas of the skin have been in contact with HF, medical care is mandatory, because considerable amounts of HF may penetrate the epidermis and lead to poisoning of deeper tissue and bone necrosis, which is both extremely painful and slow to heal. HF burns are usually treated by injecting 10% calcium gluconate in and under the exposed skin tissue. Note that HF poisons tissue rapidly, but it may take hours to cause pain.

In addition to the standard laboratory protection, such as safety goggles and chemically resistant butyl rubber gloves, a personal HF gas monitor with audible alarm and a safety sensor for liquids, as described in Section 10.4, are commercially available [2]. For detailed information about the toxic effects of HF, see references Fi5, Wa8 and Re4.

The other chemicals mentioned in this book are less dangerous and safety goggles and rubber gloves, which should always be used, are usually sufficient protection. Elementary silicon is inert and shows no toxic effects. In this respect, silicon is different from many other semiconductors, which may contain poisonous compounds. However, sufficient eye protection is required while cleaving wafers, because of the risk of fragmentation.

Legal safety regulations for HF and other chemicals have been issued [Br1, Du1, Ku1, Mu1, St1, Us1].

### 1.3

#### The Basic Properties of Silicon

Pure crystalline silicon is a brittle material with a gray metallic appearance. Its mechanical properties, such as Knoop hardness (950–1150 kg mm<sup>-2</sup>), Young's modulus (190 GPa for ⟨111⟩, 170 GPa for ⟨110⟩, 130 GPa for ⟨100⟩), torsion modulus (4050 kg mm<sup>-2</sup>) and compression breaking strength (5000 kg cm<sup>-2</sup>) vary slightly with crystal orientation. Silicon has a low thermal expansion coefficient (2.33×10<sup>-6</sup> K<sup>-1</sup>) and a high thermal conductivity (148 W K<sup>-1</sup>m<sup>-1</sup>). Crystalline silicon melts at 1413 °C (1686 K).

The atomic weight of silicon is 28.086 (4.6638×10<sup>-23</sup> g per atom). Its density of 2.328 g cm<sup>-3</sup> corresponds to roughly 5×10<sup>22</sup> atoms cm<sup>-3</sup>. Silicon has the same crystal structure as diamond (face-centered cubic, fcc) with a lattice constant of 0.543095 nm.

The electronic properties of silicon are essential in the understanding of silicon as an electrode material in an electrochemical cell. As in the case of electrolytes, where we have to consider different charged particles with different mobilities, two kinds of charge carriers – electrons and holes – are present in a semiconductor. The energy gap between the conduction band (CB) and the valence band (VB) in silicon is 1.11 eV at RT, which limits the upper operation temperature for silicon devices to about 200 °C. The band gap is indirect; this means the transfer of an electron from the top of the VB to the bottom of the CB changes its energy and its momentum.

Silicon is probably the solid element that has been produced in the most pure form. Contamination levels as low as a few parts per trillion (ppt), corresponding to less than 10<sup>11</sup> cm<sup>-3</sup>, are achievable [Ha2]. Such a pure silicon crystal is termed intrinsic and shows a specific resistivity of about 10 kΩ cm at RT, corresponding to a concentration of charge carriers of 1.45×10<sup>10</sup> cm<sup>-3</sup> at RT. This low concentration of impurities can be increased by intentional doping with Group III elements (B, Al, Ga, In), producing p-type Si, or by doping with Group V elements (P, As, Sb), producing n-type Si. Single crystalline Si is commercially available with doping levels ranging from 10<sup>13</sup> to 10<sup>20</sup> cm<sup>-3</sup>. Electrons are the majority carriers in an n-type doped material, while defect-electrons or holes are the majority carriers in p-type doped material. The mobilities,  $\mu$ , of electrons and holes are different and decrease with increasing doping density  $N_d$ . Therefore, the specific conductivity  $\sigma$  does not depend linearly on  $N_d$ :

$$\sigma = 1/\rho = e\mu N_d \quad (1.1)$$

The figure on the inner front cover of this book can be used to convert between doping density, carrier mobility and resistivity  $\rho$  for p- or n-type doped silicon substrates. One of the major contaminants in silicon is oxygen. Its concentration depends on the crystal growth method. It is low in FZ material and high (about 10<sup>18</sup> cm<sup>-3</sup>) in Czochralski (CZ) material.

A piece of silicon immersed in an electrolyte behaves similarly to a Schottky diode, a metal-semiconductor contact, as discussed in Chapter 3. Under reverse

bias (anodic for n-type, cathodic for p-type), a space charge region (SCR) is present in a semiconductor electrode. The width  $W$  of the SCR in the electrode depends on the type and density  $N_d$  of the dopant and the bias  $V$  according to:

$$W = (2\varepsilon V / eN_d)^{1/2} \quad (1.2)$$

where  $e$  is the elementary charge and  $\varepsilon$  the dielectric constant. The latter is the product of the dielectric constant of the vacuum,  $\varepsilon_0$ , and the relative dielectric constant of silicon ( $\varepsilon_{Si} = 11.9$ ). The bias  $V = V_{bi} - V_{appl} - kT/e$  depends on the built-in potential  $V_{bi}$  of the contact (about 0.5 V), the applied potential  $V_{appl}$  and  $kT/e$  (25 mV at RT). The electric field strength  $E$  shows a maximum  $E_m$  at the interface to the electrolyte ( $x=0$ ) and decreases linearly to zero at  $x=W$  for a homogeneously doped electrode according to:

$$E(x) = eN_d(W - x)/\varepsilon \quad (1.3)$$

The maximum field strength is calculated using Eqs. (1.2) and (1.3) to be:

$$E_m = (2eN_d V / \varepsilon)^{1/2} \quad (1.4)$$

$E_m$  is limited by the breakdown field strength  $E_{BD}$  of silicon, which is about  $3 \times 10^5 \text{ V cm}^{-1}$ . The figure on the inner front cover shows the width of the SCR as a function of doping density and applied bias, as well as the limitation by avalanche breakdown.

The capacitance  $C$  of the SCR is usually much smaller than that of the double layer in the electrolyte and dominates the AC behavior of the whole system. The capacitance for an electrode of interface area  $A$  and an SCR of width  $W$  can be calculated according to

$$C = A\varepsilon/W \quad (1.5)$$

The SCR capacitance for a given doping density and applied bias is given in the figure on the inner front cover.

Besides doping density and carrier mobility the minority carrier lifetime is another important parameter of silicon substrates [Sc17]. The bulk minority carrier lifetime is limited by three main recombination mechanisms: radiative, Auger and Shockley-Read-Hall (SRH). Recombination of an electron-hole pair under emission of a photon is important for direct bandgap materials, but is relatively unimportant in an indirect bandgap material like silicon. Auger recombination involves three charge carriers and depends therefore on doping density and injection level. For doping levels of  $10^{18} \text{ cm}^{-3}$ , for example, the lifetime is limited to values in the order of  $\mu\text{s}$ . SRH recombination involves a deep level impurity and the energy of the electron-hole pair is dissipated by lattice vibrations (phonons). For high-purity silicon with contamination levels below  $10^{11} \text{ cm}^{-3}$  the lifetime is in the order of milliseconds. The diffusion lengths,  $L_D$ , of electrons or holes can be calculated

from their lifetime  $\tau$  and their diffusion constant  $D_{e,h}$  ( $D_e=36.8 \text{ cm}^2 \text{ s}^{-1}$ ,  $D_h=12.4 \text{ cm}^2 \text{ s}^{-1}$ ) using:

$$L_D = (\tau D_{e,h})^{1/2} \quad (1.6)$$

The diffusion length of electronic grade silicon wafers is about 0.5 mm and therefore in the order of the wafer thickness. Illumination of the backside of a silicon electrode may, as a result, influence the electrochemistry at the front side, as discussed in Section 10.3.

#### 1.4 Common Electrolytes

Electrolytes commonly used for electrochemical processing of silicon can be categorized according to their constituents or according to their pH. Aqueous electrolytes dominate the electrochemical processing of silicon. However, for some applications, such as anodic oxidation, organic electrolytes with little or no water are used. Electrochemical etching of silicon in a water-free mixture of acetonitrile and HF [Ri1, Pr7] or dimethylformamide (DMF) and HF [Oh5] has also been reported, showing that water is not a necessary constituent. Such water-free HF electrolytes are favorable if a low etch rate on Al or SiO<sub>2</sub> is required. Anions, such as BF<sub>4</sub><sup>-</sup>, PF<sub>6</sub><sup>-</sup>, CF<sub>3</sub>SO<sub>3</sub><sup>-</sup>, AsF<sub>6</sub><sup>-</sup> and SbF<sub>6</sub><sup>-</sup>, have been proposed as substitutes for HF in such water-free electrolytes [Ri3].

Aqueous electrolytes of high pH etch silicon even at open circuit potential (OCP) conditions. The etch rate can be enhanced or decreased by application of anodic or cathodic potentials respectively, as discussed in Section 4.5. The use of electrolytes of high pH in electrochemical applications is limited and mainly in the field of etch-stop techniques. At low pH silicon is quite inert because under anodic potentials a thin passivating oxide film is formed. This oxide film can only be dissolved if HF is present. The dissolution rate of bulk Si in HF at OCP, however, is negligible and an anodic bias is required for dissolution. These special properties of HF account for its prominent position among all electrolytes for silicon. Because most of the electrochemistry reported in the following chapters refers to HF electrolytes, they will be discussed in detail.

Pure HF is a liquid, with a melting point of  $-83.36^\circ\text{C}$  and a boiling point of  $19.46^\circ\text{C}$  at ambient pressure. Its density is extremely sensitive to temperature, increasing from  $0.987 \text{ g cm}^{-3}$  at  $19^\circ\text{C}$  to  $1.658 \text{ g cm}^{-3}$  at  $-97^\circ\text{C}$  [Le7]. HF is soluble in water in any proportion. The electrical conductivity and density of solutions of HF in water are shown in Fig. 1.1 [Hi3].

Aqueous solutions of HF are usually not prepared from pure HF and water, but by dilution from commercially available aqueous solutions of higher concentration, e.g. 10, 40 or 50% of HF [3]. Unfortunately there is no convention for a single unity of concentration. In the relevant literature one will find:

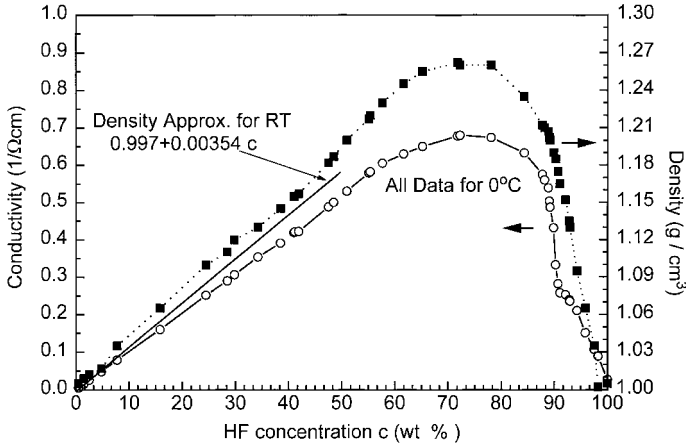


Fig. 1.1 Density and conductivity of an aqueous HF solution as a function of HF concentration, measured at 0°C. Redrawn from [Hi3].

A: weight%=mass of solute in 100 unit masses of solution

B: mole%=atom%

C: moles per kg substance

D: moles per liter solution

volume%, or simple mixing ratios by volumes, are also used

The relationship between C and A is simple:

$$C = 10A/M_{\text{HF}} \quad (1.7)$$

Using the molar weight of HF,  $M_{\text{HF}}=20.00637$ , C (moles HF  $\text{kg}^{-1}$ ) is found to be 0.49975 or roughly 0.5 times A (weight% HF).

The relationship between weight% and mole% is not as simple. Using the molar weight of water ( $M_w=18.0153$ ) the equation for the conversion is:

$$B = 100A/(A + (100 - A)M_{\text{HF}}/M_w) \quad (1.8)$$

If the unit relates not to the weight but to the volume of the solution, like moles per liter, the density  $\rho$  of the solution must also be known:

$$D = 10A\rho/M_{\text{HF}} \quad (1.9)$$

The density of HF is not a linear function of the concentration in weight%, as shown in Fig. 1.1 [Hi3]. However, for concentrations  $c$  between 0 and 50 weight% a close linear fit is found at RT, as shown in Fig. 1.1:

$$\rho(\text{kg l}^{-1}) = 0.997 + 0.00345c(\%) \quad (1.10)$$

For the same regime of concentrations the resistivity of HF at 0 °C can be fitted from the data of Fig. 1.1 to be:

$$R (\Omega \text{ cm}) = 1/0.0104c (\%) \quad (1.11)$$

To avoid ubiquity in the following chapters the concentration  $c$  of a solution will be given as follows:

A concentration given in % always refers to weight % (A).  
Concentrations may also be given in mol kg<sup>-1</sup> (C) or mol l<sup>-1</sup> (D).

In the literature many solutions are given as parts per volume, and so this notation is unavoidable and is used a few times.

If the concentration of only one component is given (in weight% or mol l<sup>-1</sup>) then the other component is pure water.

Any desired dilution of HF  $c_x$  (in weight%) can be prepared from a concentrated HF solution whose concentration  $c_{\text{HF}}$  (in %) and specific weight  $\rho_{\text{HF}}$  (in kg l<sup>-1</sup>) are known, by mixing a certain volume of pure water  $V_{\text{H}_2\text{O}}$  (in l) with the calculated volume of concentrated HF (in l):

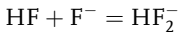
$$V_{\text{HF}} = V_{\text{H}_2\text{O}} / \{ \rho_{\text{HF}} [(c_{\text{HF}}/c_x) - 1] \} \quad (1.12)$$

Mixing ratios according to Eq. (1.12) using dilutions of commercial 50% HF solution are given in the figure in the inner back cover of this book, together with other concentration-dependent properties of HF.

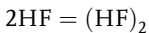
In contrast to the other three hydrohalic acids, HF is a weakly dissociating acid. One consequence of this property is that ion exchange is superior to distillation for HF reprocessing [Da3]. When diluted in water HF dissociates into H<sup>+</sup>, F<sup>-</sup> and various hydrofluoric species such as HF<sub>2</sub><sup>-</sup> and (HF)<sub>2</sub> according to the reactions:



$$\text{with } K_1 = ([\text{H}^+][\text{F}^-]) / [\text{HF}] \quad (1.13)$$



$$\text{with } K_2 = [\text{HF}_2^-] / ([\text{HF}][\text{F}^-]) \quad (1.14)$$



$$\text{with } K_3 = [(\text{HF})_2] / ([\text{HF}]^2) \quad (1.15)$$

These equilibrium constants vary with molarity of the HF solution. Measured values corrected for zero ionic strength at 25 °C are  $K_1 = 6.71 \times 10^{-4} \text{ mol l}^{-1}$ ,  $K_2 = 3.86 \text{ l mol}^{-1}$ , and  $K_3 = 2.7 \text{ l mol}^{-1}$  [Br10, Iu1, Wa11], implying a dissociation of only a few percent. This unusual behavior is still controversial and has been attributed to the greater strength of the H-F bond compared to the other hydrogen halides [Pa1], to the presence of the dimer (HF)<sub>2</sub> [Wa1], or to polymers that may

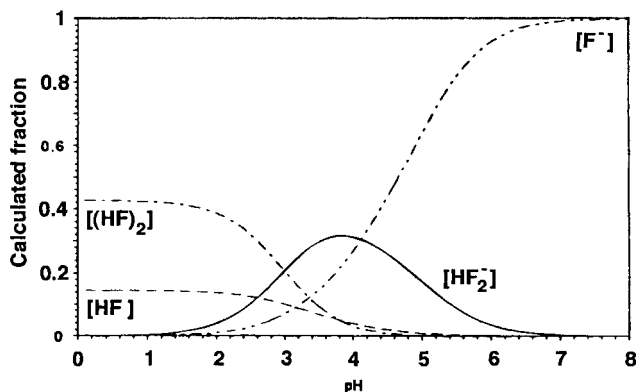


Fig. 1.2 The calculated fraction of each component in an aqueous HF solution as a function of pH for a fixed total fluoride concentration of  $7.5 \text{ mol l}^{-1}$ . Redrawn from [Ve1].

form ring structures [Hy1]. Spectroscopic measurements indicate the formation of a hydrogen-bonded ion-pair  $\text{H}_3\text{O}^+\text{F}^-$  or proton-transfer complex, which may be responsible for the observed weakness of HF [Gi1]. Species like  $(\text{HF})_2\text{F}^-$ ,  $(\text{HF})_3\text{F}^-$  and  $(\text{HF})_4\text{F}^-$  that are not present below  $1 \text{ mol l}^{-1}$  [Fa1] may contribute to the low ionic strength for higher concentrations [Mc1]. In any case, undissociated HF and its polymers are the main constituents of aqueous HF solutions of moderate and high concentrations. The concentrations of HF,  $(\text{HF})_2$ ,  $\text{HF}_2^-$  and  $\text{F}^-$  are shown as a function of  $c_{\text{HF}}$  in Fig. 1.2. For unbuffered HF of concentrations above  $0.25 \text{ mol l}^{-1}$  the composition is roughly constant, as follows: 90% HF and  $(\text{HF})_2$ , 4%  $\text{HF}_2^-$  and 2%  $\text{F}^-$ . The  $\text{pH} = -\log([\text{H}^+])$  of the solution can be calculated for a known HF concentration  $[c_{\text{HF}}] = [\text{HF}] + 2[(\text{HF})_2] + 2[\text{HF}_2^-] + [\text{F}^-]$  using the above equations and neutrality:

$$[\text{H}^+] = [\text{HF}_2^-] + [\text{F}^-] \quad (1.16)$$

Note that the exact concentrations of the species  $\text{H}^+$ , HF,  $\text{HF}_2^-$  and  $\text{F}^-$  in dilute HF solutions of a certain molarity can be obtained from  $K_1$  and  $K_2$  only with some function to represent the activity coefficients [Ha13]. Equilibrium constants, obtained from measurements of pH, differ slightly from the values given above ( $K_1 = 7.7 \times 10^{-4} \text{ mol l}^{-1}$ ,  $K_2 = 5.59 \text{ l mol}^{-1}$  [Se2]). The pH for different HF concentrations, as given in the table shown in the inner back cover of this book, has been calculated using the latter constants. Note that the dissociation of HF is further reduced by addition of ethanol to the solution [Ga3].

For the case of  $\text{SiO}_2$  etching, HF,  $(\text{HF})_2$  and  $\text{HF}_2^-$  are assumed to be the active species [Ve1, Ju1]. If HCl is added to the solution the concentration of the  $\text{HF}_2^-$  ion becomes negligible, which leaves HF and its polymers to be the active species [Ve3]. Because for high current densities the electrochemical dissolution of silicon occurs via a thin anodic oxide layer it can be concluded that, at least for this regime, the same species are active. This is supported by the observation that  $\text{F}^-$  is



inactive in the electrochemical dissolution kinetics [Se2]. It is found that  $\text{HF}_2^-$  is also inactive for the pH range investigated – which again leaves HF and its polymers to be the active species in the electrochemical dissolution reaction of silicon [Se2].

The diffusion coefficient  $D_{\text{HF}}$  of the HF molecule has been determined from the etch rate on oxide films to be between  $2 \times 10^{-6}$  and  $2 \times 10^{-5} \text{ cm}^2 \text{ s}^{-1}$  [Mo5]. A conductimetric technique gave  $D_{\text{HF}} = 1.68 \times 10^{-5} (\pm 0.02) \text{ cm}^2 \text{ s}^{-1}$  for concentrations of aqueous HF in the order of 0.2% at 25 °C [No1]. In ethanoic solutions values in the order of  $2.2 \times 10^{-5} \text{ cm}^2 \text{ s}^{-1}$  have been reported [Me14]. Due to ionization of neutral HF molecules to  $\text{F}^-$  ( $1.473 \times 10^{-5} \text{ cm}^2 \text{ s}^{-1}$ ),  $\text{HF}_2^-$  ( $2.35 \times 10^{-5} \text{ cm}^2 \text{ s}^{-1}$ ) and highly mobile  $\text{H}^+$  ( $9.315 \times 10^{-5} \text{ cm}^2 \text{ s}^{-1}$ ), the measured average diffusion coefficient increases rapidly for HF concentrations below 0.02%. The water molecule, by comparison, has a diffusion coefficient of  $2 \times 10^{-5} \text{ cm}^2 \text{ s}^{-1}$  at RT. The viscosity of solutions is dependent on temperature, which produces a temperature dependence of  $D_{\text{HF}}$ . From measurements of viscosity versus temperature, activation energies of 0.16 and 0.12 eV have been calculated for diffusion-controlled reactions in water and ethanol, respectively. These results are supported by rotating disk electrode (RDE) measurements of  $J_{\text{PS}}$  in ethanoic HF, which gave an activation energy of 0.125 eV for  $D_{\text{HF}}$  [Me14].

The product of the dissolution process of silicon electrodes in HF is fluosilicic acid,  $\text{H}_2\text{SiF}_6$ . In contrast to HF,  $\text{H}_2\text{SiF}_6$  is mostly (75%) dissociated into  $\text{SiF}_6^{2-}$  and  $2\text{H}^+$  in aqueous solution at RT. The diffusion coefficient of the  $\text{SiF}_6^{2-}$  at RT decreases from  $1.2 \times 10^{-5} \text{ cm}^2 \text{ s}^{-1}$  for  $0.83 \text{ mol l}^{-1}$  to  $0.45 \text{ cm}^2 \text{ s}^{-1}$  for  $2.5 \text{ mol l}^{-1}$ , with values of activation energy around 0.2 eV [We7].

So far only aqueous solutions have been considered; however, mixtures of HF and ethanol or methanol are quite common, because this addition reduces the surface tension and thereby the sticking probability of hydrogen bubbles. While substantial quantities of ethanol or methanol are needed to reduce the surface tension, cationic or anionic surfactants fulfill the same purpose in concentrations as low as 0.01 M [So3, Ch16].

If aluminum is present on the electrode (for example if used for interconnects), an ammonium fluoride-based electrolyte is more desirable than HF, because Al is only stable in the pH range of about 4 to 8.5 [Oh4]. Note that PS formation is observed in ammonium fluoride-based electrolytes [Ku5], as well as in water-free mixtures of acetonitrile and HF [Ri1, Pr7], but not in alkaline electrolytes.

## 1.5 The Electrodes

This section deals with the electrodes in the electrochemical set-up, with special emphasis on the silicon electrode and its semiconducting character. An electrochemical cell with its complete electrical connections, as shown in Fig. 1.3 a and b, is similar to the well-known four-point probe used for applying a defined bias to a solid-state device. The two lines that supply the current are connected to

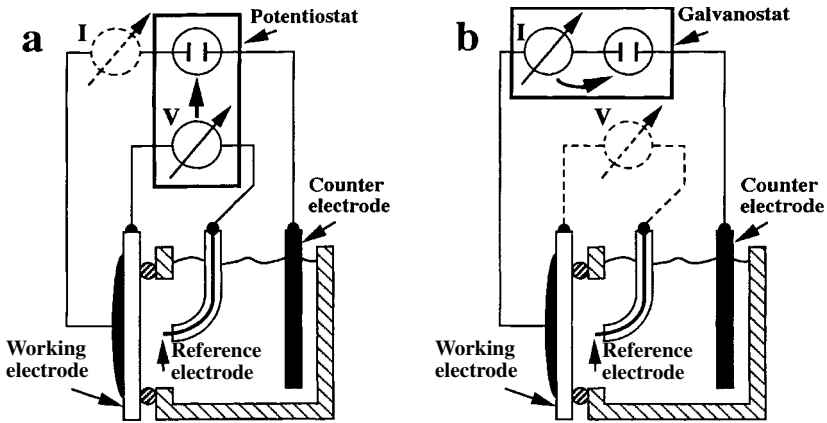


Fig. 1.3 An electrochemical cell with all its electrical connections in (a) potentiostatic mode and (b) galvanostatic mode. The dashed meters are optional.

the counter electrode and the working electrode, which is the silicon sample. One probe contact is connected to the sample and the other to a reference electrode that is placed close to the silicon surface in the electrolyte. By measuring the potentials at the probe contacts, all potential drops caused by ohmic losses in the counter electrode, the connections and the electrolyte are eliminated. The standard, four-terminal power supplies for electrochemical experiments are potentiostats, which are commercially available from various vendors [4]. It enables working under constant bias (potentiostatically, Fig. 1.3a) or under constant current (galvanostatically, Fig. 1.3b). By a scan of the potential (current) the potentiostatic (galvanostatic)  $I$ - $V$  characteristics of the electrode can be recorded.

The counter electrode is commonly realized by a platinum mesh or sheet, a carbon plate or a highly doped silicon wafer. The position and geometry of the counter electrode is of great importance for the resulting etched geometry. A pin-like electrode, for example, can even be used to micromachine the working electrode if short current pulses are applied [Sc19]. A homogeneous current distribution, as desired in most applications, is best achieved by using a counter electrode of the same size and in-plane orientation as the working electrode. If a Pt mesh is used its total surface area must be comparable to that of the Si electrode and the size of the mesh openings smaller than the distance to the Si electrode. Platinum black coating of the mesh can reduce the required mesh area.

The measurement of potentials in electrolytes is not as easy as it is for solid-state devices. Depending on the composition of the electrolyte and the electrode material a monolayer of adsorbates or a thin passivation layer may be formed on the electrode, and can significantly shift the electrode potential. These effects have to be taken into account for the working as well as for the counter electrode. The potential at the latter becomes irrelevant if a reference electrode is used. The reference electrode should be placed as close as possible to the Si electrode or it can access the Si electrode via a capillary. The size of the reference electrode is not rel-

evant, because it carries no significant current. The internationally accepted primary reference is the normal hydrogen electrode (NHE), which consists of a Pt electrode in a stream of hydrogen bubbles at 1 atm in a solution of unit hydrogen ion activity. The most common reference is the saturated calomel electrode (SCE) with a potential of 0.242 V versus NHE [5].

For a metal electrode, as a working electrode, its resistivity is in most cases negligible compared to the electrolyte resistivity and space charges in the electrode do not to be taken into account due to a high number of free charge carriers. This is in stark contrast to a semiconducting electrode where the number of free carriers is orders of magnitude smaller than in a metal. Ohmic losses in the electrode have therefore to be taken into account, especially for low doped substrates. Under reverse bias, in addition, a significant part of the applied bias may drop across an SCR. Another source for a potential difference is a surface passive film, for example  $\text{SiO}_2$ , which may be present in the anodic regime. The correct determination of potential distribution at the interface of a silicon electrode is therefore complicated, even if a reference electrode is used. Fortunately, it is found that the electrochemical condition of the silicon electrode is in most cases well described by the current density across the interface. This quality of the current density is probably due to the fact that a certain bias across the interface between electrolyte and semiconductor surface corresponds to a certain current density under constant values of temperature, doping density and electrolyte concentration. In the few cases where the applied bias is a parameter independent of the current density, as in the case of macropore formation on n-type electrodes, larger potentials are involved and a platinum wire as a pseudo-reference is usually found to be sufficient.

Because the silicon working electrode is the focus of study in this book, the details of its preparation from a wafer are worth discussing. Silicon is commercially available as a single-crystalline wafer in diameters of 100, 125, 150, 200 and 300 mm, or even larger [6]. The thickness is usually in the range of 0.4–0.7 mm. The crystal orientation of the majority of wafer used today is (100). For certain applications (111) and (110) oriented wafers are available in diameters up to 150 mm. For commercial wafers, n-type doping is realized by P, As or Sb, while for p-type doping only boron is used. Bulk dopant concentrations usually range from  $10^{13}$  to  $10^{20}$   $\text{cm}^{-3}$ , which corresponds to specific resistivities between 1000 and 0.001  $\Omega$  cm, according to the figure in the inner front cover of this book. Doping and crystal orientation of wafers below 200 mm diameter are marked by a primary and sometimes by a smaller secondary flat, as shown in Fig. 1.4. The crystal orientation of 200 and 300 mm wafers is marked by an edge-notch. For many electrochemical experiments the desirable sample size is considerably smaller than the whole wafer. Single crystalline wafers can easily be cleaved along the (110) planes using a diamond tip scribe [7] to scratch the wafer and two pairs of tweezers to bend and cleave it, as shown in Fig. 1.4. Polycrystalline substrates are mainly fabricated for solar energy conversion and have a square or rectangular shape. Such wafers are difficult to cleave and dicing by a diamond saw is recommended.

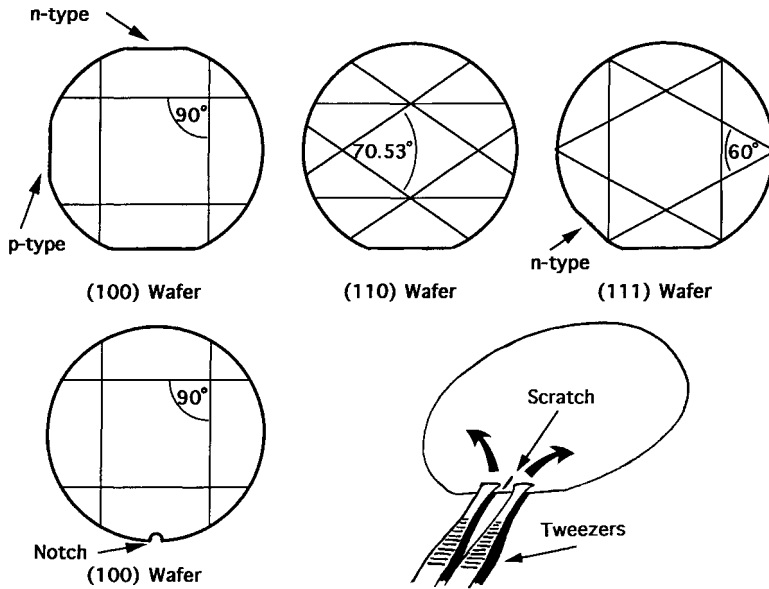


Fig. 1.4 The three common orientations of single crystalline silicon wafers are indicated by flats, while for wafers with diameters of 200 mm and larger the orientation is indicated by a small notch. Cleaving along the

lines, as indicated for each wafer orientation, can be performed by scratching the wafer at the edge with a diamond tip and bending it with tweezers, as shown on the lower left.

Most electrochemical experiments need an electrical contact of some kind to the silicon substrate. Because of the semiconducting nature of silicon a metallic tip or clip attached to the surface will not produce an ohmic contact but constitutes a Schottky junction. However, for some applications, like the ELYMAT (Section 10.3), where the contact is only operated under forward conditions at low current densities, such a contact is sufficient. For silicon samples with a doping concentration in excess of  $10^{19} \text{ cm}^{-3}$  the contact to a metal becomes ohmic. An ohmic contact to a silicon sample with a doping concentration below  $10^{19} \text{ cm}^{-3}$  can be achieved in different ways:

1. Rubbing GaIn eutectic (24% In, 76% Ga) with a piece of fine grinding paper on the backside of the sample.
2. Deposition of a metal film on the backside by evaporation or CVD techniques and subsequent annealing.
3. Doping the back of the sample in excess of  $10^{19} \text{ cm}^{-3}$  in order to produce an  $\text{nn}^+$  or a  $\text{pp}^+$  structure.
4. Providing the backside with an electrolyte contact, which is forward biased or alternatively reverse biased and intensely illuminated.

Method 1 is quick but contaminates the samples with Ga and In, which usually prohibits further processing with standard semiconductor equipment. The same

is basically true for method 2. Methods 3 and 4 circumvent this problem and in addition provide a transparent contact that is advantageous for experiments with backside illumination. For methods 1 to 3 a metallic clip or an aluminum foil are sufficient to connect the conducting backside of the sample to the terminal of the power supply. Note that the contacts realized by method 1 are not stable if exposed to HF vapor.

The geometry of the contact and the electrode area exposed to the electrolyte are crucial because ohmic losses, which may be significant for low or moderately doped silicon electrodes, lead to potential gradients. A consequence of these gradients is an inhomogeneous distribution of current density. Silicon samples are commonly platelets cleaved from a wafer. A current flowing parallel to the surface of the plate, as, for example, in immersion cell designs, leads to an inhomogeneous current density. A large contact on the backside of the sample and a current flow normal to the surface, as is the case for O-ring cells, produces a homogeneous current density at the front side, exposed to the electrolyte. For some applications, like the etching of trough-holes, current density gradients are desirable [Le20]. In such cases small, local backside contacts, as depicted in Fig. 4.17 a, can be used.

## 1.6 Cell Designs

The design of an electrochemical set-up is governed by a multitude of different requirements such as different sample sizes, low contact resistance, high current density, laminar flow of electrolyte, easy observation of the sample surface, adjustable illumination conditions, etc. This multitude of requirements is in stark contrast to the small number of cells specialized on silicon electrochemistry commercially available [8]. Doing electrochemistry with silicon therefore commonly begins with designing a suitable cell, which is usually a source of frustration as a result of broken samples, leaky set-ups and corroded contacts. The different cell designs discussed in this section may give some inspiration as to how such problems can be avoided. Emphasis is put on critical points such as materials, sealants, contacts and easy handling.

The properties of different illumination sources that can be combined with the set-ups discussed above are presented in Section 4.6.

### 1.6.1 The Cell Materials

Which materials are best for cell design depends essentially on the type of electrolyte used. Because HF acid is quite common in the electrochemistry of silicon, materials resistant to HF are preferable. Polyvinyl chloride (PVC), polypropylene (PP), polytetrafluoroethylene (PTFE) and polyvinylidene fluoride (PVDF) can be used for the cell body. PVC is a good choice for most designs because it is inex-

pensive, inert in HF, and its mechanical performance is superior to that of PTFE. In addition PVC parts can easily be glued, which is not the case for PTFE. Note that standard plastic screws are made of polyamide, which is not resistant to concentrated HF. They should be replaced by PP or PVC screws.

Materials used for transparent windows are clear PVC, Plexiglas (polymethylmethacrylate, PMMA) and sapphire. PMMA shows a good transparency in the visible and the IR, it is easily machinable, and stable at low HF concentrations. In concentrated HF (>10%), however, it becomes opaque after the initial contact. Clear PVC, which is of lower transmission coefficient than PMMA, is therefore preferable for high HF concentrations.

Standard black O-rings made of an acrylonitrile-butadiene copolymer (such as Perbunan) have proved to be stable in HF at concentrations up to 50%. If contamination of the silicon sample is an issue, the nitrile O-rings may be replaced by vinylidene fluoride-hexafluoropropylene (Viton) O-rings [9].

It is important to provide a good ohmic contact to a semiconductor like silicon. The ohmic contact is especially critical for open cell designs, like the immersion cell, because it is exposed to HF vapors from the electrolyte, which are corrosive. Platinum or gold are inert contact materials with respect to HF, however some kind of spring or clip is needed to press the noble metal to the sample. Metals commonly used to make springs, like stainless steel or brass, are found to corrode rapidly in HF vapor. Tungsten shows a better performance, but a more elegant way to solve this problem is to use the elastic properties of the sample holder material itself to effect a non-metallic clip, as shown in Fig. 1.5 a. For sample contacts that are not directly exposed to HF, other metals, e.g. aluminum, can be used. Such contacts, however, should be easily exchangeable in case of corrosion. For moderate currents, needle tip contacts at the edge of the wafer are useful – such contacts are commercially available as spring contact probes for electronic testing of PCBs [10].

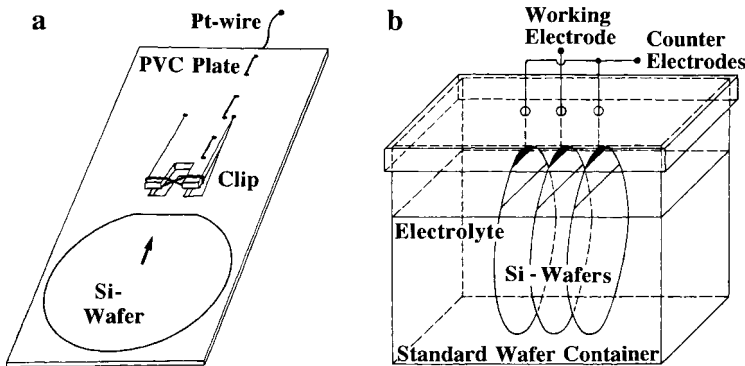


**Fig. 1.5** (a) Sample fixture for an immersion cell. The elasticity of the PVC body is used to clamp the Pt wire contact to the wafer.

(b) Standard wafer container used as an immersion cell for anodic oxidation experiments.

## 1.6.2

**The Immersion Cell**

The simplest way to realize a basic electrochemical cell is to partially immerse a strip-shaped silicon sample (working electrode) and a platinum wire (counter electrode) in a beaker filled with electrolyte. If a power supply is connected to the electrodes, the cell is ready for operation. This simple set-up has several advantages. It is a clean way of sample preparation, because the sample is not in contact with an O-ring and the area contaminated by the contact can easily be removed by cleaving it off. This is advantageous if subsequent high-temperature processing of the sample is desirable. The flexibility of immersion cell designs is shown in Fig. 1.6.

An inevitable property of this cell concept is a current flow along the strip. This causes an inhomogeneous potential distribution along the stripe due to ohmic losses, especially for low doped substrates. Porous layers, as a result, often show a thickness gradient along the stripe. The potential drop along the strip can usually be neglected for silicon samples of a sufficiently high conductivity or for small anodization currents. If, however, the transformation of the whole thickness of a strip into mesoporous silicon is desired, a slight beveling of the strip or an immersion scanning technique is required, even in the case of highly doped silicon [Ba4, Ju2].

Another drawback of the immersion cell concept is that the active area is badly defined, because of the meniscus formed at the electrolyte-air interface. The form of the meniscus greatly depends on whether the sample is hydrophilic or hydrophobic, which again is a function of applied potential. This problem can be circumvented, if the active area of the sample is defined by a window in an inert layer, for example resist or CVD nitride, which is fully immersed into the electrolyte, as shown in Fig. 1.6a.

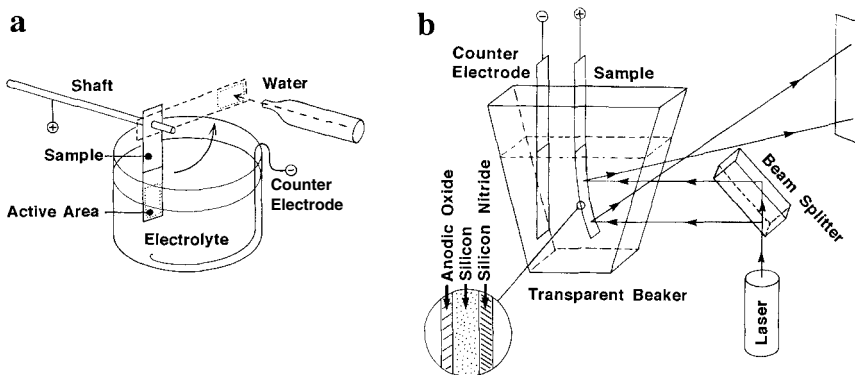


**Fig. 1.6** Two different immersion cell designs optimized for special applications. (a) Set-up for fast removal and rinsing of a strip-shaped electrode by fast rotation of the shaft (solid arrow). This set-up is useful for measurements of transient electrode processes like

anodic oxide growth during electrochemical oscillations. (b) PMMA immersion cell set-up for *in situ* determination of stress by optical measurement of the electrode curvature. Stress is induced by the growth of anodic films. After [Le4].

The simple immersion cell design is most suitable for applications for which the current densities involved are very low, such as anodic oxidation. In this case ohmic losses in the substrate become negligible, even for moderate doping densities and large samples, like whole wafers. Position and geometry of the counter electrode, however, become important, because the oxide thickness is sensitive to spacing of the electrodes. Large counter cathodes of the same size and shape as the oxidized wafer can be realized by two highly doped wafers, which avoids expensive platinum sheets or meshes. The slits of a standard wafer container provides an easy way of positioning of the wafers sufficiently accurately to produce homogeneous anodic oxides. Holes in the top of the container allow for contacting. Figure 1.5b shows such a simple set-up, where a wafer container is used as an anodization cell. A more sophisticated cell for anodic oxide formation is described in the literature [Ba13].

If the wafer is not fixed in the cell, a mechanical wafer support is advisable. The ohmic contact can be an integral part of such a sample fixture, as shown in Fig. 1.5a. During formation of mesoporous silicon on highly doped substrates at low bias (0–1.5 V), it was found that such a contact can even be immersed into the electrolyte without a significant degradation of its electrical properties. It is remarkable that mesoporous silicon formation takes place under the contact, too, without significant degradation of the contact properties.

### 1.6.3

#### The O-Ring Cell

The immersion cell design discussed above can be achieved with standard laboratory equipment within a few minutes; however, it suffers from an inhomogeneous current density along the strip and the badly defined active area of the sample. These drawbacks are overcome if the sample area exposed to the electrolyte is defined by an O-ring seal. The backside of the sample is accessible in this case and can be used to realize an ohmic contact. Now the current flows normal to the sample surface, which reduces ohmic losses significantly and leads to a homogeneous current density distribution. However, at a distance of about the wafer thickness from the O-ring the current flow is not normal to the surface and the current density is therefore slightly enhanced there. This effect has been found to be responsible for thickness inhomogeneities of porous layers [Kr3]. To reduce such inhomogeneities the O-ring should be of a diameter in excess of a centimeter and its section thickness as small as possible.

The sample has to be pressed against the O-ring in order to seal the cell. This can be done by various means, as shown in Fig. 1.7 a–f. Simple fixtures use the weight of the upper part of the cell or screws to press the O-ring against the silicon sample. A fixture using magnets is advantageous if fast handling is required [Ch14]. For whole wafers pneumatic pistons or a vacuum seal [Ba13] are preferable. Note that the use of a vacuum chuck, as shown in Fig. 1.7e, requires support of the wafer backside by a chuck to reduce its bow to values below 0.5 mm, in order to avoid fracture. An advantage of the set-ups shown in Fig. 1.7 a–f is that



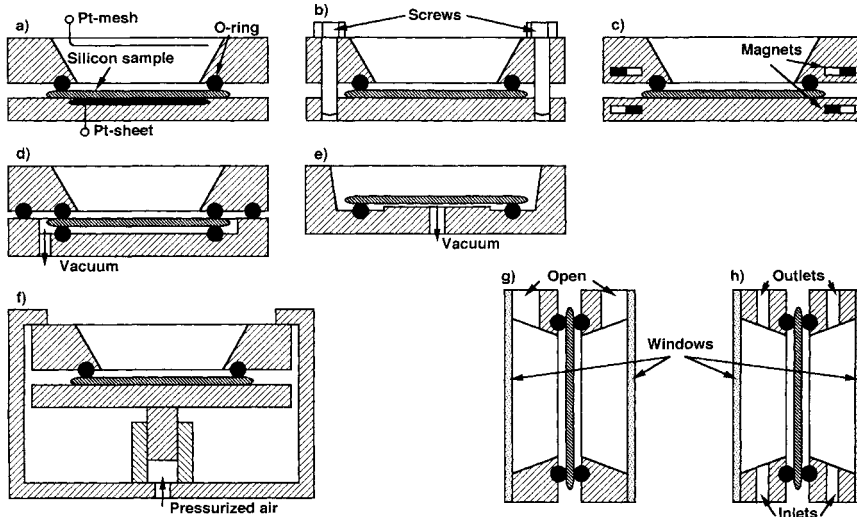


**Fig. 1.7** Cross-sectional views of various types of O-ring cells. The O-ring can be pressed against the sample (a) by the weight of the upper part of the cell, (b) by screws,

(c) by magnets, (d, e) by vacuum or (f) by pneumatic pistons. These designs can be extended to double O-ring cells: this requires (g) a vertical sample position or (h) a closed cell.

they can be filled like a beaker and allow for easy observation of the sample from the top without a window. The option of electrolyte agitation, however, is limited. The upper right figure on the front cover of this book shows the top view of a simple O-ring cell according to Fig. 1.7b.

#### 1.6.4

#### The Double Cell

An advantage of the electrochemical double cell is the possibility of replacing the ohmic contact, usually established by some kind of metal pressed against the wafer, by an electrolytic contact. This not only avoids a potential source of contamination but also establishes a transparent contact. A disadvantage of this arrangement is that the potential of the wafer is not known. The double cell shown in Fig. 1.8 combines the simplicity of the immersion cell with the homogeneous current distribution of the O-ring cell [La5, La9]. The two cells are separated by the wafer carrier, which has to fit so tightly into the set-up that leakage currents become negligible compared to the current across the wafer. O-rings can be used if leakage currents are not acceptable, as is the case for anodic oxidation. Tight sealing of double O-ring cells for whole wafers requires pneumatic elements or an evacuable recess as shown in Fig. 1.7 d and f [Ba13]. Such a double cell designed for ELYMAT measurements of 200 mm wafers with a sophisticated sample holder is shown on the upper left of the front cover of this book. The electrical contacts

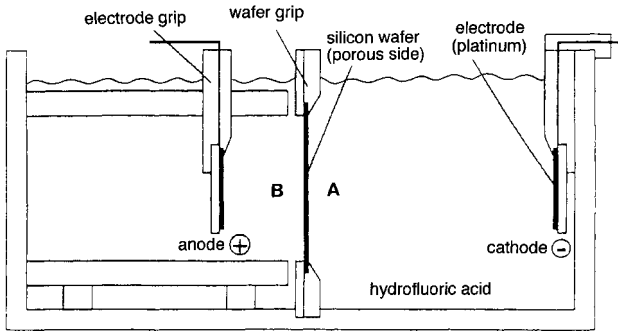


**Fig. 1.8** Immersion double cell separated by the fixture of the silicon electrode. Note that no ohmic contact to the silicon wafer is

necessary. Illumination is needed for moderately doped samples, to generate a current in the reversely biased junction. After [La5].

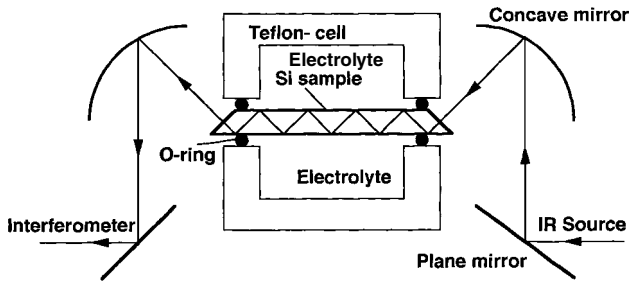


**Fig. 1.9** For *in situ* IR vibrational characterization of an electrochemical interface the silicon electrode in the double O-ring cell has to be shaped as an ATR prism.

of this set-up are realized by pneumatic tungsten carbide needles outside the O-ring, close to the wafer edge.

In order to produce significant currents across moderately doped wafers the reverse biased junction has to be illuminated. Hence the anode (for the case of p-type substrates) or the cathode (for the case of n-type substrates) should be made of a platinum mesh to be sufficiently transparent.

A special O-ring cell design is needed for *in situ* infrared (IR) vibrational characterization of an electrochemical interface. The absorption of one monolayer (i.e.  $<10^{15} \text{ cm}^{-2}$  vibrators) can be measured if the silicon electrode is shaped as an attenuated total reflection (ATR) prism, which allows for working in a multiple-internal-reflection geometry. A set-up as shown in Fig. 1.9 enhances the vibrational signal proportional to the number of reflections and restricts the equivalent path in the electrolyte to a value close to the product of the number of reflections by the penetration depth of the IR radiation in the electrolyte, which is typically a tenth of the wavelength. The best compromise in terms of sensitivity often leads to about ten reflections [Oz2].

## 1.6.5

**The Rotating Disk Electrode**

None of the set-ups discussed so far provides stirring of the electrolyte for bubble removal or for enhancement of the reaction rates. A standard set-up developed to study kinetic electrode processes is the rotating disc electrode [11]. The electrode is a small flat disc set in a vertical axle. The hydrodynamic flow pattern at the disc depends on rotation speed and can be calculated. An additional ring electrode set at a different potential provides information about reaction products such as, for example, hydrogen. However, because this set-up is designed to study kinetic processes and is usually equipped with a platinum disc, it becomes inconvenient if silicon samples of different geometries have to be mounted.

## 1.6.6

**Cells with Electrolyte Circulation**

Circulation of the electrolyte is essential for many experiments, because it reduces concentration gradients at the electrode surfaces. It can remove bubbles from the electrode and it allows for better temperature control. A magnetic or mechanical stirrer can be integrated in open cell designs, as shown in Fig. 1.7a–g. However, high flow rates can only be obtained with closed cell designs, as shown in Fig. 1.7h. Polytetrafluoroethylene membrane pumps [12] and non-metallic valves [13], as commonly used for pumping of HF in wafer fabs, are sufficient to provide good circulation. Peristaltic pumps are not advisable because of their relatively low flow rates. In order to produce a homogeneous flow of electrolyte from the intermittent pumping action a partly air-filled reservoir is added for damping. A second reservoir at ambient pressure serves as a container for the reflow from the cell and for refilling the set-up. Note that special safety regulations apply to pumping HF.

A closed O-ring double cell with in- and outlets for electrolyte circulation, as shown in Fig. 1.10, is quite complex, but it shows superior experimental flexibility. This set-up, which combines several features such as a window for illumination, an optional second electrolyte contact on the back of the sample, and the possibility to enhance the electrolyte convection by pumping, will be described briefly. The electrochemical double cell shown in Fig. 1.10 is based on a commercially available optical microbench system [14]. It allows for a maximum active sample area of 260 mm<sup>2</sup>, if a mounting plate with a 35.5 mm opening is used. The front side and the backside cells are symmetric and consist of a PVC body, shown on the left of Fig. 1.10. The windows are easily exchangeable using the window screw. An electrolyte inlet hole is located at the bottom of the cell body, the outlet is on the top. A counter electrode and a pseudoreference electrode are realized by platinum wires that are electrolyte-tight fed through the PVC body using an epoxy resin. The width of the rectangular-shaped sample is given by the distance of the rods (23 mm), whereas the length is usually somewhat larger in order to have enough space for contacting. The sample is introduced between the two cell bodies, which are pressed together by four springs. Illumination sources such as a halo-

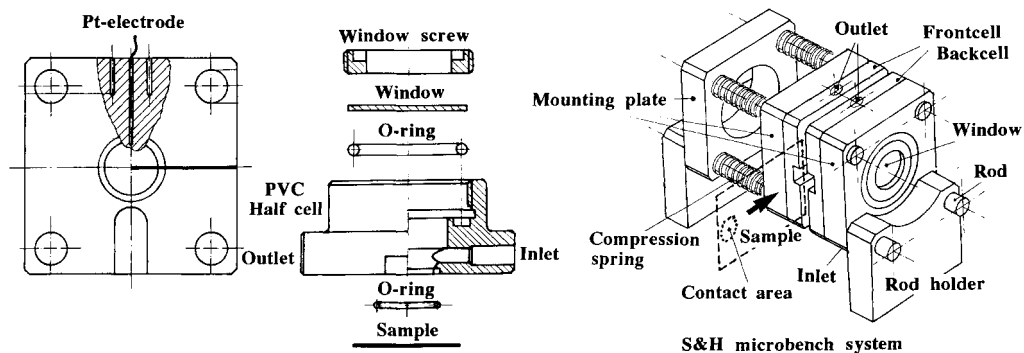


**Fig. 1.10** A closed double O-ring cell for electrochemical experiments with silicon electrodes, based on a standard optical microbench system. Top and side views of a PVC half-cell

are shown on the left. Two identical PVC half-cells are mounted on the four rods of the microbench such that the front cell is moveable for sample exchange (right side).

gen lamp, LEDs or lasers, as well as filters and other optical parts, can easily be fixed on the optical bench allowing for a high flexibility of front side or backside illumination conditions.

### 1.6.7

#### Lithographic Patterning

All the cell designs discussed so far show active working electrode areas in the order of  $\text{cm}^2$ . If much smaller active areas are desirable, photolithographic patterning of a thin surface film, e.g. resin, silicon oxide or silicon nitride is required [Na6, Kr3, Du6]. With this technique electrode areas in the order of  $\mu\text{m}^2$  and below can be achieved. However, some problems, known from the O-ring cell, also apply to patterned electrodes. On the one hand the current distribution becomes inhomogeneous for area diameters in the order of the sample thickness and below, especially for low-doped substrates. This may, for example, produce inhomogeneities of PS layer thicknesses. On the other hand, undercutting of the pattern cannot be avoided. In HF electrolytes the undercutting is isotropic for oxide or nitride masking, while resin patterns show large undercutting which eventually leads to lift-off. Figure 6.6 shows PS layer profiles obtained for different substrates and masking layers.

## 2 The Chemical Dissolution of Silicon

### 2.1 The Basics of Wet Processing of Silicon

Chemical dissolution of silicon can be performed in liquid as well as gaseous media. The latter is known as dry etching or reactive ion etching (RIE) [Ja3] and is an irreplaceable technique in today's microelectronic manufacturing. However, about 30% of the total number of process steps for the fabrication of today's integrated circuits are still wet etching and cleaning procedures, illustrating the importance of wet processing.

To treat all the different wet processes for silicon wafers developed in the last five decades exhaustively would make up a book of its own. However, a few basic aspects are important, because chemical etching of silicon is closely related to the electrochemical behavior of Si electrodes, especially to the OCP condition. A brief overview of the most common etching and cleaning solutions will be given, with emphasis on the electrochemical aspects.

In the early days of silicon device manufacturing the need for surfaces with a low defect density led to the development of CP solutions. Defect etchants were developed at the same time in order to study the crystal quality for different crystal growth processes. The improvement of the growth methods and the introduction of chemo-mechanical polishing methods led to defect-free single crystals with optically flat surfaces of superior electronic properties. This reduced the interest in CP and defect delineation.

Cleaning and the control of surface passivation then became a major issue, because traces of heavy metals in concentrations of less than a thousandth of a monolayer on the surface of a silicon wafer are sufficient to degrade device performance.

The high selectivity of wet etchants for different materials, e.g. Al, Si, SiO<sub>2</sub> and Si<sub>3</sub>N<sub>4</sub>, is indispensable in semiconductor manufacturing today. The combination of photolithographic patterning and anisotropic as well as isotropic etching of silicon led to a multitude of applications in the fabrication of microelectromechanical systems (MEMS).

In the following sections the wet treatments most common in the manufacture of silicon devices will be presented according to their main application:

1. Cleaning and passivation of silicon surfaces.
2. Silicon removal in an anisotropic manner.
3. Silicon removal in an isotropic manner.
4. Defect and junction delineation.
5. Selective etching of layers of different chemical composition.

## 2.2

### Silicon Surface Conditions and Cleaning Procedures

The surface condition of a silicon crystal depends on the way the surface was prepared. Only a silicon crystal that is cleaved in ultra high vacuum (UHV) exhibits a surface free of other elements. However, on an atomistic scale this surface does not look like the surface of a diamond lattice as we might expect from macroscopic models. If such simple surfaces existed, each surface silicon atom would carry one or two free bonds. This high density of free bonds corresponds to a high surface energy and the surface relaxes to a thermodynamically more favorable state. Therefore, the surface of a real silicon crystal is either free of other elements but reconstructed, or a perfect crystal plane but passivated with other elements. The first case can be studied for silicon crystals cleaved in UHV [Sc4], while unreconstructed silicon (100) [Pi2, Ar5, Th9] or (111) [Hi9, Ha2, Bi5] surfaces have so far only been reported for a termination of surface bonds by hydrogen.

Under ambient atmospheric conditions a native oxide is formed on cleaved Si surfaces. The properties of native and chemical oxides are discussed in Section 5.2. The well-defined surface conditions produced by wet processes like rinsing and cleaning procedures will be discussed below.

All standard cleaning processes for silicon wafers are performed in water-based solutions, with the exception of acetone or (isopropyl alcohol, IPA) treatments, which are mainly used to remove resist or other organic contaminants. The most common cleaning procedure for silicon wafers in electronic device manufacturing is the deionized (DI) water rinse. This and other common cleaning solutions for silicon, such as the SC1, the SC2 [Ke1], the SPM [Ko7] and the HF dip do remove silicon from the wafer surface, but at very low rates. The etch rate of a cleaning solution is usually well below  $1 \text{ nm min}^{-1}$ .

Chemomechanical polishing (CMP) solutions [16] for Si show somewhat higher etch rates than cleaning solutions, as shown in Fig. 2.1 a. CMP has been used since the late 1960s to prepare smooth, defect-free silicon wafer surfaces of optical quality [Me3]. CMP is based on the combined mechanical grinding action and chemical etching action of an alkaline suspension of colloidal silica: stock removal rate and the contact angle are shown in Fig. 2.1 a and b. The silicon surface is mainly covered with Si-H groups when the removal rate peaks at  $\text{pH}=11$ . The dissolution reaction is assumed to occur according to the mechanism shown in Fig. 4.1 with  $\text{OH}^-$ ,  $\text{H}_2\text{O}$  and  $\text{O}_2$  being the active species [Pi3]. If ammonia or amines and traces of copper are added to the CMP solution acceptor neutralization takes place because of incorporation of atomic hydrogen in the bulk silicon crystal [Pr2].

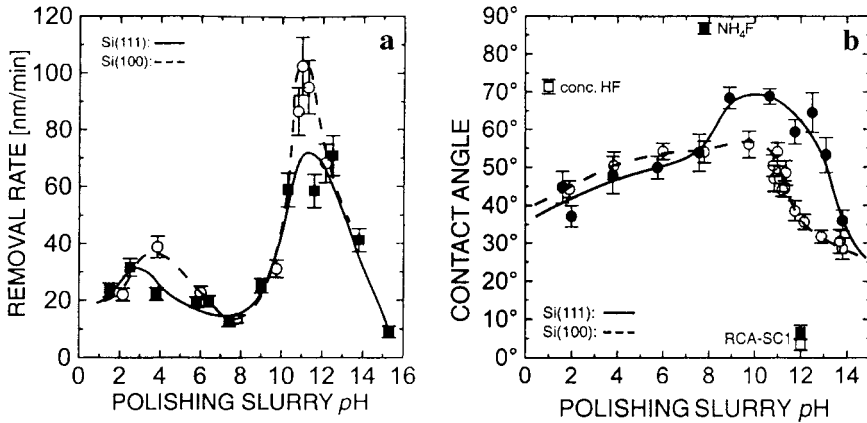


**Fig. 2.1** (a) Stock removal rate during CMP as a function of slurry pH for Si (100) surfaces (open circles) and Si (111) surfaces (filled squares), respectively.

(b) Surface contact angles of a 5  $\mu\text{l}$  droplet for hydrophilic and hydrophobic cleaning procedures and for CMP of Si (100) surfaces (open circles) and Si (111) surfaces (filled circles), as a function of slurry pH. After [Pi2].

Different chemical treatments for silicon can be categorized depending on the condition of the Si surface after the clean. The two basic surface conditions for a silicon surface are hydrophobic and hydrophilic.

### 2.2.1

#### The Hydrophobic Silicon Surface

A characteristic feature of a hydrogen-terminated silicon surface is its water repelling property. Such a surface exhibits a large contact angle for a drop of water [He1, Ra1] and is therefore called hydrophobic. The dependence of the contact angle of a water droplet on the chemical treatments applied to the silicon surface are shown in Fig. 2.1 b. A common procedure to establish a hydrophobic, hydrogenated surface condition is dipping the sample in 1% HF for 15 s (HF dip). Concentrated HF, mixtures of HF and  $\text{NH}_4\text{F}$  or pure  $\text{NH}_4\text{F}$  will show similar results concerning contact angle. The microscopic flatness of the silicon surface, however, depends on the type of etchant. While an HF dip usually induces a certain roughness, a short treatment in 40%  $\text{NH}_4\text{F}$  is reported to produce atomically flat surfaces for (111) as well as (100) oriented silicon surfaces [Hi9, Th9].

A hydrophobic Si surface condition is also observed after alkaline treatments, like CMP at a pH of about 11 or after etching in alkaline solutions, as shown in Fig. 2.1 b. Hydrophobic Si surfaces are very susceptible to hydrocarbon contamination, for example from the ambient atmosphere or from hydrocarbon films floating on a liquid. To avoid the latter case, water rinses and HF dips are often performed in an overflow wet bench.

## 2.2.2

**The Hydrophilic Silicon Surface**

A hydrophilic surface condition has been related to the presence of a high density of silanol groups (Si–OH) or to a thin interfacial oxide film. Such an oxide can be produced chemically by hot HNO<sub>3</sub> or by solutions containing H<sub>2</sub>O<sub>2</sub>. The three most common cleaning solutions for silicon are based on the latter compound:

1. SPM or pirhanja-clean: 1:1 (30% H<sub>2</sub>O<sub>2</sub>: 98% H<sub>2</sub>SO<sub>4</sub>), 10 min at 110 °C.
2. SC-1 or RCA-clean: 1:1:5 (30% H<sub>2</sub>O<sub>2</sub>: 25% NH<sub>4</sub>OH: H<sub>2</sub>O) 10 min at 80 °C.
3. SC-2: 1:1:6 (30% H<sub>2</sub>O<sub>2</sub>: 37% HCl: H<sub>2</sub>O), 10 min at 80 °C.

A standard cleaning sequence for silicon wafers starts with SPM, which is only required if organic residues are present. Between the following three steps (SC-1, HF dip, SC-2) the wafer should be removed from the solutions after 1 min of overflow quench with DI water and brought wet into the next cleaning solution. Final drying is done in a wafer centrifuge (spin-dryer) [Ke1]. Wafer handling should be done with PTFE or PP tweezers. An alternative concept without alkaline chemicals has been proposed [Me4].

Details of the chemical oxidation process are discussed in Section 5.2. The stringent requirements concerning metal contamination and the trend to more environmentally friendly processing are a constant force to improve cleaning procedures in today's semiconductor manufacturing [Me4, Sa1, Oh1].

Note that a native oxide film also forms under dry conditions in ambient air; the oxidation rate of this process can be enhanced by ultraviolet (UV)-ozone photooxidation [Ta1, Vi1]. Oxide-covered Si surfaces exhibit low contact angles. Only if the oxide surface is contaminated, for example by a monolayer of absorbed hydrocarbons, may larger contact angles be observed.

For a silanol-covered surface the contact angle depends on the relationship between Si–OH and Si–H groups, which gives rise to a dependence on pH, as shown in Fig. 2.1 b. A DI water rinse is sufficient to generate both basic Si surface conditions, depending on temperature and dissolved oxygen concentration (DOC). If a hydrogen-terminated silicon surface is exposed to DI water of moderate or high DOC at RT for several minutes the Si–H is slowly replaced by silanol groups (Si–OH) and a native oxide is formed for long rinsing times. This reduces the contact angle, and the surface becomes hydrophilic. In DI water of very low DOC (<0.004 ppm), in contrast, the reverse reaction is observed for elevated temperatures (80 °C) and long etching times (60 min) [Wa2]; the thin oxide is removed and a hydrogen-terminated surface is established again.



## 2.3

## Chemical Etching in Alkaline Solutions

Alkaline etchants are mainly used for two purposes: for CMP, as discussed in Section 2.2, or to remove silicon in an anisotropic manner, which is applied in the micromachining of silicon. Alkaline etchants are aqueous solutions of inorganic compounds like LiOH [Se3], NaOH [Al1, Al2], KOH [Se3, Sa6, Pr1, Xi1], RbOH [Wa3], CsOH [Cl1, Ya2, Ya3] or  $\text{NH}_4\text{OH}$  [Ke1, Go1, Sc4], as well as aqueous solutions of organic compounds, such as ethylenediamine [Re1], hydrazin [Me1, Ce1, Xu1], tetramethyl ammonium hydroxide (TMAH) [Ta2, Me2], cholin [As1], and amine gallates [Li2]. All these etchants show a similar etching behavior, which has been attributed to  $\text{OH}^-$  and  $\text{H}_2\text{O}$  being the active species, the cation being of minor importance. Details of the chemical dissolution reaction are discussed in Section 4.1. Common features of the alkaline etchants are:

1. Alkaline etchants are anisotropic. The etch rate for the (111) crystal planes of the Si crystal is smaller by about two orders of magnitude than the etch rate of any other crystal plane. The etch rate ratio between other crystal planes like (100) and (110) depends on etchant concentration and temperature, but doesn't usually exceed a factor of two [Sa6]. Addition of oxidizing agents reduces the anisotropy. The etch rate of (100) Si and  $\text{SiO}_2$  in KOH at different temperatures is shown in Fig. 2.2.
2. The etch rate of highly p-doped silicon ( $>10^{19} \text{ cm}^{-3}$ ) is found to be reduced by orders of magnitude compared to the etch rate of low doped or highly doped n-type silicon of (100) orientation. This effect is shown in Fig. 2.3 for KOH; note that the etch rate is significantly affected by the amount of dissolved oxygen

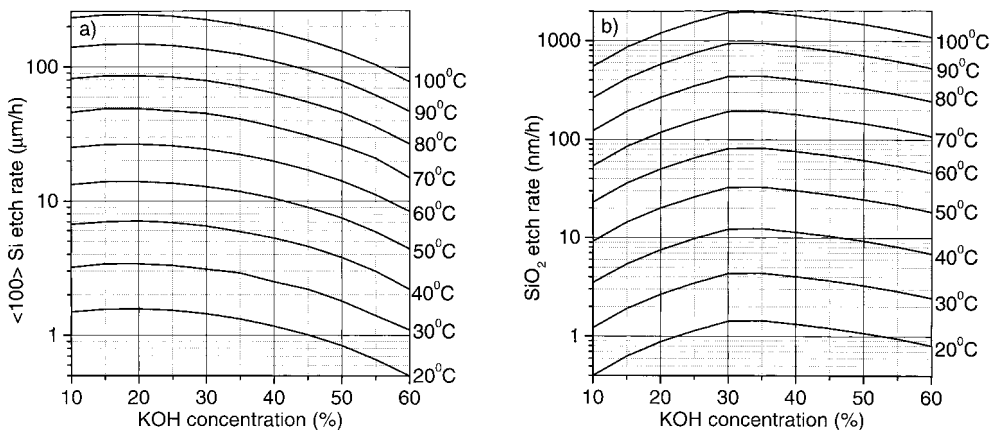


Fig. 2.2 The etch rate of (a) (100) bulk silicon and (b) thermal  $\text{SiO}_2$  as a function of KOH concentration and temperature.

In the temperature regime shown the etch rate of (110) silicon is roughly 1.5 times that of (100) silicon. After data of [Se3].

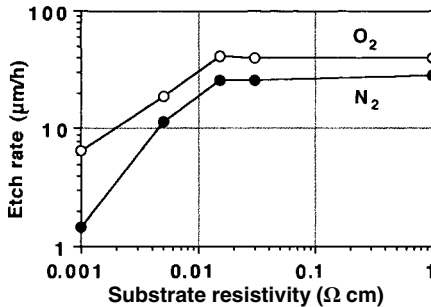


Fig. 2.3 Etch rate of (100) bulk silicon in 1M KOH of low and high DOC at 70°C as a function of p-type dopant concentration. The DOC of the solution was controlled by bubbling with pure O<sub>2</sub> or N<sub>2</sub>.

present in the alkaline solution. A silicon surface becomes resistant to alkaline etchants if implanted with a high dose of C [Le2], N [Ac1] or Ge [Fi6]. Thin films of SiO<sub>2</sub>, Si<sub>3</sub>N<sub>4</sub> or SiC are sufficient for masking in alkaline etchants.

3. The (100) etch rates show an Arrhenius dependency on temperature with activation energies of about 0.3–0.6 eV, depending on the alkaline solution used [Kr1, Se3].
4. Etching of silicon in alkaline solutions occurs under evolution of hydrogen with a ratio of two molecules H<sub>2</sub> per dissolved Si atom. This ratio is found to be reduced under positive bias [Pa6] or by addition of oxidizing agents like H<sub>2</sub>O<sub>2</sub> [Sc6]. If the anodic bias is increased beyond the passivation potential (PP), the dissolution rate is reduced by orders of magnitude.
5. The morphology of alkaline-etched (100) and (110) silicon surfaces varies from rough surfaces that exhibit micron-sized pyramids or ridges [Sc5] to smooth orange peel-like surfaces, depending on the etchant composition and substrate doping density. Mirror-like surfaces can be obtained on (111) crystal planes.
6. During the alkaline etching process the silicon surface is covered with Si–OH and Si–H. The ratio of this surface species depends on pH and temperature [Pi3, Al3].

Points 1 and 2 of the above list provide perfect conditions for the micromachining of silicon. Using a SiO<sub>2</sub> or Si<sub>3</sub>N<sub>4</sub> layer patterned by photolithography, all kinds of geometric structures can be realized, of which the basic ones are pyramids and V-grooves on (100) wafers [Ba1] or deep U-grooves on (110) wafers [Ke2, Kr1, Ya3, Ka5]. If deep structures have to be formed, patterning Si<sub>3</sub>N<sub>4</sub> or SiC are superior to SiO<sub>2</sub> because their etch rate in alkaline solutions is orders of magnitude smaller than that of thermal oxide, which is shown for the case of a KOH etchant in Fig. 2.2b. Other common masking materials like organic films (resists) or metals are rapidly dissolved or under-etched in alkaline solutions. Only epoxy-based resists, like SU-8 [15], are found to be quite stable.

Highly p-doped layers can also be used as masking layers. If the p-type doping level of silicon substrates is high enough to cause degeneracy ( $N_A > 10^{19} \text{ cm}^{-3}$ ), a decrease in etch rate with doping density is observed in all alkaline solutions inde-

pendent of their composition. This low etch rate is ascribed to a passivating oxide film present on the electrode [Pa5]. This interpretation is supported by the fact that the etch rates of thermal SiO<sub>2</sub> and p<sup>+</sup> show qualitatively the same dependence on KOH concentration. The absolute etch rate of p<sup>+</sup> Si in alkaline solutions, however, is one or more orders of magnitude larger than that of thermal SiO<sub>2</sub> [Se4]. Note that the etch stop on p<sup>+</sup> substrates is lost if made mesoporous. In the porous skeleton acceptors are still present in high concentration, while the free carrier concentration becomes negligible [Le14]. This indicates that the etch stop is related to the Fermi level position and is not caused by the chemical stability of the Si–B bonds. Low-doped silicon germanium alloys show a similar decrease in etch rate if the Ge concentration is raised above 20%. This effect has also been attributed to a passivating oxide [Fi6]. Note that the low etch rate of (111) surfaces in alkaline solutions is not attributed to a passivating oxide but to the slow dissolution kinetics caused by the bonding configuration of a monohydride silicon surface, as discussed in Section 4.1.

Silicon etch rates in alkaline solutions commonly increase monotonically with temperature. For KOH, for example, the etch rate  $r$  can be calculated according to:

$$r = K [\text{H}_2\text{O}]^4 [\text{KOH}]^{1/4} \exp(-E_a/kT) \quad (2.1)$$

with  $K=2480 \mu\text{m h}^{-1} (\text{mol l}^{-1})^{-4.25}$  and  $E_a=0.595 \text{ eV}$  for a (100) surface and with  $K=4500 \mu\text{m h}^{-1} (\text{mol l}^{-1})^{-4.25}$  and  $E_a=0.6 \text{ eV}$  for a (110) surface [Se3]. Values of  $r$  for a (100) silicon surface as calculated from Eq. (2.1) are shown in Fig. 2.2a. The often reported aging of alkaline etching solutions, accompanied by reduced etch rates, has been attributed to the formation of silica in the etchant, polymerizing from the silicate monomer formed as initial etching product [Ni6, Le29].

The surface morphology of (100) silicon planes in alkaline solutions depends strongly on concentration. High OH<sup>-</sup> concentrations (e.g. > 40% for KOH) produce smooth, orange peel surfaces, while the etched surface becomes rough at low OH<sup>-</sup> concentrations. A microscopic investigation reveals that the surface becomes rough because of the formation of pyramidal hillocks, as shown in Fig. 2.4a. This effect has been used for decades to reduce the reflectivity of solar cells, but the origin of this surface morphology is still controversial. The effect has been correlated with the sticking probability of hydrogen bubbles [Pa3, Sc6] or contamination of the solution [Kw1]. A detailed study revealed that pyramid formation is suppressed under oxidizing conditions [Br5]. This means that holes are available for the dissolution reaction. Hole supply enables attack of silicon back-bonds and thereby reduces anisotropy. Such conditions can be achieved by the addition of an oxidizing agent such as dissolved oxygen, ferricyanide or hypochlorite [Xi1], or the application of an anodic potential [Pa6], or an increase in the p-type doping density to values above  $10^{19} \text{ cm}^{-3}$ , as shown in Fig. 2.4b. That such different parameters show the same effect on etching morphology is an example of the close connection between chemical, electrochemical and electronic conditions.

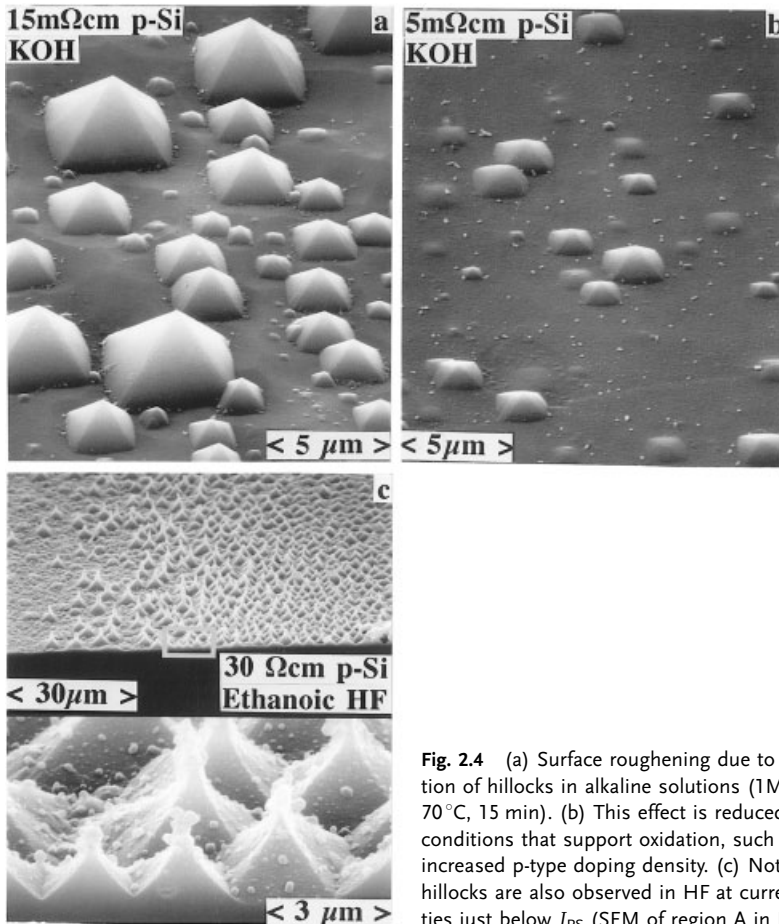


**Fig. 2.4** (a) Surface roughening due to the formation of hillocks in alkaline solutions (1M KOH, 70°C, 15 min). (b) This effect is reduced under conditions that support oxidation, such as an increased p-type doping density. (c) Note that hillocks are also observed in HF at current densities just below  $J_{PS}$  (SEM of region A in Fig. 4.17c).

## 2.4

### Chemical Etching in Acidic Solutions

Acidic silicon etchants are mainly used for two purposes: for the delineation of crystal defects, as discussed in Section 2.5, or to remove silicon in an isotropic manner. Isotropic etching adds another degree of freedom to the design of micro-mechanical structures, because all alkaline etches are anisotropic. Most isotropic etchants for silicon were developed in the early days of silicon crystal technology and exhaustive reviews on this topic are available [Tu3, Ru1]. A brief summary is given below.

Silicon is stable in acidic solutions that do not contain fluoride because the silicon surface is passivated by a native oxide. If only HF is present in an aqueous solution the etch rate remains low, showing values below  $0.1 \text{ nm min}^{-1}$  on single crystalline silicon depending on the  $\text{OH}^-$  concentration [Hu2]. This low etch rate

of HF can be considerably enhanced by addition of an oxidizing agent. The DOC of the aqueous HF may already significantly increase the etch rate [Og1], as shown in Fig. 2.5. For gravimetric measurements of such minute etch rates macroporous Si substrates of a well-defined, large surface-to-volume ratio are favorable.

The etch rate is further increased if  $\text{H}_2\text{O}_2$  is added to the solution, as shown in Fig. 2.5b. At such low rates the reaction is controlled by the kinetics of the reaction at the interface and not by diffusion in the solution. This etching solution is therefore found to be perfect to remove micro- and mesoporous silicon selectively from a bulk silicon substrate or to increase the diameter of meso- or macropores in an well-controlled, isotropic manner [Sa3].

Such low etch rates can be considerably enhanced by addition of stronger oxidizing agents, such as  $\text{HNO}_3$ ,  $\text{NaNO}_2$ ,  $\text{KBrO}_3$ ,  $\text{K}_2\text{Cr}_2\text{O}_7$ ,  $\text{KIO}_3$  or  $\text{CrO}_3$ . In some cases the etching in such mixtures proceeds under formation of a porous silicon film, a so-called stain film, as discussed in Section 7.7.

Addition of  $\text{HNO}_3$  to HF increases the etch rate by several orders of magnitude, to values as high as  $1500 \mu\text{m min}^{-1}$  for a mole ratio of 4.5 HF to 1  $\text{HNO}_3$  [Sc8, Sc9, Ro1, Ro2]. The dependence of etch rate on the ratio of HF and  $\text{HNO}_3$  is shown in Fig. 2.6. Usually mixtures with a reduced concentration of HF and additions of  $\text{CH}_3\text{COOH}$  or  $\text{H}_3\text{PO}_4$ , like for example the CP4 etch, are used for CP of silicon [Vo1, Ku7]. From the dependence of etch rate and viscosity on temperature it has been concluded that the reaction is diffusion limited [Bo3]. However, other studies propose the reaction to be under mixed control [Ku7]. Mixtures with an even lower HF concentration, for example a 30:1 (70%  $\text{HNO}_3$ : 50% HF), are commonly used to etch polysilicon layers. The etch rate of such mixtures becomes very low if the HF content is reduced to a few tenths of a percent [Jo1]. The same is true for small amounts of  $\text{HNO}_3$  in HF. If an acid of high viscosity, like  $\text{H}_3\text{PO}_4$ , is added, smoother silicon surfaces are obtained. Such solutions are used for surface finishing of the wafer backside [Ku7]. Rough surfaces, in contrast, are

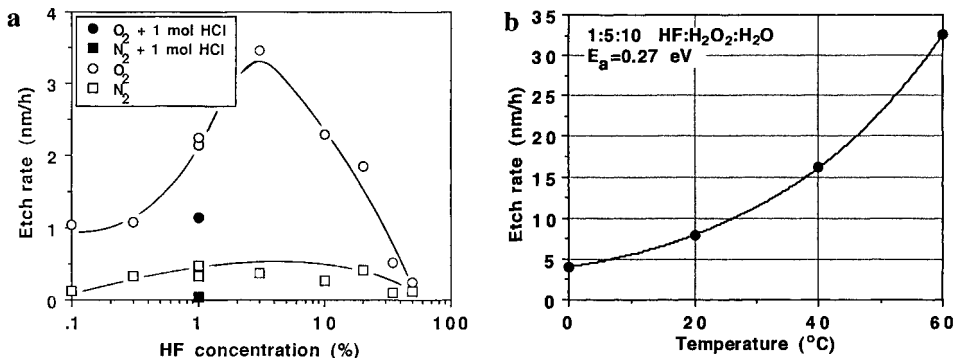
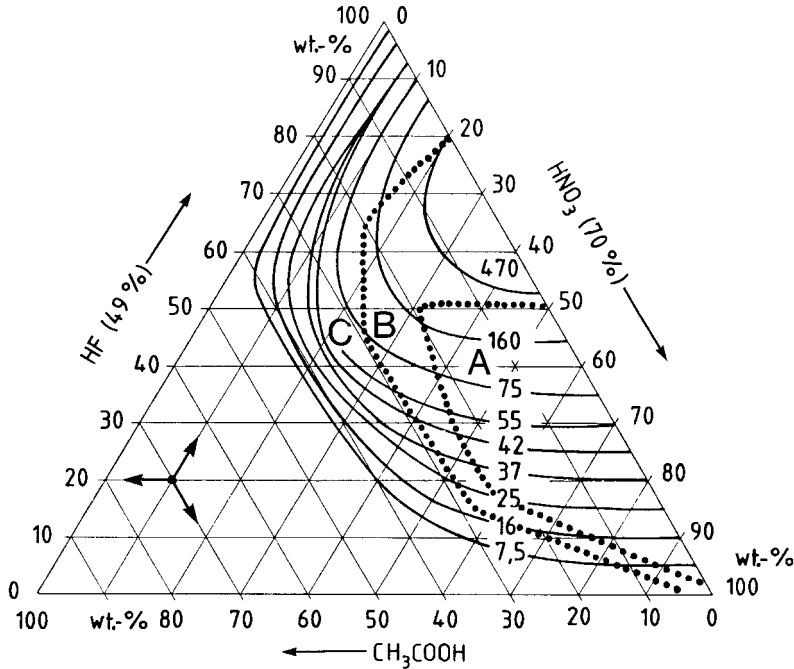


Fig. 2.5 (a) The etch rate of Si in aqueous HF bubbled with oxygen or nitrogen.

(b) Etch rate of silicon in an etchant composed of HF (50%) and  $\text{H}_2\text{O}_2$  (30%).



**Fig. 2.6** Curves of constant etch rate (in  $\mu\text{m min}^{-1}$ ) as a function of etchant composition. Compositions in region A give smooth, specular surfaces and rounded edges, while

rough surfaces and peaked corners are generated for compositions in region C. Region B is intermediate. Redrawn from [Sc9].

reported for addition of a surface active agent. This effect is exploited for texturization of multicrystalline solar cells for which alkaline texturing is inefficient [Ni5].

One of the interesting features of this etching system is its electrochemical component [Tu4]. The initial step of the reaction is proposed to be reduction of  $\text{HNO}_3$  and hole injection into the VB of silicon:



This reaction is complicated and very likely requires the participation of  $\text{HNO}_2$  as a catalyst and of  $\text{NO}_2$  as an intermediate [Ko14, Ve1]. The injected holes are consumed in the dissolution reaction of silicon, which proceeds in the same way as the tetravalent electrochemical dissolution path, as shown in Fig. 4.4. If the  $\text{HNO}_3$  concentration is low, the formation of a thin PS layer is observed, indicating that hole supply might be the limiting factor, as is the case in the divalent electrochemical dissolution path, as depicted in Fig. 4.3. The final dissolution product is a tetravalent hexafluoride complex ( $\text{SiF}_6^{2-}$ ) as is the case for the electrochemical dissolution process. The majority of the gas that evolves during silicon dissolution is hydrogen, with considerable amounts of  $\text{N}_2\text{O}$  and traces of  $\text{NO}$  and  $\text{NO}_2$  [Ko14].

The OCP etch rate of p-type and highly doped n-type Si electrodes in HF–HNO<sub>3</sub> mixtures increases by an order of magnitude under sufficiently anodic bias [Le20]. In the cathodic regime significant dark-currents are observed for p-type electrodes, as shown in Fig. 4.12. This is ascribed to hole injection from the electrolyte [Ko14]. Note that hole injection is not observed in aqueous HF free of oxidants.

Another characteristic feature of this etchant is the autocatalytic nature of reaction (2.2). As a result, the reaction must proceed first through an induction period in which the build-up of HNO<sub>2</sub> increases the etch rate to its steady-state value [Ro2]. This delay depends greatly on the condition and the size of the silicon sample surface and the volume and the convection of the etchant. It becomes short for a damaged or a porous silicon surface, for small ratios of etchant volume to sample surface and low convection rates. Under such conditions the etch rate increases fast, which may eventually lead to a significant increase in temperature, which again increases the etch rate. This effect is especially pronounced for porous layers, for which the solution can heat up to the boiling point within seconds and may cause hazard to the user. Note that mixtures of micro PS and an oxidizing agent show an explosive interaction even at cryogenic temperatures [Mc3, Ko24]. The strong temperature dependence and the autocatalytic effect limit the reproducibility of this etchant concerning etch depth and etch geometry. The induction period is specific to HNO<sub>3</sub> and not observed for other oxidants like, for example, KBrO<sub>3</sub> [Se6] or CrO<sub>3</sub> [Me5].

It is known that HF–HNO<sub>3</sub>-based solutions etch highly doped substrates faster by a factor of about three compared to moderately doped ones. A higher selectivity is reported on addition of chemicals that reduce the HNO<sub>2</sub> concentration, like H<sub>2</sub>O<sub>2</sub> or NaN<sub>3</sub> [Mu1]. However, this report suffers from the fact that the etch rate was measured for separate wafers of a homogeneous doping density. For pp<sup>+</sup> or nn<sup>+</sup> structures, which are not spatially separated, only a low selectivity is observed, because of the autocatalytic behavior of the etchant.

Masking is required for many micromechanical applications. While Si<sub>3</sub>N<sub>4</sub> is only suitable for a small etching depth because of its significant etch rate in HF, noble metals like gold are sufficient mask materials. In contrast to alkaline etchants, organic materials like certain resists or even some adhesive tapes are well suited to protect the silicon surface in isotropic etchants.

## 2.5 Defect and Junction Delineation

There are several techniques for characterizing lattice defects in a silicon crystal. Transmission electron microscopy (TEM) gives very detailed information about a single defect because of its high spatial resolution, as shown in Fig. 2.7a, but the method is rather time-consuming. A projection of all defects in a wafer is given by an X-ray topography (XRT) picture. XRT is non-destructive and the preparation time is in the order of hours. Small angle neutron scattering (SANS) provides information about the average size, form and density of lattice defects. This method is especially suited for small defects of about 10 nm. The high penetration depth

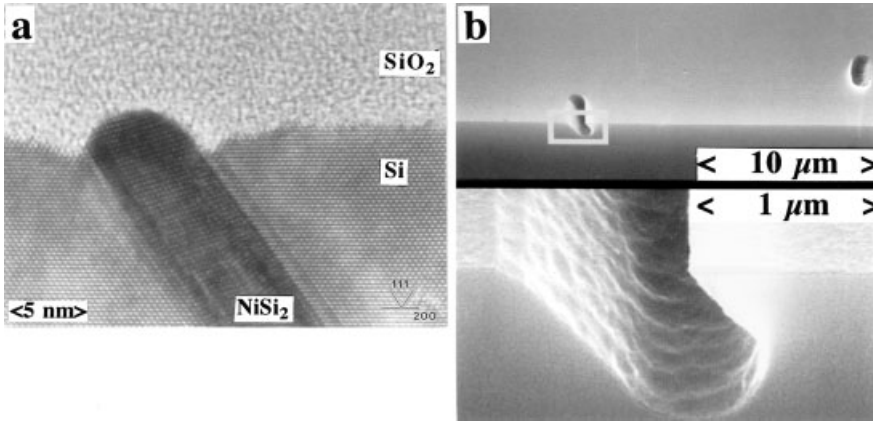


**Fig. 2.7** (a) Nickel silicide precipitates in disks parallel to the (111) Si crystal planes. Such a  $\text{NiSi}_2$  platelet in bulk Si is revealed by high-resolution electron microscopy (HREM); the tip of the platelet is penetrating the thermal oxide layer.

(b) After Secco etch the platelet and the surrounding silicon are preferentially etched. Note the different magnifications. A high density of etch pits produce a haze-like appearance of the wafer surface.

of neutrons allows us to investigate slugs several centimeters thick. Preferential chemical etching is the fastest characterization technique, but it is destructive and reveals only defects located in, or close to, the wafer surface. An advantage of preferential etching is its magnifying effect. As shown in Fig. 2.7a, the thickness of the actual lattice defect is a few nanometers, while the etch pit it causes is measured in micrometers, as shown in Fig. 2.7b, and is therefore detectable by optical methods, as shown in Fig. 10.6f.

Etchants for defect and junction delineation are usually composed of HF and an oxidizing agent such as  $\text{HNO}_3$  [Da1, Gr4, Ka4, Ne1],  $\text{K}_2\text{Cr}_2\text{O}_7$  [Se5] or  $\text{CrO}_3$  [Si1, Je1, Sc7, Ya4, Me5]. Alkaline solutions are rarely used for defect delineation [Ma12].

An etch pit will form on a silicon surface if the dissolution rate is enhanced locally. Enhancement of the etch rate may occur for various reasons:

1. The higher chemical energy of the elastic strain field present around a dislocation.
2. A high impurity concentration caused by gettering of impurities by a dislocation.
3. An impurity that has formed a precipitate, for example a metal silicide.
4. A different doping density.
5. Bubbles sticking randomly at the surface.

Etch pit formation as a result of the factors given in 1–4 above can be used to characterize silicon materials. A summary of common defect etchants for silicon is given in Table 2.1.

Single etch pits can be inspected and counted under an optical microscope, as shown in Fig. 2.7b. The scattering of light shining onto a wafer surface under a



**Tab. 2.1** Composition and etch rates of common defect etchants for silicon.

<i>Etchant</i>	<i>Composition in parts of volume</i>			<i>r (μm/min)</i>	<i>Ref.</i>
	<i>HF (ml)</i> 50%	<i>HNO<sub>3</sub> (ml)</i> 70%	<i>CH<sub>3</sub>COOH (ml)</i> 100%		
HF	1	–	–	<0.0001	[Hu2]
John	0.15	100	–	0.018	[Jo1]
Graff	1	20	4	1.85	[Gr4]
Dash	1	3	10	3	[Dal4]
CP4	3	5	3	50–75	[Vo1]
Sirtl	1 Vol (100 ml H <sub>2</sub> O+50 g CrO <sub>3</sub> ) 1 Vol (48% HF)			3.5	[Si1]
Schimmel	1 Vol (100 ml H <sub>2</sub> O+7.5 g CrO <sub>3</sub> ) 2 Vol (48% HF)			1.7–3.2	[Sc7]
Yang	1 Vol (100 ml H <sub>2</sub> O+15 g CrO <sub>3</sub> ) 1 Vol (49% HF)			1.5	[Ya4]
Secco	1 Vol (100 ml H <sub>2</sub> O+45 g CrO <sub>3</sub> ) 2 Vol (48% HF)			1.5	[Se5]
Wright	1 Vol (90 ml H <sub>2</sub> O+45 g CrO <sub>3</sub> ) 1 Vol (180 ml H <sub>2</sub> O+6 g CuNO <sub>3</sub> ) 1 Vol (90 ml HNO <sub>3</sub> +180 ml CH <sub>3</sub> COOH+180 ml HF)			1	[Je1]
Seo	12 M HF+0.05 M KBrO <sub>3</sub>			0.15–0.5	[Se6]

small angle gives a macroscopic image of the etch pit density across the wafer. Areas of high etch pit concentration show a bright haze-like picture while areas of no defects remain dark, as shown in Fig. 10.6f.

The sensitivity of this haze method is about  $10^{12} \text{ cm}^{-3}$  for Cu and Ni [Gr4], while contamination by Fe can only be detected if the iron forms precipitates, which is only the case in wafers of a sufficiently high oxygen concentration. This property of the haze test has been exploited as a qualitative indicator of gettering efficiency of oxygen-related defects in CZ silicon [Fa2, Fa3]. Because it has been shown that there is no difference between the results obtained with Cr-based solutions and HNO<sub>3</sub>-based ones, the latter are preferred for environmental reasons [Ch1, Gr4, Ka4]. A study that compared images of polycrystalline substrates obtained by electron beam induced current (EBIC), by chemical defect etching, and by anodic etching showed that electrically active defect sites are preferentially etched under applied bias [Fo1].

Methods of characterizing the dopant distribution based on metal plating or selective chemical etching of doped layers and subsequent microscopy have been used since the early days of device fabrication [Si5, Wu2]. Despite the fact that other methods, for example secondary ion mass spectroscopy (SIMS) or spreading resistance profiling (SRP), are sensitive over a wider range and give better calibra-

tion, chemical etching is still indispensable, because it is time efficient and gives a two-dimensional image. HF- and HNO<sub>3</sub>-based solutions show an enhanced etch rate for n-type layers with doping densities in excess of 10<sup>18</sup> cm<sup>-3</sup> if compared to the etch rate on low doped n-type or p-type Si [Ne1]. For the delineation of p-type layers alkaline solutions can be used because the etch rate is significantly reduced for dopant densities in excess of 10<sup>19</sup> cm<sup>-3</sup> [Se4]. Differences in doping concentration below this level, for example moderately doped p-n junctions, can also be delineated, but these methods are electrochemical in nature and are therefore discussed in Sections 4.5 and 4.6.

## 2.6

### Selective Etching of Common Thin Film Materials

One of the properties that makes wet etchants indispensable in silicon device manufacturing today is their high selectivity for layers of different chemical composition. Most prominent are the oxide etchants based on HF. In semiconductor manufacturing thin oxide layers are commonly etched by diluted HF [Ki1]. For thicker oxide layers a buffered oxide etchant (BOE), a mixture of HF, NH<sub>4</sub>F and water is preferred. The commonly used ratio of NH<sub>4</sub>F to HF in BOE is 7 to 1. The addition of NH<sub>4</sub>F increases the etch rate of HF [Pr3] on oxide, while the etch rate on aluminum interconnects remains low. Equation (4.5) gives the overall dissolution reaction of SiO<sub>2</sub> in HF. Note that the reaction product fluosilicic acid (H<sub>2</sub>SiF<sub>6</sub>) still shows a significant etch rate for silicon dioxide [Th8]. The simple assumption that 6 moles of HF remove 1 mole of SiO<sub>2</sub> according to Eq. (4.5) is therefore not correct. The etch rates of thermal oxide for different concentrations of aqueous HF at RT are well studied [Ju1, Ki1, Ve1]. The activation energy of chemical dissolution of SiO<sub>2</sub> in 1% HF is determined to be 0.34 eV [Ki1].

Data from different authors are summarized in Fig. 2.8. Equation (2.3) is a fit of these experimental values (for  $r$  in nm min<sup>-1</sup> and  $c_{\text{HF}}$  in % of aqueous HF):

$$r_{\text{oxide}} = -0.25 + 5.5 c_{\text{HF}} + 0.047 c_{\text{HF}}^2 + 0.0065 c_{\text{HF}}^3 \quad (2.3)$$

The etch rates of other oxides such as borophosphosilicate glass (BPSG), phosphosilicate glass (PSG), tetraethylorthosilicate (TEOS), spin-on glass (SOG), anodic oxides and oxidized PS in HF are generally larger by factors of up to two orders of magnitude compared to the value for thermal oxides [So2, Bu6, Mo5]. Comprehensive reviews of SiO<sub>2</sub> etching in HF are available in the literature [Bu6, Mo6].

The etch rate of CVD silicon nitride in HF is sensitive to the details of the deposition process. Values measured for the etch rate of Si<sub>3</sub>N<sub>4</sub> deposited at 850°C are shown in Fig. 2.8. The best fit to these etch rates is found to be (for  $r$  in nm min<sup>-1</sup> and  $c_{\text{HF}}$  in % of aqueous HF):

$$r_{\text{nitride}} = 0.18 c_{\text{HF}} + 0.0013 c_{\text{HF}}^2 \quad (2.4)$$

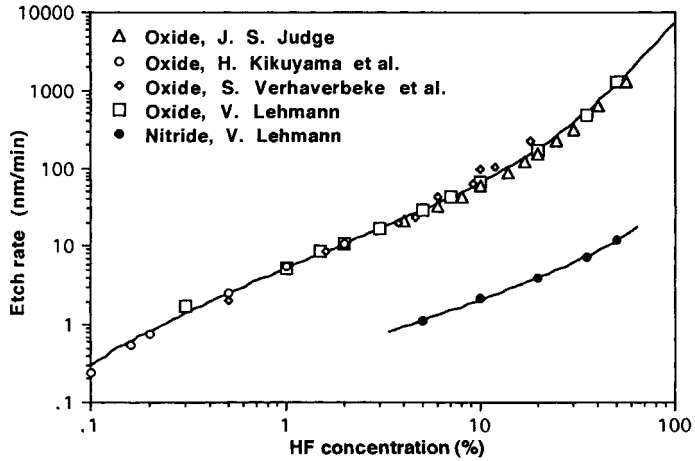


Fig. 2.8 Etch rate of thermal oxide and CVD nitride (deposited at 850°C) as a function of aqueous HF concentration at RT.

Tab. 2.2 Etch rates of common materials used in semiconductor manufacturing in the most popular wet etching solutions. Note that this table gives only a rough overview; etch rates may vary significantly depending on the details of thin film formation parameters, etchant composition, temperature and additives, e.g. surfactants.

Etch rates in $\text{nm s}^{-1}$	Thermal oxide	CVD- nitride	Undoped poly-Si	Bulk Si (100)	Aluminum
1% HF, RT	0.09	0.006	0.0005	0.0005	1.5
BOE, RT	1.70	0.02	0.0005	0.0005	0.02
30:1 $\text{HNO}_3$ :HF, RT	0.5	0.025	50	38	2
80% $\text{H}_3\text{PO}_4$ , 155°C	0.0015	0.065	0.003	0.0003	7400
10% KOH, 90°C	0.075	0.0006	22	60	2300
50% KOH, 90°C	0.2	0.0003	29	34	4300
25% $\text{NH}_4\text{OH}$ , RT	0	0	0.04	0.008	0.15

The reaction rate of silicon nitride dissolution has been found to be mainly determined by the concentrations of  $\text{F}^-$  and HF, while  $\text{HF}_2^-$  is active during dissolution of  $\text{SiO}_2$ , as discussed in Section 4.1. This enables us to engineer the etching selectivity.  $\text{Si}_3\text{N}_4$  is preferably etched at high temperatures, low HF concentrations and a low degree of ionization. The latter factor can be tuned by addition of organic solvents, like ethanol, that reduce ionization [Kn1]. At RT and HF concentrations commonly used for electrochemical etching of Si, however, the  $\text{Si}_3\text{N}_4$  etch rate is much lower than that of  $\text{SiO}_2$ . This favors  $\text{Si}_3\text{N}_4$  as a masking material for micromechanical applications and local formation of PS [Kr3]. If a high selectivity to  $\text{SiO}_2$  is desired, hot phosphoric acid is used commonly as an etchant for  $\text{Si}_3\text{N}_4$ .

An aqueous solution of 91.5%  $\text{H}_3\text{PO}_4$  heated to the boiling temperature of  $180^\circ\text{C}$  produces an etch rate of  $10 \text{ nm min}^{-1}$  for  $\text{Si}_3\text{N}_4$ ,  $0\text{--}2.5 \text{ nm min}^{-1}$  for  $\text{SiO}_2$ , and  $0.3 \text{ nm min}^{-1}$  for Si [Ge4]. Etch rates as calculated by Eqs. (2.3) and (2.4) are listed in the table in the inner back cover of this book.

Table 2.2 gives an overview of the most common materials in silicon device manufacturing and their etch rates in different etching solutions.

## 3 The Semiconductor-Electrolyte Junction

### 3.1 Basics of the Semiconductor-Electrolyte Contact

This chapter is dedicated to the basics of the silicon-electrolyte contact, with emphasis on the semiconductor side of the junction. The phenomenology of the I–V curve is discussed, together with basic charge states of semiconductor electrode like accumulation, depletion and inversion. Electrostatic and electrodynamic properties will be described, with emphasis on the direct current (DC) properties of the semiconductor electrode, while alternating current (AC) properties are discussed in Section 10.2. Details of charge exchange and mass transport as well as details of the reactions at the microscopic level are considered in Chapter 4.

The mobile charge carriers in a metal are electrons. If a metal electrode is immersed in an electrolyte electrons will accumulate or deplete at the interface. Ions are the mobile species in the electrolyte. A monolayer of ions or molecular dipoles accumulate at the interface to an electrode. This thin (0.3 nm) rigid layer is described by the Helmholtz model. Any charge transfer across this layer involves a chemical reaction. If the available energy, or the applied bias respectively, is too low to initiate this reaction, the charge carriers in the electrode and the dipoles in solution accumulate at the interface, without being separated by a dielectric. The capacitance of this double layer is of the order of  $0.1 \text{ F m}^{-2}$  for metal electrodes. Supercapacitors are an application of this charge separation without a dielectric.

If the metal electrode is replaced by a semiconducting electrode the number of free charge carriers is reduced from values in the order of  $10^{23} \text{ cm}^{-3}$  to much lower values, depending on doping density. Charging of a semiconductor interface immersed in an electrolyte may be due to majority charge carriers, ionized dopants, or minority charge carriers. The corresponding charge states are called accumulation, depletion and inversion, respectively. In contrast to electrons and holes, which are free charge carriers, the ionized doping atoms are not mobile. They therefore form SCRs that may extend up to several tens of microns into the bulk of the electrode, depending on doping concentration, as described by Eq. (1.2). The thickness of the accumulation and inversion layers in contrast is in the order of a nanometer, because they are due to free charge carriers. Note that the ionized doping atom in a p-type semiconductor is negatively charged, for example

$B^-$ , while for an n-type semiconductor the reverse is true. An analog to the SCR in the semiconductor is an extended layer of ions in the bulk of the electrolyte, which is present especially in the case of electrolytes of low concentration (typically below  $0.1 \text{ mol l}^{-1}$ ). This diffuse double layer is described by the Gouy-Chapman model. The Stern model, a combination of the Helmholtz and the Gouy-Chapman models, was developed in order to find a realistic description of the electrolytic interface layer.

Now we have discussed the electrostatics dealing with where the charges 'stay', but how about the electrodynamics, how do they 'move' in space and energy? In contrast to a semiconductor where a current is caused by the movement of free electrons and holes, an electrolyte can be understood as a phase through which charge is carried by the movement of ions. Hence the mobilities of electrons or holes in silicon ( $\mu_e, \mu_h > 100 \text{ cm}^2 \text{ V}^{-1} \text{ s}^{-1}$ ) and ions in solutions ( $\mu_{H^+} = 36.2 \times 10^{-4} \text{ cm}^2 \text{ V}^{-1} \text{ s}^{-1}$ ,  $\mu_{OH^-} = 20.6 \times 10^{-4} \text{ cm}^2 \text{ V}^{-1} \text{ s}^{-1}$ ,  $\mu_{F^-} = 5.7 \times 10^{-4} \text{ cm}^2 \text{ V}^{-1} \text{ s}^{-1}$ ) differ by orders of magnitude. However, the electrical conductivities of a common electrolyte and a moderately doped silicon electrode are of the same order of magnitude, because the ratio of density of charge carriers in an electrolyte ( $10^{21} \text{ cm}^{-3}$  for  $1 \text{ mol l}^{-1}$ ) and in moderately doped silicon ( $10^{14}$ – $10^{17} \text{ cm}^{-3}$ ) is about the inverse of the ratio of mobilities.

Any transfer of a charge between the electrode and the host ion in the electrolyte is accompanied by a chemical reaction. If an electron moves from the electrode to the solution, the host ion is reduced. If it moves in the other direction the host ion is oxidized. The electron is a term used in physics as well as chemistry. This is in contrast to the concept of a hole, a positive charge carrier, which describes the behavior of an electron vacancy in the periodic potential of a semiconductor crystal. This term, however, loses its meaning at the interface to the electrolyte. Concerning the chemical reaction, any hole crossing the interface can be replaced by an electron going in the other direction. Energetically, however, there is a difference, because the injection of an electron from the host ion into the silicon conduction band (CB) requires an energy 1.1 eV larger than that required for a hole in the valence band (VB) going in the other direction. In many cases the interaction of holes with the electrode surface can be understood if two holes at the interface are replaced by one broken bond of a surface atom.

Not only the movement of charges in space but also changes in energy occur in different ways in the semiconductor and the electrolyte. The well established semiconductor band model where an excited electron may jump from one energy level to another is not applicable to an electrolyte. In a solution the energy levels itself fluctuate in energy due to thermal fluctuations of the surrounding solvent dipoles, carrying the electron with it. A detailed description of the latter model is given in the literature [Mo2, Ge1, Ge3].

The current-voltage (I–V) characteristic of a semiconductor-electrolyte contact is determined by both the semiconducting nature of the electrode, as well as by the ionic and molecular species present in the electrolyte. The current density at the electrode for a certain potential is limited by the reaction kinetic at the interface, or by the charge supply from the electrode or the electrolyte.

If the charge transfer is limited by charge supply from the silicon electrode the basic I-V curve of the silicon-electrolyte junction is very similar to that of a silicon-metal junction, a Schottky diode, as shown in Fig. 3.1 a and b. A p-type electrode, for example, is reversely biased in the cathodic regime. Therefore the current is minimal in the dark and increases upon illumination or for a bias high enough to initiate breakdown (Fig. 3.1 a). In the anodic regime the junction is under forward conditions and the current is described by the diode equation. The case of an n-type electrode is only different insofar as the forward and the reverse regime are exchanged in the I-V curve, as shown in Fig. 3.1 b.

A Schottky diode is always operated under depletion conditions; flat-band condition would involve giant currents. A Schottky diode, therefore, models the silicon electrolyte interface only accurately as long as the charge transfer is limited by the electrode. If the charge transfer becomes reaction-limited or diffusion-limited, the electrode may as well be under accumulation or inversion. The solid-state equivalent would now be a metal-insulator-semiconductor (MIS) structure. However, the I-V characteristic of a real silicon-electrolyte interface may exhibit features unlike any solid-state device, as

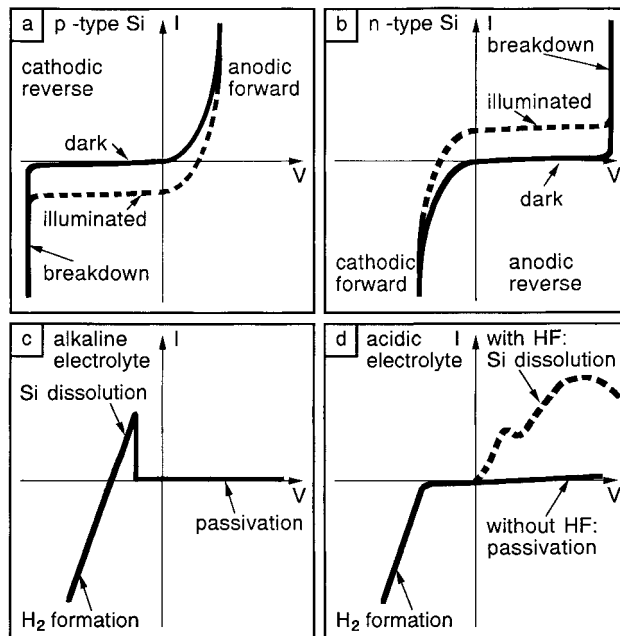


**Fig. 3.1** The I-V characteristic of (a) a p-type and (b) an n-type silicon electrode under the assumption that the current is dominated by the properties of the semiconductor and is not limited by interface reactions or by diffusion in the electrolyte. (c) The characteristic I-V curve in an alkaline electrolyte under the

assumption that the current is not limited by charge supply from the electrode (which is the case for a highly doped or strongly illuminated electrode). (d) The I-V curve under the same assumption as in case (c) is shown for an acidic electrolyte without (full line) and with fluoride (broken line).

shown for example in Fig. 4.7. This is due to details of the chemical reaction at the interface, like for example the formation of an anodic oxide film for a certain bias or current density. In Fig. 3.1 c and d the basic I–V curve in alkaline and acidic electrolytes respectively are shown for a silicon substrate doped in excess of  $10^{19} \text{ cm}^{-3}$ . The same characteristics are observed if low doped substrates are strongly illuminated. Under such conditions the blocking effect of the reversed biased Schottky diode is lost and the basic characteristic of the I–V curve is the same for all silicon substrates independent of doping type and density. This is a consequence of the fact that the chemical reactions at the silicon electrode are independent of the minute traces of dopants. However, while the chemical dissolution reaction is not sensitive to doping density the Fermi energy is. As a result, there is a significant potential shift of the I–V curves and the open circuit potentials with doping density, as shown in Fig. 3.3.

The I–V characteristic of a real silicon electrode is usually superpositions of the basic potentiostatic curves shown in Fig. 3.1 a–d. The galvanostatic I–V curves are deductible in many cases from the potentiostatic ones. This holds true for a constant potential or a very slow scan of the applied potential, for fast changes of potential or current, however, the I–V curve may show transient contributions. Transient effects at the silicon electrodes can be due to chemical or capacitive effects as well as to changes of the interface morphology for example by pore formation. Chemically caused effects are usually slow and current or bias show transients on a time scale in the order of seconds. The most prominent example for such effects are electrochemical oscillations observed at silicon electrodes anodized in HF, as discussed in Section 5.5. Transient currents due to oxide passivation and electron injection during oxide dissolution are shown in Fig. 4.14. Pore formation does significantly change the surface area and morphology of the electrode and it thereby affects the I–V characteristic. The reverse current of an n-type electrode, for example, increases by orders of magnitude due to formation of mesopores of the breakdown type, as discussed in Section 8.4. However, even hydrogen bubbles sticking to the electrode surface are found to generate a considerable noise pattern in the I–V curves. The charge values involved in charging interfacial capacities, due to the SCR, an anodic oxide or the Helmholtz layer, are commonly much smaller than the charges exchanged during chemical reactions, such as anodic oxide formation. The measurement of interfacial capacities is discussed in Section 10.2.

In the next section the charge states of the electrode and the electrochemical reactions are discussed for acidic, especially fluoride-containing electrolytes followed by a section dealing with alkaline electrolytes.

### 3.2

#### The I–V Characteristics of Silicon Electrodes in Acidic Electrolytes

In this section the I–V characteristic of a silicon electrode in acidic, and specially hydrofluoric electrolytes is discussed with emphasis on the different charge states of the semiconductor. The accompanying chemical reactions are briefly mentioned, but are discussed in detail in Chapter 4.



While the cathodic characteristic of the I–V curve is dominated by hydrogen reduction and therefore not very sensitive to the kind of ions present in an aqueous electrolyte, the anodic part is. If a silicon electrode is anodized in an acidic electrolyte that is free of fluoride, a passivating oxide layer is formed. Details of the formation and the properties of anodic oxides are given in Chapter 5. An I–V curve in the common sense does not exist for such electrolytes, because a certain anodic bias does not correspond to a constant current density, but rather to a constant charge of a few  $\text{mAs cm}^{-2}$  which is consumed during the formation of an oxide layer. In this respect there is no current-voltage curve, but a charge-voltage curve for the anodic regime, as shown in Fig. 5.1. Only for short anodization times and small current densities in the  $\mu\text{A cm}^{-2}$  range the I–V curve is not dominated by oxide formation but by the semiconducting properties of the electrode [Ch10].

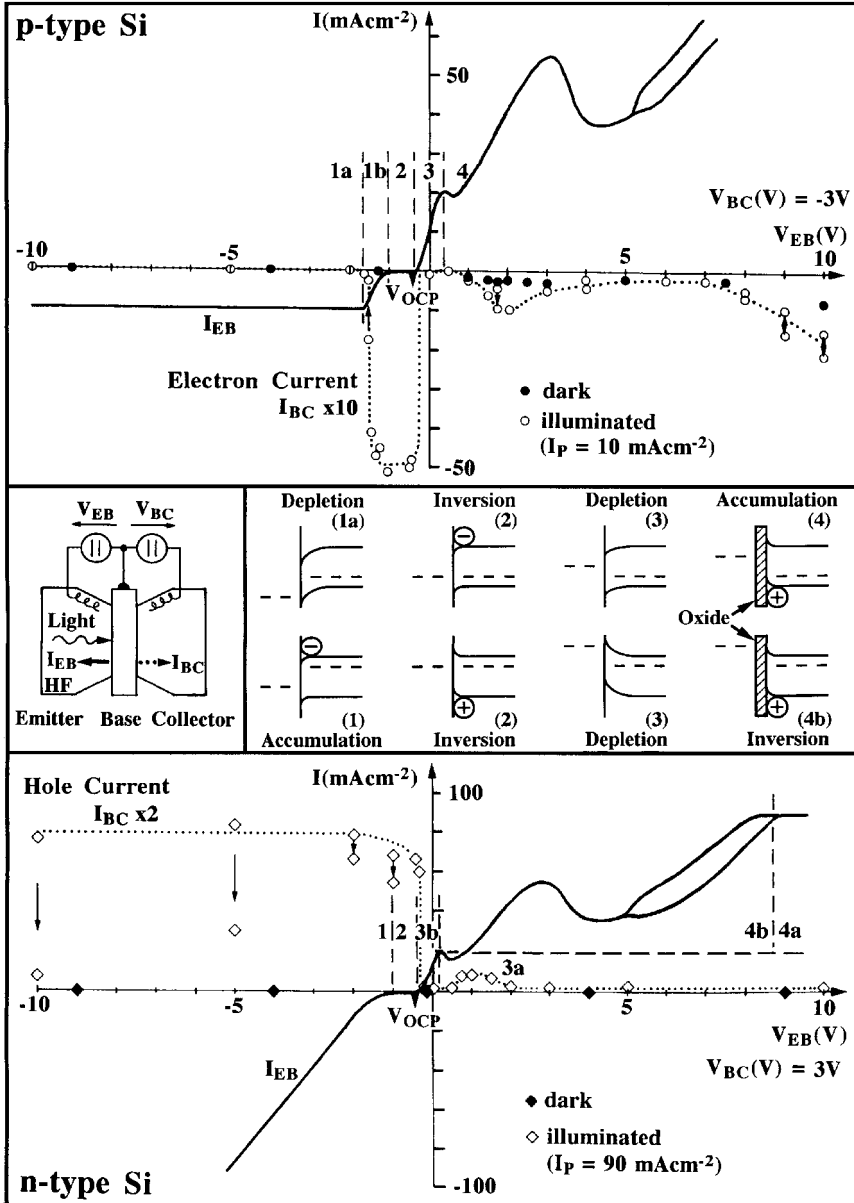
A passivating oxide is formed under sufficiently anodic potentials in HF, too. However, there are decisive differences to the case of alkaline and fluoride-free acidic electrolytes. For the latter electrolyte the steady-state current density prior to passivation is zero and it is below  $1 \text{ mA cm}^{-2}$  for alkaline ones, while it ranges from  $\text{mA cm}^{-2}$  to  $\text{A cm}^{-2}$  in HF. Furthermore, in HF silicon oxide formation does not lead to passivation, because the anodic oxide is readily etched in HF. This gives rise to an anodic I–V curve specific to HF, it shows two current maxima and two minima and an oscillatory regime, as for example shown in Fig. 4.7.

There are several methods to investigate the charge states of a semiconductor electrode, for example high-frequency resistometry (HFR) [Ot1]. Below a transistor-like set-up, as shown in the inset of Fig. 3.2, will be discussed because it shows in an exemplary way the similarities and differences of solid-state junctions and liquid junctions.

The electrochemical set-up, as depicted in the inset of Fig. 3.2, consists of a 0.5 mm thick silicon slice in an electrolytic double cell, as shown in detail in Fig. 1.10. This establishes a transistor-like configuration with the backside electrolyte as collector, the front side electrolyte as emitter and the silicon electrode as base in between. However, this ‘transistor’ is not operated in a common amplifying transistor circuit. A constant reverse bias  $V_{\text{BC}}$  of 3 V is applied between collector and base in order to collect the minority carriers diffusing through the base, while the emitter-base voltage is switched from  $V_{\text{OCP}}$  to values of  $V_{\text{EB}}$  between  $-10 \text{ V}$  and  $+10 \text{ V}$  ( $I_{\text{EB}}$  according to the solid line in Fig. 3.2). Prior to switching the electrode has been cleaned by electropolishing to ensure a virgin interface of the electrode free of contaminants or PS. The measurements are performed with and without illumination of the front electrode. The IR light of the light source was blocked by a filter, to insure that minority carriers are only generated in the vicinity of the front surface. Note that the base-collector junction could as well be a solid-state junction, for example a Schottky junction. Only the electrolytic nature of the emitter-base junction is probed by this set-up.

If minority carrier current ( $I_{\text{BC}}$ , dotted line, symbols in Fig. 3.2) is detected at the collector, it can be concluded that the emitter is no sink for minorities. The absolute value of  $I_{\text{EB}}$  depends not only on the charge state of the emitter-base junction and surface recombination velocity, but as well on bulk diffusion length and on sample thickness. However, the latter two parameters are constants for a given sample.

Four different regimes of the I-V curve for moderately doped silicon electrodes in an HF electrolyte are shown in Fig. 3.2. These regimes will now be discussed in terms of the charge state of the electrode, the dependence on illumination conditions, the charge transfer, the mass transport, and accompanying chemical reactions. Transient effects are indicated in Fig. 3.2 by a symbol with an arrow.



### Regime 1

This is the regime of cathodic currents. The silicon atoms of the electrode do not participate in the chemical reaction in this regime. An n-type electrode is under forward bias and the current is caused by majority carriers (electrons). The fact that photogenerated minority carriers (holes) are detectable at the collector indicates that the front is under flat band or accumulation. A decrease of  $I_{BC}$  with cathodization time is observed. As Fig. 3.2 shows, the minority carrier current at the collector after switching to a cathodic potential is identical to that at  $V_{OCP}$  in the first moment, but then it decreases within seconds to lower values, as indicated by arrows in Fig. 3.2. This can be interpreted as an increase of the surface recombination velocity with time under cathodic potential. It can be speculated that protons, which rapidly diffuse into the bulk of the electrode, are responsible for the change of the electronic properties of the surface layer [Al7]. However, any other effect sufficient to produce a surface recombination velocity in excess of  $100 \text{ cm s}^{-1}$  would produce similar results.

A p-type electrode shows only a small reverse current density in the cathodic regime, if it is kept in the dark as shown in detail in Fig. 4.11. If defects are present in the electrode surface, this small dark current increases by orders of magnitude [Wa4]. If  $V_{EB}$  is increased breakdown of the junction is observed, at a bias, which depends on the doping density of the substrate, as displayed in the figure of the front inner cover of this book. If the electrode is illuminated a photocurrent is observed and the number of electrons transferred to the electrolyte per absorbed photon is one, if losses by recombination in the bulk of the electrode are neglected, as shown in Fig. 4.13. On the other hand, current multiplication effects, as observed for anodized n-type electrodes, are not present in the cathodic regime. Under illumination two different cases can be distinguished. In one case the bias is sufficiently cathodic to keep the front side of the electrode under depletion and so a cathodic emitter current proportional to the photon flux and independent of applied bias is generated. In this case no electrons are detected at the collector (region 1a in Fig. 3.2). In the other case the bias is closer to  $V_{OCP}$  and not all photogenerated electrons are immediately consumed in the cathodic reaction. Electrons now accumulate and it can be concluded that the electrode is under inversion or in flat-band condition. A certain fraction of the photogenerated elec-

**Fig. 3.2** The inset (center left) shows the electrochemical double-cell set-up with the two applied potentials  $V_{EB}$  and  $V_{BC}$ , which constitute a circuit similar to a solid-state bipolar transistor. The emitter-base current  $I_{EB}$  (full line) of a moderately doped p-type electrode illuminated corresponding to a photocurrent of  $10 \text{ mA cm}^{-2}$  is shown in the upper part of the figure. Below  $I_{EB}$  is shown for an n-type electrode illuminated with an intensity corresponding to  $90 \text{ mA cm}^{-2}$ . The base-

collector current  $I_{BC}$  for a constant reverse bias of  $U_{BC} = 3 \text{ V}$  is monitored without (filled symbols) and with illumination of the emitter-base junction (open symbols, dotted line as a guide to the eye). For each regime of the  $I_{EB}$ – $V_{EB}$  characteristic (indicated by numbers and broken lines) the proposed band diagram is shown (center right) for the illuminated case assuming a quasi Fermi level to be present in the electrolyte.

trons diffuse through the base and can be detected at the collector (region 1b in Fig. 3.2).

### Regime 2

This is the region of the OCP. For an HF electrolyte without an oxidizing agent the electrode is inert, because no chemical reaction occurs at the front (emitter) at this potential range. The OCP depends on illumination condition, substrate doping density, illumination condition, HF concentration and DOC [Ot1]. For moderately doped Si substrates in 5% aqueous HF the OCP is usually close to  $-0.6$  V versus SCE in the dark. Under illumination a small negative (cathodic) shift to  $-0.64$  versus SCE is observed for n-type electrodes, while the OCP for p-type substrate shifts significantly in positive (anodic) direction to  $-0.2$  V versus SCE [Be9].

Because the emitter-base current is zero in this regime, the electrode behaves similar to an MIS contact. It can be assumed that the number of thermally generated minority carriers is not sufficient to produce inversion; the electrode is therefore under depletion if kept in the dark. Under illumination the generation rate is high and minority carriers accumulate at the emitter because there is no chemical reaction path for them to enter the electrolyte, at OCP. Therefore the emitter is under inversion or under flat-band conditions. Under such conditions the collector shows a high and stable minority charge carrier collection efficiency for n-type as well as p-type doping. This property of the electrode under OCP is exploited for bulk diffusion length measurements as discussed in Section 10.3. A prerequisite of the high collection efficiency is a very low surface recombination velocity in the order of  $1 \text{ cm s}^{-1}$ , which has been reported for a silicon surface in contact with HF at OCP [Ya1]. By using different electrolytes, the presence of an inversion layer and not a reduced density of electrical trap sites on the silicon surface has been found to be primarily responsible for these low values of surface recombination velocity [Ro9].

### Regime 3

This is the regime of anodic current densities below  $J_{PS}$ . A hole approaching the interface initiates the divalent electrochemical dissolution of a silicon surface atom at the emitter. The dissolution proceeds under formation of  $\text{H}_2$  and electron injection, as shown in Fig. 4.3. The formation of PS structures is confined to this region.

Let us now consider the charge state of the electrode. The emitter is positively biased. A p-type silicon electrode is therefore under forward conditions. If the logarithm of the current for a forward biased Schottky diode is plotted against the applied potential (Tafel plot) a linear dependency with 59 meV per current decade is observed for moderately doped Si. The same dependency of  $I_{EB}$  on  $V_{EB}$  is observed at a silicon electrode in HF for current densities between OCP and the first current peak at  $J_{PS}$ , as shown in Fig. 3.3 [Ga1, Ot1]. Note that the slope in Fig. 3.3 becomes less steep for highly doped substrates, which is also observed for highly doped Schottky diodes. This, and the fact that no electrons are detected at the collector, indicates that the emitter-base interface is under depletion. This interpretation is sup-

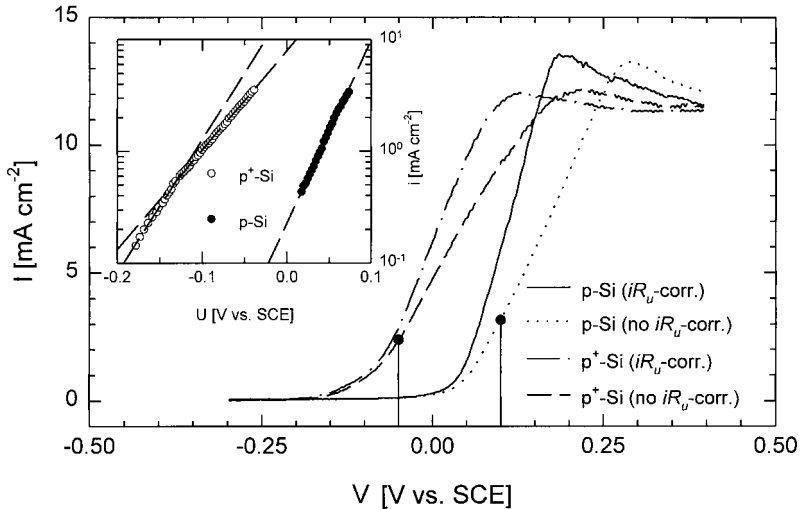


**Fig. 3.3** The I–V curves, as recorded and compensated for ohmic losses ( $iR_{\text{cor}}$ ), of Si electrodes in aqueous HF (1M HF, 0.5M  $\text{NH}_4\text{Cl}$ ) are found to shift cathodically with increasing p-type doping density. In a  $V$  versus  $\log(i)$  plot (inset) a p-type electrode (1  $\Omega$  cm,

full circles) shows a slope of 59 mV per current decade, while a p<sup>+</sup>-type electrode (5 m $\Omega$  cm, open circles) shows a slope increasing from 80 to 115 mV per current decade. After [Ot1].

ported by capacitance measurements as well as IR measurements [Ga1, Se7, Oz2, Oz4]. The formation of PS shows little effect on the basic I–V characteristic. However, a transient current-time behavior after a potential step from OCP to a potential in region 3, due to pore initiation has been observed [Po3].

As shown in Fig. 3.3, the I–V curve in this regime shows a cathodic potential shift and a slight change of slope, if the doping density is increased. Compared to p-type substrates the I–V curve of p<sup>+</sup> is shifted cathodically by about 0.1 V and that of n<sup>+</sup> by about 0.2 V [Ga1, Zh5]. This shift can be exploited for etch stops and selective formation of PS, as discussed in Section 4.5.

An n-type electrode is under reverse bias in this anodic regime, and so only a small dark current density in the order of a few  $\mu\text{A cm}^{-2}$  is observed, as shown in Fig. 4.11. The dark current increases by orders of magnitude if the breakdown field strength is reached at the electrode surface or at a pore tip present in the electrode, as discussed in Section 8.4.

If the n-type electrode is illuminated, no holes are observed at the collector in regime 3. This and the Tafel characteristic of  $I_{\text{EB}}$  are indications of a depletion of the emitter-base junction. Depletion is obvious for regime 3a, because  $V_{\text{EB}}$  generates a large SCR sufficient to collect all photogenerated holes and to drive them to the emitter. However, in region 3b no holes are detected at the collector, too. This is in stark contrast to the corresponding region 1b of the p-type electrode, where electrons not consumed at the emitter are allowed to diffuse through the base to

the collector. A high value of surface recombination velocity for photogenerated holes at n-type electrodes in regime 3b would explain this behavior. A similar high surface recombination velocity also appears to be present at the p-type electrode in regime 3, because electrons, known to be injected during the divalent dissolution reaction, as shown in Fig. 4.3, are not detected at the collector.

If  $V_{EB}$  is increased,  $I_{EB}$  increases and the current density at the electrode eventually becomes equal to  $J_{PS}$ . It has been speculated that this first anodic current peak is associated with flat-band condition of the emitter-base junction. However, data of flat-band potential of a silicon electrode determined from Mott-Schottky plots show significant scatter, as shown in Fig. 10.3. However, from C-V measurement it can be concluded that all PS formation occurs under depletion conditions independent of type and density of doping of the Si electrode [Ot1].

#### Regime 4

For anodic current densities above  $J_{PS}$  tetravalent electrochemical dissolution of the electrode is observed. The chemical reaction proceeds in two steps, first the electrode is anodically oxidized, and then the oxide is chemically dissolved in HF. The overall reactions, as given in Eqs. (4.2) and (4.5), show that the dissolution of one silicon atom consumes four holes. In regime 4 the current density exceeds  $J_{PS}$  and the simple diode behavior disappears. The I-V characteristic shows a more complex structure with another current maximum and a region of current oscillations, the latter is indicated by a splitting of the solid line in Fig. 3.2. These features of the I-V curve are related to the properties of a thin anodic oxide present on the electrode surface, details are discussed in Chapter 5. The dependence of  $I_{EB}$  on electrolyte convection in regime 4 indicates that the current is not limited by charge supply from the electrode any more, but by diffusion in the electrolyte. The solid-state analog for this regime would be an MIS structure with a leaky insulator.

For a bias positive of the flat-band potential holes accumulate at the interface of a p-type electrode. These free holes produce a sizable absorption at wavenumbers below  $2000\text{ cm}^{-1}$ , which offers another way to measure the charge state of the electrode. The charge state of p-type electrodes in an HF electrolyte has been probed by such *in situ* IR absorption measurement [Oz2, Oz4]. Negligible absorption at negative potentials and below the first current peak at  $J_{PS}$  support the observation that the electrode is in depletion in regime 3. At positive potentials between  $J_{PS}$  and the second current peak at  $J_3$  (Fig. 4.7) the free-carrier absorption remains weak. This has been ascribed to an oxide of low blocking capability covering the electrode. For more positive potentials, at and above the second current peak, the absorption increases rapidly, indicating significant accumulation due to a dense oxide of low defect density. In the regime of current oscillations the free-carrier density is found to oscillate, too. This is shown in Fig. 5.12.

For the p-type substrate a significant number of electrons are collected at the backside, as shown in the top part of Fig. 3.2. This is true not only for the illuminated p-type electrode but also if the electrode is kept in the dark, which indicates that electrons are injected during the tetravalent dissolution reaction. In the regime of oscillations the electron injection current is found to oscillate, too [Ca10].

For higher  $V_{EB}$  ( $>7$  V) electron injection increases and  $I_{BC}$  oscillates when  $I_{EB}$  does. Capacitance measurements indicate a surface charge of holes at the front, this means a p-type electrode is under accumulation.

A current of photogenerated holes observed in regime 4 at the collector at low  $V_{EB}$  of about 1 V for an illuminated n-type substrate indicates that no significant SCR is present at the front side; the n-type electrode is in inversion. If the bias is increased this current disappears indicating an SCR or an increased surface recombination velocity at the emitter. In regime 4a all photogenerated holes are consumed by  $I_{EB}$ . Breakdown of the junction in regime 4 does not lead to pore formation.

Note that in contrast to a solid-state transistor, hole injection from the HF electrolyte into the base is not observed independent of  $V_{EB}$  (full diamonds in Fig. 3.2). Hole injection becomes sensible if an oxidizing agent is added to the HF, as shown in Fig. 4.12.

### 3.3

#### The I–V Characteristics of Silicon Electrodes in Alkaline Electrolytes

There are fewer studies devoted to the electrochemistry of silicon in alkaline electrolytes than is the case for HF. This can partly be ascribed to the fact that pore formation is not observed in alkaline electrolytes, which limits the field of applications. This section gives a brief overview of the characteristic features of I–V curves of silicon electrodes in alkaline electrolytes.

In contrast to acidic electrolytes, chemical dissolution of a silicon electrode proceeds already at OCP in alkaline electrolytes. For cathodic potentials chemical dissolution competes with cathodic reactions, this commonly leads to a reduced dissolution rate and the formation of a slush layer under certain conditions [Pa2]. For potentials slightly anodic of OCP, electrochemical dissolution accompanies the chemical one and the dissolution rate is thereby enhanced [Pa6]. For anodic potentials above the passivation potential (PP), the formation of an anodic oxide, as in the case of acidic electrolytes, is observed. Such oxides show a much lower dissolution rate in alkaline solutions than the silicon substrate. As a result the electrode surface becomes passivated and the current density decreases to small values that correspond to the oxide etch rate. That the current density peaks at PP in Fig. 3.4 are in fact connected with the growth of a passivating oxide is proved using *in situ* ellipsometry [Pa2]. Passivation is independent of the type of cation. Organic compounds like hydrazin [Su1], for example, show a behavior similar to inorganic ones, like KOH [Pa8]. Because of the presence of a passivating oxide the current peak at PP is not observed for a reverse potential scan.

The potential separation between PP and OCP, as well as the anodic current density corresponding to PP, increase with temperature. Current density values in the order of  $100 \mu\text{A cm}^{-2}$  for example are found for a (100) Si electrode in 2 M KOH at RT. This current increases by one order of magnitude if the temperature is increased from RT to  $60^\circ\text{C}$  [Pa5]. A similar temperature dependence is observed for chemical etching of Si in KOH, as shown in Fig. 2.2a.

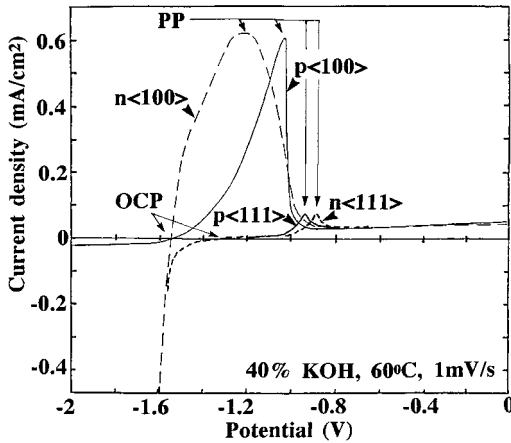


**Fig. 3.4** The electrochemical I–V characteristic of n-type and p-type silicon electrodes of (100) and (111) orientation in 40% aqueous KOH solution at 60°C in the dark. The potential is scanned from cathodic to anodic at a sweep rate of  $1 \text{ mV s}^{-1}$ . Redrawn from results of [Sm6].

The anodic current density corresponding to PP shows no significant dependence on doping for n-type and moderately doped p-type Si electrodes. This indicates that the anodic currents at n-type electrodes are caused by electron injection [Pa6, Xi1]. If the p-type doping density approaches  $10^{19} \text{ cm}^{-3}$  the PP current density becomes reduced and for  $10^{20} \text{ cm}^{-3}$  the passivation peak disappears. This has been interpreted as a passivating oxide being already present on highly p-doped electrodes at OCP. That the separation of a few hundred mV between the PP and the OCP decreases with increasing doping density and becomes negligible at p-type doping densities in excess of  $10^{20} \text{ cm}^{-3}$ , supports this interpretation [Fa7, Pa5, Sm6].

As expected from the anisotropy of chemical etching of Si in alkaline solutions, the electrochemical dissolution reaction shows a strong dependence on crystal orientation. For all crystal orientations except (111) a sweep rate independent anodic steady-state current density is observed for potentials below PP. For (111) silicon electrodes the passivation peak becomes sweep rate dependent and corresponds to a constant charge of  $2.4 \pm 0.5 \text{ mC cm}^{-2}$  [Sm6]. OCP and PP show a slight shift to more anodic potentials for (111) silicon if compared to (100) substrates, as shown in Fig. 3.4.

It has been speculated that there is a common origin of the reduced chemical etch rate for (111) oriented silicon substrates and for highly p-type doped substrates. But the electrochemical investigations discussed above indicate that the passivation of highly doped p-type Si can be ascribed to an oxide film already present at OCP, while no such oxide film is observed on (111) silicon below PP. This supports models that ascribe the reduced chemical etch rate on (111) planes to a retarded kinetic for Si surface atoms with three backbonds, present at (111) interfaces [Gl1, Al2], as discussed in Section 4.1.

The charge states of the silicon electrode in alkaline electrolytes have not been investigated in detail. It can be assumed that the electrode represents an MIS structure above PP, while it behaves similarly to a Schottky junction for potentials below PP.



## 4

# The Electrochemical Dissolution of Silicon

### 4.1

#### Electrochemical Reactions

This section and the next are dedicated to the basics of the silicon-electrolyte contact with focus on the electrolyte side of the junction and the electrochemical reactions accompanying charge transfer. The current across a semiconductor-electrolyte junction may be limited by the mass transport in the electrolyte, by the kinetics of the chemical reaction at the interface, or by the charge supply from the electrode. The mass transport in the bulk of the electrolyte again depends on convection as well as diffusion. In a thin electrolyte layer of about a micrometer close to the electrode surface, diffusion becomes dominant. The stoichiometry of the basic reactions at the silicon electrode will be presented first, followed by a detailed discussion of the reaction pathways as shown in Figs. 4.1–4.4.

#### 4.1.1

##### Overall Reactions

While the electrochemical reaction in the cathodic regime is similar for most commonly used aqueous electrolytes, the anodic reaction depends on composition and pH of the electrolyte.

In the cathodic regime the silicon atoms of the electrode do not participate in the chemical reaction. Therefore, an n-type or a strongly illuminated p-type silicon electrode behave like a noble metal electrode and hydrogen evolution or metal plating reactions are observed. For the case of an aqueous electrolyte free of metal ions the main reaction is electrochemical hydrogen evolution according to:



It is shown that the rate-limiting step in the photoelectrochemical evolution of hydrogen in an HF electrolyte is linearly dependent on the excess electron concentration at the surface of the p-type silicon electrode. The rate of this step does not depend on the electrode potential and the  $H^+$  concentration in the solution, but is sensitive to the surface pretreatment [Sc11]. The plateau in the I–V curve, slightly

cathodic of OCP, as shown in Fig. 3.2 (regime 2) can be ascribed to the hydrogen evolution overpotential. This assumption is supported by the fact that upon addition of  $\text{H}_2\text{O}_2$  to the electrolyte a convection-dependent cathodic current density can be observed in this regime.

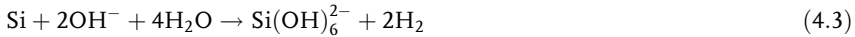
Under cathodic bias hydrogen or deuterium may be incorporated in p-type electrodes in concentrations of up to the doping level and depth in the order of a micrometer. In the hydrogenated region the acceptors become passivated, causing a dramatic increase in resistivity [Mi5]. Acceptor compensation is also observed during CMP if copper ions are present in the slurry [Pr2]. Since precleaning in the electrochemical investigations, mentioned above [Mi5], was also performed in a copper-containing solution it can be speculated that the presence of Cu is a prerequisite for acceptor compensation.

Under anodic potentials in acidic electrolytes free of fluoride, silicon is passivated by formation of an anodic oxide under consumption of four holes ( $\text{h}^+$ ), according to the reaction:



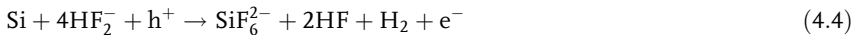
Details of the formation process and the properties of anodic oxides are discussed in Chapter 5.

In alkaline electrolytes silicon is dissolved chemically at OCP. From the observed stoichiometric ratio of approximately  $2\text{H}_2/\text{Si}$ , a overall reaction can be derived [Fi1]:



For moderate anodic potentials the dissolution rate becomes enhanced and the ratio of  $\text{H}_2/\text{Si}$  is reduced due to the contribution of the electrochemical reaction path [Pa6]. At the electrode surface Si-H as well as Si-OH groups are present. For higher concentrations of the silicate monomer produced by reaction (4.3) silicate polymerization takes place [Ni6]. Passivation takes place for more anodic potentials, due to formation of Si-O-Si bonds according to reaction (4.2).

In acidic electrolytes with fluoride, silicon is stable at OCP, while electrochemical dissolution takes place for anodic potentials. For anodic current densities below the critical current density  $J_{\text{PS}}$  PS is formed and the electrolyte-electrode interface is found to be Si-H covered. Species active in the dissolution process are HF,  $(\text{HF})_2$  and  $\text{HF}_2^-$ . A dissolution reaction proposed for this regime is:



If the anodic potential is increased, the current density becomes larger than  $J_{\text{PS}}$  and dissolution occurs via an intermediate anodic oxide film. Hence the reaction can be separated into electrochemical oxide formation according to reaction (4.2) and chemical dissolution of the oxide due to HF,  $(\text{HF})_2$  or  $\text{HF}_2^-$  [So2]:



The overall reactions described above give no information about the actual reaction pathways on the atomic scale. Models proposed for the dissolution pathways in alkaline and in hydrofluoric electrolytes are discussed below.

#### 4.1.2

#### Chemical Dissolution of Si in Alkaline Solutions

The common etching behavior of different alkaline solutions, as discussed in Section 2.3, is attributed to  $\text{H}_2\text{O}$  and  $\text{OH}^-$  being the active species in the dissolution process while the cations play a minor role [Fi1, Pa2, Se3]. This interpretation is supported by the fact that the etch rate of organic alkaline liquids approaches zero if no water is added. Furthermore, anisotropic etch rates as high as  $0.2 \mu\text{m min}^{-1}$  have been observed in pure water under certain conditions (2.54 GHz microwaves,  $183^\circ\text{C}$ , 37 bar) [Dz1]. A model for the dissolution process of silicon in alkaline media that is in accordance with the characteristics mentioned above is shown in Fig. 4.1. The silicon (100) surface is assumed to be hydrogen terminated. The dissolution is initiated by nucleophilic attack of  $\text{OH}^-$ , as shown in step 1 of Fig. 4.1. An Si–OH bond is established under formation of  $\text{H}_2$ . In step 2 the second Si–H bond of the Si surface atom is replaced by Si–OH under formation of another  $\text{H}_2$ . The attraction of electrons by the ligands now weakens the silicon backbonds sufficiently that water can break these bonds as shown in steps 3 and 4 of Fig. 4.1. The silicon surface atom is dissolved with  $\text{SiO}_2(\text{OH})_2^{2-}$  being the final etching product and the surface remains covered with Si–H bonds [Pa4]. If step 1 is rate limiting the silicon surface will be hydrogen passivated and hydrophobic. Whereas a rate limitation by step 3 will lead to a silanol-covered, hydrophilic surface. As shown in Fig. 2.1, the highest degree of hydrophobicity has been observed at  $\text{pH}=11$ , indicating the highest concentration of Si–H surface groups. Under anodic potentials below PP the alkaline dissolution process is enhanced as a result of an electrochemical contribution. While the dissolution rate increases, the ratio of  $\text{H}_2$  per dissolved Si decreases. Significant anodic currents observed for n-type electrodes kept in the dark indicate electron injection during anodic dissolution [Pa6].

In the frame of this model the anisotropy of alkaline etchants, the low etch rate observed for (111) oriented silicon surfaces, can be interpreted as an insufficient polarization of three silicon backbonds by only one Si–OH surface bond that can

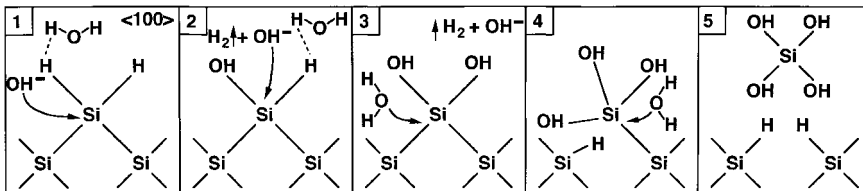


Fig. 4.1 Reaction scheme proposed for the chemical dissolution of (100) oriented silicon surfaces in alkaline solutions.

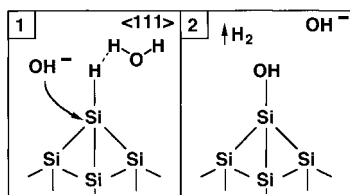


Fig. 4.2 The chemical dissolution rate of (111) oriented silicon surfaces in alkaline solutions is negligible as a result of insufficient polarization of the Si backbonds by only one OH group.

be established on a monohydride surface, as shown in Fig. 4.2. Whereas two Si backbonds are polarized by two Si–OH bonds for the dihydride surfaces present for (100) or (110) surfaces, as shown in Fig. 4.1. The weak polarization induced by only one Si–OH efficiently reduces the probability of nucleophilic attack of the backbonds [G11, Al2]. Scanning tunneling microscopy (STM) investigations revealed that the etching of (111) surfaces proceeds at kink-sites present at the edges of terraces, while the surface of the terrace itself is not attacked [Al1]. Therefore, etch rates observed for (111) silicon surfaces are sensitive to minute misorientations of the substrate. At high DOC, high p-type doping or if holes are available at the interface, due to an applied potential, direct attack of the terrace surface seems to be more likely [Be23] and the anisotropy becomes significantly reduced, as for example indicated in Fig. 2.4. Why the etch rate ratio between (100) and (110) planes is affected by temperature or additions of organic or inorganic agents is not fully understood [Zu1].

#### 4.1.3

#### Divalent Electrochemical Dissolution of Si in HF

The first models for the electrochemical dissolution process of silicon in HF assumed a fluoride-terminated silicon surface to be present in electrolytes containing HF [Ge6, Du3]. However, by IR spectroscopy it was found that virtually the whole surface is covered by hydride (Si–H) [Ni3]. No evidence of Si–F groups is found in IR spectra independent of HF concentration used [Ch9]. This is surprising insofar as the Si–F (6 eV) bond is much stronger than the Si–H (3.5 eV) bond, and so it cannot be assumed that Si–F is replaced by Si–H during the electrochemical dissolution. This led to the conclusion that if a silicon atom at the surface establishes a bond to a fluorine atom it is immediately removed from the surface.

This fast removal of Si–F species can be ascribed to the weakening of the Si backbonds induced by the strong polarizing effect of F [Ub1]. The weak backbonds are then attacked by HF or H<sub>2</sub>O. This reaction scheme for the dissolution process is supported by quantum-chemical calculations [Tr1]. The observed dissolution valence of two for  $J < J_{PS}$  [Tu1], the photocurrent doubling indicating injection of an electron [Me11, Ma1], and the observed proportionality between electron injection current and Si–F bond density [Be22] are experimental findings that are in support of the divalent dissolution mechanism, as shown in Fig. 4.3 [Le1, Ge7, Ho6].

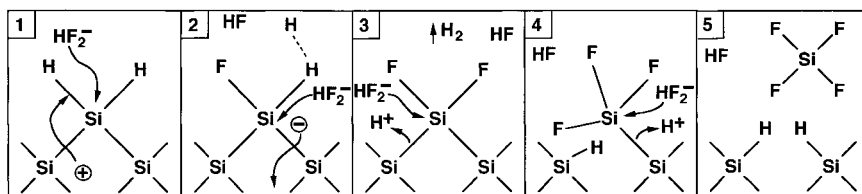


Fig. 4.3 Reaction scheme proposed for the anodic, divalent dissolution of silicon electrodes in HF.

Divalent dissolution is initiated by a hole from the bulk approaching the silicon-electrolyte interface which allows for nucleophilic attack of the Si atom (step 1 in Fig. 4.3). This is the rate-limiting step of the reaction and thereby the origin of pore formation, as discussed in Chapter 6. The active species in the electrolyte is HF, its dimer  $(\text{HF})_2$ , or bifluoride  $(\text{HF}_2^-)$ , which dissociates into HF monomers and  $\text{F}^-$  ions near the surface [Ok1]. The  $\text{F}^-$  ions in the solution seem to be inactive in the dissolution kinetics [Se2]. Because holes are only available at a certain anodic bias, the Si dissolution rate becomes virtually zero at OCP and the surface remains Si-H covered in this case, which produces a hydrophobic silicon surface.

If the Si-F bond is established, the second nucleophilic attack occurs under injection of an electron (step 2). Note that step 2 is not initiated by a charge carrier. Electron injection, which is by 1.1 eV more energetic than hole consumption, is a result of the reaction. The hydrogen escapes as gaseous  $\text{H}_2$  [Me11]. The ionic nature of the two Si-F bonds polarizes the remaining two silicon backbonds sufficiently to be broken by HF or  $\text{H}_2\text{O}$  (steps 3 and 4). The remaining silicon surface atoms are again hydrogenated (step 5).

The reaction product  $\text{SiF}_4$  would be gaseous, but it reacts with two HF to  $\text{SiF}_6^{2-}$  and two protons and stays in solution [Me11]. The solubility of  $\text{SiF}_6^{2-}$ , which is in the order of  $\text{mol l}^{-1}$  is significantly reduced in the presence of alkali metal ions. Especially for Rb, K or Cs, a micrometer thick, insoluble layer of metal hexafluoro-silicate may be formed on the electrode surface [Ha12]. The divalent electrochemical dissolution reaction is dominant during PS formation. The effects of the reaction products  $\text{SiF}_6^{2-}$  and  $\text{H}_2$  on pore growth are discussed in Section 9.5.

The main difference from the alkaline dissolution scheme is the hole needed to initiate step 1 of the divalent reaction. The polarizing effect on the Si backbonds is the same for Si-F and Si-OH. From this similarity a certain crystal anisotropy is expected for the divalent reaction, too. Faceting along (111) planes in HF electrolytes is observed when the current density is close to  $J_{\text{PS}}$  and micro PS formation becomes suppressed. This is the case for the electrode surface shown in Fig. 2.4 or at the tips of macropores as shown in Fig. 9.13b.

## 4.1.4

**Tetravalent Electrochemical Dissolution of Si in HF**

At higher anodic potentials an anodic oxide is formed on silicon electrode surfaces. This leads to a tetravalent electrochemical dissolution scheme in HF and to passivation in alkaline electrolytes. The hydroxyl ion is assumed to be the active species in the oxidation reaction [Dr1]. The applied potential enables  $\text{OH}^-$  to diffuse through the oxide film to the interface and to establish an Si–O–Si bridge under consumption of two holes, according to Fig. 4.4, steps 1 and 2. Details of anodic oxide formation processes are discussed in Chapter 5. This oxide film passivates the Si electrode in aqueous solutions that are free of HF.

The dissolution of the anodic oxide in HF involves nucleophilic attack of Si by fluorine, bound in HF,  $(\text{HF})_2$  or  $\text{HF}_2^-$  and electrophilic attack of the  $\text{H}^+$  ion on the oxygen backbonded to the Si [Mo6], as shown in Fig. 4.4, steps 3 and 4. These are the rate-limiting steps and the origin of electropolishing, as discussed in Section 5.6. The assumption that  $\text{HF}_2^-$  is again the active species [Ok3] is supported by the observation that HF vapor etches  $\text{SiO}_2$  only in the presence of trace amounts of water, which is an indication that dissociation of HF is required for dissolution [Mc2]. The formation and dissolution of the oxide film occur simultaneously or in an oscillatory manner during the electrochemical dissolution of silicon in HF. Four charge carriers are consumed for the dissolution of a single Si atom in the tetravalent dissolution scheme shown in Fig. 4.4, and so no hydrogen evolution is observed. No dependence on crystal orientation is observed for anodic oxidation, and the same is found to be true for the tetravalent dissolution reaction. The dissolution of the  $\text{SiO}_2$  is accompanied by electron injection, as shown in the top of Fig. 3.2 or in Fig. 4.14.

For the electrochemical dissolution of Si in electrolytes composed of anhydrous HF and an organic solvent a reaction is proposed that is similar to the divalent dissolution in aqueous HF. However, molecular hydrogen is not observed and four charge carriers are consumed per dissolved silicon atom, as in the tetravalent case [Pr7, Ri1].

Chemical etching of Si in acidic solutions, as described in Section 2.4, can also be understood as an oxidation of Si by  $\text{HNO}_3$  or  $\text{H}_2\text{O}_2$  and a subsequent dissolu-

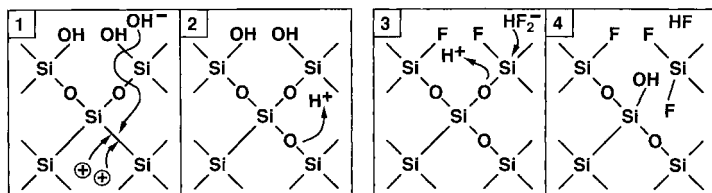


**Fig. 4.4** Reaction scheme proposed for the anodic, tetravalent dissolution of silicon electrodes in aqueous HF. The reaction can be separated into two parts: first an oxide is

formed anodically (steps 1 and 2), followed by chemical dissolution of the oxide in HF (steps 3 and 4).

of the oxide by HF. Some of the cleaning solutions discussed in Section 2.1 assumed to work on a similar basis. In SC-1, for example, the alkaline component ( $\text{NH}_4\text{OH}$ ) would rapidly etch Si but this reaction is prevented by a chemical formed by the oxidizing component ( $\text{H}_2\text{O}_2$ ).

### Dissolution Valence

dissolution valence  $n_v$  of the electrochemical reaction is the ratio of exchanged charge carriers  $n_{\text{he}}$  per dissolved silicon atom  $n_{\text{Si}}$ :

$$= n_{\text{he}}/n_{\text{Si}} \quad (4.6)$$

The total number of exchanged holes and electrons  $n_{\text{he}}$  can be calculated from anodization time  $t$ , the applied current  $I$  and the elementary charge  $e$  ( $1.602 \times 10^{-19}$  C). While the total number of dissolved silicon atoms  $n_{\text{Si}}$  is given by corresponding weight loss of the sample  $\Delta m$ , measured gravimetrically, divided by the atomic mass of silicon  $m_{\text{Si}}$  ( $4.6638 \times 10^{-23}$  g):

$$= (It/e)/(\Delta m/m_{\text{Si}}) \quad (4.7)$$

alkaline solutions electrochemical dissolution of Si ( $n_v > 0$ ) is accompanied by chemical dissolution ( $n_v = 0$ ), and so  $n_v$  is determined by the ratio of both processes [Pa6]. In HF free of oxidants, in contrast, only electrochemical dissolution ( $n_v > 0$ ) is observed. Because the valence of silicon is four one expects  $n_v = 4$ .

a tetravalent electrochemical dissolution is observed in mixtures of an organosolvent and anhydrous HF [Pr7, Ri1, Ch17] or for the electropolishing regime aqueous HF (regime 4 in Fig. 3.2). In aqueous HF, however,  $n_v$  decreases to values around 2 for current densities below the critical value  $J_{\text{PS}}$ , as shown in 4.5 [Le9]. This change from a divalent to a tetravalent dissolution at the critical current density  $J_{\text{PS}}$  is a consequence of a change in the dissolution reaction pathway, as discussed in the preceding section.

possible source of error in the measurement of  $n_v$  is the slow, purely chemical dissolution of silicon, because  $n_v$  becomes zero for dissolution at OCP. This effect becomes significant for long etching times and large interfacial areas, which are present in meso PS and micro PS layers. Values of  $n_v$  in excess of four may well be measured at high bias, for which dissolution is accompanied by anodic oxygen evolution.

While  $n_v$  shows no dependence on doping density, current density or electrolyte concentration in the electropolishing regime, it does in the PS regime [Le23, Fr6]. Generally  $n_v$  increases with current density. This is shown for the mesoporous regime in Fig. 6.9a, and microporous regime in Fig. 4.6. From the data of the latter figure the dependence of  $n_v$  on formation current density  $J$  (in  $\text{mA cm}^{-2}$ ) in ethanolic HF can be fitted to:

$$n_v = 1.86 + 0.242 \log_{10}(J) \tag{4.8}$$

While  $n_v$  is not very sensitive to changes in doping density for micro PS and macro PS formation it is for the meso PS regime. For p-type doping  $n_v$  shows values close to 2 in the micro PS regime and increases in the mesoporous regime at doping densities in excess of  $10^{18} \text{ cm}^{-3}$  to values close to 3. While for mesoporous n-type electrodes formed by anodization in the dark, the effect of doping density on  $n_v$  is relatively small, as shown in Fig. 6.9 a. If the electrolyte concentration is increased, a slight increase of the dissolution valence is observed for micro- and mesoporous films [Pa10].

The dependence of  $n_v$  on PS formation parameters as discussed above reflects the dependence of  $n_v$  on the microstructure of the porous film. A change of illumination

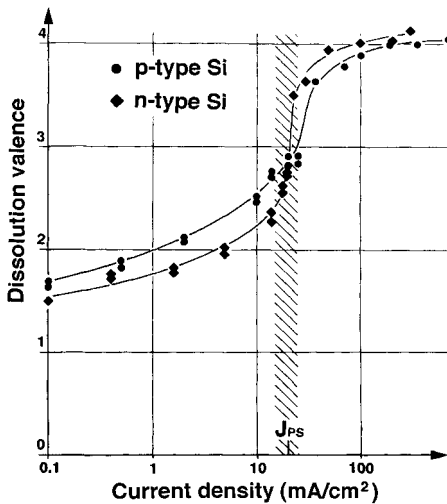


Fig. 4.5 Dissolution valence  $n_v$  as a function of anodic current density for low doped p-type and strongly illuminated, low doped n-type samples ( $< 10^{17} \text{ cm}^{-3}$ , 2.5% HF, at RT). For current densities below  $J_{PS}$  the samples were measured with and without the microporous layer. This produces a minor difference in  $n_v$ , indicated by two data points.

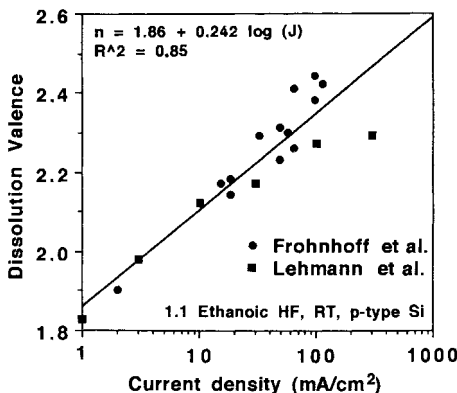


Fig. 4.6 Dissolution valence  $n_v$  as a function of anodic current density for micro-pore formation on low doped p-type electrodes anodized in ethanoic HF (1:1, ethanol : HF 50%).



intensity, for example, is sufficient to decrease  $n_v$  from 3 (dark) to 2.3 (illuminated), if all other parameters are kept constant [Le23]. The sample shows breakdown-type mesopores in the prior case, while illumination leads to macropore formation. This dependence on microstructure can be understood if the current density distribution at a pore tip is studied. Because of their large dimensions, this is easiest for macropores. As shown in Fig. 9.12, the current density at the center of a macropore tip in n-type Si is always  $J_{PS}$  and therefore close to the electropolishing regime, while it decreases towards the pore walls. It is justified to assume that  $n_v$  is close to 4 at the tip center and decreases to  $n_v=2$  towards the pore walls, producing a mean value around  $n_v=2.6$  for macropores [Le9]. For p-type macropores for which the pore tip current density has been found to be significantly below  $J_{PS}$ , the dissolution valence is always close to 2 in aqueous HF [Le21]. For micro and meso PS the pore tip current distribution is not known, but by analogy it can be concluded that the high values of  $n_v$  observed for mesopore formation are due to tip current densities close to  $J_{PS}$ .

If the electrolyte is composed of HF and an organic solvent a dependence of  $n_v$  on the kind of solvent and on the residual water content is observed, while the substrate orientation showed no effect on  $n_v$  [Ch15].

### 4.3

#### The Characteristic Anodic Currents in HF

The characteristic shape of the anodic voltammogram of a Si electrode in aqueous fluoride media, as shown for example in Fig. 3.1d, is surprisingly stable against changes in fluoride concentration ( $c_F$ ) or pH. When the potential of a p-type Si electrode is swept anodic of OCP a steep current rise near 0 V is observed, followed by a sharp peak ( $J_1$ ) and a narrow plateau ( $J_2$ ). Then a second broad maximum ( $J_3$ ) is found around a positive bias of 1.5–2.5 V, followed by a broad plateau ( $J_4$ ) extending over several volts, as shown in Fig. 4.7. When electrode rotation is used, these curves are pen-reproducible for a given solution. The hysteresis of the curves approaches zero for slow sweeps [Ch3].

In a detailed rotating-disk electrode study of the characteristic currents were found to be under mixed control, showing kinetic as well as diffusional limitations [Ha3]. While for low HF concentrations (<1 M) kinetic limitations dominate, the regime of high HF concentrations (> 1 M) the currents become mainly diffusion controlled. However, none of the relevant currents ( $J_1$  to  $J_4$ ) obeys the Levich equation for any values of  $c_F$  and pH studied [Et1, Ha3]. According to the Levich equation the electrochemical current at a rotating disk electrode is proportional to the square root of the rotation speed [Le6]. Only for HF concentrations below  $1 \text{ mol l}^{-1}$  and a fixed anodic potential of 2.2 V versus SCE the traditional Levich behavior has been reported [Ca13].

The characteristic currents  $J_1$  to  $J_4$  are a unique property of aqueous HF, they are not observed in electrolytes composed of anhydrous HF and an organic solvent or in electrolytes free of HF [Ri1]. All currents  $J_1$  to  $J_4$  show a similar dependence on the

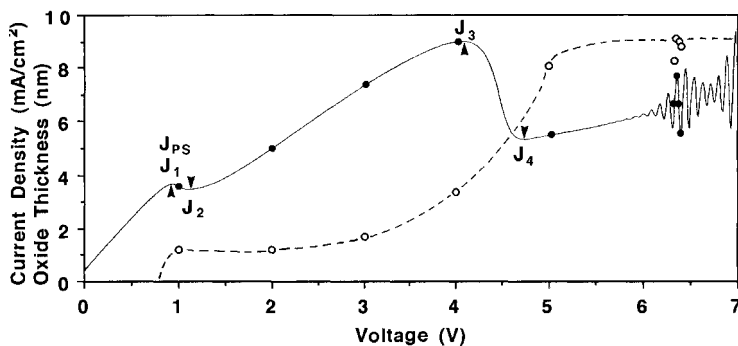


Fig. 4.7 The current density-voltage curve of a (100) p-type Si electrode in  $0.3 \text{ mol kg}^{-1} \text{ NH}_4\text{F}$  ( $\text{pH}=3.5$ ) recorded with  $50 \text{ mV s}^{-1}$  showing the characteristic current maxima and minima. At the points indicated by filled

circles the electrode was quickly removed from the electrolyte and the oxide thickness was measured by ellipsometry (open circles, broken line fitted as a guide to the eye).

pH of the electrolyte, characterized by a maximum between  $\text{pH}=2$  and  $\text{pH}=4$  and a rapid decrease for higher pHs [Ch3], as shown in Fig. 4.8. This behavior correlates with the pH dependence of  $[\text{HF}]$  and  $[\text{HF}_2^-]$  concentrations but not with  $[\text{F}^-]$ , which indicates that  $\text{HF}$  and  $\text{HF}_2^-$  are the active species in the dissolution process.

The currents  $J_1$  to  $J_4$  and thereby the dissolution rate in fluoride media shows a dependence on the nature and concentration of the cation present in the electrolyte.  $J_1$  to  $J_4$  increase by more than one order of magnitude if a small cation, like  $\text{Li}^+$ , is replaced by a large one, like  $\text{Rb}^+$  or  $\text{Cs}^+$ . A catalytic effect of the cation on breaking of Si-O bonds is assumed [Ha11, Ha12].

The first of the four characteristic currents  $J_1$  to  $J_4$  has a prominent position. It indicates the crossover from a charge supply limited reaction to a kinetically and mass transfer limited reaction. This crossover is accompanied by pronounced changes in charge state, chemical dissolution reaction, dissolution valence, pore formation and anodic oxide formation. Therefore its dependence on other parameters, such as crystal orientation, temperature or HF concentration deserves further investigation. In the literature  $J_1$  is usually termed  $J_{\text{crit}}$ ,  $J_{\text{PS}}$  or  $J_{\text{PSL}}$ . In the following the symbol  $J_{\text{PS}}$  will be used.

The critical current density  $J_{\text{PS}}$ , easily identified by the first anodic peak in the current voltage plot, is shown for p-type samples of different crystal orientation in Fig. 4.9. Note that  $J_{\text{PS}}$  is largest for silicon electrodes of (100) crystal orientation, independently of the electrolyte concentration used (inset of Fig. 4.9). This indicates that the dissolution process has an anisotropic component [Le9].

Because  $J_{\text{PS}}$  is limited by reaction kinetics and mass transport a dependency on the HF concentration  $c_{\text{HF}}$  and the absolute temperature  $T$  can be expected. An exponential dependence of  $J_{\text{PS}}$  on  $c_{\text{HF}}$  has been measured in aqueous HF (1% to 10%) using the peak of the reverse scan of the voltammograms of (100) p-type electrodes. If the results are plotted versus  $1/T$ , a typical Arrhenius-type behavior

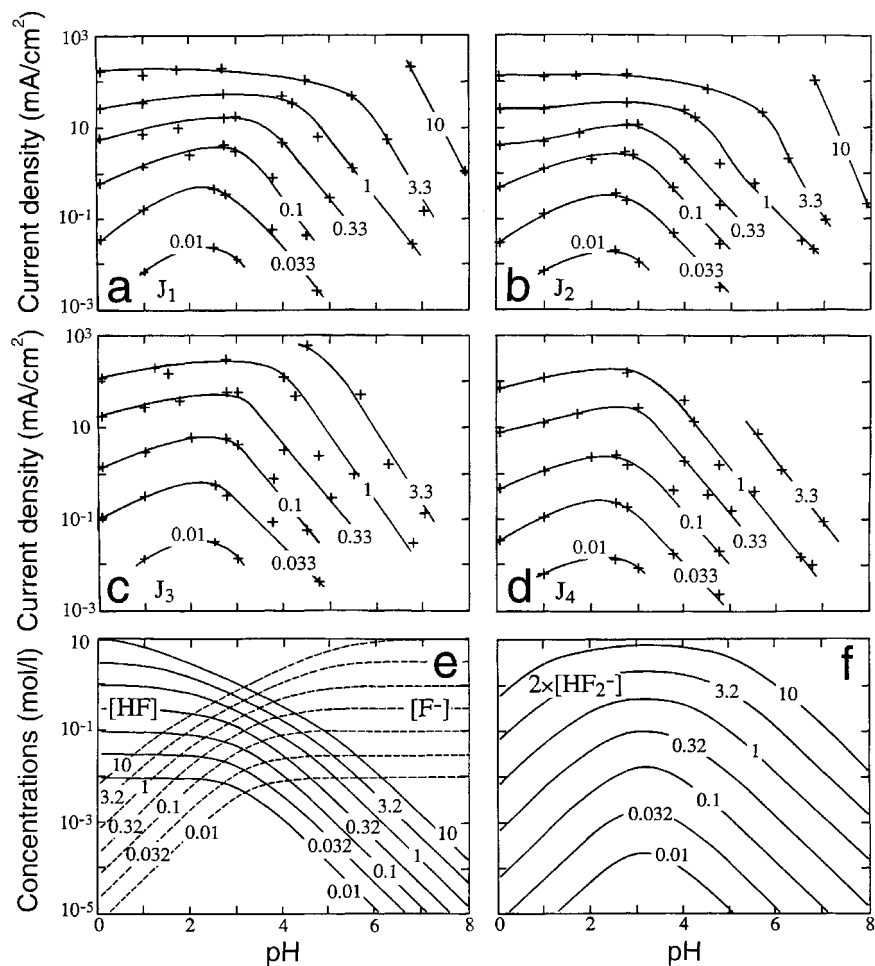


Fig. 4.8 Plots of the characteristic current densities (a)  $J_1$ , (b)  $J_2$ , (c)  $J_3$  and (d)  $J_4$ , as a function of pH, for various values of  $c_F$  labeled on the curves in units of  $\text{mol l}^{-1}$ .

Calculated values of (e)  $[\text{HF}]$ ,  $[\text{F}^-]$  and (f)  $2[\text{HF}_2^-]$  as a function of pH, for different values of  $c_F$ . After [Ch3].

is found, as shown in Fig. 4.10. The critical current density  $J_{PS}$  (in  $\text{A cm}^{-2}$ ) as a function of  $c_{\text{HF}}$  (in wt% aqueous HF) and  $T$  (in K) is described by the equation:

$$J_{PS} = C_{PS} c_{\text{HF}}^{\xi} \exp(-E_a/kT) \quad (4.9)$$

with the constant  $C_{PS} = 3300 \text{ A cm}^{-2} (\% \text{HF})^{-\xi}$ , the activation energy  $E_a = 0.345 \text{ eV}$  and the exponent  $\xi = 1.5$ . These values are used to calculate  $J_{PS}$  as a function of  $c_{\text{HF}}$  at RT, as shown in the table in the inner back cover of the book. The value  $\xi = 1.5$  has been determined for a reverse scan (from high values of anodic bias to

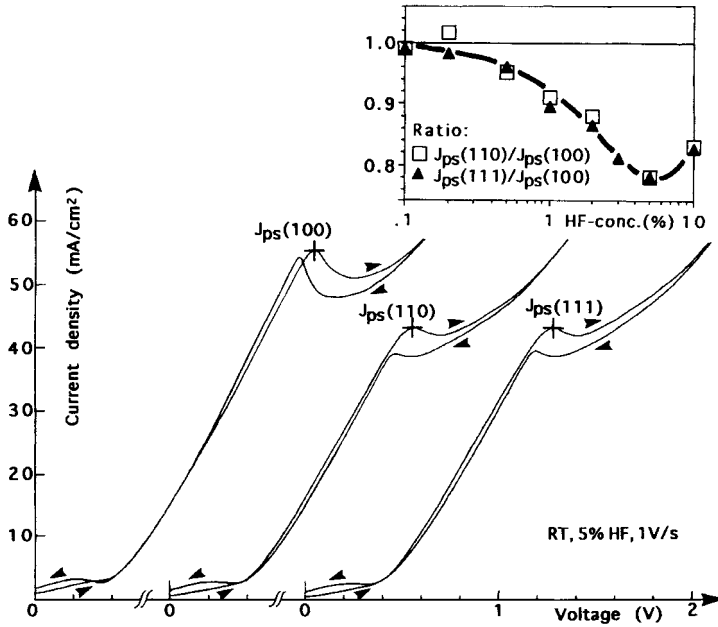


Fig. 4.9 Cyclic voltammograms of silicon anodes of different crystal orientation ( $10^{15} \text{ cm}^{-3}$ , boron doped, versus a Pt pseudoreference electrode in 5% HF), with the characteristic

peak that indicates the critical current density  $J_{PS}$ .  $J_{PS}$  was found to be largest for (100) oriented samples independently of the HF concentration used (inset upper right).

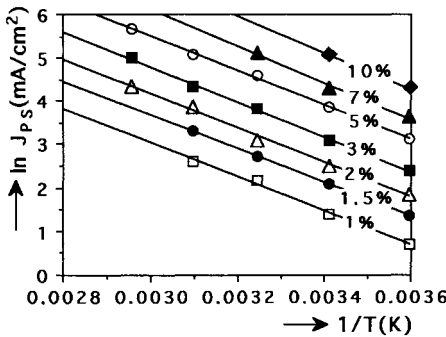


Fig. 4.10 Critical current density  $J_{PS}$  of (100) oriented silicon electrodes for different HF concentrations plotted versus the inverse absolute temperature  $1/T$ . Arrhenius-type behavior, with an activation energy of 0.345 eV, is observed.

low ones) of the voltammogram, while  $\zeta=1.3$  has been found for a forward scan [Le9]. This discrepancy may be due to the microporous layer that covers the electrode in the latter case, while in the first case the electrode is electropolished and therefore free of PS when  $J_{PS}$  is measured. The above values are supported by investigations using a rotating disk electrode [Me14].

Values reported for the exponent  $\zeta$  show a significant scatter between 1 and 1.5 [Ed2, Zh5, Ge10]. For the modeling of macropore formation  $E_a=0.415 \text{ eV}$ ,  $\zeta=1.35$

and  $C_{PS} = 68431 \text{ A cm}^{-2} (\% \text{HF})^{-\xi}$  are found to give the best fit to experimental results.

Little is known about the mechanisms that cause the three other current extrema  $J_2$  to  $J_4$ . The kinetic and diffusional contributions of the characteristic currents  $J_1$  to  $J_4$  show a different concentration dependence. While the diffusion current is found to be roughly proportional to  $c_F$ , the kinetic current shows an exponent of  $2 < \xi < 2.5$  [Ha3]. No dependence of the characteristic currents  $J_1$  to  $J_4$  on doping kind and density is observed. This indicates again that  $J_1$  to  $J_4$  depend on mass transport and reaction kinetics rather than on charge supply. For n-type electrodes, of course, strong illumination is necessary in order to generate a sufficient number of minority carriers to support the currents.

The second current maximum  $J_3$  corresponds to an oxide thickness at which tunneling of charge carriers becomes negligible, as shown in Fig. 4.7. At the bias corresponding to  $J_3$  the formation of anodic oxides in electrolyte-free HF shows a change of growth kinetics, as shown in Fig. 5.2.

#### 4.4

#### Reverse Currents, Electron and Hole Injection

The existence of two types of mobile charge carriers in semiconductors enables us to distinguish between a majority charge carrier transferred from the electrode into the electrolyte and a minority charge carrier injected from the electrolyte into the electrode. Minority carrier injection causes significant reverse currents, but may also contribute to the total current under forward conditions.

##### 4.4.1

#### Electron Injection under Anodic Bias without Illumination

If an n-type electrode is kept in the dark, the anodic dark current depends on properties of the semiconductor as well as on the chemical composition of the electrolyte. Measurements of dark current density need a defect-free Si surface. Scratches, barely visible to the eye, may increase the dark current by orders of magnitude. For the dark current density of a defect-free silicon electrode a dependence on the chemical environment is observed.

The steady-state current for an n-type Si electrode in the dark anodized at 0.5 V positive of OCP in 1M  $\text{NH}_4\text{F}$  shows a strong dependence on pH. While it is about  $5 \mu\text{A cm}^{-2}$  for pH 2–6, it peaks at pH=7 with values above  $10 \mu\text{A cm}^{-2}$ , followed by a decrease to about  $1 \mu\text{A cm}^{-2}$  for pH>8 [Ho6]. As shown in Fig. 4.11, the dark current of an n-type silicon electrode in 3% HF increases significantly with increasing DOC. This chemically-induced electron injection current is about one order of magnitude larger than the one observed for low DOC. A similar dependence of reverse current on DOC has also been observed in pure water. Atomic force microscopy (AFM) inspections of the electrode showed an atomically flat

step-terrace surface to be formed at low DOC on (111) Si electrodes, while at high DOC the electrode surface remains rough [Be23].

C–V and I–V measurements of Si electrodes of different doping density in electrolytes free of fluoride show that in this case the dark current becomes dominated by thermally activated electron transfer over the Schottky barrier rather than by carrier generation in the depletion region [Ch10]. Note that the dark currents discussed above may eventually initiate the formation of breakdown type mesopores, which causes a rapid increase of the dark current by local breakdown at the pore tips, as shown in Fig. 8.9. This effect is enhanced for higher values of anodic bias or doping density.

The current transients observed upon immersion of n-type Si electrodes in HF of low concentration (2%) depend on the sample pretreatments. Immersion in 50% HF prior to anodization, for example, leads to current densities of up to  $30 \mu\text{A cm}^{-2}$ , which decreases within 1 s to the steady-state dark current value, producing a charge density of  $24 \mu\text{C cm}^{-2}$ . This effect has been ascribed to the density of Si–F bonds present on the electrode surface electrode prior to anodization [Be22].

For alkaline electrolytes significant electron injection currents are also observed. Values as high as  $600 \mu\text{A cm}^{-2}$  have been found for n-type silicon electrodes anodized in the dark in KOH, as shown in Fig. 3.4 [Sm6]. This can be understood as an electrochemical contribution to the chemical reaction path, as shown in Fig. 4.1. Electron injection can be expected to occur during step 2 of this reaction, because the interface configuration present is very similar to that during step 2 of the divalent dissolution scheme, as shown in Fig. 4.3. The observed decrease of hydrogen production with increasing electron injection current supports this model [Pa6]. In CMP solutions like Syton [16] (pH=10.3), the electron injection current density is low ( $1\text{--}2 \mu\text{A cm}^{-2}$ ), but it is enhanced under the action of a soft polishing pad by nearly two orders of magnitude [He6].

#### 4.4.2

##### **Hole Injection under Cathodic Bias without Illumination**

Hole injection into p-type electrodes under cathodic bias in the dark is not observed in aqueous HF or alkaline solutions and the small reverse current, as shown in Figs. 4.11 or 3.4, can be understood as caused by carrier generation in the depletion region or at defects. If, however, oxidants like  $\text{HNO}_3$  are added, hole injection in the cathodic regime, as well as electron injection in the anodic regime, are observed [Ko14]. This produces considerable reverse currents at Si electrodes without any illumination, as shown in Fig. 4.12. Note that a cathodic bias of about 0.5 V is needed to passivate a silicon electrode against the dissolving action of the HF– $\text{HNO}_3$  mixture.

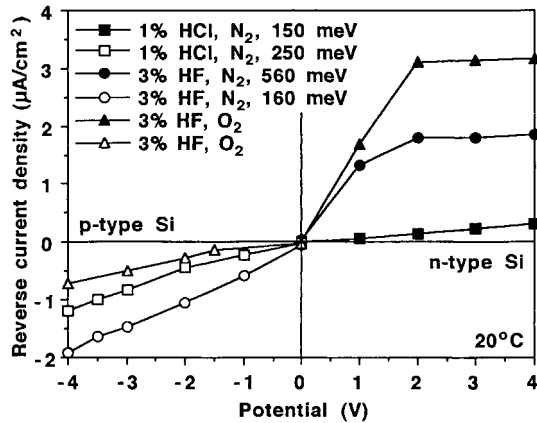


Fig. 4.11 Reverse current densities of moderately doped n-type (filled symbols) and p-type (open symbols) silicon electrodes in 3% HF and 1% HCl as a function of applied potential without illumination. The electrolyte was

bubbled with either nitrogen or oxygen. The reverse current density shows an Arrhenius dependency for the temperature range under investigation (5–50°C); observed activation energies are given in the legend.

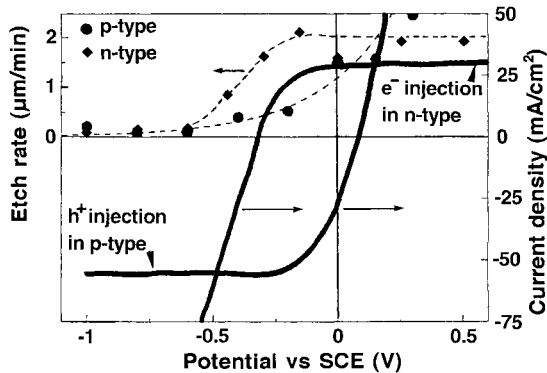


Fig. 4.12 Current-potential and etch rate-potential curves of p-type and n-type silicon electrodes in an electrolyte composed of 6 M HNO<sub>3</sub> and 6 M HF. Redrawn from [Ko14].

4.4.3 Electron Injection under Anodic Bias with Illumination

Significant reverse currents at semiconductor electrodes are not only observed for breakdown but also under illumination. For the latter case a quantum efficiency  $q$ , the number of exchanged holes and electrons  $n_{he}$  per incident photons  $n_p$ , can be defined:

$$q = n_{he}/n_p \tag{4.10}$$

The quantum efficiency for solid-state devices, e.g. solar cells, is always below unity. For n-type silicon electrodes anodized in aqueous or non-aqueous HF electrolytes, quantum efficiencies above unity are observed because one or more electrons are injected into the electrode when a photogenerated hole enters the electrolyte. Note that energy conservation is not violated, due to the enthalpy of the electrochemical dissolution reaction of the electrode.

A p-type electrode is in depletion if a cathodic bias is applied. Illumination generates one electron per absorbed photon, which is collected by the SCR and transferred to the electrolyte. It requires two electrons to form one hydrogen molecule. If the photocurrent at this electrode is compared to that obtained by a silicon photodiode of the same size the quantum efficiencies are observed to be the same for the solid-state contact and the electrolyte contact, as shown in Fig. 4.13. If losses by reflection or recombination in the bulk are neglected the quantum efficiency of the electrode is 1.

If the same experiment is performed with an n-type Si electrode under identical illumination intensity the anodic photocurrent is found to be larger than for the p-type electrode under cathodic conditions. This increase is small (about 10%) for current densities in excess of  $J_{PS}$ . Figure 3.2 shows that in this anodic regime injected electrons are also detected at p-type electrodes. This allows us to interpret the 10% increase in photocurrent observed at n-type electrodes as electron injection during anodic oxide formation and dissolution.

For current densities below  $J_{PS}$  the photocurrent in aqueous HF is found to be increased by a factor of 2 or even up to a factor of 4 for small photocurrent densities [Br2, Ma1, Pe1]. This effect is shown in Fig. 4.13. For non-aqueous HF electrolytes factors between 2 and 3 are observed. For further reduction of the illumination intensity the multiplication factor approaches infinity, because of the illu-

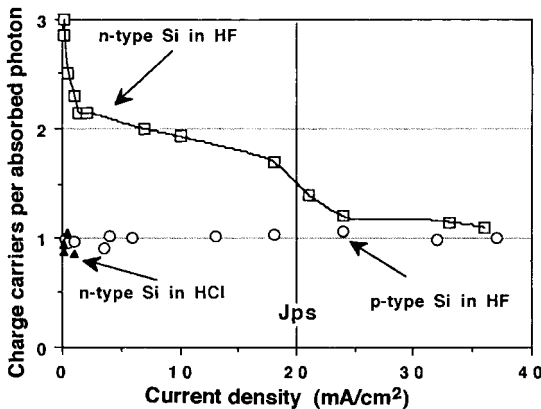


Fig. 4.13 Number of observed charge carriers per absorbed photon as a function of the current density. The photoinduced current at n-type electrodes in HF (squares) is increased compared to a photodiode or p-type electrode

(circles). For an n-type electrode photooxidized in HCl no current multiplication is observed after formation of the first monolayer (triangles).



mination-independent electron injection during the slow chemical dissolution of the n-Si electrode in HF, as shown in Fig. 4.11.

If an oxide-free, hydrogen-terminated, n-type electrode is anodized under illumination in an electrolyte free of HF (for example HCl), a quantum efficiency of close to 2 is observed for the initial contact of the electrode to the electrolyte. During the oxidation of the first hydrogenated monolayer the quantum efficiency decreases to 1 and remains at that value during the formation of the first few nanometers of anodic oxide, as indicated by filled triangles in Fig. 4.13. For a further increase of oxide thickness the quantum efficiency decreases to values significantly below 1 [Ch14].

The photocurrent doubling discussed above can be understood as a consequence of the divalent dissolution reaction as shown in Fig. 4.3. Dissolution for current densities below  $J_{PS}$  is initiated by a hole in step 1 and proceeds under injection of an electron in step 2. For the case of an n-type electrode, one photon is required to generate one hole, but the electron injected in the dissolution process doubles the current without consumption of another photon. Hence the resulting current density is twice as large as observed at a reference photodiode. Because step 2 of the reaction depicted in Fig. 4.3 is independent of type of doping it can be concluded that electron injection also takes place at p-type electrodes. There is, however, no simple way to detect these injected electrons because the electrode is under depletion in this regime, as discussed in Section 3.2.

For anodic oxidation of a silicon electrode in fluoride-free electrolytes, the reaction of step 2 is only expected during the first seconds of anodization, until all Si-H surface groups are replaced by Si-OH.

#### 4.4.4

#### Electron Injection Caused by a Dissolving Oxide Film

Electron injection has been observed during the chemical dissolution of an oxide film in HF [Ma1, Oz1, Bi5]. The injected electrons are easily detected if the anodized electrode is n-type and kept in the dark. Independently of oxide thickness and whether the oxide is thermally grown or formed by anodization, injected electrons are only observed during the dissolution of the last few monolayers adjacent to the silicon interface. The electron injection current transient depends on dissolution rate respectively HF concentration, however, the exchanged charge per area is always in the order of  $0.6 \text{ mC cm}^{-2}$ . This is shown in Fig. 4.14 for an n-type silicon electrode illuminated with chopped light. The transient injection current is clearly visible in the dark phases.

The origin of the electron injection peak at the end of the dissolution of an oxide film is not understood in detail. Silicon interface atoms with three Si-O bonds and a single Si-Si bond are proposed to be responsible for the effect [Ma1]. On the other hand, during the dissolution process silicon interface atoms with one Si-O bond and three Si-Si bonds lead to a configuration identical to the one for which electron injection is observed during divalent dissolution (Fig. 4.3, step 2). In any case, the injected charge exceeds by a factor of 3 to 5 the charge expected

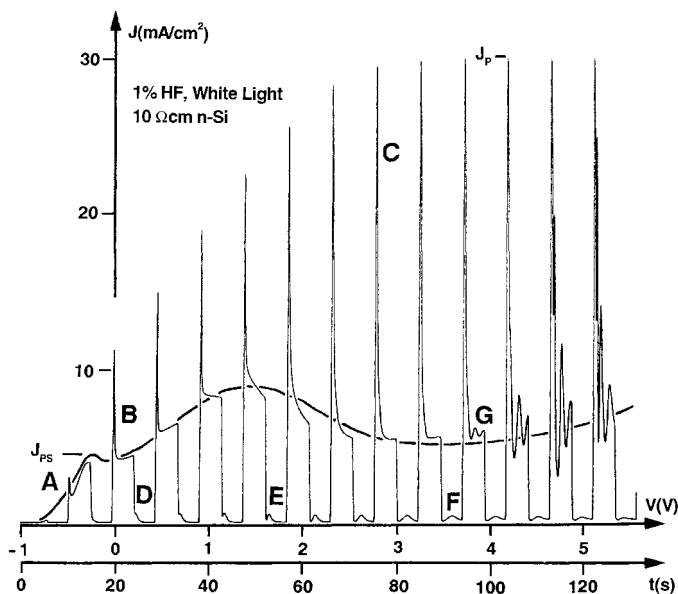


Fig. 4.14 Anodic potential scan ( $50 \text{ mV s}^{-1}$ ) of an n-type Si electrode in 1% HF under constant (bold broken line) and chopped illumination (solid line, illumination intensity corresponding to  $J_p$ ). Point A: Current transients are minimal below  $J_{PS}$ . Points B, C: Current

peaks due to anodic oxidation. Points D, E, F: Transient electron injection currents due to dissolution of an anodic oxide of increasing thickness. Note that the injection becomes delayed with increasing oxide thickness. Point G: Onset of current oscillations.

for a single monolayer. This cannot simply be explained by roughness effects at the interface between oxide and silicon because, at least for thermal oxides, TEM studies indicate an atomically flat interface. It can be speculated that electron injection already takes place if the remaining oxide thickness is small enough to permit electron tunneling.

#### 4.5 Electrochemical Etch Stops

If the relevant literature is surveyed for the keywords etch stops and silicon, a confusing multiplicity of methods is found using different electrolytes, different bias and differently doped silicon substrates. This section does not aim to be a comprehensive review of all these techniques [Co2], but an introduction to the basic principles of electrochemical etch stops, which will be illustrated by a few typical examples.

An etch stop is a method that allows for selective removal of a specific material. Selectivity, therefore, is the most important property of an etch stop. It is defined as the etch rate of the faster etching material divided by the etch rate of the slower etching material.

It is usually simple to find a selective etchant, if the two materials are different in their chemical composition, as discussed in Section 2.6. It is more difficult to develop etchants sensitive to different doping densities of bulk silicon, as discussed in Section 2.5. Applying a bias during etching adds another degree of freedom to the process and is in many cases found to be useful in producing the desired selectivity. Selective etching as a result of an applied potential is termed an electrochemical etch-stop technique. The source of bias needed for this technique can be external, e.g. a power supply. In this case an electrical contact to the silicon electrode is required. This is not necessary if an internal source is used. This can be a galvanic element or an illuminated p–n junction. The latter case will be treated in the next section dealing with photoelectrochemical etching.

A sufficiently anodic bias and the availability of holes are the two necessary conditions for the dissolution of silicon aqueous HF. In this case the Si dissolution rate is proportional to the current density divided by the dissolution valence. In all other cases silicon is passivated in HF; this is the case under OCP, or under cathodic conditions, or under anodic conditions if the sample is moderately n-type doped and kept in the dark. If an oxidizing agent like  $\text{HNO}_3$  is added silicon will already dissolve at OCP, but the dissolution rate remains bias dependent. If an anodic bias is applied the dissolution rate will be enhanced, whereas a cathodic bias effectively decreases the rate of dissolution.

In alkaline electrolytes, in contrast, silicon is readily dissolved at OCP. Under cathodic conditions the dissolution becomes reduced, while under low anodic potentials the dissolution rate is enhanced compared to the OCP rate. If, however, the anodic potential becomes larger than the PP, the silicon electrode is passivated due to a thin anodic oxide film and the dissolution rate becomes negligible. The current density needed to keep the electrode in the passive state corresponds to the dissolution rate of the anodic oxide in the alkaline electrolyte used and is usually very low.

All electrochemical etch stops of silicon are based on the dissolution behavior discussed above and a method to have different parts of the electrode interface under different potentials.

The easiest way to have different parts of the electrode surface under different bias is to disconnect them by an insulator. This method is elucidated by an experiment in which an electrochemical etch-stop technique has been used to localize defects in an array of trench capacitors. In a perfect capacitor the polysilicon in the trench is insulated from the substrate whereas it is connected in a defect capacitor, as shown in Fig. 4.15a. If an anodic bias is applied the bulk silicon and the polysilicon in the defect trench will be etched, while the other trenches are not etched if an aqueous HF electrolyte is used, as shown in Fig. 4.15b. The reverse is true for a KOH electrolyte, because the only polysilicon electrode in the defect trench is passivated by an anodic oxide, as shown in Fig. 4.15c.

More sophisticated than the use of an insulator to disconnect a part of the sample is the use of an electronic insulation realized by a p–n junction. Because the potential required to passivate a silicon electrode in alkaline solutions [Pa8] is smaller than the bias required to forward a junction, only the side of the junction that is connected will be passivated [Ja1, Ge5], as shown in Fig. 4.16a. Note that a temporary

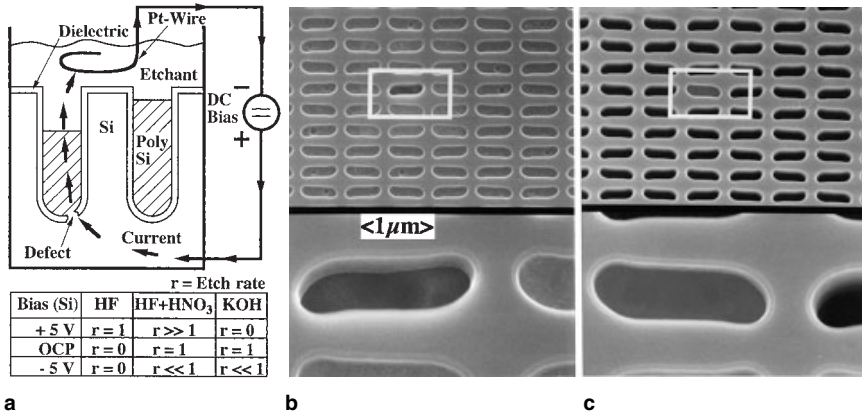


**Fig. 4.15** The use of etch stops to visualize defects in a dynamic random access memory (DRAM) structure for subsequent electron microscopy inspection. If a bias is applied to the silicon substrate, as shown in (a), the polysili-

con electrode of a defect trench capacitor will either etch at (b) higher rate  $r$  than the other electrodes or (c) passivate, depending on the kind of electrolyte and bias used, as listed in the table below the diagram.

n-type doping can be established by proton implantation and a subsequent 500 °C anneal. The initial p-type doping can easily be resumed by a 1050 °C anneal [Im1].

Small leakage currents or a transistor-like action of the junction are sufficient to generate a small current that may cause undesired passivation. This can be circumvented by application of an additional potential to the etching layer, shown by the broken line in Fig. 4.16a. This electrochemical etch-stop technique is favorable compared to the conventional chemical  $p^+$  etch stop in alkaline solutions, because it does not require high doping densities. This etch stop has mainly been applied for manufacturing thin silicon membranes [Ge5, Pa7, Kl1] used for example in pressure sensors [Hi1].

However a p–n junction is not necessarily needed to generate an electrochemical etch stop. A difference in doping density may be sufficient, because it changes the width of the SCR and thereby charge transfer mechanism in HF. Charge carrier tunneling, which is possible at high doping, requires a bias about 0.1 V lower than that required for thermionic emission over the barrier, as shown in Fig. 3.3. Mesoporous silicon can therefore be formed in the  $p^+$  doped regions at potentials at which micropore formation on the low doped p-type or n-type areas is still suppressed. The mesoporous silicon can be removed with a high selectivity to the low doped regions by subsequent etching in a silicon etch of low etch rate, for example in KOH at RT. Selectivities in excess of 100 are reported for doping densities in excess of  $5 \times 10^{18} \text{ cm}^{-3}$  [Ts5, Th1, Li8, Ta12]. A similar etch stop is found for p-type regions in contact with  $n^+$  areas [Th1, Be18]. Note that all etch stops discussed above refer to silicon electrodes kept in the dark. If the electrode is illuminated, the etch rate ratios change and may even be reversed. If, for example, an

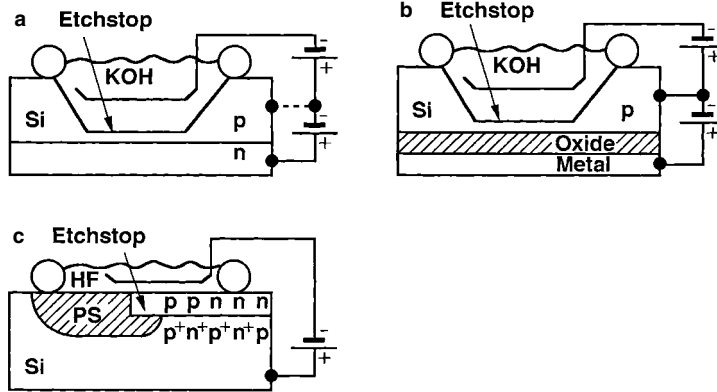


**Fig. 4.16** (a) The dissolution of a silicon substrate in alkaline etchants stops at or close to the reversely biased junction. (b) A similar etch stop can be achieved using an MOS (metal oxide semiconductor) structure to induce an SCR. (c) An etch stop in aqueous HF

can be realized by different doping densities. The top layer of the five doping combinations shown is passivated, while the bottom layer is transformed into PS. The PS can then be removed selectively by chemical etching.

n-type substrate with implanted p-type regions is illuminated, the n-type region is reported to etch preferably at anodic potentials in HF [M1, Tu6].

In contrast to minute potential differences used above, low doped n-type regions on an  $n^+$  doped substrate are passive in HF even at anodic potentials well in the electropolishing regime [Di1, Th1]. This is due to the fact that holes are not available in n-type silicon if it is kept in the dark. At high potentials, however, spiking of mesopores into the low doped region, as discussed in Section 8.4, may negatively affect the properties of the etch stop layer. Anodization at low potentials and selective removal of the mesoporous silicon formed selectively in the  $n^+$  regions are therefore advisable. An etch stop for low doped n-type Si reported for  $np^+$ -structures [We3, Th1] and np-structures [Br7] is based on the same principles. Note that due to bipolar effects the etch stop is not necessarily located at the metallurgical junction [An3]. The different doping combinations sufficient for producing etch stop layers in aqueous HF are summarized in Fig. 4.16c.

For doping-dependent anodic etch stops in HF, a general hierarchy of dissolution is observed [La5]: illuminated n-doped and  $n^+$ -doped areas are most easily dissolved, followed by  $p^+$ -doped areas. Next likely to be dissolved are p-type areas. Moderately n-type doped areas kept in the dark are least likely to be etched. This hierarchy corresponds to the potential shift of the I–V curve in the regime of PS formation [Ga1, Zh5].

But even in a homogeneously doped material an etch stop layer can be generated by an inhomogeneous charge carrier distribution. If a positive bias is applied to the metal electrode of an MOS structure, an inversion layer is formed in the p-type semiconductor. The inversion layer passivates in alkaline solutions if it is kept at the PP using a second bias [Sm5], as shown in Fig. 4.16b. This method is used to reduce the thickness variations of SOI wafers [Og2]. Illuminated regions

of a homogeneously doped n-type electrode in HF are also dissolved preferably, as discussed in the next section.

A prerequisite for all etch-stop techniques discussed so far is an electrical connection to an external power supply. However, if the potential required for passivation in alkaline solutions is below 1 V, it can be generated by an internal galvanic cell, for example by a gold-silicon element [As4, Xi1]. An internal galvanic cell can also be realized by a p–n junction illuminated in the etchant, as discussed in the next section. Internal cells eliminate the need for external contacts and make this technique suitable for simple batch fabrication.

#### 4.6

#### Photoelectrochemical Etching

The surprising variety of photoelectrochemical effects observed at silicon electrodes anodized in HF is solely a consequence of the semiconducting nature of the electrode, because the electrolyte is not photoactive.

Photons of wavelength below 1100 nm, which corresponds to an energy in excess of the silicon band gap energy of 1.1 eV, are absorbed in bulk silicon under generation of an electron hole pair. The absorption coefficient as shown in Fig. 7.6 is strongly energy dependent and so light penetrates deep into the silicon bulk for wavelengths near 1100 nm, as shown in Fig. 10.4a. Above this wavelength silicon appears transparent and absorption bands in this region are impurity related.

This spectral dependence of absorption is important for selection of an adequate light source for illumination. Filament lamps show a broad spectrum and high intensity. They are useful if a whole wafer has to be illuminated homogeneously. Various optical low pass filters and a few high pass filters are available and can be used to cut off undesirable parts of the spectrum [17]. A disadvantage of filament lamps is the high IR intensity, which heats up the silicon and the filters. Sodium lamps [18] and fluorescent lamps show a better light to heat ratio, but tuning of the light intensity is a major problem. Light-emitting diodes (LEDs) are favorable if a monochromatic illumination is desirable. The intensity can be regulated very fast and over a wide range. For high-intensity applications IR-LEDs (820 nm) [18] are preferable. For illumination of whole silicon wafers LED arrays in wafer size show best results. Lasers are favorable if local illumination with monochromatic light is desirable. Using a mirror scanner enables rapid scanning of the wafer surface, which is exploited in the ELYMAT technique, as discussed in Section 10.3. Intensity tuning is feasible for semiconductor lasers.

Illumination is a relevant parameter in the electrochemistry of silicon because photogenerated carriers may initiate or contribute to the charge exchange at the electrolyte-silicon interface. If an electrode is illuminated, photogenerated electron-hole pairs are generated corresponding to the number of absorbed photons. This number depends on spectral distribution, total illumination intensity and losses due to optical reflection and transmission. The number of electron-hole

pairs is reduced by recombination processes caused by impurities or defects in the crystal. Under sufficient reverse bias the remaining photogenerated minority carriers are collected by the SCR and can initiate dissolution at the interface to the electrolyte.

Illumination-induced effects at silicon electrodes are used in different ways. For some of these applications illumination is a minor attribute. The sections in which these topics are discussed in detail are summarized below.

Under anodic conditions hole transfer to HF electrolytes is accompanied by electron injection that may lead to quantum efficiencies greater than 1. This effect is known as current multiplication and is discussed in Section 4.4.

The dependence of photocurrent on bulk recombination rate allows us to realize an analytical tool for the characterization of silicon, as discussed in Section 10.3.

Photogenerated carriers are needed for the formation of macropores in n-type electrodes, as discussed in Chapter 9.

Illumination of a microporous silicon layer during anodization changes the PL spectrum significantly, as discussed in Section 7.4, and may also be applied for structuring of microporous layers [As2, Do1].

An initially flat silicon electrode surface will develop a surface topography if the photocurrent varies locally. This variation can be caused by a lateral variation of the recombination rate or by a lateral variation of the illumination intensity. The photoelectrochemical etching of a silicon electrode is related to the etch-stop techniques discussed in Chapter 3. While different etching rates for different areas of the electrode may be obtained by electrical insulation or by a different doping density, the etch rate may also be altered by a difference in illumination intensity. Basically four photoelectrochemical etching modes are possible for homogeneously doped substrates:

1. The etch rate of an illuminated area on p-type Si is reduced under cathodic potential in alkaline solutions, while an area kept in the dark shows the OCP etch rate [Ve2].
2. An illuminated area on n-type Si is anodically passivated in alkaline solutions for potentials in excess of PP, whereas an area kept in the dark is not passivated and is therefore etched with the OCP etch rate.
3. Due to the anodic shift of the OCP potential with illumination [Be9], a p-type Si electrode under anodic bias in HF is preferably etched in the dark areas.
4. The etch rate of moderately or low doped n-type silicon in HF is proportional to the number of photogenerated holes for current densities below  $J_{PS}$  [Da2, Tu6, Le19].

A characteristic property of these different modes is their spatial resolution. A spatial resolution in the order of the illumination wavelength used can be obtained if lateral diffusion of the photogenerated charge carriers is suppressed. This is not the case in mode 2, or in mode 4 if the electrode is under inversion (with  $J > J_{PS}$ ). If the electrode is kept under depletion as in modes 3 or 4 (with  $J < J_{PS}$ ) or in mode 1, diffusion becomes minimal. If light of sufficiently short wavelengths is

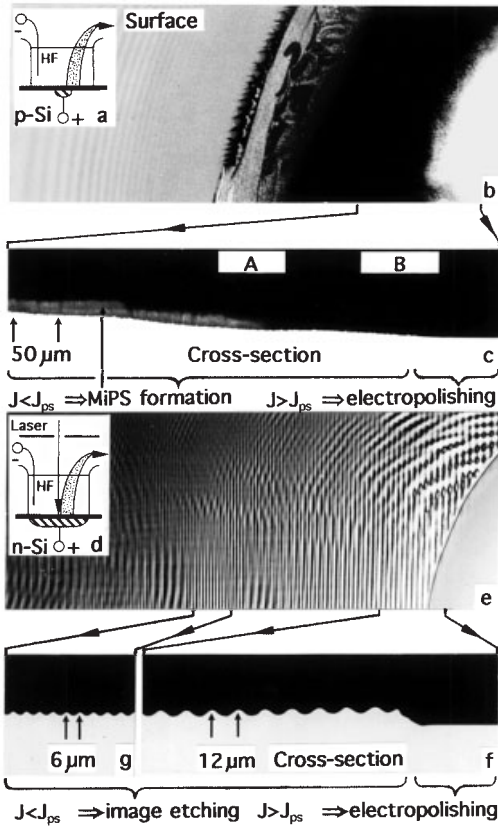


**Fig. 4.17** Optical micrographs showing the effect of a lateral increase (from left to right) in anodization current density on sample morphology. (b) Surface and (c) cross-section of a p-type (100) substrate anodized in the dark ( $4 \times 10^{14} \text{ cm}^{-3}$ , 60 s, 10 V, 1:1 HF 50%: ethanol) using a set-up with a small, local ohmic back contact, as shown in (a). An SEM micrograph of the center of (c) is shown in Fig. 6.11c. SEM images of regions A and B are shown in Figs. 6.11c and 2.4c, respec-

tively. (e) Surface and (f, g) cross-sections of an n-type (100) substrate anodized under illumination ( $10^{15} \text{ cm}^{-3}$ , 600 s, 2 V, 6% aqueous HF) using an interference pattern generated by a HeNe laser (633 nm) and a slit as shown in the inset (d). The micro PS layer visible for the p-type sample in the left part of (c) was removed for the n-type sample by a short KOH rinse for better visibility of the wave pattern. After [Le19].

used, virtually all charge carriers are generated close to the surface and so spatial resolution of the order of a few micrometers becomes possible. The proportionality between illumination intensity and etch rate favors mode 4 for microstructuring of silicon by photoelectrochemical etching.

The dependence of spatial resolution on the charge state of the electrode in mode 4 is visualized in Fig. 4.17 d–g. A red HeNe laser and a slit have been used to project a diffraction pattern on an n-type sample surface as shown in the inset



(d) of Fig. 4.17. For current densities in excess of  $J_{PS}$  the surface shows homogeneous electropolishing, producing the flat area (f) in Fig. 4.17. For current densities below  $J_{PS}$ , etching is proportional to the illumination intensity and a wavy pattern (g) is observed. Note that the whole sample was illuminated with a diffraction pattern, the pronounced border between the wavy region (g) and the flat region (f) in Fig. 4.17 is solely due to the change from depletion to inversion at  $J=J_{PS}$ . The minimal wavelength of the sine wave topography obtained in this experiment was about  $4\ \mu\text{m}$  [Le19]. Photochemical etching of n-type Si is performed under conditions sufficient for the formation of micro and macro PS. The undesirable formation of macropores can be suppressed if a substrate of low resistivity ( $>5\ \Omega\ \text{cm}$ ) and low bias ( $<2\ \text{V}$ ) is used. The formation of micro PS cannot be avoided, however micro PS can selectively etch by a slow silicon etchant, as for example in alkaline solutions at RT. Photochemical etching is a perfect tool for producing patterned structures without the use of standard lithographic techniques simply by projecting the desired pattern on the electrode while anodizing [Da4, Ho2, Le19].

If a p–n junction is present in the substrate, a potential difference and a photocurrent can be generated by illumination. This photocurrent can be used to form a stain film (micro PS) on the p-type side of the junction and thereby mark it [Fu3, Mi6, Pr8, Wu2] or to deposit a noble metal on the n-type side of the junction [Tu7]. The internal power supply formed by the illuminated junction can also be used for electrochemical etch-stop techniques, replacing an external source as discussed in the previous section [La3]. Such photoelectrochemical etch stops have the advantage that no external connections are required. A disadvantage, on the other hand, is the limited value of the potential difference, which is usually below  $0.6\ \text{V}$ . The combination of illumination, different doping densities and applied potentials gives a high degree of freedom to optimize an etch stop according to the desired application [M11, Tu6].

## 5

### Anodic Oxidation

#### 5.1

##### Silicon Oxidation Techniques

One of the properties that makes silicon the elephant in the zoo of semiconducting materials used in microelectronic manufacturing is the superior dielectric properties of its oxide [So1]. An SiO<sub>2</sub> layer can be formed by a simple thermal oxidation process in a wet (water vapor) or dry (oxygen) atmosphere. The growth process is found to be diffusion limited and can be described by a parabolic growth law [De1]. By rapid thermal annealing (RTA), oxidation times in the order of tens of seconds become feasible [Fu1, Go2]. However, independent of the kind of furnace used, the two drawbacks of thermal oxidation remain, which are the high thermal budget that inevitably leads to a smear-out of steep doping profiles and the restriction that thermal oxides can only be formed on a bulk or a polysilicon substrate. Therefore alternative methods of oxide formation such as CVD, LPD and anodic oxidation have been developed.

Anodic oxidation is a very common process in the electrochemical industry, used for example in the manufacture of aluminum and tantalum capacitors. The anodic oxidation of silicon is not of comparable importance, because the electrical properties of anodic oxides are inferior to those of thermal oxides.

To understand the electrochemical behavior of silicon, however, the formation and the properties of anodic oxides are important. The formation of an anodic oxide on silicon electrodes in HF and HF-free electrolytes will therefore be discussed in detail in this chapter. The formation of native and chemical oxides is closely related to the electrochemical formation process and will be reviewed briefly. The anodic oxidation of porous silicon layers is closely related to the morphology and the luminescent properties of this material and is therefore discussed in Section 7.6.

## 5.2

### Native and Chemical Oxides

An oxide layer of about 1 nm thickness is present on a silicon wafer as received from the supplier. This oxide is called a native oxide and forms on every bare silicon surface exposed to ambient air. A 'bare' silicon surface can be generated, for example, by cleaving a silicon crystal in high vacuum.

Native oxidation also takes place at hydrogen-passivated silicon surfaces, which can easily be generated by an HF dip. The oxidation process of a hydrogen-passivated surface in air is rather slow and it takes several hours for the native oxide to be formed [Gr5, Hi2, Ni1]. A detailed study of the oxidation process in air using X-ray photoelectron spectroscopy (XPS) revealed that the amount of suboxide species,  $\text{SiO}_x$  with  $x < 2$ , does not increase above an oxide thickness of 0.5 nm. For an oxide thickness in excess of 0.5 nm a continuous stoichiometric oxide film is present [Ai1]. During the oxidation reaction of hydrophobic surfaces with water vapor in air,  $\text{SiH}_4$  is formed as a by-product in the ppm range [La1]. The rate of native oxide formation is found to be enhanced if the sample is exposed to UV light. This effect has been used to generate a patterned native oxide by a lateral variation of the light intensity, without the use of a resist [Kr2].

If a hydrogen-terminated silicon surface is exposed to DI water at RT for several minutes the Si-H is slowly replaced by silanol groups (Si-OH). This reaction starts at the most unstable trihydrides, continues at the dihydrides, and finally at the most stable monohydrides [Gr1, Gr2, Mo1]. The silanol groups reduce the contact angle and the surface becomes hydrophilic. At this stage, no oxide is incorporated into the Si-Si backbonds. It needs long rinsing times (>100 min) to form Si-O-Si bridges. For such a thin surface oxide formed in water or other electrolytes at ambient conditions without an applied potential the term 'chemical oxide' will be used. The thickness of chemical oxides, for example formed in one of the common hydrophilic cleaning procedures or in ozonized water, is limited. The measured oxide thicknesses deviate significantly depending on the technique used. While thicknesses of 0.95 nm (SC1) [Su2] and 1.1 nm (SC2) [Ko8] were determined by X-ray reflectivity measurements, TEM images indicate a thickness of about 1.5 nm [Oh3]. The density of chemical oxides is lower than that of bulk thermal oxides. Values between 2.07 and 2.25 g cm<sup>-2</sup> are reported, depending on the amount of bound hydrogen. The hydrogen concentration itself depends on the chemical solution used [Aw1, Ko7, Su3]. However, chemically produced oxides do not exceed a thickness of about 2 nm under ambient conditions and electrons can easily tunnel through such thin layers [Sa2]. Under high pressures and high temperatures chemical oxides of up to 20 nm have been reported to form in  $\text{HNO}_3$  [Uc1].

The formation of a chemical oxide in pure DI water was found to depend critically on the DOC of the water [Gr3, Mo1, Li9]. In DI water of very low DOC (< 0.004 ppm), no native oxide forms. Furthermore the reverse reaction is observed; for elevated temperatures (80 °C) and long etching times (60 min) thin native or chemical oxides are removed and a hydrogen-terminated surface is established [Wa2].

Chemical oxides are reported to show non-uniformities of the thickness or the etch rate on a length scale of 30–100 nm, independent of crystal orientation or doping of the substrate. This is in contrast to oxides formed in the gas phase, which are very uniform [Ao1].

### 5.3

#### Anodic Oxide Formation and Ionic Transport

If a silicon electrode is anodically oxidized in an acidic electrolyte free of HF, the oxide thickness increases monotonically with anodization time. This is also true for alkaline electrolytes if the oxide formation rate exceeds the slow chemical dissolution of the anodic  $\text{SiO}_2$ . This monotonic behavior, however, is not necessarily associated with monotonic current-time or potential-time curves.

Typical anodization curves of silicon electrodes in aqueous electrolytes are shown in Fig. 5.1 [Pa9]. The oxidation can be performed under potential control or under current control. For the potentiostatic case the current density in the first few seconds of anodization is only limited by the electrolyte conductivity [Ba2]. In this respect the oxide formation in this time interval is not truly under potentiostatic control, which may cause irreproducible results [Ba7]. In aqueous electrolytes of low resistivity the potentiostatic characteristic shows a sharp current peak when the potential is switched to a positive value at  $t=0$ . After this first current peak a second broader one is observed for potentials of 16 V and higher, as shown in Fig. 5.1 a. The first sharp peak due to anodic oxidation is also observed in low concentrated HF, as shown in Fig. 4.14. In order to avoid the initial current peak, the oxidation can be performed under potentiodynamic conditions ( $V/t = \text{const}$ ), as shown in Fig. 5.1 b. In this case the current increases slowly near  $t=0$ , but shows a pronounced first maximum at a constant bias of about 19 V, independently of scan rate. The charge consumed between  $t=0$  and this first maximum is in the order of  $0.2 \text{ mAs cm}^{-2}$ . After this first maximum several other maxima at different bias are observed.

For galvanostatic anodization a first potential maximum is again observed at about 19 V, and the thickness of the anodic oxide at this maxima has been determined to be about 11 nm, as shown in Fig. 5.4. Note that these values correspond to an electric field strength of about  $17 \text{ MV cm}^{-1}$ . The first maximum may be followed by several more, as shown in Fig. 5.1 c and d. Note that these pronounced maxima become smeared out or even disappear for an increase in anodization current density (Fig. 5.1 d), a reduction in temperature (Fig. 5.1 c), or an increase in electrolyte resistivity. The latter value is usually too large for organic electrolytes to observe any current maxima. A dependence of these maxima on crystal orientation [Le4] or doping kind and density [Pa9] is not observed. The rich structure of the anodization curves is interpreted as transition of the oxide morphology and is discussed in detail in the next section.

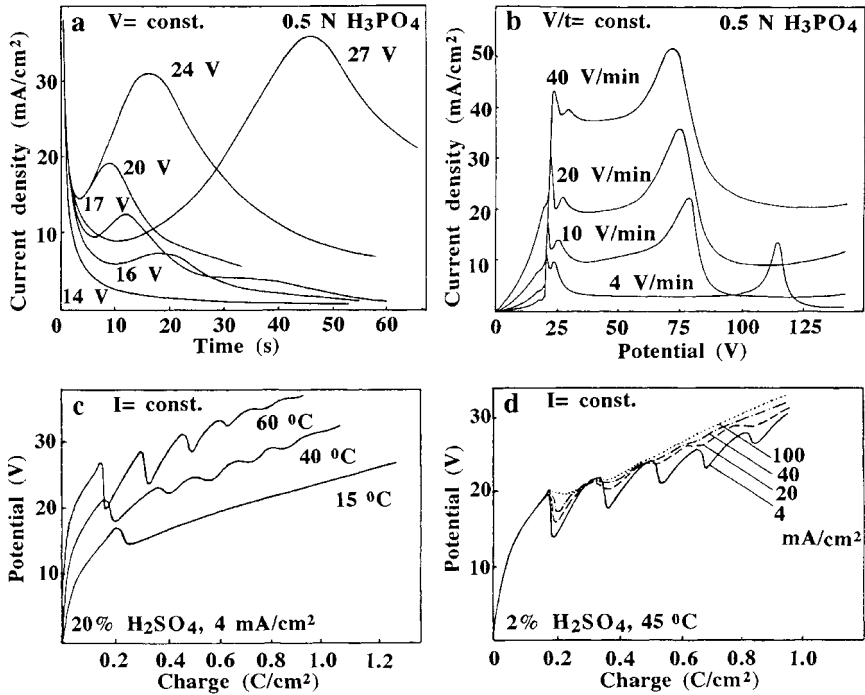


Fig. 5.1 (a) Current density versus time curves for potentiostatic oxidation at different potentials. (b) Current density versus potential curves for potentiodynamic oxidation at different scan rates. (c, d) Potential versus

charge curves for galvanostatic oxidation at different temperatures and current densities. A (111) p-type silicon electrode was used as anode. Redrawn from [Pa9].

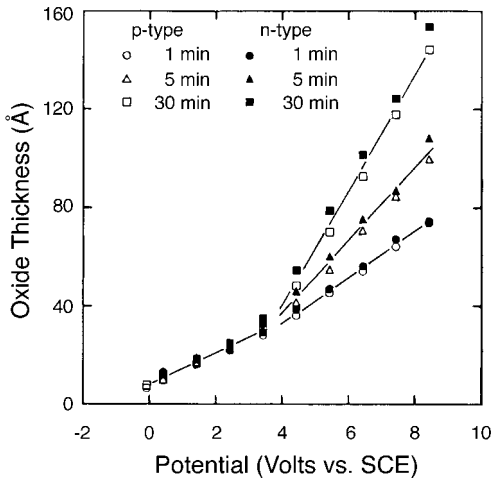


Fig. 5.2 Thickness of anodic oxides formed potentiostatically on (100) Si in 3%  $\text{NH}_4\text{OH}$ , as a function of applied potential for various anodization times. Illumination was provided for n-type Si. After [Ba14].

The growth rates of anodic oxides depend on electrolyte composition and anodization conditions. The oxide thickness is reported to increase linearly with the applied bias at a rate of  $0.5\text{--}0.6\text{ nm V}^{-1}$  for current densities in excess of  $1\text{ mA cm}^{-2}$  and ethylene glycol-based electrolytes of a low water content [Da2, Ja2, Cr1, Me12] (for  $D$  in nm and  $V$  in V):

$$D = 1.7 + 0.5V \quad (5.1)$$

In electrolytes of high water content no such correlation of oxide thickness on applied bias is observed; the oxide thickness, in contrast, increases monotonically under constant applied bias. In aqueous electrolytes, three different anodic oxidation regimes can be identified. In a first growth regime below 3 nm of oxide thickness, where the growth is assumed to be dominated by tunneling of charge carriers, the thickness depends on applied bias only and does not increase with anodization time, as shown in the potentiostatic curves of Fig. 5.2. Above a thickness of 3 nm, corresponding to a potential of 4 V, the oxide thickness increases with time under constant bias [Ba14].

Under galvanostatic conditions in 10% acetic acid the thickness  $D$  of the anodic oxide is found to depend on anodization time  $t$  according to:

$$\log D = a + b \log t \quad (5.2)$$

where constants  $a$  and  $b$  are a function of the applied current density; a graphical representation of Eq. (5.2) is given in Fig. 5.3 [Le22]. At an oxide thickness of 11 nm a pronounced change of the slope ( $b$ ) is observed, indicating a second and third growth regime. A change in oxide growth rate at an oxide thickness of about 10 nm was also found in alkaline electrolytes [Fa7].

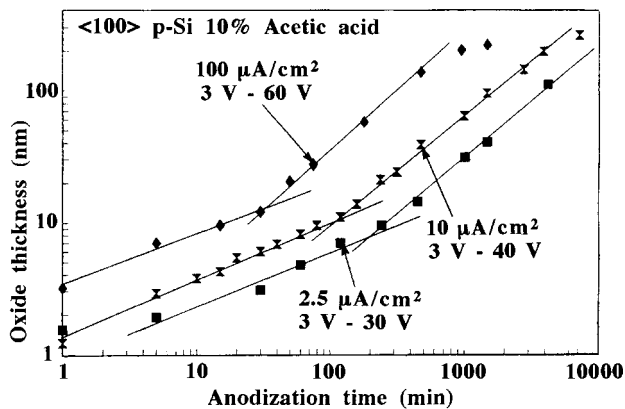


Fig. 5.3 The thickness of anodic oxides formed galvanostatically on (100) Si in 10% acetic acid as a function of anodization time for three applied current densities. The range

of potentials, observed at the end of anodization, is labeled for each value of current density. After [Le22].

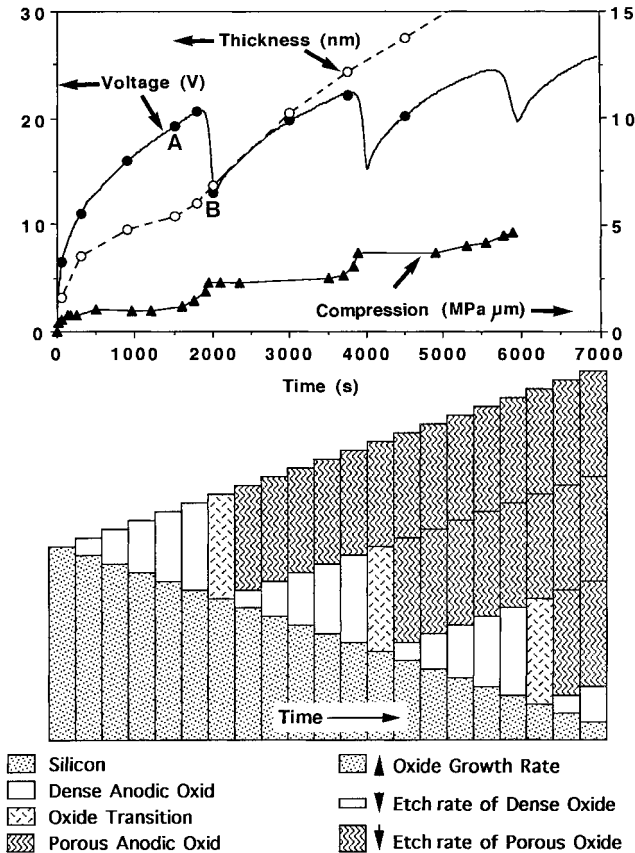


Fig. 5.4 Voltage-time curve for a p-type silicon electrode anodized galvanostatically at  $0.1 \text{ mA cm}^{-2}$  in 10% acetic acid. Silicon electrodes were removed from the electrolyte after various anodization times (filled circles) and the thickness of the anodic oxide was measured by ellipsometry (open circles). The curvature of the sample was monitored *in situ* and is plotted as the value of stress times oxide thickness (filled triangles). The bar graph below the  $V(t)$  curve shows a proposed formation mechanism. Galvanostatically a

dense oxide of increasing thickness is formed, producing a monotonic increase in the potential. At a thickness of about 11 nm a transition of the dense oxide to a porous modification occurs. Now ions can penetrate the porous oxide, resulting in a sudden drop in the potential. The growth of the next layer of dense oxide begins the next cycle. Because the total thickness of the oxide increases monotonically the oscillations are damped after a few periods. After [Le4].

A wide variety of electrolyte compositions used for anodic oxidation of silicon can be found in the literature. The electrolytes can be categorized in inorganic or organic solutions. In the latter case electrolytes like ethylene glycol [Ja2, Me6, Ma5, Me13], methanol [Ma2] or tetrahydrofuryl alcohol [Be3] are used, with salts such as  $\text{KNO}_3$  added in order to improve the conductivity. Studies with pure water [Ga2, Mo3, Hu3] as an electrolyte were performed, as well as with additions

of  $\text{NH}_3$  [Ba2],  $\text{KOH}$  [Fa7],  $\text{HCl}$  [Ba6],  $\text{CH}_3\text{COOH}$  [Le22],  $\text{H}_3\text{PO}_4$  or  $\text{H}_2\text{SO}_4$  [Pa9]. Despite this diversity in electrolyte composition, water is commonly assumed to be the active species in the oxidation process. Even in organic electrolytes traces of water or water formed by electrochemical processes at the electrode are assumed to be active.

According to Eq. (4.2), the anodic oxidation of silicon consumes four holes for the formation of one  $\text{SiO}_2$  group. This predicted ratio of four divided by the experimentally observed ratio is termed current efficiency. The current efficiency decreases with increasing oxide thickness and with increasing current density. For thin oxides of a few nanometers thickness the current efficiency may even be above unity, indicating a contribution of pure chemical oxidation. For an oxide thickness in the order of 100 nm, in contrast, values below 0.1 are observed, indicating a contribution of other anodic processes at the electrode, like oxygen evolution. Light emission during anodic growth of oxides above 15 nm thickness due to inelastic scattering of hot electrons has been reported [Zh1].

Several  $^{16}\text{O}/^{18}\text{O}$  tracer studies have been performed to determine the mobile species during the anodic oxidation process [Ma4, Me7, Pe8, Cr2, Me13]. As in the case of thermal oxides, oxygen was found to diffuse through the  $\text{SiO}_2$  to be built in at the Si– $\text{SiO}_2$  interface. This process is termed short circuit diffusion. An activation energy of 0.66 eV indicates that hydroxyl is the diffusing species in the anodic oxidation process [Dr1]. The rate of this field-enhanced diffusion seems to be the kinetically limiting process during anodic oxidation. During the growth of the first 3 nm of oxide the growth is dominated by lattice diffusion of oxygen, as observed in experiments performed with  $^{18}\text{O}$ -enriched electrolytes [Ba2]. Interestingly, an enhanced growth rate below a thickness of 3 nm is also observed for thermal oxides [Ma3]. It has been speculated that tunneling of charge carriers is a decisive factor during the growth of the first 3 nm [Be4], which becomes negligible for thicker oxides.

## 5.4

### Oxide Morphology, Chemical Composition and Electrical Properties

While the growth of thermal oxides is dominated by high-temperature diffusion of oxygen in the oxide matrix, anodic oxide growth is dominated by field-enhanced hydroxyl diffusion at RT. These different growth mechanisms result in pronounced differences in the morphological, chemical and electrical properties of the oxide.

#### 5.4.1

##### Morphology of Anodic Oxides

The morphology of the anodic oxide is sensitive to oxidation parameters and electrolyte composition. At water concentrations below about 5% in the electrolyte the oxide is usually more dense and shows a lower etch rate in HF than for concen-



trations above 5% [Me13]. The complexity of the galvanostatic and potentiostatic anodization curves in electrolytes of high water content, as for example shown in Figs. 5.1 and 5.3, has been ascribed to a morphological transition of the anodic oxide at a certain thickness, which results in a layered structure for thicker films [Pa9, Ch12, Le4].

An indication of such a morphological transition is a pronounced enhancement of oxide film roughness at a thickness of 11 nm, observed by AFM, as shown in Fig. 5.5. The appearance of this surface ripple corresponds to the first potential peak in Fig. 5.4. An investigation using differential IR spectroscopy revealed that the peak position, width and degree of symmetry of the Si–O absorption bands

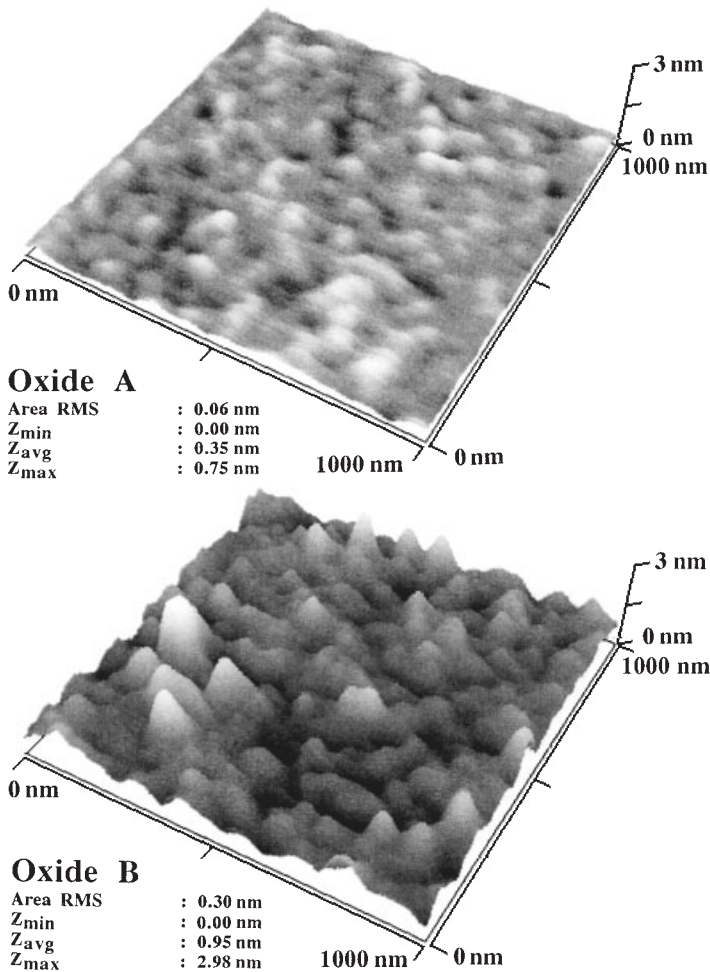


Fig. 5.5 AFM micrographs of the surface topography of anodic oxides (A) before and (B) after the potential drop as shown in Fig. 5.4. After [Le4].

depend upon film thickness below 10 nm, while for thicker films the spectral behavior was found to represent the bulk properties of the anodic oxide. This has been interpreted as a strain effect originating at the Si–oxide interface [Bo4, Cl2]. *In situ* measurements of stress during the growth of the anodic oxide showed a step-like behavior in phase with the potential peaks in the galvanostatic curve, as shown in Fig. 5.4.

Evidence for a layered structure is provided by X-ray reflection. For the oxide film present at point A in Fig. 5.4, a thickness of 10.8 nm and a density of  $2.1 \text{ g cm}^{-3}$  has been determined. While the film present at point B shows an angular reflectance that could best be fitted assuming a double layer structure with a thin (2.9 nm), dense ( $2.1 \text{ g cm}^{-3}$ ) oxide at the silicon interface and a thick (10.2 nm), less dense ( $1.75 \text{ g cm}^{-3}$ ) oxide on top. The density value found for the top oxide is in good agreement with density values obtained for thick (100 nm) anodic oxides using gravimetric methods.

From these observations, a basic oxide formation mechanism has been developed, as shown in the lower part of Fig. 5.4. The bars show the proposed oxide structure at the same time scale as the potential plotted above. First a dense oxide of homogeneous thickness is formed. At about 11 nm oxide thickness the transition from the dense to the porous type oxide occurs, indicated by a change of bar pattern in Fig. 5.4. After the transition the anodic oxide is porous, indicated by bars with a wavy pattern. The electrolyte now penetrates the oxide, which leads to a sudden drop in potential, if the electrolyte conductivity is large enough to ‘short-circuit’ the electric field in the porous region. During and after the potential drop the formation of a dense oxide continues at the interface to the substrate, which leads to a periodic behavior. Because of the overlying layers of porous oxide the oscillations become less pronounced with increasing anodization time. However, the microscopic details of the transition are still controversial. The porous nature of the low-density oxide film is ascribed to an accumulation of oxide defects [Ch12], to successive pitting of the film [Le13], or to an inhomogeneous distribution of stress [Le4].

Macroscopically the lateral thickness inhomogeneity of an anodic oxide (as measured by ellipsometry) can be less than 1% across the wafer for low current densities (e.g.  $10 \mu\text{A cm}^{-2}$ ), highly conductive electrolytes (e.g. 10% acetic acid) and an appropriate counter electrode geometry (e.g. Fig. 1.5b). For an oxide thickness above 100 nm the anodic oxide may develop a visible, haze-like roughening. It is not clear whether this effect is caused by stress or by dielectric breakdown. Microscopic inspection reveals that the roughening starts with a local increase in oxide thickness, as shown in Fig. 5.6a and b. This leads to mechanical fracture and fast regrowth of oxide under the defect (Fig. 5.6c–f). A high density of such defects (Fig. 5.6d) produces a macroscopic haze. Under severe oxide regrowth (Fig. 5.6e and f) millimeter-sized white spots appear on the electrode surface. Fast oxide regrowth can be avoided if the maximum bias is limited to values below 20 V.

Thinning of the anodic oxide coverage is found at sharp  $90^\circ$  edges of the substrate. This effect has been ascribed to oxide stress, because similar results are found for low-temperature thermal oxidation under conditions where viscous flow is not present. For oxide thicknesses in excess of about 100 nm, cracks develop in

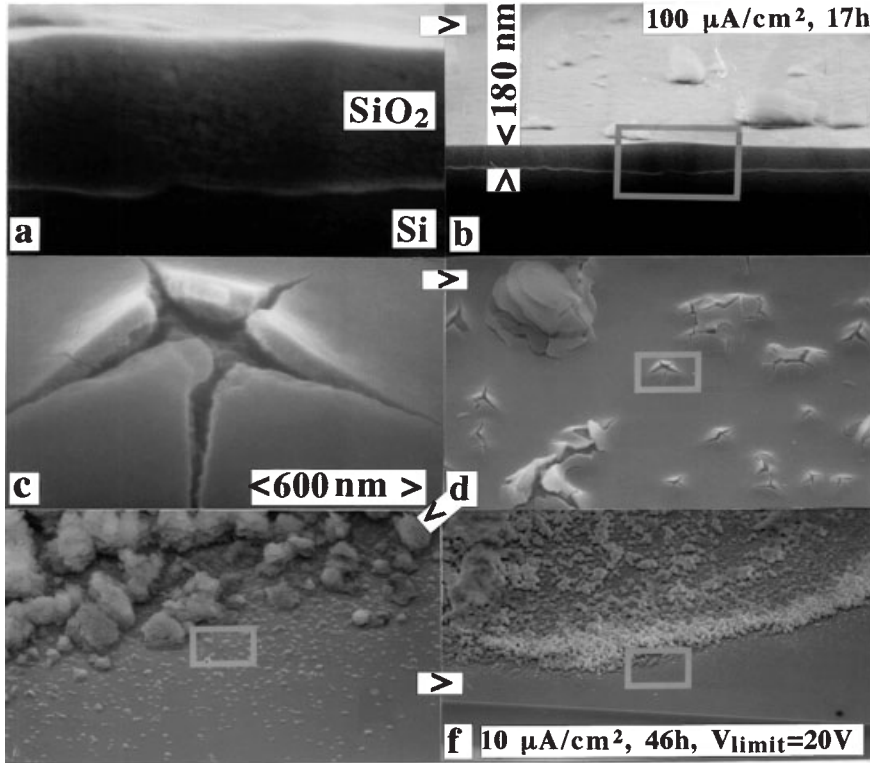


**Fig. 5.6** SEM micrographs of (a, b) a thickness inhomogeneity of an anodic oxide grown galvanostatically in 10% acetic acid without a bias limit. Such inhomogeneities develop into

(c, d) oxide defects that agglomerate to (e, f) extended defect areas by fast regrowth of oxide.

the strained regions at the edge as shown in Fig. 5.7b. This leads to erosion of the edge, if the applied bias is not limited, as a result of rapid regrowth of oxide, as shown in Fig. 5.7c and d. Note that a dependence of oxide thickness on crystal orientation is not observed in Fig. 5.7 – this is in stark contrast to low-temperature thermal oxidation where the oxide growth rate on (110) and (111) planes is roughly a factor of 1.5 higher than for (100) planes.

#### 5.4.2

#### Chemical Composition of Anodic Oxides

If the properties of anodically grown oxides are compared to those of thermal oxides, distinct differences are observed. Anodic oxides formed in water-rich electrolytes exhibit a lower refractive index ( $n_r < 1.4$ ) than thermal oxides ( $n_r = 1.46$ ) [Du2]. The density of thick anodic oxides is a weak function of the current density for galvanostatic anodization and increases from 1.8 to about  $2.1 \text{ g cm}^{-3}$  (thermal oxide:  $2.2 \text{ g cm}^{-3}$ ) if

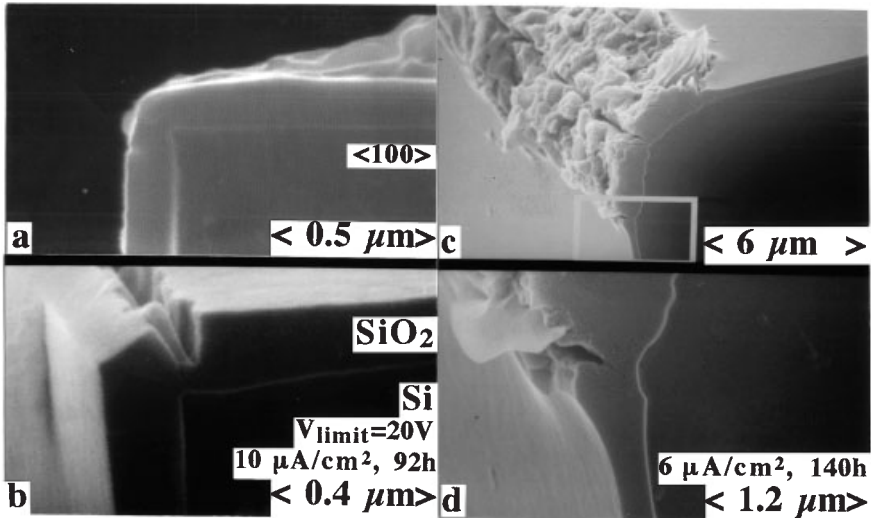


Fig. 5.7 (a) Anodic oxides exhibit thinning at sharp convex edges. (b) Cracks develop with increasing oxide thickness, eventually leading

to (c, d) erosion of the edge, if the anodization potential is not limited during galvanostatic anodization.

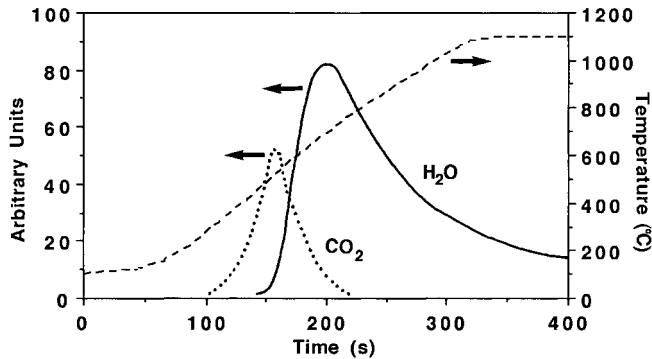


Fig. 5.8 Thermal effusion of  $\text{H}_2\text{O}$  and  $\text{CO}_2$  from a 196 nm thick anodic oxide film for a temperature ramp from RT to  $1100^\circ\text{C}$ . After [Le22].

the current density is reduced from  $1 \text{ mA cm}^{-2}$  to  $10 \mu\text{A cm}^{-2}$ . This indicates differences in the structural and chemical composition. However, it has been shown that anodic oxides behave like thermal ones upon annealing and that anodization of thermal oxides in water leads to properties similar to those of anodic oxides [Sc10]. This can be interpreted as a result of removal of  $\text{OH}^-$  groups in the  $\text{SiO}_2$  network, or to their introduction.

During a temperature scan from RT to  $1100^\circ\text{C}$  the effusion of  $\text{CO}_2$  and  $\text{H}_2\text{O}$  has been observed from an anodic oxide film, as shown in Fig. 5.8. The detected amount of  $\text{CO}_2$  could be explained by a monolayer of hydrocarbons adsorbed on

the oxide surface. The amount of  $\text{H}_2\text{O}$  was found to be in excess of  $2 \mu\text{g cm}^{-2}$ , corresponding to more than  $0.1 \text{ g cm}^{-3} \text{ H}_2\text{O}$  in the oxide or roughly one molecule of  $\text{H}_2\text{O}$  per five molecules of  $\text{SiO}_2$ . This value is about two orders larger than the value found for thermal oxide films [Be3]. The high effusion temperature indicates that  $\text{H}_2\text{O}$  or  $\text{OH}$  are not absorbed but chemically bound in the oxide. Annealing produces a 10% decrease in oxide thickness for thick oxides ( $>11 \text{ nm}$ ). Thinner oxides in contrast show an increase in thickness and in roughness upon annealing. The oxide etch rate (e.g. in 1% HF) decreases by one order of magnitude after an anneal at  $1100^\circ\text{C}$  [Le22].

### 5.4.3

#### Electrical Properties of Anodic Oxides

The electrical properties of an anodic oxide are found to depend on the formation conditions and subsequent treatments such as annealing. As-prepared anodic oxides show high leakage currents and a diode-like behavior known from anodic oxides of valve metals. A short high-temperature anneal, which removes the bound hydroxyl, reduces the leakage current to values typical of thermal oxides, as shown in Fig. 5.9.

An anodic oxide grown in pure water at  $10 \mu\text{A cm}^{-2}$  to thicknesses between 4 and 10 nm and subsequently annealed at  $700^\circ\text{C}$  in  $\text{N}_2$  for 1 hour, showed an interface charge density ( $10^{11} \text{ eV}^{-1} \text{ cm}^{-2}$ ) and a dielectric breakdown field strength ( $11\text{--}14 \text{ MV cm}^{-1}$ ) that are comparable with known values for thermal oxides [Ga2]. While the breakdown field strength of anodic oxides is comparable to thermal

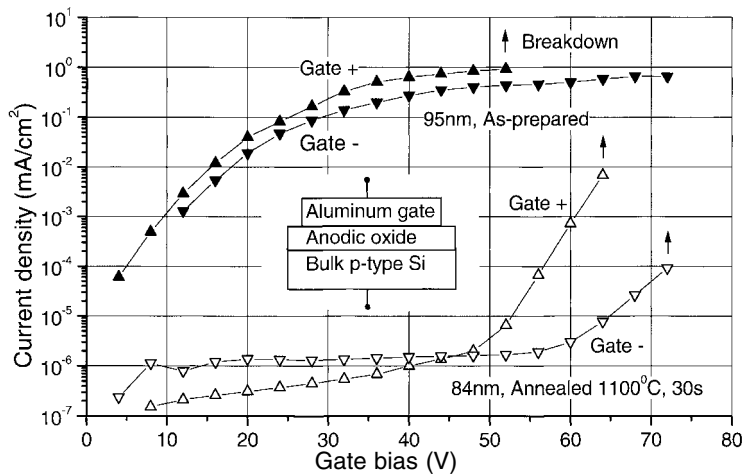


Fig. 5.9 Leakage current density of an as-prepared anodic oxide as a function of applied gate bias (filled symbols). Note that the leakage current density can be reduced by orders

of magnitude by a short anneal of the oxide in nitrogen (open symbols). After data of [Le22].

oxides the charge-to-breakdown is not. The charge-to-breakdown values of 50 anodic oxides were found to peak at  $0.1 \text{ As cm}^{-2}$ , which is two orders of magnitude below values found for thermal oxides [Le22].

Using an MOS structure, the metal-to-oxide barrier height was found to be 2.5–2.8 eV, which is about 0.3 eV lower than values found for thermal oxides [Ga2, Mo3, Ba14]. Such low values of interface charge density favor anodic oxide as a surface passivation layer, if a low thermal budget is desirable [Me12]. A low applied potential during the growth of the first few oxide layers is found to improve the electrical performance of the oxide [Ba14].

As a rule of thumb it can be said that the electrical properties of an anodic oxide are found to improve for thin layers that are grown slowly, at low potentials and low current densities. A subsequent RTA process is mandatory if low leakage currents are required.

To summarize, thermal silicon oxides are superior to anodic oxides for most applications. However, for special requirements, for instance if a very low thermal budget or a homogeneous oxide thickness on polysilicon layers is required, anodic oxides offer some benefits.

## 5.5

### Electrochemical Oscillations

Oscillations have been observed in chemical as well as electrochemical systems [Fr1, Fi3, Wo1]. Such oscillatory phenomena usually originate from a multivariable system with extremely nonlinear kinetic relationships and complicated coupling mechanisms [Fr4]. Current oscillations at silicon electrodes under potentiostatic conditions in HF were already reported in one of the first electrochemical studies of silicon electrodes [Tu1] and ascribed to the presence of a thin anodic silicon oxide film. In contrast to the case of anodic oxidation in HF-free electrolytes where the oscillations become damped after a few periods, the oscillations in aqueous HF can be stable over hours. Several groups have studied this phenomenon since this early work, and a common understanding of its basic origin has emerged, but details of the oscillation process are still controversial.

A typical I–V curve for a silicon electrode under potentiostatic control in aqueous HF is shown in Fig. 4.7. Sine-like current oscillations are observed for potentials positive of the one corresponding to the second current minimum  $J_4$ ; between 6 and 7 V in Fig. 4.7. These oscillations may occur spontaneously or can be initiated by a potential or current pulse – the latter case is shown in Fig. 4.14. Under galvanostatic conditions, potential oscillations are observed for current densities in excess of  $J_3$ . In this case the potential oscillations are not sine-like; a slow increase in potential is followed by a sudden drop, as shown in Fig. 5.10. The exchanged charge per oscillation period is by orders of magnitude too large to be explained simply by capacitive charging, even under the assumption of the maximum capacitance given by the Helmholtz layer, which is about  $0.5 \mu\text{F cm}^{-2}$  for silicon electrodes in HF [Na7]. A variation in pH or HF concentration changes the

frequency and the shape of the oscillations [Oz1], as well as the absolute values of the characteristic current density minima and maxima  $J_{PS}$ ,  $J_2$ ,  $J_3$  and  $J_4$ . However, the basic characteristic of the I–V curve and the position of the oscillation regime remain unaffected [Ch3].

For low HF concentrations in the order of 0.1%, the behavior of the interface is not oscillation, but rather resonant: if the potential is set to a fixed value and time is allowed for stabilization, a steady-state constant current is finally reached. Addition of a series resistor in the order of  $1 \text{ k}\Omega \text{ cm}^{-2}$  leads to sustained potentiostatic oscillations [Ch5]. For higher HF concentrations of about 2–5% aqueous HF, the system is self-oscillating, if the series resistivity of the electrolyte itself is not electronically compensated. For even higher concentrations the periodicity is lost and

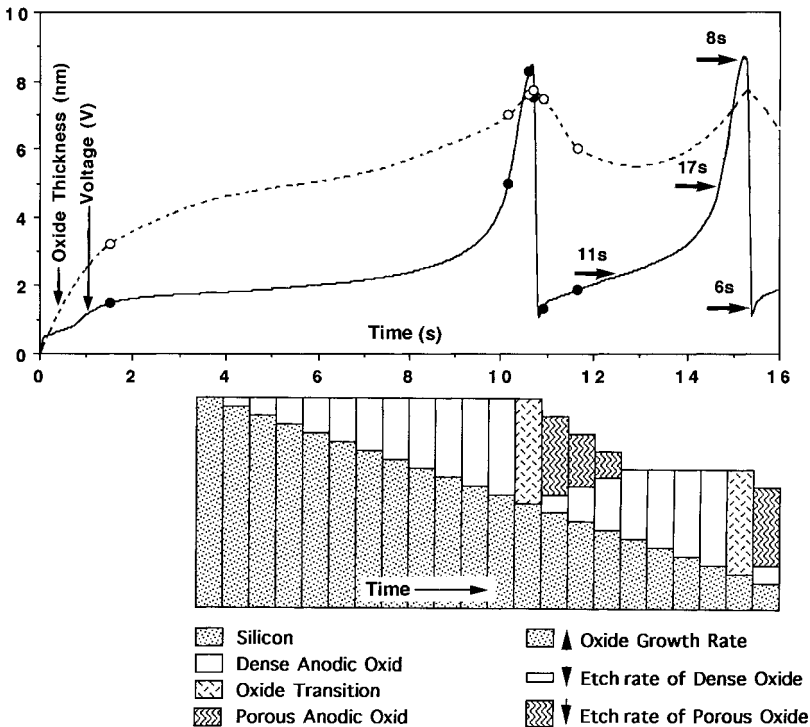
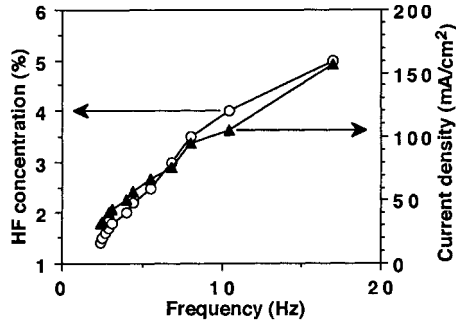


**Fig. 5.10** Voltage-time curve (solid line) for an  $n^-$ -type silicon electrode ( $3 \text{ m}\Omega \text{ cm}$ ) anodized with a constant current density of  $6.25 \text{ mA cm}^{-2}$  for  $t > 0$  (sample at OCP for  $t < 0$ ) in  $0.3 \text{ mol kg}^{-1} \text{ NH}_4\text{F}$  ( $\text{pH}=3.5$ ). The thickness of the anodic oxide was measured by ellipsometry (open circles, broken line fitted as a guide to the eye). The etch rate of the anodic oxide in the electrolyte was measured (values above arrows) at different

points of the oscillation by switching to OCP. The bar graph below shows a proposed oscillation mechanism. At first a dense oxide with a low etch rate is formed, which induces a monotonic increase in potential. At a thickness of about 8 nm a change in the oxide morphology leads to an increase in etch rate and a sudden decrease in potential. After this layer is etched away a dense oxide is formed again and the next cycle begins. After [Le4].

Fig. 5.11 The frequency  $f$  of potentiostatic electrochemical oscillations at a p-type silicon electrode in aqueous HF solutions is plotted versus the concentration  $c_F$  and the average current density  $J$ .



the system oscillates in a chaotic way. The dependence of the frequency of current oscillations on the average current density is roughly linear, according to Fig. 5.11. The exchanged charge per period is constant ( $13 \text{ mAs cm}^{-2}$ ) and corresponds to an anodic oxide thickness of 10 nm, assuming an oxide density of  $2.1 \text{ g cm}^{-3}$  and the consumption of four holes for the formation of an  $\text{SiO}_2$  molecule [Le4]. Under galvanostatic control potential oscillations are observed for a certain range of current densities. These oscillations are self-sustained for a wide range of HF concentrations.

There have been many attempts to characterize transient properties of the interfacial oxide during an oscillation cycle. A simple method is to remove the silicon electrode quickly from the electrolyte at different points of the I–V curve and flush with water. Then the thickness of the anodic oxide can be measured by standard ellipsometry, as shown by open circles in Fig. 4.7. An anodic oxide layer is present for current densities above  $J_{PS}$ . Between  $J_{PS}$  and the second current density maximum ( $J_3$ ) the oxide thickness increases from 1 nm to about 3 nm. In this oxide thickness regime tunneling of charge carriers is sufficient to produce current densities well in the mA regime [Fu4]. Beyond  $J_3$  the oxide thickness increases rapidly and reaches about 8 nm at  $J_4$ . Above  $J_4$  and in the regime of oscillations the oxide is 6–9 nm thick. In this thickness range the contribution of tunneling to the total current density depends greatly on oxide thickness, its porosity and applied bias. For slow oscillations, as present in electrolytes of low HF concentration (0.1 M), the oxide thickness and the free-carrier density can be determined *in situ* by Fourier transform infrared (FTIR) spectroscopy. The results are shown for the galvanostatic as well as the potentiostatic case in Fig. 5.12. Measurements of bulk PL at 1050 nm indicate an anticorrelation between interface recombination velocity and current density for the oscillation regime [Ra2]. Compared to the exchanged charge per period, the variation in oxide thickness during one oscillation cycle is found to be surprisingly small. The thickness variation is in most cases well below a factor of two, as shown by *in situ* [St2, Ag1] and *ex situ* ellipsometry [Le4], by XPS [Le12], by FTIR spectroscopy [Ca10], by charge measurements and by capacitive methods [Ch4]. This observation excludes oscillation models that are based on a complete dissolution and regrowth of a thin anodic oxide during one cycle. The oscillation process is accompanied by hydrogen evolution and electron in-



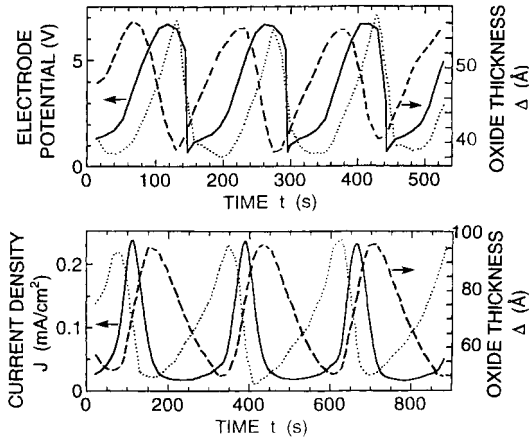


**Fig. 5.12** The oxide thickness (broken line) and the free carrier absorption (dotted line, in arbitrary units) determined by FTIR spectroscopy for galvanostatic (top,  $58 \mu\text{A cm}^{-2}$ ) and potentiostatic (bottom, 7 V) conditions in buffered HF (0.1 M, pH=4.5). Redrawn from [Ch12].

jection. The former has its maximum together with the oxide thickness maximum, while the latter is then at its minimum [Ca10].

A key to understanding the oscillation process is the observation that two forms of anodic oxide are present on the electrode. A dense, slow dissolving type of anodic oxide and a soft, fast dissolving type. A first indication of different dissolution rates is the shape of the I–V curve itself. For current densities above  $J_{PS}$  it is mainly determined by the dissolution rate of the thin anodic oxide. The existence of the current maximum  $J_3$  and the current minimum  $J_4$  can be interpreted as an indication of anodic oxides of different dissolution rates [Se9]. The oxide etch rates at different times of the oscillation cycle can be determined *in situ*, if the time delay between switching the electrode to OCP and the appearance of hydrophobic surface conditions is measured. Despite the fact that the oxide thickness changes by only about 20%, the time required for etching of the total oxide thickness varies by a factor as high as 3, as shown by arrows in Fig. 5.10. This modulation of the oxide etch rate itself is sufficient to generate an oscillation loop, as shown in the lower part of Fig. 5.10. The bars in this figure show the proposed oxide structure at the same time scale as the potential plotted above. The initial formation of an oxide with a low dissolution rate leads to an increase in potential under galvanostatic conditions with increasing oxide thickness. If the potential across the oxide is constant over the whole sample area, which is fulfilled for a good conductivity of electrolyte and substrate, the oxide becomes very homogeneous in thickness. This is a self-adjusting process, because the electric field across a thin oxide would be higher than for an area with a thicker oxide, generating a higher oxide growth rate at the thin spot until a homogeneous oxide thickness is reached. This effect is sufficient to synchronize the oscillations. At a certain thickness a change in the oxide morphology occurs, which transforms the dense oxide into the soft, porous form, indicated by a change in the bar pattern in Fig. 5.10. After this change the anodic oxide shows a high permeability for ions of the electrolyte. This leads to the sudden drop in the potential and an increase in

etch rate, indicated by bars with a wavy pattern in Fig. 5.10. Now the etch rate exceeds the growth rate and the total oxide thickness decreases until the fast etching layer is etched away. The next slow etching oxide is exposed to the electrolyte and its thickness increases again, and so on. There is strong evidence for such a layered structure of the oxide and the transient behavior of its etch rate, which is proposed to be the driving force of the oscillation process [Ch12, Le4].

The transformation of dense oxide into the soft form and the pertinent oscillations have also been observed during anodic oxide growth in HF-free electrolytes, as discussed in Section 5.4. However, the microscopic origin of this change in oxide morphology is as yet unidentified. Different oscillation models are under discussion. In one oscillation model the modulation of dissolution rate is ascribed to the presence of charged or neutral defects in the oxide that are generated depending on the current density [Ch4]. This model is connected with a model assuming small self-oscillating domains [Ch6, Ca12]. However, oscillation models based on local effects like electrical breakdown of the anodic oxide [Fo2] or the existence of small self-oscillating domains [Oz1, Ch6] usually suffer from the inability to explain the synchronization of the oscillations over large sample areas.

In another model, the modulation of oxide etch rate is ascribed to a stress-induced change in oxide morphology. This change is characterized by a crossover from a homogeneous stress distribution to an inhomogeneous one, which leads to highly stressed, fast etching regions in the oxide film. This model is supported by *in situ* stress measurements during an oscillation period [Le4].

The observation of pores in the anodic oxide with a density in the order of  $10^{11} \text{ cm}^{-2}$  [Ag1] supports the so-called fluctuating pore model [Le13]. This model assumes that randomly distributed pores in the oxides work as charge collecting centers, which lead to oscillations synchronized by the applied external electric field. It should be noted that the observed pore density corresponds well with the roughness at the oxide-electrolyte interface observed after the stress-induced transition of an anodic oxide, as shown in Fig. 5.5.

Other models are based on electric breakdown of the oxide [Fo2, Ch12]. It is not clear whether this breakdown should be thought of in terms of an electronic or an ionic effect. However, in both cases breakdown may cause a degradation in the oxide morphology, which leads to an enhanced etch rate. An electric field strength in the order of  $10 \text{ MV cm}^{-1}$ , the observation of an electroluminescent burst associated with the current peak of the oscillation, and the presence of an electronic component in the interface current are in favor of this model [Ca10, Ch12].

## 5.6 Electropolishing

In some ways electropolishing and electrochemical pore formation can be understood as the two sides of the same coin. In the first case the rate-limiting species in the chemical reaction is HF, while in the second it is the supply of holes from the electrode. If we assume a rough silicon wafer surface and a reaction that is

limited by the diffusion of HF, it is obvious that hillocks will dissolve faster than depressions because they are more exposed to the source of the rate-limiting species. If the reaction is limited by charge supply from the electrode the center of a depression will dissolve faster. The latter process will lead to pore formation while the former will lead to smoothing of the surface [Fo2]. However, this is a simplified picture of the electropolishing effect; real systems are more complex and electropolishing of metal and semiconductors commonly involves the presence of a thin oxide film.

The need for defect-free, flat silicon surfaces led to the first investigations in this field, which were performed as early as 1958 [Tu1]. It was found that electropolishing of silicon is possible in HF if the applied anodic potential is sufficient to produce current densities in excess of the critical value  $J_{PS}$ .

The reaction at any solid-state electrode is limited by the reaction kinetics, by charge supply or by ionic diffusion. Depending on electrolyte and electrode materials a change of dissolution reaction or growth of a passivating layer is often observed at the transition between the charge-limited and ionic diffusion-limited regimes. For the case of a silicon electrode the transition from the charge supply-limited to the ionic diffusion-limited case is characterized by the critical current density  $J_{PS}$ , as discussed in detail in Section 4.3. Electropolishing requires current densities in excess of  $J_{PS}$ . During electropolishing of an n-type substrate the electrode has to be illuminated with a light intensity sufficient to generate a current density  $J > J_{PS}$ .

If the electropolishing is performed in the regime of current oscillations (Section 5.5), silicon surfaces of an extremely low surface state density, in the order of  $10^{10} \text{ eV}^{-1} \text{ cm}^{-2}$  minimum, can be obtained. The remaining surface states are predominantly of donor type and have been related to water molecules adsorbed at surface imperfections. They can act as fixed positive surface charge ( $10^{10} \text{ cm}^{-2}$ ) as well as fast surface states, depending on the surface morphology and applied field. The fixed charge for an HF-dipped Si surface in comparison has been found to be two orders of magnitude larger [Ra3, Di5]. Electropolishing can therefore be applied as a simple *in situ* cleaning process during electrochemical experiments with silicon electrodes. For aqueous HF concentrations below 10%, for example, an anodic bias of 6–10 V or a current density of two times  $J_{PS}$  is sufficient to remove a microporous silicon film and to establish a surface of low recombination velocity within a few seconds.

Electropolishing under galvanostatic conditions can be used to remove bulk silicon in a well-defined manner. This can for example be used to profile doping density or diffusion length versus the thickness of the sample, as discussed in Sections 10.2 and 10.3. The thickness  $D$  of the removed silicon layer can be calculated from the applied current density  $J$ , the anodization time  $t$ , the dissolution valence  $n_v$ , the atomic density of silicon  $N_{Si}$  and the elementary charge  $e$ .

$$D = Jt / N_{Si} e n_v \quad (5.3)$$

As shown in Fig. 4.5, the dissolution valence  $n_v$  shows a relatively constant value of 4 for electropolishing current densities well above  $J_{PS}$  and a bias below 10 V.

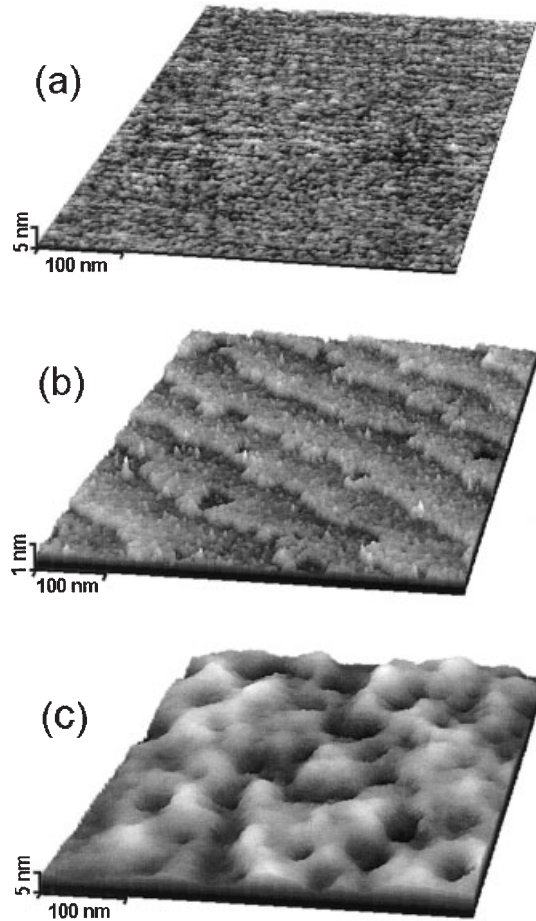


**Fig. 5.13** STM images of hydrogenated Si(111) surfaces after (a) immersion in aqueous 48% HF, (b) in 40%  $\text{NH}_4\text{F}$  and (c) after anodization in the oscillating regime

(+6 V vs SCE) in 0.1 M  $\text{NH}_4\text{F}$  for 30 min followed by electrochemical hydrogenation (−0.4 V). After [Di5].

For higher bias oxygen evolution is observed in some cases, which leads to values of  $n_v$  in excess of 4.

STM micrographs of the surface topography of silicon samples after different wet etching treatments are shown in Fig. 5.13. From the low number of surface states it could be speculated that the electropolished surface is atomically flat. In Fig. 5.13c, however, it can be seen that the low surface-state density after electro polishing is not associated with an atomically flat surface, but with a surface that is very smooth on a nanometer scale, while being wavy on a larger scale of about 100 nm. Note that a roughness on the same scale is observed for anodic silicon oxides grown on flat silicon electrodes, as shown in Fig. 5.5. Silicon surfaces

chemically etched in HF or  $\text{NH}_4\text{F}$  are much rougher on the nanometer scale, as shown in Fig. 5.13 a and b. On the micrometer scale electropolished surfaces are very smooth again, as shown for example in the right part of cross-sections in Fig. 4.17 c and f. On the millimeter scale flatness deviations may appear, because of inhomogeneous convection of the electrolyte. This effect can be minimized by using a low concentration of HF (1–3%), by increasing the electrolyte viscosity, for example by addition of glycerol to the electrolyte, and by the use of a rotating disk cathode [Ba11]. Concerning surface flatness from nanometer to millimeter scale, today's CMP methods are found to be superior to electropolishing.

Electropolishing is well established as a simple, *in situ* method to separate porous silicon layers from the silicon electrode. By switching the anodic current density from values below  $J_{\text{PS}}$  to a value above  $J_{\text{PS}}$ , the PS film is separated at its interface to the bulk electrode. The flatness of a PS surface separated by electropolishing is sufficient for optical applications, as shown in Fig. 10.10.

## 6 Electrochemical Pore Formation

### 6.1 Basics of Pore Formation

In order to use a consistent terminology in the following chapters it is emphasized that the term 'hole' will always refer to a defect electron, while an etched feature in the electrode will be designated as a 'pore' if its depth exceeds its width or otherwise as an etch pit. All values of current density refer to the initial surface of the electrode exposed to the electrolyte, which is for example defined by the O-ring of the set-up.

Pore formation is a common feature of many metal and semiconductor electrodes under anodic conditions in various electrolytes. Common products, for example aluminum capacitors, have been manufactured for decades using electrochemical pore formation techniques. Nevertheless in many cases the physics of pore initiation and propagation is poorly understood.

What causes the remarkable difference in dissolution rate between the pore tip and pore wall is the basic question for any system that shows pore formation. In this section a general view of this process is presented, without discussing details of the chemistry or of the pore morphology.

A common feature of all electrochemical pore formation processes in solid-state electrodes of a homogeneous chemical composition is the remarkable difference in dissolution rate between pore tip and pore wall. This is usually discussed in terms of an active-passive transition between the pore tip interface and the pore wall interface. But this still leaves the question open as to what quality of the pores makes their tips active and the remaining surface passive. On a basic level the active-passive transition has been ascribed to three distinct causes [Le31]:

1. The difference between pore tips and pore walls may originate from the initial state of the electrode prior to anodization.
2. The pore tips are different from the rest of the electrode surface by their geometry.
3. The pore tips are different from the remaining interface by their position in the electrode.

These three features are proposed to be basic causes for pore formation and will be illustrated by a few examples.

## 6.1.1

**Initial State of the Electrode**

Let us assume that the total surface of an electrode is in an active state, which supports dissolution, prior to anodization. The application of a constant anodic current density may now lead to formation of a passive film at certain spots of the surface. This increases the local current density across the remaining unpassivated regions. If a certain value of current density or bias exists at which dissolution occurs continuously without passivation the passivated regions will grow until this value is reached at the unpassivated spots. These remaining spots now become pore tips. This is a hypothetical scenario that illustrates how the initial, homogeneously unpassivated electrode develops pore nucleation sites. Passive film formation is crucial for pore nucleation and pore growth in metal electrodes like aluminum [Wi3, He7], but it is not relevant for the formation of PS.

The process described above is expected to produce a random distribution of active and passive spots on the electrode interface. But the electrode surface may also be artificially patterned prior to anodization in order to form nucleation centers for pore growth. This may be a lithographically formed pattern in said passive film or a predetermined pattern of depressions in the electrode material itself, which become pore tips upon subsequent anodization. The latter case applies to silicon electrodes and is discussed in detail in Chapter 9, which is devoted to macropore formation in silicon electrodes.

Both the examples discussed above show that the differences between pore tip and pore wall may have their origin in the initial state of the electrode.

## 6.1.2

**Pore Geometry**

The most obvious difference between pore walls and pore tips is their different geometry. For many porous samples the radius of the pore becomes minimal at the pore tip. This produces a maximum of the electric field strength and a minimum of the SCR width at the tip. This is even true if the radius of curvature is constant, due to the transition from the cylindrically curved pore wall to the spherical pore tip. As a result, electrical breakdown of a passive film or an SCR preferably occurs at the pore tip. The breakdown current promotes dissolution, and the pore grows. Junction breakdown is discussed in Chapter 8, which describes the growth of mesopores.

Another consequence of pore geometry is that for crystalline electrodes, other crystal planes are exposed to the electrolyte at the pore tip than at the pore walls. The dependence of pore growth on crystal orientation of the silicon electrode is discussed in Chapters 8 and 9.

### 6.1.3

#### **Pore Position**

At first sight the position of the pore tip in the electrode seems to be a badly defined parameter because its position changes while the pore is propagating. However, the pore tip is always farthest away from the bulk of the electrolyte. Diffusion thereby produces a minimal concentration of active ions and a maximum concentration of reaction products at the pore tip. This condition may already be sufficient for a passivation of the pore walls if the passivation mechanism is sensitive to ionic concentrations.

But even more important than the pore position in relation to the electrolyte is its position in relation to neighboring pores. The distance between the pores defines the pore wall thickness. For many cases of electrochemical pore formation, the pore tips are located close to each other and form a well-defined interface that separates the porous region from the bulk electrode. This close spacing of pore tips can effectively passivate the pore walls in semiconductor electrodes due to a depletion of charge carriers that support the dissolution process. The fact that it is virtually impossible to etch a single pore in a silicon electrode emphasizes the importance of pore spacing. The different mechanisms that produce pore wall depletion and their relation to the different pore size regimes will be discussed in the following sections.

## **6.2**

### **Porous Silicon Formation Models**

It is surprising that a defect-free, monocrystalline piece of silicon develops minute sponge-like porous structures or straight pores along certain crystal orientations upon simple anodization in HF. The explanation of such effects is a challenge to the imagination of any researcher and many different pore formation models have been discussed extensively in the literature. A brief summary of the basic models will be given here. Pore formation models specific to a certain pore size regime are presented at the beginning of Chapters 7–9.

### 6.2.1

#### **Linear Stability Analyses**

A theoretical framework for investigating pore initiation is provided by linear stability analyses. This method describes the stability of a propagating front upon introduction of a small perturbation [Mu4]. Let us for example assume a silicon surface with a small sine wave perturbation of its flatness. The interface will be stable if solving the equations of the system leads to damping of the perturbation with proceeding dissolution. Such a damping is expected for electropolishing conditions. Otherwise the interface will be unstable, which may result in pore initiation and growth. This method is a powerful tool for investigating the behavior of the dissolving interface, depending on all stabilizing and destabilizing effects pre-



sent. It is, however, quite difficult to find the correct mathematical description of stabilizing or destabilizing physical effects, for example quantum size effects or the SCR field [Ka1, Va3, Ch13, We6].

### 6.2.2

#### Probability Analyses

One approach to understanding the steady-state growth of a pore and the passive state of the pore wall is a simulation based on a reaction kinetic limited by the supply of a reactant, which diffuses to the reaction site [Sm3]. The diffusional distribution can be investigated by probability considerations for the reactants. Usually holes in the electrode are assumed to be the rate-limiting species during pore formation. Such statistical methods have been developed to describe non-equilibrium, kinetic depositions in terms of rate-limiting steps. Dissolution is inverse to deposition and a growing pore can be modeled in the same way as a growing dendrite. Two useful models for describing such growth phenomena are the Eden model [Ed1] and the diffusion-limited aggregation (DLA) model [Me8]. For the Eden model the growth of a cluster is assumed to be restricted by the reaction kinetics at the interface, while for the DLA model the rate-limiting step is assumed to be the diffusion of the reactants to the interface. In the latter case the introduction of a finite diffusion length enables us to study the dependence of cluster growth on the release point of a particle [Sm1]. Computer simulations proceed by releasing a particle from a random point at a distance of  $L$  lattice sites from the interface. The particle is then allowed to diffuse towards the interface with a two-dimensional random walk. When the particle contact an active site, defined as a lattice site immediately adjacent to the interface, the particle is added to the growing structure at the hit site. For the case of pore growth in silicon electrodes the particle would be for example a hole and the active site a pore wall or pore tip. Such simulations demonstrate a fractal to non-fractal transition at the diffusion length  $L$ . Or in other words there is a strong tendency for the pores to maximally space themselves at a distance of  $2L$  [Bo5].

This approach is favored by the striking similarity between the structural topologies of pore structures simulated by random walk and real mesoporous or macroporous silicon structures, as shown by various authors [Sm2, Pa11, Ya5, He3, Jo2, Va1]. However, it remains difficult to find the physical equivalent of the mathematical parameters used in the model. The diffusion length  $L$ , for example, has been interpreted as Debye length, minority carrier diffusion length or SCR width. A shortcoming of most simulations is the assumption of an unlimited collection efficiency of the pore tips. As a result, pore tips that collect more charge carriers grow faster and win the 'race', while others 'die'. This produces strongly branched and fractal pore geometries. For real pores, however, the charge transfer rate at the pore tip is limited by diffusion in the electrolyte. Nevertheless, an important result of the simulation approach is that the average dimensions of the porous network, given by the mean pore diameter and the mean pore spacing, are expected to be in the same order of magnitude as the diffusion layer width.

## 6.2.3

**Passivity and Passivity Breakdown**

The above models describe pore formation from a mathematical point of view and the parameters of the models are subsequently assigned to physical values. The models described below are based on the specific chemistry or physics of the semiconducting electrode.

A basic requirement for electrochemical pore formation is passivation of the pore walls and passivity breakdown at the pore tips. Any model of the pore formation process in silicon electrodes has to explain this difference between pore tip and pore wall conditions. Three different mechanisms have been proposed to explain the remarkable stability of the silicon pore walls against dissolution in HF, as shown in Fig. 6.1.

Anodic oxide formation suggests itself as a passivating mechanism in aqueous electrolytes, as shown in Fig. 6.1a. However, pore formation in silicon electrodes is only observed in electrolytes that contain HF, which is known to readily dissolve  $\text{SiO}_2$ . For current densities in excess of  $J_{PS}$  a thin anodic oxide layer covers the Si electrode in aqueous HF, however this oxide is not passivating, but an intermediate of the rapid dissolution reaction that leads to electropolishing, as described in Section 5.6. In addition, pore formation is only observed for current densities below  $J_{PS}$ . Anodic oxides can therefore be excluded as a possible cause of pore wall passivation in PS layers. Early models of pore formation proposed a

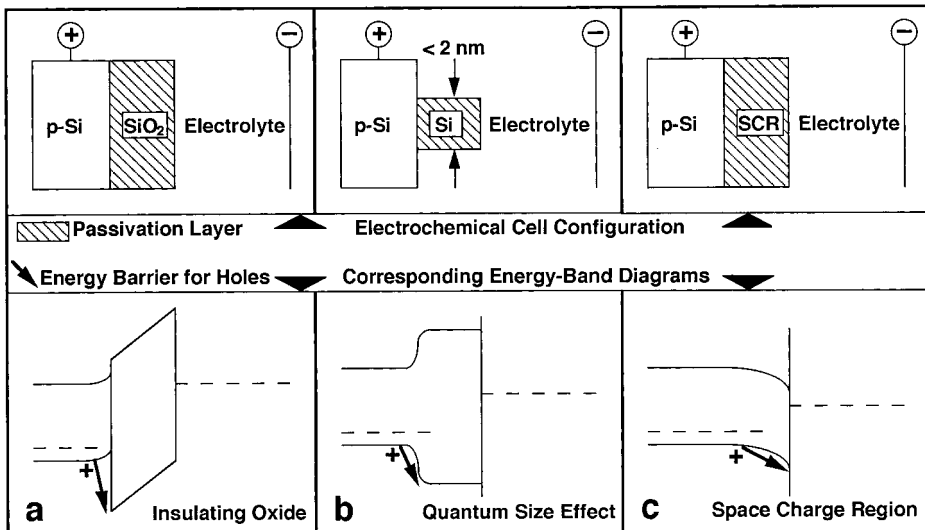


**Fig. 6.1** Mechanisms that could produce a passivation of the silicon–electrolyte interface (top) and the corresponding band diagrams (bottom). Note that passivation by an anodic

oxide (a) is not relevant for pore formation on silicon electrodes, while passivation by quantum confinement (QC) (b) or by an SCR (c) are.

passivating film consisting of silicic acid that passivates the pore walls [Un1, Un2]. However, this assumption contradicts several experimental observations. Chemical analyses, for example, show only silicon and hydrogen to be present in porous layers in significant concentrations. In conclusion, there is no evidence for the existence of a passive thin film with a chemical composition different from the bulk electrode.

Passivation can be understood as an energy barrier to charge transfer. This energy barrier, however, does not necessarily have to be constituted by an interfacial film of a chemical composition different from the bulk electrode. The energy of electrons and holes increases, for example, if they are confined in a tiny volume. This effect becomes significant in silicon, if the structural dimensions approach a few nanometers. Such tiny structures become passivated against dissolution because holes from the bulk need additional energy to enter the confined volume, as shown in Fig. 6.1b. Note that no electric field is involved – the energy barrier is a result of quantum confinement (QC) in the minute silicon structure. An inherent property of the QC model is that it explains not only the passive state of the pore walls but also the active state of the pore tips. QC is not only proposed to be responsible for the formation of microporous silicon [Le1], but also for its optical properties, like blue shift of the optical absorption edge and visible PL, as discussed in Sections 7.3 and 7.4.

An electric field in the semiconductor may also produce passivation, as depicted in Fig. 6.1c. In semiconductors the concentration of free charge carriers is smaller by orders of magnitude than in metals. This permits the existence of extended space charges. The concept of pore formation due to an SCR as a passivating layer is supported by the fact that n-type, as well as p-type, silicon electrodes are under depletion in the pore formation regime [Ro3]. In addition a correlation between SCR width and pore density in the macroporous and the mesoporous regime is observed, as shown in Fig. 6.10 [Th1, Th2, Zh3, Le8].

In contrast to QC, which is only present in the confined pore walls, the SCR is present at the pore tip, also. The active state of dissolution present at the pore tip, therefore, requires a mechanism of passivity breakdown. Morphology and the size regime of PS structures depend to a great extent on the way charge carriers transfer through the SCR at the pore tips. Charge transfer is limited by charge supply from the electrode in the pore formation regime and not by reaction kinetics or ionic diffusion. Therefore charge transfer across the SCR can be modeled using a Schottky diode with a non-planar interface as a solid-state analog for the electrode.

The proposed cause of pore wall passivation according to the above model is shown in the top row of Fig. 6.2. The cause of passivation breakdown at the pore tip is given in the middle row. In the bottom row of Fig. 6.2 the respective substrate doping densities and the resulting size regimes are given. A definition of the size regimes is given in Section 6.3. According to Fig. 6.2, the proposed pore formation mechanism and its dependence on doping density can be summarized:

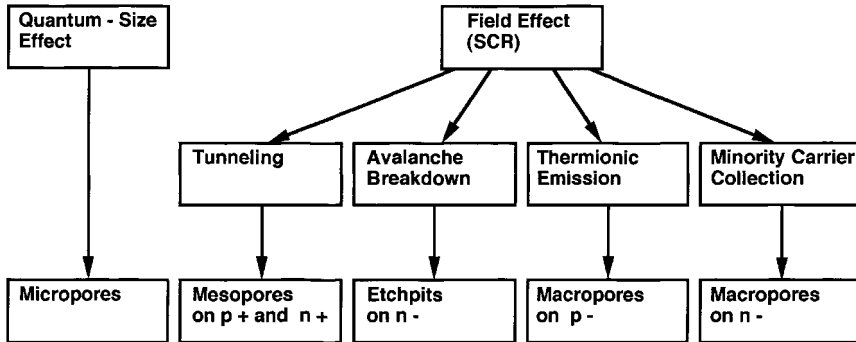


Fig. 6.2 Effects thought to be responsible for pore wall passivation (top row). Effects that can lead to passivation breakdown at the pore tip (middle row) and the resulting kinds of PS structure together with substrate doping type (bottom row). After [Le23].

1. QC in silicon structures requires dimensions of a few nanometers and is therefore proposed to be responsible for the formation of microporous films on Si electrodes, as discussed in Chapter 7. QC is independent of doping and is often found as a superposition to pore formation by SCR effects. Only for p-type silicon electrodes of doping densities of  $10^{16}$ – $10^{17}$   $\text{cm}^{-3}$  is no formation of SCR-related pores observed upon anodization in aqueous HF. This substrate doping regime is therefore best suited for formation of purely microporous layers.
2. Charge transfer at p-type electrodes, which are under forward conditions in the anodic regime, is dominated by tunneling through the SCR, for doping densities in excess of  $10^{18}$   $\text{cm}^{-3}$ . For n-type electrodes that are under reverse conditions, tunneling is the dominant charge transfer mechanism, also, if the doping densities are in excess of  $10^{18}$   $\text{cm}^{-3}$  or if the anodization bias is below 10 V. Tunneling is proposed to be the dominant process during formation of mesopores, as discussed in Chapter 8.
3. For p-type electrodes with doping densities below  $10^{18}$   $\text{cm}^{-3}$  diffusion and thermionic emission of charge carriers across the SCR is dominant. For p-type doping densities below  $10^{16}$   $\text{cm}^{-3}$  this charge transfer is associated with the formation of macropores, as discussed in Chapter 9.
4. For n-type electrodes with doping densities below  $10^{18}$   $\text{cm}^{-3}$ , avalanche breakdown in the SCR dominates for an anodization bias in excess of about 10 V. Avalanche breakdown corresponds to a radius of curvature in excess of about 100 nm and is proposed to be the cause of the formation of large etch pits, which will be termed macropits, as discussed in Chapter 8.
5. Another mechanism that can produce significant anodic pore tip currents across the SCR in low doped n-type electrodes ( $<10^{18}$   $\text{cm}^{-3}$ ) is collection of minority carriers (holes). Minority carriers can be generated by illumination or by injection from a p-type region. Macropore formation is observed in this regime, as discussed in Chapter 9.

In conclusion it should be emphasized that the passivation of the pore walls is electronic in nature. It therefore is not specific to silicon, but applies to all semi-conducting electrodes. This is in contrast to chemical passivation, which is usually specific to a certain electrode material and electrolyte chemistry.

### 6.3

#### Pore Size Regimes and Pore Growth Rates

The average pore size of PS structures covers four orders of magnitude, from nanometers to tens of micrometers. The pore size, or more precisely the pore width  $d$ , is defined as the distance between two opposite walls of the pore. It so happens that the different size regimes of PS characterized by different pore morphologies and different formation mechanisms closely match the classification of porous media, as laid down in the IUPAC convention [Iu2]. Therefore the PS structures discussed in the next three chapters will be ordered according to the pore diameters as mostly microporous ( $d < 2$  nm), mostly mesoporous ( $2 \text{ nm} < d < 50$  nm), and macroporous ( $d > 50$  nm). Note that the term ‘nanoporous’ is sometimes used in the literature for the microporous size regime.

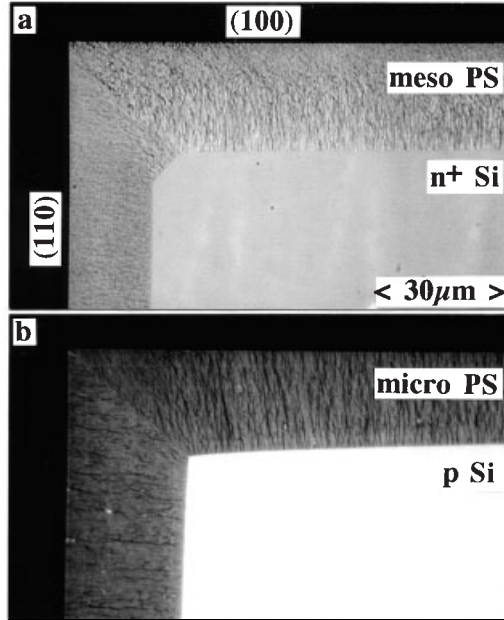
The smallest pores that can be formed electrochemically in silicon have radii of  $< 1$  nm and are therefore truly microporous. However, confinement effects proposed to be responsible for micropore formation extend well into the lower mesoporous regime and in addition are largely determined by skeleton size, not by pore size. Therefore the IUPAC convention of pore size will not be applied strictly and all PS properties that are dominated by quantum size effects, for example the optical properties, will be discussed in Chapter 7, independently of actual pore size. Furthermore, it is useful in some cases to compare the properties of different pore size regimes. Meso PS, for example, has roughly the same internal surface area as micro PS but shows only negligible confinement effects. It is therefore perfectly standard to decide whether observations at micro PS samples are surface-related or QC-related. As a result, a few properties of microporous silicon will be discussed in the section about mesoporous materials, and vice versa. Properties of PS common to all size regimes, e.g. growth rate, porosity or dissolution valence, will be discussed in this chapter.

The growth rate  $r_p$  of a pore can be defined as the increase in length  $dl$  divided by the required etch time  $dt$ . For a constant pore etching current and negligible diffusion gradients in the pore the growth rate becomes constant versus time and can be calculated using the total pore length  $l$  and total etching time  $t$ .

$$r_p = l/t \quad (6.1)$$

For the special case of straight pores growing orthogonal to the electrode surface forming a flat interface to the bulk, the pore length  $l$  becomes equivalent to the layer thickness  $D$ . Equation (6.1) then also defines the growth rate of the whole porous layer  $r_{PS}$ . The growth rate  $r_{PS}$  of a porous layer depends on several

**Fig. 6.3** Optical micrographs of edges of cleaved Si wafers showing different crystal planes anodized at  $100 \text{ mA cm}^{-2}$  in ethanoic HF (1:1). (a) The growth rate of meso PS formed on a highly doped n-type substrate ( $2 \times 10^{18} \text{ cm}^{-3}$ , 2 min) shows a clear dependence on crystal orientation. (b) An orientation dependence is not observed for micro PS formed on moderately doped p-type samples ( $1.5 \times 10^{16} \text{ cm}^{-3}$ , 4 min) but the PS thickness becomes inhomogeneous because of local variations in the current density caused by the edge geometry.



parameters such as substrate doping density, crystal orientation, HF concentration, current density and temperature. This is shown in Fig. 6.3a and b. The cleaved edge of a highly doped n-type sample shows that the meso PS growth rate is increased on (100) surfaces by a factor of about 1.5 compared to (110) surfaces. This orientation effect is not observed for micro PS grown on a moderately doped p-type substrate. In this case, however, current density variations caused by the edge geometry produce inhomogeneities in PS layer thickness.

The growth direction of mesopores and macropores formed electrochemically in silicon electrodes shows a certain dependence on crystal orientation. Generally the orientation dependence increases when the pore tip current density approaches  $J_{PS}$ . The pore growth rate is found to show an absolute maximum along the (100) direction. For the case of macropores a second relative maximum along the (311) direction has been observed [Ro8]. For other substrate orientations the pores do not grow orthogonal to the electrode surface. In this case the growth rate of an individual pore  $r_P$  equals  $r_{PS}/\cos a$ , with  $a$  being the angle between pore direction and the vector normal to the surface plane. The dependence of  $r_{PS}$  on substrate orientation is shown in Fig. 6.4. Note that no orientation dependence is observed for micro PS.

If one studies the growth rate as a function of anodization current density for different PS structures prepared in the same electrolyte, as shown in Fig. 6.5, some inherent laws can be observed. In the regime of stable macropore formation on n-type silicon the growth rate is found to be virtually independent of the applied current density. This is simply a consequence of  $J_{PS}$  being present at any pore tip, as described by Eq. (9.5). For the growth rate  $r_{PS}$  (in  $\text{nm s}^{-1}$ ) of micro PS in ethanoic

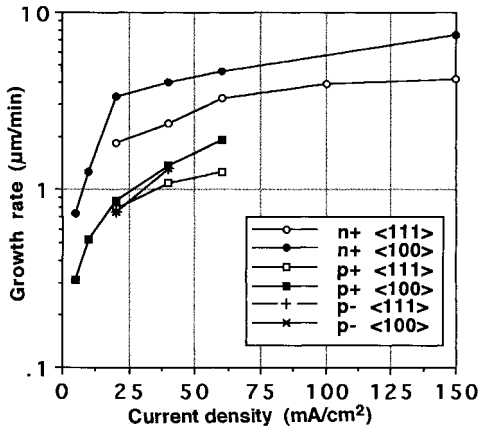


Fig. 6.4 Dependence of pore growth rates on crystal orientations of the substrate for different substrate doping densities and applied current densities (in HF:H<sub>2</sub>O:ethanol, 2.5:1). After data of [Gu4].

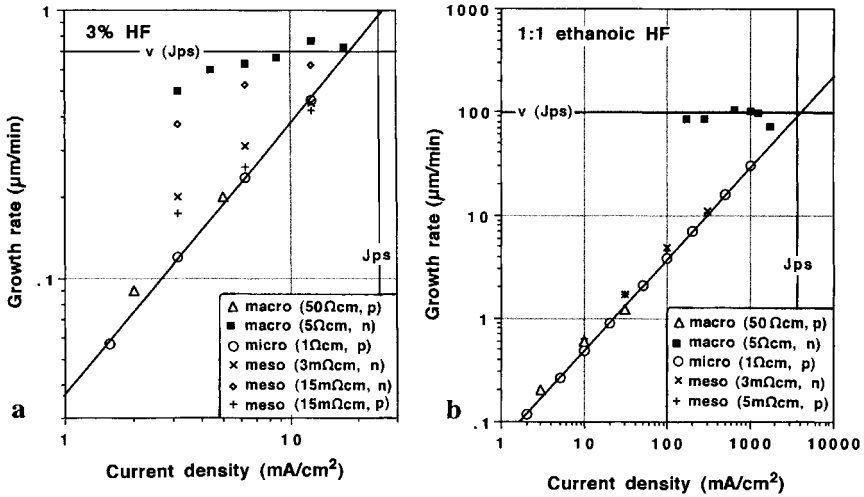


Fig. 6.5 Pore growth rates in (a) 3% aqueous HF and (b) ethanoic HF for different types of substrate doping and doping densities, as in-

dicated. Note that high growth rates are observed for low and moderately doped n-type substrates.

HF (ethanol: 50% HF, 1:1), in contrast, a power law dependence on current density  $J$  (in  $\text{mA cm}^{-2}$ ) over three orders of magnitude has been observed [Le5]:

$$r_{PS} = 1.05 J^{0.89} \tag{6.2}$$

For 3% aqueous HF an exponent close to 1 is observed, as shown in Fig. 6.5a.

The absolute values of micro PS growth rate are remarkably insensitive to HF concentration for a certain  $J$ . Equation (6.2) can therefore be used as an approximation for any concentration of aqueous HF. Note that the micropore growth rate according

to Eq. (6.2) and the constant macropore rate intersect at a growth rate equal to the silicon dissolution rate at  $J_{PS}$ , as shown in Fig. 6.5. Even if ethanoic HF is replaced by 3% aqueous HF there is little variation in  $r_{PS}$ , as shown by the data of Fig. 6.5 a and b. This is in stark contrast to macropore formation, where  $r_{PS}$  is coupled to  $J_{PS}$  and is therefore reduced by two orders of magnitude if ethanoic HF is replaced by 3% HF, as shown in Fig. 6.5. The dependence of macropore growth rate on concentration of aqueous HF is shown in Fig. 9.17. Note that a decrease in HF concentration due to ionic diffusion along the macropore leads to a decrease in growth rate with pore depth, as shown in Fig. 9.18. This effect is most pronounced for high HF concentrations, because the diffusion coefficient  $D_{HF}$  shows no strong dependence on HF concentration  $c$ , while the growth rate of macropores is proportional to the critical current density  $J_{PS}$ , which increases with about  $c^{1.35}$ , as described by Eq. (4.9). Thus low HF concentrations (<10%) are favorable for the formation of deep macropores.

While the micro and macro PS pore growth rates show little dependence on changes in the doping density the meso PS growth rate does, as shown in Fig. 6.9b. For p-type substrates  $r_{PS}$  shows a maximum for doping densities between  $10^{18}$  and  $10^{19}$   $\text{cm}^{-3}$ . For n-type substrates  $r_{PS}$  increases monotonically with decreasing doping density approaching the macro PS growth rate.

The PS layer thickness may show fluctuations over the electrode area on different length scales. The thickness variations may originate from a waviness of the bulk-PS interface, or the electrolyte-PS interface. The latter case, which is usually due to a dissolution of PS during anodization or a collapse of the PS microstructure due to capillary forces during drying, is discussed in Section 6.5.

A roughness on the millimeter scale is observed for micro, meso and macro PS if the HF concentration or temperature varies over the interface. HF concentration variations may be caused by inhomogeneous electrolyte convection at the electrolyte-electrode interface, another common cause are bubbles that stick to the electrode surface. Lateral temperature variations may be a problem during illumination-assisted PS formation.

A lateral variation of the anodization current will produce different growth rates and consequently an interface roughness for porous layers. Note that this is not the case for stable macro PS formation on n-type, because here the growth rate is independent of current density. An inhomogeneous current distribution at the O-ring seal of an anodization cell or at masked substrates produces PS layer thickness variations, as shown in Fig. 6.6. Inhomogeneities of the current distribution become more pronounced for low doped substrates, as shown in Figs. 6.3 b and 6.5 d [Kr3].

As a result of the crystal growth process Si wafers usually show striations, a variation in the bulk Si resistivity in a concentric ring pattern with a spacing in the order of millimeters. This variation of the bulk Si resistivity modulates the current density and thereby the porosity, which results in an interface roughness [Le16]. Mesopore formation due to breakdown at the pore tips is very sensitive to striations and can be used for their delineation.

A PS-bulk-interface roughness on the  $\mu\text{m}$  scale is found to develop for meso and micro PS layers with increasing PS thickness. This roughness especially impairs reflectivity measurements and the manufacture of optical superstructures



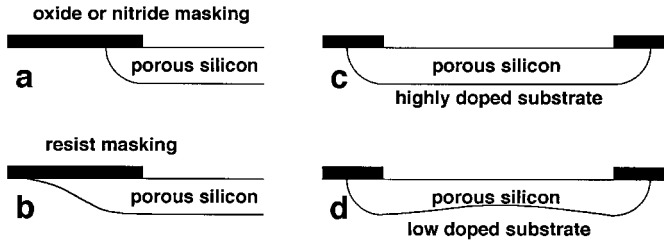


**Fig. 6.6** PS layer thickness inhomogeneities as a result of different kinds of masking layers and doping densities. (a) While under-etching is minimal for a silicon nitride mask, (b) a resist mask shows severe under-etching.

(c) On substrates of low resistivity the etch profile is isotropic, (d) while the PS thickness increases towards the edges of the pattern for high substrate resistivities.

(Section 10.5). The roughness frequency shows no strong dependence on doping density, while the amplitude increases from a few nm for degenerately doped material to several tens of nanometers for low doped substrates [Le16].

#### 6.4

##### Porosity, Pore Density and Specific Surface Area

Porosity is defined as the fraction  $p$  of the total volume of the sample  $V_{PS}$  that is attributed to the pores  $V_{pores}$ , detected by the method used:

$$p = V_{pores}/V_{PS} \quad (6.3)$$

Porosity relates to the ratio of the pore diameter  $d$  and the pore wall thickness  $w$ , but it contains no information about the absolute dimensions of the porous network.

The porosity is usually determined gravimetrically. The density of the porous layer  $\rho_{PS}$  is defined as the ratio of the PS mass  $m_{PS}$  and the PS volume  $V_{PS}$ .

$$\rho_{PS} = m_{PS}/V_{PS} \quad (6.4)$$

The porosity  $p$  is obtained if the porous layer density  $\rho_{PS}$  is normalized on the silicon bulk density  $\rho_{Si}$ .

$$p = 1 - \rho_{PS}/\rho_{Si} \quad (6.5)$$

The mass of the porous layer can either be determined by weighing the sample before and after anodization and determination of the dissolved mass  $\Delta m_D$  or by weighing the sample with and without the PS layer and determination of  $m_{PS}$ . The latter case needs an etchant with a high selectivity between bulk and PS, which is not required for the former case. The PS volume is given by the layer thickness  $D$  and the electrode area  $A$  exposed to the electrolyte.

$$p = \Delta m_D / (DA\rho_{Si}) = 1 - [m_{PS} / (DA\rho_{Si})] \quad (6.6)$$

The measurement of  $p$  for micro PS of high porosities is difficult because thick layers shrink or even disintegrate during drying, making it impossible to determine  $D$ , while for thin layers determination of the weight loss becomes critical. If  $p$  is assumed to be constant over  $D$  this problem can be circumvented by measuring both values separately. The thickness  $D$  and thereby the growth rate  $r_{PS}$ , as shown in Fig. 6.5, can easily be measured by ellipsometry for thin PS films, while the weight loss and thereby the dissolution valence  $n_v$ , as shown in Fig. 4.5, can be determined gravimetrically for thicker films. The porosity can then be calculated from both results using

$$p = J / (r_{PS} n_v e N_{Si}) \quad (6.7)$$

where  $e$  is the elementary charge and  $N_{Si}$  the atomic density of Si. For the special case of stable macropore formation the porosity is simply given by the ratio between the formation current density  $J$  and  $J_{PS}$ , according to Eq. (9.1). For ordered macropore arrays, the center-to-center distance of pores, termed the pitch  $i$ , is usually a constant. In this case the porosity can be calculated from the ratio  $d/i$ , as shown in Fig. 6.7.

In general the porosity of PS layers increases with increasing formation current density, as shown for micro PS in Fig. 6.8 and for meso PS in Fig. 6.9c. The porosity decreases with increasing HF concentration of the electrolyte [Un3, Be5]. The porosity is sensitive to the type of pores and therefore on substrate doping density, as shown in Fig. 6.9c. For a given electrolyte composition, current density and tempera-

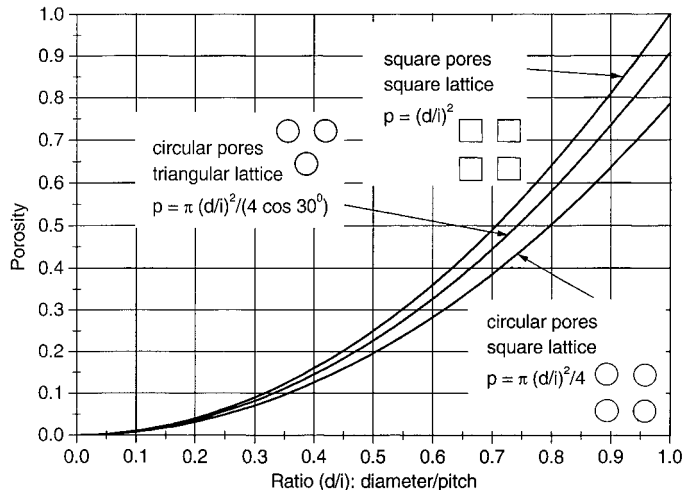
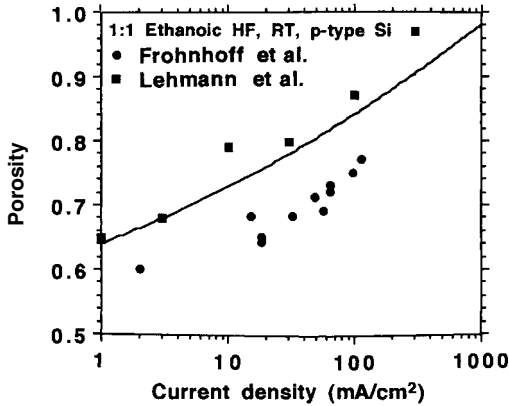


Fig. 6.7 Calculated values of porosity as a function of the pore diameter to pore pitch ratio for pore arrays of different pore shapes and pore patterns.



**Fig. 6.8** Porosity of micro PS formed in (1:1) ethanoic HF, RT, p-type Si together with porosity (line) calculated from growth rate and dissolution valence using Eqs. (6.7), (6.2) and (4.8).

ture, microporous layers are commonly found to be of higher porosity than mesoporous layers and these are again more porous than macroporous layers.

In Eqs. (6.3) to (6.7) the porosity is assumed to be constant over the PS volume. There are several cases for which this assumption is incorrect, because of a porosity gradient in the PS film. If the doping density, the current density, the HF concentration or the temperature are fluctuating over the sample surface or over anodization time, the porosity does accordingly. This effect is exploited in the manufacture of optical superlattices, as discussed in Section 10.5. If the formation parameters are kept constant, the porosity can be assumed to be constant for short anodization times and thin layers. However, for long anodization times pure chemical dissolution in the porous structure cannot be neglected and will lead to a decrease in porosity with pore depths. This effect is most pronounced for micro PS layers, because of their large inner surface [Un3, He4, Th4]. For meso and macro PS layers, in contrast, an increase in porosity with pore depth is observed. This effect, which is caused by a decrease in the HF concentration with pore depth due to diffusional limitations, is most pronounced for thick layers and high current densities, as shown for a meso PS layer in Fig. 8.5 [Th4, Le9]. The latter effect can be avoided if the anodization is interrupted to restore the equilibrium electrolyte concentration at the pore tips. If the break intervals are one order of magnitude longer than the anodization intervals no increase of porosity with depth is observed [Bi2].

In contrast to porosity, the pore density and the specific surface area are quantities directly related to the actual size of pores and pore walls. The pore density  $N_p$  is defined as the number of pores per unit area and it usually refers to a plane normal to the pore axis. For (100) oriented substrates this plane is parallel to the electrode surface, but for other orientations or strongly branched pores, there is no preferred plane orientation and  $N_p$  refers to an average of the pore density of different planes. For arrays of straight pores the pore density can be directly calculated from the array geometry. For cylindrical pores of diameter  $d$  orthogonal to the electrode surface, for example, the average pore density  $N_p$  is given by:

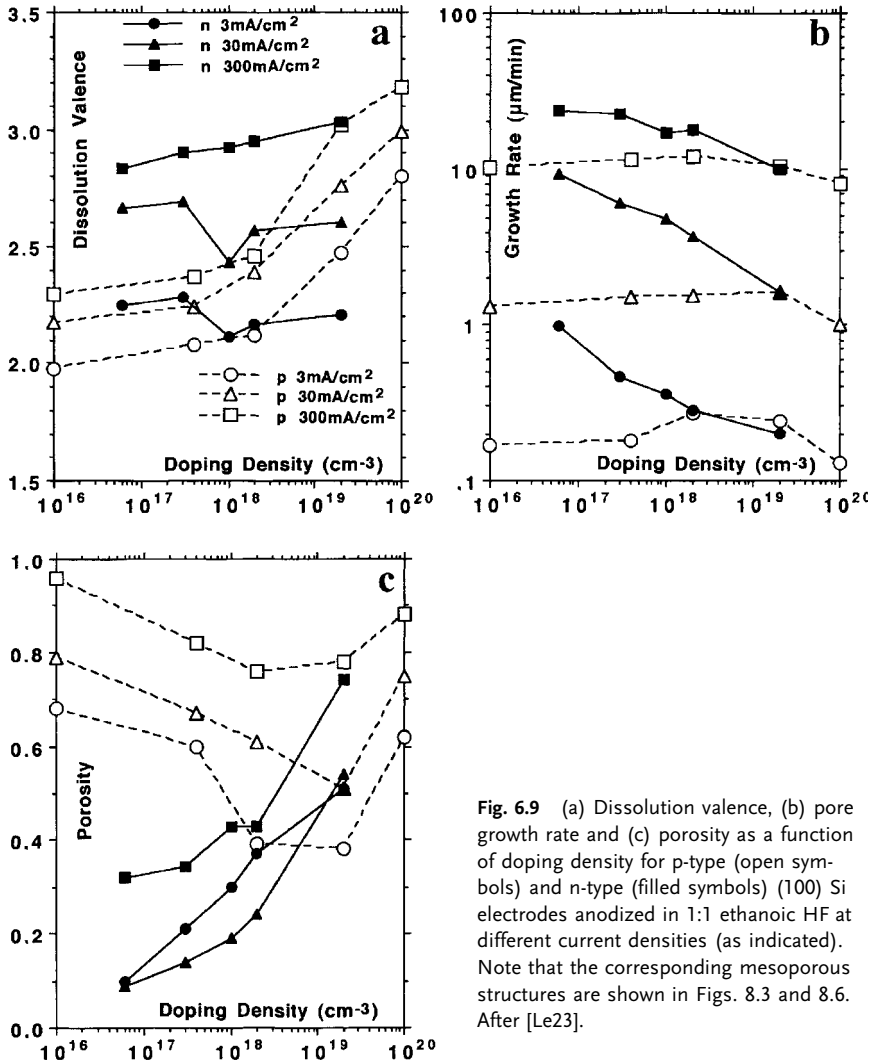
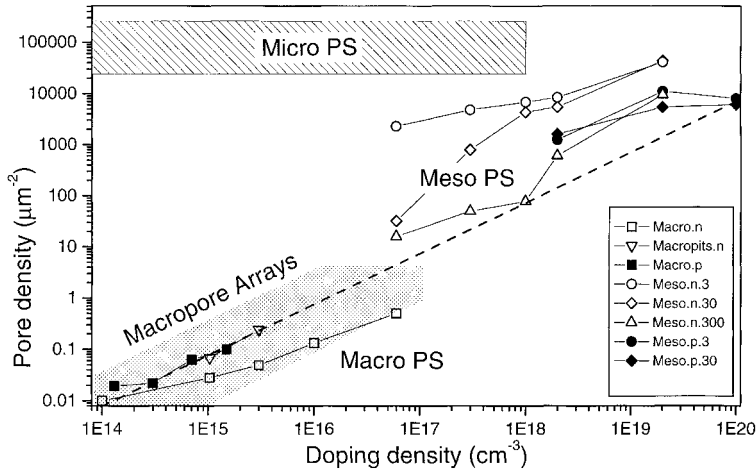


Fig. 6.9 (a) Dissolution valence, (b) pore growth rate and (c) porosity as a function of doping density for p-type (open symbols) and n-type (filled symbols) (100) Si electrodes anodized in 1:1 ethanoic HF at different current densities (as indicated). Note that the corresponding mesoporous structures are shown in Figs. 8.3 and 8.6. After [Le23].

$$N_p = p/\pi(d/2)^2 \quad (6.8)$$

If the pore density is plotted versus the doping density of the silicon electrode, it can be seen that the micropore density is independent of doping, while the macropore and mesopore densities increase linearly with doping density, as shown in Fig. 6.10. This is a consequence of the QC formation mechanism being independent of doping, while the SCR-related mechanisms are not, as discussed in Section 6.2.

The specific surface area is defined as the accessible area of solid surface per unit mass of material. For an array of macropores the specific surface area can be



**Fig. 6.10** Pore density versus silicon electrode doping density for PS layers of different size regimes. The broken line shows the pore density of a triangular pore pattern with a pore pitch equal to twice the SCR width for 3 V applied bias. Note that only macropores on n-type substrates may show a pore spac-

ing significantly exceeding this limit. The regime of stable macropore array formation on n-type Si is indicated by a dot pattern. Type of doping and formation current density (in  $\text{mA cm}^{-2}$ ) are indicated in the legend. After [Le23].

calculated directly from its geometrical dimensions. For example an orthogonal array of circular macropores with a pitch of  $2.5 \mu\text{m}$  and a diameter of  $2 \mu\text{m}$  has a specific surface area of  $0.859 \text{ m}^2 \text{ g}^{-1}$  (or  $1 \text{ m}^2 \text{ cm}^{-3}$ ). The porosity of such an array is 50%. For a pore depth of  $100 \mu\text{m}$  the surface area is enlarged by a factor of about 100 compared to the initial electrode surface. If the sizes of pores and pitch are shrunk by a factor of two, the porosity remains at 50%, while the specific surface area is doubled to  $1.718 \text{ m}^2 \text{ g}^{-1}$ . A surface enlargement of 100 is now realized with a pore depth of  $50 \mu\text{m}$ . Table 6.1 shows the increase in surface area with shrinking dimensions from the macroporous to the microporous regime and its consequences for the chemical composition of the porous layer. The values in the figure have been calculated for straight, cylindrical pores in an orthogonal pattern, as depicted in the lower right of the table. Micro and meso PS structures do not show such a well ordered morphology, nevertheless, the values in Table 6.1 can be used as an approximation.

While for macroporous structures the inner surface can be calculated from the geometry, meso and micro PS layers require other methods of measurement. First evidence that some PS structures do approach the microporous size regime was provided by gas absorption techniques (Brunauer-Emmet-Teller gas desorption method, BET). Nitrogen desorption isotherms showed the smallest pore diameters and the largest internal surface to be present in PS grown on low doped p-type substrates. Depending on formation conditions, pore diameters close to, or in, the microporous regime are reported, while the internal surface was found to

**Tab. 6.1** The left-hand side shows spectroscopic and excited-state kinetic properties of spherical silicon nanocrystals together with the sizes of biological building blocks. After [Br9, Ca11]. The right-hand side shows properties of an orthogonal array of cylindrical pores of 50% porosity. Pore density, specific surface area and the ratio of bulk atoms to surface atoms are displayed assuming an atomic density of  $7 \times 10^{14} \text{ cm}^{-3}$ , corresponding to a (100) Si surface, and a bulk density of Si atoms of  $5 \times 10^{22} \text{ cm}^{-3}$ . The chemical composition of the porous layer for a dihydride surface coverage and for a 0.5 nm thick (stoichiometric) native oxide layer are also given.

Biological objects	Spectroscopic regions	Kinetic regions	Atoms	Diameter (nm)	Size regime	Pore density ( $\mu\text{m}^{-2}$ )	Specific surface ( $\text{m}^2/\text{g}$ )	Atoms <sub>surf</sub> / Atoms <sub>bulk</sub>	Surface condition:
Drug molecules	Molecule	Unimolecular	$10^1$	0.7	Micro	$5 \times 10^5$	1718	0.28	$\text{Si}_{1.8}\text{H}$ $\text{SiO}_{1.2}$
DNA helix	Bulk exciton diameter	e-h Kinetics	$10^2$	1.6					
Proteins	Quantum Dot		$10^3$	3.4					
Viruses			$10^4$	7.3	Meso				
			$10^5$	16					
			$10^6$	34					
			$10^7$	73					
			$10^8$	156					
			$10^9$	337					
			$10^{10}$	726					
			$10^{11}$	1560					

Surface condition:	Atoms <sub>surf</sub> / Atoms <sub>bulk</sub>	Specific surface ( $\text{m}^2/\text{g}$ )	Pore density ( $\mu\text{m}^{-2}$ )	Diameter (nm)	Size regime	Surface condition:
$\text{Si}_{1.8}\text{H}$ $\text{SiO}_{1.2}$	0.28	1718	$5 \times 10^5$	0.7	Micro	$\text{Si}_{1.8}\text{H}$ $\text{SiO}_{1.2}$
$\text{Si}_{3.6}\text{H}$ $\text{Si}_{1.8}\text{O}$	0.14	859	$12 \times 10^4$	1.6		$\text{Si}_{3.6}\text{H}$ $\text{Si}_{1.8}\text{O}$
$\text{Si}_9\text{H}$ $\text{Si}_{5.6}\text{O}$	$5.6 \times 10^{-2}$	344	$2 \times 10^4$	3.4		$\text{Si}_9\text{H}$ $\text{Si}_{5.6}\text{O}$
$\text{Si}_{18}\text{H}$ $\text{Si}_{12}\text{O}$	$2.8 \times 10^{-2}$	172	5000	7.3	Meso	$\text{Si}_{18}\text{H}$ $\text{Si}_{12}\text{O}$
$\text{Si}_{36}\text{H}$ $\text{Si}_{24}\text{O}$	$1.4 \times 10^{-2}$	86	1250	16		$\text{Si}_{36}\text{H}$ $\text{Si}_{24}\text{O}$
$\text{Si}_{90}\text{H}$ $\text{Si}_{61}\text{O}$	$5.6 \times 10^{-3}$	34.4	200	34		$\text{Si}_{90}\text{H}$ $\text{Si}_{61}\text{O}$
$\text{Si}_{180}\text{H}$ $\text{Si}_{123}\text{O}$	$2.8 \times 10^{-3}$	17.2	50	73		$\text{Si}_{180}\text{H}$ $\text{Si}_{123}\text{O}$
$\text{Si}_{360}\text{H}$ $\text{Si}_{249}\text{O}$	$1.4 \times 10^{-3}$	8.6	12.5	156		$\text{Si}_{360}\text{H}$ $\text{Si}_{249}\text{O}$
$\text{Si}_{900}\text{H}$ $\text{Si}_{617}\text{O}$	$5.6 \times 10^{-4}$	3.44	2	337	Macro	$\text{Si}_{900}\text{H}$ $\text{Si}_{617}\text{O}$
$\sim\text{Si}$	$2.8 \times 10^{-4}$	1.72	0.5	726		$\sim\text{Si}$
$\sim\text{Si}$	$1.8 \times 10^{-4}$	0.86	0.125	1560		$\sim\text{Si}$

Biological objects

Drug molecules

DNA helix

Proteins

Viruses

Bacteria

Cells

Spectroscopic regions

Molecule

Bulk exciton diameter

Quantum Dot

Polariton

Kinetic regions

Unimolecular e-h Kinetics

Band bending

Many-body kinetics

Atoms

$10^1$

$10^2$

$10^3$

$10^4$

$10^5$

$10^6$

$10^7$

$10^8$

$10^9$

$10^{10}$

$10^{11}$

Diameter (nm)

0.7

1.6

3.4

7.3

16

34

73

156

337

726

1560

Size regime

Micro

Meso

Macro

Pore density ( $\mu\text{m}^{-2}$ )

$5 \times 10^5$

$12 \times 10^4$

$2 \times 10^4$

5000

1250

200

50

12.5

2

0.5

0.125

Specific surface ( $\text{m}^2/\text{g}$ )

1718

859

344

172

86

34.4

17.2

8.6

3.44

1.72

0.86

Atoms<sub>surf</sub> / Atoms<sub>bulk</sub>

0.28

0.14

$5.6 \times 10^{-2}$

$2.8 \times 10^{-2}$

$1.4 \times 10^{-2}$

$5.6 \times 10^{-3}$

$2.8 \times 10^{-3}$

$1.4 \times 10^{-3}$

$5.6 \times 10^{-4}$

$2.8 \times 10^{-4}$

$1.8 \times 10^{-4}$

Surface condition:

$\text{Si}_{1.8}\text{H}$   $\text{SiO}_{1.2}$

$\text{Si}_{3.6}\text{H}$   $\text{Si}_{1.8}\text{O}$

$\text{Si}_9\text{H}$   $\text{Si}_{5.6}\text{O}$

$\text{Si}_{18}\text{H}$   $\text{Si}_{12}\text{O}$

$\text{Si}_{36}\text{H}$   $\text{Si}_{24}\text{O}$

$\text{Si}_{90}\text{H}$   $\text{Si}_{61}\text{O}$

$\text{Si}_{180}\text{H}$   $\text{Si}_{123}\text{O}$

$\text{Si}_{360}\text{H}$   $\text{Si}_{249}\text{O}$

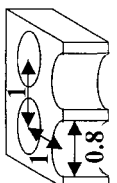
$\text{Si}_{900}\text{H}$   $\text{Si}_{617}\text{O}$

$\sim\text{Si}$

$\sim\text{Si}$

Pore array

Porosity=0.5



be about  $600\text{--}900\text{ m}^2\text{ cm}^{-3}$ . Note that the latter value is comparable to the internal surface of activated charcoal. Pores of similar diameters were also reported for PS grown on highly doped p-type substrates, however, the specific surface was found to be somewhat smaller ( $300\text{ m}^2\text{ cm}^{-3}$ ) [He4, Ca8, Ru3].

Hydrogen, which covers the internal surface of PS, can also be used to estimate its structural dimensions. IR measurements indicated a stoichiometry of roughly SiH for electrochemically prepared micro PS [Be2]. If dihydride groups are assumed to cover the internal surface, every second atom must be a surface atom. This is the case for a cube of about 1000 atoms that has a diameter of approximately 2 nm. A stoichiometry of  $\text{SiH}_{0.4}$  obtained by thermodesorption measurements points to a crystallite diameter in the order of 4 nm [Pe2]. The chemical composition for a hydride coverage surface and for a 0.5 nm thick native oxide layer are given in Table 6.1.

## 6.5

### Mechanical Properties and Drying Methods

The mechanical properties of an array of macro PS can be calculated based on the properties of bulk Si and the specific array geometry. The internal surface of macro PS is usually too small to contribute significantly to the mechanical properties of the material. The stress induced by a native oxide coverage, for example, is negligible for macro PS, and so an as-prepared macroporous layer is found to be free of intrinsic stress. However, processes such as diffusion doping, oxidation or deposition of a nitride layer are sufficient to induce considerable stresses, which in turn may lead to bowing of the wafer. The drying of macroporous material is not critical. Only if the porosity becomes high enough for pores to join ( $d/i=1$  in Fig. 6.7), leaving free-standing silicon pillars or sheets, do these structures tend to bend and stick together during drying.

The strain induced by surface forces increases if the internal surface is enlarged, which is the case for meso- and microporous silicon. For as-prepared meso PS an increase in lattice spacing between  $10^{-3}$  and  $10^{-4}$  [Ba8] compared to the bulk value is reported, while for micro PS values of up to 1% have been reported [Yo2, Ya7]. This strain leads to a macroscopic curvature of the anodized silicon substrate. Microscopically compressive as well as tensile stresses seem to be present in the distorted network of highly microporous samples, which increases or decreases the interatomic spacing by several per cent [Le10]. The strain has been proposed to originate from interactions between the Si-H groups covering the internal surface of PS [Su4, Bu5].

The thermal expansion coefficient of bulk silicon is positive at RT ( $2.6 \times 10^{-6}\text{ K}^{-1}$ ), but becomes negative below 120 K. The thermal expansion coefficient of micro PS for heating from 290 to 870 K is found to be negative ( $-4.3 \times 10^{-6}\text{ K}^{-1}$ ), which can be ascribed to hydrogen desorption and oxidation of the inner surface [Di7]. For meso PS the thermal expansion coefficient was found to increase with porosity in the temperature regime between 90 K and 300 K, from  $0.4 \times 10^{-6}\text{ K}^{-1}$  to

$1.6 \times 10^{-6} \text{ K}^{-1}$  [Fa8]. The latter effect, which has been ascribed to surface stress, also, is found to be reversible, in contrast to measurements at higher temperatures.

The elastic properties of PS depend on its microstructure and porosity. The Young's modulus for meso PS, as measured by X-ray diffraction (XRD) [Ba8], acoustic wave propagation [Da5], nanoindentation [Be13] and Brillouin spectroscopy [An2], shows a roughly  $(1-p)^2$  dependence. For the same values of porosity (70%), micro PS shows a significantly lower Young's modulus (2.4 GPa) than meso PS (12 GPa). The Poisson ratio for meso PS (0.09 for  $p=54\%$ ) is found to be much smaller than the value for bulk silicon (0.26) [Ba8].

The hardness, defined as the resistance to plastic deformation, of microporous silicon decreases with porosity  $p$  from the bulk silicon value of about 11.5 GaP to values around 4 GaP for porosities in the order of 75% following a  $(1-p)^{2/3}$  dependence. For porosities above 75% a further decrease in hardness is observed. The hardness of PS formed on highly doped p-type substrates is found to be somewhat less than that observed for low doped substrates, which may be caused by the more columnar structure of meso PS [Du5].

The thermal conductivity of bulk silicon ( $148 \text{ W K}^{-1} \text{ m}^{-1}$ ) is dominated by phonons; electronic contributions are negligible. Due to restrictions of the mean free path of phonons in the porous network the thermal conductivity of micro PS is reduced by two or three orders of magnitude at RT, compared to the bulk value. Because of the larger dimensions of its network, meso PS shows a thermal conductivity several times larger than that of micro PS, for the same value of porosity. Thermal oxidation at low temperatures ( $300^\circ\text{C}$ ) is found to decrease the thermal conductivity of meso PS by a factor of about 0.5 [Pe9]. In contrast to bulk Si the thermal conductivity of PS is found to decrease with decreasing temperature [Be21, La4, Ge9, Ly1].

The surface tension at liquid-gas interfaces is responsible for the pressure in a capillary liquid. The pressure increases linearly with decreasing pore diameter. The cracking and peeling of meso and micro PS films of high porosity during drying, as shown in Fig. 6.11, is a consequence of these capillary forces. This effect and the resulting morphology is the same as in a dried lake-bed. Cracking of a PS film can be expected if the film exceeds a critical thickness  $D$ , which is approximated by:

$$D = (d/2\gamma_L)^2 E_{\text{Si}}(1-p)^3 \gamma_{\text{Si}} \quad (6.9)$$

with  $d$  being the pore diameter,  $p$  the porosity of the film,  $\gamma_L$  the surface tension of the liquid,  $\gamma_{\text{Si}}$  the average surface tension of silicon ( $1 \text{ J m}^{-2}$ ) and  $E_{\text{Si}}$  the Young's modulus (140 GPa). Figure 6.12 shows values of the critical thickness  $D$  as a function of  $p$  for different  $d$ . The problem of film cracking due to capillary forces can be reduced if the samples are not dried in water ( $\gamma_L=72 \text{ mJ m}^{-2}$ ) but in a liquid of low surface tension, e.g. pentane ( $\gamma_L=14 \text{ mJ m}^{-2}$ ) [Be12]. In this case pure ethanol should be used as a transition liquid between water and pentane, which are not miscible.



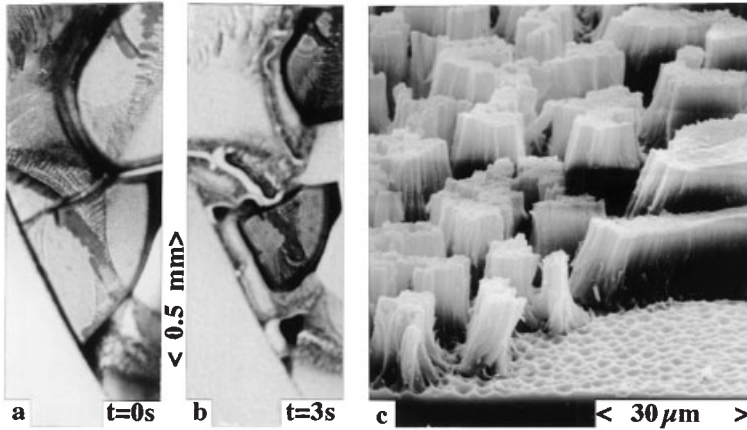


**Fig. 6.11** Optical microscopy of the surface of a 25 μm thick micro PS layer on the Si substrate, showing (a) crack formation in the wet film ( $t=0$  s) and (b) subsequent ( $t=3$  s) shrinkage of the micro PS pieces due to capil-

lary forces during drying of propanol [Le19]. (c) SEM micrograph of a disintegrated micro PS film formed at high current density (SEM of region A in Fig. 4.17).

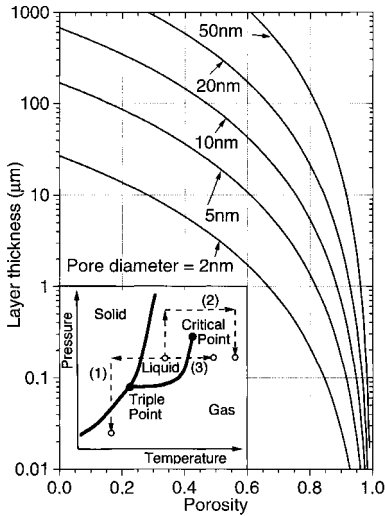
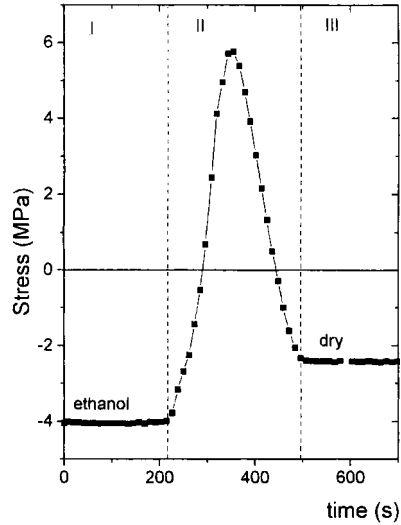


**Fig. 6.12** Critical PS thickness above which cracking of the PS film during evaporation of water is expected, according to Eq. (6.9). Note that drying in pentane or ethanol increases the critical thickness by a factor of about 26 or 11, respectively. Inset: Cracking can be avoided by freeze drying (1) or critical point drying (2), which removes the solvent without crossing the fluid-gas boundary in the phase diagram (3).

Cracking of PS because of capillary forces can be circumvented if one avoids crossing the liquid-vapor boundary in the phase diagram of the solvent. This is the case for supercritical drying [Ca4] or freeze drying [Am1], as shown in the inset of Fig. 6.12.

Detailed measurements of stress have revealed that microporous layers on bulk silicon are under compressive stresses that decrease with increasing porosity,

**Fig. 6.13** Stress-time evolution during the drying of a PS film grown on a low doped p-type substrate in ethanol [Gr6].



from about 5 MPa to values around 1 MPa if kept wet after formation. During the drying process the stress is tensile up to values around 10 MPa, which leads to cracking of highly porous samples. Dry PS samples are under compressive stress again, however the compression is by about 1–2 MPa lower than that observed under wet conditions. The latter effect is ascribed to attractive forces due to instantaneous dipole moments of the surface hydrogen atoms, known as Van der Waals forces [Gr6]. The stress-time curve during the drying process is shown in Fig. 6.13. Re-immersion of the sample and repetition of the cycle showed that the changes in stress are fully reversible. It should be noted that freshly dried PS samples are strongly hydrophobic and re-wetting is suppressed without addition of a surfactant to the aqueous solution.

The compressive stress in PS decreases with annealing temperature and is reversed for temperatures above 350 °C, indicating that the PS is under tension [Su4]. These changes are reversible if the hydrogen coverage is restored by a short HF dip; however, at annealing temperatures above 500 °C the PS microstructure is irreversibly changed [Ha4].

## 6.6 Chemical Composition and Ageing Effects

In micro PS a considerable number of silicon atoms are located at the inner surface, as shown in Table 6.1. Therefore, oxidation or absorption of hydrocarbons in the order of a monolayer will significantly change the chemical composition of the material. It is therefore essential for the comparison of chemical data if they have been obtained *in situ*, directly after preparation, or after longer storage peri-

ods. In the first part of this section the freshly prepared sample will be discussed, while ageing effects are discussed in the second part.

Infrared (IR) spectroscopy is a perfect tool for investigating the chemical composition of PS because it can be used *in situ* and the frequency positions of the characteristic absorption band indicate not only the element but also its binding configuration, as shown in Fig. 6.14. The *in situ* IR investigation of bulk silicon surfaces in dilute HF solutions has revealed that the silicon surface is terminated with hydrogen. Hydrogen-associated Si fluorides, such as  $\text{SiH}_2(\text{SiF})$ ,  $\text{SiHF}_3$  and  $\text{SiH}_2\text{F}_2$ , expected from the dissolution reaction as shown in Fig. 4.3, have not been detected by IR. If they exist, their lifetime is shorter than 0.3 ms [Ve4]. The total fluorine concentration in PS is usually below 1% [Ea1] and is below the detection limit after a short DI water rinse. In the latter case only the Si–H, the Si–H<sub>2</sub> and the Si–H<sub>3</sub> vibrational modes are observed. No Si–O surface species are detectable [Ni3]. The same is basically true for PS if it is formed in aqueous HF: no oxygen is detectable in electrochemically formed PS during, or right after, the preparation [Ve4, Li3]. Only in very dilute solutions ( $[\text{HF}] < 0.1 \text{ M}$ ) are submonolayer oxide films found to be present at the porous-bulk interface during formation at current densities well below  $J_{\text{PS}}$  [Be20]. The PS stoichiometry is reported to be between SiH and SiH<sub>2</sub>. These results for electrochemically formed PS are in contrast to PS formed chemically in an HF–HNO<sub>3</sub> solution. In this case the composition is reported to be between H<sub>2</sub>SiO and HSiO<sub>1.5</sub> [Be2]. Significant oxygen incorporation is also observed for PS formed by anodization in HF under UV illumination, while addition of H<sub>2</sub>O<sub>2</sub> to the HF electrolyte showed no increase in the oxygen content of PS [Ya11].

On storage in ambient air or immersion in H<sub>2</sub>O<sub>2</sub> the Si–O–Si vibrational mode becomes detectable for electrochemically formed PS, without a significant change in the number of Si–H<sub>x</sub> bonds, as shown in Fig. 6.15 [Th5]. This supports the assumption that oxygen penetrates the Si lattice and breaks the backbonds of the

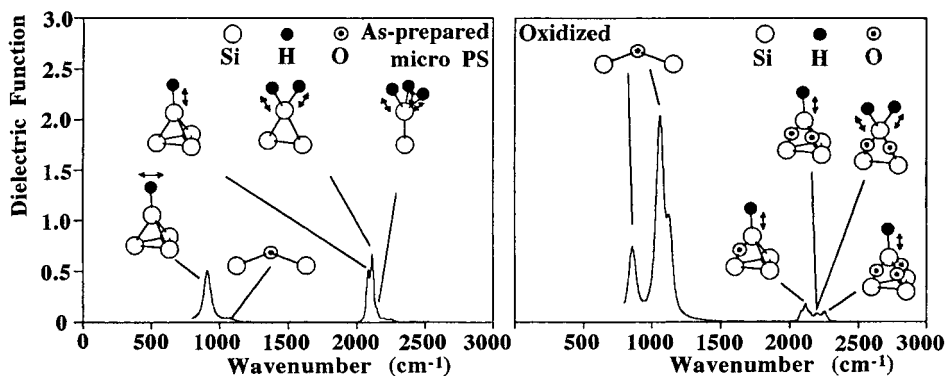
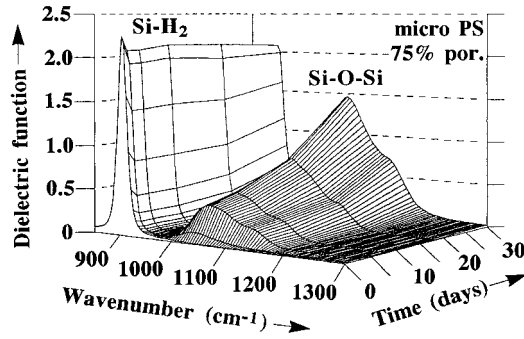


Fig. 6.14 Characteristic dielectric functions (imaginary part), as observed by IR spectroscopy for the solid component of as-prepared

PS (left) and an oxidized sample (right), with the most important vibrational modes assigned as indicated. After [Th6].

**Fig. 6.15** The increase in the Si–O–Si vibrational modes ( $980\text{--}1200\text{ cm}^{-1}$ ) upon storage of a high porosity (75%) micro PS layer formed on a p-type substrate ( $0.2\ \Omega\text{ cm}$ ) in ambient air. The Si–H<sub>2</sub> scissors mode ( $905\text{ cm}^{-1}$ ) shows little time dependence. After [Th7].



Si–H surface groups, as observed for native oxidation of bulk Si surfaces [Gr5]. The oxidation at ambient conditions is accompanied by a desorption of traces of SiH<sub>4</sub> from the surface [La1, Ca2]. An investigation of the reaction of atomic hydrogen with hydrogenated PS revealed that trihydride is the surface precursor of SiH<sub>4</sub>. As far as the etch rate in atomic hydrogen is concerned ( $30\text{ nm min}^{-1}$ ,  $10\text{ mTorr}$ , RT), the inner PS surface still behaves like the single crystal silicon surface [Gl2].

As observed for the case of hydrophobic bulk silicon surfaces [Li11], PS attracts organic matter from the ambient atmosphere. The hydrocarbon coverage may be in the order of a monolayer, which leads to C/Si atom ratios as high as 1 [Hi6]. Upon longer storage in ambient air at RT the hydrogen-passivated surface of PS gradually converts to a heavily hydrocarbon-contaminated native oxide [Ca3]. It is worth mentioning that these processes, known as ageing, usually increase the PL efficiency of the sample [Ma6].

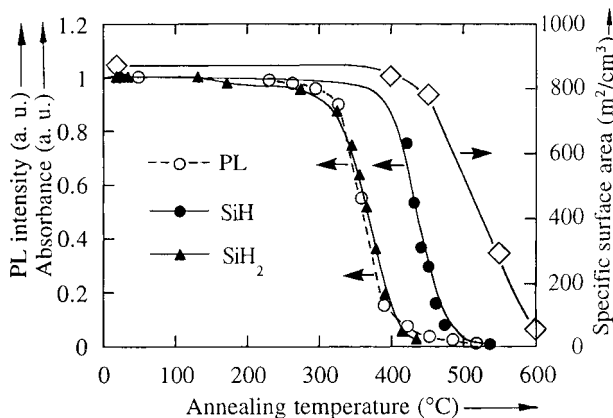


**Fig. 6.16** The normalized integrated absorbance of SiH and SiH<sub>2</sub> species (filled symbols), the PL intensity (open circles) and the specific surface area (open diamonds) as a

function of annealing temperature for a porous layer formed on a low doped p-type substrate. After data of [Ha4].

The absorption of water in the microporous silicon network was evaluated by exposing the porous samples to H<sub>2</sub>O and D<sub>2</sub>O vapor at low pressure (10<sup>-5</sup> Torr). FTIR spectral analyses revealed that water dissociates at the PS internal surface to SiH (SiD) and SiOH (SiOD). Upon annealing to 350 °C, Si–O–Si is formed from the SiOH (SiOD) groups while H<sub>2</sub> (D<sub>2</sub>) is desorbed [Gu3].

If a freshly prepared micro PS sample is annealed, hydrogen desorbs from the inner surface, as shown in Fig. 6.16. Thermodesorption measurements using a low ramping rate of 1 K min<sup>-1</sup> showed that most hydrogen is initially bound as Si–H<sub>2</sub>, which converts to monohydride Si–H at 610 K, producing a first effusion peak [Pe2]. A detailed IR investigation revealed that the monohydride Si–H is present in a dimer structure (Si–H)<sub>2</sub> formed by a surface reconstruction after the first desorption peak [Og3], while at 720 K the rest of the hydrogen from the dimer is desorbed, resulting in a second peak. A stoichiometry of SiH<sub>0.4</sub> has been obtained by these measurements. In an earlier study, however, the initial concentrations of monohydride and dihydride in PS (measured by FTIR) were reported to be the same within 5%, while desorption peaked at 680 and 810 K respectively for fast ramping (8 K s<sup>-1</sup>). Hydrogen on the PS surface was observed to be very similar to hydrogen on Si (100) 2×1. A desorption activation barrier of 1.86 eV (SiH<sub>2</sub>) and 2.82 eV (SiH) has been observed. These activation barriers yield upper limits of 3.19 eV (SiH<sub>2</sub>) and 3.67 eV (SiH) [Gu2]. For temperatures above the second desorption peak, a decrease in the specific surface area by more than one order of magnitude is found, which indicates a significant change in the PS microstructure [Ha4].

## 6.7

### Electrical Properties of Porous Silicon

The focus of this section is charge transport in PS, and electrical properties such as resistivity, carrier mobility, capacitance and photoconductivity are discussed.

#### 6.7.1

##### Contacts to Porous Films

The measurement of properties such as the resistivity or dielectric constant of PS requires some kind of contact with the PS layer. Evaporation of a metal onto the PS film-covered silicon sample produces a metal/PS/Si sandwich, which behaves like an MIS structure with an imperfect insulator. Such sandwich structures usually exhibit a rectifying behavior, which has to be taken into account when determining the resistivity [Si3, Be14]. This can be circumvented by four-terminal measurements of free-standing PS films, but for such contacts the applied electric field has to be limited to rather small values to avoid undesirable heating effects. An electrolytic contact can also be used to probe PS films, but the interpretation of the results is more complicated, because it is difficult to distinguish between ionic and electronic contributions to the measured conductivity. The electrolyte in the porous matrix may short-circuit the silicon filaments, and wetting of PS in-

creases the average dielectric constant and leads to screening of surface charges, which may change the values of the electrical properties of PS by orders of magnitude.

### 6.7.2

#### Definition of Conductivity and the Macroporous Case

The conductivity of porous structures depends on the size of the conducting filaments making up the silicon skeleton [An5] and will therefore be discussed for each of the three size regimes separately.

For a homogeneous porous layer a specific conductivity  $\sigma$  can be defined:

$$\sigma = ID/VA \quad (6.10)$$

where  $I$  is the current due to an applied potential  $V$  across the PS film of thickness  $D$  and area  $A$ . The specific resistivity of this film is  $1/\sigma$ .

According to the macropore formation mechanisms, as discussed in Section 9.1, the pore wall thickness of PS films formed on p-type substrates is always less than twice the SCR width. The conductivity of such a macroporous silicon film is therefore sensitive to the width of the surface depletion layer, which itself depends on the type and density of the surface charges present. For n-type substrates the pore spacing may become much more than twice the SCR width. In the latter case and for macro PS films that have been heavily doped after electrochemical formation, the effect of the surface depletion layer becomes negligible and the conductivity is determined by the geometry of the sample only. The conductivity parallel to the pores is then the bulk conductivity of the substrate times  $1-p$ , where  $p$  is the porosity.

### 6.7.3

#### Conductivity of Mesoporous Silicon

For mesoporous silicon, where QC effects are still negligible, depletion of the porous skeleton due to charges located at the large internal surface becomes the dominant factor. A mesoscopic void like an etched pore compensates charges from shallow dopants by capture at dangling bond (DB) centers and a depletion region is formed around such a void. Calculations show that a spherical void of 10 nm diameter can compensate about 25 charges of either sign [No2]. Even if we assume that the majority of surface bonds will reconstruct and that the effective DB density in meso PS is as low as  $10^{12} \text{ cm}^{-2}$ , the large internal surface area of about  $100 \text{ m}^2 \text{ cm}^{-3}$  will still generate an effective density of states (DOS) in the order of  $10^{18} \text{ cm}^{-3}$ . This high density of surface states is compatible with the pinning of the Fermi level at mid-gap. As a result, the mesoporous sample becomes insulating because of a complete trapping of free majority carriers at the inner surface, which produces a depletion of the porous volume. This idea is supported by optical transmission measurements, which show that the sub-bandgap absorp-

tion due to free carriers is significantly suppressed in the porous material compared to the bulk substrate, as shown in Fig. 7.8. Detrapping of the charge carriers has been observed for a meso PS film exposed to a polar gas, for example  $\text{NO}_2$  [Bo7]. This effect has been interpreted as a screening of surface traps by absorbed polar species [St11, Le14]. Hall effect measurements show that the concentration of free electrons and their mobility in meso PS formed on highly doped n-type silicon is about  $10^{13} \text{ cm}^{-3}$  and  $30 \text{ cm}^2 \text{ V}^{-1} \text{ s}^{-1}$  respectively [Si2], and so the material behaves similarly to intrinsic Si. It should be noted that the reduction of free carriers is not caused by a reduction of dopant atoms due to a preferential etching of these atoms compared to silicon atoms during the PS formation process [Le14]. The resistivity of mesoporous silicon varies between  $10^4$  and  $10^7 \Omega \text{ cm}$ , depending on substrate doping density and anodization conditions. Screening of the surface states by ions present in an electrolyte may increase the conductivity of wet meso PS to values comparable to those of the bulk substrate.

The temperature dependence of meso PS resistivity can be understood if Coulomb blockade effects are taken into account. For a silicon nanocrystallite to become conducting, it must first overcome the Coulomb blockade barrier,  $E_B$  [Le14, Ha14, Mi8]:

$$\Delta E_B = e^2/2C \quad (6.11)$$

where  $e$  is the electron charge and  $C$  the self-capacitance of an isolated, spherical Si nanocrystal, which is given by:

$$C = 2\pi\epsilon_r\epsilon_0d \quad (6.12)$$

Here  $d$  is the crystallite diameter,  $\epsilon_r$  and  $\epsilon_0$  are the dielectric constants of the surrounding medium and a vacuum, respectively. The probability of electrons overcoming the barrier shows an Arrhenius dependency on temperature. A significant increase in conductivity of the PS film, however, is only expected if the density of unblocked sites in the porous network is high enough to form continuous pathways from one electrode to the other. The continuous connection of unblocked crystallites is expected to produce an abrupt increase in conductivity at a critical temperature  $T_c$ , as shown in Fig. 6.17. A Coulomb blockade indicated by a plateau in the I–V characteristic at low applied bias is shown in the inset of this figure. Above  $T_c$ , the I–V characteristic becomes linear and the activation energy approaches the bulk silicon value of about 0.5 eV for large crystallites, while below  $T_c$  the activation energy is significantly lower.  $T_c$  is expected to increase with decreasing crystallite mean size [Mi8].

#### 6.7.4

#### Conductivity of Microporous Silicon

The resistivity of micro PS in dry air at RT is observed to increase with porosity and shows high values ranging from  $10^7$  to  $10^{14} \Omega \text{ cm}$ , with the maximum of the

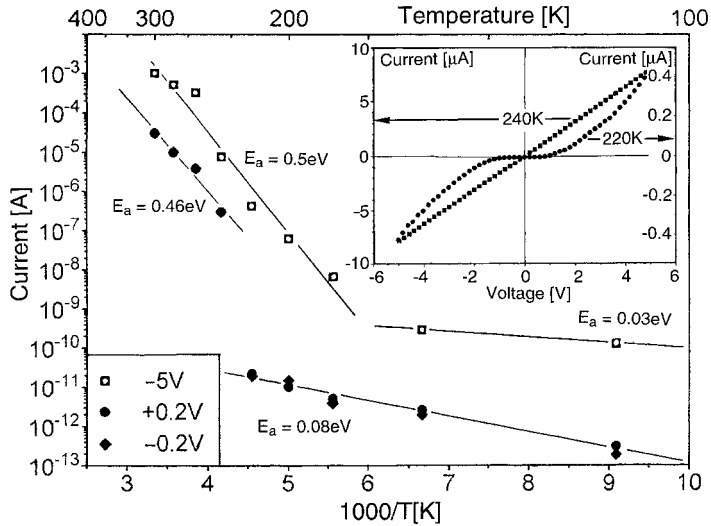


**Fig. 6.17** Temperature dependence of the current through a metal-meso PS-silicon sandwich for different applied potentials ( $3 \text{ m}\Omega \text{ cm}$  n-type,  $100 \text{ mA cm}^{-2}$ ,  $24 \mu\text{m}$ ,  $8 \text{ mm}^2$  evaporated aluminum contacts,

freshly prepared). The I–V curves for 220 and 240 K, shown in the inset, indicate a sharp transition from a Coulomb blockade characteristic to a linear one.

distribution around  $10^{11} \Omega \text{ cm}$ . For micro PS-based EL devices a mobility of the order of  $3 \times 10^{-4} \text{ cm}^2 \text{V}^{-1} \text{s}^{-1}$  has been reported [Co5]. The conductivity shows a  $V^{1/2}$  dependence on applied bias and is thermally activated, with an activation energy of 0.3–0.7 eV. The resistivity increases upon cooling to 200 K by five orders of magnitude and is found to be roughly constant below 150 K, as shown in Fig. 6.18 [Ko2], which is similar to the behavior observed for meso PS, as shown in Fig. 6.17. The observed anti-correlation between resistivity and PL intensity is a result of the long lifetime of the luminescent state. If the probability of a charge carrier leaving the crystallite is higher than that of the radiative recombination channel, the PL becomes quenched.

For micro PS a decrease in the specific resistivity by two or three orders of magnitude is observed if the dry material is exposed to humid air [Ma8] or vapors of polar solvents, e.g. methanol [Be6]. This sensitivity of PS to polar vapors can be used to design PS-based gas sensors, as discussed in Section 10.4. This change in resistivity with pore surface condition becomes dramatic if the pores are filled with an electrolyte. From the strong EL observed under low anodic as well as low cathodic bias in an electrolyte it can be concluded that micro PS shows a conductivity comparable to that of the bulk substrate under wet conditions [Ge8]. Diffusion doping has been found to reduce the PS resistivity by more than five orders of magnitude, without affecting the PL intensity [El1].

The interpretation of these different experimental observations is complicated by the fact that for micro PS, not only do the Coulomb blockade effects have to be



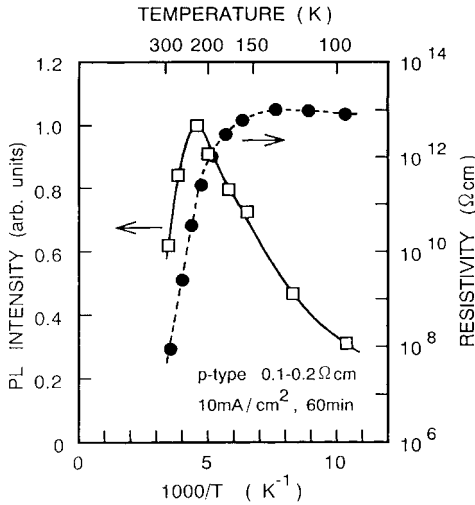


**Fig. 6.18** Temperature dependence of the micro PS resistivity (filled circles) and the PL intensity (open squares) for a self-supporting PS film of 40  $\mu\text{m}$  thickness. Anodization conditions in ethanoic HF (1:1) are indicated on the lower left. After [Ko2].

taken into account, but also quantum size effects. The non-linear electric field dependence has been interpreted in terms of the Onsager model: an electron at the Fermi level can jump from its crystallite and leave behind a positive trap, which gives rise to a Poole-Frenkel-like functional behavior for temperatures above 200 K [Be8]. AC measurements indicate hopping of charge carriers and no polarization of atoms or particles [Be7]. It has been argued that the activation energy of 0.5 eV is too large for hopping, and other transport channels such as thermionic emission above energy barriers [Ko10] and transport in extended states have been suggested [Lu2]. For a more detailed discussion of conduction mechanisms in PS, see [Be15].

#### 6.7.5

##### Photoconductivity of Porous Silicon

So far all values of resistivity have referred to measurements performed in the dark. If the porous layer is illuminated, a photoconductivity is found that is almost independent of polarity and value of the applied bias, but is sensitive to the wavelength of the light. The photoresponse of micro PS is largest for wavelengths between 500 and 600 nm, because at longer wavelengths the light is not effectively absorbed, while short-wavelength illumination will only excite the topmost region of the porous layer [Se13]. Even for moderate illumination intensities the resistivity of dry micro PS is reduced by two or three orders of magnitude compared to the value observed in the dark [Ko2]. This is because the free charge carrier concentration in PS is very low compared to the bulk material. It increases by orders of magnitude under illumination.

From photocarrier grating measurements at low laser intensities ( $100 \text{ mW cm}^{-2}$ ), the value of the ambipolar diffusion coefficient of meso PS is deduced to be about

$10^{-6} \text{ cm}^2\text{s}^{-1}$ , which gives a small diffusion length of a few tens of nanometers between the repeated trapping of photogenerated carriers [Sc13]. This is in contrast to diffusion constants of  $5\text{--}50 \text{ cm}^2\text{s}^{-1}$  reported for micro PS. The latter results were obtained for excitation energies of up to  $170 \text{ mW cm}^{-2}$ , where bipolar plasma-like diffusion prevails [To1]. The use of porous polysilicon as cold cathode, as discussed in Section 10.6, indicates that charge drift lengths in the order of  $1 \mu\text{m}$  are realistic at high fields ( $10^5 \text{ V cm}^{-1}$ ) [Kl4, Se13]. Measurements of the photoconductivity of PS using transparent liquid contacts show that the porous structure is not necessarily short-circuited by a conducting electrolyte inside the pores [Se10].

### 6.7.6

#### Carrier Mobility in Porous Silicon

The application of an electric field  $E$  to a conducting material results in an average velocity  $v$  of free charge carriers parallel to the field superimposed on their random thermal motion. The motion of charge carriers is retarded by scattering events, for example with acoustic phonons or ionized impurities. From the mean time  $\tau$  between such events, the effective mass  $m^*$  of the relevant charge carrier and the elementary charge  $e$ , the velocity  $v$  can be calculated:

$$v = e\tau E/m^* \quad (6.13)$$

At low electric fields  $v$  is proportional to  $E$  and a mobility  $\mu = e\tau/m^*$  can be defined. The mobility of electrons and holes in bulk silicon is shown in the figure on the inner front cover of this book.

Measurements of mobility in PS suffer from the fact that the number of free charge carriers is usually small and very sensitive to illumination, temperature and PS surface condition. Hall measurements of meso PS formed on a highly doped substrate ( $10^{18} \text{ cm}^{-3}$ , bulk electron mobility:  $310 \text{ cm}^2 \text{ V}^{-1} \text{ s}^{-1}$ ) indicated an electron mobility of  $30 \text{ cm}^2 \text{ V}^{-1} \text{ s}^{-1}$  and a free electron density of about  $10^{13} \text{ cm}^{-3}$  [Si2]. Values reported for effective mobility of electron and hole space charges in micro PS are about five orders of magnitude smaller ( $10^{-3}$  to  $10^{-4} \text{ cm}^2 \text{ V}^{-1} \text{ s}^{-1}$ ) [Pe10]. The latter values are much smaller than expected from theoretical investigations of square silicon nanowires [Sa9]. For in-depth information about carrier mobility in PS see [Si6].

### 6.7.7

#### Dielectric Constant of Porous Silicon

The macroscopic dielectric constant of PS is very sensitive to the frequency range investigated. For very high frequencies the dielectric constant can be obtained by optical measurements. In this regime the effective medium approximation has been found to be an adequate description [Th3]. For lower frequencies the dielectric constant  $\epsilon$  is commonly obtained by capacitance measurements of metal/PS/Si structures. AC conductivity measurements of such structures indicate a hop-

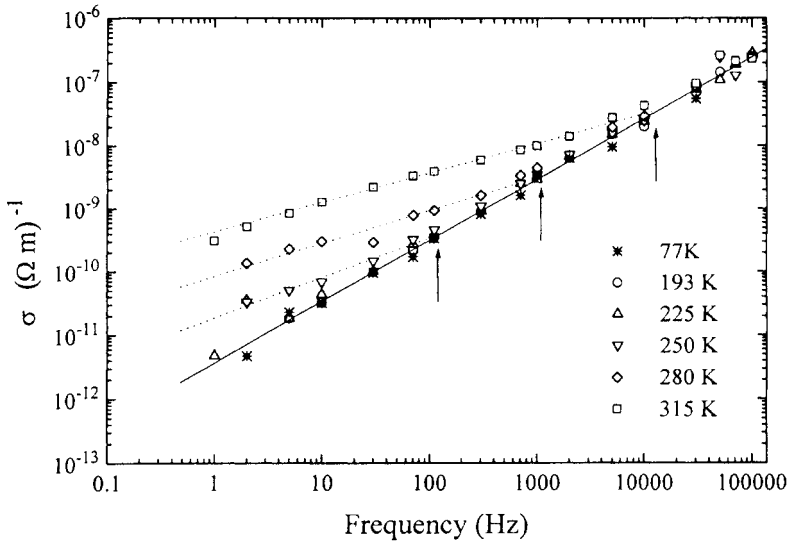


**Fig. 6.19** Frequency dependence of the conductivity at different temperatures for a micro PS film ( $5 \Omega \text{ cm}$  p-type,  $30 \text{ mA cm}^{-2}$ , ethanoic HF). The transition from a frequency regime

of 0.95 slope (full line) to a regime of 0.5 slope (broken line) is indicated by arrows. After [Be7].

ping of charge carriers and no polarization of atoms or particles [Be7]. The resistivity is found to decrease with increasing frequency, as shown in Fig. 6.19, a behavior typical of disordered solids. The full line in Fig. 6.19 corresponds to a dielectric constant of about 2.3, which is in agreement with values of refractive index obtained by IR ellipsometry. This indicates that the Bruggeman effective medium model is still valid in the MHz regime for micro and meso PS of porosities greater than 50%. The relative dielectric constant in this regime can therefore be approximated by  $\epsilon = 1 + 10.4(1-p)$ . For lower frequencies and low porosity, however, higher values of the dielectric constant may be observed. Note that for partially oxidized micro and meso PS films the dielectric constant may reach values in the order of  $10^3$  for the low-frequency regime (1 kHz) [Un1]. Completely oxidized PS, in contrast, shows low values of  $\epsilon$ , which correspond to  $\text{SiO}_2$  ( $\epsilon = 3.9$ ) of a certain porosity. For more information about PS layer capacitance see [Co3].

## 7

### Microporous Silicon

#### 7.1

##### Micropore Formation Mechanism

This section is devoted to the mechanism responsible for the formation of micropores on silicon electrodes. Micropore formation on silicon electrodes illustrates the importance of the pore position with respect to the neighboring pores, i.e. the pore wall thickness.

If the dimensions of a silicon crystallite are reduced to a few nanometers, its bandgap increases as a result of QC effects, as discussed in detail in Section 7.5. The same holds true for the thin silicon walls separating the micropores. The increase in bandgap energy  $\Delta E_C$  in the wall region compared to the bulk electrodes produces an energy barrier for holes  $\Delta E_V$ , as schematically shown in Fig. 7.1a. If  $\Delta E_V$  is larger than the bias-dependent energy of holes, the porous region becomes depleted of holes and therefore passivated against further dissolution. It is energetically more favorable for a hole to enter the electrolyte at the pore tip directly, than via the porous structure [Le1]. Note that for the case of pore formation due to QC no additional effect is required to explain the active state of the pore tip, which is in contrast to passivation by an SCR. The pore tip is active, because it is in contact with the unconfined bulk electrode, while the pore walls are passive due to the close spacing of the pore tips. Direct consequences of this condition are a distinct porous-bulk interface and significant values of porosity.

A few further conclusions can be drawn from this model. If, for example, the formation current density is increased, the bandgap of the porous structure is expected to increase, too. A higher current density requires an increase in the anodization bias, thus holes have more energy to cross the barrier  $\Delta E_V$ . Therefore, the nanometer-sized structures that form the porous skeleton will be etched further, until their bandgap is large enough to become passivated again. The same is true for illumination during anodization. By illumination with sufficiently energetic photons, electron-hole pairs are generated in the porous structure. The photogenerated holes initiate further dissolution of the pore walls, as shown in Fig. 7.1 b. This reduces their size and thereby increases their bandgap energy until it is higher than the photon energy, which establishes passivation again. The increase in bandgap results in a blue shift of the PL from PS formed under illumination, as shown in Fig. 7.10 [Ni2, Le10]. However, it is not

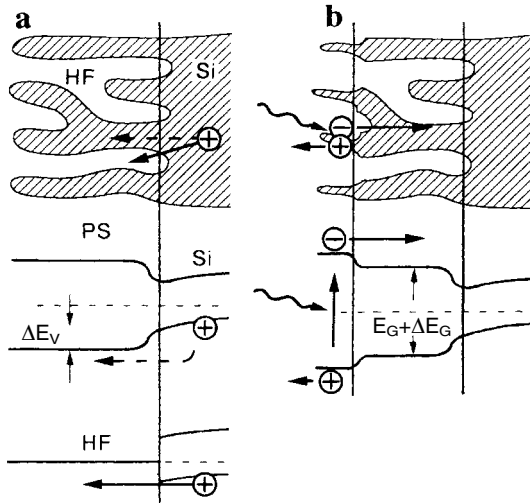


**Fig. 7.1** (a) Schematic illustration of the interface between PS and bulk silicon (top) and the corresponding band diagrams for charge transfer from the bulk to the porous skeleton (middle) and from the bulk to the electrolyte in the pore tip (bottom). Note that hole transition at the pore tip, indicated by a solid

arrow, is energetically favorable compared to the transition into the pore wall (broken arrow). (b) Illumination during anodization leads to further thinning of the porous skeleton, because photons of an energy higher than  $E_{P5}$  are absorbed. After [Le24].

only during the formation process of micro PS that the charge transfer is expected to be sensitive to the degree of confinement. Generally any charge transfer to and in the confined structures in micro PS depends on  $\Delta E_V$  and  $\Delta E_C$ . These effects dominate the electrical and EL properties of the material, as discussed in Sections 6.7 and 10.5, respectively.

An extension of this QC model, including tunneling probabilities between the confined crystallites and the bulk, has been developed [Fr6]. The QC model for microporous silicon formation, however, is still qualitative in character, and a quantitative correlation between anodization parameters and the morphology and properties of the porous structure is at yet beyond the capability of the model.

## 7.2

### Morphology of Microporous Silicon

The dimensions of the microporous silicon skeleton are too minute to be resolved by microscopy techniques that generate a direct image of the morphology, e.g. SEM. However, an understanding of the morphology of microporous silicon has emerged from a superposition of results from a multitude of investigations carried out by different techniques such as TEM, Raman spectroscopy (RS), XRD, BET or small angle X-ray scattering (SAXS). A short summary of these investigations and a conclusive idea of the morphology of the material are presented in this chapter.

## 7.2.1

## Transmission Electron Microscopy

Even under magnifications of the order of  $10^5$ , micro PS looks rather homogeneous under the transmission electron microscope, as shown in Fig. 7.2 a. This is in contrast to the microstructure of meso PS, which can be revealed at this magnification, as shown in Fig. 7.2 b. It requires HREM techniques to reveal the struc-

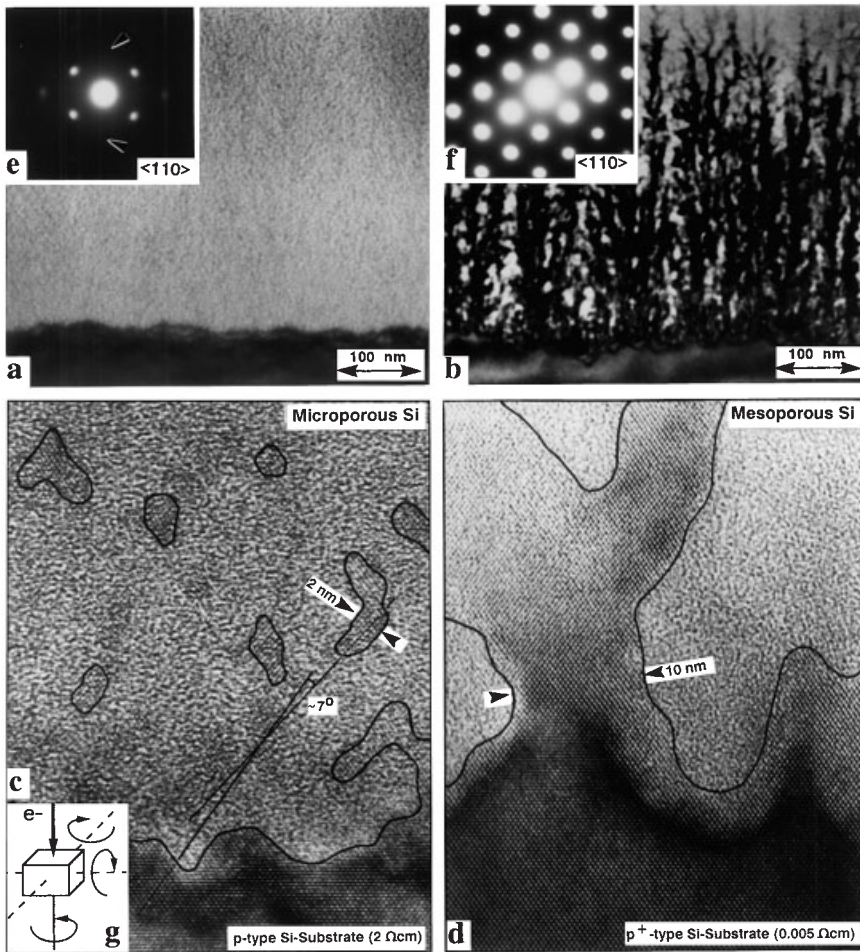


**Fig. 7.2** TEM (a, b) and HREM (c, d) micrographs showing the interface between PS (formed at  $100 \text{ mA cm}^{-2}$  in 1:1 ethanoic HF) and the (100) substrate for the cases of micro PS (left) and meso PS (right). The insets (e, f) show the corresponding electron diffraction patterns. In the bottom figures lines are

drawn around crystallites as guides to the eye. Note that micro PS crystallites may be misaligned with the substrate, as indicated by the lines in (c). Only crystallites rotated around the solid axis, as shown in (g), reveal lattice fringes in the image (c). After [Le15].

tural details of microporous material. In Fig. 7.2c lattice fringes of crystallites of about 2–4 nm in diameter can be identified in a matrix that looks like an amorphous material. A closer inspection of the crystallites in Fig. 7.2c reveals a rotation to each other by several degrees. Only crystallites that are rotated around an axis parallel to the electron beam will reveal lattice fringes in the HREM image, as shown in Fig. 7.2g. Crystallites rotated around the other two axes, indicated by the broken axis in the inset to Fig. 7.2g, are imaged with a contrast like amorphous silicon. HREM images obtained under different angles to the sample showed no anisotropy in the rotation of crystallites. These HREM investigations [Le10] indicate that a high density of Si microcrystallites is present in micro PS. However, no conclusions can be drawn from HREM images if an amorphous fraction is present in the sample. It should be noted that the thickness of TEM and HREM samples as shown in Fig. 7.2 is a few tens of nanometers, and so the electrons of the beam penetrate several crystallites.

The transmission electron diffraction patterns of meso PS, as shown in Fig. 7.2f, shows sharply defined Bragg diffraction spots that are characteristic of crystalline bulk silicon. The diffraction spots of micro PS, as shown in Fig. 7.2e, still show the material to be single crystalline, however, the spots are less well defined, higher orders are missing and much diffuse scattering is observed. In conclusion, TEM observations indicate that microporous silicon can be visualized as a sponge-like silicon crystal with average dimensions of a few nanometers [Ph1, Be5, Le15]. Some morphological investigations of PS have been performed using AFM and STM [Yu1]. These techniques, however, suffer from the fact that the aspect ratio of the tip used for inspection is usually not sufficient to reproduce the micropore morphology.

### 7.2.2

#### Raman Spectroscopy

RS is another method that has been used to investigate the morphology of micro PS. In single crystalline silicon only first-order scattering at the optical phonon in the center of the Brillouin zone is allowed, which produces a sharp (FWHM  $3.3 \text{ cm}^{-1}$ ) Raman peak at  $520 \text{ cm}^{-1}$ . Confinement of the phonon leads to a momentum uncertainty, and so the Raman peak broadens and shifts to lower energy. This effect can be used to determine the size of silicon microcrystallites using Raman measurements [Pa14]. The analysis of Raman data, however, is complicated by the fact that the Raman signal is also sensitive to temperature and stress, as well as shape and surface conditions of the crystallite. Nevertheless, dimensions observed by RS agree well with values of size obtained by other techniques such as HREM or XRD. Broadening and shift of the Raman peak is also observed for acoustic phonons (at  $20 \text{ cm}^{-1}$ ) [Fu2]. But nearly all investigations of PS refer to optical phonons.

Raman measurements of free-standing PS films have indicated crystallite dimensions as small as 2 nm [Ka3]. Investigations of PS films grown on substrates of different doping density showed a broad size distribution (2–10 nm) for  $p^+$ -type substrates, while the size distribution for PS films on low doped  $p$ -type substrates

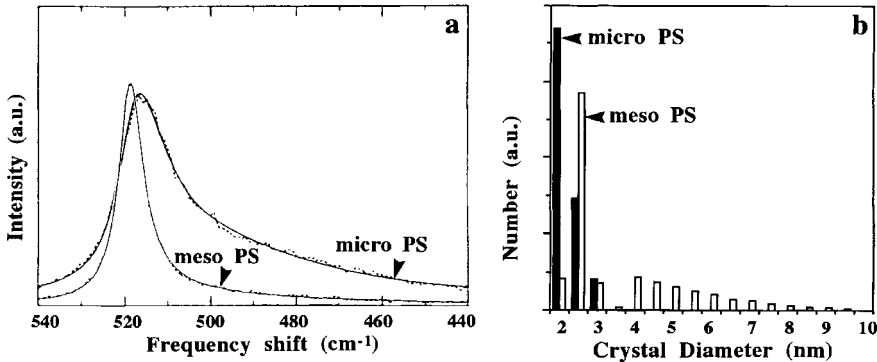


Fig. 7.3 (a) Raman spectra (dotted lines) of PS films of 65% porosity formed on moderately ( $1 \Omega \text{ cm}$ , micro PS) and highly ( $0.01 \Omega \text{ cm}$ , meso PS) doped substrates,

together with calculated fits (full lines), assuming the distributions of crystallite diameters as shown in (b). Redrawn from [Mu2].

showed only contributions below 3 nm, as shown in Fig. 7.3. The presence of an amorphous contribution in the Raman spectra of PS is still controversial [Go3, Zh4]. It is not clear whether the observed broad peak is due to an amorphous phase or if the insertion of oxygen atoms leads to a relaxation of the lattice expansion and to its distortion, which could result in the relaxation of the Raman selection rules and the appearance of an enhanced amorphous-like component of the spectrum [Ta7]. The amorphous contribution in the Raman spectra is found to be larger by nearly one order of magnitude near the surface of the sample. This is interpreted as being caused by progressive chemical etching of the topmost region of the PS layer [Mu3].

### 7.2.3

#### X-Ray Analysis

X-rays with a wavelength comparable to interatomic distances are diffracted by the crystal lattice. The diffraction signal contains information about crystal orientation, particle size and strain. The XRD signal of an as-anodized micro PS layer that is still on the substrate shows no significant misorientations of the crystallites to the substrate and so PS can be imagined as a single crystalline sponge-like structure [Fa8]. A significant amount of amorphous material in PS would produce a broad peak at low diffraction angles. The fact that such a peak is not observable for freshly prepared PS limits the maximal amount of amorphous silicon or silicon oxide present in PS to values below 10% [Le10].

The broadening of the characteristic peaks of the silicon XRD signal provides information about stress and size of the crystallites. Figure 7.4 shows the diffraction pattern of microporous silicon powders scraped from p-type Si electrodes and of a bulk silicon powder sample. The peak broadening increases with increasing formation current density. For low formation current densities a superposition of



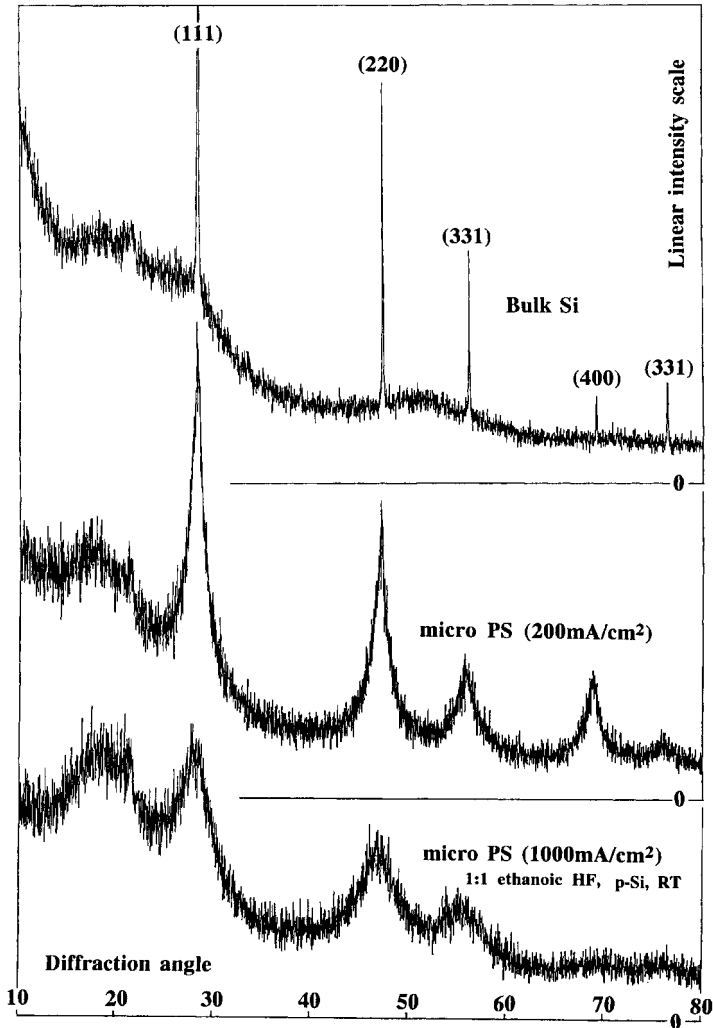


Fig. 7.4 XRD signal for powder samples prepared from bulk Si (top) and micro PS films produced on p-type electrodes using different anodization current densities, as indicated in

the figure. From the broadening of the diffraction peaks the crystallite size was calculated to be 3.5 nm (middle) and 2.8 nm (bottom). After [Le10].

a sharp peak and a broad peak is observed. In the light of HREM and Raman observations this is interpreted as being due to a long-range order that produces coherent diffraction and not as an indication of the presence of two different crystallite sizes. The average crystallite diameter is in the order of 3–4 nm. For high formation current densities a change in lattice constant of the order of  $\Delta a/a=0.1$  is found [Le10], which corresponds to high values of stress. Values below  $\Delta a/a=0.01$  have been reported for lower current densities [Mu2].

SAXS is sensitive to variations in the electronic density in a material, and so provides information about the shape and size of clusters in micro PS. In contrast to the quantum wire structure proposed in early publications [Ca1, Le1], the crystallites in micro PS are found to be almost spherical. There has been some evidence that the dimensions in the growth direction are somewhat smaller than those parallel to the surface [Fr2]. The latter result, however, is still controversial because investigations by spectroscopic techniques indicate an opposite elongation [Mi4]. A combination of grazing incidence diffraction (GID) and SAXS measurements on various free-standing micro PS films showed crystallite diameters from about 1.5 to 4 nm, depending on formation conditions. A good correlation between size reduction and blue shift of the PL peak position has been observed [Bi3].

The X-ray absorption fine structure (EXAFS and NEXAFS) provides information about the next neighbor atoms. A comparison of data from small oxidized silicon spheres of known size with micro PS indicate that the average dimension of the microstructures in luminescent PS is about 1.5–2 nm [Sc12]. Photoemission and X-ray absorption spectroscopy gives information about the binding energy of electrons. This method enables us to measure separately the change in energy of the conduction and valence bands. As shown in Fig. 7.16, the VB shift  $\Delta E_V$  has been found to be about a factor of two larger than the CB shift  $\Delta E_C$  [Bu2, Mo8]. In addition a ratio of 1:3 has been observed between the increase in  $\Delta E_C$  and the increase in PL emission energy [Da6]. These results have been interpreted in terms of QC present in the microporous silicon structures, as discussed in Section 7.5.

### 7.3

#### Absorption, Reflection and Nonlinear Optical Effects

The interaction of photons with electrons in the porous structure, which is the topic of this section, provides information about the PS band structure, while the excitation of vibrational modes of molecules present in the porous structure by photons gives information about its chemical composition, as discussed in Section 6.6.

The dependence of the optical properties of silicon on its microstructure is shown by the color figure in the lower left corner of this book's cover. Despite the fact that the thickness of all PS samples shown has been chosen to correspond to a 20  $\mu\text{m}$  thick film of bulk silicon, the difference in light transmission is dramatic [Le27].

The structural dimensions of macro PS are of the same order as the wavelength of photons in the visible regime and in the near IR. Therefore macro PS is a strongly scattering material. As a result, a two-dimensional photonic bandgap has been observed for certain regular pore patterns under illumination with IR light in a plane orthogonal to the macropore axis. For illumination parallel to the macropore axis transmission through the pores is observed. With decreasing pore diameter the transmittance becomes reduced for long wavelength, and the material acts as an optical short-pass filter. Therefore a macropore sample appears blue if illuminated by

white light from the backside, as shown on the lower left of the book's cover. These effects have been exploited for optical applications, as discussed in Section 10.5.

The structural dimensions in meso PS and micro PS, in contrast, are too small to scatter photons of energies in the visible or below, and the transmittance becomes independent of the pore growth direction. This allows us to treat such structures in the framework of the effective medium concept. Now the electronic properties, namely the bandgap of the material, dominate the optical properties. Bulk Si, as well as micro PS and meso PS, show an optical low pass filter characteristic. The films shown in the lower left of the book's cover, however, appear in different colors, despite the fact that the total amount of silicon in the beam path is roughly constant. The microporous film appears bright yellow, showing an even higher transmittance than a 7  $\mu\text{m}$  thin bulk Si film, which appears orange. A mesoporous film appears red, which indicates a transmittance between that of the 7  $\mu\text{m}$  thick Si film and the 20  $\mu\text{m}$  thick bulk Si grid. This blue shift of the absorption edge has been interpreted in terms of QC, as discussed below [Le1].

The propagation of light waves inside the effective medium established by the porous structure as well as the reflected and transmitted fractions can be described by the complex refractive index [Th3]. The real part of the function describes the difference between the vacuum wavelength of a photon and its wavelength in the material, while the imaginary part of the dielectric function gives the exponential decay (or absorption) of the wave in the material. A reliable method of determining the refractive index is to measure the interference fringes of a free-standing PS layer or a PS layer on the Si substrate. A reflectance spectra of a PS film on the Si substrate that exhibits several interference maxima and minima is shown in Fig. 7.5a. The complex refractive index of the PS film, as shown in Fig. 7.5b, can be obtained by a complete simulation of the measured spectra (broken line in Fig. 7.5a). The refractive index of bulk silicon is shown in Fig. 7.5b for reference. The distinct maxima of the refractive index of bulk silicon correlated to direct transitions of bulk Si (at 3.4 and 4.3 eV) can be identified in reflectance spectra of meso PS and micro PS samples of low porosity, but disappear for micro PS if the porosity increases above about 70% [Ko17, Th7].

A certain anisotropy of the refractive index along specific crystallographic axes indicates that the microstructures in the porous network are not spherical but somewhat elongated along the PS growth direction [Mi4]. This birefringence is below 1% for micro PS, while it may reach values in the order of 10% for meso PS films formed on (110) oriented silicon wafers [Ko22].

The refractive index of micro PS,  $n_{\text{PS}}$ , for wavelengths in the visible or near IR regime is found to decrease with porosity  $p$  [Lo1] and can be roughly approximated if the refractive index of bulk silicon  $n_{\text{Si}}$  for the wavelength in question is known, using

$$n_{\text{PS}} = (n_{\text{Si}} - 1)(1 - p) + 1 \quad (7.1)$$

This dependence of  $n_{\text{PS}}$  on  $p$  can be used to fabricate optical superlattices, e.g. Bragg filters, by modulating the porosity of a PS layer, as discussed in Section 10.5.

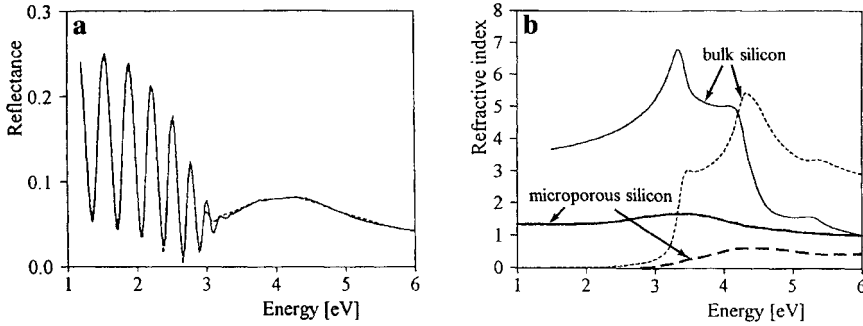


**Fig. 7.5** (a) Measured reflectivity of a micro PS film (1  $\mu\text{m}$  thick, 71% porosity) on the Si substrate (solid line) together with the simulated reflectivity (broken line). (b) Real part (bold solid line) and imaginary part (bold

broken line) of the refractive index obtained from the simulation, together with the refractive index of bulk Si for comparison. Redrawn from [Th7].

The imaginary part of the dielectric function describes the optical absorption in PS and thereby gives information about the bandgap. Details of the optical transitions responsible for absorption and emission of photons in Si are shown in Fig. 7.12 and will be discussed in the next section. The absorbed fraction  $P(x)$  of the non-reflected light intensity  $P$  depends on the sample thickness  $x$  and on the absorption coefficient  $a$  according to

$$P(x) = P[1 - \exp(-ax)] \quad (7.2)$$

This function is shown for bulk silicon and different values of light wavelength in Fig. 10.4a. The transmitted fraction  $T(x)$  is  $T(x) = P - P(x)$ :

$$T(x) = P \exp(-ax) \quad (7.3)$$

The optical absorption coefficient  $a$  as a function of wavelength for free-standing micro- and mesoporous silicon layers determined by transmission measurements in comparison with that of bulk silicon and amorphous silicon is shown in Fig. 7.6. The absorption coefficient of the mesoporous silicon sample fits closely that of bulk silicon over the entire investigated range of photon energies if the data are corrected for porosity (effective medium approximation). The bandgap of the meso PS sample, defined by extrapolation of the data shown in Fig. 7.6 to zero absorption, is found to be 1.13 eV, which is only 10 meV higher than observed for bulk Si [Ko15]. For the micro PS sample results are different. While for photon energies above the direct bandgap (3.3 eV) the effective medium approximation describes  $a$  well,  $a$  is significantly reduced for lower energies. In this region  $a$  depends exponentially on the photon energy. This blue shift of the absorption edge of micro PS compared to bulk silicon can be interpreted in terms of QC [Le1]. An observable blue shift is only expected if the majority of crystallites that form the porous skeleton are small enough to show a significant QC, otherwise

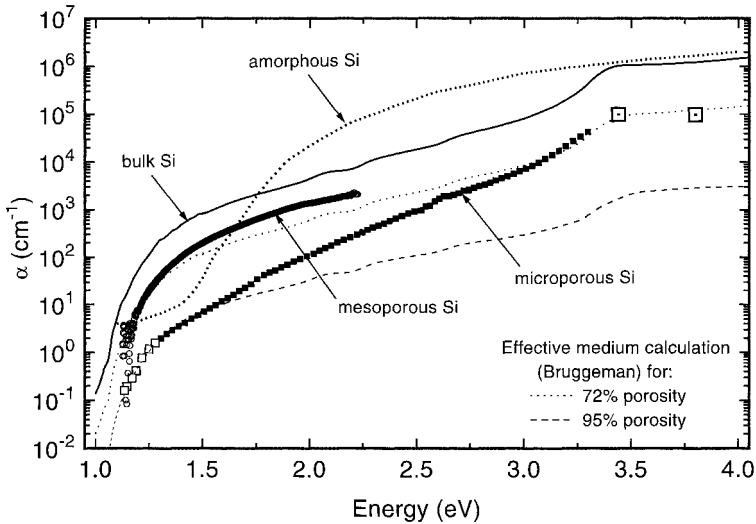


**Fig. 7.6** Spectral dependence of the absorption coefficient for free-standing micro PS (72% porosity), meso PS (45% porosity), bulk Si and amorphous Si:H at RT. While the meso porous film can be roughly fitted to a Bruggeman effective medium calculation for

Si spheres embedded in a vacuum with 45% nominal porosity [Ko15], micro PS shows a significantly lower absorption in the visible than expected from a calculation for 72% nominal porosity. After [Ko4].

the non-confined crystallites would dominate the absorption spectrum. However, a small fraction, in the order of 5% of the total volume of the sample of larger crystallites, seems to be present and to dominate the absorption at energies below 1.5 eV [Ko4].

Between 7 and 470 K  $\alpha$  is found to increase with temperature. This increase is reversible and corresponds well with that of bulk silicon [Ko4]. If PS is annealed in nitrogen at higher temperatures (600 °C), hydrogen desorption takes place, which changes the condition of the inner surface drastically. At these temperatures an irreversible increase in  $\alpha$  is observed for micro PS. A similar increase in  $\alpha$  after annealing is found for meso PS. Changes that affect the core of the crystallites, e.g. stress effects [Ko4], as well as surface-related effects like the formation of surface states [Ko5, Ba10], are proposed to be responsible for the observed increase of  $\alpha$  with  $T$ .

The optical transmission of free-standing micro PS shows a non-linear behavior on the picosecond time-scale for high intensities. The increase in absorption with increasing incident power can be interpreted as being caused by additional absorption by photogenerated free charge carriers [Ma9]. Carrier thermalization [Ow1] or excitation transfer from core states to surface states [Ma10] is proposed to be responsible for the observed fast decay in the first picoseconds. At high carrier densities ( $>10^{18} \text{ cm}^{-3}$ ), fast Auger recombination dominates the following 200 ps [Ma9], followed by trapping of the free carriers, while the radiative recombination

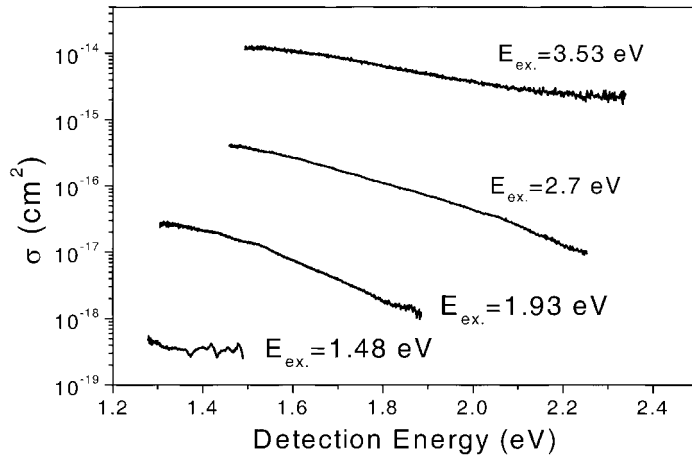


**Fig. 7.7** Absorption cross-section of Si nanocrystals versus detection energy. Excitation energies are indicated in the figure. After [Ko19].

process is much slower. The latter observation supports the idea that PS behaves like an indirect bandgap material [Be10]. PL measurements in the regime of Auger saturation can be used to determine the optical absorption cross-section of the Si nanocrystals in micro PS. This parameter is found to vary by over five orders of magnitude, depending on excitation energy, as shown in Fig. 7.7 [Ko19].

As a result of carrier localization the nonlinear optical response is expected to be strongly enhanced for micro PS compared to bulk silicon. This property is described by the third-order nonlinear susceptibility, whose real part is proportional to the nonlinear refractive index, while the imaginary part is proportional to the nonlinear absorption coefficient. For weak excitation at RT micro PS shows a large nonlinear absorption change. The third-order nonlinear susceptibility is found to be in the order of  $10^{-12}$  esu cm for high switching frequencies ( $10^{12}$  s $^{-1}$ ) and increases to values in the order of  $10^{-3}$  esu cm for the kHz regime [Kl2, Ka7, Ma13].

While the above-bandgap absorption of meso PS roughly resembles that of the substrate, as shown in Fig. 7.6, the below-bandgap absorption shows pronounced differences to that of the substrate. The free carriers in heavily doped silicon absorb photons below the fundamental bandgap with increasing absorption towards small photon energies, as shown in Fig. 7.8. If such substrates are made mesoporous by anodization, the absorption coefficient of the dry layers decreases by orders of magnitude with increasing porosity, as observed by photothermal displacement spectroscopy (PDS) [Ch7]. Because dopant atoms are still present in the porous layer, as proved by SIMS, the reduced  $\alpha$  for the IR regime in mesoporous silicon has been interpreted as being caused by trapping of free charge carriers by deep levels relating to surface states [Le14].

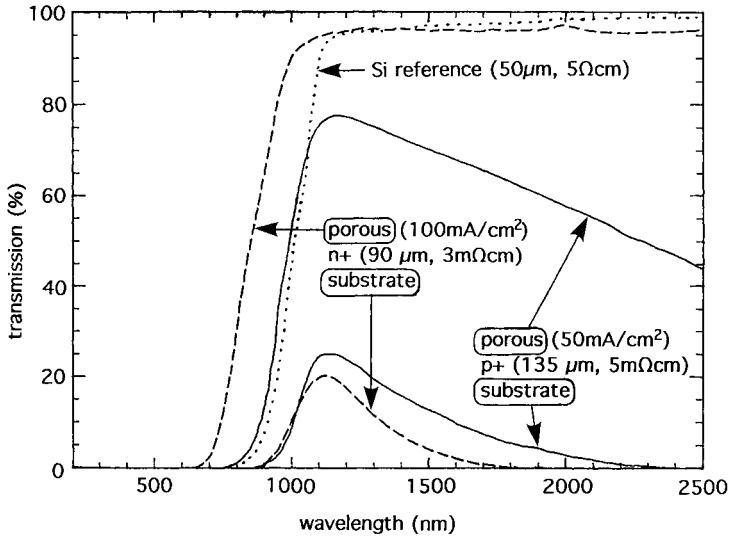


Fig. 7.8 The below-bandgap transmission of free-standing mesoporous silicon compared to the bulk transmission of the corresponding  $n^+$  and  $p^+$  substrates. The strong increase in

IR transmission for the porous samples has been ascribed to a reduced free carrier concentration in the porous material due to trapping in surface states. After [Le14].

#### 7.4

#### Luminescence Properties

Bulk silicon is a semiconductor with an indirect band structure, as schematically shown in Fig. 7.12c. The top of the VB is located at the center of the Brillouin zone, while the CB has six minima at the equivalent  $\langle 100 \rangle$  directions. The only allowed optical transition is a vertical transition of a photon with a subsequent electron-phonon scattering process which is needed to conserve the crystal momentum, as indicated by arrows in Fig. 7.12c. The relevant phonon modes include transverse optical phonons (TO: 56 meV), longitudinal optical phonons (LO: 53.5 meV) and transverse acoustic phonons (TA: 18.7 meV). At very low temperature a splitting (2.5 meV) of the main free exciton line in TO and LO replicas can be observed [Ko15].

Because of its indirect bandgap, bulk crystalline silicon shows only a very weak PL signal at 1100 nm, as shown for RT and 77 K in Fig. 7.9. Therefore optoelectronic applications of bulk silicon are so far limited to devices that convert light to electricity, such as solar cells or photodetectors. The observation of red PL from PS layers at room temperature in 1990 [Ca1] initiated vigorous research in this field, because efficient EL, the conversion of electricity into light, seemed to be within reach. Soon it was found that in addition to the red band, luminescence in the IR as well as in the blue-green region can be observed from PS.

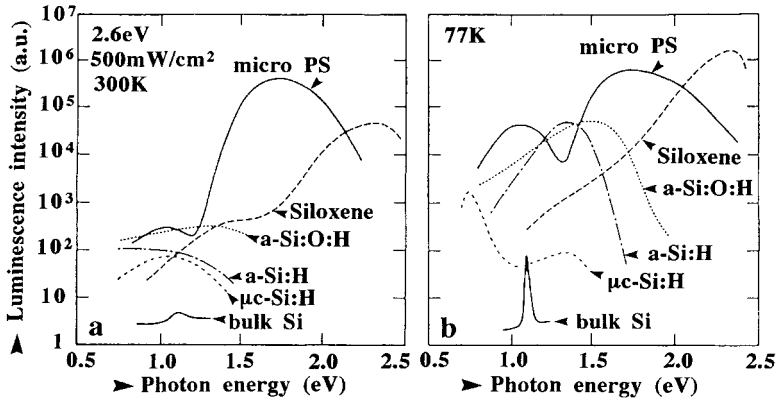


Fig. 7.9 The PL spectra of various silicon-based materials (a) at RT and (b) at 77 K (note the logarithmic scale of the PL intensity) (a-Si: amorphous Si,  $\mu$ c-Si: microcrystalline Si). After [St8].

#### 7.4.1

##### The Red Photoluminescence Band

More than 1000 scientific publications address the PL of PS and make this single property of PS probably its best studied one [Cu2]. Of the different luminescence bands the red PL band is usually the most intense. This band is the subject of most investigations and is usually addressed if the wavelength of PL is not specified explicitly. The PL peak intensity of the red band extends from about 1.3 eV (950 nm) to 2.1 eV (590 nm). Towards the low-energy side the PL intensity becomes small even for high excitation intensities. This is in contrast to the high-energy side, for which efficiencies of up to 10% have been reported [Be11]. The PL peak intensity of the red band can be shifted by a variation of the anodization conditions. A blue shift is observed for an increase in formation current density, for a decrease in HF concentration and for intense illumination during anodization. However, a PL peak energy of 2.1 eV seems to be an upper limit for as-anodized PS samples exposed to air. The decay times at RT are of the order of several microseconds, and the red band is therefore also termed the slow-band (S-band). For most of the luminescent PS samples the red PL peak can be fitted to a Gaussian.

#### 7.4.2

##### Dependence on Formation Current Density

The formation of luminescent PS requires HF to be present in the electrolyte, while the presence of water is not essential [Pr7]. The intensity as well as the peak energy of the PL emission increases with the PS formation current density  $J$  for a fixed electrolyte concentration. If various electrolytes are compared, the ratio between formation current density  $J$  and the critical current density  $J_{PS}$  is more relevant than the absolute value of  $J$ . Because the porosity itself depends on  $J/J_{PS}$ , in many studies



the PL intensity is plotted versus the porosity. At this point it should be emphasized that the PL depends not directly on porosity, but on the structural dimensions of the porous network, which usually decrease with increasing porosity. This relationship, however, holds true only for a certain doping density. If for example PS is formed on highly doped substrates in the dark, the PL is red shifted and its intensity is reduced by orders of magnitude compared to low doped p-type samples of the same porosity. For low doped as well as highly doped substrates the PL intensity increases by more than three orders of magnitude for an increase in porosity from 70% to 94% [Be11].

### 7.4.3

#### Dependence on Illumination

If the electrode is illuminated during anodization, the PL of the resulting PS depends strongly on the wavelength of the light source. If the wavelength is short enough to be absorbed by PS, a higher porosity and a higher PL efficiency at shorter PL wavelength are observed, as shown in Fig. 7.10 [Le24, Su7]. This has been ascribed to further etching of the porous network producing a smaller structure, as shown in Fig. 7.1b. That the same effect can also be observed for prolonged soaking of the PS in the HF electrolyte in the dark [Ca1] or under illumination [Mi3] following the anodization, supports the idea that the increase in PL intensity and peak energy can be ascribed to a size reduction of the porous skeleton.

Surprisingly it was found that PS luminescence excited by polarized light emerges from the sample preferentially with the same sense of polarization. This memory effect has been observed despite the fact that the electron-hole pair loses energy in the order of 1 eV in elastic processes with lifetimes in the order of

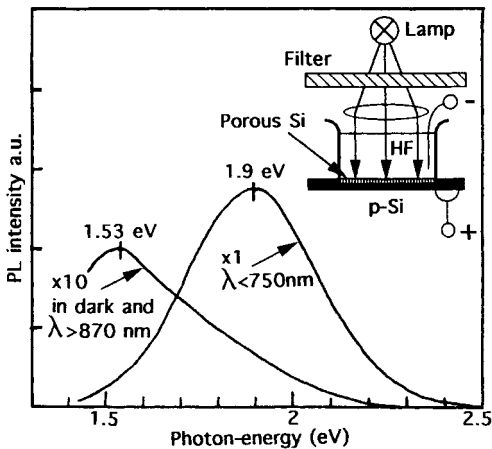


Fig. 7.10 PL spectra (RT) of micro PS samples anodized in the dark and under illumination using the set-up shown in the upper right of the figure (1  $\Omega$  cm p-type, (100),

50 mA cm<sup>-2</sup>). A blue shift and an increase in PL intensity by one order of magnitude is observed for short wavelength illumination. After [Le24].

10  $\mu\text{s}$ . The polarization memory has been ascribed to elongated crystals in the porous network which act as dipole radiators. This idea is supported by experiments in which micro PS was formed under illumination with polarized light. In this case luminescence excitation with unpolarized light led to a partly polarized PL. These investigations point to extended states as recombination centers, in a sense that wave functions 'occupy' a major part of the microcrystallite and depend therefore on their shape and orientation. For local defect states of atomic dimension no polarization memory would be expected [Ko11].

#### 7.4.4

##### **Dependence on Magnetic Field and Hydrostatic Pressure**

Anodization of Si in HF under an applied magnetic field produces an enhancement of the PL efficiency at RT, accompanied by an enhanced porosity compared to PS samples prepared without an applied field. The degree of polarization of the emitted PL is reduced for field-assisted preparation [Na3]. At low temperatures (4.2 K), the Stokes shift and the decay time of the PL are found to be increased, if compared to PS formed under zero magnetic field. This has been interpreted as Zeeman splitting of the spin-triplet exciton states. It indicates that the ground state of the luminescing silicon crystallite is a triplet state [Ko13].

The dependence of PL on hydrostatic pressure has been investigated in a diamond anvil cell up to pressures of 17 GPa [Ze1]. At moderate pressures of up to 3 GPa the PL peak shows a blue shift followed by a significant red shift and a decrease in PL intensity at higher pressures. However, it needs pressures in the order of 17–18 GPa to make the PL vanish. This is astonishing at first sight, because the diamond phase silicon crystal undergoes an irreversible phase transition to the metallic  $\beta$ -tin phase at 12–13 GPa, followed by a transition to the primitive hexagonal phase at 16–17 GPa. However, measurements of the PL and Raman intensity for hydrostatic pressures up to 21 GPa indicated that the phase transitions of silicon are sensitive to cluster size [Pa13].

#### 7.4.5

##### **Dependence on Chemical Environment**

The intensity and wavelength of PL depend greatly on the chemical environment of the luminescing crystallites. This addresses the medium present in the pores, as well as the effects of species chemically bonded to the surface [Le25]. A reversible decrease in the luminescence intensity, for example, is found if the pores are filled with a vapor or a liquid solvent. This quenching increases with increasing gas phase dipole moment of the liquid or the vapor [La7]. Desorption of the hydrogen from the internal PS surface, which starts at temperatures as low as 350 °C, is sufficient to reduce the PL intensity by a factor of 10, as shown in Fig. 6.16 [Ts3, Ha4]. The decrease in PL intensity associated with annealing to the first hydrogen desorption peak is fully reversible by a short HF dip, while annealing above the temperature range of the second peak leads to an irreversible loss of the PL [Ha4].

The dependence of PL on the presence of Si-H led to the idea that the luminescent species is the silicon hydride itself [Pr6]. However, *in situ* PL and FTIR studies during annealing of PS from RT to 350 °C revealed that the quenching of the PL signal significantly precedes H<sub>2</sub> desorption from most of the SiH<sub>2</sub> surface species. In addition, no correlation was found between the IR absorbance due to Si-H<sub>x</sub> and the PL intensity during chemical etching of PS in HF [Ro6]. Furthermore, the PL is restored if oxidized PS is formed by annealing above 600 °C in oxygen [Pe1, Ro6]. The role of hydrogen became clearer when the anticorrelation between the PL intensity and the defect density of PS during the thermal treatment was observed. Electron paramagnetic resonance (EPR) measurements revealed that the defect density increases from 10<sup>16</sup> cm<sup>-3</sup> for as-prepared PS to densities close to 10<sup>19</sup> cm<sup>-3</sup> for samples annealed at 600 °C, as shown in Fig. 7.20. The latter value of defect density corresponds to roughly one defect per crystallite, if the crystallites are assumed to be 5 nm in diameter [Me9]. The defects in as-prepared PS are mainly dangling bonds of the P<sub>b0</sub> type [Ro7, Ba12]. Further annealing under the presence of oxygen forms a thin oxide film that sufficiently passivates the crystallites to restore the PL, as discussed in Section 7.6.

Deuterium-terminated PS shows the same microstructure and VB energy shift, but the PL is significantly blue shifted if compared to hydrogen-terminated PS. This indicates that the surface vibration of terminated atoms couples to the excited energy states of quantum-confined charge carriers [Ma11].

#### 7.4.6

##### Photoluminescence Excitation Spectroscopy

The PL spectrum of a PS sample is usually recorded using a certain excitation wavelength well above the PL signal range. However, if the excitation energy is reduced to values close to the emission energy or even below, the absorption processes connected with light emission and the bandgap energy can be investigated. This technique is called photoluminescence excitation spectroscopy (PLE). It measures the PL signal intensity for a certain wavelength in the PL spectrum while the excitation wavelength is scanned.

A typical PLE spectrum, together with the PL spectrum of a red-emitting PS sample, is shown in Fig. 7.11 a. A quadratic increase in intensity with excitation energy is observed for most PLE spectra of micro PS. This can be interpreted as a reminiscent of indirect absorption in the crystallite core and allows us to extrapolate a bandgap. By extrapolation to zero absorption a bandgap of about 1.8 eV for crystallites emitting at the detection energy of 1.55 eV is determined, for example [Ku4]. Values for the bandgap energy in micro PS extrapolated from PLE correspond well to values calculated from the IR PL band, as shown in Fig. 7.13. The energy loss between absorption and emission of about 0.4 eV for the red band and of 1.1 eV for the IR band, as shown in Fig. 7.11, is called the Stokes shift. PLE investigations show that the red emission from dry PS and OPS, as well as the green emission of PS in HF are significantly Stokes-shifted. Only the blue emission from OPS can be excited close to the emission energy.

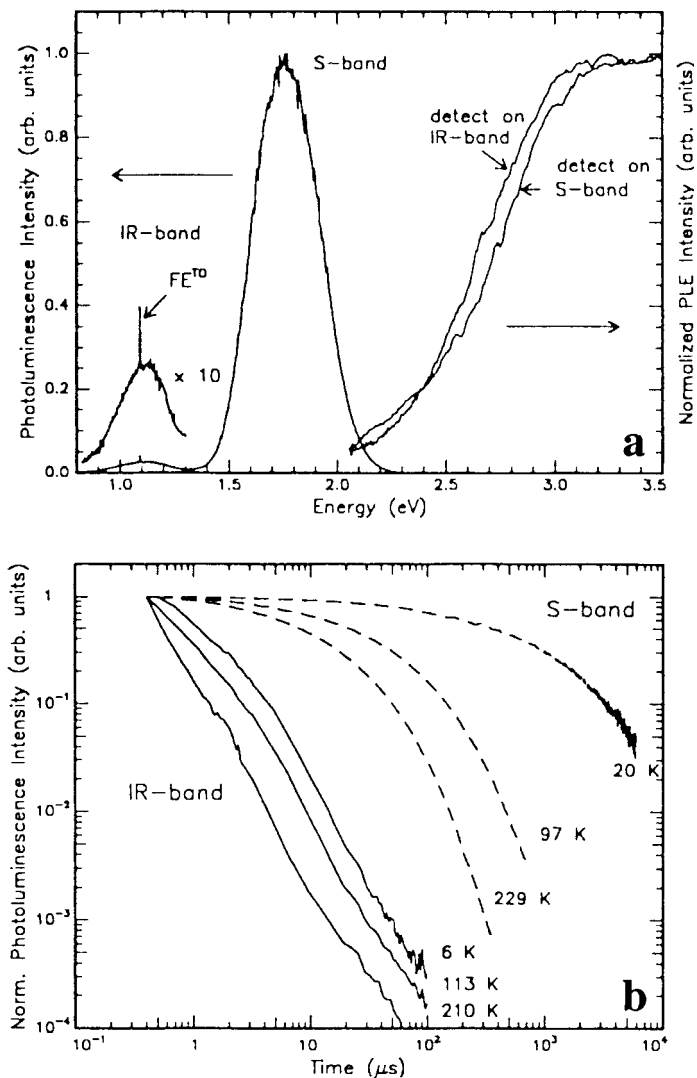


**Fig. 7.11** (a) PL and PLE spectra of the IR and the red S-band for a micro PS sample of 80% porosity at 4.2 K. (b) Double-logarithmic plot of the decays of the IR and red PL intensities

at emission energies of 1.181 eV (IR) and 1.907 eV (red) for different temperatures of the sample [Ma17].

At low temperatures the PLE of hydrogen-terminated PS reveals that phonons and the exciton exchange splitting contribute significantly to the observed Stokes shift [Ca6, Ku4, Ro5, Ka8, Ko13]. For oxidized PS the picture is not usually so clear, due to a recombination path that may involve surface states.

In indirect bandgap semiconductors, like silicon, optical transitions are allowed only if phonons are absorbed or emitted to conserve the crystal momentum. Phonons are not involved in luminescent recombination processes at surface molecules. The observation of phonon-related structures in the PL signal is therefore a fingerprint for the absorption and emission pathways, as shown in Fig. 7.12c and d. Time-resolved, resonantly excited PL spectroscopy of PS and OPS at low temperatures revealed momentum-conserving phonon satellites, as shown in Fig. 7.12a and b. Each localized exciton state is split by the exchange interaction into a spin singlet and a spin triplet, with the triplet lower in energy. The exchange splitting of excitons is found to be enhanced by QC, compared to the bulk Si value. That the optical transitions are phonon-assisted supports the idea of crystalline silicon being the luminescing species in PS and indicates that the indirect

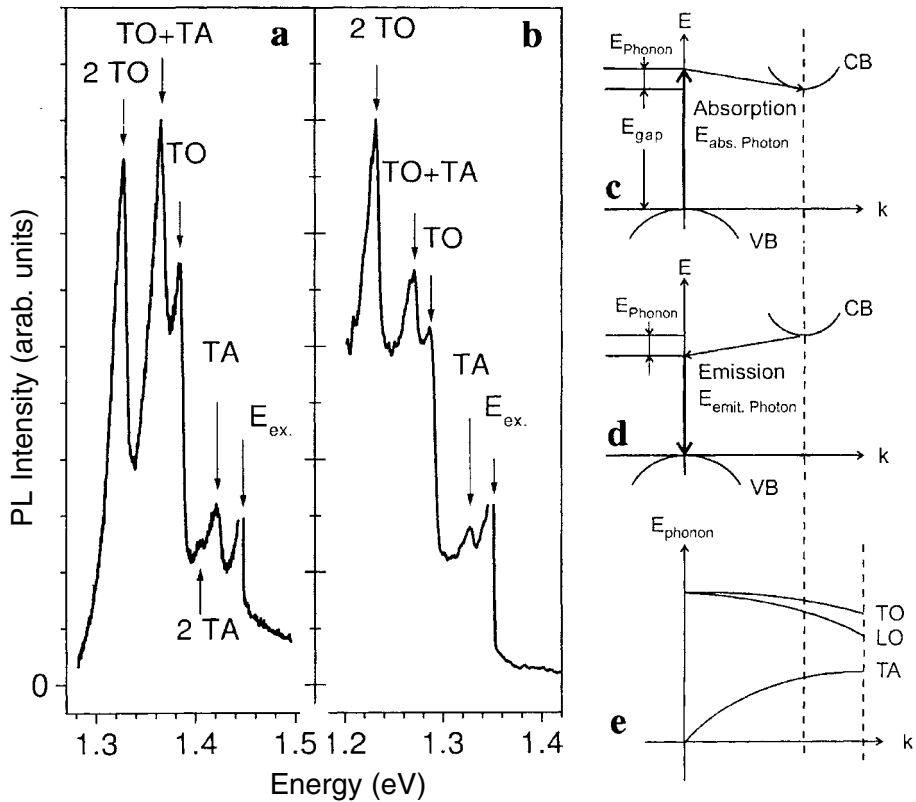


**Fig. 7.12** The resonant PL spectra of (a) naturally and (b) heavily oxidized micro PS at 1.8 K. The arrows show the energy position of silicon TA and TO momentum-conserving phonons with respect to the triplet exciton ground state.

The band structure of bulk silicon, with possible optical transitions for (c) absorption and (d) emission of a photon, together with (e) the dispersion curves of phonon branches, is shown on the right. After [Ko15].

character of silicon is preserved in PS. However, the spatial confinement of electrons and holes inside a small crystallite increases the uncertainty of their crystal momentum, thus allowing optical transitions in which phonons are not involved. This breakdown of the k-conservation rule with increasing confinement energy is theoretically predicted [Hy2] and observed experimentally [Ko13]. The crossover from phonon-assisted to no-phonon recombination occurs at emission energies around 1.8–1.9 eV.

#### 7.4.7

##### **Auger Saturation**

The PL intensity is proportional to the excitation energy over several orders of magnitude. At high excitation levels an occupation of a nanocrystal by two electron-hole pairs can be achieved. In this case fast, non-radiative Auger recombination of one pair leads to PL saturation. The excitation level needed for saturation depends on lifetime and therefore decreases with temperature. The Auger saturation phenomenon can be used to determine the optical absorption cross-section of the Si nanocrystals in micro PS. As shown in Fig. 7.7, the absorption cross-section varies over five orders of magnitude depending on excitation energy. In the light of these findings the significant Stokes shift between absorption edge and the PL peak energy becomes an artificial fact arising from the very small DOS in the vicinity of the energy of the exciton ground state [Ko19].

#### 7.4.8

##### **Thermostimulated Luminescence**

The red PL band of PS can not only be excited by above bandgap photons, but also by an intense IR (1064 nm) pulse [Di6]. Such a thermostimulated luminescence is known for the case of glasses. This observation was attributed to PS having about 100 times the third-order nonlinear optical susceptibility of bulk Si, as discussed in Section 7.3. Multiphoton excitation of the red PL band by resonant pumping of the vibrational modes of surface groups like Si–O [Di4] or Si–H [Ch8] provided evidence for excitation modes that involve the porous skeleton surface.

#### 7.4.9

##### **Photoluminescence Decay**

The PL decay following a short excitation pulse provides valuable information about absorption and emission processes. Therefore the temporal behavior of the PL spectra has been studied at time-scales from picoseconds to tens of milliseconds for different temperatures.

Microcrystallites of direct semiconductors usually show a simple exponential decay of the PL intensity  $P$  with time, with time constants  $\tau$  in the ps and ns range at RT. A similar simple exponential decay ( $\tau=20$  ms at 2 K) is observed for PL from mesoporous silicon of high porosity, which shows a weak confinement effect

[Po2]. For microporous silicon a more complex time behavior extending well into the ms range is observed, as shown in Fig. 7.11b. The experimentally observed dependence of intensity  $P$  on time  $t$  has been fitted to an exponential [Ho3, Fi4, Ma10] or a stretched-exponential function according to Eq. (7.4) [Ka6, Pa12, Oo1].

$$P(t) = P_0 \exp[-(t/\tau)^\beta] \quad (7.4)$$

The exponent  $\beta$  describing the distributions of PL decay rates is found to be in the range 0.4–0.5 for most temperatures and PL energies investigated. In contrast, the PL lifetime  $\tau$  decreases with increasing PL energy.

The decay on a picosecond time-scale, the so-called fast band, is understood as a quasi-direct recombination process in the silicon crystallites or as an oxide-related effect [Tr2, Mg1]. This fast part of the luminescence requires an intense excitation to become sizable; it then competes with non-radiative channels like Auger recombination. The observed time dependence of the slow band is explained by carrier recombination through localized states that are distributed in energy, and dimensionally disordered [Gr7].

The PL lifetime values  $\tau$  obtained by fitting a stretched exponential function decrease with increasing PL peak energy  $E_{\text{PL}}$ . For micro PS dried in a vacuum, for which the PL energies range from 1.5 to 3.5 eV, this dependence can roughly be fitted to the empirical relation:

$$\tau = 10^{(5-2 E_{\text{PL}})} \quad (7.5)$$

for the PL peak energy  $E_{\text{PL}}$  in eV and the lifetime  $\tau$  in  $\mu\text{s}$  at RT [Mi3]. Equation (7.5) fits well with the data shown in Fig. 7.19b, which indicate that the dependence of PL lifetime on confinement energy can be traced smoothly down to the fundamental bandgap of bulk silicon [Ko15].

#### 7.4.10

##### Temperature Dependence

The variation of PL intensity, wavelength and decay with temperature is strongly dependent on the history of the specific PS sample under investigation. In respect of the PL intensity, three basic temperature regimes are observed. The PL intensity is low at low temperatures ( $T < 60$  K). This can be interpreted as a PL being dominated by temporary traps and the thermal activation of charge carriers from these traps competing with non-radiative recombination. At medium temperatures ( $60 \text{ K} < T < 250 \text{ K}$ ) the PL intensity shows a maximum. The thermal energy is now sufficient for activation from shallow traps, but still too low to separate the photogenerated electron-hole pair by thermally activated diffusion of one charge carrier to the next crystallite. A further increase in temperature ( $T > 250 \text{ K}$ ) results in a decrease in the PL intensity. In this temperature regime hopping and diffusion of charge carriers is activated and non-radiative recombination becomes effective. This basic behavior of PL intensity is shown in Fig. 6.18, together with the

PS resistivity versus temperature. Note that the PL intensity reaches its maximum at the onset of thermally-activated electrical transport. This supports the assumption that the quenching of the PL at elevated temperatures is caused by a separation of the photogenerated electron-hole pairs by thermally-activated diffusion of one charge carrier to the next crystallite [Oo1, Ko2]. The change in the PL characteristic of PS upon cooling to temperatures below RT is usually fully reversible, because it is a result of the temperature dependence of diffusion, trapping and thermal activation processes of charge carriers. This is in contrast to the irreversible change in the PL observed for heating above RT.

The dependence of the PL spectra on temperature is again quite complicated. The change from a Gaussian-shaped PL spectrum at RT to a multi-peak spectrum at 5 K for low excitation energies was initially interpreted in terms of an interference effect in the thin porous layer [Ho3]. Later work, however, showed that the peak positions are independent of PS layer thickness, excitation wavelength and sample rotation [Ke3]. The spacing of the peaks is about 61 meV. The origin of this fine structure is still controversial [Ro4].

The picture is more consistent for the dependence of the PL decay time on temperature. The dependence of  $\tau$  on  $T$  can be fitted to  $\ln \tau = T^{-\zeta}$ , with  $\zeta$  increasing with decreasing PL energy [Oo1]. In the temperature range 50–150 K the average lifetime becomes thermally activated by a characteristic energy of 10–20 meV. This energy can be interpreted as the relevant phonon energy in a phonon-mediated transition and in terms of the singlet-triplet splitting of confined excitons. In the latter case only the lower triplet state with a long lifetime is populated at low temperatures. With increasing temperature the faster singlet state becomes populated [Ho3, Ma14].

#### 7.4.11

#### The Green-blue Photoluminescence Band

In contrast to the red PL band, the green-blue PL band of PS commonly shows decay times in the nanosecond regime and is therefore termed the fast band or F-band. This PL band can be observed under several conditions:

1. From porous samples that are still in the HF electrolyte a weak green PL (peak energy 2.1–2.4 eV) is detected, while the red PL is quenched. The green PL shows a blue shift and an increase in intensity with illumination time. If such samples are dried they show the usual red PL band. This green-red switching is reversible and only observed for polar liquids or vapors [Ku2, Li6, Oz3]. This effect has been attributed to a screening of luminescent impurity states by a high dielectric constant of the embedding medium [Ts1].
2. Microporous samples that have been illuminated in the electrolyte after anodization are found to exhibit a green or blue luminescence (peak energy from 2.1–3.0 eV) after drying in a vacuum or in an inert gas such as Ar. This PL red shifts within seconds to the common red PL-band if the PS is exposed to oxygen. This effect has been attributed to the formation of Si=O double bonds,



which generate deep levels in Si crystallites of diameters below 2.5 nm [Mi3, Wo2]. For anodization in an  $\text{H}_2\text{O}_2$ -HF-based electrolyte, a more stable green PL is reported for dried samples [Ya10], while for microcrystallites dispersed in solution a blue PL, peaking at 390 nm, is found [Ak1].

3. A green-blue PL (peak energy 2.3–2.7 eV) is observed from PS samples that have been exposed to some kind of oxidizing treatment, like formation in an HF- $\text{H}_2\text{O}_2$  mixture, storage under ambient air for a prolonged period [Ha6, Mg1], boiling in water [Ho5], oxidizing in  $\text{H}_2\text{O}_2$  [Ya9] or oxidizing by rapid thermal oxidation (RTO) [Ko6]. The origin of this PL is still a matter of controversy. The silanol group (Si-OH) has been proposed as the luminescent center responsible for this blue band [Ta10, Ku3]. Other potential emission centers are the neutral oxygen vacancy (2.7 eV) and the two-fold coordinated silicon lone pair center (3 eV), which are known to cause efficient PL in silica [Yu2].

#### 7.4.12

##### The Infrared Photoluminescence Band

In addition to the red PL band, an IR PL band between about 0.8 and 1.3 eV is usually present in most PS samples [Fa6, Pi3, Ma17, Mo7, Ku4, Pe5], as shown in Fig. 7.9. At RT the intensity of the IR band is weak. At cryogenic temperatures it becomes much stronger and can even be more intense than the red band. The PLE spectra for the red and the IR bands are identical despite their large difference in PL peak energy, as shown in Fig. 7.11a. Furthermore a correlation between the peak position of the two bands has been observed, as shown in Fig. 7.13 [Ku6]. The PL decay, however, is found to be different. For the IR band a  $\tau^{-2}$  dependence of PL intensity on time, with little dependence on temperature, is observed, while a stretched exponential decay with strong temperature dependence is observed for the red band, as shown in Fig. 7.11b.

The IR band has been ascribed to radiative recombination from the CB to a DB center [Ku6]. Such a recombination process is sensitive to changes in the CB energy only and is therefore expected to show a weaker dependence on confinement than the red PL. This interpretation, together with the observation that the increase in VB energy is about twice the increase in CB energy, as shown in Fig. 7.16, has been used to approximate the bandgap energy in micro PS, as shown in Fig. 7.13.

#### 7.4.13

##### Wet Electroluminescence

EL from PS is observed for electrolytic contacts as well as solid-state contacts. The latter subject is discussed in Section 10.5 while this section discusses wet EL.

While the external quantum efficiency of PS reported for solid-state contacts is usually low, wet contacts are found to give high EL efficiencies at low applied bias under anodic [Vi2, It1, Ge2, Ha7] as well as cathodic conditions [Bs1]. An example of bright EL from a micro PS sample in acetic acid under anodic bias is shown

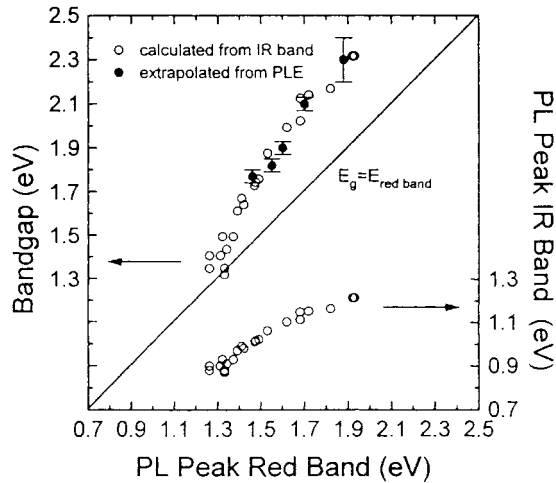


**Fig. 7.13** Bandgap of PS for different types of samples as determined from PLE measurements with detection on the PL maximum (filled circles) and from the position of the IR PL band (open circles). The correlation between the peak energy of the red PL band

and the IR PL band is shown in the lower part of the figure (open circles). The diagonal line indicates the case where the PL peak energy is identical to the bandgap energy, corresponding to zero Stokes shift. After [Ku6].

on the upper right of the book's cover. The orange glowing PS region of the circular sample has been formed in HF at a higher current density ( $200 \text{ mA cm}^{-2}$ ) than the red glowing PS part ( $10 \text{ mA cm}^{-2}$ ). According to the QC model of PS formation, the higher formation current density leads to smaller crystallites that emit at shorter wavelength [Le3]. Under anodic conditions the EL is transient, because it is accompanied by irreversible oxidation of the PS network. During the anodic oxidation of mostly meso PS a shift of the EL and PL bands to shorter wavelength has been observed. This has been interpreted in the frame of the QC model as a successive passivation according to the size of the Si crystallites in PS [Bi1]. The anodic current flows through the largest and non-confined structures first. No light emission is observed during this step. The oxide growth induces a potential drop at their oxidized surface. Under galvanostatic conditions the bias will increase and charge transfer to confined crystallites becomes possible. This produces red EL, which is blue shifted with further anodization. Finally oxidation leads to electrical isolation of the PS from the substrate and light emission ceases.

An IR study of electro-oxidized PS showed a decrease in the OH signal and an increase in the SiO signal with anodization time. This can be interpreted as oxide formation on the PS surface and a removal of electrolyte from the pores. Furthermore a correlation in intensity of localized carrier IR absorption and luminescence indicates that localized states are involved in the red EL [Du4].

In contrast to the anodic case, cathodic EL is persistent. Cathodic EL can be observed from PS layers formed on n-type substrates in aqueous solutions contain-

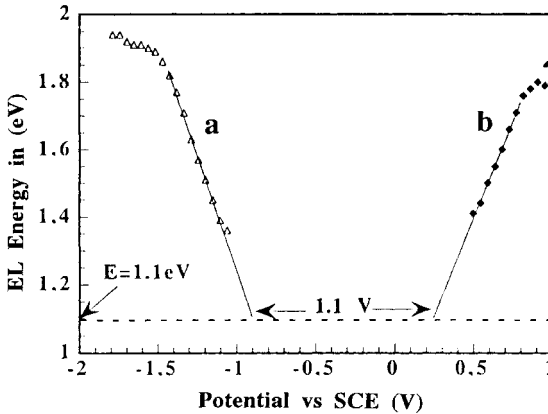


Fig. 7.14 EL peak energy from a 1  $\mu\text{m}$  microporous Si film in an  $\text{H}_2\text{SO}_4$ ,  $(\text{NH}_4)_2\text{S}_2\text{O}_8$  electrolyte as a function of the applied (a) cathodic and (b) anodic polarization. Redrawn from [Bs1].

ing the persulphate ion. The amplitude of the EL is found to be proportional to the current, while the spectral position is only determined by the applied voltage. The shift of the EL peak position with cathodic bias is shown together with the corresponding shift for the anodic regime in Fig. 7.14. Note that the extrapolation of the linear regimes to an EL energy of 1.1 eV, corresponding to the bulk silicon bandgap, leads to a polarization gap of 1.1 V. This suggests that the injected energy level is directly determined by the polarization [Bs1]. A model for the voltage tunability of wet EL based on the QC concept has been developed [Me10].

## 7.5

### Quantum Confinement and Models of the Luminescence Process

This section gives a brief overview of theoretical investigations dealing with the properties of quantum-confined silicon structures.

Every atom shows specific, discrete energy levels for electrons. These levels are either empty or occupied by one or two (spin-paired) electrons according to the Pauli exclusion principle. The energy of the levels can be found by solving the Schrödinger equation. Exact solutions, however, can only be obtained for single electron atoms (hydrogenic atoms).

If many atoms are bound together, for example in a crystal, their atomic orbitals overlap and form energy bands with a high density of states. Different bands may be separated by gaps of forbidden energy for electrons. The calculation of electron levels in the periodic potential of a crystal is a many-electron problem and requires several approximations for a successful solution.

The minute network structure of microporous silicon is between the two extremes of a single atom and a large crystal. A crystallite of a few hundred silicon atoms is large enough to have a rich electronic band structure but is still small enough to show an increase in the energy of an electron-hole pair (exciton) due to

QC. The effect of an increase in fundamental bandgap due to size quantization is not specific to silicon, but common to all semiconductors [He2, Br3, We1].

### 7.5.1

#### Bandgap Calculations

A very crude model to calculate the increase in bandgap energy is the effective-mass particle-in-a-box approximation. Assuming parabolic bands and infinitely high barriers the lowest conduction band (CB) level of a quantum wire with a square cross-section of side length  $w$  is shifted by  $\Delta E_C$  compared to the value  $E_C$  of the bulk crystal [Le1, Ho3]:

$$\Delta E_C = z\hbar^2 / (8m_e^* w^2) \quad (7.6)$$

where  $\hbar$  is Planck's constant and  $m_e^*$  denotes the effective electron mass. The change in VB energy  $\Delta E_V$  is calculated analogously using the effective hole mass  $m_h^*$ . The total increase in the bandgap energy  $\Delta E_G$  is the sum of both changes ( $\Delta E_G = \Delta E_V + \Delta E_C$ ). For the case of a two-dimensional confinement the factor  $z$  is 2. If the thickness of the wire fluctuates, the confinement energy will change along the wire. As soon as the magnitude of these variations becomes comparable to the thermal energy  $kT$  the mobility of carriers along the wire decreases. This eventually leads to confinement in three dimensions, a quantum dot. However, the approximation of Eq. (7.6) is too simplistic. It ignores the detailed shapes of the valence and conduction bands, the influence of neighboring bands, excitonic contributions, and surface effects. More sophisticated calculation methods give more reliable results. An introduction to the different methods of band structure calculation can be found in the literature [As3].

The main questions that are addressed in the theoretical studies are:

1. How does  $\Delta E_G$  depend on  $w$ ?
2. Is the bandgap direct or indirect?
3. What are the lifetimes of excitons in the confined structures?

The methodology used to answer these questions can be classified as either semi-empirical or based on first principles. The confined structure is assumed to be two-dimensional (2D=quantum well), one-dimensional (1D=quantum wire) or zero-dimensional (0D=quantum dot).

All authors who calculated the increase in bandgap energy  $\Delta E_G$  found that the approximation of Eq. (7.6), based on an infinite energy barrier, overestimates the size dependence. A linear [Re2, Bu1, De2, Hi4, Hi8] dependence between  $\Delta E_G$  and  $1/w$  or a  $w^{-1.47}$  law [Pr4] has been found to be more realistic, as shown in Fig. 7.15. In order to simulate the complicated structure of the sponge-like silicon network the band structures for wires along different crystal orientations [Fi2], as well as for wires with constrictions, have been calculated [Hi5]. The calculated en-

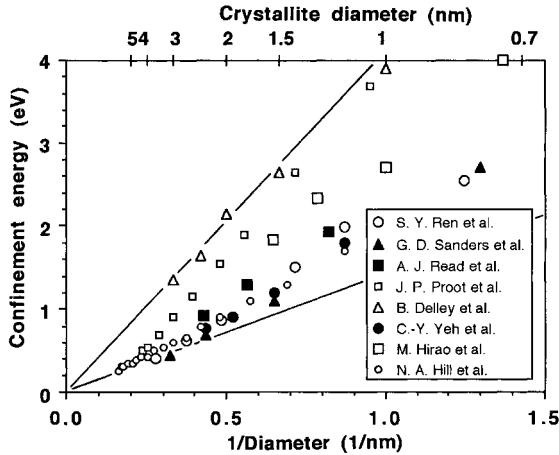


Fig. 7.15 Increase in bandgap energy  $\Delta E_C$  with decreasing diameter of a silicon cluster or dot (open symbols) or a silicon wire (filled symbols), as predicted by various theoretical investigations.

ergy gaps are in good agreement with values determined by optical absorption measurements.

High-resolution measurements of the L-edge absorption in electrochemically prepared micro PS have shown that the absorption is shifted to higher energies relative to the bulk Si value. The CB edge shift  $\Delta E_C$  increases with formation current density and post-anodization soaking time in HF [Bu7]. By monitoring the photoluminescent yield during such X-ray absorption fine structure measurements (XAFS), it becomes possible to correlate the change in emission energy to the relative CB shift. From these measurements a ratio  $\Delta E_V/\Delta E_C$  of about 3 has been observed [Da6]. In the above investigations, as well as for photoemission and X-ray absorption near edge structure (XANES) spectroscopies, the ratio between VB shift and CB shift  $\Delta E_V/\Delta E_C$  has been observed to be about 2 [Mo8].

Theoretical investigations of  $\Delta E_V$  and  $\Delta E_C$  have indicated that the ratio  $\Delta E_V/\Delta E_C$  is greater than 1 [Zh2, Vo2, Ne2] and may be as high as 3 for the case of hydrogenated silicon clusters [Re3]. In a similar calculation for thin silicon films, even-odd oscillations of  $\Delta E_V$  according to the number of Si monolayers have been found [Zh2]. For the latter case the ratio  $\Delta E_V/\Delta E_C$  showed values between 1 and 2. The results of a study [Wa5] including the decrease in the static dielectric constant with size are close to the experimentally [Bu2] observed values of about 2 for the ratio  $\Delta E_V/\Delta E_C$ , as shown in Fig. 7.16. In this work [Wa5], it is concluded that the electron-hole pair is confined by the physical dimension of the quantum dot, not by Coulomb attraction.

The question of whether the bandgap of the quantum structures is direct or indirect has been discussed by several authors. However, it has been pointed out that the electron and hole wave functions are spread in  $k$  space, breaking the

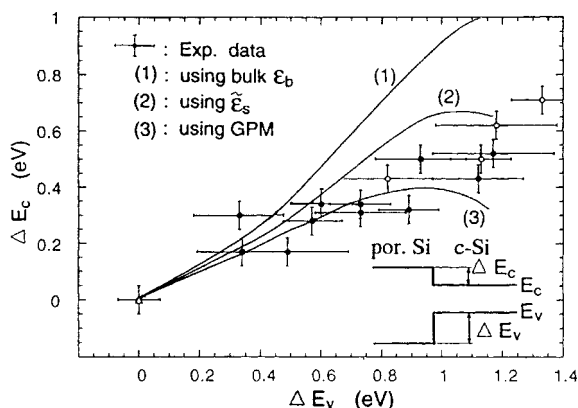


**Fig. 7.16** CB edge shifts versus VB edge shifts calculated for silicon clusters under different assumptions for the value of the dielectric constant  $\epsilon$  (lines). After [Wa5]. For comparison the experimental results obtained by

photoelectron spectroscopy measurements on electrochemical (filled circles) and stain-etch (open circles) PS samples in comparison to bulk silicon (open triangles) are shown. Redrawn from [Bu2].

usual crystal momentum selection rules, so that it is no longer meaningful to debate whether the gap is direct or indirect [Hy2]. Physically, the required momentum derives from scattering from the crystallite surface. The question of whether the luminescence occurs via a zero-phonon or a phonon-assisted transition can be answered if the lifetimes for both mechanisms are calculated and compared. The data shown in Fig. 7.18 suggest that, at least for the red luminescence band ( $\Delta E_G = 0.5\text{--}1.0$  eV), phonon-assisted transitions are expected to dominate. Experimentally no-phonon transitions have been found to dominate for  $\Delta E_G > 1.9$  eV [Ko13].

The energy difference between optical absorption and emission, the Stokes shift, is predicted to be below 0.1 eV for crystallites in the order of 1.5 nm diameter [Ma7]. However, values as high as 1 eV have been reported from experiments. This discrepancy is explained by the localization of the electron-hole pair on one particular single bond, leading to a longer bond length and a lower luminescence energy. Because the elastic response of the environment is weaker at the surface than in the bulk, such a self-trapped exciton is probably found at the crystallite surface [Al5]. Another explanation for the large Stokes shift is based on interactions between neighboring quantum wires. For closely packed quantum wires new interface-localized states appear in the bandgap, reducing its value significantly (about 0.5 eV) [Os2]. The fact that large Stokes shifts are observed for PS exposed to air, while a much smaller shift is found for PS dried in vacuum or Ar, indicates that an oxygen bond is involved in the recombination process [Mi3]. This assumption is supported by simulation of the electronic structure of Si clusters with Si=O double bonds at the surface. This model suggests that recombination in a silicon crystallite passivated solely by hydrogen is via free exciton states for all crystallite sizes, while in the presence of Si=O

double bonds excitons with energies above 2.1 eV get trapped [Wo2]. In the light of experimental findings, which show a variation of the absorption cross-section of PS over five orders of magnitude, the large Stokes shift can be interpreted as an artificial fact arising from a very small density of electronic states in the vicinity of the energy of the exciton ground state [Ko19].

### 7.5.2

#### The Dielectric Constant and Doping of a Quantum Dot

The role of the dielectric constant of the microcrystallite and the medium in the pores deserves further discussion. While the response of the porous layer to high frequencies or light is adequately described by an effective medium approximation [Th3], this macroscopic model is not sufficient to describe the behavior of charge carriers in the minute crystallites in the porous structure. Calculations based on the Penn model [Ts1], pseudopotential calculations [Wa5], as well as self-consistent linear screening calculations of hydrogenic impurities [Al4, La8], predict a reduction of the dielectric constant in a small crystallite compared to the silicon bulk value. Figure 7.17 shows calculated values for the dielectric constant in small silicon clusters with a hydrogen-saturated surface based on different models. A decreasing dielectric constant is reported to increase the energy splitting between the two lowest excitonic levels in asymmetric crystallites [Ma7].

In a study that addressed the effect of doping on quantum dots, the donor and acceptor levels were found to be practically independent of particle size [De3]. In other words, shallow impurities become deep ones if the dot size is reduced. Experimental observations show that the luminescence is not affected by doping if a thermal diffusion process, for example using a  $\text{POCl}_3$  source, is used [El1]. Implantation, in contrast, is observed to effectively quench the PL [Ta14]. If the pores are filled with a medium of a large low-frequency dielectric constant, such as water or any other polar solvent, it is found that deep impurity states still exist,

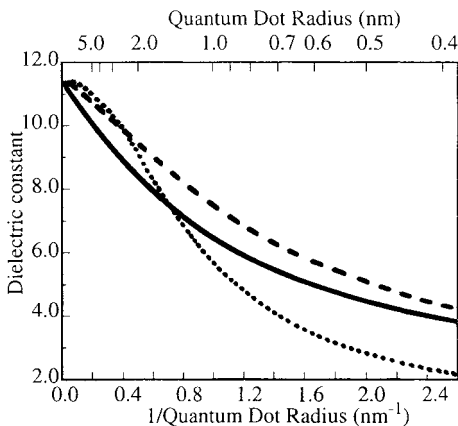


**Fig. 7.17** Plot of the calculated dielectric constant in silicon crystallites of different size. The broken curve corresponds to calculations based on the Penn model [Ts1], the dotted line corresponds to pseudopotential calculations [Wa5], while the full line is based on self-consistent linear screening calculation of hydrogenic impurities [Al4]. Redrawn from [Al4].

but a free carrier can hardly get trapped into them, because of slow dielectric relaxation effects [Ch2, Br4, Ba3, Ts1]. This screening of the electric field of an ionized impurity by the embedding medium is assumed to be responsible for the green-to-red switching of the PL, as well as the reduction in the free carrier density, observed if the porous layer is dried [Ch2].

### 7.5.3

#### Lifetime Calculations and Surface Passivation

An approximation of the lifetime in PS at RT using an electron-hole pair density equal to one pair per crystallite and the radiative recombination parameter of bulk silicon give values in the order of 10 ms [Ho3]. The estimated radiative lifetime of excitons is strongly size dependent [Sa4, Hi4, Hi8] and increases from fractions of microseconds to milliseconds, corresponding to an increase in diameter from 1 to 3 nm [Hy2, Ta3], as shown in Fig. 7.18. For larger crystallites a recombination via non-radiative channels is expected to dominate. The experimentally observed stretched exponential decay characteristic of the PL is interpreted as a consequence of the randomness of the porous skeleton structure [Sa5].

The dependence of lifetime on temperature in the range above RT shows an activation energy in the order of 10–25 meV [Bu3, Oo1]. This was proposed to be a consequence of the exchange splitting of the exciton between the singlet and the triplet state. While at RT both states are populated, only the lower triplet state is populated at temperatures below 20 K. However, it has been shown that even for crystallites of low symmetry the calculated values of the exchange splitting are too low compared with experimental observations [De3]. Calculations of the radiative lifetime of the triplet exciton that take into account spin-orbit interactions are reported to be consistent with experimental results [Na1].

Values of  $\Delta E_G$  calculated on the basis of the effective mass model are sensitive to the height of the barrier present at the surface of the confined structures [De4, Xu2]. For the case of oxidized PS, it is obvious that the silicon crystallites are embedded in a wide-gap material. In the case of a hydrogen termination of the crys-

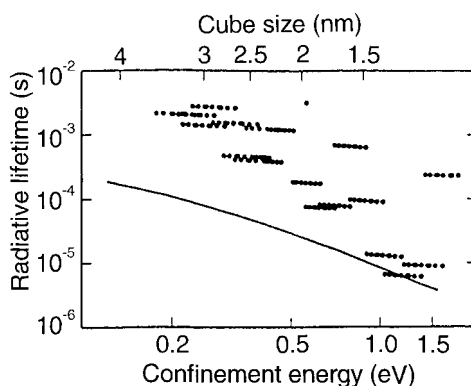


**Fig. 7.18** The radiative recombination time  $\tau$  as a function of the blue shift of the photon energy  $\Delta E$  from the bulk silicon band edge: zero-phonon transitions (dots); TO phonon-assisted transitions (line). This scatter plot shows the radiative time for each member of an ensemble uniformly distributed around a cubic geometry. The top scale indicates the equivalent cube size. Redrawn from [Hy2].



tallite surface it is argued that the bonding-antibonding splitting of the Si-H bonds mimics a wide-gap material [De4]. However, the assumption of a finite barrier gives more realistic results, especially for very small structures where the effective mass model overestimates the gap.

A hydrogen termination of the crystallite surface is assumed in most studies. Calculations show that a small part of the hydrogen can be removed without the formation of DBs, as shown for the transformation of  $\text{Si}_{29}\text{H}_{36}$  to  $\text{Si}_{29}\text{H}_{34}$  [Hi4]. Further dehydrogenation, however, leads to the formation of DBs that are efficient recombination centers and thus effectively suppress the luminescence [De2, Hi4, De5]. The observed IR luminescence has been proposed to be due to recombination via DB centers [De3].

The lifetime for Auger recombination was calculated to be in the 1 ns regime [De3]. This may explain the saturation observed in the excitation of crystallites, which seems to be limited to one exciton per crystallite [Mi1].

It should be noted that other structures, such as siloxene [De6] or polysilane [Ta4], that have been proposed to play a role in the luminescence mechanism of PS have also been studied on a theoretical level.

#### 7.5.4

#### Conclusions from Calculations

It is possible to draw some conclusions about the physical properties of microporous silicon from the results of the theoretical studies:

1. The increase in bandgap energy  $\Delta E_C$  shows an approximately linear dependence on  $1/w$ .
2. The increase in VB energy  $\Delta E_V$  is expected to be considerably larger than the increase in the CB energy  $\Delta E_C$ .
3. Fluctuations in the thickness of quantum wires can be assumed to be present in a porous network and will drastically reduce the carrier mobility.
4. A visible red luminescence corresponds to a silicon cluster size between about 1 and 2.5 nm.
5. For the red luminescence band, lifetimes of about  $10^{-3}$  to  $10^{-6}$  s are expected and the recombination is most probably phonon assisted.
6. A DB at the quantum structure surface is expected to efficiently suppress visible luminescence.
7. The dielectric constant in the crystallite is significantly reduced compared to the bulk value.
8. Donor and acceptor levels are assumed to remain practically unaffected by particle size and thus become deep levels in confined crystallites.
9. If the pores are filled with a medium of a high dielectric constant, a screening of impurity states is probable.
10. The large Stokes shift for confinement energies above 2.1 eV can be explained by the electronic states produced by an Si=O double bond.

A detailed review of theoretical studies of PS is available in the references [Jo3].

## 7.5.5

**Models of the Luminescence Process**

With roughly 1000 atoms, the size of the silicon clusters that constitute the micro PS network is between the bulk crystal and a molecule. Hence models of the luminescence process based on size reduction of the crystal, as well as models based on molecular structures, have been proposed, which are reviewed in detail in [Ca7, Ju3]. Generally the various models of the luminescence of PS can be classified into three major categories:

1. **The molecular recombination model.** Absorption of a photon and its radiative reemission occurs in chemical compounds such as siloxenes [Br6], polysilanes [Ta4] or silicon hydrides [Pr6]. This luminescence mechanism is independent of whether or not QC is present in PS.
2. **The surface-state model.** The absorption of a photon generates an exciton within a quantum-confined silicon crystallite but its radiative recombination occurs at localized electronic states on the surface of the crystallites [Ko5] or in defects in the oxide coverage of the crystallites [Pr5].
3. **The quantum recombination model.** The photogeneration of an exciton and its luminescent decay occur within a quantum-confined silicon crystallite [Ca6].

1. The molecular recombination model was proposed because the PL spectra of some silicon compounds, e.g. siloxene, are very similar to the PL observed from PS [Br6, St4, Mc3]. In addition aged PS is rich in H and O and the presence of silicon hydrides, polysilanes or siloxene could therefore not be excluded. Detailed investigations, however, showed that PS free of oxygen [Pr7], as well as OPS free of hydrogen, do luminesce. The PL of micro PS is not very sensitive to its stoichiometry, which would be the case if the luminescent species is molecular in nature. For the special case of siloxene ( $\text{Si}_6\text{H}_6\text{O}_3$ ), detailed investigations of the PL spectra revealed quantitative differences to the PL from PS, which led to the conclusion that light emission from PS is not directly associated with siloxenes [Sh3, Mo4].

2. The surface-state model, in which the luminescent recombination occurs via surface states, was proposed to explain certain properties of the PL from PS, for example long decay times or sensitivity of the PL on chemical environment. In the frame of this model the long decay times are a consequence of trapping of free carriers in localized states a few hundred meV below the bandgap of the confined crystallite. The sensitivity of the PL to the chemical environment is interpreted as formation of a trap or change of a trap level by a molecule bonding to the surface of a PS crystallite. The surface-state model suffers from the fact that most known traps, e.g. the  $\text{P}_b$  center, quench the PL [Me9], while the kinds of surface state proposed to cause the PL could not be identified.

3. A strong argument in favor of the QC model is the observation of step-like features in the low-temperature PL spectrum of PS, as shown in Fig. 7.12, which correspond well with the energies of momentum-conserving phonons in crystal-

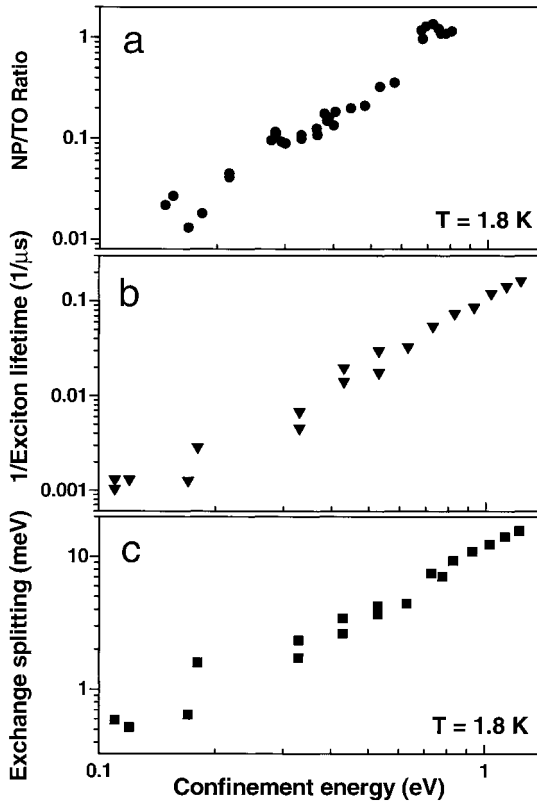


Fig. 7.19 Influence of QC on the basic properties of excitons localized in Si nanocrystals. Confinement energy dependence of (a) relative strength of no-phonon and TO phonon-

assisted recombination channels; (b) inverse lifetime of the optically active exciton state; (c) exciton exchange splitting. After [Ko15].

line silicon [Ca6, Ko13]. It has been argued that this observed weak luminescence signal very close to the excitation energy is not identical to the strong red band observed at room temperature [Ro5]. However, hole burning spectroscopy of PS showed the same phonon-related structures, proving that the PL mainly originates from quantum-confined states inside the Si crystallites [Ko12]. The observed phonon structures also exclude amorphous silicon as a potential source of the PL [Va2]. In the frame of the confinement model the sensitivity of the PL on the surface condition is explained as being due to polarization-induced changes in the energy level of the quantum-confined states [Ts1].

The most fundamental properties of the confined exciton are confinement energy, the type of recombination process (indirect or quasi-direct) and the exciton exchange splitting. As shown in Fig. 7.19, each quantity follows the expected strongly nonlinear enhancement over a large dynamic range with increasing confinement energy and decreasing crystallite size. All these quantities can be traced

continuously and smoothly from bulk Si PL up to the visible spectrum, where the confinement energy of more than 1 eV is as large as the fundamental silicon bandgap itself [Ko13]. This smooth transition from bulk Si properties to the properties of micro PS are in favor of the QC model.

## 7.6

### Oxidized Porous Silicon

In this section the properties of chemically and thermally oxidized and nitridized PS will be discussed. Wet anodic oxidation of PS is commonly accompanied by luminescence and is therefore discussed in Section 7.4.

Microporous and mesoporous silicon can be partly oxidized by chemical or electrochemical methods, while thermal oxidation is needed for a complete conversion of the porous layer to oxide. This complete conversion was the aim of the first studies in this field.

Thermal oxidation of bulk silicon requires high temperatures and the maximum oxide thickness is limited to a few micrometers. The complete oxidation of highly porous silicon, in contrast, can be performed in wet oxygen at temperatures as low as 850–900 °C, independent of layer thickness. During the oxidation the optical absorption edge of the material is blue shifted, which is ascribed to a decreasing size of the microcrystallites [Pe1]. For films of several micrometers in thickness this shift corresponds to a change in color from brown via red and yellow to a glassy appearance. This color change can be used as a simple indicator of whether the oxidation was complete or not.

The porosity of the initial PS layer determines the density of the resulting oxide. Oxidation of PS at temperatures below 1000 °C leads to porous oxides if the initial porosities were in excess of 56%, while PS layers of lower porosity show residual silicon crystallites in an oxide matrix after oxidation. Porous oxides have a lower dielectric constant than thermal oxides and are therefore favorable for reducing parasitic capacitance [Ar4]. In addition the thermal budget of a manufacturing process can be reduced if the thermal oxide is not formed from bulk silicon but from PS. The resistivity of OPS is rather low for low oxidation temperatures (600 °C), which are known to produce a high density of DBs [Ha9], while high resistivities ( $10^{16}$ – $10^{17}$  Ω cm) and low interface trap densities ( $10^{12}$  cm<sup>-2</sup>) are observed for higher temperatures [Wu1].

The stress of oxidized PS layers is always compressive. For porous oxides, values below  $10^8$  N m<sup>-2</sup> are reported [Ba5], which is nearly one order of magnitude smaller than values of intrinsic stress generated by low-temperature thermal oxidation of bulk silicon. The compressive stress in OPS has successfully been used to lift up released mesoporous films and thereby fabricate 3D microstructures [La9].

Annealing of porous oxides at temperatures above 1000 °C leads to a densification. If the porosity of the initial PS was optimized to 56% the densification does not affect the layer thickness, while otherwise the layer thickness increases (for

$p < 56\%$ ) or decreases (for  $p > 56\%$ ). The stress in the densified oxides is caused by the difference in thermal expansion coefficients between oxide and substrate. It is therefore identical to that observed for high-temperature thermal oxidation. The densified oxides are comparable to thermal oxides with respect to their etch rate and refractive index. Fully oxidized PS is a good dielectric insulator, exhibiting reasonable breakdown field strengths of around  $5 \text{ MV cm}^{-1}$ , low leakage currents and moderate interface state densities [Wu1]. The densification process has an activation energy of 3 eV and is probably associated with the viscous flow of silica [Yo1]. While the dielectric constant for the densified oxide is identical to that of a thermal oxide, it is one or two orders of magnitude larger for incomplete oxidized PS, especially for oxidized meso PS. This effect has been ascribed to the polarizability of the remaining silicon crystallites in the OPS film [Un1].

The doping dependence of the PS formation process and the possibility of transforming PS to oxide at relatively low temperatures has been used to form dielectrically isolated silicon islands, as shown in Fig. 10.23.

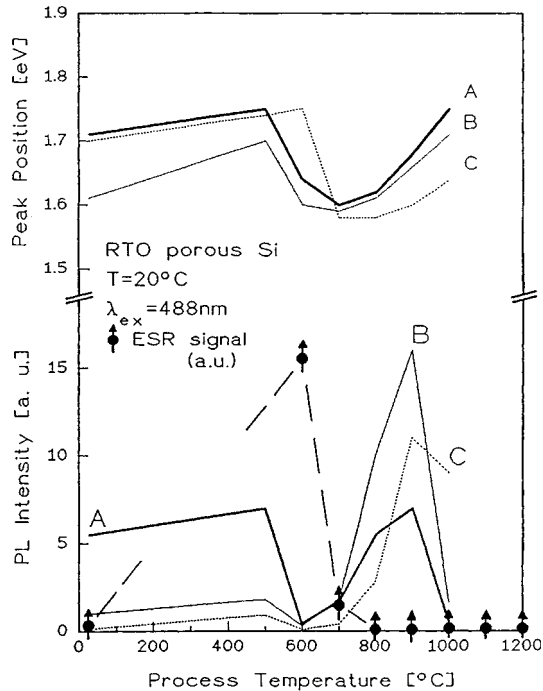
The observation of visible PL from as-prepared microporous silicon led to the question of whether the PL is still present after partial oxidation of this material [It2, Le15]. Investigations of this matter are not aiming at full conversion of PS to  $\text{SiO}_2$  but to a surface passivation of the silicon crystallites. Therefore, the effects of soft oxidation methods such as storage of PS in dry or wet air at RT [Di2] and boiling of PS in water [Ho5] or soaking with  $\text{H}_2\text{O}_2$  [Ko18] have been investigated. It was found that backbond oxidation without an attack of the surface Si-H bonds is the initial step in the oxidation reaction at low temperatures [Ka2]. The PL intensity is found to increase during this process [Ok1]. Full oxidation of PS at room temperature is reported using ozone and UV light. This treatment, however, quenches the visible PL effectively [Ho4].

Partial oxidation of PS can be performed thermally, if the oxidation rate is reduced by using dry oxygen, by dilution of the oxygen with an inert gas, by a low oxidation temperature or by short oxidation intervals. Oxidation times in the order of seconds can be achieved by RTO, for which oxidation rates and details of the kinetics are given in the literature [Fu1, Go2].

The dependence of the PL intensity and peak position on oxidation temperature for three different PS samples is shown in Fig. 7.20. Oxidation at  $600^\circ\text{C}$  destroys the PL, while the initial PL intensity is restored or even increased after oxidation at  $900^\circ\text{C}$ . This effect can be understood as a quenching of PL because of a high density of defects generated during the desorption of hydrogen from the internal surface of PS. Electron spin resonance (ESR) investigations show a defect with an isotropic resonance ( $g=2.0055$ ) in densities close to  $10^{19} \text{ cm}^{-3}$  for oxidation at  $600^\circ\text{C}$  [Pe1, Me9]. This corresponds to one defect per crystallite, if the crystallite diameter is assumed to be about 5 nm in diameter.

The spectral distribution of the PL from OPS is found to be similar to that of as-prepared PS [Ta6]. In some cases a green band is found and has been ascribed to point defects in  $\text{SiO}_2$  [Ka9]. The slow red-orange band is dominant, while the fast blue-green band contributes significantly to the PL intensity for highly oxidized samples [Ko1]. While the red band is correlated with the presence of small

**Fig. 7.20** Luminescence intensity and peak position versus RTO processing temperature for PS samples grown on p-type silicon substrates (A: 1  $\Omega$  cm, B: 1  $\Omega$  cm, C: 0.07  $\Omega$  cm). Note the anti-correlation of the PL intensity and of the ESR signal (taken for sample series A). After [Pe1].



silicon crystallites [Cu1], it is uncertain whether the blue PL is caused by QC effects [Mi7] or by hydroxyl groups absorbed on defects in the silica network [Ta5, Ya6]. The fact that the blue PL remains even at high annealing temperatures (1050°C), for which the red PL is quenched, supports the latter proposal [Se12]. As in the case of as-prepared samples, the peak wavelength of the red band depends on crystallite size, however, it cannot be blue shifted above 1.9 eV by prolonged oxidation. Hydrogen-related peaks in the FTIR spectra disappear during RTO [Sh1], which allows us to conclude that polysilane species are not responsible for the visible PL. The observation of momentum-conserving phonon signals in PLE measurements of OPS, as shown in Fig. 7.12b, indicate a common origin of the red luminescence band for non-oxidized and oxidized PS.

Concerning long-term stability of the PL, OPS is superior to PS. Even under laser illumination in air, no degradation of the PL was observed for OPS [Sh1]. OPS has been found to have lower resistivity and higher photoelectric efficiency than as-anodized material [Li4]. The quite high electrical conductivity of incompletely oxidized OPS can be understood if we recall that the average oxide thickness between two crystallites is below 3 nm, which is sufficient for tunneling of charge carriers.

Analogous to oxidized PS, nitridized PS can be fabricated by thermal treatment of PS in  $N_2$  or  $NH_3$  [Ts2, Sm4, Li5]. The dependence of PL intensity on annealing temperature is found to be similar to that of OPS. For low annealing tempera-

tures (600–800 °C) the PL is quenched, while the PL is restored for high annealing temperatures (800–1100 °C) [Li5]. The optimal initial porosity of PS required for a complete transformation of PS to Si<sub>3</sub>N<sub>4</sub> is 20%. Thick silicon nitride layers can be formed in ammonia (at 0.1 bar) in 1 h at 730 °C.

## 7.7

### Related Materials

This section summarizes the properties of materials similar to PS but not formed by anodization of a bulk silicon electrode. These materials fall into the following categories:

1. PS formed chemically without an applied potential in a mixture of HF and an oxidizing agent.
2. PS formed anodically on amorphous or polycrystalline silicon in HF.
3. Porous layers formed anodically on other semiconductors than silicon.
4. Luminescent silicon microstructures formed by other methods than anodization and stain etching.

#### 7.7.1

##### Stain Films

PS formed chemically without an applied potential in a mixture of HF and an oxidizing agent, e.g. HNO<sub>3</sub>, is called a stain film. The similar nature of electrochemically formed micro PS and stain films was pointed out in 1960 [Ar1]. Stain films are usually microporous. They are of predominantly monocrystalline character and show visible PL [Sc16, Ji1]. If metal films are present on the silicon surface, mesopore formation may also be observed [Li10].

The formation mechanism of stain films is not understood in detail. The chemical identity of the oxidizing agent seems to be of minor importance, because HNO<sub>3</sub>, NaNO<sub>2</sub>, CrO<sub>3</sub>, K<sub>2</sub>Cr<sub>2</sub>O<sub>7</sub>, KBrO<sub>3</sub> and KMnO<sub>4</sub> showed similar results [Be19, Fa5, Na5, Ya9]. Cathodic and anodic sites present at the silicon interface have been proposed to be responsible for stain film formation. In the case of a p–n junction, especially if it is illuminated in the electrolyte, the different sites are easily identified: the built-in potential between differently doped areas constitutes a galvanic element. In the early years of semiconductor device manufacturing this effect was exploited to determine the depth of a diffused p–n junction.

That the assumption of such spatially separated sites is justified has been demonstrated by experiments using evaporated metal films, acting as catalytic sites [Li10]. In an electrolyte composed of aqueous HF, H<sub>2</sub>O<sub>2</sub> and ethanol, stain film formation has been observed under and close to evaporated thin films of Au, Pt and Pd, while silicon samples free of metal films showed no PS formation. The metal is assumed to act as a cathodic site, where H<sub>2</sub>O<sub>2</sub> is reduced to H<sub>2</sub>O under injection of two holes into the silicon VB. These holes are consumed by the for-

mation of PS, according to the reaction shown in Eq. (4.4). If the metal films are patterned, most holes are consumed directly under the metal film, however, a fraction diffuses away and leads to PS formation in regions nearby. The doping type and density of the silicon substrate determines pore morphology and thereby film porosity.

For homogeneously doped silicon samples free of metals the identification of cathodic and anodic sites is difficult. In the frame of the quantum size formation model for micro PS, as discussed in Section 7.1, it can be speculated that hole injection by an oxidizing species, according to Eq. (2.2), predominantly occurs into the bulk silicon, because a quantum-confined feature shows an increased VB energy. As a result, hole injection is expected to occur predominantly at the bulk-porous interface and into the bulk Si. The divalent dissolution reaction according to Eq. (4.4) then consumes these holes under formation of micro PS. In this model the limited thickness of stain films can be explained by a reduced rate of hole injection caused by a diffusional limitation for the oxidizing species with increasing film thickness.

Formation rate and morphology of stain films are strongly dependent on etchant composition and on substrate doping. A delay of stain film formation of up to 10 min has been observed, which is ascribed to the autocatalytic character of the reaction in HF–HNO<sub>3</sub> mixtures, as discussed in Section 2.4. In order to accelerate the process, the etchants are commonly primed by briefly etching a piece of silicon in the concentrated solution prior to adding DI water. A mixture of HF(50%):HNO<sub>3</sub>(70%):H<sub>2</sub>O for example produces rough surfaces consisting of small hillocks with lateral dimensions of several hundred nanometers if the HNO<sub>3</sub> concentration is high (mixing ratio 1:5:10) while for low HNO<sub>3</sub> concentrations (e.g. mixing ratio 4:1:5) smoother surfaces are observed [Fa5, Sc18, Ca5, Wi1]. In both solutions spontaneous staining is observed for Si samples of doping densities in excess of 10<sup>19</sup> cm<sup>-3</sup>, while lower doped samples show delayed staining even for primed solutions. For very low HNO<sub>3</sub> concentrations (mixing ratio 1000:1:0) the staining behavior changes and all doping densities except highly doped p-type Si show spontaneous PS film formation. In this case the growth rate shows a parabolic rate law that is ascribed to the limiting diffusion of the oxidizing species. Growth rates of the order of 1 nm s<sup>-1</sup> are observed. The porosity of such stain films increases rapidly with thickness and saturates at values around 70% or more [Fr3, Sh6]. Acetic acid is sometimes used in place of water as diluent in order to relieve the surface tension, which reduces the sticking probability for gas bubbles evolved during etching [Je1]. In all etchants the thickness of chemically formed porous films is limited to values below about a micrometer. In some cases a double layer structure of the stain film has been observed; TEM images have shown a 100 nm thick continuous layer of micro PS at the bulk interface and oxide-rich flakes on top [Wi1]. The neutral P<sub>b</sub> center concentration is an order of magnitude higher than in comparable anodically formed micro PS films, indicating a higher degree of oxidation in the as-prepared stain film [Sc16].

Stain films show an intense PL at a peak wavelength of about 1.9 eV, independent of substrate doping density [St7, Li10]. This is in contrast to anodically



formed PS, for which the visible PL intensity decreases rapidly if the substrate doping density exceeds  $10^{18} \text{ cm}^{-3}$ . The PL is observed from stain films grown on single- as well as polycrystalline substrates, but not from stained amorphous thin films [St9]. Visible EL is reported from solid-state devices using a stain-etched film in between the bulk and an ITO (indium tin oxide) electrode [Xu3].

### 7.7.2

#### **Porous Silicon on Amorphous and Polycrystalline Silicon**

If a p-type polycrystalline silicon electrode is anodized in HF the dependence of PS formation rate on the crystal orientation leads to thickness variations between the grains, which become significant for highly doped polysilicon. In addition pore formation is enhanced along grain boundaries, which may result in an uneven interface and eventually lead to remaining non-anodized silicon grains in a porous matrix [Ko21]. However, no significant difference is observed for optical and electrical properties of PS formed on polycrystalline electrodes if compared to PS formed on single-crystalline silicon [Ha8].

The picture is less clear if the electrode is made of amorphous Si. Device-grade amorphous silicon is usually produced by radio-frequency glow discharge of  $\text{SiH}_4$  at substrate temperatures between 100 and 300 °C. Amorphous silicon is a highly disordered material with an elastic scattering length below 1 nm for thermalized carriers. Bulk amorphous silicon exhibits a more efficient PL (1.2–1.5 eV) than crystalline silicon at low temperatures. The origin of PL from bulk amorphous silicon, as well as from anodized porous amorphous silicon, is still under discussion [Oh2, Al6, St3, Bu4, We2].

### 7.7.3

#### **Pore Formation in Semiconductor Electrodes Other Than Si**

The pore formation models discussed in Section 6.2 are based on the semiconducting properties of the electrode but not on its chemical identity. Consequently electrochemical pore formation has been observed for many semiconductors.

There is no solubility limit for Ge in Si, and so  $\text{Si}_{1-x}\text{Ge}_x$  layers, with  $x$  varying from a few per cent to 100%, have been investigated. Porous  $\text{Si}_{1-x}\text{Ge}_x$  layers ( $x=5\text{--}20\%$ ) formed by anodization in HF showed red luminescence under UV excitation and the morphology seems to change from microporous to mesoporous with increasing p-type doping level, as observed for PS [Sc14]. Even on pure p-type Ge a porous layer is formed upon anodization in HF. This porous germanium shows a broad PL band well above the bandgap at 1.17 eV, which blue shifts to 2.15 eV after oxidation at 600 °C [Mi2]. Mesoporous structures have been observed on n-type 6H-SiC electrodes in HF under UV illumination [Sh5].

The electrochemical formation of porous structures is also observed for III–V semiconductors like GaP [An1, Er1], GaN [Pe7, My1], InP [Ki2, Ko16, Ta13, La10] or GaAs [Be5, Fa4, Sc15]. Structural dimensions in the macroporous regime are observed for n-type GaAs of moderate doping ( $10^{17} \text{ cm}^{-3}$ ) anodized in KOH in the

dark [Fa4] or in  $\text{NH}_4\text{OH}$  under illumination [Mo9], as well as for GaN anodized under UV illumination in KOH or  $\text{H}_3\text{PO}_4$  [Pe7]. Macroporous structures are also observed for n-type InP after anodization in HCl [Ko16, Ta13, La10]. Mesoporous films are found on highly doped GaAs anodized in HF [Be5]. Green PL (540 nm) from porous GaAs, intense enough to be visible to the naked eye, has been reported [Sc15]. Porous films have also been observed after photoelectrochemical anodization of II–VI semiconductors such as CdSe [Te1], CdTe [Mu5, Er2] and ZnSe [Te2].

#### 7.7.4

#### Luminescent Silicon Microstructures

The visible luminescence from PS has been ascribed to QC effects [Ca1]. This interpretation is supported by the observation of a similar luminescence from silicon clusters in the nanometer regime or large silicon molecules that are not produced by anodization but by alternative methods.

Silicon microstructures can be categorized according to the dimensionality of the confinement. Most PL studies deal with silicon structures confined in three dimensions; such dot-like structures are designated zero-dimensional (0D). An overview of size-dependent properties of silicon spheres is given in Table 6.1. Standard methods of generating such microstructures are gas-phase synthesis [Di3, Li7, Sc12], plasma CVD [Ru2, Co1, Ta8] or conventional chemical synthesis [Ma15].

The visible blue and red EL, observed from silicon-rich oxides formed by CVD of  $\text{SiO}_2$  with excess Si, was attributed in 1984 to QC effects in the tiny Si precipitates present in the films [Di3]. The blue luminescence was later attributed to OH groups in the silica network, while the red luminescence is believed to be due to QC effects [Ta5, Ko3]. Only the red PL band is observed for silicon microcrystallites that are not in an  $\text{SiO}_2$  matrix but covered by hydrogen, as is the case for microwave plasma decomposition of  $\text{SiH}_4$  in hydrogen [Ta8]. *In situ* PL measurements of hydrogenated silicon particles suspended in a silane plasma at RT showed that the PL intensity is sensitive to the onset of agglomeration but not to the oxygen content of the plasma [Co1]. Comparative studies of PS and oxide-passivated silicon microcrystallites, formed at  $1000^\circ\text{C}$  in He by decomposition of disilane and subsequent oxidation, indicate that particles of 1–2 nm in diameter are present in red luminescing PS [Sc12, Br9].

High-frequency spark discharge is also found to be a sufficient method to generate a porous layer at silicon cathodes that exhibit visible PL bands in the green (2.2–2.4 eV) and in the blue (3.2 eV). The PL shows a rapid decay (5–10 ns), a quantum efficiency in the order of 1% and is found to be stable up to annealing temperatures of  $1000^\circ\text{C}$ . These properties of the PL, and the dependence of the PL on the presence of oxygen and nitrogen during the spark processing, indicate an  $\text{SiO}_2$ -related PL, rather than a quantum dot-related one [Lu1].

Silicon wires or pillars are one-dimensional (1D) structures that are confined in only two dimensions. Weak red PL as well as EL is observed from silicon pillars

with diameters below 10 nm fabricated by standard semiconductor manufacturing techniques such as lithography, dry etching followed by thermal oxidation [Na2].

A sheet of silicon is a two-dimensional (2D) structure that is confined in only one dimension. Such a sheet has been fabricated by magnetron sputtering [Su6] or from a silicon-on-insulator (SOI) wafer if the thin superficial Si layer is further thinned by thermal oxidation [Ta11]. An advantage of such  $\text{SiO}_2/\text{Si}/\text{SiO}_2$  sandwich structures is that the thickness of the Si quantum well can be adjusted and measured with high precision. The PL of these 2D structures at 10 K is very similar to that observed from PS concerning peak energy and blue shift with size reduction. A 2 nm well for example shows a PL maximum at 1.65 eV, while for 1.4 nm a maximum at 2 eV is observed. The temperature dependence, however, is very different. While the PL intensity of PS shows a maximum between 50 and 150 K, the PL of the 2D structures decreases monotonically with increasing temperature. Annealing of the sandwich structure at 1100°C for 30 min is found to increase the PL at RT by two orders of magnitude.

For inorganic and organic silicon compounds the same dimensional hierarchy applies. Oligosilanes, for example, can be understood as quantum dots, polysilanes as quantum wires and polysilynes as quantum planes. For all of these structures luminescence is quite a common phenomenon. The HOMO/LUMO gap decreases with increasing Si backbone dimension. Because of their smaller size, the PL peak energy of these compounds is usually higher than observed for PS. Polysilanes, for example, show PL peak energies from 3 to 3.8 eV and Stokes shifts ranging from 0.05 to 0.5 eV [Ma15, Hi8]. Octasilacubane, a cube-like molecule of eight silicon atoms, which can be viewed as a model of the smallest three-dimensionally bonded Si nanocrystal, shows a PL peaking at about 2.5 eV at RT [Ma16]. The PL properties of a few silicon-based compounds are discussed briefly in Section 7.5.

## 8

# Mesoporous Silicon

### 8.1

#### Mesopore Formation Mechanisms

This section is devoted to the mechanisms responsible for the formation of mesopores on p-type and n-type silicon electrodes. Pore formation in silicon electrodes is only observed under anodic conditions in HF for current densities below  $J_{PS}$ . In this case a depletion region is present in silicon electrodes independent of type and density of doping, as discussed in Section 3.2. With increasing doping density the electric field strength increases and the width of the depletion region decreases. This enables charge carriers to pass through the SCR by band-to-band tunneling. For a planar silicon junction tunneling dominates the charge transfer for doping densities in excess of  $10^{18} \text{ cm}^{-3}$ , corresponding to a maximum field strength of about  $1 \text{ MV cm}^{-1}$ , while avalanche breakdown dominates at lower doping densities. Note that in contrast to solid-state devices, where breakdown leads to high currents and may eventually destroy the device by thermal heating, the currents in the electrochemical cell are always limited by mass transport of chemical reactants in the electrolyte and by reaction kinetics.

The electric field depends not only on doping and on applied bias, but also on geometry. Around a depression in the electrode the depletion region width is decreased and the field strength is increased, which increases the tunneling probability of charge carriers and thereby the local current density there [Zh3]. This effect becomes significant if the radius of curvature of the etch pit is smaller than the SCR width. If the geometry of a pore tip is assumed to be hemispherical, the breakdown bias can be approximated by calculating the breakdown bias for a spherical junction, which is plotted as a function of its radius of curvature in Fig. 8.1b. Breakdown at the pore walls can be approximated by calculating the breakdown conditions for the cylindrical case, which is shown in Fig. 8.1a. In these calculations breakdown by band-to-band tunneling is assumed to start at an electric field strength in excess of  $1.2 \text{ MV cm}^{-1}$  at the junction, while avalanche breakdown is assumed to occur if the ionization integral equals unity [Le23]. The curves in Fig. 8.1 show that:

The bias needed for breakdown decreases with pore diameter and becomes as low as 1 V independent of doping density for pore tip diameters below 20 nm.

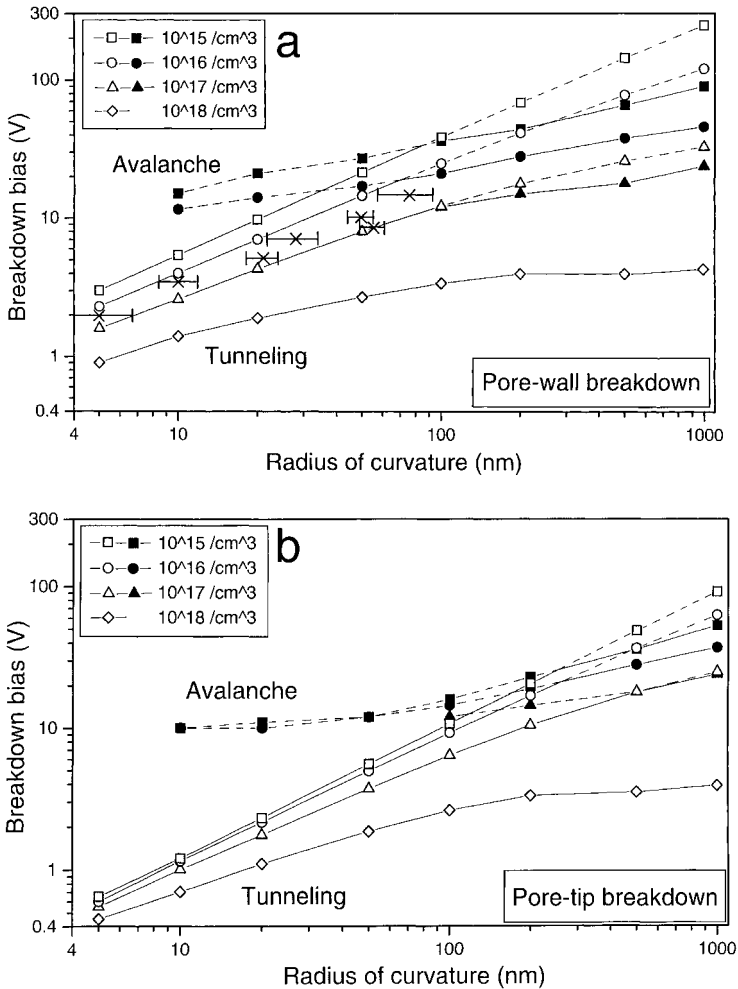


**Fig. 8.1** (a) Calculated breakdown bias for a cylindrical Schottky junction as a function of radius of curvature for tunneling (open symbols) and avalanche multiplication (full symbols) of charge carriers, for substrates of different doping density. The mechanism active

at lower bias dominates (full line). Experimental results (in 1:1 ethanoic HF) for pore radius as a function of anodization bias are plotted as crosses with error bars. (b) Calculated breakdown bias for a spherical Schottky junction. After [Le23].

For moderately doped substrates the crossover from tunneling to avalanche breakdown occurs at pore diameters of about 500 nm, corresponding to a bias in excess of 10 V. Above doping densities of  $10^{17} \text{ cm}^{-3}$  breakdown is always dominated by tunneling. Tunneling is therefore expected to dominate all pore formation in the mesoporous regime and extends well into the lower macropore regime, while avalanche breakdown is expected to produce structures of macroporous size.

The bias needed for breakdown at the cylindrical pore wall is a factor of 2 to 5 larger than for the pore tip. A comparison of the calculated results with experimental observations shows that the bias dependence of the actual pore diameters is well described by the calculation for the cylindrical case, as shown in Fig. 8.1 a. This can be understood if one recalls the current distribution at a real pore tip, according to Fig. 9.12 f. The current density decreases from the tip towards the wall according to a cosine law and becomes zero when the pore wall is truly cylindrical. At the wall segment that is close to being cylindrical, the current density becomes small, but not zero. Because any current flow is associated with the breakdown condition, the pore diameter increases until the limiting value for tunneling at the pore wall, according to Fig. 8.1 a, is reached.

Now the consequences of type and density of substrate doping on pore geometry and pore spacing will be addressed. Below the concept of a homogeneous SCR with a constant width  $W$ , as described in Eq. (1.2), is used, independently of the absolute value of the doping density. However, it should be noted that for doping densities of  $10^{19} \text{ cm}^{-3}$  and 1 V applied bias the SCR width (10 nm) exceeds the average distance of dopants (6 nm) only by a factor of two, as shown in the diagram on the inner front cover of this book. The width and the electric field in the SCR is therefore inhomogeneous and it can be assumed that the growth of a mesopore depends on the local field distribution.

If the distances between the pores become significantly larger than twice the SCR width  $W$ , the pore wall regions will no longer be depleted. This enables branching at the pore tips and side pores would penetrate this region until depletion is established again. As a result of this mechanism, pores tend to space themselves at distances below  $2W$ , as shown by the broken line in Fig. 6.10. In highly doped p-type or n-type silicon the pore diameter is comparable to  $W$ , and so mesoporous layers of significant porosity are formed. For low doped n-type electrodes, on the other hand, the pore diameter is much smaller than  $W$ , and so mesoporous layers of very low porosity are preferably formed in this case.

Not only the doping density but also the type of doping is important, because it determines whether the silicon electrode is under forward or reverse conditions. A p-type silicon electrode is under forward conditions in the anodic regime. The solid-state equivalent is a forward-biased non-planar Schottky junction. Depending on doping density the forward current of a Schottky diode is dominated by diffusion, thermionic emission over the barrier, or by tunneling through the barrier. At room temperature and for planar junctions the crossover between thermionic emission and tunneling occurs at a doping density of about  $10^{18} \text{ cm}^{-3}$ . The field at a spherical pore tip is significantly larger than in the planar case and mesopore formation due to tunneling is observed for p-type doping densities up to  $3 \times 10^{17} \text{ cm}^{-3}$ . The forward bias of a Schottky diode does not exceed 1 V. Therefore only small mesopores with radii around 5 nm are expected in this doping regime, according to the calculations shown in Fig. 8.1 a. This is in accordance with experimental observation, as shown in the SEM micrographs of Section 8.2. Avalanche breakdown in p-type electrodes is, of course, confined to the cathodic regime, and is therefore not relevant to pore formation.

In contrast, n-type electrodes are under reverse conditions in the anodic regime. However, no significant morphological differences to the p-type case are expected, as long as the n-type substrate doping density is in excess of about  $10^{18} \text{ cm}^{-3}$ . In this case the formation bias is in the order of 1 V, which again produces mesopore radii around 5 nm, as shown in the SEM micrographs in Section 8.3. With decreasing doping density, however, the bias required for breakdown increases. In this regime the dependence of pore wall radius on applied bias becomes clearly observable, as shown by the measurement in Fig. 8.1a (crosses). Because the tip radius is always less than or equal to the wall radius, the pore tip current density is not limited by charge carrier tunneling. This leaves reaction kinetics or ionic diffusion as limiting mechanisms for the pore tip current. This fact, together with the observation that the dissolution valence is greater than 2 for macropore formation supports the assumption that the pore tip current density is identical to the critical current density  $J_{PS}$ . The dependence of  $J_{PS}$  on crystallographic orientation now becomes important.  $J_{PS}$  is highest along the  $\langle 100 \rangle$  directions of the Si crystal, as shown in Fig. 4.9, and so mesopores tend to grow in this direction. Mesoporous films therefore exhibit the maximum thickness on  $\langle 100 \rangle$  planes, as shown in Fig. 6.3. In addition side pores are formed orthogonal to the main pore along the other  $\langle 100 \rangle$  directions. This mechanism is called spiking. If the main pore grows deep into the bulk of the electrode the diffusional limitations become significant and the pore growth rate may decrease to values close to zero. Mesopore formation and spiking on low doped n-type Si are discussed in Section 8.4.

For n-type doping densities below  $10^{17} \text{ cm}^{-3}$  and an anodization bias above 10 V, avalanche breakdown becomes relevant. The interface morphology generated in this regime is very complex and shows large etch pits, macropores and mesopores. The formation of this structure is not understood in detail. A hypothetical model will be discussed in Section 8.5.

A good example of the consequences of the pore formation mechanisms discussed so far is the pore morphology formed in a p/p<sup>+</sup> multilayer structure. In order to manufacture interference mirrors, a stack of 75 nm thick homogeneously p-doped ( $10^{17}$  and  $10^{19} \text{ cm}^{-3}$ ) Si layers have been grown by LPCVD, as shown in the inset of Fig. 10.14. After anodization of the stack at  $50 \text{ mA cm}^{-2}$  in ethanoic HF, the TEM micrograph (Fig. 10.14), as well as a simulation of the measured spectral reflectivity (Fig. 10.15), indicated a triple layer structure with a significant porosity gradient [Be16]. That three layers of different porosity have been formed from only two doping densities can be understood in the frame of the mesopore formation mechanisms:

The electric field in an anodized silicon electrode of a p-type doping density of  $10^{17} \text{ cm}^{-3}$  is too small for breakdown, and so the charge transfer is dominated by thermionic emission over the barrier and only micro PS of high porosity (67%) is formed. The bias across the junction can be approximated to 0.1 V, as discussed in Section 9.2. This corresponds to an SCR width of about 35 nm. If the micropores reach a depth of 40 nm the SCR reaches the highly doped p-region. For solid-state pin diodes this effect is known as punch-through. Because of the high doping density in the p<sup>+</sup> region ( $10^{19} \text{ cm}^{-3}$ ), the SCR width now monotonically de-

creases with the increasing micropore depth. This in turn increases the field strength at the pore tips until it approaches the value required for junction breakdown by tunneling. Let us assume that this value is reached at a total micro PS thickness of 50 nm. The bias required for tunneling now becomes less than the bias for thermionic emission and micropore formation stops, while a few mesopores grow by tunneling through the remaining 25 nm of low doped p-Si until they reach the interface to the  $p^+$  region. Note that the entire low doped region is depleted, pore wall passivation is therefore established there, even for pore separations of tens of nanometers, and so a layer of very low porosity (5%) is formed. In the  $p^+$  region in contrast pore wall passivation requires a pore wall thickness of the order of 3.5 nm. As a result, the pores start to branch when they reach the  $p^+$  region and a network of closely spaced mesopores of moderate porosity (55%) is formed. Due to the fact that the SCR now only extends 3.5 nm, the next low doped p-type region does not affect the field at the pore tips until they are as close as 3.5 nm. The sequence is then repeated.

## 8.2

### Mesopores in Highly Doped p-Type Silicon

The morphology of mesoporous structures can be investigated by TEM, as shown in Fig. 7.2b and d. However, sample preparation for TEM is time-consuming. Fortunately the mesoporous regime can also be studied by today's most advanced SEMs. For SEM inspection no sample preparation is required, and even sputtering of the sample is dispensable, as shown by the SEM micrographs displayed in this and the next section.

The initiation process of mesopores shows similarities to macropore initiation. The growth of mesopores can be initiated by a depression in the electrode, for example an alkaline etch pit [Le23]. On flat electrodes a doping-dependent density of etch pits is generated during the first seconds of anodization in HF, as shown in Fig. 8.2. A certain fraction of these etch pits develop into mesopores, for which the density is again a function of doping density, as shown in Fig. 6.10. The charge consumed during pore nucleation on a flat electrode until stable pore growth is reached can be determined by impedance measurements. During the initiation period of mesopores on highly doped p-type Si a charge of about  $100 \text{ mAs cm}^{-2}$  is consumed, which is significantly larger than the charge observed for micropore initiation on low doped p-type Si ( $25 \text{ mAs cm}^{-2}$ ) [Po3].

In order to investigate the mesopore morphology versus pore depth, samples are cleaved along a (110) plane after anodization. The dependence of mesopore morphology on doping density and formation current density is shown in Fig. 8.3 for anodization in ethanoic HF and in Fig. 8.4 for 6% aqueous HF. Values of porosity, growth rate and dissolution valence are given for each sample above the micrograph and are plotted as a function of doping density in Fig. 6.9. A common feature of all mesoporous layers formed on highly doped substrates is a distinct interface between the mesoporous region and the bulk. This interface is easily



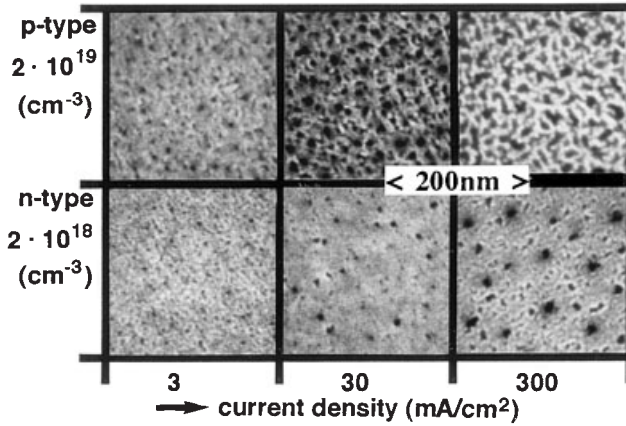


Fig. 8.2 SEM micrographs of the initially polished (100) silicon electrode surfaces after galvanostatic anodization in ethanoic HF. After [Le23].

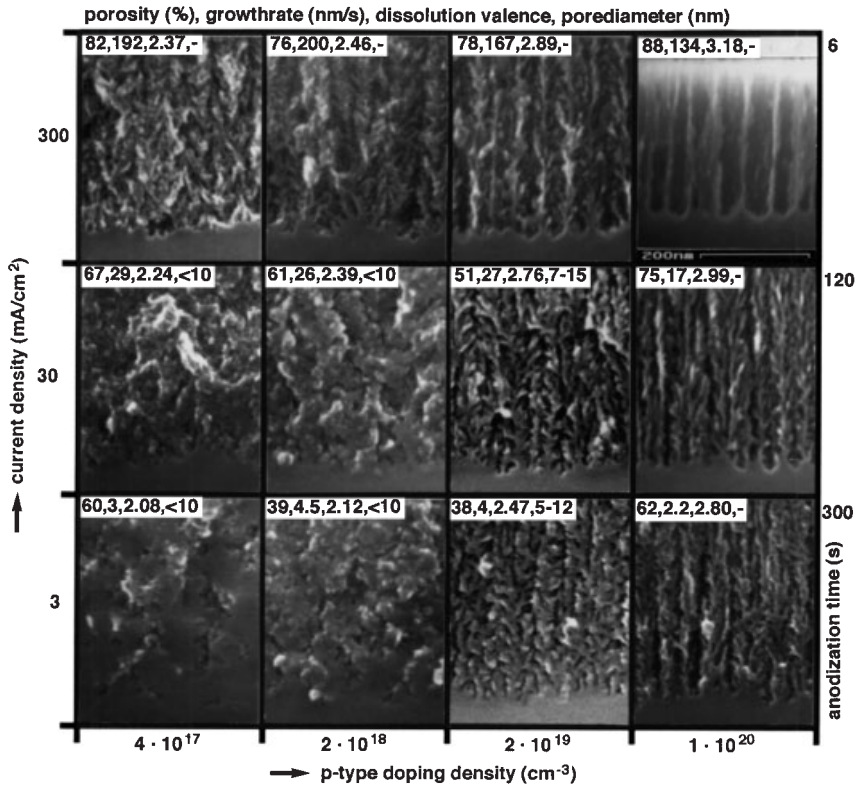


Fig. 8.3 SEM micrographs of the interface between bulk and meso PS for p-type doped (100) silicon electrodes anodized galvanostatically in ethanoic HF. After [Le23].

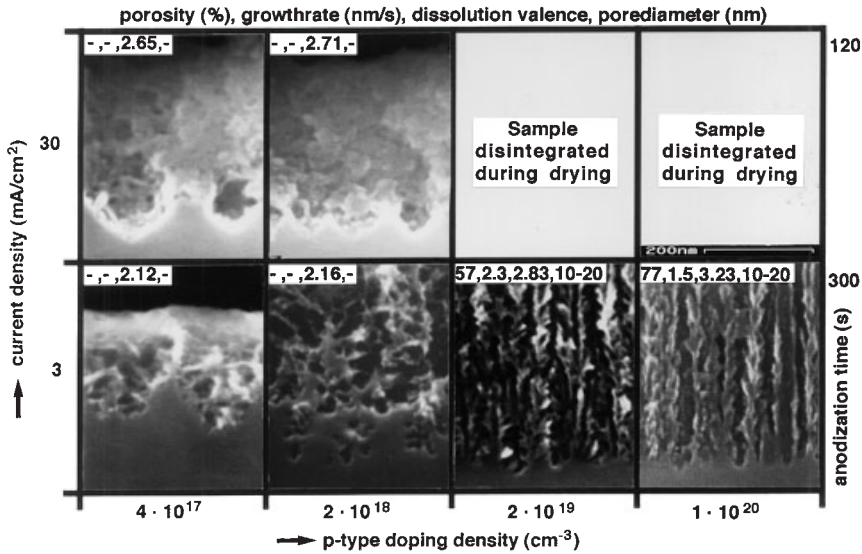


Fig. 8.4 SEM micrographs of the interface between bulk and meso PS for p-type doped (100) silicon electrodes anodized in 6%

aqueous HF. For high current densities and high doping densities (upper right) the PS layers disintegrate during drying. After [Le23].

identified even by optical microscopy if the sample is cleaved, as shown in Fig. 6.3. This distinct interface is an indication of a depletion of charge carriers which promote dissolution in the pore walls, as is the case during microporous silicon formation.

For very high doping densities and large formation current densities, the pore dimensions approach the macroporous regime, as shown in the upper right of Fig. 8.3. In this regime the pore diameter depends approximately exponentially on current density. For p-type substrates of  $1 \text{ m}\Omega \text{ cm}$  anodized in ethanoic HF at  $600 \text{ mA cm}^{-2}$ , pore diameters of  $1 \mu\text{m}$  and porosities above 90% have been observed [Ja4].

Using SIMS or elastically recoiling particle detection spectroscopy (ERDA) the remaining concentration of acceptors and donors was measured in meso PS formed on highly doped substrates. No preferential dissolution of dopant atoms has been observed [Le14, Po2]. As expected from the dimensions of the mesoporous skeleton, which show no or minimal QC, the optical behavior of meso PS is similar to that of bulk silicon for photon energies above the Si bandgap. The luminescence efficiency in the visible regime is usually negligible. Only meso PS samples of high porosity, which contain a certain fraction of small crystallites, show a weak PL signal one- or two-tenths of eV above the Si bandgap energy [Po2]. However, the optical absorption for below bandgap photons is significantly reduced for dry mesoporous layers, if compared to the highly doped substrate, as shown in Fig. 7.8. This has been ascribed to a depletion of free charge carriers in

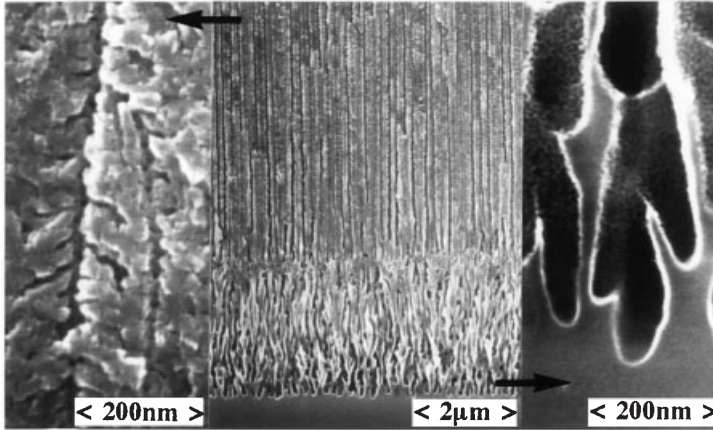


**Fig. 8.5** SEM micrographs of an Si electrode ( $n$ -type  $10^{18} \text{ cm}^{-3}$  (100),  $300 \text{ m A cm}^{-2}$ , 60 s) anodized galvanostatically in ethanoic HF.

An increase in pore diameter and porosity with depth is observable. After [Le23].

the porous region due to a trapping in surface states present at the large inner surface [Le14]. For wet mesoporous silicon these surface states appear to be partly passivated, because the conductivity of wet mesoporous silicon is higher than for the dry case. The passivation of  $p^+$  type substrates in alkaline solutions is lost if it is made mesoporous, as discussed in Section 2.3.

### 8.3 Mesopores in Highly Doped n-Type Silicon

An overview of the morphologies of mesopores grown under galvanostatic conditions on  $n$ -type substrates of different doping densities is shown in Figs. 8.6 and 8.7. Note that the mesopore morphology depends on doping density, not on the elementary nature of the dopant. Even implanted protons activated by a post-implant anneal are reported to form a highly  $n$ -doped layer sufficient for mesopore formation [Tu5].

The decisive difference to the  $p$ -type case is that  $n$ -type silicon electrodes are under reverse conditions during mesopore formation. This becomes apparent if the pore morphologies are compared. While the morphology of mesoporous silicon formed on  $n$ -type substrates of doping densities in excess of  $10^{19} \text{ cm}^{-3}$  is very similar, as can be seen by comparison with Figs. 8.3 and 8.6, the difference becomes apparent at lower doping densities. For  $p$ -type substrates the SCR field becomes insufficient for breakdown below doping densities of  $10^{17} \text{ cm}^{-3}$  and only micro PS or macro PS formation is observed in this regime. For  $n$ -type electrodes, in contrast, mesopore formation is not quenched for doping densities below  $10^{17} \text{ cm}^{-3}$ . The bias required for breakdown at the flat  $n$ -type electrodes of this doping den-

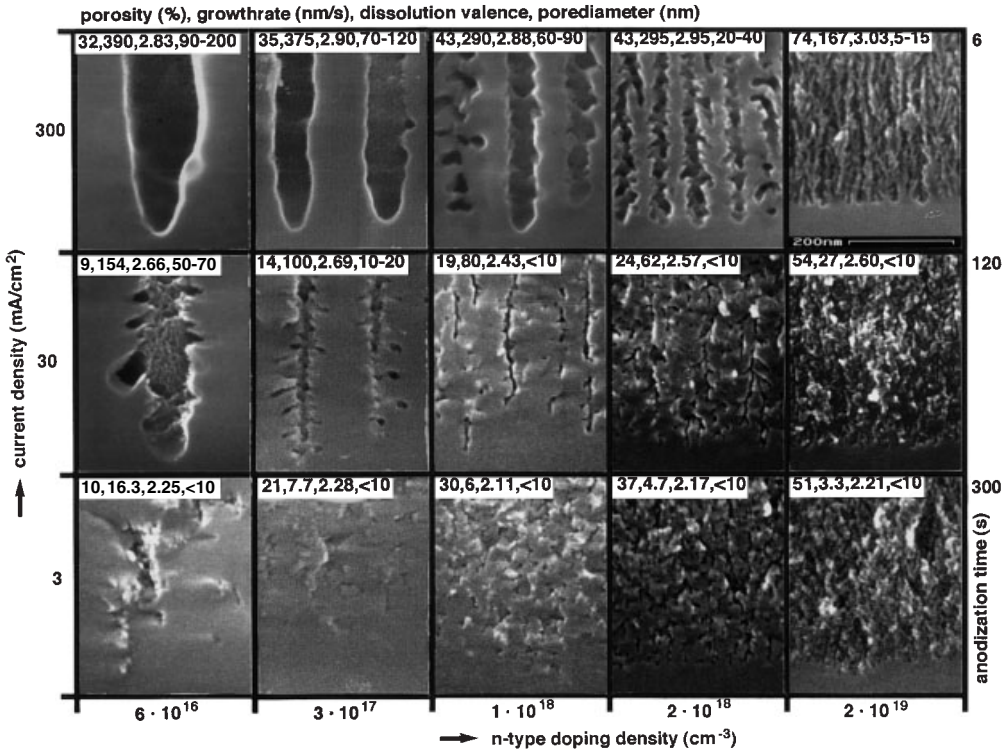


Fig. 8.6 SEM micrographs of the interface between bulk and meso PS for n-type doped (100) silicon electrodes anodized galvanostatically in ethanoic HF. After [Le23].

sity in the dark is in excess of 10 V. It decreases with decreasing radius of curvature of the pore. The pore diameter in this doping regime can therefore be adjusted by anodization bias, as shown by the experimental data plotted in Fig. 8.1a. In contrast to electrochemical macropore formation, spiking and formation of side pores cannot be avoided, because of the high applied bias. The technological impact of this method of tuning the mesopore diameter is therefore limited.

Another consequence of the SCR width being significantly larger than for the corresponding p-type case, is the lower porosity observed for meso PS on n-type electrodes, as shown in Fig. 6.9c. The porosity increases with current density and decreases with HF concentration [Na8, Le23]. But porosity is also a function of meso PS layer thickness, especially for high current densities [It3, Th4, Le23]. The morphology of mesopores changes with depth, from narrow, strongly branched pores to wider unbranched ones, as shown in Fig. 8.5. This can be understood as a consequence of diffusion-limited mass transfer in the pores. Because of the diffusion gradient the HF concentration decreases with increasing pore depth. This again reduces the limiting pore tip current density  $J_{PS}$  according to Eq. (4.9), which results in an increase in pore diameter under galvanostatic conditions. An

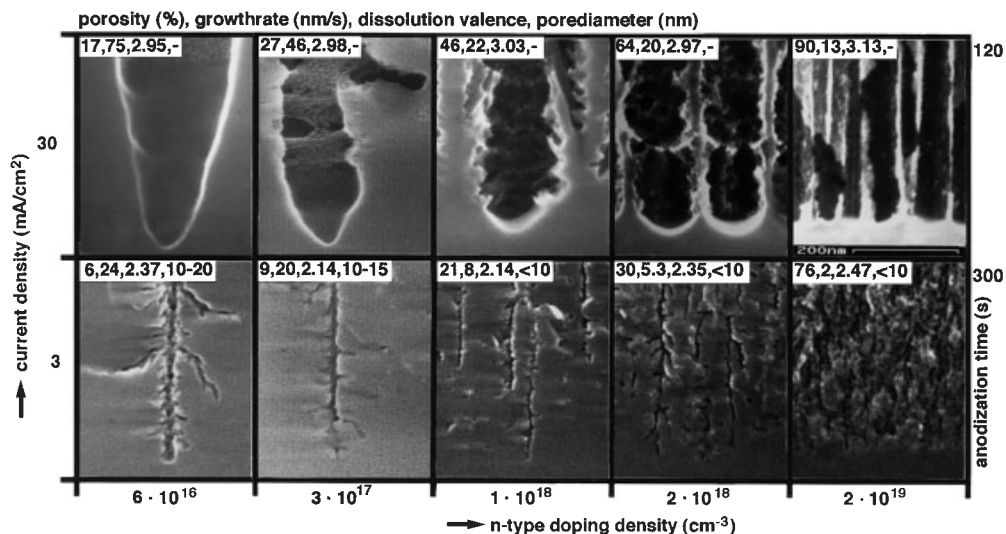
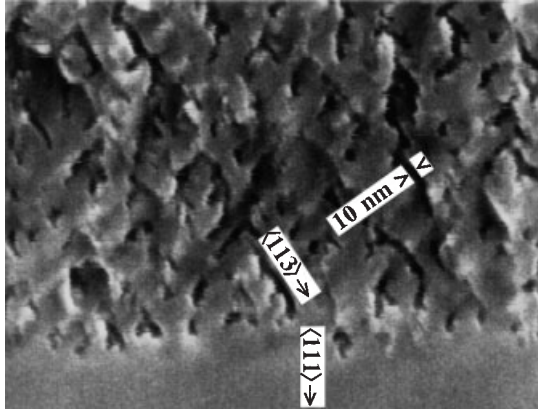


Fig. 8.7 SEM micrographs of the interface between bulk and meso PS for n-type doped (100) silicon electrodes anodized galvanostatically in 6% aqueous HF. After [Le23].

increase in applied current density may even lead to a separation of the mesoporous layers from the substrate, which is a common method of producing free-standing films.

The dependence of mesopore formation on crystal orientation becomes apparent in Figs. 8.6 and 8.7. For moderate doping densities or high current densities preferential growth in the  $\langle 100 \rangle$  direction is observed. This anisotropy is enhanced further if anodization is performed under a magnetic field [Na8]. On (111) substrates the  $\langle 113 \rangle$  direction can be identified as a preferred growth direction, as shown in Fig. 8.8. Note that the same orientation dependence has been observed for macropore formation on (100) and (111) substrates, as shown in Figs. 9.7 and 9.14, respectively. The preferential direction of mesopore growth is reduced for high doping densities and moderate to low current densities due to severe branching of pores, as shown in the lower part of Fig. 8.6. It can be speculated that the growth direction of a pore at high doping densities becomes dominated by the local electric field distribution at the pore tip, which depends on the position of individual dopant atoms in reference to the pore tip. The average growth rate of mesoporous films, however, is still found to be highest on (100) substrates, as illustrated by the etched sample edge in Fig. 6.3 or by the data displayed in Fig. 6.4.



**Fig. 8.8** SEM micrograph of the interface between bulk and meso PS for an n-type doped electrode of (111) crystal orientation anodized

galvanostatically in ethanoic HF ( $5 \times 10^{18} \text{ cm}^{-3}$ ,  $50 \text{ mA cm}^{-2}$ ). After [Le23].

#### 8.4

#### Mesopore Formation and Spiking in Low-Doped n-Type Silicon

The formation of pores during anodization of an initially flat silicon electrode in HF affects the I–V characteristics. While this effect is small for p-type and highly doped n-type samples, it becomes dramatic for moderate and low doped n-type substrates anodized in the dark. In the latter case a reproducible I–V curve in the common sense does not exist. If, for example, a constant potential is applied to the electrode the current density usually increases monotonically with anodization time [Th1, Th2]. Therefore the I–V characteristic, as shown in Fig. 8.9, is sensitive to scan speed. The reverse is true for application of a certain current density. In this case the potential jumps to values close to the breakdown bias for the flat electrode and decreases to much lower values for prolonged anodization. These transient effects are caused by formation of pores in the initially flat surface. The lowering of the breakdown bias at the pore tips leads to local breakdown either by tunneling or by avalanche multiplication. The prior case will be discussed in this section while the next section focuses on the latter.

According to Fig. 8.1a the diameter of mesopores decreases with decreasing substrate doping density for anodization at a certain bias. The pore spacing, on the other hand, depends on SCR width and therefore increases with doping density. As a result, the porosity of the porous layer on low doped n-type silicon is very low and, in contrast to other types of PS, no clear interface between the mesoporous region and the bulk can be identified in microscopic images. Simple optical microscopy, even at magnifications of 1000, is usually not sufficient to reveal individual mesopores. In the optical micrograph of an n-type Si electrode cleaved after anodization, as shown in Fig. 8.10a, only a few larger pores normal to the electrode surface are visible. If interference contrast is used, the porous region

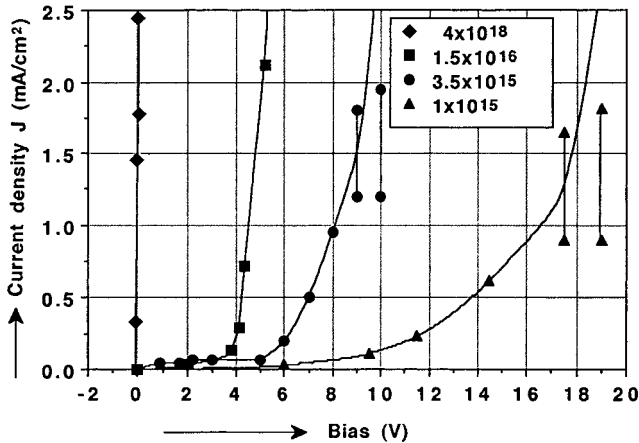
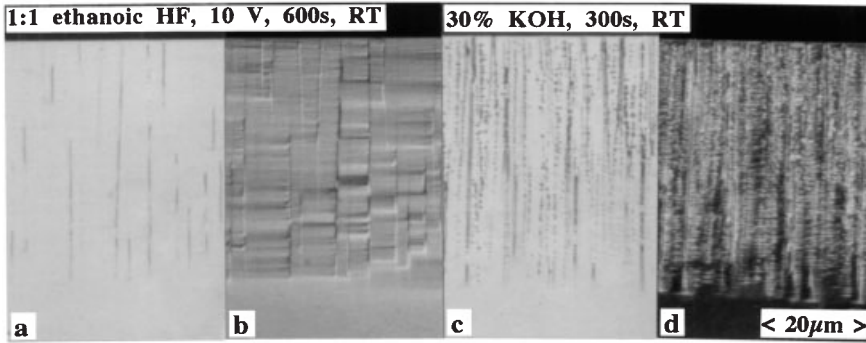


Fig. 8.9 Current density versus potential for n-type electrodes of different doping density anodized in 5% aqueous HF. The current density has been measured 30 s after a step-wise increase in bias. Redrawn from [Th2].

can be identified better because of the increase in roughness of the cleaved surface it induces, as shown in Fig. 8.10b. By a short etch in a silicon defect etchant the pores are sufficiently enlarged to become visible by optical microscopy. Now mesopores spiking out of the main pore in the other  $\langle 100 \rangle$  directions become visible, as shown in Fig. 8.10c and d. Under the high magnification of a TEM the needle spiking pores can be directly revealed, as shown in Fig. 8.11. However, it requires formation of an oxide replica and etchback to give a clear idea of the mesopore morphology [Le9]. This technique is used in Fig. 8.12 to reveal the morphology of mesopores spiking out of macropore walls. Such spiking is usually undesirable during macropore array fabrication. The formation of spiking mesopores can be suppressed if low bias, low substrate doping density and high array porosity are used.

Pore growth in silicon electrodes shows a crystal anisotropy [Hi7, Ch11, Le8, Ro8, Ch17]. This effect is most pronounced for mesopores in low doped n-type electrodes and will therefore be discussed here. Mesopores in low doped n-type silicon are found to always grow along the  $\langle 100 \rangle$  directions of the silicon crystal. The resulting pore morphology is shown for a  $\langle 100 \rangle$  and a  $\langle 111 \rangle$  Si substrate in Fig. 8.13. This orientation dependence has been ascribed to the anisotropy of the critical current density  $J_{PS}$  [Le9]. As shown in Fig. 4.9,  $J_{PS}$  is found to show a maximum on  $\langle 100 \rangle$  substrates, independent of the HF concentration used. As discussed in Section 8.1, the current density at the mesopore wall is limited by tunneling, while at the pore tip charge supply is not the limiting factor. Therefore the tip current approaches  $J_{PS}$  and the anisotropy of  $J_{PS}$  becomes decisive. The dissolution rate is maximum for the  $\langle 100 \rangle$  directions and so pore tips are formed preferentially along these directions. This orientation dependence increases with increasing anodization bias. If pores grow into the depletion region of neighboring



**Fig. 8.10** (a) Optical microscopy (magnification 1000) of a cleaved (100) n-type Si electrode after 300 s at 10 V in ethanoic HF. (b) The roughness in the porous region of the cleaved interface becomes visible if inter-

ference contrast mode is used. (c) The high density of breakdown pores becomes apparent after pore widening by chemical etching in KOH. (d) Same area as in (c) with interference contrast.

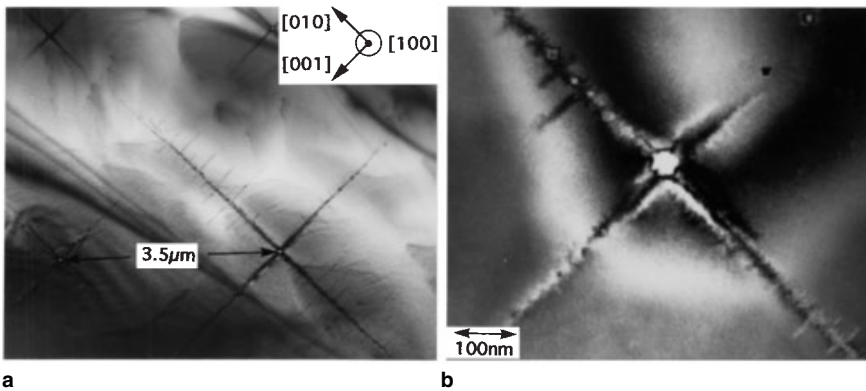


**Fig. 8.11** (a) TEM micrograph of mesopores (in a plane parallel to the sample surface) initiated by a surface pattern of etch pits (5 V, 3% HF, RT,  $10^{15} \text{ cm}^{-3}$  n-type, pattern according

to inset of Fig. 9.9). (b) While the center pore shows a diameter of about 40 nm, the diameter of the smallest spiking pores is not resolved ( $< 5 \text{ nm}$ ). After [Le9].

pores, the electric field at the tip is reduced and eventually the pore stops growing. This leads to morphologies as depicted in Fig. 8.13. Mesopore formation on low doped n-type substrates has been observed to occur exclusively along the  $\langle 100 \rangle$  directions of the Si crystal, independent of substrate orientation [Ro8]. This is in contrast to macropores (Fig. 9.14) or mesopores on highly doped substrates (Fig. 8.8), for which pores along the  $\langle 113 \rangle$  directions are found on (111) oriented electrodes.



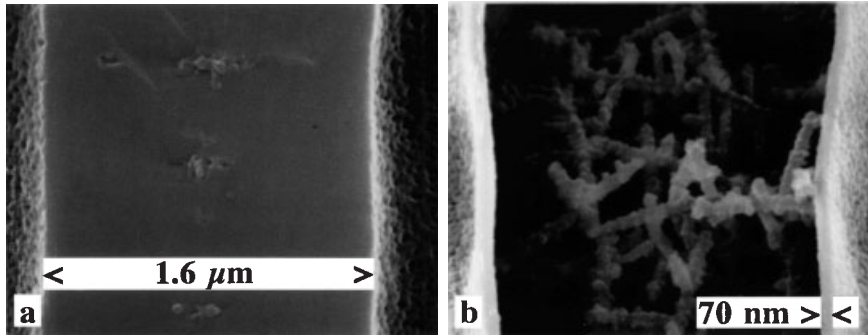


**Fig. 8.12** (a) SEM micrograph of the cleaved wall area between two macropores that have been anodically oxidized (70 nm) after their formation. The existence of breakdown spikes is only indicated by a small surface roughness

of the cleaved macropore wall. (b) After Si etchback the oxide replica of a high density of spiking breakdown mesopores is revealed. Note that the spikes appear distorted because of stress in the oxide film.

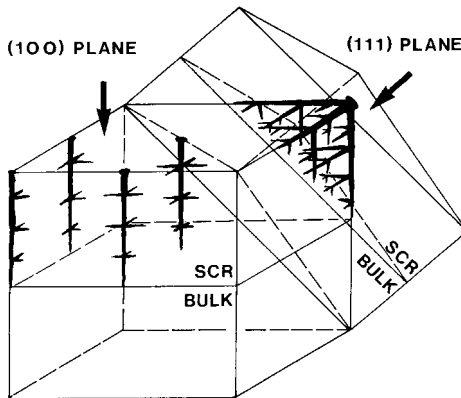


**Fig. 8.13** Dependence of the mesopore morphology on the crystal orientation of the silicon substrate. After [Le8].

## 8.5

### Etch Pit Formation by Avalanche Breakdown in Low-Doped n-Type Silicon

From the calculated curves in Fig. 8.1 it can be concluded that breakdown in n-type substrates of a doping density below  $10^{17} \text{ cm}^{-3}$  at an applied bias in excess of 10 V is dominated by avalanche breakdown. Anodization in this regime produces a complex morphology, dominated by large spherical etch pits with diameters in the order of tens of micrometers, as shown for different substrate doping densities in Fig. 8.14. The density of these etch pits increases with increasing doping density, as indicated by downward-pointing triangles in Fig. 6.10. If the cross-section of such a pit is inspected by SEM, macro- as well as mesopores are found in the outer perimeter of the pit [Le23]. The inner perimeter shows significant etching but no pore formation, except the large central cavity. The position of the etch

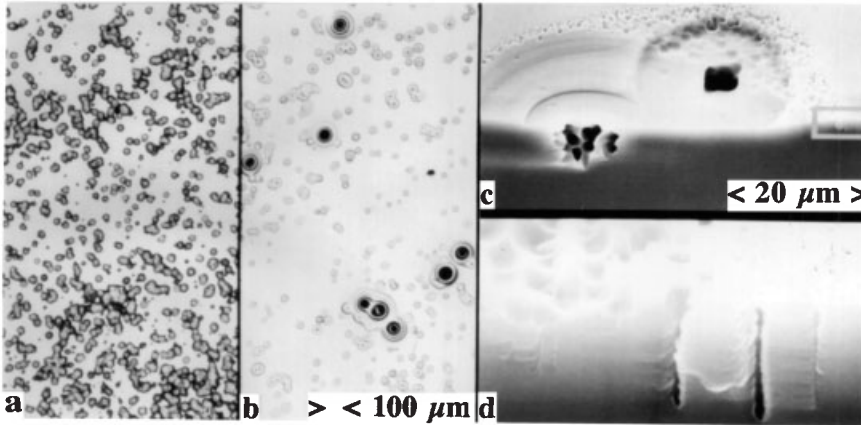


**Fig. 8.14** The density of avalanche etch pits depends on substrate doping density, as shown by optical micrographs of two n-type electrodes anodized at high bias in 6% aqueous HF in the dark (a) 50 V, 30 s, 1.5  $\Omega$  cm;

(b) 100 V, 30 s, 5  $\Omega$  cm. (c, d) SEM micrographs of the sample shown in (b) reveal a circle of macro- and mesopores around the central pit. After [Le23].

pits is random on a polished electrode surface, but can be predetermined by a depression, as for example produced by alkaline etching.

The regime of avalanche breakdown has not been studied in detail and only a rough picture of the formation mechanism can be drawn [Le23]. In contrast to solid-state devices where breakdown results in high current densities that may destroy the device by thermal heating, the current density in electrolyte-filled pores and pits is limited by mass transport of chemical reactants to values below  $J_{PS}$ . It can therefore be assumed that avalanche breakdown occurs in a transient manner. Prior to breakdown only a small dark current density is present, which is too small to generate a concentration gradient in the HF. The local current density then increases dramatically by avalanche multiplication. It is, however, limited by electrolyte conductivity and ionic diffusion. Most of the generated charge is now consumed to form the central etch pit, which reduces the HF concentration in and around the pit considerably and drives this interface area into the electropolishing regime. The potential drop across the anodic oxide film and in the electrolyte now efficiently reduces the field in the SCR and thereby stops the avalanche multiplication process. The circular region of dissolution and macropore formation around the large etch pit can be understood as being a result of etching caused by charge carriers generated by avalanche multiplication in the bulk of the electrode but not consumed to form the large central pit. These remaining charge carriers diffuse to the surface, generating a current density that decreases with the radial distance to the central pit, thus generating a pore-free inner ring of a dissolution rate close to or in the electropolishing regime and a surrounding ring showing macropore and mesopore formation.

## 9

# Macroporous Silicon

### 9.1

#### Macropore Formation Mechanisms

This section is devoted to the formation mechanisms that have been proposed as being responsible for formation of macropores on p-type and n-type silicon electrodes.

First models for macropore formation on p-type Si electrodes were based on surface passivation by organic molecules [Po1] or on electrostatic considerations [We5]. These models, however, were found to contradict experimental observations [Le21]. Thermionic emission over the Schottky barrier and Fermi level pinning at the silicon electrode surface were originally proposed to cause micro PS formation. It has been argued that because the barrier's height and not its width controls the current density, pores can grow into each other's depletion region and the structural sizes may become very small [Be5]. The observation of micropore formation on n-type electrodes contradicts this model, because in this case no interfacial barrier for minority carriers (holes) is present. But the proposed mechanism can account for macropore formation on p-type Si electrodes. As discussed below, pore formation can be understood as a consequence of charge transfer across the Schottky barrier, if the non-planar interface constituted by a pore is taken into consideration [Le21].

A p-type electrode is under forward conditions during macropore formation. The basic charge distribution around pores in a p-type electrode is shown in Fig. 9.1. No electric field is present in the bulk electrode and neutrality requires the hole concentration  $n_h$  to equal the acceptor concentration  $N_A$  there. Close to the interface to the electrolyte an SCR exists in the semiconductor electrode. The width  $W$  of the SCR depends on the difference between the Fermi levels of electrolyte and semiconductor, called the built-in potential  $V_{bi}$ , on the p-type doping density, on the applied bias  $V$  (according to Eq. (1.2)) and on the interface geometry. The latter factor is key to the understanding of pore formation and will be discussed in some detail. By solving the Poisson equation,  $W$  can be calculated for different geometries. Assuming a doping density of  $N_A = 10^{15} \text{ cm}^{-3}$  and a potential ( $V_{bi} - V - 2kT/e$ ) of 1 V,  $W$  is 1150 nm for the planar interface. At the walls of a cylindrical pore of radius  $r = 500 \text{ nm}$ ,  $W$  is reduced to 950 nm, due to geometrical field

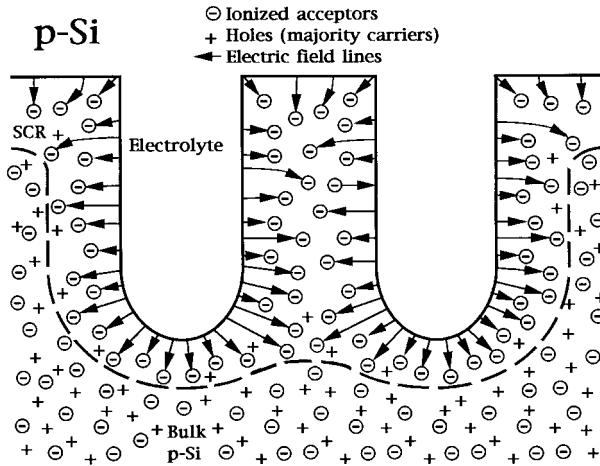


**Fig. 9.1** The charge distribution around pores in a low doped p-type silicon electrode. Two types of charge carriers are present in

the electrode: holes, the majority charge carriers (crosses) and immobile ionized impurities (circles).

enhancement. At a hemispherical pore tip of the same radius,  $W$  is further reduced to 800 nm.  $W$  becomes even smaller for conical pore tips. In conclusion,  $W$  is minimal at the pore tip, while the barrier height  $E_b = e(V_{bi} - V) - 2kT$  is independent of geometry.

After having discussed the electrostatics, charge transfer is the next topic. A p-type silicon electrode anodized in HF behaves basically like a solid-state Schottky diode under forward conditions. The forward current of a Schottky diode is dominated by diffusion, or thermionic emission, or tunneling of holes. At zero bias and under forward conditions the SCR is not fully depleted of holes and so a diffusion current  $I_{diff}$  exists that is caused by the concentration gradient of holes  $dn_h/dr$ , according to Schottky's theory. At thermal equilibrium and with no applied bias (OCP),  $I_{diff}$  is compensated by the field current  $I_{field}$  and  $I_{diff} = I_{field}$  is fulfilled at the pore walls as well as at the pore tip. However, the absolute values of  $I_{diff}$  and  $I_{field}$  are larger at the pore tip, because the concentration gradient  $dn_h/dr$ , as well as the electric field strength, increase with decreasing  $W$ , as shown in the left part of Fig. 9.2. If a forward bias  $V$  is applied,  $I_{field}$  decreases, while  $I_{diff}$  increases. The higher current density values at the pore tip now become decisive. The total current density at the tip,  $I_{tip} = (I_{diff} - I_{field})_{tip}$ , is always larger than the current density at the wall  $I_{wall} = (I_{diff} - I_{field})_{wall}$ . Therefore a depression in the electrode etches faster than a planar area – a pore tip develops. If the distance between two neighboring pores becomes less than  $2W$  their SCRs overlap and the pore wall becomes passivated due to the depletion of holes.

The above model is sufficient to qualitatively understand the basic properties of macroporous layers formed on p-type substrates, for example their porosity, which is usually high. However, the observed suppression of macropore formation in

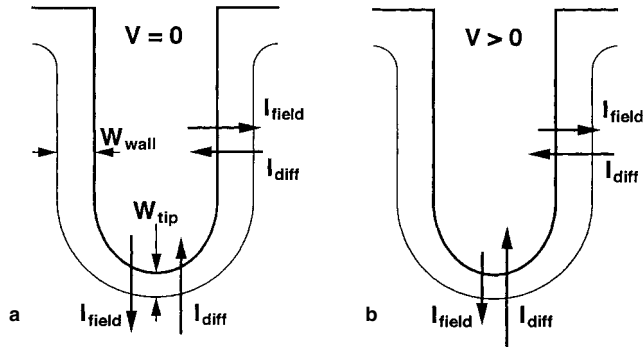


**Fig. 9.2** (a) Equilibrium ( $V=0$ ) field currents and diffusion currents across the SCR for a macropore geometry in p-type Si.

(b) Field currents and diffusion currents under forward bias ( $V>0$ ). Note that because of field enhancement around the pore tip the tip currents are always larger than the pore wall currents.

aqueous electrolytes for p-type doping densities in excess of  $N_A=10^{16} \text{ cm}^{-3}$  cannot be understood using the Schottky diffusion theory. It has been proposed that the change from a diffusion-dominated charge transfer to a thermionic emission-dominated is responsible for this effect [Le21]. According to the theory of Bethe, the thermionic emission current  $I_{\text{therm}}$  is due to holes that have sufficient energy to overcome the potential barrier  $E_b$  and are traversing normal to the interface. Thermionic emission is sensitive to barrier height but not to barrier width, if the width is less than the main free path of holes. If the charge transfer is dominated by thermionic emission, depressions show no increase in current density compared to planar areas, and so pore formation is not initiated. However, the upper limit of p-type doping density for macropore formation calculated from this model ( $10^{17} \text{ cm}^{-3}$ ) is about one order of magnitude larger than the value observed experimentally in aqueous electrolytes ( $10^{16} \text{ cm}^{-3}$ ). At doping densities in excess of  $10^{18} \text{ cm}^{-3}$ , tunneling becomes dominant, which leads to the formation of mesoporous silicon, as discussed in Section 8.1.

In contrast to p-type electrodes, an n-type electrode is under reverse conditions in the anodic regime. This has several consequences for pore formation. Significant currents in a reverse biased Schottky diode are expected under breakdown conditions or if injected or photogenerated minority carriers can be collected. Breakdown at the pore tip due to tunneling generates mainly mesopores, while avalanche breakdown forms larger etch pits. Both cases are discussed in Chapter 8. Macropore formation by collection of minority carriers is understood in detail and a quantitative description is possible [Le9], which is in contrast to the pore formation mechanisms discussed so far.

Holes, which initiate the dissolution process, are minority charge carriers in n-type electrodes. The concentration of holes  $n_h$  is very low in n-type Si under equilibrium conditions. The hole concentration can be increased by illumination or by

injection. Three kinds of charge carriers are now present in the bulk electrode: holes (of concentration  $n_h$ ), electrons ( $n_e$ ) and the ionized donors ( $N_D$ ). Neutrality is established if  $n_e = N_D + n_h$ . Concentration gradients of holes in the bulk semiconductor may therefore exist in n-type electrodes, because their charge can always be compensated by the electron distribution, as shown in Fig. 9.3. Hence the strict requirement for p-type macropore formation, i.e. that the wall thickness  $w$  needs to be less than  $2W$  for passivation, no longer applies to n-type electrodes. Note that the condition  $w = 2W$  has been proposed to be valid for macropore formation on n-type Si, also [Le8, Zh3, Se8]. But it has been experimentally shown that macropores on n-type Si may be separated by as much as  $10W$  [Le21, Ri4]. In this case the concentration of holes becomes close to zero between the pore walls, due to their diffusional distribution, as shown in Fig. 9.3. The distance between two n-type macropores required for passivation is therefore limited by the minority carrier diffusion length [Le21] rather than by the SCR width [Se8]. In terms of the DLA model [Me8] discussed in Section 6.2, the minority carrier diffusion length  $L_D$  becomes the parameter  $L$  of the model, rather than the SCR width  $W$ .

Having discussed the causes of pore wall passivity, we will now focus on the active state of the pore tip, which is caused by its efficiency in minority carrier collection. Usually the current density at the pore tip is determined by the applied bias. This is true for all highly doped as well as low doped p-type Si electrodes and so the pore growth rate increases with bias in these cases. For low doped, illuminated n-type electrodes, however, bias and current density become decoupled. The anodic bias applied during stable macropore formation in n-type substrates is

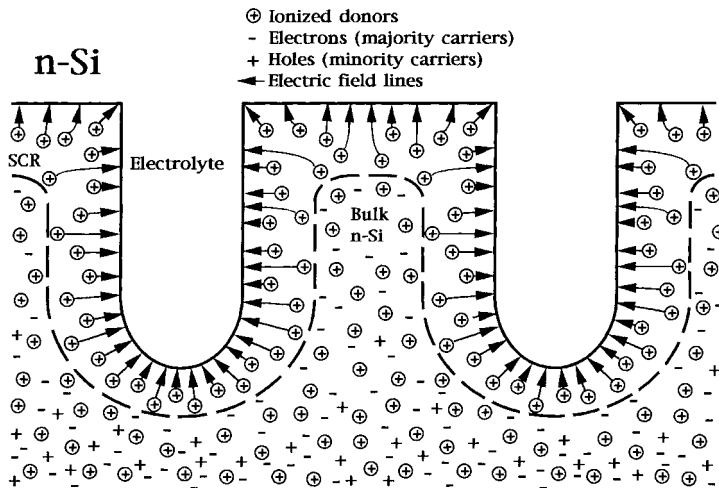


**Fig. 9.3** The charge distribution around pores in a low doped, illuminated n-type silicon electrode. Three types of charge carriers are present: electrons, which are the majority carriers (dashes), holes, which are the minor-

ity carriers (crosses), and immobile ionized impurities (circles). Note that a concentration gradient of holes is possible, because of compensation by electrons.

sufficient to produce current densities well in the electropolishing regime, while the current density remains low because it depends on minority carrier generation rate only. Under this condition of relatively high bias and a limited supply of holes, the current density at every pore tip increases until the pore tip is close to electropolishing. A further increase in current density would cause a decrease in the dissolution rate because of the increase in the dissolution valence from 2 to 4, as discussed in Section 4.2, and a change in the pore tip condition from depletion to inversion. Holes would accumulate around the tip and eventually enter the pore walls and thereby destroy their passivity. The crossover from depletion to inversion for Si electrodes in HF is characterized by the critical current density  $J_{PS}$ , which is reached at any macropore tip during stable growth [Le9].  $J_{PS}$  is a function of the HF concentration and the temperature only, as shown in Eq. (4.1). A fixed value of current density for every pore tip produces a very stable dissolution condition. If, for example, the hole supply for a single pore is increased, the pore has to increase its diameter, because the tip current density is fixed. Another consequence of  $J_{PS}$  being the pore tip current density, is a tip growth rate independent of tip collection efficiency. This growth rate, common to all macropores in the electrode, produces a condition of 'coexistence' for the pore tips, rather than a 'survival of the fittest'. Hence the pore density is usually constant during stable macropore growth and changes in this value are mainly observed during pore initiation.

Pore initiation mechanisms and the initial state of the Si electrode prior to anodization have so far been neglected. This is on the one hand because the investigation of pore initiation in the micro- and mesoporous regimes requires high-resolution techniques. Simulations, on the other hand, show that mechanisms supporting pore formation are based on an interfacial instability, which is also sufficient to explain pore initiation, even on surfaces without lateral inhomogeneities. As a result, micro- and mesoporous films, discussed in the preceding sections, have usually been formed by anodization of single crystalline, defect-free, polished and homogeneously doped Si electrodes. This leaves open the question of in what way is pore formation affected the topography of the electrode. The macropore regime, because of its larger dimensions, is well suited for such investigations. For all kinds of macropores it has been found that pits or depressions, generated artificially prior to anodization, are sufficient to initiate macropores [Le8].

## 9.2

### Macropores in p-Type Silicon

Macropore formation on p-type silicon electrodes was first observed for anodization in water-free mixtures of anhydrous HF and an organic solvent [Pr7, Ri1]. Later it was observed that organic HF electrolytes with a certain fraction of water [Po1, We5], or even non-organic, aqueous HF electrolytes [We2, Le21], are also sufficient for the formation of macropores on p-type Si electrodes. This indicates that macropore formation on such electrodes cannot be ascribed to the chemical iden-

tivity of a certain electrolyte. Only the presence of HF in the electrolyte is required, as is the case for the other pore size regimes. The pore morphology and stability of pore growth, however, depend on electrolyte composition and concentration, as well as on additives such as surfactants [Le21, Ch16].

The morphology of macroporous layers formed on p-type Si electrodes can be understood as a consequence of the stringent requirement for pore wall passivation in low doped p-type substrates: pore walls are depleted if their thickness is less than twice the SCR width  $W$ .  $W$  depends on doping density and applied bias. The change in pore morphology with p-type doping density is shown in Fig. 9.4, together with an n-type sample for comparison. If the average pore wall thicknesses from Fig. 9.4 a–d are plotted versus the substrate doping density, the square root dependence, expected from Eq. (1.2), is observed, as shown in Fig. 9.5. The SCR width obtained from Fig. 9.5 is found to correspond to a bias of about 0.1 V.

For n-type as well as p-type Si, the dependence of macropore density on doping density is linear. However, the absolute values of pore density observed on non-structured p-type substrates is about one order of magnitude larger than for n-type electrodes, as shown in Fig. 6.10. This produces high values of porosity ( $p > 0.5$ ) for random p-type macropore structures as well as for arrays [We5, Le21]. The pore walls become fragile if the doping density is increased above  $10^{16} \text{ cm}^{-3}$  and usually only a roughening of the electrode surface is observed for anodization in aqueous HF.

For macropore formation on low doped p-type substrates, the applied bias and current density are coupled: a change in the applied bias produces a corresponding change in anodization current density. For macropore growth on p-type Si

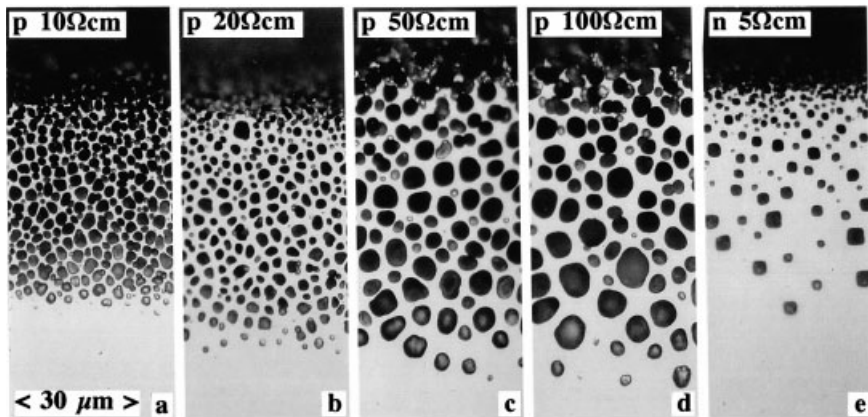
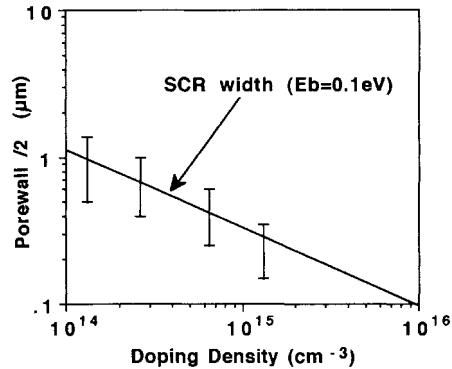


**Fig. 9.4** (a–d) Optical micrographs of p-type substrates of different doping densities polished under a small angle to the electrode surface, after anodization under identical conditions in the dark (10% aqueous HF,

$3 \text{ mA cm}^{-2}$ , 90 min, RT). (e) An n-type substrate anodized under similar conditions is shown for comparison (10% HF,  $5 \text{ Ω cm}$ ,  $3 \text{ mA cm}^{-2}$ , 30 min, RT). After [Le21].



**Fig. 9.5** Values of pore wall thickness from Fig. 9.4 a–d as a function of doping density (error bars), together with the SCR width for a potential ( $V_{bi} + V - 2kT/e$ ) of 0.1 V (line). After [Le21].



electrodes an increase in the current density has little effect on pore diameter, but produces a roughly proportional increase in pore growth rate [Le21]. Note that just the opposite is true for macropore formation in n-type Si. Concerning growth rate and the dissolution valence ( $n_v=2.0-2.3$ ), macropore formation on p-type Si shows similarities to micro PS formation. This can be understood as a consequence of the fact that depletion in p-type substrates is only present for an applied bias significantly lower than that corresponding to the critical current density  $J_{PS}$ . Thus  $J_{PS}$  is never reached at the pore tips or pore walls during macropore formation on p-type Si electrodes. This is supported by the observation that microporous silicon covers not only the macropore walls but also the pore tips. For higher HF concentrations the whole pore volume can be filled with micro PS, as shown in Fig. 9.6.

The dependence of pore morphology on crystal orientation is found to be weak in aqueous HF. The tendency of the pores to branch is enhanced on (110) and (111) substrates if compared to (100) substrates. Some faceting can be observed at the pore tips. In organic solvents the orientation dependence becomes stronger and the  $\langle 100 \rangle$  and  $\langle 113 \rangle$  directions are observed to be preferred for pore growth. At high HF concentrations or in mixtures with organic solvents, most of the pore volume is found to be filled with micro PS. The presence of an oxidizing species, like water, reduces the amount of pore filling [Ch15].

The growth of a macropore on a p-type substrate can be initiated by artificial etch pits. The growth of predefined pore arrays is observed to be more stable than the growth of random pores on flat electrodes [Ch16, Le21]. If a slit is used for pore initiation the formation of trenches separated by thin walls has been observed on (100) p-type substrates [Oh5]. Note that for slits along the  $\langle 110 \rangle$  direction the walls become (110) planes, in contrast to trenches produced by alkaline etchants, for which only (111) oriented walls can be formed on (110) oriented silicon substrates.

In conclusion it can be said that the flexibility of pore array design on low doped p-type Si is less than that for macropore formation on n-type substrates, because of the limitations in array porosity and substrate doping range.

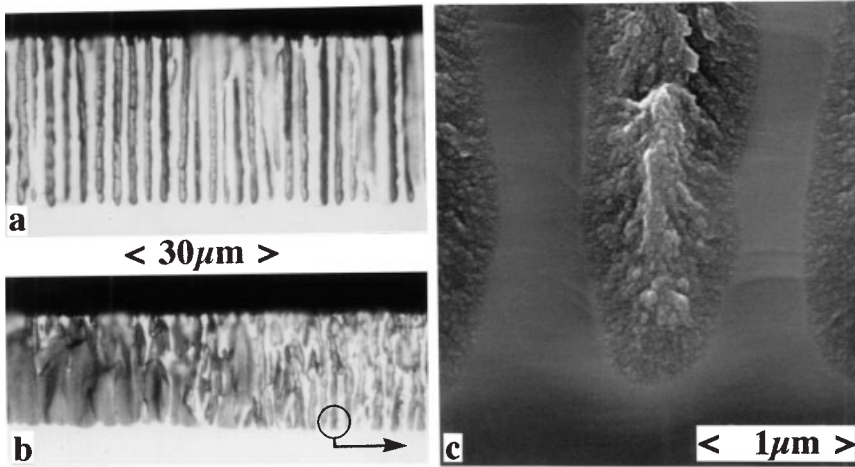


**Fig. 9.6** Cross-sectional optical micrographs of a macropore formed by anodization of (100) p-type Si electrodes in (a) 2 M HF in acetonitrile ( $20\ \Omega\ \text{cm}$ ,  $3\ \text{mA}\ \text{cm}^{-2}$ , 90 min, RT) and in (b) 30% aqueous HF ( $20\ \Omega\ \text{cm}$ ,

$40\ \text{mA}\ \text{cm}^{-2}$ , 7.5 min, RT). (c) A SEM micrograph of the macropores in (b) reveals that most of the pore volume is filled with microporous silicon.

### 9.3

#### The Phenomenology of Macropore Formation in n-Type Silicon

A specific feature of macropore formation in n-type silicon is the possibility of controlling the pore tip current by illumination and not by applied bias. This adds another degree of freedom that is not available for mesopore or macropore formation on p-type substrates. The dark current density of moderately doped n-type Si electrodes anodized at low bias is negligible, as shown in Fig. 4.11, therefore all macropore structures discussed below are formed using illumination of the electrode to generate the flux of holes needed for the dissolution process. Illumination, however, is not the only possible source of holes; for example, hole injection from a p-doped region is expected to produce similar results.

If the sample is illuminated from the side that is exposed to the electrolyte, hole generation in the depleted pore walls is inevitable. Under this frontside illumination, a full passivation of the pore walls is not obtained and for short wavelengths ( $< 700\ \text{nm}$ ), macropore growth even becomes suppressed. Under illumination with long wavelength light ( $700\text{--}1100\ \text{nm}$ ) the resulting pores are conically shaped, as shown in the center column of Fig. 9.7. An electrode surface covered with such tapered pores appears pitch black to the eye. This is due to light trapping in the porous layer, which reduces the reflectivity to values below 1% for the visible regime. The minority carrier density profile generated by frontside illumination is shown in Fig. 10.4b.

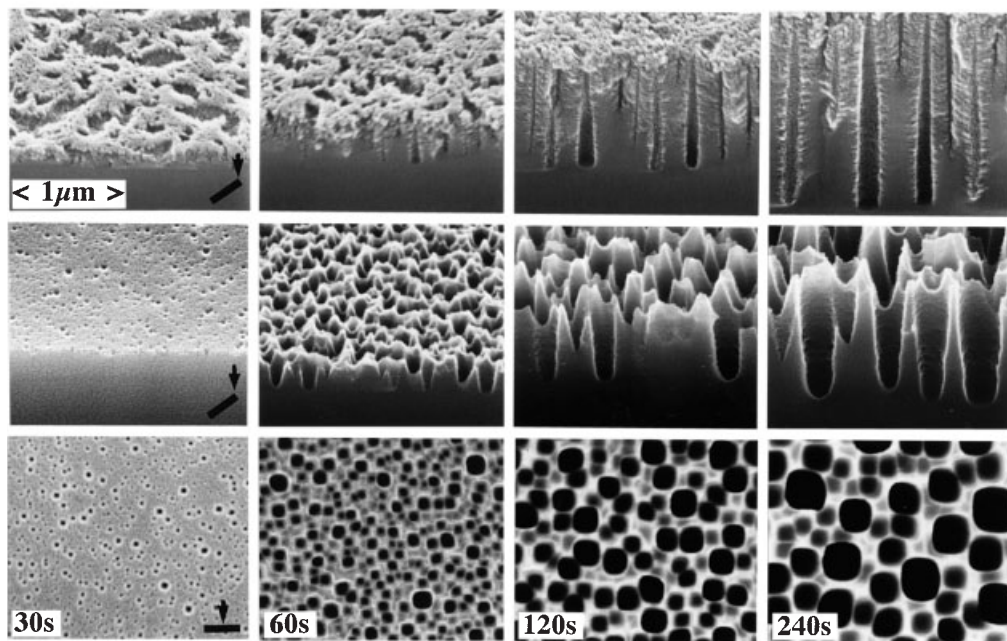


**Fig. 9.7** SEM micrographs of surface and cross-section of an n-type Si electrode anodized for the indicated times under white light illumination of the front side ( $0.4 \Omega \text{ cm}$ , (100), 2.5% HF,  $10 \text{ mA cm}^{-2}$ , 14 V). Micro-

porous silicon covering the macropores, as shown in the top row, has been removed by alkaline etching for better visibility of the macropore initiation process in the center and bottom rows. After [Le8].

Under backside illumination carrier generation in the pore walls can be avoided, if the wavelength of the light source is significantly lower (900 nm) than the wavelength corresponding to the bulk silicon bandgap (1100 nm). For the latter wavelength the absorption coefficient of bulk silicon becomes very low, as displayed in Fig. 7.6, and the light penetrates deep into the bulk, as shown in Fig. 10.4a. A significant fraction may even reach the porous region and produce an undesirable generation of minority carriers in the pore walls. Light sources recommended for macropore formation are discussed in Section 4.6. Backside illumination, however, is only applicable for samples of moderate surface recombination velocity and a bulk diffusion length of about the sample thickness. Otherwise the majority of photogenerated holes are lost by recombination before they reach the pore tips to support dissolution. A low surface recombination velocity can be realized by a diffused or implanted  $n^+$  layer on the backside of the electrode. A benefit of such a layer is that it serves well as a transparent and homogeneous ohmic contact. The minority carrier density profile generated by backside illumination is shown in Fig. 10.4c.

The way in which pore initiation occurs and how it can be controlled will be considered next. If a polished, illuminated n-type Si electrode of (100) orientation

is anodized in aqueous HF, the topmost few micrometers of the electrode are etched homogeneously until tiny etch pits appear, which develop into stable pores, as shown in Fig. 9.7. Only a certain fraction of the initial etch pits develop into macropores by a kind of Ostwald ripening process, which can easily be observed for a sample polished under a small angle to the electrode surface, as shown in Fig. 9.4e. The decrease in pore density causes an increase in pore tip current for the surviving pores, which leads to a bottleneck at the pore opening due to the dependence of pore diameter on current, according to Eq. (9.3). After this initiation and ripening period pore growth becomes stable and a pattern of randomly distributed pores penetrates the electrode without a further significant change in the number of pores, as shown in Fig. 9.8. The average pore density of such random structures increases with doping density, as shown in Fig. 6.10. The absolute values, however, are significantly lower than for macropore formation on p-type substrates of the same doping density [Ri4].

The question arises as to what effects are responsible for the generation of the very first tiny etch pits on the surface. However, this question is misleading in some respects. A flat n-type surface anodized in HF is in an unstable condition. Tiny inhomogeneities of flatness in the electrode surface, inevitably produced by the dissolution process, are amplified, because the concave areas will focus the electric field and thereby become more efficient in collection holes than flat areas. An increase in anodization bias accelerates pore initiation at flat electrodes.

This understanding of pore initiation led to the idea of producing an ordered rather than a random array of pores by using an artificial pattern of etch pits formed prior to anodization. This approach proved to be successful [Le8]. Artificial pits can, for example, be generated by standard lithography of an oxide film and subsequent alkaline etching, which leads to the well-known inverted pyramids, as shown in the inset of Fig. 9.9. Anodization of such a textured electrode leads to a well ordered array of macropores, as shown in the same figure. The etch pit geometry is important. For example, incompletely etched pyramids may lead to formation of four pores per pit, located at the corners of the flat pyramid bottom. Note that the same principle of a pre-textured electrode has successfully been applied to the electrochemical formation of ordered pore arrays in alumina [As5].

If the pore density of arrays as well as random structures is plotted versus the doping density, a linear dependency is observed over several orders of magnitude, as shown in Fig. 6.10. If the pore density, pre-set by the pitch of a predefined pore pattern, is mis-adjusted to the natural pore density determined by substrate doping density, to a certain extent the system will change its pore density. An increase in the number of pores, as shown in Fig. 9.10a, has been called branching, while a decrease, as shown in Fig. 9.10c, has been called dying of pores [Le17]. Note that branched pores are still macropores, because of an illumination-induced photocurrent, while spiking pores, in contrast, are mesopores caused by breakdown of the SCR at the pore tip. Branching or dying of pores does not affect properties like porosity or pore growth rate.

It has been proposed that depletion of the pore walls requires their thickness to be  $2W$  [Zh3, Se8]. However, this does not apply for n-type electrodes. Because the

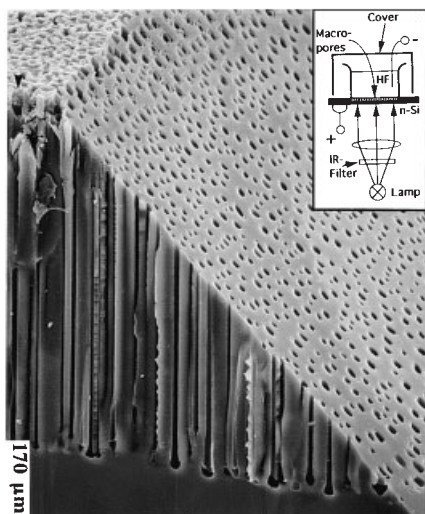


**Fig. 9.8** SEM micrograph of the surface, cross-section and a 45° level of an anodized n-type silicon sample (5  $\Omega$  cm, (100), 6% HF) showing a random pattern of macropores. Pore initiation was enhanced by applying 10 V bias in the first minute of anodization followed by 149 min at 3 V. The current density was kept constant (10 mA cm<sup>-2</sup>) by adjusting the backside illumination. After [Le9].

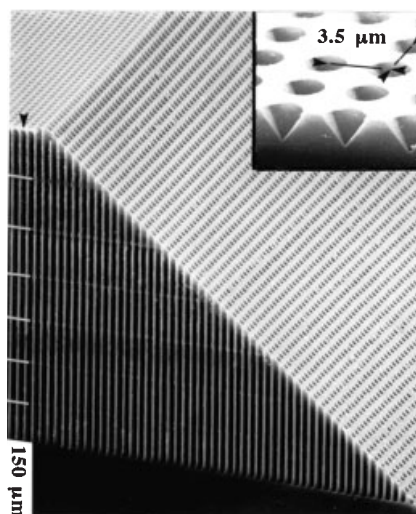


**Fig. 9.9** SEM micrograph of an n-type silicon electrode with an etched macropore array (5  $\Omega$  cm, (100), 3 V, 350 min, 2.5% HF). Pore growth was induced by a square pattern of pits produced by standard lithography and subsequent alkaline etching (inset upper right). In order to measure the depth dependence of the growth rate, the current density was periodically kept at 5 mA cm<sup>-2</sup> for 45 min and then reduced to 3.3 mA cm<sup>-2</sup> for 5 min. This results in a periodic decrease in the pore diameter, as indicated by the white labels on the left-hand side. After [Le9].

porosity depends on the applied current density, according to Eq. (9.1), pore walls can be much thinner than  $2W$ . On the other hand, in low doped substrates wall dimensions as large as  $10W$  are observed, as shown in Fig. 9.11 b. In the latter case the pore wall region is not fully depleted. Holes diffuse into the wall region, but their numbers are small, because the pore tips drain most of the hole current. If the number of holes in the pore walls is not sufficient to initiate branching, only a roughening of the pore walls is observed, as shown in Fig. 9.11 b.

Because the SCR width depends not only on doping density but also on bias, the average pore density is expected to decrease with the square root of bias. This, however, is not observed. An increase in bias often leads to the formation of breakdown-type mesopores at the macropore walls. Because these spiking pores show diameters on the order of a few tens of nanometers they are hard to identify even in an SEM. Spiking pores can be identified if they are enlarged by subsequent chemical etching, as shown in Fig. 8.10. Details of their branched morphology become visible by formation of an oxide replica and after etchback of the sub-

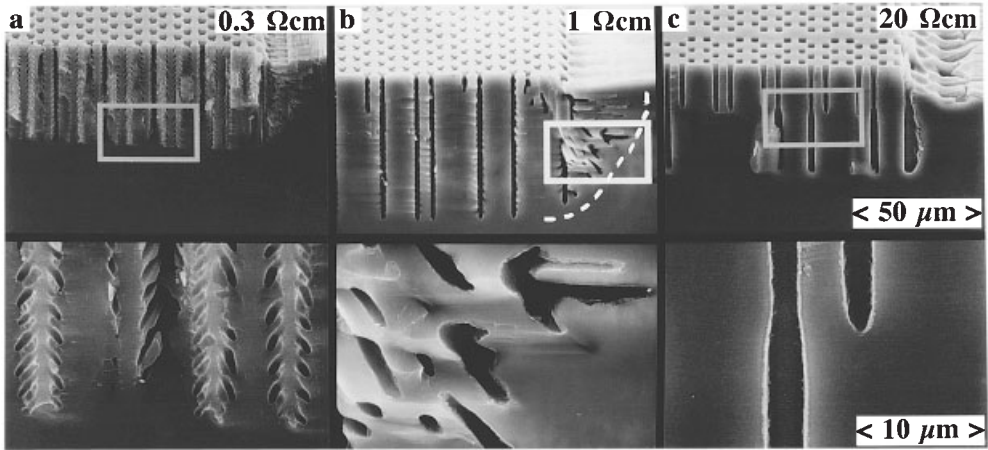


**Fig. 9.10** SEM micrographs showing the dependence of macropore morphology on n-type doping density (2.5% HF,  $5 \text{ mA cm}^{-2}$ , 2 V). (a) High doping leads to branching, while (c) low doping results in drying of pores.

(b) Strong branching is observed at the border to an unpatterned area producing under-etching in an isotropic manner (white broken line). After [Le17].

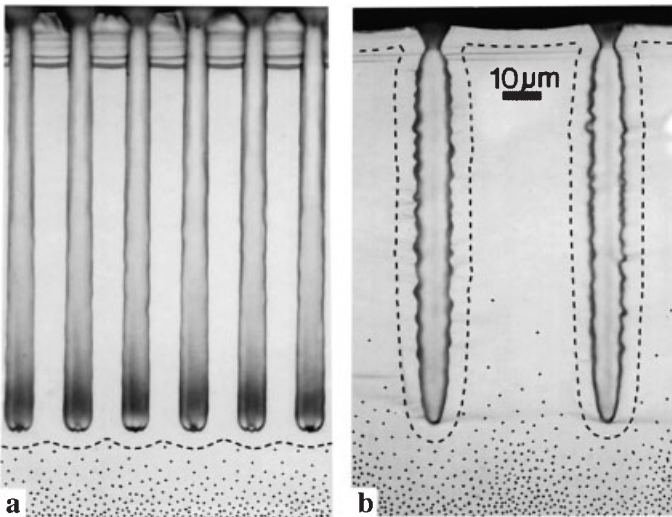


**Fig. 9.11** Optical micrograph of macropore arrays with (a) densely and (b) widely spaced pores (n-type,  $40 \Omega \text{ cm}$ , 4% HF, 143 min, 2 V).

The broken line indicates the interface between bulk and SCR. The dots represent the hole distribution. After [Le 21].

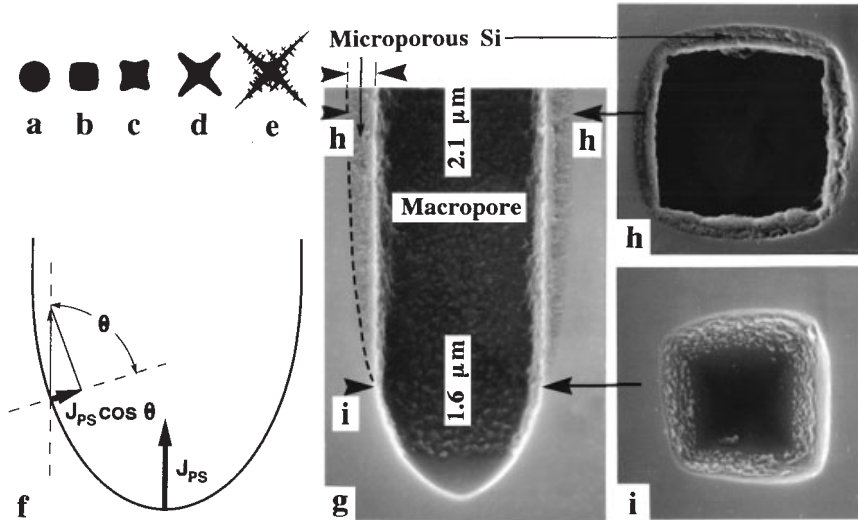


**Fig. 9.12** By an increase in bias or doping density the round (a) or slightly faceted (b) cross-section of macropores becomes star-shaped by branching (c, d) or spiking (e) along the  $\langle 100 \rangle$  directions orthogonal to the growth direction. (f) The current density distribution at a pore tip. (g) SEM micrograph

of a macropore grown on  $\langle 100 \rangle$  n-type Si. The macropore walls are covered by micro PS, indicated by a broken line at the interface to bulk Si. (i, h) Sectional views of the pore shown in (g) at positions h and i. (i) Note that the pore tip is free of micro PS.

strate, as shown in Fig. 8.12b. Spiking leads to pore cross-sections as in Fig. 9.12e. Because spikes are mesopores formed by breakdown, their formation current is independent of photogenerated carriers, as discussed in Section 8.1. This is the decisive difference from branching pores, as for example shown in Figs. 9.10a and 9.14, which are still macropores etched by the photocurrent. A consequence of severe spiking is an increase in the anodic current density with etching time under constant illumination conditions. Note that the decrease in remaining bulk thickness during macropore growth also leads to an increase in current density with etching time under constant illumination conditions according to Eq. (10.10). Both cases can be easily distinguished if the illumination is switched off, as spiking produces a considerable dark current. Spiking, which is usually undesirable in macropore array fabrication, puts an upper limit to the bias. This limit is as low as 2 V for high doping densities ( $> 10^{16} \text{ cm}^{-3}$ ), while for low doped substrates a bias in the order of 10 V is required to initiate spiking.

A lower limit of bias is given by the onset of unstable macropore formation. This is shown in Fig. 9.13, which shows the pore morphology and the corresponding formation conditions in the current density-voltage plot. The current density  $J$  is held constant by the intensity of the backside illumination, so that the influence of the applied bias can be studied independently. At  $-0.4 \text{ V}$ , versus a platinum wire as a pseudoreference electrode, the current density is constant over the

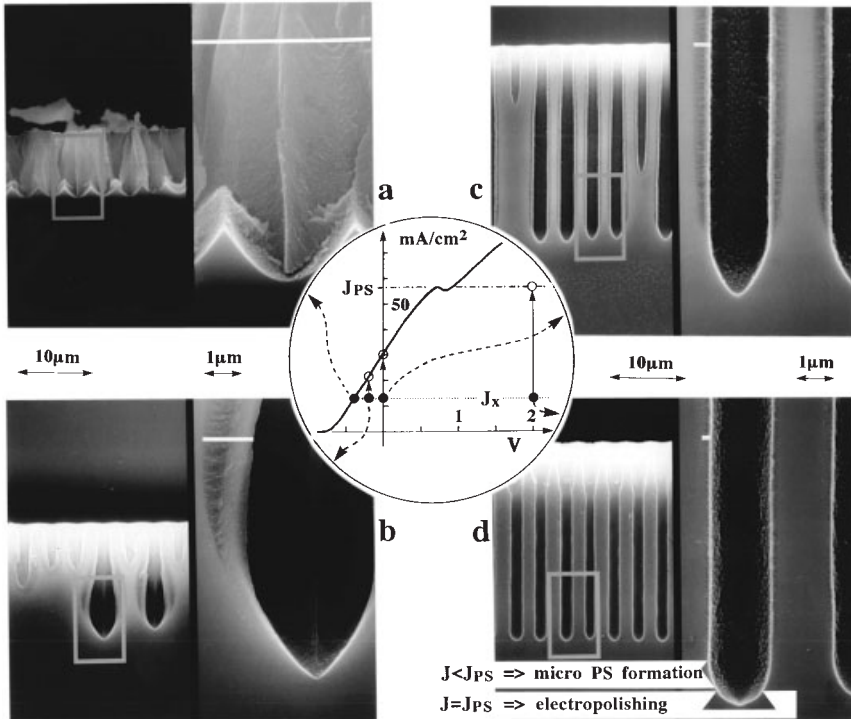


**Fig. 9.13** SEM micrographs of pre-patterned n-type electrodes anodized at different bias (a:  $-0.4$  V, b:  $-0.2$  V, c:  $0$  V, d:  $2$  V, versus Pt-reference, 5% HF,  $12.5 \text{ mA cm}^{-2}$ ,  $5 \Omega \text{ cm}$ , (100)). The four micrographs correspond to positions in the I-V curve as indicated by bro-

ken arrows. The current density as adjusted by illumination is indicated by full circles; open circles indicate the pore tip current density. (d) Stable macropore formation requires a bias sufficient to produce  $J_{PS}$  at the pore tip. After [Le9].

entire sample surface and only homogeneous formation of microporous silicon is observed. At  $-0.2$  V the current density at depressions in the electrode may reach the value indicated by the open circle in the center diagram; macropores are initially formed but their depth is small compared to the thickness of the microporous layer. For a bias of  $0.0$  V the macropore formation is more pronounced but not all pores have the same depth. Stable macropore formation is observed at a bias of  $2$  V, as shown in Fig. 9.13d. In general stable macropore formation requires an applied bias sufficient to generate the current density  $J_{PS}$  (about  $1$  V).

The behavior discussed above shows that in the regime of stable macropore formation the pore current divided by the cross-sectional area of the pore is equal to  $J_{PS}$ . Because of the hemispherical shape of the pore, only the current density at the center of the tip is equal to  $J_{PS}$ , while the interfacial current density decreases towards the pore wall with a cosine dependency, as shown in Fig. 9.12f [Zh3]. As a result the pore walls become covered with micro PS film, while the center of



the pore tip is close to electropolishing and therefore free of micro PS for a sufficient bias of 2 V, as shown in Fig. 9.12 g–i. A more quantitative proof of the condition  $J_{\text{tip}}=J_{\text{PS}}$  is the measurement of the macropore growth rate, which is found to depend only on HF concentration and temperature [Le9], but not on applied current density, as shown by solid squares in Fig. 6.5. Note that the increase in pore diameter induced by the death of a neighboring pore, as shown in Fig. 9.10 c, or the formation of bottlenecks at the pore openings during pore initiation without a predetermined pattern [La2] are direct consequences of the condition  $J_{\text{tip}}=J_{\text{PS}}$ . If the number of pores decreases, the tip current of dying pores is added to the tip currents of the neighboring pores, thus increasing their diameter. An increase of  $J_{\text{tip}}$  to values in excess of  $J_{\text{PS}}$  would cause carrier accumulation at the tip as discussed in Section 3.2, thus effectively destroying the depletion in the pore walls. In addition,  $J_{\text{tip}}>J_{\text{PS}}$  would be accompanied by an increase in the dissolution valence from 2 to 4, which would imply a reduction in the tip growth rate. The latter effect could explain the remarkable flatness of the plane that is formed by all pore tips of a macropore array [Le17]. The consequences of the condition  $J_{\text{tip}}=J_{\text{PS}}$  for a quantitative description of macropore formation are discussed in detail in the next section.

The extraordinary straightness of macropores is not only a consequence of the lithographic pattern but also of the crystal nature of the substrate. The direction of macropore growth depends on the crystal orientation of the substrate and on the source of holes that support the dissolution. As observed for the case of mesopores in low doped n-type electrodes, macropores also have a tendency to grow along the  $\langle 100 \rangle$  directions of the crystal, as illustrated in Fig. 8.13 [Ha10, Ch11, Le8]. This orientation dependence can be ascribed to the anisotropy of the pore tip current density  $J_{\text{PS}}$ .  $J_{\text{PS}}$  is found to be maximum on  $\langle 100 \rangle$  substrates, as shown in Fig. 4.9. Note that  $J_{\text{tip}}$  becomes smaller than  $J_{\text{PS}}$  for an applied bias below about 1 V, and so the orientation dependence as well as the homogeneity of macropore growth is reduced at low bias. However, in contrast to the case of the mesopores where the hole generation occurs directly by the high field present at the pore tip, the source of holes, for example the illuminated backside of the sample, is spatially separated from the drain of holes, the pore tips, for the case of macropore formation. Therefore the direction of pore growth is under mixed control. If a  $\langle 100 \rangle$  direction of the crystal is pointing towards the source of holes, which is the case for  $\langle 100 \rangle$  substrates illuminated homogeneously from the backside, the formation of perfectly straight pores is observed, as shown in Fig. 9.9. However, even for a considerable misalignment of the substrate, the pores still grow along  $\langle 100 \rangle$ , but the tendency to branching is enhanced, as shown in Fig. 9.14 a. For  $\langle 110 \rangle$  oriented substrates pores form along both  $\langle 100 \rangle$  directions, but branching along the  $\langle 113 \rangle$  directions is also observed. For  $\langle 111 \rangle$  oriented substrates the  $\langle 113 \rangle$  directions of the crystal become the preferred pore growth directions, producing a three-fold symmetry. However, such pores are strongly branched, also, as shown in Fig. 9.14 b [Ro8, Ch17].

The geometry of the pore cross-section in a plane parallel to the electrode surface is also dominated by the crystal orientation. Usually shapes between a circle

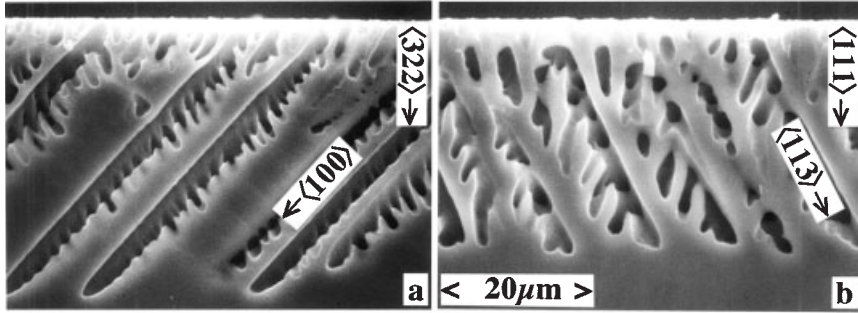


Fig. 9.14 While the preferred macropore growth direction on a (322) substrate is still  $\langle 100 \rangle$ , it becomes  $\langle 113 \rangle$  for (111) substrates (4% HF,  $5.6 \text{ mA cm}^{-2}$ ,  $4 \Omega \text{ cm n-type Si}$ ). After [Ro8].

and a square are observed for (100) substrates as shown in Fig. 9.12a–c. An increase in formation bias leads to spiking. All spiking occurs along  $\langle 100 \rangle$  directions and so the pore shape becomes distorted to a four-pointed star, as shown in Fig. 9.12e.

The geometry of the pore tips is pyramidal, with facets formed by (111) planes, for  $J_{\text{tip}} < J_{\text{PS}}$ . This is the case when the current density is limited by the applied bias, as is the case for the samples shown in Fig. 9.13 b and c. If the bias is increased, dissolution at the pore tip occurs partially in the isotropic electropolishing regime ( $J_{\text{tip}} = J_{\text{PS}}$ ). This reduces the tendency to form facets and the tip geometry becomes almost hemispherical, as shown in Fig. 9.13d.

## 9.4

### Calculating Macropore Growth and Mass Transport

In contrast to the micro- and mesoporous regimes, for which only a few empirical laws for the growth rate and porosity are available, the detailed pore geometry for macropore arrays in n-type silicon can be pre-calculated by a set of equations. This is possible because every pore tip is in a steady-state condition characterized by  $J_{\text{tip}} = J_{\text{PS}}$  [Le9]. This condition enables us to draw conclusions about the porosity of a macroporous film. The etching current, controlled by illumination divided by the initial sample surface area as defined for example by the O-ring of the cell, gives the applied current density  $J$ . If temperature and HF concentration present at the pore tip are known,  $J_{\text{PS}}$  can be calculated according to Eq. (4.9). The porosity  $p$  is then simply given by the ratio of the applied current density  $J$  and  $J_{\text{PS}}$ :

$$p = J/J_{\text{PS}} \quad (9.1)$$

This equation holds true even for thick porous layers, if the decrease in the HF concentration in the pores, which leads to a decrease in  $J_{\text{PS}}$  at the pore tip, is taken into account.

Note that Eq. (9.1) applies to pore arrays as well as to randomly distributed pores. For simple orthogonal or hexagonal arrays of macropores with one pore per unit cell of the pattern, the porosity can be defined locally as the ratio between the cross-sectional area of the pore  $A_p$  and the area of the unit cell  $A_u$ , as shown in Fig. 9.15 a:

$$p = A_p/A_u \quad (9.2)$$

The cross-section of a macropore may have all shapes between a circle and a four-pointed star, as shown in Fig. 9.12 a–e. In addition the pore walls are covered with a microporous silicon layer, as shown in Fig. 9.12 h, which makes the determination of  $A_p$  difficult. In most cases, however, the approximation of the pore cross-section by a square of size  $d$  is found to be sufficient. Under this assumption and for a square pattern of pitch  $i$ , as shown in Fig. 9.15 a,  $d$  becomes simply:

$$d = i(J/J_{ps})^{1/2} \quad (9.3)$$

For arrays of complex geometry where the unit cell contains several pores, or for random pore distributions, the cross-sectional area of each pore  $A_p$  is proportional to the area from which it collects charge carriers, indicated by broken lines in Fig. 9.15 b and c. Equation (9.3) offers an elegant way of tuning the pore diameters during pore growth by a corresponding variation of  $J$ . Periodic changes of  $J$ , for example, produce corresponding variations of the pore diameter, as illustrated by Fig. 9.16.  $J$  is usually adjusted by the backside illumination intensity. Interestingly, a modulation of pore diameter with anodization current has been observed for pore formation in aluminum, too, and has likewise been interpreted in terms of a pore growth velocity independent of applied current [He8].

For a square pattern and square pores the pore wall thickness  $w$  is given by:

$$w = i[1 - (J/J_{ps})^{1/2}] \quad (9.4)$$

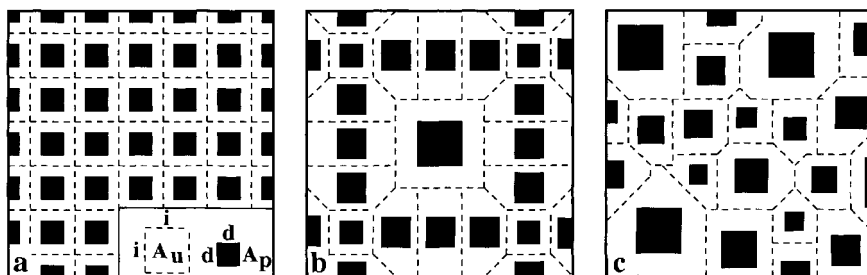
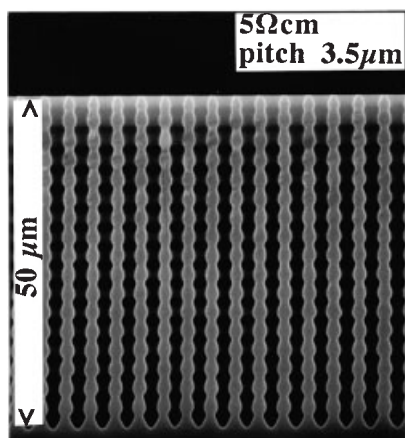


Fig. 9.15 Cross-sections of macropore arrays parallel to the electrode surface (a) for a square, (b) for an ordered and (c) for a random pattern. The pores (black squares)

collect holes from the area indicated by the broken lines. The porosity (ratio of black area to total area) is 0.25 for all patterns.



**Fig. 9.16** A sine wave modulation of the etching current produces an array of macropores with a corresponding modulation of diameter. After [Le17].

The steady-state condition ( $J_{\text{tip}}=J_{\text{PS}}$ ) at the pore tip determines not only the pore diameter but also the pore growth rate. The rate  $r_p$  of macropore growth can be calculated if the local current density at the pore tip is divided by the dissolution valence  $n_v$  (number of charge carriers per dissolved silicon atom), the elementary charge  $e$  ( $1.602 \times 10^{-19}$  C) and the atomic density of silicon  $N_{\text{Si}}$  ( $5 \times 10^{22}$   $\text{cm}^{-3}$ ):

$$r_p = J_{\text{PS}} / (n_v e N_{\text{Si}}) \quad (9.5)$$

$J_{\text{PS}}$  and  $n_v$  are the only variables in this equation. The dissolution valence  $n_v$  shows a steep increase from 2 to 4 at  $J_{\text{PS}}$ , as shown in Fig. 4.5. Because  $J_{\text{PS}}$  is a function of temperature  $T$  and electrolyte concentration  $c$  only, the macropore growth rate on n-type substrates is dependent on  $c$ ,  $T$  and  $n_v$ . Gravimetric measurements of macroporous samples show that  $2.2 < n_v < 3$  is valid in most cases [Le9]. This is shown in Fig. 9.17; the experimentally observed macropore growth rates that are plotted as a function of the HF concentration fit well with growth rates calculated for  $n_v=2$  and  $n_v=4$  using Eq. (9.5). Assuming an average dissolution valence of  $n_v=2.6$ , the macropore growth rate  $r_p$  has been calculated according to Eqs. (9.5) and (4.9); it is given as a function of HF concentration in the table on the inner back cover of this book.

It should be emphasized that  $n_v$  and  $J_{\text{PS}}$ , and therefore  $c$  and  $T$ , refer to the condition at the pore tip. The dissolution valence and the temperature can be assumed to be independent of pore depth. This is not the case for the HF concentration  $c$ . Because convection is negligible in macropores, the mass transport in the pore occurs only by diffusion. A linear decrease in HF concentration with depth and a parabolic growth law for the pores according to Fick's first law is therefore expected, as shown in Fig. 9.18a. The concentration at the pore tip can be calculated from the concentration in the bulk of the electrolyte  $c$ , the pore length  $l$ , the diffusion coefficient  $D_{\text{HF}}$  (Section 1.4) and the flow of HF molecules  $F_{\text{HF}}$ , which is proportional to the current density at the pore tip:

**Fig. 9.17** Calculated growth rates of macropores for  $n_v=2$  and  $n_v=4$  (lines) and experimentally obtained initial macropore etch rates  $r_p$  (squares) versus the HF concentration  $c_{HF}$  of the electrolyte ( $J/J_{PS}=0.25$ ,  $10^{15} \text{ cm}^{-3}$  n-type, RT, square pattern). After [Le9].

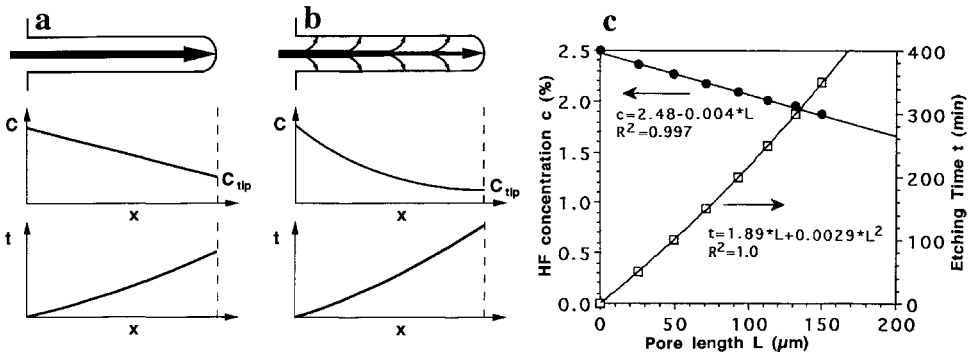
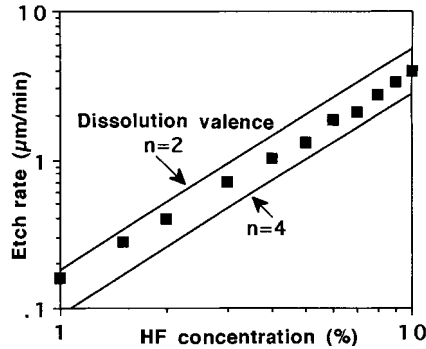


**Fig. 9.18** (a) If the pore tip is the only reaction site, a linear HF concentration gradient and a parabolic pore growth is observed. (b) If HF is consumed at the pore walls, also, the concentration gradient is nonlinear and pore growth becomes retarded. (c) Using depth

markers, as shown in Fig. 9.9, the depth of macropores  $l$  is plotted versus the anodization time  $t$  (squares). The decrease in HF concentration  $c_{HF}$  (circles) in the pore is calculated from the observed  $l$  using Eqs. (9.5) and (4.9). After [Le9].

$$c_{tip} = c - F_{HF} l / D_{HF} \tag{9.6}$$

The experimentally observed parabolic increase in pore depth and linear decrease in concentration shown in Fig. 9.18c indicate that Eq. (9.6) is valid [Le9]. The macropore growth rate decreases linearly with  $l$  according to Eq. (9.6). If, therefore, a constant pore diameter is desired for a macropore array, a decrease in etching current or illumination intensity, respectively, with time is required.

For deep and narrow pores, however, the slow etching of the pore walls, which produces a small dark current density in the order of  $1\text{--}10 \mu\text{A cm}^{-2}$ , as shown in Fig. 4.11, cannot be neglected. Unfortunately the dissolution at the pore walls not only depends on the total wall area but also on parameters such as temperature, DOC and amount of surfactants added to the electrolyte. It is therefore difficult to quantify this effect. The consumption of HF in the dissolution process at the pore

walls leads to a non-linear decrease in the HF concentration along the pore, as shown in Fig. 9.18b. As a result, a non-linear term is superimposed on the linear decrease in growth rate with depth.

Note that during macropore formation in p-type silicon electrodes the pore tip current density is usually well below  $J_{PS}$ , and so Eqs. (9.1) to (9.5) are not applicable to p-type macropore formation [Le21].

## 9.5

### Design Rules and Limits of Macropore Array Fabrication

Not all desirable macropore array geometries can be achieved by the electrochemical etching process. This section gives the upper and lower limits for pore dimensions and a few design rules. Macropores in n-type substrates will be discussed first [Le17].

The realization of a desired pore pattern requires a certain doping density of the n-type Si electrode. A good rule of thumb for the selection of an appropriate substrate is to multiply the desired pore density given (in  $\mu\text{m}^{-2}$ ) by  $10^{16}$  and take this number as doping density (in  $\text{cm}^{-3}$ ). This dependency is shown in Fig. 6.10. A square pattern of  $10\ \mu\text{m}$  pitch, for example, produces a pore density of  $0.01\ \text{pores}\ \mu\text{m}^{-2}$ , which can best be etched using a n-type substrate doping density of  $10^{14}\ \text{cm}^{-3}$ .

The number of possible arrangements for the pore pattern is only limited by the requirement that under homogeneous backside illumination the porosity has to be constant (Eq. 9.1) on a length scale above about three times the pitch. This means it is possible to etch a pattern with a missing pore, a missing row of pores or even two missing rows. Patterns as shown in Fig. 9.15b can also be etched; a single pore, however, cannot be etched. It is also possible to enlarge or shrink the pitch of a pattern across the sample surface by a maximum factor of about three. But a pattern with an abrupt border to an unpatterned area will lead to severe under-etching, according to Fig. 9.10 b, and random pore formation in the unpatterned area.

A local variation in porosity can be produced by an inhomogeneous illumination intensity. However, any image projected on the backside of the wafer generates a smoothed-out current density distribution on the frontside, because of random diffusion of the charge carriers in the bulk. This problem can be reduced if thin wafers or illumination from the frontside is used. However, sharp lateral changes in porosity cannot be achieved.

Arrays with pore diameters  $d$  as small as about  $0.3\ \mu\text{m}$  have been achieved [Le17]. The lower limit for the pore diameter is established by breakdown, according to Fig. 8.1b, which leads to light-independent pore growth and spiking. There seems to be no upper limit for the pore diameter, because the formation of  $100\ \mu\text{m}$  wide pores has been shown to be feasible [KL3]. Array porosities may range from 0.01 to close to 1. The porosity, which is controlled by the etching current, determines the ratio between pore diameter and pitch of the pore pattern.

This means that for a square pattern, any pore diameter between a tenth of the pitch and nearly the pitch can be realized.

The pore diameter can be varied over the length of the pore by a factor of up to about 3 for all pores simultaneously by adjusting the current density, as shown in Fig. 9.16. This means that the porosity normal to the surface can be varied. The taper of such pore geometries is limited by dying of pores to values below about  $30^\circ$  for a pore diameter decreasing in growth direction, while values in the order of  $45^\circ$  have been realized for an increase in pore diameter in the growth direction [Mu6]. Note that narrow bottlenecks will significantly reduce the diffusion in the pore and the formation of deep modulated pores becomes more difficult than formation of straight pores. Bottlenecks at the pore entrance may result from the transition of the pyramidal etch pit into a pore tip. They can be avoided by an increase in the current density during the first minutes of pore array fabrication.

The pore cross-section under stable array formation conditions is usually a rounded square, as shown in Fig. 9.12 b and h. Following electrochemical pore formation, the cross-section can be made round by oxidation steps or can be made square by chemical etching at RT in aqueous HF or weak alkaline solutions like diluted KOH or  $\text{NH}_4\text{OH}$ . Formation of side pores by branching or spiking, as shown in Figs. 9.10 a and 8.12, can be suppressed by an increase in current density or a decrease in doping density, bias or HF concentration. The dying of pores, as shown in Fig. 9.10 c, is suppressed by an increase in current density, doping density or bias.

The pore length  $l$  can be as large as the wafer thickness (up to 1 mm). However, the growth of deep pores requires low electrolyte concentrations, low temperatures and etching times in the order of a day or more, because the etch rate in deep pores is limited by HF diffusion to values in the order of  $0.5 \mu\text{m min}^{-1}$  and below. Shorter pores ( $l < 0.1 \text{ mm}$ ) can be etched much faster ( $5 \mu\text{m min}^{-1}$ ). Under stable etching conditions all pores have the same length. Pore arrays with through-pores can be realized by an increase in the etching current density into the electropolishing regime, which separates a free-standing porous plate from the substrate. Macropores penetrating the whole wafer thickness can also be etched, but pore formation becomes unstable in the vicinity of the backside. The formation of dead-end pores and subsequent oxidation and alkaline etchback is technologically favorable.

Another effect that limits the obtainable pore length is shown in Fig. 9.19 a. This effect is characterized by a sudden drop in the growth rate at the pore tip to negligible values and an increase in pore diameter close to the tip. This degradation of pore growth establishes an upper limit for the pore length for a given set of anodization parameters. The fact that pore degradation is delayed for a reduced formation current, which produces conical pores as shown in Fig. 9.19 b, indicates a diffusion-related phenomenon. The observed dependence of degradation on the concentration of the dissolution product  $\text{H}_2\text{SiF}_6$  in the electrolyte points to a poisoning of the dissolution reaction. The maximum obtainable pore depth decreases rapidly with increasing HF concentration, as shown in Fig. 9.20. This effect can be ascribed to the rate of  $\text{H}_2\text{SiF}_6$  production being proportional to  $J_{\text{PS}}$ , which again depends exponentially on HF concentration (Eq. 4.9), while the diffusion of  $\text{H}_2\text{SiF}_6$  is expected to show little dependence on HF concentration.

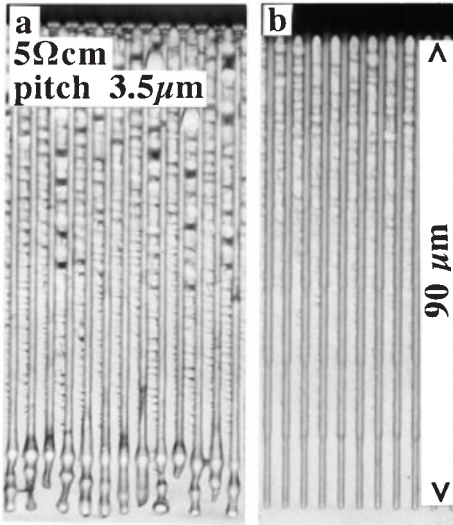


**Fig. 9.19** Optical micrographs of (a) cylindrical pores showing a degradation effect at the pore tips, ascribed to a limitation of mass transport (15% HF, 3 V, 1200 s). (b) Conical pores do not show this degradation at the same depth (15% HF, 3 V, 720 s). After [Le17].

According to Eq. (4.4), hydrogen is another dissolution product. This raises the question of whether hydrogen bubbles are present inside the pore. Direct experimental observations relating to this question are not available. However, the growth of perfect macropore arrays seems unlikely under the assumption of randomly distributed microbubbles in the pores, which would hinder or even block the continuous mass transfer. It can therefore be assumed that hydrogen is supersaturated in the electrolyte inside the pores and that bubbles are formed at the pore entrance. This assumption is supported by the observation that a change in ambient pressure between 0.3 and 100 bar shows little or no effect on electrochemical pore formation in aluminum electrodes, which is also accompanied by hydrogen evolution [Be24].

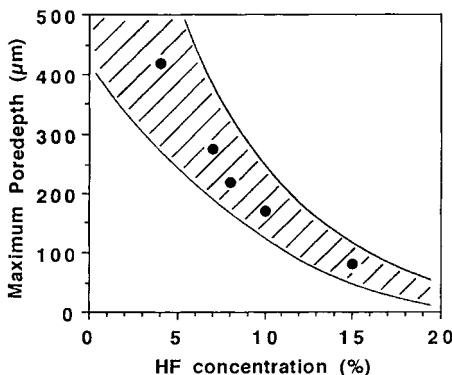


**Fig. 9.20** The maximum pore length for cylindrical pores that can be achieved without a degeneration of the pore tips is shown as a function of the electrolyte concentration at RT (circles). The shaded area indicates the degeneration depth for a decrease or increase in pore diameter versus pore depth. After [Le17].



The pore growth direction is along the  $\langle 100 \rangle$  direction and toward the source of holes. For the growth of perfect macropores perpendicular to the electrode surface (100), oriented Si substrates are required. Tilted pore arrays can be etched on substrates with a certain misorientation to the (100) plane. Misorientation, however, enhances the tendency to branching and angles of about  $20^\circ$  appear to be an upper limit for unbranched pores. For more details see Section 9.3.

Pore array formation is also feasible for p-type substrates [Le21]. Under optimized conditions a pore depth of up to  $400\ \mu\text{m}$ , at a growth rate of  $0.6\text{--}0.8\ \mu\text{m}\ \text{min}^{-1}$  has been reported [Ch16]. A detailed investigation of the limits of pore geometry and design rules are not available for p-type electrodes. The condition that the pore wall thickness is always less than  $2W$ , however, reduces the flexibility in array design significantly. The fact that the pore growth rate depends on current density, on the other hand, could be applied to form pores of different depth by lateral variations of current density. The latter is not possible for stable macropore formation on n-type substrates.

In conclusion it can be said that the limits of macropore array formation are in some way complementary to the limitations of plasma etching [Ja3]. The latter technique gives a higher degree of freedom in lateral design, while the freedom in vertical design and the feasible pore aspect ratios are limited.

An interesting question is whether such well-ordered pore arrays can also be produced in other semiconductors than Si by the same electrochemical etching process. Conversion of the macropore formation process active for n-type silicon electrodes on other semiconductors is unlikely, because their minority carrier diffusion length is usually not large enough to enable holes to diffuse from the illuminated backside to the front. The macropore formation process active in p-type silicon or the mesopore formation mechanisms, however, involve no minority carrier diffusion and it therefore seems likely that these mechanisms also apply to other semiconductor electrodes.

## 10 Applications

### 10.1 Overview

A complete review of the multitude of applications based on electrochemical properties of silicon is beyond the scope of this chapter and so selected examples representing the different categories of applications are given. Two fundamental categories of applications can be identified: in the first, the properties of the silicon-electrolyte contact are exploited for analytical purposes [Fo2]. The HF tester and the pin hole detector directly exploit special properties of the electrochemical reactions at anodically or cathodically polarized silicon electrodes, while for diffusion length mapping and carrier concentration profiling the electrolyte serves mainly as a transparent, homogeneous and easy-to-use contact with the substrate. The second category exploits the properties of electrochemically formed materials to create new devices. An anodic oxide is an example of such an electrochemically formed material. Because of its electrical performance, which is inferior to a thermal oxide, however, device-related applications of anodic SiO<sub>2</sub> are limited to cases where the thermal budget is crucial, e.g. nuclear radiation detectors [Me13]. This is in contrast to the different kinds of porous silicon, for which anodization in HF or stain etching are the only known fabrication techniques. PS-related applications can be found in various fields. Electronic applications include cold cathodes and capacitors, while optical applications include anti-reflective coatings, LEDs, short-pass filters, interference filters, waveguides and photonic crystals. The high internal surface area of PS can be exploited for chemical and biological applications such as biocompatible interfaces or biochips used in genomics, as well as for a multitude of different sensing devices. The use of PS as a sacrificial layer opens new doors in micromechanical engineering. A selection of the wide variety of PS-based applications is given below.

## 10.2

## AC Properties of Silicon Electrodes and Carrier Concentration Profiling

This section summarizes the AC behavior of a silicon electrode and introduces an application of these properties, the carrier concentration profiling technique.

Several factors contribute to the impedance behavior of a silicon electrode. Figure 10.1a shows a proposal for an equivalent circuit that considers most of these factors, which are:

1. A resistance  $R_U$  due to the sum of the ohmic contact resistance, the silicon bulk resistance and in part to the electrolyte resistance.
2. The capacitance  $C_{SC}$  and the resistance  $R_{SC}$  due to the SCR in the Si electrode.
3. The capacitance  $C_{SS}$  and the resistance  $R_{SS}$  connected parallel to  $C_{SC}$ , which are introduced to describe the effect of surface states.
4. An additional RC element  $C_S$  and  $R_S$ , to describe interfacial layers, such as an anodic oxide.
5. The capacitance  $C_H$  and the charge transfer resistance  $R_{CT}$  representing the Helmholtz layer.

At high electrolyte concentrations ( $>1 \text{ mol l}^{-1}$ ) the Helmholtz capacitance  $C_H$  of the electrode shows values in the order of  $C_H/A = 0.5 \mu\text{F cm}^{-2}$  [Na7] and is thereby at least one order of magnitude larger than  $C_{SC}/A$ . Therefore it can be neglected

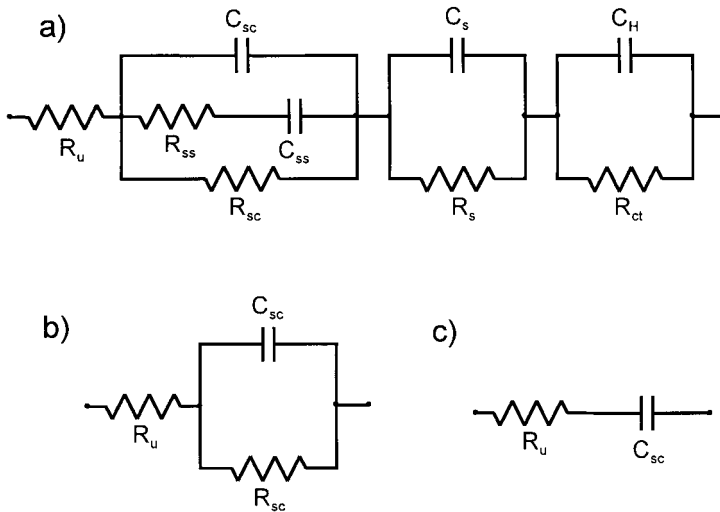


**Fig. 10.1** Equivalent circuits used to represent the semiconductor-electrolyte interface. (a) A more complete approach taking into account the series resistance ( $R_U$ ), the depletion layer ( $C_{SC}$ ,  $R_{SC}$ ), an oxide surface film

( $C_S$ ,  $R_S$ ), the Helmholtz layer ( $C_H$ ) with a transfer resistance ( $R_{CT}$ ), and surface states ( $C_{SS}$ ,  $R_{SS}$ ). Simplified equivalent circuits are shown in (b) and (c). After [Ot1].

for AC measurements under depletion conditions. If the electrode is free of surface films and shows a low surface state density it is sufficient to use the simplified equivalent circuit shown in Fig. 10.1b. In case leakage currents are negligible, the circuit can be further reduced to two elements, as shown in Fig. 10.1c.

The potential dependence of the SCR capacity  $C_{SC}$  on applied potential  $V$  is described by the Mott-Schottky relation:

$$1/C_{SC}^2 = 2(V - V_{fb}) / (\epsilon N_d \epsilon_0 A^2) \quad (10.1)$$

where  $A$  is the interfacial area,  $e$  the elementary charge,  $N_d$  the doping density,  $V_{fb}$  the flat-band potential and  $\epsilon$  the dielectric constant of the semiconductor. From Eq. (10.1) the flat band potential for an electrolytic contact can be calculated from measurements of  $C_{SC}$  ( $V$ ) if  $N_d$  is known; or  $V_{fb}$  can be graphically determined by extrapolation of a  $C_{SC}^{-2}$  versus  $V$  plot to zero capacitance, as shown in Fig. 10.2. The value of 0.75 V found for p-type Si, however, is unrealistically high. By HFR the flat band voltage of a p-type and an n-type Si electrode in 0.5 M HF + 1 M  $NH_4Cl$  are determined to be 0.14 V (SCE) and -0.54 V (SCE), respectively [Ot1]. A similar value of -0.35 V (SCE) is observed for n-type Si in 1 M HF by microwave reflectivity measurements [Na7]. Figure 10.3 summarizes values of  $V_{fb}$  obtained by different methods. Note that the scatter in these data is much larger for p-type silicon electrodes than for n-type. A similar scatter has been observed in the determination of the OPC potential of p-type electrodes, which is found to be more sensitive to parameters such as, for example, illumination intensity than that of n-type electrodes, as discussed in Section 3.2.

Equation (10.1) can be used to determine the doping density of a silicon substrate and its depth profile, even if the flat band potential is not known accurately. Diffusion doping, ion implantation or the growth of an epitaxial layer are common methods of producing doped regions in semiconductor substrates. The dopant concentration close to the surface can be measured by SRP or capacitance-

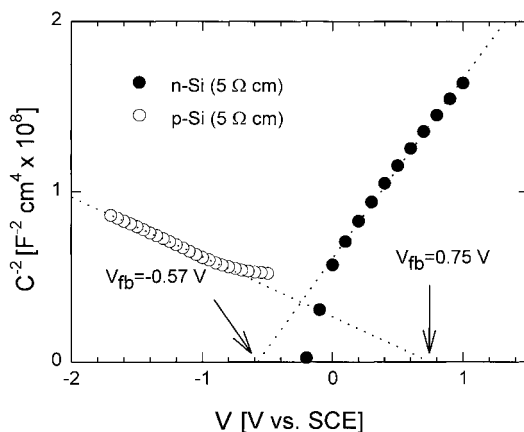


**Fig. 10.2** Mott-Schottky plots of an n-type and a p-type silicon electrode in an electrolyte composed of 0.5 mol l<sup>-1</sup> HF and 0.5 mol l<sup>-1</sup>  $NH_4Cl$ . Dotted lines correspond to  $N_D = 1.1 \times 10^{15} \text{ cm}^{-3}$  and  $N_A = 3.4 \times 10^{15} \text{ cm}^{-3}$ . After [Ot1].

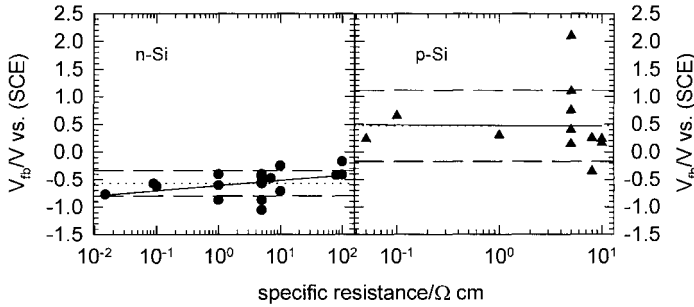


**Fig. 10.3** Graphical representation of flat band potentials of silicon electrodes as determined by different methods. The solid lines represent the mean value and the broken lines represent the standard deviation from mean. After [Ot1]. The dotted lines show a linear regression, the dotted lines

voltage (CV) techniques. In order to determine the carrier concentration depth profile, we need a method of removing material and continuously probing its dopant concentration. SIMS is now the standard analytical tool to investigate doping profiles. However, in some cases, e.g. very deep or ultra-shallow dopant profiles, electrochemical methods can be beneficial.

By varying the applied bias the CV technique itself gives a certain depth resolution, but the investigated depth is limited by reverse bias breakdown. It is therefore advantageous to use the electrolyte not only for measurement but also for material removal. Silicon can be etched by anodic oxidation in HF-free electrolytes and subsequent etching in HF or directly by electropolishing in HF. The prior method is very accurate but slow, and most suited for shallow implants. Formation and removal rates of anodic oxides and silicon are given in Sections 5.3 and 5.6, respectively. Determination of dopant depth profiles by anodic sectioning of silicon and other semiconductors is an analytical tool that has been applied for many years in semiconductor manufacturing [Ta9, Qu1, Am2, Bl1, Sh2, Ba9, Se11]. The dopant concentration  $N(W)$  at the edge of the SCR of width  $W$  to the bulk can be calculated from the change in capacitance  $dC_{SC}$  with bias  $dV$ , according to the Mott-Schottky relation:

$$N(W) = -(C_{SC}^3 / \epsilon \epsilon_0 A^2) / (dC_{SC} / dV) \tag{10.2}$$

$$W = \epsilon A / C_{SC} \tag{10.3}$$

The doping densities calculated from the slope of the  $C^{-2}$  versus  $V$  plots, as shown for example in Fig. 10.2, agree well with values measured by other methods [Ot1]. Deviation between results obtained by spreading resistance measurements and electrochemical CV measurements are usually found to be below 20% for doping densities between  $10^{12}$  and  $10^{18} \text{ cm}^{-3}$  [Pe3].

The carrier concentration depth profile can be monitored by repeated CV measurement and controlled electrochemical removal of the substrate. An optimum

for smooth and homogeneous removal of the substrate has been reported for an electrolyte composed of ammonium bifluoride (0.1 M  $\text{NH}_4\text{F}\cdot\text{HF}$ ) with a few drops of a non-ionic wetting agent and dissolution in the tetravalent regime ( $n=3.7 \pm 0.1$ ) at about  $3 \text{ mA cm}^{-2}$  [Pe4]. A computerized electrochemical set-up for carrier concentration profiling has been commercialized [20]. A drawback of the electrochemical CV technique is its limited spatial resolution, usually given by the size of the O-ring, which cannot be reduced significantly below  $1 \text{ mm}^2$ . This value is comparable to the area needed for a spreading resistance measurement. The doping density has to be homogeneous over this electrode area. This limitation can be overcome by the use of photoresist patterning, which provides a lateral resolution of down to  $0.01 \text{ mm}^2$  [Se11].

An extension of the CV technique to a method comparable to deep level transient spectroscopy (DLTS) is possible if the electrode is illuminated during the capacitance measurement. Plots of capacitance versus wavelength, for a sweep from low to high photon energies, yield a series of plateaus or peaks, each corresponding to the population or depopulation of a given deep level in the bandgap. The onset energy of the capacitance change yields the energy of the state, relative to the appropriate band edge. This technique is known as electrochemical photocapacitance spectroscopy (EPS) [Ha5].

### 10.3 Diffusion Length and Defect Mapping

Contamination of silicon wafers by heavy metals is a major cause of low yields in the manufacture of electronic devices. Concentrations in the order of  $10^{11} \text{ cm}^{-3}$  [Ha2] are sufficient to affect the device performance, because impurity atoms constitute recombination centers for minority carriers and thereby reduce their lifetime [Sc17]. In addition, precipitates caused by contaminants may affect gate oxide quality. Note that a contamination of  $10^{11} \text{ cm}^{-3}$  corresponds to a pinhead of iron ( $1 \text{ mm}^3$ ) dissolved in a swimming pool of silicon ( $850 \text{ m}^3$ ). Such minute contamination levels are far below the detection limit of the standard analytical techniques used in chemistry. The best way to detect such traces of contaminants is to measure the induced change in electronic properties itself, such as the oxide defect density or the minority carrier lifetime, respectively diffusion length.

#### 10.3.1 Diffusion Length Mapping

The basic idea of most diffusion length measurement techniques is to generate a certain number of minority carriers inside the bulk Si, for example by illumination, and to measure the fraction of these carriers that diffuse to a collecting interface. This fraction can be determined capacitively [Bo6], as well as by measurements of the steady-state photocurrent [Dr2, Le11]. The parameter obtained by these measurements is the minority carrier diffusion length  $L_D$  of electrons in

p-type Si or of holes in n-type Si, respectively.  $L_D$  can be converted into the lifetime  $\tau$  of minority carriers using

$$\tau = L_D^2 / D_{e,h} \quad (10.4)$$

where  $D_{e,h}$  is the diffusion coefficient for the relevant minority charge carrier in silicon. The diffusion coefficient itself depends on the mobility  $\mu$  of the relevant species according to

$$D_{e,h} = (kT/e)\mu_{e,h} \quad (10.5)$$

The frontside of the sample will now be illuminated. Let us first assume that the collecting SCR is located at the frontside, too, as shown in the inset of Fig. 10.4b. This mode of operation will be termed frontside photocurrent mode (FPC). The collected photocurrent  $I_{\text{FPC}}$  is a result of minority charge carriers generated in the SCR producing the current  $I_{\text{SCR}}$  and in the bulk of the electrode producing  $I_{\text{DIFF}}$ .

$$I_{\text{FPC}} = I_{\text{SCR}} + I_{\text{DIFF}} \quad (10.6)$$

The number of charge carriers generated in the SCR depends on the absorbed flux of incident photons per unit area  $P$ , the width  $W$  of the SCR and the wavelength-dependent absorption coefficient  $a$  of bulk Si. The latter parameter is shown in Fig. 7.6, while the resulting penetration depth for light of different wavelengths is shown in Fig. 10.4a.

$$I_{\text{SCR}} = eP[1 - \exp(-aW)] \quad (10.7)$$

If the sample thickness is much larger than  $L_D$ , the backside condition becomes irrelevant and  $I_{\text{DIFF}}$  is simply given by:

$$I_{\text{DIFF}} = eP a L_D \exp(-aW) / (aL_D + 1) \quad (10.8)$$

If the photon energy approaches the bandgap energy of Si (1.1 eV),  $I_{\text{SCR}}$  becomes small and  $I_{\text{FPC}}$  is dominated by  $I_{\text{DIFF}}$ . In contrast, for illumination with light of a short wavelength, the absorption coefficient  $a$  of Si is large and minority carrier generation occurs close to the illuminated surface, in a region smaller than the width of the SCR  $W$ . If we assume the latter case, all absorbed photons contribute to the collected current,  $I_{\text{FPC}} = I_{\text{SCR}} = eP$ .

Let us now assume that the collecting SCR is located at the backside, as shown in the inset of Fig. 10.4c. This mode of operation will be termed backside photocurrent mode (BPC). The collected photocurrent  $I_{\text{BPC}}$  again depends on generation in the bulk and in the SCR:

$$I_{\text{BPC}} = I_{\text{SCR}} + I_{\text{DIFF}} \quad (10.9)$$

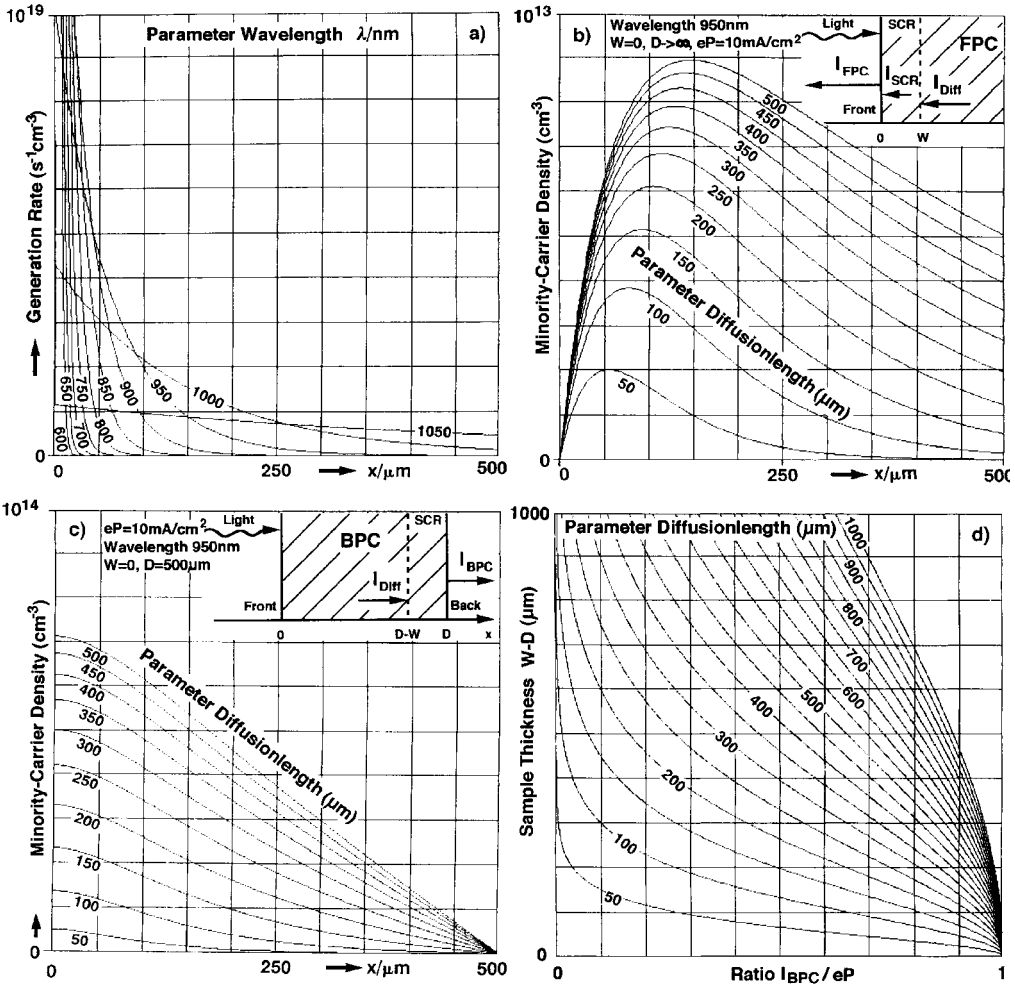


**Fig. 10.4** (a) Computed minority carrier generation rate in bulk silicon for different wavelengths of monochromatic illumination of an intensity corresponding to a photocurrent density of  $10 \text{ mA cm}^{-2}$ . (b) Bulk minority carrier density for carrier collection at the illum-

nated frontside ( $\lambda=950 \text{ nm}$ ,  $eP=10 \text{ mA cm}^{-2}$ ). (c) Minority carrier density for carrier collection at the backside ( $\lambda=950 \text{ nm}$ ,  $eP=10 \text{ mA cm}^{-2}$ ,  $D-W=500 \mu\text{m}$ ). (d) Computed values of  $L_D$  as a function of the ratio  $I_{\text{BPC}}/eP$  and the sample thickness ( $D-W$ ) according to Eq. (10.10).

For not too low doped samples ( $D \gg W$ ), however, the contribution of  $I_{\text{SCR}}$  is usually negligible. If the surface recombination velocity at the illuminated front is low,  $I_{\text{BPC}}$  then only depends on sample thickness  $D$ , illumination intensity  $eP$ , and minority charge carrier diffusion length  $L_D$ .

$$I_{\text{BPC}} = eP / \cosh[(D - W)/L_D] \quad (10.10)$$



Equation (10.10) is the solution of the one-dimensional continuity equation under several assumptions, such as a lifetime independent of the carrier concentration, a negligible electric field inside the wafer, and no coupling between injected electrons and holes. However, despite these crude approximations, the results for  $L_D$  correlate well with values obtained by other methods such as surface voltage spectroscopy (SPV). The sensitivity of the method for iron, for example, has been found to be better than  $10^{11} \text{ cm}^{-3}$  [Be17, Wa9]. Plots for different values of  $L_D$  over the ratio  $I_{\text{BPC}}/eP$  and the thickness  $D-W$  according to Eq. (10.10) are shown in Fig. 10.4d. For large values of diffusion length, the measurement range in BPC mode is limited to about four times the wafer thickness, while for small diffusion length the limit is about one-fifth of the wafer thickness. The  $L_D$  of electronic grade silicon is usually well above the lower limit, but for solar silicon materials, the diffusion length may be too low for the BPC mode. In the latter case,  $L_D$  can still be obtained if the FPC value measured with short wavelength illumination is compared to the FPC value for long wavelength illumination, using Eqs. (10.7) and (10.8).

Double-sided electrolytic contacts are favorable for this method of diffusion length measurement because they are transparent and the required SCRs are easily induced by application of a reverse bias. Therefore homogeneously doped wafers need no additional preparation, such as evaporation of metal contacts or diffusion doping, to produce a p-n junction. Furthermore, a record low value of surface recombination velocity has been measured for silicon surfaces in contact with an HF electrolyte at OCP [Ya1]. Note that this OCP value cannot be further decreased by a forward bias at the frontside, because any potential other than OCP has been found to increase the surface recombination velocity, as shown in Fig. 3.2. Note that contaminations in the HF electrolyte, such as Cu, may significantly increase the surface recombination velocity. This effect has been used to detect trace levels (20 ppt) of Cu in HF [Re5].

Double cells that allow the establishment of an Si-HF contact to both interfaces of the wafer are shown in Fig. 1.7g and h and Fig. 1.10. A photograph of an ELYMAT double cell designed for diffusion length measurement of 200 mm wafers is shown on the upper left of the front cover of this book. Tungsten carbide tips pressed to the edge of the wafer are found to produce a sufficiently ohmic contact for the majority carrier current. The applied reverse bias at the collector side should be low (1–3 V) in order to reduce contributions to the reverse current because of metal precipitates or other crystal defects present in the SCR, as shown in Fig. 10.6c and d. The illumination intensity  $eP$  can either be measured by an independent method or, for short wavelength and large values of  $L_D$ , it can be replaced by  $I_{\text{FPC}}$  in Eq. (10.10). Thus,  $L_D$  can be determined by measurements of  $I_{\text{BPC}}$  and  $I_{\text{FPC}}$ , if the sample thickness and doping are known.

The method described so far measures diffusion length but provides no information about the element responsible for the contamination. This information can for some cases be obtained indirectly, if the change in lifetime with temperature or injection level is measured. Injection levels in the FPC mode are generally one or two orders of magnitude smaller compared to the BPC mode at the same

light intensity, as shown in Fig. 10.4 b and c. Combining both modes for injection level spectroscopy, the accessible levels cover four orders of magnitude. This enables us to distinguish, for example, titanium from iron contamination, because in the case of Fe the lifetime increases by one order of magnitude for an increase in injection level of three orders of magnitude, while the lifetime shows little dependence on injection level in the case of Ti. In addition iron contamination in p-type Si can be identified by the characteristic decrease in lifetime upon low-temperature annealing (210 °C). This effect is caused by a break-up of Fe–B pairs at elevated temperatures. Other elements such as Ni can be identified, because they produce a decrease in lifetime accompanied by a significant increase in the dark current, because of nickel silicide precipitates in the SCR, as shown in Fig. 2.7 [Wa4, Zo1, Ei1, Wi2].

If different wavelengths are used for illumination, the effects of bulk and surface recombination can be decoupled. Surface recombination velocities between  $10^2$  and  $10^5$  cm s<sup>-1</sup>, as well as the bulk diffusion length  $L_D$ , have been measured simultaneously using this multi-color method [Os1]. Different wavelengths can also be used to obtain a certain depth resolution. For the case of oxygen-rich CZ wafers, for example, the depth of the denuded zone, the region free of oxygen precipitations, has been found to be measurable using an 820 nm and a 905 nm laser diode for illumination [Ob1]. This technique is not only advantageous because it is non-destructive, it also offers to map the lateral distribution of oxygen precipitations with high resolution, as discussed below.

If the homogeneous illumination is replaced by a point-like source, a laser for example, diffusion length mapping of the wafer becomes possible. In this case the equations, discussed above, become approximations, because the carrier diffusion profile is no longer one-dimensional. However, the use of point-like illumination is not intended to give a better quantitative determination of  $L_D$ , but rather to produce a lateral resolution. The maximum obtainable resolution is determined by the diffusion profile of minority carriers. It is therefore in the order of the wafer thickness for the BPC mode and in the order of 50 μm for FPC measurements [Ca9]. This lateral resolution is much better than for any comparable technique, such as SPV [Go4], photoconductive decay (PCD) [De7], or microwave absorption [Na4, Ya8]. The use of a laser for illumination also enables fast scanning, which is not possible with other methods, for example a moving Hg drop used as a Schottky contact [Su5]. The lateral resolution of the technique was first demonstrated for wafers that had been intentionally contaminated with different metals [Le11], as shown, for example, in Fig. 10.6a. The diffusion length of the contaminated wafer was then measured for every square millimeter of surface inside the O-ring, using BPC mode. The observed values are represented by dots of different sizes. In the diffusion length plot, as shown in Fig. 10.6b, the contamination pattern is clearly visible.

The high spatial resolution of the technique enables identification of a source of contamination by the characteristic fingerprint left on the wafer. This is illustrated in Fig. 10.5, which shows lifetime maps of wafers contaminated in different ways. The concentric circles shown in Fig. 10.5a are caused by oxygen precipitates. The

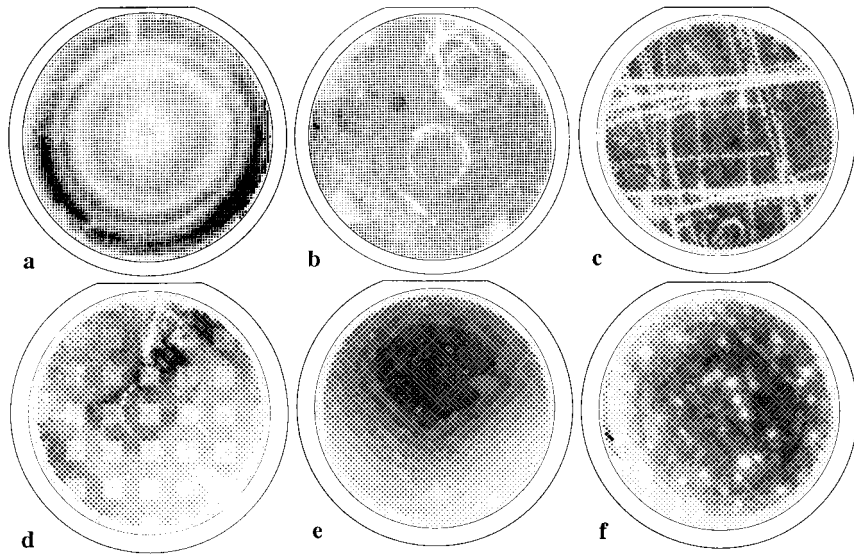


**Fig. 10.5** Diffusion length maps characteristic of certain sources of contamination. Each dot corresponds to one measurement, with dark regions representing areas of high diffusion length. (a) Concentric rings indicate oxygen precipitates caused by a high oxygen level

during wafer growth. Contamination induced by wafer handling: (b) vacuum tweezers, (c) transport belts, (d) wafer chucks, (e) boat contamination in the furnace, and (f) contamination by particulates.

oxygen originates from the crystal growth process and is therefore incorporated in a circular manner. Such precipitates can also be revealed by XRT, although diffusion length mapping has been found to be more sensitive. In contrast to such bulk contamination, surface contaminants show up only after a thermal drive-in process. This is visualized by the imprints of vacuum tweezers shown in Fig. 10.5b, which were detected on as-received wafers after an RTA step (1200 °C, 30 s). Other contamination sources present in a wafer fab and their characteristic fingerprints are shown in Fig. 10.5c–f. Even after the full device manufacturing process, contamination incorporated during processing can be resolved, if the top-most 10 μm of the wafer are removed prior to the diffusion length measurement.

The result described above generated sufficient interest for commercialization of this technique. The ELYMAT (electrolytic metal tracer) [21] is equipped with laser diodes (670 and 905 nm), two rotatable mirrors, and an electrolytic double cell. The time needed for 10000 single measurements, which are necessary for one wafer map, is in the order of a few minutes, with a lifetime measurement range of 0.01 to 10 μs in FPC mode and 10 μs to 1 ms in BPC mode [Ei1, Os1].

## 10.3.2

**Defect Mapping**

While the local variation of a laser-induced current can be used for diffusion length mapping, as discussed above, the local formation of hydrogen bubbles or metal plating can be used for defect mapping. The yield of a semiconductor fabrication process depends critically on the defect density of insulating layers such as an  $\text{SiO}_2$  or an oxide-nitride-oxide (ONO) dielectric. Average defect densities are in the order of  $1\text{--}1000\text{ cm}^{-2}$ , while the size of the actual defect is usually below a micrometer, as shown, for example, in Fig. 2.7a. The small size and the low density make it very difficult to find such defects by microscopic inspection only. It is more advisable to detect the electric current that flows through the defect. This can be done, for example, by a liquid crystal, which changes its reflection due to heating by the high local current. In an electrolyte the chemical reaction caused by the current through the defect can be sensed. For anodic currents the reaction at the defect is electrochemical etching, as discussed in Section 4.5, while for cathodic currents the defect is detected by metal plating or hydrogen bubble formation [Or1]. If an n-type wafer with an insulating oxide is immersed in an electrolyte, for example 10% acetic acid, and cathodically biased, hydrogen bubbles will form at defects in the oxide. For the case of a p-type wafer additional illumination is needed because it is under reverse bias. Such measurements can be performed in simple O-ring cells or in double cells, as shown in Fig. 1.7. In Fig. 10.6 the technique is demonstrated using an intentionally contaminated wafer. Oxide defects induced by mechanical damage or by copper contamination of the backside are clearly visible because they are decorated by hydrogen bubbles, as shown in Fig. 10.6e. Microscopic investigations have revealed that copper silicide precipitates penetrate the oxide [We4]. If a more permanent decoration is desirable the Pt counter electrode can be replaced by a copper plate. In this case the cathodic current at the defects leads to copper deposition and after a few minutes the copper crystallites become large enough to be identified [Ok2].

Defects in a SCR, which is present under reverse bias, can be tested in a similar way. Figure 10.6c shows the same wafer as in Fig. 10.6e after removal of the oxide and under cathodic polarization in the dark. Hydrogen bubbles caused by the dark current now decorate nickel silicide precipitates that short-circuit the SCR. Nickel precipitates are known to increase the dark current of a p-type Si electrode under reverse bias by orders of magnitude [Wa4]. If the bias is increased the copper silicide precipitates also become visible, as shown in Fig. 10.6d. This method, like defect etching (Fig. 10.4f), is only sensitive to precipitated metals. Metals that stay in solution, like iron, do not show up in defect mapping and have to be determined by other methods, for example diffusion length mapping.

If mapping of the defects is dispensable and only the average contamination level is of interest, measurements of the reverse dark current are sufficient to provide this information [Wi2]. This method is also applicable to n-type samples, which is in contrast to decoration of SCR defects by hydrogen bubbles, which is not possible in the anodic regime.

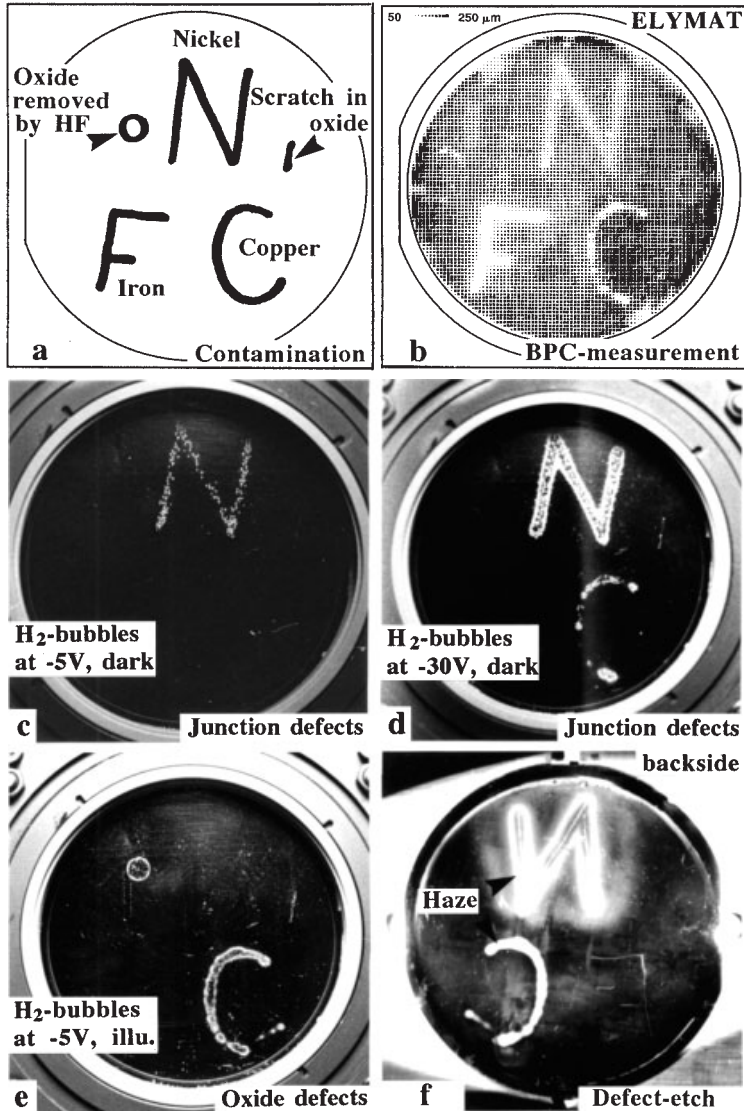


**Fig. 10.6** A p-type Si wafer with a 20 nm thick thermal oxide has been contaminated by scratching the backside with metal wires (Ni, Cu, Fe), according to the pattern shown in (a) and later annealed at 1200 °C for 30 s. (e) Under cathodic bias in acetic acid, oxide defects become decorated by hydrogen bubbles. (c, d) After oxide removal junction defects caused by metal precipitates are decorated by hydrogen bubbles, if sufficient catho-

dic bias is applied in the dark. (f) The removal of the precipitates by a defect etchant, like Secco etch [Se5], produces a surface roughness, visible as haze under small angle illumination (wafer backside is shown). (b) Non-precipitating metals, like Fe, have to be traced by other methods, e.g. diffusion length mapping. Scale:  $L_D=50\ \mu\text{m}$  (white) to  $L_D=250\ \mu\text{m}$  (black).

## 10.4

### Sensors and Biochips

Silicon-based sensors can be classified as physical, chemical or biological, depending on the parameter to be measured.

Sensors for measurements of physical parameters such as pressure, rotation or acceleration are commonly based on elongation or vibration of membranes, cantilevers or other proof masses. The electrochemical processes used to achieve these micromechanical structures are commonly etch-stop techniques, as discussed in Section 4.5, or sacrificial layer techniques, discussed in Section 10.7.

For the fabrication of chemical sensors, either the unique properties of the silicon electrode itself or a variation in PS properties with absorption of molecules at the large internal surface, are exploited for sensing. Both principles are addressed below.

#### 10.4.1

##### Hydrofluoric Acid Sensor

The HF tester is a commercial safety tool for sensing whether an unidentified liquid contains HF [2]. It shows in an exemplary way how the electrochemical properties of a silicon electrode, namely its I–V curve in HF, can be applied for sensing. The ability to dissolve an anodic oxide layer formed on silicon electrodes in aqueous electrolytes under anodic bias is a unique property of HF. HF is therefore the only electrolyte in which considerable, steady-state anodic currents are observed, as shown schematically in Fig. 3.1. This effect has been exploited to realize a simple but effective safety sensor, which allows us to check within seconds if a liquid contains HF. This is useful for safety applications, because HF constitutes a major health hazard in semiconductor manufacturing, as discussed in Section 1.2.

The electronic circuit of the safety sensor consists of a p-type silicon electrode, an LED, a resistor, two 3 V lithium batteries, and a platinum wire as a counter electrode, connected in series, as shown in the right part of Fig. 10.7. These components are assembled in a pen-like housing, optimized to measure even thin layers of liquid on a flat surface, as shown in the left part of Fig. 10.7. This configuration is advantageous if a puddle, observed for example under a wet bench or other equipment, is to be analyzed.

The working principle of the sensor is simple. If the tip of the sensor, which contains the electrodes, is immersed in a liquid free of HF, an anodic oxide is formed and the anodic current decreases within a second to very low values: the LED is off. For the case of a liquid containing more than 5% HF, a constant anodic current flows which is only limited by the series resistor and the LED emits with its maximum intensity. If the liquid contains between 0.5% and 5% HF the intensity of the LED becomes roughly proportional to the HF concentration. In contrast to other chemical sensors where the electrodes are very sensitive to contamination or drying, the HF sensor is quite robust. The sensor electrode can be

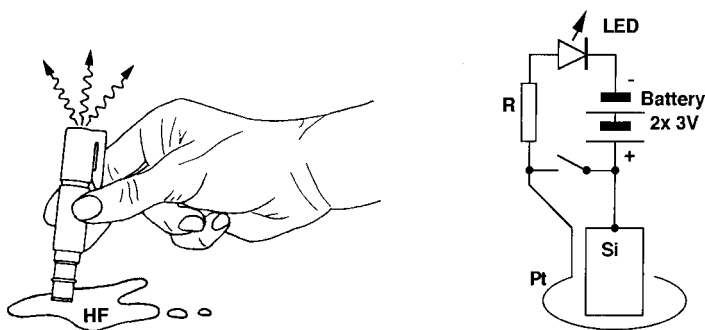


Fig. 10.7 The HF safety sensor (left) and its electronic circuit (right).

cleaned with acetone or even grinding paper if it is for example contaminated with oil or resist. Because the resistor limits the current, the etch rate at the electrode remains low even in highly concentrated HF and the lifetime of the electrode is in the order of 1000 tests.

The safety sensor, however, gives only qualitative information. For a quantitative determination of the concentration of HF in a solution, it is necessary to determine  $J_{PS}$ , which can be done by scanning the anodic potential from about 3 V to 0 V and measuring the relative current maximum in a unstirred solution. If  $J_{PS}$  and the temperature  $T$  are determined, the electrolyte concentration  $c$  can be calculated using Eq. (4.9). This method of determining the concentration of HF is superior to simple measurements of the conductivity of the solution, because it is insensitive to dissolution products of Si or  $\text{SiO}_2$ , or to other ionic species in the analyte.

#### 10.4.2

##### Porous Silicon-Based Gas Sensors

Chemical sensors based on changes in work function, refractive index, dielectric constant, PL intensity or resistivity of PS with absorption of chemical species, such as  $\text{H}_2\text{O}$ , NO,  $\text{NO}_2$ ,  $\text{Cl}_2$ ,  $\text{Br}_2$ , alcohols, ethers, aromatic and chlorinated hydrocarbons, have been proposed by several groups [Sa7, Wa6]. The sensitivity to adsorbates is usually discussed in terms of a change in surface charge by polar molecules, which produces a change in capacitance [An4] or resistivity [Bo7]. The observed decrease in resistivity, for example, has been attributed to detrapping of charge carriers from surface states, as discussed in Section 6.7 [Be6, St11, Le14]. A change in resistivity of a PS layer can easily be measured with a device structure as shown in the inset of Fig. 10.8. In this example of a sensor application, a 20–30  $\mu\text{m}$  thick meso PS film has been formed by anodization of a p-doped substrate ( $10^{19} \text{cm}^{-3}$ ) in ethanoic HF at  $10 \text{ mA cm}^{-2}$ . An oxide, serving as an insulating layer, has then been sputtered on top. After deposition of two Pt or Au contacts the resistivity can be measured between the two terminals. Figure 10.8

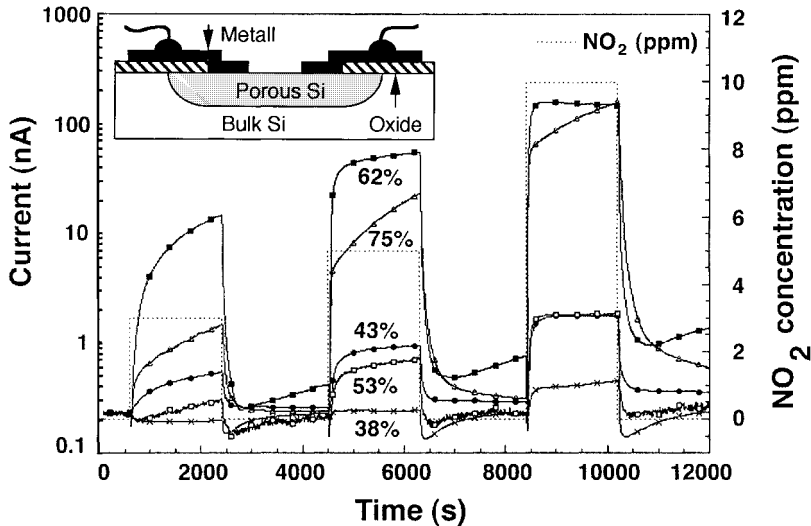


**Fig. 10.8** Dynamic response of meso PS gas sensors of different porosities to low concentrations of  $\text{NO}_2$ . Measurements were per-

formed at RT and 20% relative humidity. The structure of the sensor is shown on the upper left. After [Bo7].

shows the response to  $\text{NO}_2$  as a function of exposure time for meso PS layers of different porosity. While a significant increase in conductivity has been observed for an oxidizing species like  $\text{NO}_2$ , a decrease has been observed for exposure to a reducing gas like  $\text{NO}$ . At RT the sensor shows a high sensitivity – around 1 ppm for  $\text{NO}_2$  – and a moderate sensitivity of 5 ppm to  $\text{NO}$ . No response is observed to non-polar gases like  $\text{CO}$  and  $\text{CH}_4$ , up to levels of 1000 ppm. The ambient humidity level, however, affects the sensitivity of the sensor [Bo7].

The inability to differentiate between different gases, e.g.  $\text{NO}_2$  and water vapor, is one of the drawbacks of the resistive sensor approach described above. This problem can be circumvented by gas spectroscopy. The tunable light source needed for this method can again be achieved using PS. Figure 10.9 illustrates the working principle of the spectrometer. A broadband IR source illuminates a gas cell. Depending on the specific gas inside the cell certain bands in the IR are absorbed. By changing the tilt angle of the interference filter an IR spectrum is recorded by the thermopile detector.

The IR filter is realized by a PS layer with a modulation of porosity, which constitutes an interference filter as described in detail in the next section. The 30  $\mu\text{m}$  thick porous layer is then released from the substrate by electropolishing, which is easily done *in situ* by increasing the etching current density above  $J_{\text{PS}}$ . This process is commonly applied to form free-standing PS membranes and PS tubes [T]1]. The internal strain between the  $\text{Si}_3\text{N}_4$  layer used for masking and the porous layer lifts the filter up to its rest position, as shown in Fig. 10.10. The filter is suspended at two microactuator arms, which work as thermal bimorph actua-



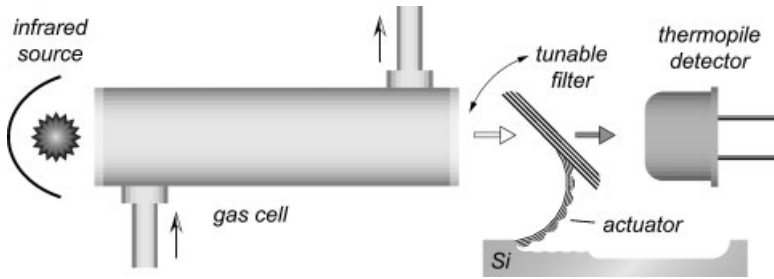


**Fig. 10.9** A MEMS IR gas spectrometer, which measures the IR absorption of a gas at different wavelengths selected by a tunable interference filter. After [La11].



**Fig. 10.10** SEM micrograph of a tunable IR Bragg filter ( $1.1 \times 1.85$  mm) of density-modulated PS, suspended at two microactuator arms. Its rest position is more than  $180^\circ$

out of plane, showing the remarkable flatness of the interface, which has been separated from the substrate by electropolishing. After [La11].

tors if heated by a current applied to the CrNi film that has been deposited on the arms. More than  $90^\circ$  deviation has been achieved with a DC power of 100 mW. It has been shown that the system is able to differentiate between gases even at low levels (for example 0.5% CO and 1% CO<sub>2</sub> in N<sub>2</sub>) [La9, La11].

The above examples show that it is possible to envisage the application of PS in electronic artificial nose chips [Le26].

## 10.4.3

**Biochips**

While silicon has for decades been the dominant material for electronic and micro-mechanical devices, it has only recently been used for medical and biological applications [St13]. PS is advantageous for some of these applications because of its large surface area. Micro and meso PS, for example, are found to be biocompatible materials that bond directly with healthy bone by calcification, which is an advantage if implantation in living tissue is desirable [Ca11] [23]. Because of its biodegradability and non-toxicity, mesoporous silicon doped with trace elements has been proposed to serve as an implanted long-term delivery source [Ca14] [23].

Other applications are aimed at using PS for sensing of biochemical compounds. It is well known that the CV characteristics of an electrolyte-insulator-semiconductor (EIS) structure can be used to sense the pH of a solution. A chemical reaction can therefore be sensed if it results in a change in pH. This principle has been successfully used to sense penicillin. First the enzyme penicillinase is immobilized on an  $\text{SiO}_2$ ,  $\text{Si}_3\text{N}_4$  passivated silicon surface enlarged by macropores. Then the analyte is brought into contact with the surface. The more penicillin present in the analyte, the more molecules are converted to penicilloic acid, resulting in a measurable decrease in pH near the sensor surface [Sc20].

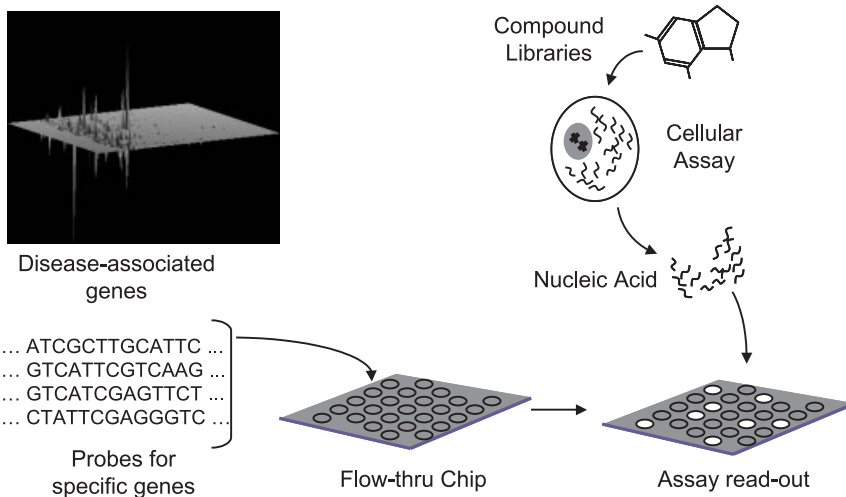


**Fig. 10.11** Schematic diagram of a drug screening concept. Disease-associated genes are identified using different display technologies. Probes for disease-associated genes are designed and are spotted onto the porous chip. Libraries of pharmaceutical compounds are screened against a validated cell model

system. Messenger RNA is collected from the cells and analyzed using the porous chip to determine efficiency of the drug against multiple gene targets. Hybridization events are detected by optical readout of the chip, as shown in Fig. 10.12. After [St12].

Another large area of biological applications of PS is micro array technology. The concept of fabricating miniaturized molecular assay systems that are capable of performing thousands of analyses simultaneously has its roots in the electronics and semiconductor chip industry. The arrangement of transistors, resistors and capacitors that make up electronic components on a silicon chip are analogous to an array of molecular recognition elements on a biochip. The state of each element on the biochip is determined by the abundance of the complementary analyte in a sample mixture. Molecular recognition events are translated into an analytical signal via a signal transduction mechanism, for example fluorescence, which is measured by some detection device. Biochip recognition elements and analytes can be small molecules, nucleic acids or proteins, such as ligand receptor's antibodies and enzymes. A comparison of the sizes of important biological building blocks and pore sizes in PS is given in Table 6.1.

Macro PS satisfies three major requirements of micro array technology: a large surface area for attachment, an intense contact between analyte and recognition elements, and a geometry that supports the optical readout [St12] [19, 24]. For this application macropores penetrating the full substrate thickness are required. Such through-pores can be obtained by etchback in KOH, if a CVD nitride is deposited inside the pores as etch stop layer prior to etchback. The recognition elements are usually spotted onto the chip and are attached to the pore walls by linker molecules. The analyte is then pumped through the pores, which guarantees intimate

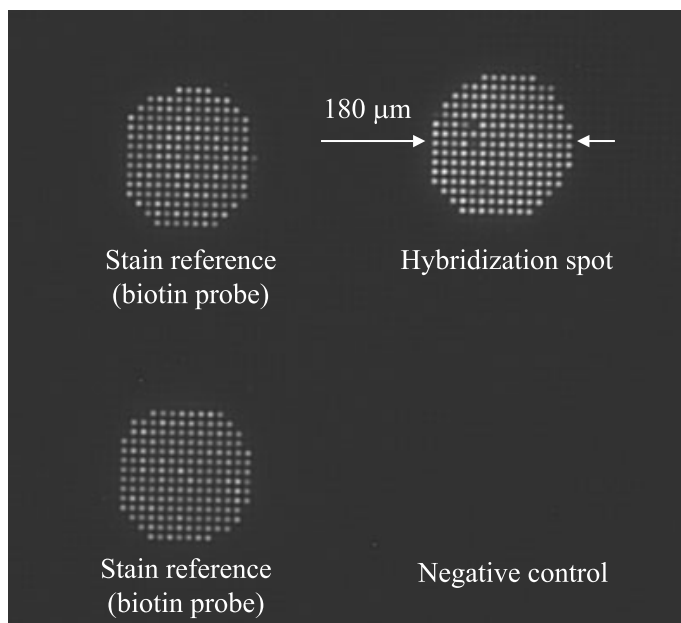


**Fig. 10.12** Chemiluminescence image of four spotted probes on a macroporous silicon-based flow-through chip after hybridization.

The total number of spots on a chip is in the order of 100–1000.

contact with the recognition elements. This reduces the time needed for hybridization by an order of magnitude compared to flat substrates. A schematic diagram of the application of a flow-through chip in drug discovery is shown in Fig. 10.11. For the final readout the macroporous silicon chip is illuminated with an excitation wavelength and the emanating fluorescent signal is recorded. An excitation source is not necessary if chemiluminescence readout is used, as shown in Fig. 10.12.

## 10.5 Passive and Active Optical Devices

PS layers formed by anodization of silicon in HF show a variety of interesting optical properties. For example, free-standing layers of micro PS behave like an optical long-pass filter, as discussed in Section 7.3. However, high-quality low-pass filters based on doped glasses are available for a multitude of cut-off wavelengths [17]. The property of macroporous silicon to behave as a short-pass filter for light transmission along the pores is of particular value, because it is difficult to produce high-pass filters for the visible regime. The different transmission properties of free-standing micro-, meso- and macroporous silicon films are shown on the lower left corner of the front cover of this book.

Optical filters with a well-defined transmission band can be manufactured by periodic variations of the dielectric constant. PS offers two ways to realize such periodic dielectric structures. Either variations in the optical density of meso- or microporous films can be exploited or the contrast of the dielectric constant between the air-filled core of a macropore and its solid wall can be exploited. Both approaches are discussed below.

However optical applications of PS are not restricted to passive devices. It has been shown that electroluminescent solid-state devices based on silicon are feasible.

### 10.5.1 Optical Short-pass Filters

Bulk silicon constitutes an optical long-pass filter, as shown in Fig. 7.6. The same is true for micro- and mesoporous silicon, for which the effective medium approximation (EMA) is valid in the visible regime. The dimensions of macroporous silicon are in the visible regime and the EMA becomes invalid.

To calculate the optical transmittance of a single macropore, it can be modeled by two opaque screens with an aperture of diameter  $d$  at a distance  $l$ , as shown in the inset of Fig. 10.13. For such an arrangement the ratio  $n_t$  of transmitted power to incident power of a wavelength  $\lambda$  can be approximated by

$$n_t = \pi^2 (d/2)^4 / (\lambda^2 l^2) \quad (10.11)$$

The short-pass characteristic of Eq. (10.11) is evident. Measurements of the spectral transmittance of macropore arrays with the pore axis parallel to the inci-

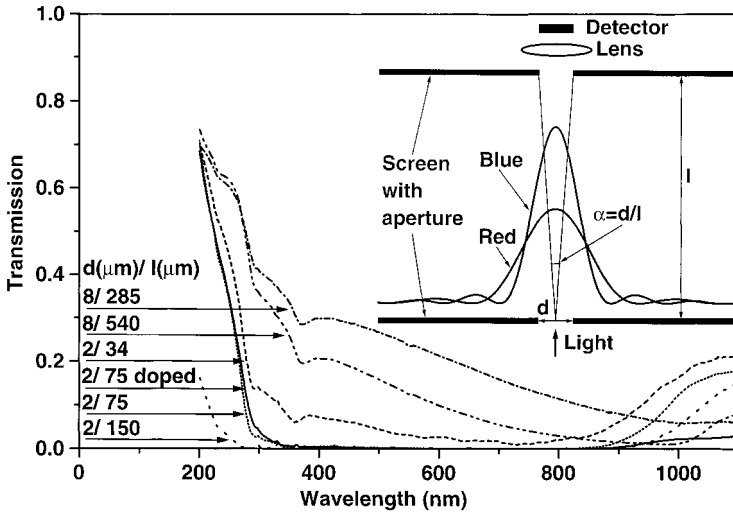


Fig. 10.13 The measured transmittance of macropore arrays of pore diameter  $d$  and pore length  $l$ , with the pore axis parallel to the light beam. The data are corrected for porosity ( $p=1$ ). The transmittance of a single

macropore can be calculated assuming two opaque screens with an aperture of diameter  $d$  at a distance  $l$ , as shown in the inset. After [Le27].

dent light beam confirm these calculations, as shown in Fig. 10.13. The dips in the transmission characteristic at 290 and 370 nm have been interpreted as reminiscent of the direct transitions in bulk silicon, which indicates that the assumption of zero reflection inside the pores is not justified.

Optical short-pass filters based on macropore arrays show several advantages compared to conventional filters: macropore filters are true short-pass filters, because light is transmitted in empty space, not in matter. As a result, functionality down to wavelengths in the order of a few nanometers is expected if operated in vacuum. The cut-off wavelengths can simply be tuned by pore diameter and pore length. Despite the fact that light is diffracted at the pore entrance and the pore exit, the macropore filters are of optical quality because of constructive interference between the high number of pores in an array [Le27].

### 10.5.2

#### Dielectric Thin Films

The structural features of micro- and mesoporous silicon are much smaller than the wavelength of visible light, and so these materials may be treated according to the EMA. The dependence of the porosity of micro- and mesoporous silicon on formation current density and substrate doping density can be used to generate layers with a single or a periodic change in the dielectric constant.

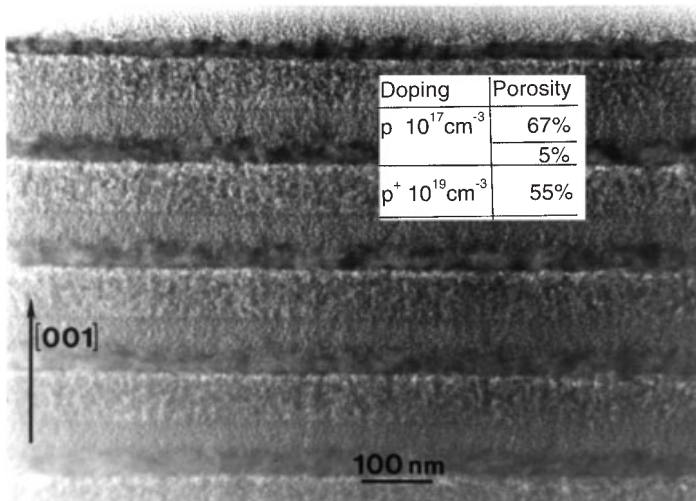


**Fig. 10.14** TEM cross-sectional micrograph of a one-dimensional porosity superlattice. Anodization was performed on a periodically p-doped substrate (75 nm of  $10^{17} \text{ cm}^{-3}$ , 75 nm of  $10^{19} \text{ cm}^{-3}$ ) using a current density of

$50 \text{ mA cm}^{-2}$  in ethanoic HF. Values of porosity as labeled are determined by measurements of spectral reflectivity, shown in Fig. 10.15. After [Fr5].

A single layer of a micro PS film on a silicon substrate always reduces its reflectivity, because of its lower refractive index compared to bulk Si. Hence micro and meso PS films of a thickness around 100 nm have been proposed as anti-reflective coatings for solar cells [Pr8, Gr9, Po1, Bi4, Sc18, St10].

The dependence of PS porosity on doping density has been exploited to fabricate optical waveguides. Such structures require only a single variation of refractive index. If a p-type substrate with implanted  $p^+$  lines is anodized and partially oxidized, mesoporous lines of high refractive index are embedded in a low refractive index material. An obtained refractive index contrast between core and clad of 30% is promising for future applications [Ta12].

A substrate with a periodic variation of the doping density can be formed by epitaxy. If such sandwich structures are anodized under constant current conditions a surface film with periodic variations of refractive index is obtained. Such a porosity superlattice formed by anodization of a sample with epitaxially grown layers of high and low p-type doping density is shown in the TEM micrograph of Fig. 10.14. The optical reflectance spectra of such periodic layered structures exhibits characteristic transmission and reflection bands as shown in Fig. 10.15 [Be16]. It is worth noting that the TEM micrograph, as well as the simulation of the density distribution from the reflectance spectra, as given in the inset of Fig. 10.15, reveals a more complex structure than expected from the simple bilayer doping scheme, as discussed in detail in Section 8.1.

Another way of producing periodic porosities is a variation of anodization current density. Drawbacks of this approach are a certain roughness of the different

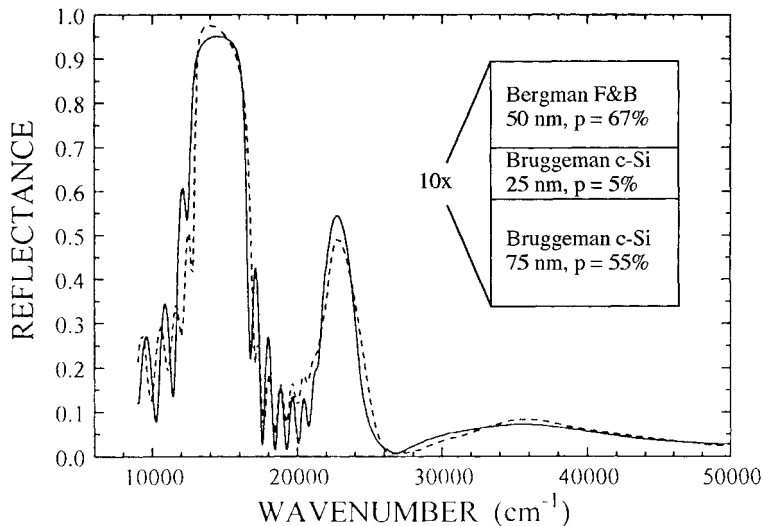


**Fig. 10.15** Measured reflectance spectrum (solid line) of 10 periods of the superlattice shown in Fig. 10.14. The fit (broken line) has been calculated based on porosities shown as in the inset. For the 67% porosity layer the

Bergman effective medium theory, in conjunction with a model dielectric function for the particles, has been used. For the other layers the Bruggeman effective medium theory was used. After [Be16].

layers, which increases with etch depth and the limited range of obtainable porosities. For  $p^+$  type substrates the porosity of the mesoporous layer can be varied from about 30% to 75%, corresponding to current densities between 10 and 240  $\text{mA cm}^{-2}$ , while for moderately doped p-type substrates, this range is considerably smaller (60–75%). The roughness has been ascribed to lateral variations of PS growth rate [Fr5].

An optical microcavity produced by the latter process has been applied to tune the emission from erbium-doped PS [Zh6]. Erbium compounds like  $\text{Er}_2\text{O}_3$  are known to exhibit a narrow emission band at 1.54  $\mu\text{m}$ , which is useful for optical telecommunications. Several methods have been used to incorporate erbium in PS. A simple and economical way is cathodic electrochemical doping. External quantum efficiencies of up to 0.01% have been shown from erbium-doped PS films under electrical excitation [Lo2]. The emission band, however, is much broader than observed for  $\text{Er}_2\text{O}_3$ . This drawback can be circumvented by the use of an optical cavity formed by PS multilayers. In this case the band is narrowed and the intensity is increased because emission is only allowed into optical cavity modes [Lo3].

In conclusion, it has been demonstrated that the manufacture of waveguides, Bragg reflectors, Fabry-Perot filters and anti-reflective coatings can be based on PS thin films. Such filters are applied for example in gas sensors, as described in the preceding section.

## 10.5.3

**Photonic Crystals**

The periodic structures discussed so far are one-dimensional. This is an inevitable property of the formation method, which produces layers parallel to the surface. The periodicity of macropore arrays offers a method for varying the dielectric constant in two dimensions. This, and the high contrast in the dielectric constant, which is 11.7 for the pore walls and 1 for the air-filled pores, enables us to fabricate a photonic crystal with a complete two-dimensional photonic bandgap in the IR regime [Gr8]. A photonic bandgap is a frequency range where photons are not allowed to propagate. The propagation of photons in the periodic dielectric lattice of a photonic crystal is analogous to the propagation of electrons in the periodic potential of a semiconductor crystal, with the difference that the Coulomb interaction of electrons has to be considered while photon interactions can be neglected. The Brillouin zone of a triangular lattice, together with the calculated photonic band structure for a lattice constant of  $2.3\ \mu\text{m}$  and H-polarization, is shown in the center of Fig. 10.16.

The manufacture of a photonic crystal requires extreme process control because a deviation from perfect periodicity in the order of a few percent of the wavelength worsens the optical performance. Macroporous silicon is a potential candidate for the realization of such structures because of its photolithographic patterning. The precision of the macroporous structures is reflected in the transmission measurements along the  $\Gamma$ -M and  $\Gamma$ -K directions, which exhibit a photonic bandgap centered at  $5\ \mu\text{m}$ , as shown in Fig. 10.16. For measurement the macroporous

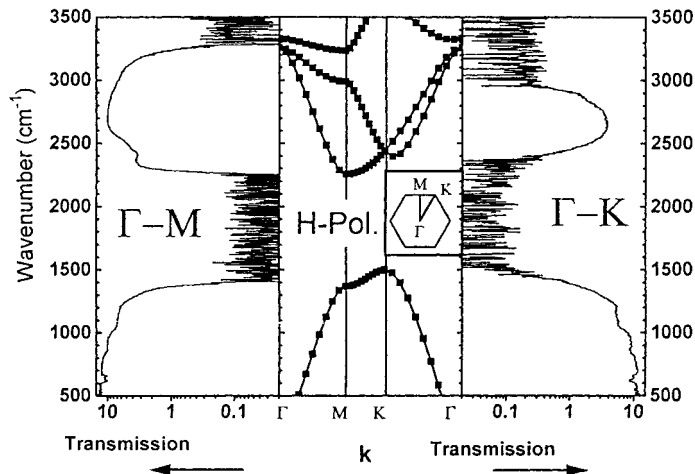


**Fig. 10.16** In the center part, the calculated photonic band structure (TE-pol.) of a two-dimensional photonic crystal of lattice constant  $2.3\ \mu\text{m}$  is plotted, while the inset shows the

first Brillouin zone. On the sides the measured transmission spectra of the macroporous film for the  $\Gamma$ -M and  $\Gamma$ -K directions are shown. After [Gr8].



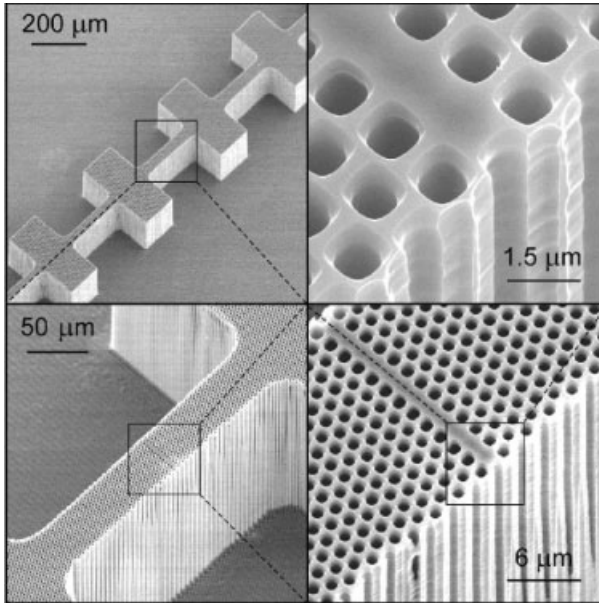


**Fig. 10.17** Microstructured bar of macroporous silicon with a waveguide oriented in the  $\Gamma$ -K direction. The triangular lattice of pores

cladding the waveguide has a pitch of 1.5  $\mu\text{m}$ , producing an optical bandgap ranging from 3.3 to 5.5  $\mu\text{m}$ . After [Le28].

layer has been structured into bars, as shown for example in Fig. 10.17, by a second photolithography and subsequent plasma etching [Ot2].

The use of photolithography to determine the pore positions enables us to create artificial defects in the photonic crystal. By leaving out a row of pores, for example, propagating modes confined within the defect can be created for frequencies within the photonic bandgap. Such a line defect can therefore act as a waveguide, with the confinement achieved by means of the photonic bandgap and not by total internal reflection as in traditional waveguides. It has been shown that the line defect as shown in Fig. 10.17 exhibits a single-mode transmission characteristic [Le28].

A review of silicon-based photonic crystals is available in the literature [Bi6].

#### 10.5.4

#### Electroluminescent Devices

The majority of application-related work exploiting the visible PL from PS is aimed at the fabrication of electroluminescent solid-state devices. Only a few other applications of the PL of PS, e.g. the use of luminescent PS for fluorescent labels in biosensing [Ak1] or for chemical sensing [Le26], have been proposed. This section therefore focuses on PS-based EL devices. Note that EL from porous structures using wet contacts is discussed in Section 7.4.

Shortly after the observation of visible PL from micro PS at room temperature [Ca1], the first EL from a solid-state device was reported [Ri2]. This initiated vigorous research, because silicon-based optoelectronic devices seemed to be within reach. After several years of intense research the potential and the main problems involved with the EL from PS have been clarified.

The external quantum efficiency of the EL from PS-based devices has been increased from low initial values of 0.001% [Ko9] to values close to 1% [Ni4, La6, Co5]. This, however, is still about one order of magnitude smaller than the maximum quantum efficiency of state-of-the-art LEDs based on III–V semiconductor heterostructures.

For data transfer applications the modulation speed of an emitter is a decisive parameter. Here the long lifetime of the excited state in PS becomes problematic. The fall time of the EL is usually in the  $\mu\text{s}$  regime, while somewhat shorter values are reported for the rise time. Only for devices based on OPS has a significantly shorter fall time (0.03  $\mu\text{s}$ ) been reported [Wa10]. For small signal modulations of the EL from PS, frequencies in the order of 1 MHz are reported [Ts4, Co5]. Such modulation frequencies are sufficient for display applications. For data transfer via optical interconnects, however, they are much too low.

The requirements for spectral position and width of the EL emission depend strongly on the application. While for display applications the three colors blue, green and red are crucial, compatibility with the waveguide technology and the detector are more important for data transfer. The FWHM of the EL from PS is usually in the range 0.2–0.4 eV. Peak emission wavelengths in the red are usually reported from electrochemically and stain-etched films [Xu3]. However, wavelengths from 450 to 700 nm have been reported for porous layers that have been illuminated during anodization [St5].

The threshold voltage, the lowest voltage at which EL is observed, has been drastically reduced from values in the order of hundreds of volts to values as low as about 3 V for visual detection [Si4]. The threshold current density is usually in the order of  $\text{mA cm}^{-2}$ , however values as low as  $10 \mu\text{A cm}^{-2}$  have been reported to be sufficient for visual detection of the EL [Si4].

The long-term stability of devices based on as-prepared PS films is generally poor. Under emission conditions the degradation is measured usually in minutes or hours. The stability of devices based on chemically [Ko18], anodically [Ge11] or thermally oxidized PS films [It4] is usually better; however the standard lifetime requirement for microelectronic devices ( $>10^5$  h) has not been met.

The different parameters of EL discussed above illustrate that considerable advances have been made, but more are still needed to meet today's specifications for EL devices. So far the basic properties of EL devices have been discussed. For details of the EL device structure, including contact type, doping and geometry, a comprehensive review is available [Co4].

## 10.6

### Porous Silicon-Based Electronic Devices

The material properties of PS offer new ways of making electronic devices. For the manufacture of cold cathodes, for example, oxidized microporous polysilicon has been found to be a promising material. The application of basic semiconductor processing steps such as doping, oxidation and CVD to a macroporous material enable us to fabricate silicon-based capacitors of high specific capacitance. Both devices will be discussed below.

#### 10.6.1

##### Cold Cathodes

In many electronic applications, e.g. vacuum tubes, an electron emitting cathode is an indispensable part of the device. For many such devices cold electron emission is favorable because of its lower energy consumption.

In an early study of electron emission from PS it was proposed that the observed emission is caused by extremely sharp silicon tips present at the interface between PS and bulk silicon [Yu3], thus assuming PS to work by the same principle as conventional field emitting arrays [Sp1]. However, later studies indicate that ballistic transport through the porous layer is more likely [Ko20, Sh4, Ko21]. This is supported by time-of-flight (TOF) measurements, which show that the drift length of carriers under a strong electric field ( $10^5 \text{ V cm}^{-1}$ ) within a PS layer may reach  $1 \mu\text{m}$  [Kl4].

A schematic view of the cold cathode fabrication process is shown in Fig. 10.18. The cold cathode is fabricated by low pressure chemical vapor deposition (LPCVD) of  $1.5 \mu\text{m}$  of non-doped polysilicon on a silicon wafer or a metallized glass substrate. The topmost micrometer of polysilicon is then anodized ( $10 \text{ mA cm}^{-2}$ , 30 s) in ethanoic HF under illumination. This results in a porous layer with inclusions of larger silicon crystallites, due to faster pore formation along grain boundaries. After anodization the porous layer is oxidized ( $700^\circ\text{C}$ , 60 min) and a semi-transparent (10 nm) gold film is deposited as a top electrode.

If a sufficient bias is applied between the metallized glass and the Au electrode, an electron emission current  $I_e$  can be observed, as shown in Fig. 10.19a. A Fowler-Nordheim plot of the emission current, shown in Fig. 10.19b, indicates that field-induced tunneling occurs during electron emission from the porous polysilicon. The emission has been found to be homogeneous over the emitting surface and to be stable over time. Spike-like fluctuations of the emission current, as commonly observed for field-emission devices, have not been found. The stability of operation has been ascribed to a quasi-ballistic drift of electrons in the porous layer. This may also be the cause of the low sensitivity of the emission current against variations in vacuum quality, of up to 10 Pa for Ar,  $\text{N}_2$  or  $\text{O}_2$ .  $I_e$  may reach values in the  $\text{mA cm}^{-2}$  range and efficiencies in the order of 1%. The feasibility of a  $20 \text{ cm}^2$  multicolor matrix panel with a porous polysilicon cold cathode has been demonstrated, which is promising for application of this technique in future large flat panel displays [Ko23].

**Fig. 10.18** Schematic view of the fabrication process of a porous polysilicon-based cold cathode. Note that metallized glass may also serve as a substrate. Redrawn from [Ko21].

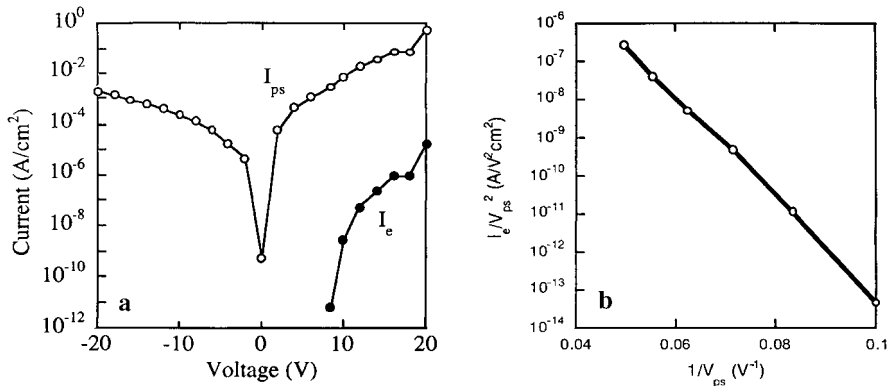
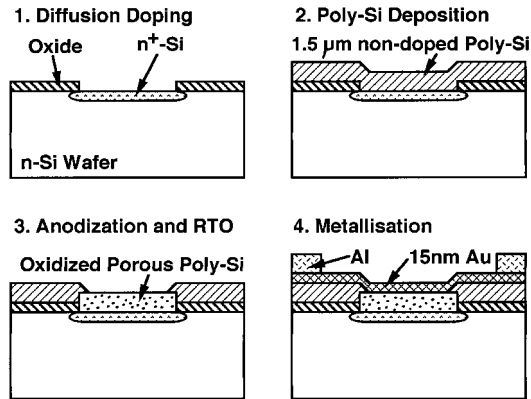


**Fig. 10.19** (a) Current-voltage characteristic of the cold cathode according to the circuit shown in Fig. 10.18. (b) A Fowler-Nordheim plot indicates that the emission current is caused by tunneling of electrons. After [Ko21].

10.6.2  
**Silicon Capacitors**

Since the invention of the Leiden jar in 1745 there has been tremendous progress in capacitor technology; in particular, capacitance-to-volume ratios have been increased by orders of magnitude. But today's capacitors still suffer from a few drawbacks: either one selects a superior dielectric like polystyrene or SiO<sub>2</sub> and has to cope with low surface-to-volume ratios of the electrodes or one increases the electrode area by etching or sintering techniques and has to accept the disadvantages of anodically formed oxides, which is the case for aluminum or tantalum capacitors. Ceramic dielectrics have been developed to solve this problem by increasing the dielectric constant instead of the electrode area. A drawback of this approach is the strong temperature and electric field dependence of the dielectric constant in these materials. A solution to these problems is offered by a capacitor

concept based on macroporous silicon that combines an electrochemically enlarged electrode surface with a superior dielectric; this device has been termed SIKO [Le18] [19].

A macroporous silicon substrate with pores of about a micrometer and a pore depth of a few tenths of a millimeter offers a surface area enhancement of about two or three orders of magnitude compared to an unetched silicon surface. An example of such a macroporous substrate used for fabrication of a silicon capacitor (SIKO) is shown in Fig. 10.20 b.

All process steps after electrochemical etching are standard techniques in micro-electronic manufacturing. The porous part of the low doped n-type substrate is highly doped using a phosphorus silicate glass (PSG) diffusion process ( $n^+$  region in Fig. 10.20d). After removal of the PSG layer by wet etching, an ONO dielectric is formed inside the pores. For the device as shown in Fig. 10.20, the ONO consists of 5 nm of a thermally grown  $\text{SiO}_2$ , 20 nm of CVD  $\text{Si}_3\text{N}_4$  and 5 nm of  $\text{SiO}_2$  formed by thermal oxidation of the  $\text{Si}_3\text{N}_4$ . The second electrode of the capacitor is realized by CVD of a phosphorus-doped polysilicon film. The two contacts to the electrodes can either be realized separately on the front- and backside of the chip or both on the top side using patterned Al or Au layers. In the latter case the substrate contact is realized by removing the poly-Si and the ONO in the contact area by lithography and etching. A few microns of aluminum are sputtered onto the surface to provide the pads for bonding, as shown in Fig. 10.20 a.

The electrical characteristics of the SIKO are summarized below. The specific capacitance of the device shown in Fig. 10.20 is close to  $4 \mu\text{FV mm}^{-3}$ , and with smaller designs values of up to  $20 \mu\text{FV mm}^{-3}$  are feasible. The range of manufacturable capacitance is not only a question of chip size but also of defect density of the ONO. Surprisingly, a defect density of  $<10^{-3} \text{ cm}^{-2}$  has been observed for the porous structure, which is much smaller than the defect density of planar ONO layers, which is in the order of  $0.1 \text{ cm}^{-2}$ . This low defect density can be understood if the defect density of planar films is assumed to be due to particles that do not penetrate into the pores.

The remarkable stability of the capacitance of the SIKO against variations in bias, temperature, frequency and time of operation is a consequence of the superior properties of its ONO dielectric. In contrast to aluminum and tantalum capacitors, the SIKO is a symmetrical device. It shows no significant voltage dependence of the capacitance, as the high  $\epsilon$  ceramic capacitors do. Only polymeric capacitors show a lower dependence of capacitance on bias than a SIKO.

The change of capacitance in relation to the temperature is very small and a linear function of the substrate temperature. Unlike the change in metal film capacitors it is completely reversible. The maximum operating temperature of the capacitor chip (more than  $200^\circ$ ) is determined by its aluminum gate. For encapsulated systems the bond contacts and the material of the package will determine the upper temperature limit.

The change of capacitance in relation to frequency is a matter of the polarizability of the dielectric. This change is very large for ceramics and large for most polymer dielectrics, but very small for  $\text{Si}_3\text{N}_4$  and  $\text{SiO}_2$ .

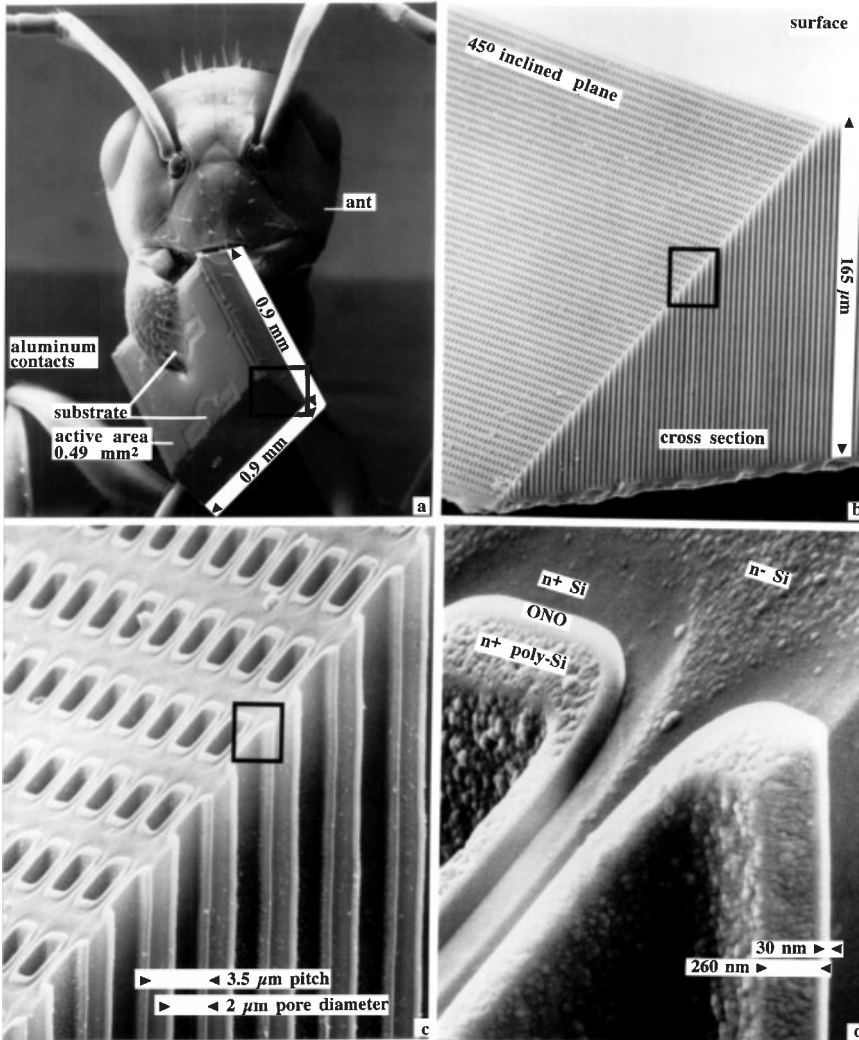


**Fig. 10.20** The SIKO chip with its aluminum contacts to the substrate and the active area is shown together with the head of an ant for size comparison. One side of the chip was beveled in order to reveal the details. (b) Ten-fold magnification of the marked area in (a) shows a rectangular array of pores generated

by electrochemical etching. (c) Hundred-fold magnification reveals the homogeneity of pore diameters and spacings. (d) Thousand-fold magnification shows the heart of the capacitor: a highly doped substrate and polysilicon layer with a thin ONO dielectric in between.

For ceramic capacitors there is a continuous decrease of capacitance with time. The higher the dielectric constant, the higher is this decrease. In metal film capacitors the best values given for 63 V capacitors are changes of 0.5% in 2 years. The SIKO shows the same long-term stability of the capacitance as the trench capacitors in DRAMs.

The dissipation factor of capacitors at high frequencies is determined by the series resistance. For low frequencies there may be losses caused by leakage currents as well as by slow components in the polarizability, especially of high  $\epsilon$  ceramics and polymer dielectrics. The dissipation factor of the SIKO at room temperature is below  $10^{-4}$ . At  $200^\circ\text{C}$  it is still very low ( $2 \times 10^{-4}$ ).

The ohmic series resistance is determined by the geometrical layout of the capacitor as well as by the conductance of its electrodes. The electrochemically etched array of straight pores produces a comb-like electrode structure and gives very low values of electrical series resistance (ESR) for the capacitor chip.

## 10.7

### Sacrificial Layer Applications

Despite the fact that dry etching techniques have improved dramatically in recent decades, the manufacture of microelectromechanical systems (MEMS) is still a domain of wet etching and silicon electrochemistry. The multiplicity of structures that can be achieved with silicon, together with its excellent mechanical properties [Pe6], have led to an immense variety of micromechanical applications.

In the manufacture of micromechanical devices electrochemistry is commonly used to realize etch stop structures or to form porous layers. The first of these is discussed in Section 4.5. In the latter case, the use of PS as a preserved layer or as a sacrificial layer can be distinguished. In the first case PS is an integral part of the ready device, as discussed in Sections 10.4 to 10.6, while in the latter case the PS serves as a sacrificial layer and is removed during the manufacturing process.

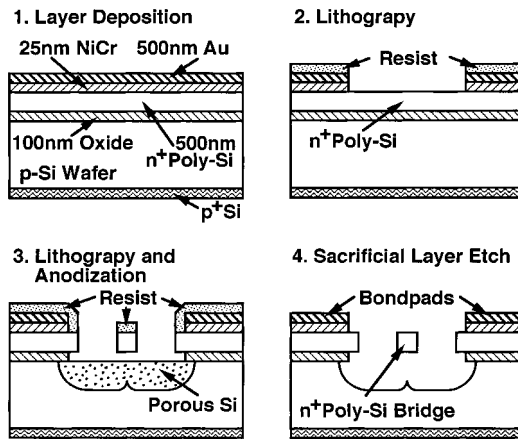
#### 10.7.1

##### Microporous Silicon

Microporous silicon is suitable for sacrificial layer applications because of its high etch rate ratio to bulk silicon, because it can be formed selectively, and because of the low temperatures required for oxidation. PS can be formed selectively if the substrate shows differently doped areas, as discussed in Section 4.5, or if a masking layer is used. Noble metal films can be used for masking as well as  $\text{SiO}_2$ ,  $\text{Si}_3\text{N}_4$  and SiC. Oxidation conditions are given in Section 7.6, while the etch rates of an etchant selective to PS are given in Fig. 2.5 b.

The use of micro PS as a sacrificial layer is illustrated by the fabrication of a free-standing polysilicon bridge, as used for example in a hot-wire anemometer [St6]. The process sequence is depicted in Fig. 10.21. A sandwich of thermal  $\text{SiO}_2$ , n-type poly Si, NiCr and Au is deposited on a moderately doped p-type Si substrate. After producing these layers, micro PS is formed under the poly Si bridges by anodization in an electrochemical double cell, as shown in Fig. 1.8. The PS is then removed by KOH etching at RT. The resulting structure is shown in Fig. 10.22. By bonding another silicon wafer with a similar groove on top of the

**Fig. 10.21** The process steps for the fabrication of a free-standing poly Si bridge. After [St6].



structure a closed channel is formed. The use of a PS sacrificial layer is advantageous compared to conventional alkaline etching because in the prior case there are no geometrical restrictions due to crystal orientation. This decreases the required chip area and thereby reduces production costs [He5].

For applications where micro PS is transformed into SiO<sub>2</sub> it can be argued that micro PS is not truly a sacrificial layer. However, the application described next has been included in this section for the sake of completeness.

The doping dependence of the PS formation process and the possibility of transforming PS to SiO<sub>2</sub> at relatively low temperatures can be used to form dielectrically isolated silicon islands [Ho1, Im1]. This process is also known as full isolation by oxidized porous silicon (FIPOS). The process sequence is shown in Fig. 10.23. First a p-type wafer with a nitride layer patterned by a resist is implanted by boron ions to form highly doped p-type regions in the unmasked areas. After resist removal, protons are implanted through the nitride film. After annealing at 500°C n-type regions are formed under the nitride film by the implanted protons. The proton dose, however, is not sufficient to reverse the doping

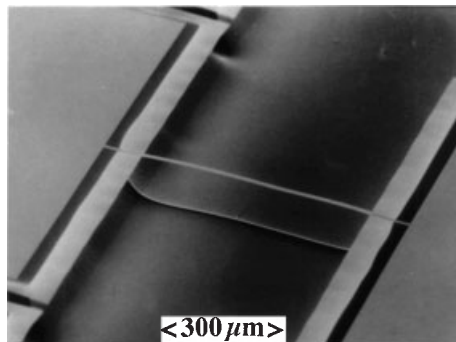


**Fig. 10.22** SEM micrograph of the 500 nm thick polysilicon bridge (straight line, center) that is the heart of the hot-wire anemometer. The bridge crosses a 80 μm deep groove produced by a micro PS sacrificial layer. After [St6].



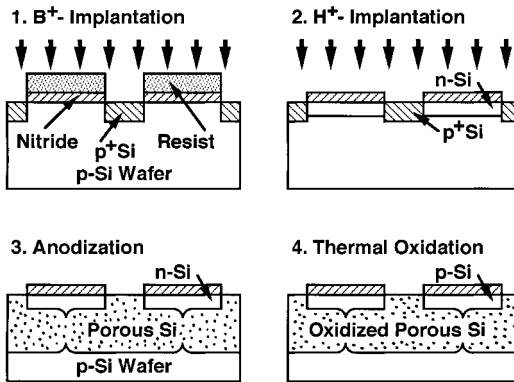


Fig. 10.23 Fabrication of a silicon island using the FIPOS process. Redrawn from [Im1].

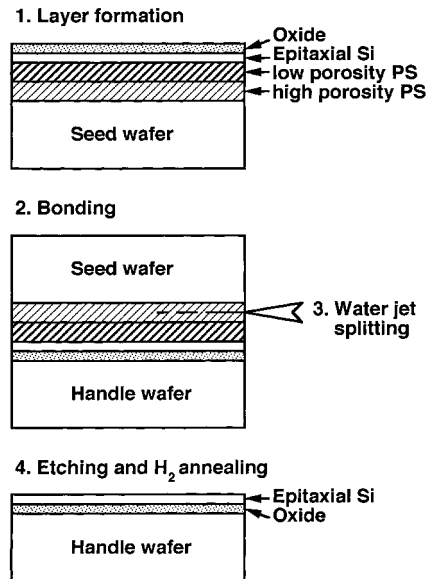
of the heavily doped p-type regions. These areas, as well as the p-type substrate, are then converted into PS by anodization in HF, while the n-type regions remain unetched. Finally the PS is oxidized at 1050°C in wet oxygen. At this temperature the protons diffuse away and the isolated islands resume the initial p-type doping of the bulk silicon wafer. The feasibility of the FIPOS approach has been demonstrated by successful application of a complementary metal oxide semiconductor (CMOS) process to such FIPOS substrates [Im1]. A drawback of this approach is the limited size of the islands, because of the under-etching required.

### 10.7.2

#### Mesoporous Silicon

A method of producing an SOI structure that circumvents the shortcomings of the FIPOS process described above, is based on the use of mesoporous silicon as a sacrificial layer. In mesoporous silicon the perfect bulk lattice is preserved, while the oxidation rate and the etch rate are only somewhat lower than for micro PS. These properties favor meso PS as a sacrificial layer for production of SOI material [Sa3, Sa8]. The process sequence is depicted in Fig. 10.24. A heavily doped seed wafer is anodized to form 4 μm of low porosity meso PS on top of a high porosity meso PS layer of about the same thickness. A pre-bake in H<sub>2</sub> (900–1040°C) forms a continuous silicon film at the surface, by filling the pore openings with migrating silicon surface atoms. This pre-bake reduces the defect density of the subsequently deposited epitaxial silicon layer (0.5–2 μm thick) significantly. After forming a thin thermal oxide on top of the epitaxial layer, the wafer is bonded to a handle wafer and annealed to increase the bonding strength. Using a water jet the two bonded wafers are then cleaved at the weakest interface, which is the high porosity meso PS. Thus the epitaxial layer has been transferred to the handle wafer. By selective chemical etching, e.g. in a mixture of HF and H<sub>2</sub>O<sub>2</sub> at RT, the remaining PS is removed. A final H<sub>2</sub> anneal smoothes the surface of the epitaxial silicon film. Advantages of this process are the reusability of the seed wafer and the freedom to choose the silicon film thickness, from ultra

**Fig. 10.24** Process for the fabrication of the SOI wafer based on meso PS. Redrawn from [Sa3].



thin (< 50 nm) up to several micrometers. This technique has been commercialized under the name ELTRAN (epitaxial layer transfer) [22]. A similar technique has been proposed for the fabrication of low-cost monocrystalline Si photovoltaic thin film cells [Br8].

### 10.7.3

#### Macroporous Silicon

One of the remarkable properties of macroporous silicon is the straightness of its pores. This property makes macropore arrays a perfect template for forming other materials with the same geometric precision. An example of such a process is the fabrication of anti-scatter grids for radiology applications. In radiology, a collimator located between the patient and the photographic plate is used to absorb scattered X-ray photons, which otherwise would blur the image. Such collimators are termed anti-scatter grids. Conventional grids consist of alternating layers of lead as the absorbing medium, together with paper or aluminum coupled together. As a result of this fabrication process the number of lines per millimeter and their precision are limited, which reduces the resolution of the image and has become a limiting factor in the performance of today's radiology system.

In order to circumvent these shortcomings, a fabrication process based on macro PS as a sacrificial layer has been proposed [Le30]. The process sequence is shown in Fig. 10.25. First etch pits in the desired pore pattern are formed on the n-type silicon wafer surface by photolithography and subsequent alkaline etching. Then deep macropores are formed by electrochemical etching according to the

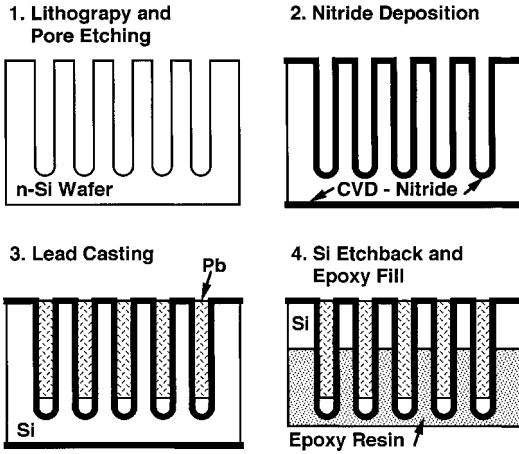


Fig. 10.25 Schematic view of the fabrication process for macro PS-based anti-scatter grids. Redrawn from [Le30].

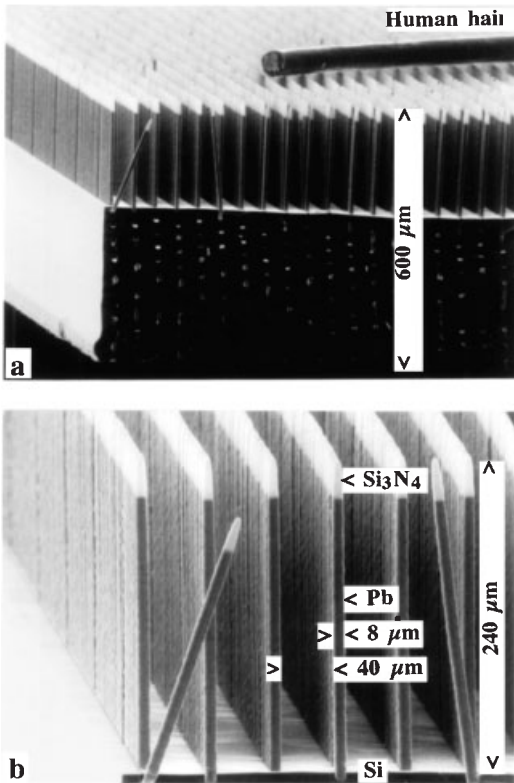


Fig. 10.26 (a) SEM micrograph of a silicon wafer with lead-filled macropores after etchback of 265  $\mu\text{m}$  of bulk Si. (b) The lead pillars are arranged in closely spaced lines (pitch: 16  $\mu\text{m}$ )

in one direction and a large spacing (pitch: 48  $\mu\text{m}$ ) in the other direction. Because of volume reduction of the lead during solidification, the pore tips remain empty. After [Le30].

process described in Chapter 9. A nitride layer is then deposited by CVD. Next the pores are filled with liquid lead under pressure. Then the wafer is cooled down to RT and the lead is solidified. After removal of the nitride on the wafer backside, about half of the wafer thickness is etched back in hot KOH. An SEM image of a sample at this stage of the fabrication process is shown in Fig. 10.26a and b. In this stage of the process the CVD nitride serves not only as an etch stop but also as a mechanical support for the soft lead pillars. The fragile structure of free-standing pillars is then further stabilized by an epoxy resin. If desired a repetition of etchback and epoxy fill generates lead pillars in an epoxy matrix. This is favorable for radiology applications in the low-energy regime (30 keV) where the silicon absorption is undesirably high.

## Appendices

### List of Symbols and Constants

$A$	area
$a$	lattice constant ( $a_{\text{Si}} = 0.543095 \text{ nm}$ )
$\alpha$	absorption coefficient
$\beta$	exponential factor
$C_{\text{PS}}$	constant
$C$	capacitance
$c$	concentration
$c_{\text{F}}$	fluoride concentration
$D$	substrate or film thickness
$D_{\text{e}}$	diffusion coefficient of electrons (in Si: $36.8 \text{ cm}^2 \text{ s}^{-1}$ )
$D_{\text{h}}$	diffusion coefficient of holes (in Si: $12.4 \text{ cm}^2 \text{ s}^{-1}$ )
$D_{\text{HF}}$	diffusion coefficient of HF (in $\text{H}_2\text{O}$ : $10^{-5} \text{ cm}^2 \text{ s}^{-1}$ )
$d$	diameter (of pore or crystallite)
$E$	electric field strength
$E_{\text{BD}}$	breakdown field strength (for Si: $3 \times 10^5 \text{ V cm}^{-1}$ )
$E_{\text{m}}$	maximum field strength
$E_{\text{Si}}$	Young's modulus (for Si: 140 GPa)
$E_{\text{a}}$	activation energy
$E_{\text{B}}$	Coulomb barrier energy
$E_{\text{C}}$	conduction band energy
$E_{\text{G}}$	bandgap energy
$E_{\text{V}}$	valence band energy
$e$	elementary charge ( $1.602 \times 10^{-19} \text{ C}$ )
$\epsilon$	dielectric constant
$\epsilon_0$	dielectric constant of a vacuum ( $8.8542 \times 10^{-12} \text{ AsV}^{-1} \text{ m}^{-1}$ )
$\epsilon_{\text{r}}$	relative dielectric constant
$\epsilon_{\text{Si}}$	relative dielectric constant of bulk silicon (11.9)
$F_{\text{HF}}$	flow of HF
$f$	frequency
$\gamma_{\text{L}}$	surface tension of liquid
$\gamma_{\text{Si}}$	surface tension of silicon ( $1 \text{ J m}^{-2}$ )

$h$	Planck's constant ( $6.6261 \times 10^{-34}$ Js)
$I$	current
$i$	pitch
$J$	current density
$J_{PS}$	critical current density
$K$	constant
$k$	Boltzmann constant ( $1.38 \times 10^{-23}$ J K <sup>-1</sup> , $8.618 \times 10^{-5}$ eV K <sup>-1</sup> )
$L$	length
$L_D$	diffusion length (for e: $L_e$ , for h: $L_h$ )
$l$	pore length
$\lambda$	wavelength
$M$	molar weight
$m$	mass
$m_e^*$	effective mass of electron
$\mu$	mobility
$\mu_e$	electron mobility (in low doped Si: $1450$ cm <sup>2</sup> V <sup>-1</sup> s <sup>-1</sup> )
$\mu_h$	hole mobility (in low doped Si: $480$ cm <sup>2</sup> V <sup>-1</sup> s <sup>-1</sup> )
$N_A$	acceptor density
$N_{Av}$	Avogadro number ( $6.022 \times 10^{23}$ mol <sup>-1</sup> )
$N_{Si}$	atomic density of silicon ( $5 \times 10^{22}$ cm <sup>-3</sup> )
$N_D$	donor density
$N_d$	doping density
$N_p$	pore density
$n_r$	refractive index
$n_{PS}$	refractive index of PS
$n_{Si}$	refractive index of Si
$n_t$	ratio of transmitted power to incident power
$n_v$	dissolution valence
$P$	photon flux
$p$	porosity
$q$	quantum efficiency
$r$	etch rate
$r_p$	pore growth rate
$r_{PS}$	porous film growth rate
$R$	resistivity
$\rho$	density
$\rho_{Si}$	density of bulk silicon ( $2.328$ g cm <sup>-3</sup> )
$\rho_{PS}$	density of porous silicon
$s$	stress
$\sigma$	specific conductivity
$T$	temperature
$T_o$	optical transmission
$t$	time
$\tau$	lifetime
$\tau_n$	lifetime of electrons

$\tau_p$	lifetime of holes
$v$	velocity
$V_{PS}$	volume of porous silicon
$V$	bias, potential, voltage
$V_{bi}$	built-in potential
$V_{fb}$	flat-band potential
$W$	width of SCR
$w$	pore wall thickness
$x$	position
$\xi$	exponential factor
$\zeta$	exponential factor
$z$	dimensional factor

### List of Abbreviations

AC	alternating current
AFM	atomic force microscopy
ATR	attenuated total reflection
BET	Brunauer-Emmet-Teller gas desorption method
BOE	buffered oxide etchant
BPC	backside photo current
BPSG	borophosphosilicate glass
CB	conduction band
CMOS	complementary metal oxide semiconductor
CMP	chemomechanical polishing
CP	chemical polishing
CV	capacitance-voltage (measurement)
CVD	chemical vapor deposition
CZ	Czochralski (crystal growth method)
DB	dangling bond
DC	direct current
DI	deionized (water)
DLA	diffusion-limited aggregation
DLTS	deep level transient spectroscopy
DNA	deoxyribonucleic acid
DOC	dissolved oxygen concentration (of water)
DOS	density of states
DRAM	dynamic random access memory
EBIC	electron beam-induced current
EIS	electrolyte-insulator-semiconductor
EL	electroluminescence
ELTRAN	epitaxial layer transfer
ELYMAT	electrolytic metal tracer
EMA	effective medium approximation

EPR	electron paramagnetic resonance
EPS	electrochemical photocapacitance spectroscopy
ERDA	elastically recoiling particle detection spectroscopy
ESR	electrical series resistance
ESR	electron spin resonance
EXAFS	extended X-ray absorption fine structure
FIPOS	full isolation by porous oxidized silicon
FPC	frontside photo current
FTIR	Fourier transform infrared spectroscopy
FWHM	full width at half maximum
FZ	float-zone (crystal growth method)
GID	grazing incidence diffraction
HF	hydrofluoric acid
HFR	high-frequency resistometry
HOMO	highest occupied molecular orbit
HREM	high-resolution electron microscopy
IR	infrared (absorption)
IPA	isopropyl alcohol
ITO	indium tin oxide
IUPAC	International Union of Pure and Applied Chemistry
LED	light-emitting diode
LPCVD	low pressure chemical vapor deposition
LUMO	lowest unoccupied molecular orbit
MBE	molecular beam epitaxy
MEMS	micro electro mechanical systems
MIS	metal-insulator-semiconductor
MOS	metal oxide semiconductor
NEXAFS	near edge X-ray absorption fine structure
NHE	normal hydrogen electrode (= SHE)
OCP	open circuit potential
ONO	oxide-nitride-oxide dielectric
OPS	oxidized porous silicon
PCD	photoconductive decay
PDS	photothermal displacement spectroscopy
PL	photoluminescence
PLE	photoluminescence excitation spectroscopy
PMMA	polymethyl methacrylate
PP	passivation potential
PP	polypropylene
PS	porous silicon
PSG	phosphosilicate glass
PSL	porous silicon layer
PTFE	polytetrafluoroethylene
PVC	polyvinyl chloride
PVDF	polyvinylidene fluoride



QC	quantum confinement
RDE	rotating disk electrode
RIE	reactive ion etching
RS	Raman spectroscopy
RT	room temperature
RTA	rapid thermal annealing
RTO	rapid thermal oxidation
SANS	small angle neutron scattering
SAXS	small angle X-ray scattering
SC	surface clean
SCE	saturated calomel electrode
SCR	space charge region
SEM	scanning electron microscopy
SIKO	silicon capacitor
SIMS	secondary ion mass spectroscopy
SOG	spin-on glass
SOI	silicon-on insulator
SPM	sulphuric peroxide mixture
SPV	surface photovoltage spectroscopy
SRH	Shockley-Read-Hall
SRP	spreading resistance profiling
STM	scanning tunneling microscopy
TA	transverse acoustic
TEM	transmission electron microscopy
TEOS	tetraethylorthosilicate
TMAH	tetramethyl ammonium hydroxide
TO	transverse optical
TOF	time-of-flight
UHV	ultra-high vacuum
UV	ultraviolet
VB	valence band
XAFS	X-ray absorption fine structure
XANES	X-ray absorption near edge structure
XPS	X-ray photoelectron spectroscopy
XRD	X-ray diffraction
XRT	X-ray topography

## Supplier References

- [1] Carl Roth GmbH, Germany
- [2] Metron Technologies, USA; Micro Sensor Technology, Germany
- [3] Merck, Germany
- [4] EG&G Instruments, USA; Gamry Instruments, USA; Perkin Elmer, USA
- [5] Cypress Systems, USA
- [6] Shin-Etsu Handotai, Japan; MEMC, USA; Wacker Siltronic, Germany
- [7] Diamond SA, Switzerland
- [8] Silicet, Germany; AMMT, Germany
- [9] American Seal, USA; K & M Seals, USA
- [10] Interconnect Devices, USA; PTR Messtechnik, Germany
- [11] Bioanalytical Systems, USA
- [12] Almatec, Germany
- [13] Entegris, USA; Gemü, Switzerland
- [14] Spindler & Hoyer, Germany
- [15] MicroChem. Corp., USA; Micro Resist Technology, Germany
- [16] DuPont, France
- [17] Schott, Germany
- [18] Osram, Germany
- [19] Infineon Technologies, Germany
- [20] Accent, USA
- [21] Hologenix, USA; GeMeTec, Germany
- [22] Canon, Japan
- [23] pSiMedica, UK
- [24] MetriGenix, USA

## References

- [Ac1] M. C. ACERO, J. ESTEVE, J. MONTSERRAT, J. BAUSELLS, A. PEREZ-RODRIGUES, A. ROMANO-RODRIGUEZ, J. R. MORANTE, *Sens. Actuators, A*, **1994**, *45*, 119–224.
- [Ag1] M. AGGOUR, M. GIERSIG, H. J. LEWENZ, *J. Electroanal. Chem.*, **1995**, *383*, 67–74.
- [Ai1] T. AIBA, K. YAMAUCHI, Y. SHIMIZU, N. TATE, M. KATAYAMA, T. HATTORI, *Jpn. J. Appl. Phys.*, **1995**, *34*, 707–711.
- [Ak1] O. AKCAKIR, J. THERRIEN, G. BELOMIN, N. BARRY, J. D. MULLER, E. GRATTON, M. NAYFEH, *Appl. Phys. Lett.*, **2000**, *76*, 1857–1859.
- [Al1] P. ALLONGUE, V. COSTA-KIELING, H. GERISCHER, *J. Electrochem. Soc.*, **1993**, *140*, 1009–1018.
- [Al2] P. ALLONGUE, V. COSTA-KIELING, H. GERISCHER, *J. Electrochem. Soc.*, **1993**, *140*, 1018–1026.
- [Al3] P. ALLONGUE, H. BRUNE, H. GERISCHER, *Surf. Sci.*, **1992**, *275*, 414–423.
- [Al4] G. ALLAN, C. DELERUE, M. LANNOO, E. MARTIN, *Phys. Rev. B*, **1995**, *52*, 11982–11988.
- [Al5] G. ALLAN, C. DELERUE, M. LANNOO, *Phys. Rev. B*, **1996**, *76*, 2961–2964.
- [Al6] G. ALLAN, C. DELERUE, M. LANNOO, *Phys. Rev. B*, **1997**, *78*, 3161–3164.
- [Al7] P. ALLONGUE, C. H. DE VILLENEUVE, L. PINSARD, M. C. BERNARD, *Appl. Phys. Lett.*, **1995**, *67*, 941–948.
- [Am1] G. AMATO, N. BRUNETTO, *Mater. Lett.*, **1996**, *26*, 295–298.
- [Am2] T. AMBRIDGE, M. M. FAKTOR, *J. Appl. Electrochem.*, **1973**, *4*, 135–143.
- [An1] A. ANEDDA, A. SEIPT, V. A. KARAVANSKII, I. M. TIGINYANU, V. M. ICHIZLI, *Appl. Phys. Lett.*, **1995**, *67*, 3316–3318.
- [An2] G. T. ANDREWS, J. ZUK, H. KIEFTE, M. J. CLOUTER, *Appl. Phys. Lett.*, **1996**, *69*, 1217.
- [An3] M. K. ANDREWS, G. C. TURNER, *Sens. Actuators, A*, **1990**, *21–23*, 835–839.
- [An4] R. C. ANDERSON, R. S. MULLER, C. W. TOBIAS, *Sens. Actuators, A*, **1991**, *29*, 49–57.
- [An5] R. C. ANDERSON, R. S. MULLER, C. W. TOBIAS, *J. Electrochem. Soc.*, **1991**, *138*, 3406–3411.
- [Ao1] T. AOYAMA, T. YAMAZAKI, T. ITO, *J. Electrochem. Soc.*, **1996**, *143*, 2280–2285.
- [Ar1] R. J. ARCHER, *J. Phys. Chem. Solids*, **1960**, *14*, 104.
- [Ar2] Y. ARITA, Y. SUNOHARA, *J. Electrochem. Soc.*, **1977**, *124*, 285–295.
- [Ar3] Y. ARITA, *J. Cryst. Growth*, **1978**, *45*, 383–392.
- [Ar4] Y. ARITA, *Jpn. J. Appl. Phys.*, **1997**, *36*, 1035–1046.
- [Ar5] K. ARIMA, K. ENDO, T. KATAOKA, Y. OSHIKANE, H. INOUE, Y. MORI, *Appl. Phys. Lett.*, **2000**, *76*, 463–465.
- [As1] M. ASANO, T. CHO, H. MURAOKA, *Electrochem. Soc. Ext. Abstr. No. 354*, **1976**, 911–913.
- [As2] T. ASANO, K. HIGA, S. AOKI, M. TONOUCHI, T. MIYASATO, *Jpn. J. Appl. Phys.*, **1992**, *31*, L373–375.
- [As3] N. W. ASHCROFT, N. D. MERMIN, *Solid State Physics*, Holt, Reinhard & Winston, Philadelphia, **1976**.
- [As4] C. M. A. ASHUF, P. J. FRENCH, P. M. M. C. BRESSERS, P. M. SARRO, J. J. KELLY, *Sens. Actuators A*, **1998**, *33*, 284–291.
- [As5] H. ASOH, K. NISHIO, M. NAKAO, T. TAMAMURA, H. MASUDA, *J. Electrochem. Soc.*, **2001**, *148*, B152–156.

- [Aw1] N. AWAJI, Y. SUGITA, S. OHKUBO, T. NAKANISHI, K. TAKASAKI, S. KOMIYA, *Jpn. J. Appl. Phys.*, **1995**, 34, L1013–1016.
- [Ba1] E. BASSOUS, E. F. BARAN, *J. Electrochem. Soc.*, **1978**, 125, 1321–1327.
- [Ba2] J. A. BARDWELL, K. B. CLARK, D. F. MITCHELL, D. A. BISAILLION, I. G. SPROULE, B. MACDOUGALL, M. J. G. BARIBEAU, *J. Electrochem. Soc.*, **1993**, 140, 2135–2138.
- [Ba3] D. BABIC, R. TSU, R. F. GREENE, *Phys. Rev. B*, **1992**, 45, 14150.
- [Ba4] E. BASSOUS, M. FREEMAN, J.-M. HALBOUT, S. S. IYER, V. P. KESAN, S. F. PESARCIK, B. L. WILLIAMS, *Mat. Res. Soc. Symp. Proc.*, **1992**, 256, 23–26.
- [Ba5] K. BARLA, R. HERINO, G. BOMCHIL, *J. Appl. Phys.*, **1986**, 59, 439–441.
- [Ba6] J. A. BARDWELL, N. DRAPER, P. SCHMUKI, *J. Appl. Phys.*, **1996**, 79, 8761–8769.
- [Ba7] J. A. BARDWELL, E. M. ALLEGRETTO, J. PHILLIPS, M. BUCHANAN, N. DRAPER, *J. Electrochem. Soc.*, **1996**, 143, 2931–2938.
- [Ba8] K. BARLA, R. HERINO, G. BOMCHIL, J. C. PFISTER, A. FREUND, *J. Cryst. Growth*, **1984**, 68, 727–732.
- [Ba9] J. A. BARDWELL, R. J. EVANS, N. DRAPER, S. J. ROLFE, A. NAEM, M. SIMARD-NORMANDIN, *J. Electrochem. Soc.*, **1996**, 143, L256–258.
- [Ba10] L. A. BALAGUROW, D. G. YARKIN, E. A. PETROVA, A. F. ORLOW, S. N. KARYAGIN, *Appl. Phys. Lett.*, **1996**, 69, 2852–2854.
- [Ba11] D. BAKER, J. R. TILLMAN, *Solid-State Electron.*, **1963**, 6, 589.
- [Ba12] H. J. VON BARDELEBEN, C. ORTEGA, A. GROSMAN, V. MORAZZANI, J. SIEJKA, D. STIEVENARD, *J. Lumin.*, **1993**, 57, 301–313.
- [Ba13] J. A. BARDWELL, L. LEBRUN, R. J. EVANS, D. G. CURRY, R. ABBOTT, *Rev. Sci. Instrum.*, **1996**, 67, 2346–2350.
- [Ba14] J. A. BARDWELL, P. SCHMUKI, G. I. SPROULE, D. LANDHEER, D. F. MITCHELL, *J. Electrochem. Soc.*, **1995**, 142, 3933–3940.
- [Be1] F. BECK, H. GERISCHER, *Z. Phys. Chem.*, **1958**, 17, 39.
- [Be2] K. H. BECKMANN, *Surf. Sci.*, **1965**, 3, 314–332.
- [Be3] K. H. BECKMANN, N. J. HARRICK, *J. Electrochem. Soc.*, **1971**, 118, 614–619.
- [Be4] R. B. BECK, B. MAJKUSIAK, *Phys. Status Solidi*, **1989**, 116, 313–329.
- [Be5] M. I. J. BEALE, J. D. BENJAMIN, M. J. UREN, N. G. CHEW, A. G. CULLIS, *J. Cryst. Growth*, **1985**, 73, 622–636.
- [Be6] M. BEN-CHORIN, A. KUX, I. SCHECHTER, *Appl. Phys. Lett.*, **1994**, 64, 481–483.
- [Be7] M. BEN-CHORIN, F. MÖLLER, F. KOCH, W. SCHIRMACHER, M. EBERHARD, *Phys. Rev. B*, **1995**, 51, 2199–2213.
- [Be8] M. BEN-CHORIN, F. MÖLLER, F. KOCH, *Phys. Rev. B*, **1994**, 49, 2981.
- [Be9] V. BERTAGNA, C. PLOUGONVEN, F. ROUELLE, M. CHEMLA, *J. Electrochem. Soc.*, **1996**, 143, 3532–3538.
- [Be10] J. V. BEHREN, Y. KOSTOULAS, K. BURAK ÜÇER, P. M. FAUCHET, *J. Non-Cryst. Solids*, **1996**, 198–200, 957–960.
- [Be11] J. V. BEHREN, P. M. FAUCHET, E. H. CHIMOWITZ, C. T. LIRA, *Met. Res. Soc. Symp. Proc.*, **1997**, 452, 565–570.
- [Be12] O. BELMONT, C. FAIVRE, D. BELLET, Y. BRECHET, *Thin Solid Films*, **1996**, 276, 219–222.
- [Be13] D. BELLET, P. LAMAGNERE, A. VINCENT, Y. BRECHET, *J. Appl. Phys.*, **1996**, 80, 3772.
- [Be14] M. BEN-CHORIN, F. MÖLLER, F. KOCH, *J. Appl. Phys.*, **1995**, 77, 4482.
- [Be15] M. BEN-CHORIN, in *Properties of Porous Silicon* (Ed. L. CANHAM), EMIS Data Review Series No. 18, IEE, London, **1997**, pp. 165–175.
- [Be16] M. G. BERGER, M. THÖNISSEN, R. ARENS-FISCHER, H. MÜNDE, H. LÜTH, M. ARNTZEN, W. THEISS, *Thin Solid Films*, **1995**, 255, 313–316.
- [Be17] W. BERGHOLZ, D. LANDSMANN, P. SCHAUBERGER, B. SCHOPPERL, *Proc. Electrochem. Soc.*, **1993**, 93-15, 69–86.
- [Be18] H. BENDER, S. JIN, J. POORTMANS, L. STALMANS, *Appl. Surf. Sci.*, **1999**, 147, 187–200.
- [Be19] M. I. J. BEALE, J. D. BENJAMIN, M. J. UREN, N. G. CHEW, A. G. CULLIS, *J. Cryst. Growth*, **1986**, 75, 408–414.
- [Be20] A. BELAIDI, M. SAFI, F. OZANAM, J.-N. CHAZALVIEL, O. GOROCHOV, *J. Electrochem. Soc.*, **1999**, 146, 2659–2664.
- [Be21] G. BENEDETTO, L. BOARINO, R. SPAGNOLO, *Appl. Phys. A*, **1997**, 64, 155–159.
- [Be22] F. BENSILMAN, M. AGGOUR, A. ENNAOUI, Y. HIROTA, M. MATSUMURA, *Electrochem. Solid State Lett.*, **2000**, 3, 566–568.

- [Be23] F. BENSLIMAN, M. AGGOUR, A. EN-NAOUI, M. MATSUMURA, *Jpn. J. Appl. Phys.*, **2001**, *39*, L1206–1208.
- [Be24] T. R. BECK, A. J. BABCHIN, K. J. MCGRATH, in *Aluminum Surface Treatment Technology* (Eds R. S. ALWITT and G. E. THOMPSON), The Electrochemical Society Proceedings Series Vol. 86-11, ECS, Pennington, NJ, **1986**, p. 334.
- [Bi1] S. BILLAT, *J. Electrochem. Soc.*, **1996**, *143*, 1055–1061.
- [Bi2] S. BILLAT, M. THÖNISSEN, R. ARENS-FISCHER, M. G. BERGER, M. KRÜGER, H. LÜTH, *Thin Solid Films*, **1997**, *297*, 22–25.
- [Bi3] M. BINDER, T. EDELMANN, T. H. METZGER, J. PEISL, *Solid State Commun.*, **1996**, *100*, 13–16.
- [Bi4] R. R. BILYALOV, L. STALMANS, L. SCHIRONE, C. LEVY-CLEMENT, *IEEE Trans. Electron Devices*, **1999**, *46*, 2035–2040.
- [Bi5] T. BITZER, M. GRUYTERS, H. J. LEWENZ, K. JACOBI, *Appl. Phys. Lett.*, **1993**, *63*, 397–399.
- [Bi6] A. BIRNER, R. B. WEHRSPORN, U. GÖSELE, K. BUSCH, *Adv. Mater.*, **2001**, *13*, 377–388.
- [Bl1] P. BLOOD, *Semicond. Sci. Technol.*, **1986**, *1*, 7–27.
- [Bo1] K. BOHNENKAMP, H. J. ENGELL, *Z. Electrochem.*, **1957**, *61*, 1184.
- [Bo2] G. BOMCHIL, R. HERINO, K. BARLA, J. C. PEISTER, *J. Electrochem. Soc.*, **1983**, *130*, 1611–1614.
- [Bo3] A. F. BOGENSCHÜTZ, W. KRUSEMARK, K.-H. LÖCHNER, W. MUSSINGER, *J. Electrochem. Soc.*, **1967**, *114*, 970–973.
- [Bo4] I. W. BOYD, J. I. B. WILSON, *J. Appl. Phys.*, **1987**, *62*, 3195–3200.
- [Bo5] R. W. BOWER, S. D. COLLINS, *Phys. Rev. A*, **1991**, *43*, 3165–3167.
- [Bo6] L. BOUSSE, S. MOSTARSHED, D. HAFEMAN, *J. Appl. Phys.*, **1994**, *75*, 4000–4007.
- [Bo7] L. BOARINO, C. BARATTO, F. GEOBALDO, G. AMATO, E. COMINI, A. M. ROSSI, G. FAGLIA, G. LERONDEL, G. SBERVEGLIERI, *Mater. Sci. Eng., B*, **2000**, *69–70*, 210–214.
- [Br1] L. BREThERICK, *Handbook of Reactive Chemical Hazards*, Butterworths, London, **1990**.
- [Br2] W. H. BRATTAIN, C. G. B. GARRETT, *Bell Syst. Tech. J.*, **1955**, *34*, 129–176.
- [Br3] L. E. BRUS, *Appl. Phys. A*, **1991**, *53*, 465–474.
- [Br4] L. E. BRUS, *J. Chem. Phys.*, **1984**, *80*, 4403.
- [Br5] P. M. M. C. BRESSERS, J. J. KELLY, J. G. E. GARDENIERS, M. ELVENSPOEK, *J. Electrochem. Soc.*, **1996**, *143*, 1744–1750.
- [Br6] M. S. BRANDT, H. D. FUCHS, M. STUTZMANN, J. WEBER, M. CARDONA, *Solid State Commun.*, **1992**, *81*, 307.
- [Br7] J. BRANEBJERG, C. J. M. EIJKEL, J. G. E. GARDENIERS, F. C. M. VAN DE POL, in *Proceedings of the IEEE Micro Electro Mechanical Systems Workshop Nara, Japan*, **1991**, pp. 221–226.
- [Br8] R. BRENDL, H. ARTMANN, S. OELTING, J. H. WERNER, H. J. QUEISSER, *Appl. Phys. A*, **1998**, *67*, 151–154.
- [Br9] L. E. BRUS, P. F. SZAJOWSKI, W. L. WILSON, T. D. WILSON, T. D. HARRIS, S. SCHUPPLER, P. H. CITRIN, *J. Am. Chem. Soc.*, **1995**, *117*, 2915–2922.
- [Br10] H. H. BROENE, T. DE VRIES, *J. Am. Chem. Soc.*, **1947**, *69*, 1644–166.
- [Bs1] A. BSIESY, F. GASPARD, R. HERINO, M. LIGEON, R. ROMESTAIN, J. C. VIAL, *Thin Solid Films*, **1995**, *255*, 80–86.
- [Bu1] F. BUDA, J. KOHANOFF, M. PARRINELLO, *Phys. Rev. Lett.*, **1992**, *69*, 1232–1235.
- [Bu2] T. VAN BUUREN, T. TIEDJE, J. R. DAHN, B. M. WAY, *Appl. Phys. Lett.*, **1993**, *63*, 2911–2913.
- [Bu3] E. BUSTARRET, M. LIGEON, I. MIHALCESCU, J. OSWALD, *Thin Solid Films*, **1995**, *255*, 234–237.
- [Bu4] E. BUSTARRET, M. LIGEON, M. ROSENBAUER, *Phys. Status Solidi B*, **1995**, *190*, 111.
- [Bu5] D. BUTTARD, D. BELLET, G. DOLINO, *J. Appl. Phys.*, **1996**, *79*, 8060–8070.
- [Bu6] J. BÜHLER, F.-P. STEINER, H. BALTES, *J. Micromech. Microeng.*, **1997**, *7*, R1–13.
- [Bu7] T. VAN BUUREN, T. TIEDJE, W. WAYDANZ, *Mat. Res. Soc. Symp. Proc.*, **1993**, *298*, 283–288.
- [Ca1] L. T. CANHAM, *Appl. Phys. Lett.*, **1990**, *57*, 1046–1048.
- [Ca2] L. T. CANHAM, S. J. SAUNDERS, P. B. HEELEY, A. M. KEIR, T. I. COX, *Adv. Mater.*, **1994**, *6*, 865–868.
- [Ca3] L. T. CANHAM, M. R. HOULTON, W. Y. LEONG, C. PICKERING, J. M. KEEN, *J. Appl. Phys.*, **1991**, *70*, 422–431.

- [Ca4] L. T. CANHAM, A. G. CULLIS, C. PICKERING, O. D. DOSSER, T. I. COX, *Nature*, **1994**, 368, 133.
- [Ca5] S. D. CAMPBELL, L. A. JONES, E. NAKAMICHI, F.-X. WEI, L. D. ZAJCHOWSKI, D. F. THOMAS, *J. Vac. Sci. Technol., B*, **1995**, 13, 1184–1189.
- [Ca6] P. D. J. CALCOTT, K. J. NASH, L. T. CANHAM, M. J. KANE, D. BRUMHEAD, *J. Lumin.*, **1993**, 57, 257–269.
- [Ca7] L. T. CANHAM, *Phys. Status Solidi B*, **1995**, 190, 9–14.
- [Ca8] L. T. CANHAM, A. J. GROSZEK, *J. Appl. Phys.*, **1992**, 72, 1558–1565.
- [Ca9] J. CARSTENSEN, W. LIPPIK, S. LIEBERT, S. KÖSTER, H. FÖLL, *ECS Proc.*, **1995**, 95-30, 83–92.
- [Ca10] S. CATTARIN, J.-N. CHAZALVIEL, C. DE FONSECA, F. OZANAM, L. M. PETER, G. SCHLICHTHÖRL, J. STUMPER, *J. Electrochem. Soc.*, **1998**, 145, 498–502.
- [Ca11] L. T. CANHAM (Ed.), in *Properties of Porous Silicon*, EMIS Data Review Series No. 18, IEE, London, **1997**, pp. 371–376.
- [Ca12] J. CARSTENSEN, R. PRANGE, H. FÖLL, *J. Electrochem. Soc.*, **1999**, 146, 1134–1140.
- [Ca13] S. CATTARIN, I. FRATEUR, M. MUSIANI, B. TRIBOLLET, *J. Electrochem. Soc.*, **2000**, 147, 3277–3282.
- [Ca14] L. T. CANHAM, C. L. REEVES, J. P. NEWBY, M. R. HOULTON, T. I. COX, J. M. BURIK, M. P. STEWART, *Adv. Mater.*, **1999**, 11, 1505–1507.
- [Ce1] M. J. CECLERCQ, L. GERZBERG, J. D. MEINDL, *J. Electrochem. Soc.*, **1975**, 122, 545–552.
- [Ch1] T. C. CHANDLER, *J. Electrochem. Soc.*, **1990**, 137, 944.
- [Ch2] J.-N. CHAZALVIEL, F. OZANAM, V. M. DUBIN, *J. Phys. I France*, **1994**, 4, 1325–1339.
- [Ch3] J.-N. CHAZALVIEL, M. ETMAN, F. OZANAM, *J. Electroanal. Chem.*, **1991**, 297, 533–540.
- [Ch4] J.-N. CHAZALVIEL, *Electrochim. Acta*, **1992**, 37, 865–875.
- [Ch5] J.-N. CHAZALVIEL, F. OZANAM, M. ETMAN, F. PAOLUCCI, L. M. PETER, J. STUMPER, *J. Electroanal. Chem.*, **1992**, 327, 343–349.
- [Ch6] J.-N. CHAZALVIEL, F. OZANAM, *J. Electrochem. Soc.*, **1992**, 139, 2501–2508.
- [Ch7] M. H. CHAN, S. K. SO, K. W. CHEAH, *Appl. Phys. Lett.*, **1996**, 79, 3273–3275.
- [Ch8] R. P. CHIN, Y. R. SHEN, V. PETROVA-KOCH, *Science*, **1995**, 270, 776.
- [Ch9] J.-N. CHAZALVIEL, F. OZANAM, *J. Appl. Phys.*, **1997**, 81, 7684–7686.
- [Ch10] J.-N. CHAZALVIEL, *Surf. Sci.*, **1979**, 88, 204–220.
- [Ch11] S.-F. CHUANG, S. D. COLLINS, R. L. SMITH, *Appl. Phys. Lett.*, **1989**, 55, 675.
- [Ch12] J.-N. CHAZALVIEL, C. DE FONSECA, F. OZANAM, *J. Electrochem. Soc.*, **1998**, 145, 964–973.
- [Ch13] J.-N. CHAZALVIEL, R. B. WEHRSPHON, F. OZANAM, *Mater. Sci. Eng. B*, **2000**, 69–70, 1–10.
- [Ch14] J.-N. CHAZALVIEL, F. OZANAM, *Mat. Res. Soc. Symp. Proc.*, **1993**, 283, 359–364.
- [Ch15] M. CHRISTOPHERSEN, J. CARSTENSEN, A. FEUERHAKE, H. FÖLL, *Mater. Sci. Eng. B*, **2000**, 69–70, 194–198.
- [Ch16] K. J. CHAO, S. C. KAO, C. M. YANG, M. S. HSEU, T. G. TSAI, *Electrochem. Solid-State Lett.* **2000**, 3, 489–492.
- [Ch17] M. CHRISTOPHERSEN, J. CARTENSEN, S. RÖNNEBECK, C. JÄGER, W. JÄGER, H. FÖLL, *J. Electrochem. Soc.*, **2001**, 148, E267–275.
- [Cl1] L. D. CLARK, J. L. LUND, D. J. EDELL, *Proceedings of the IEEE Solid-State Sensor and Actuator Workshop*, Hilton Head Island, SC, USA, **1988**, pp. 5–8.
- [Cl2] K. B. CLARK, J. A. BARDWELL, J.-M. BARIBEAU, *J. Appl. Phys.*, **1994**, 76, 3114.
- [Co1] C. COURTEILLE, J.-L. DORIER, J. DUTTA, CH. HOLLENSTEIN, A. A. HOWLING, T. STOTO, *J. Appl. Phys.*, **1995**, 78, 61–65.
- [Co2] S. D. COLLINS, *J. Electrochem. Soc.*, **1997**, 144, 2242–2262.
- [Co3] T. I. COX, in *Properties of Porous Silicon* (Ed. L. CANHAM), EMIS Data Review Series No. 18, IEE, London, **1997**, pp. 185–191.
- [Co4] T. I. COX, in *Properties of Porous Silicon* (Ed. L. CANHAM), EMIS Data Review Series No. 18, IEE, London, **1997**, pp. 290–310.
- [Co5] T. I. COX, A. J. SIMONS, A. LONI, P. D. J. CALCOTT, L. T. CANHAM, M. J. UREN, K. J. NASH, *J. Appl. Phys.*, **1999**, 86, 2764–2773.

- [Cr1] M. CROSET, E. PETREANU, D. SAMUEL, G. AMSEL, J. P. NADAI, *J. Electrochem. Soc.*, **1971**, *118*, 717.
- [Cr2] M. CROSET, D. DIEUMEGARD, *Corros. Sci.*, **1976**, *16*, 703–715.
- [Cu1] A. G. CULLIS, L. T. CANHAM, G. M. WILLIAMS, P. W. SMITH, O. D. DOSSER, *J. Appl. Phys.*, **1994**, *75*, 493–501.
- [Cu2] A. G. CULLIS, L. T. CANHAM, P. D. J. CALCOTT, *J. Appl. Phys.*, **1997**, *82*, 909–965.
- [Da1] W. C. DASH, *J. Appl. Phys.*, **1958**, *29*, 705–709.
- [Da2] A. L. DALISA, W. K. ZWICKER, D. J. DEBITETTO, P. HARNACK, *J. Appl. Phys.*, **1970**, *17*, 208–210.
- [Da3] J. DAVISON, *Solid State Technol.*, **1992**, *35*, S10.
- [Da4] A. L. DALISA, D. J. DEBITETTO, *Appl. Optics*, **1972**, *11*, 2007–2015.
- [Da5] R. J. M. DA FONSECA, *J. Mater. Sci.*, **1995**, *30*, 35.
- [Da6] G. DALBA, N. DALDOSSO, P. FORNASINI, M. GRIMALDI, R. GRISENTI, F. ROCCA, *Phys. Rev. B*, **2000**, *62*, 9911–9914.
- [De1] B. E. DEAL, A. S. GROOVE, *J. Appl. Phys.*, **1965**, *36*, 3770.
- [De2] B. DELLEY, E. F. STEIGMEIER, *Phys. Rev. B*, **1993**, *47*, 1397–1400.
- [De3] C. DELERUE, M. LANNOO, G. ALLAN, E. MARTIN, *Thin Solid Films*, **1995**, *255*, 27–34.
- [De4] B. DELLEY, E. F. STEIGMEIER, *Appl. Phys. Lett.*, **1995**, *67*, 2370–2372.
- [De5] C. DELERUE, G. ALLEN, M. LANNOO, *Phys. Rev. B*, **1993**, *48*, 11024–11036.
- [De6] P. DEAK, M. ROSENBAUER, M. STUTZMANN, J. WEBER, M. S. BRANDT, *Phys. Rev. Lett.*, **1992**, *69*, 2531–2534.
- [De7] N. DERHACOBIAN, J. T. WALTON, P. N. LUKE, Y. K. WONG, C. S. ROSSINGTON, *J. Appl. Phys.*, **1994**, *76*, 4663–4669.
- [Di1] H. J. A. VAN DIJK, J. DE JONGE, *J. Electrochem. Soc.*, **1970**, *117*, 553–554.
- [Di2] T. DITTRICH, H. FLIETNER, V. Y. TIMOSHENKO, P. K. KASHKAROV, *Thin Solid Films*, **1995**, *255*, 149–151.
- [Di3] D. J. DiMARIA, J. R. KIRTLEY, E. J. PAKULIS, D. W. DONG, T. S. KUAN, F. L. PESAVENTO, N. THEIS, J. A. CUTRO, *J. Appl. Phys.*, **1984**, *56*, 401–415.
- [Di4] J. DIENER, M. BEN-CHORIN, D. I. KOVALEV, S. D. GANICHEV, F. KOCH, *Phys. Rev. B*, **1995**, *52*, R8617.
- [Di5] T. DITTRICH, M. SCHWARTZKOPF, E. HARTMANN, J. RAPPICH, *Surf. Sci.*, **1999**, *437*, 154–162.
- [Di6] J. DIENER, D. I. KOVALEV, G. POLISSKI, F. KOCH, *Appl. Phys. Lett.*, **1999**, *74*, 3350–3352.
- [Di7] Y. DIAWARA, J. F. CURRIE, A. YELON, V. PETROVA-KOCH, A. NIKOLOV, *Mater. Res. Soc. Symp. Proc.*, **1995**, *358*, 555.
- [Do1] V. V. DOAN, M. J. SAILOR, *Appl. Phys. Lett.*, **1992**, *60*, 619–620.
- [Dr1] R. DREINER, *J. Electrochem. Soc.*, **1966**, *113*, 1210–1215.
- [Dr2] B. DRUGGE, E. NORDLANDER, *IEEE Trans. Electron Devices*, **1980**, *ED-27*, 2124–2147.
- [Du1] Dutch Association of Safety Experts, *Handling Chemicals Safely*, 2nd edn, **1980**.
- [Du2] E. F. DUFFEK, E. A. BENJAMINI, C. MYLROIE, *Electrochem. Technol.*, **1965**, *3*, 75–80.
- [Du3] V. M. DUBIN, *Surf. Sci.*, **1992**, *274*, 82–92.
- [Du4] V. M. DUBIN, F. OZANAM, J.-N. CHAZALVIEL, *Thin Solid Films*, **1995**, *255*, 87–91.
- [Du5] S. P. DUTTAGUPTA, X. L. CHEN, S. A. JENEKHE, P. M. FAUCHET, *Solid State Commun.*, **1997**, *101*, 33–37.
- [Du6] S. P. DUTTAGUPTA, C. PENG, P. M. FAUCHET, S. K. KURINEC, T. N. BLANTON, *J. Vac. Sci. Technol.*, *B*, **1995**, *13*, 1230–1235.
- [Dz1] J. A. DZIUBAN, *Sens. Actuators*, **2000**, *85*, 133–138.
- [Ea1] L. G. EARWAKER, J. P. G. FARR, I. ALEXANDER, I. M. STURLAND, J. M. KEEN, *Nuc. Instrum. Methods Phys. Res.*, **1983**, *218*, 481–4.
- [Ed1] M. EDEN, in *Proceedings of the Fourth Berkeley Symposium on Mathematical Statistics and Probability*, Vol. IV, **1961**, p. 233.
- [Ed2] M. J. EDDOWS, *J. Electroanal. Chem.*, **1990**, *280*, 297.
- [Ef1] E. A. EFIMOV, I. G. ERUSALIMCHIK, *Dokl. Akad. Nauk S.S.S.R.*, **1959**, *124*, 609.
- [Ei1] P. EICHINGER, M. ROMMEL, *Electrochem. Soc. Proc.*, **1997**, *97-22*, 363–375.

- [El1] A. EL-BAHAR, S. STOLYAROVA, Y. NEMIROVSKY, *IEEE Electron Device Lett.*, **2000**, *21*, 436–438.
- [Er1] B. H. ERNE, D. VANMEAKELBERGH, J. J. KELLY, *J. Electrochem. Soc.*, **1995**, *143*, 305.
- [Er2] B. H. ERNE, C. MATHIEU, J. VIGNERON, A. MILLION, A. ETCHEBERRY, *J. Electrochem. Soc.*, **2000**, *147*, 3759–3767.
- [Et1] M. ETMAN, M. NEUMANN-SPALLART, F. OZANAM, J.-N. CHAZALVIEL, *J. Electroanal. Chem.*, **1991**, *301*, 259.
- [Fa1] H. N. FARRER, F. J. C. ROSOTTI, *J. Inorg. Nucl. Chem.*, **1964**, *26*, 1959.
- [Fa2] R. D. FAIR, C. W. PEARCE, J. WASHBURN, *Mater. Res. Soc. Symp. Proc.*, **1985**, *36*, 19.
- [Fa3] R. FALSTER, W. BERGHOLZ, *J. Electrochem Soc.*, **1990**, *137*, 1548–1559.
- [Fa4] M. M. FAKTOR, D. G. FIDDYMENT, M. R. TAYLOR, *J. Electrochem. Soc.*, **1975**, *122*, 1566–1567.
- [Fa5] R. W. FATHAUER, T. GEORGE, A. KSENDZOV, R. P. VASQUES, *Appl. Phys. Lett.*, **1992**, *60*, 995–997.
- [Fa6] P. M. FAUCHET, E. ETTEDGUI, A. RAISANEN, L. J. BRILLSON, F. SEIFERT, S. K. KURINEC, Y. GAO, C. PENG, L. TSYBESKOV, *Mater. Res. Soc. Symp. Proc.*, **1993**, *298*, 271.
- [Fa7] J. W. FAUST, E. D. PALIK, *J. Electrochem. Soc.*, **1983**, *130*, 1413–1420.
- [Fa8] C. FAIVRE, D. BELLET, G. DOLINO, *J. Appl. Phys.*, **2000**, *87*, 2131–2136.
- [Fi1] R. M. FINNE, D. L. KLEIN, *J. Electrochem. Soc.*, **1967**, *114*, 965–970.
- [Fi2] A. B. FILONOV, G. V. PETROV, V. A. NOVIKOV, V. E. BORISENKO, *Appl. Phys. Lett.*, **1995**, *67*, 1090.
- [Fi3] R. J. FIELD, M. BURGER, *Oscillations and Traveling Waves in Chemical Systems*, Wiley, New York, **1985**.
- [Fi4] S. FINKBEINER, J. WEBER, M. ROSENBAUER, M. STUTZMANN, *J. Lumin.*, **1993**, *57*, 231–234.
- [Fi5] A. J. FINKEL, *Adv. Fluorine Chem.*, **1973**, *7*, 199–203.
- [Fi6] E. A. FITZGERALD, K. C. WU, M. CURRIE, N. GERRISH, D. BRUCE, J. BORENSTEIN, *Mater. Res. Soc. Symp. Proc.*, **1998**, *518*, 233–238.
- [Fr1] U. F. FRANK, M. VOLMER, *Z. Phys. Chem.*, **1930**, *150*, 401.
- [Fr2] H. FRANZ, V. PETROVA-KOCH, T. MUSCHIK, V. LEHMANN, J. PEISL, *Proc. Mater. Res. Soc.*, **1992**, *283*, 133–138.
- [Fr3] G. DI FRANCIA, A. CITARELLA, *J. Appl. Phys.*, **1995**, *77*, 3549–3552.
- [Fr4] U. F. FRANCK, *Faraday Symp. Chem. Soc.*, **1974**, *9*, 137.
- [Fr5] S. FROHNHOFF, M. G. BERGER, M. THÖNISSEN, C. DIEKER, L. VESCAN, H. MÜNDER, H. LÜTH, *Thin Solid Films*, **1995**, *255*, 59–62.
- [Fr6] S. FROHNHOFF, M. MARSA, M. G. BERGER, M. THÖNISSEN, H. LÜTH, H. MÜNDER, *J. Electrochem. Soc.*, **1995**, *142*, 615–620.
- [Fo1] H. FÖLL, *Appl. Phys. Lett.*, **1980**, *37*, 316–318.
- [Fo2] H. FÖLL, *Appl. Phys. A*, **1991**, *53*, 8–19.
- [Fu1] H. FUKUDA, M. YASUDA, T. IWABUCHI, *Jpn. J. Appl. Phys.*, **1992**, *31*, 3436–3439.
- [Fu2] M. FUJII, Y. KANZAWA, S. HAYASHI, K. YAMAMOTO, *Phys. Rev. B*, **1996**, *54*, R8373–375.
- [Fu3] C. S. FULLER, J. A. DITZENBERGER, *J. Appl. Phys.*, **1956**, *27*, 544–553.
- [Fu4] M. FUKUDA, W. MIZUBAYASHI, A. KOHNO, S. MIYAZAKI, M. HIROSE, *Jpn. J. Appl. Phys.*, **1998**, *37*, L1534–536.
- [Ga1] F. GASPARD, A. BSIESY, M. LIGEON, F. MULLER, R. HERINO, *J. Electrochem. Soc.*, **1989**, *136*, 3043–3046.
- [Ga2] F. GASPARD, A. HALIMAOU, G. SARRABAYROUSE, *Rev. Phys. Appl.*, **1987**, *22*, 65–69.
- [Ga3] B. GARRIDO, J. MONTERRAT, J. R. MORANTE, *J. Electrochem. Soc.*, **1996**, *143*, 4059–4065.
- [Ge1] H. GERISCHER, in *Surface Chemistry of Metals and Semiconductors* (Ed. H. C. GATOS), Wiley & Sons, New York, **1960**.
- [Ge2] A. GEE, *J. Electrochem. Soc.*, **1960**, *107*, 787–788.
- [Ge3] H. GERISCHER, *Electrochim. Acta*, **1990**, *35*, 1677–1699.
- [Ge4] W. VAN GELDER, V. E. HAUSER, *J. Electrochem. Soc.*, **1967**, *114*, 869–872.
- [Ge5] R. L. GEALER, H. K. KARSTEN, S. M. WARD, *J. Electrochem. Soc.*, **1988**, *135*, 1180–1183.
- [Ge6] H. GERISCHER, M. LÜBKE, *J. Electrochem. Soc.*, **1988**, *135*, 2782–2786.



- [Ge7] H. GERISCHER, P. ALLONGUE, V. COSTA-KIELING, *Ber. Bunsenges. Phys. Chem.*, **1993**, *97*, 753–757.
- [Ge8] B. GELLOZ, A. BSIESY, F. GASPARD, F. MULLER, *Thin Solid Films*, **1996**, *276*, 175–178.
- [Ge9] G. GESELE, J. LINSMEIER, V. DRACH, J. FRICKE, R. ARENS-FISCHER, *J. Phys. D: Appl. Phys.*, **1997**, *30*, 2911–2916.
- [Ge10] A. E. GERSHINSKII, L. V. MIRONOVA, *Sov. Electrochem.*, **1990**, *25*, 1224.
- [Ge11] B. GELLOZ, T. NAKAGAWA, N. KOSHIDA, *Appl. Phys. Lett.*, **1998**, *73*, 2021.
- [Gi1] P. A. GIGUERE, A. TURRELL, *J. Am. Chem. Soc.*, **1980**, *102*, 5473.
- [Gl1] O. J. GLEBOCKI, R. E. STAHLBUSCH, M. TOMKIEWICS, *J. Electrochem. Soc.*, **1985**, *132*, 145–150.
- [Gl2] J. A. GLASS, E. A. WOVCHKO, J. T. YATES, *Surf. Sci.*, **1996**, *348*, 325–334.
- [Go1] G. GOULD, E. A. IRENE, *J. Electrochem. Soc.*, **1989**, *136*, 1108–1112.
- [Go2] N. GONON, A. GAGNAIRE, D. BARBIER, A. GALCHANT, *J. Appl. Phys.*, **1994**, *76*, 5242–5247.
- [Go3] S. R. GOODES, T. E. JENKINS, M. I. J. BEALE, J. D. BENJAMIN, C. PICKERING, *Semicond. Sci. Technol.*, **1988**, *3*, 483–487.
- [Go4] A. M. GOODMAN, L. A. GOODMAN, H. F. GOSSENBERGER, *RCA Review*, **1983**, *44*, 326–341.
- [Gr1] D. GRÄF, M. GRUNDNER, R. SCHULZ, *J. Vac. Sci. Technol.*, **A**, **1989**, *7*, 808.
- [Gr2] M. GRUNDNER, D. GRÄF, P. O. HAHN, A. SCHNEGG, *Solid State Technol.*, **1991**, *34*, 69.
- [Gr3] M. GRUNDNER, H. JACOB, *Appl. Phys. A*, **1986**, *39*, 73–82.
- [Gr4] K. GRAFF, P. HEIM, *J. Electrochem. Soc.*, **1994**, *141*, 2825–2921.
- [Gr5] D. GRÄF, M. GRUNDNER, R. SCHULZ, L. MÜHLHOFF, *J. Appl. Phys.*, **1990**, *68*, 5155–5161.
- [Gr6] U. GRÜNING, A. YELON, *Thin Solid Films*, **1995**, *255*, 135–138.
- [Gr7] V. GRIVICKAS, J. LINNROS, *Thin Solid Films*, **1995**, *255*, 70–73.
- [Gr8] U. GRÜNING, V. LEHMANN, S. OTTOW, K. BUSCH, *Appl. Phys. Lett.*, **1996**, *68*, 747–749.
- [Gr9] K. GRIGORAS, A. KROTKUS, V. PACEBUTAS, J. KAVALIUSKAS, I. SIMKIENE, *Thin Solid Films*, **1996**, *276*, 228–230.
- [Gu1] A. GÜNTHERSCHULZE, H. BETZ, *Electrolytkondensatoren* (Ed. M. KRAYN), Techn. Verlag H. Cram, Berlin, **1937**.
- [Gu2] P. GUPTA, V. L. COLVIN, S. M. GEORGE, *Phys. Rev. B*, **1988**, *37*, 8234–8243.
- [Gu3] P. GUPTA, A. C. DILON, A. S. BRACKER, S. M. GEORGE, *Surf. Sci.*, **1991**, *245*, 360–372.
- [Gu4] M. GUENDOUZ, P. JOUBERT, M. SARRET, *Mater. Sci. Eng. B*, **2000**, *69–70*, 43–47.
- [Ha1] W. W. HARVEY, H. C. GATOS, *J. Electrochem. Soc.*, **1958**, *105*, 654.
- [Ha2] Y. HAYAMAZU, T. HAMAGUSHI, S. USHIO, T. ABE, *J. Appl. Phys.*, **1991**, *69*, 3077.
- [Ha3] H. H. HASSAN, J. L. SCULFORT, M. ETMAN, F. OZANAM, J.-N. CHAZALVIEL, *J. Electroanal. Chem.*, **1995**, *380*, 55–61.
- [Ha4] A. HALIMAOU, Y. CAMPIDELLI, A. LARRE, D. BENSACHEL, *Phys. Status Solidi B*, **1995**, *190*, 35–41.
- [Ha5] R. HAAK, D. TRENCH, *J. Electrochem. Soc.*, **1984**, *131*, 275–283.
- [Ha6] J. F. HARVEY, M. SHEN, R. A. LUX, M. DUTTA, J. PAMULAPTI, R. TSU, *Mater. Res. Soc. Sym. Proc.*, **1992**, *256*, 175.
- [Ha7] A. HALIMAOU, C. OULES, G. BOMCHIL, A. BSIESY, F. GASPARD, R. HERINO, M. LIGEON, F. MULLER, *Appl. Phys. Lett.*, **1991**, *59*, 304.
- [Ha8] P. G. HAN, M. C. POON, P. K. KO, J. K. O. SIN, H. WONG, *J. Vac. Sci. Technol. B*, **1996**, *14*, 824–826.
- [Ha9] K. HAMANO, *Denki Kagaku*, **1984**, *52*, 553.
- [Ha10] J. HARSANYI, H.-U. HABERMEIER, *Microelectron. Eng.*, **1987**, *6*, 575.
- [Ha11] H. H. HASSAN, B. FOTUHI, J. L. SCULFORT, S. S. ABDLE-REHIEM, M. ETMAN, F. OZANAM, J.-N. CHAZALVIEL, *J. Electroanal. Chem.*, **1996**, *407*, 105–113.
- [Ha12] H. H. HASSAN, J.-N. CHAZALVIEL, M. NEUMANN-SPALLART, F. OZANAM, M. ETMAN, *J. Electroanal. Chem.*, **1995**, *381*, 211–214.
- [Ha13] W. J. HAMER, Y.-C. WU, *J. Res. Natl. Bur. Std. A*, **1970**, *74*, 761–768.
- [Ha14] B. HAMILTON, J. JACOBS, D. A. HILL, R. F. PETTIFER, D. TEEHAN, L. T. CANHAM, *Nature*, **1998**, *393*, 443–435.
- [He1] R. C. HENDERSON, *J. Electrochem. Soc.*, **1972**, *119*, 772.

- [He2] A. HENGLEIN, *Chem. Rev.*, **1989**, 89, 1861–1873.
- [He3] Z. J. HE, Y. P. HUANG, R. KWOR, *Thin Solid Films*, **1995**, 265, 96–100.
- [He4] R. HERINO, G. BOMCHIL, K. BARLA, C. BERTRAND, J. L. GINOUX, *J. Electrochem. Soc.*, **1987**, 134, 1994–2000.
- [He5] F. HEDRICH, S. BILLAT, W. LANG, *Sens. Actuators*, **2000**, 84, 315–323.
- [He6] W. L. M. C. HEYBOER, G. A. C. M. SPIERINGS, J. E. A. M. MEERAKKER, *J. Electrochem. Soc.*, **1991**, 138, 774–777.
- [He7] K. R. HEBERT, H. WU, T. GESSMANN, K. LYNN, *J. Electrochem. Soc.*, **2001**, 148, B92–100.
- [He8] K. R. HEBERT, R. ALKIRE, *J. Electrochem. Soc.*, **1988**, 135, 2447–2452.
- [Hi1] M. HIRATA, K. SUZUKI, H. TANIGAWA, *Sens. Actuators*, **1988**, 13, 63.
- [Hi2] M. HIROSE, T. YASAKA, M. TAKAKURA, S. MIYAZAKI, *Solid State Technol.*, **1991**, 43–48.
- [Hi3] E. G. HILL, A. P. SIRKAR, *Proc. R. Soc. London, Ser. A*, **1909**, 83, 130–148.
- [Hi4] M. HIRAO, T. UDA, *Surf. Sci.*, **1994**, 306, 87–92.
- [Hi5] N. A. HILL, K. B. WHALEY, *J. Appl. Phys.*, **1994**, 76, 2423–2428.
- [Hi6] J. HILLIARD, D. ANDSAGER, L. A. HASSAN, H. M. NAYFEH, M. H. NAYFEH, *Appl. Phys. Lett.*, **1995**, 67, 1125.
- [Hi7] M. J. HILL, *J. Electrochem. Soc.*, **1973**, 120, 142–145.
- [Hi8] M. HIRAO, *Mater. Res. Soc. Symp. Proc.*, **1995**, 358, 3–12.
- [Hi9] G. S. HIGASHI, Y. J. CHABAL, G. W. TRUCKS, K. RAGHAVACHARI, *Appl. Phys. Lett.*, **1990**, 56, 656.
- [Ho1] R. P. HOLMSTROM, J. Y. CHI, *Appl. Phys. Lett.*, **1983**, 42, 386–388.
- [Ho2] H. J. HOFFMANN, J. M. WOODALL, *Appl. Phys. A*, **1984**, 33, 243–245.
- [Ho3] G. W. 'T HOOFT, Y. A. R. R. KESSENER, G. L. J. A. RIKKEN, A. H. J. VENHUIZEN, *Appl. Phys. Lett.*, **1992**, 61, 2344–2346.
- [Ho4] W. H. THOMPSON, Z. YAMAIN, L. H. A. HASSAN, J. E. GREEN, M. NAYFEH, M.-A. HASAN, *J. Appl. Phys.*, **1996**, 80, 5415–5421.
- [Ho5] X. Y. HOU, G. SHI, W. WANG, F. L. ZHANG, P. H. HAO, D. M. HUANG, X. F. JIN, X. WANG, *Appl. Phys. Lett.*, **1993**, 62, 1097.
- [Ho6] P. M. HOFFMANN, I. E. VERMEIR, P. C. SEARSON, *J. Electrochem. Soc.*, **2000**, 147, 2999–3002.
- [Hu1] R. M. HURD, P. T. WROTENBERY, *Recent News Paper*, Electrochem. Soc. Meeting, Chicago, **1960**.
- [Hu2] S. M. HU, D. R. KERR, *J. Electrochem. Soc.*, **1967**, 114, 414.
- [Hu3] T. F. HUNG, H. WONG, Y. C. CHENG, C. K. PUN, *J. Electrochem. Soc.*, **1991**, 138, 3747–3750.
- [Hy1] H. H. HYMAN, J. J. KATZ, in *Non-Aqueous Solvent Systems* (Ed. T. C. WADDINGTON), Academic Press, New York, **1965**, p. 62.
- [Hy2] M. S. HYBERTSEN, *Phys. Rev. Lett.*, **1994**, 72, 1514–1517.
- [Im1] K. IMAI, H. UNNO, *IEEE Trans. Electron Devices*, **1984**, ED-31, 297–302.
- [It1] T. ITO, K. MOTOI, O. ARAKAKI, A. HATA, A. HIRAKI, *Jpn. J. Appl. Phys.*, **1994**, 33, L941–944.
- [It2] T. ITO, T. OHTA, O. ARAKAKI, A. HIRAKI, *Mater. Res. Soc. Symp. Proc.*, **1992**, 256, 127.
- [It3] M. ITOH, N. YAMAMOTO, K. TAKEMOTO, O. NIITONO, *Jpn. J. Appl. Phys.*, **1996**, 35, 4182–4186.
- [It4] T. ITO, T. OHTA, K. MOTOI, O. ARAKAKI, O. ARAKAKI, A. HIRAKI, *Mater. Res. Soc. Symp. Proc.*, **1993**, 283, 263–268.
- [Iu1] IUPAC, *Stability Constants of Metal Ion Complexes, Part A*, Pergamon Press, Oxford, **1982**, p. 188.
- [Iu2] IUPAC, *Manual of Symbols and Terminology*, Appendix 2, Part 1, Pure and Appl. Chem., **1972**, 31, 578.
- [Ja1] T. N. JACKSON, M. A. TISCHLER, K. D. WISE, *IEEE Electron Device Lett.*, **1981**, EDL2, 44–45.
- [Ja2] G. C. JAIN, A. PRASAD, B. C. CHAKRAVARTY, *J. Electrochem. Soc.*, **1979**, 126, 89–92.
- [Ja3] H. JANSSEN, H. GARDENIERS, M. DE BOER, M. ELWENSPOEK, J. FLUITMAN, *J. Micromech. Microeng.*, **1996**, 6, 14–28.
- [Ja4] A. JANSHOFF, K.-P. S. DANCIL, C. STEINEM, D. P. GREINER, V. S.-Y. LIN, C. GURTNER, K. MOTESHAREI, M. J. SAILOR, *J. Am. Chem. Soc.*, **1998**, 120, 12108–12116.
- [Je1] M. W. JENKINS, *J. Electrochem. Soc.*, **1977**, 124, 757.

- [Ji1] Y. Q. JIA, L. Z. ZHANG, J. S. FU, B. R. ZHANG, J. C. MAO, G. G. QIN, *J. Appl. Phys.*, **1994**, *74*, 7615–7617.
- [Jo1] J. P. JOHN, J. McDONALD, *J. Electrochem. Soc.*, **1993**, *140*, 2622–2625.
- [Jo2] G. C. JOHN, V. A. SINGH, *Phys. Rev. B*, **1995**, *52*, 11125–11131.
- [Jo3] G. C. JOHN, V. A. SINGH, *Phys. Rep.*, **1995**, *263*, 93–151.
- [Ju1] J. S. JUDGE, *J. Electrochem. Soc.*, **1971**, *118*, 1772.
- [Ju2] K. H. JUNG, S. SHIH, D. L. KWONG, T. GEORGE, T. L. LIN, H. Y. LIU, J. ZAVADA, *J. Electrochem. Soc.*, **1992**, *139*, 3363–3372.
- [Ju3] K. H. JUNG, S. SHIH, D. L. KWONG, J. ZAVADA, *J. Electrochem. Soc.*, **1993**, *140*, 3046–3064.
- [Ka1] Y. KANG, J. JORNE, *Appl. Phys. Lett.*, **1993**, *62*, 2224–2226.
- [Ka2] Y. KATO, T. ITO, A. HIRAKI, *Jap. J. Appl. Phys.*, **1988**, *27*, L1406–1409.
- [Ka3] Y. KANEMITSU, H. UTO, Y. MASUMOTO, T. FUTAGI, T. MATSUMOTO, H. MIMURA, *Phys. Rev. B*, **1993**, *48*, 2827.
- [Ka4] Y. KASHIWAGI, R. SHIMOKAWA, M. YAMANAKA, *J. Electrochem. Soc.*, **1996**, *143*, 4079–4087.
- [Ka5] G. KAMINSKY, *J. Vac. Sci. Technol., B*, **1985**, *3*, 1015–1024.
- [Ka6] Y. KANEMITSU, *Phys. Rev. B*, **1993**, *48*, 12357.
- [Ka7] Y. KANEMITSU, S. OKAMOTO, A. MITO, *Phys. Rev. B*, **1995**, *52*, 10752–10755.
- [Ka8] Y. KANEMITSU, S. OKAMOTO, *Phys. Rev. B*, **1998**, *58*, 9652–9655.
- [Ka9] Y. KANEMITSU, Y. MASUMOTO, T. FUTAGI, T. MATSUMOTO, H. MIMURA, *Mater. Res. Soc. Symp. Proc.*, **1993**, *298*, 205–210.
- [Ke1] W. KERN, *Semicond. Int.*, **1984**, *7*, 94–99.
- [Ke2] D. L. KENDALL, *Appl. Phys. Lett.*, **1974**, *26*, 195–198.
- [Ke3] Y. A. R. R. KESSENER, G. L. J. A. RIKKEN, A. H. J. VENHUIZEN, *J. Lumin.*, **1993**, *57*, 77–81.
- [Ki1] H. KIKUYAMA, M. WAKI, M. MIYASHITA, T. YABUNE, N. MIKI, J. TAKANO, T. OHMI, *J. Electrochem. Soc.*, **1994**, *141*, 366–374.
- [Ki2] E. KIKUNO, T. TAKIZAWA, S. ARAI, *Jap. J. Appl. Phys.*, **1995**, *34*, 177–178.
- [Kl1] B. KLOECK, S. D. COLLINS, N. F. DE ROOIJ, R. L. SMITH, *IEEE Trans. Electron Devices*, **1989**, *36*, 663–669.
- [Kl2] V. I. KLIMOV, V. S. DNEPROVSKII, V. A. KARAVANSKII, *Appl. Phys. Lett.*, **1994**, *64*, 2691–2693.
- [Kl3] P. KLEINMANN, J. LINNROS, S. PETERSON, *Mater. Sci. Eng., B*, **2000**, *69/70*, 29–33.
- [Kl4] O. KLIMA, P. HLINOMAZ, A. HOSPODKOVA, J. OSWALD, J. KOCKA, *J. Non-Cryst. Solids*, **1993**, *164–166*, 961.
- [Kn1] D. M. KNOTTER, T. J. J. D. DENTENEER, *J. Electrochem. Soc.*, **2001**, *148*, F43–46.
- [Ko1] D. I. KOVALEV, I. D. YAROSHETZKII, T. MUSCHIK, V. PETROVA-KOCH, F. KOCH, *Appl. Phys. Lett.*, **1994**, *64*, 214–216.
- [Ko2] H. KOJAMA, N. KOSHIDA, *J. Lumin.*, **1993**, *57*, 293–299.
- [Ko3] A. J. KONTKIEWICZ, A. M. KONTKIEWICZ, J. SIEJKA, G. NOWAK, A. M. HOFF, P. SAKTHIVEL, K. AHMED, P. MUKHERJEE, J. LGOWSKI, *Appl. Phys. Lett.*, **1994**, *65*, 1436–1438.
- [Ko4] D. KOVALEV, G. POLISSKI, M. BEN-CHORIN, J. DIENER, F. KOCH, *J. Appl. Phys.*, **1996**, *80*, 5978–5983.
- [Ko5] F. KOCH, V. PETROVA-KOCH, T. MUSCHIK, *J. Lumin.*, **1993**, *57*, 271–281.
- [Ko6] D. KOVALEV, I. D. YAROSHETZKII, T. MUSCHIK, V. PETROVA-KOCH, F. KOCH, *Appl. Phys. Lett.*, **1994**, *64*, 214.
- [Ko7] K. KOBAYASHI, H. UNNO, H. TAKIZAWA, S. ADACHI, *Jpn. J. Appl. Phys.*, **1996**, *35*, 5925–5928.
- [Ko8] K. KOBAYASHI, T. SUZUKI, S. ADACHI, *Jpn. J. Appl. Phys.*, **1994**, *33*, L15.
- [Ko9] N. KOSHIDA, H. KOJAMA, *Appl. Phys. Lett.*, **1992**, *60*, 347–349.
- [Ko10] J. KOCKA, I. PELANT, A. FEJFAR, *J. Non-Cryst. Solids*, **1996**, *198–200*, 857.
- [Ko11] F. KOCH, D. KOVALEV, B. AVERBOUKH, G. POLISSKI, M. BEN-CHORIN, *J. Lumin.*, **1996**, *70*, 320–332.
- [Ko12] D. KOVALEV, H. HECKLER, B. AVERBOUKH, M. BEN-CHORIN, M. SCHWARTZKOPFF, F. KOCH, *Phys. Rev. B*, **1998**, *57*, 3741–3744.
- [Ko13] D. KOVALEV, H. HECKLER, M. BEN-CHORIN, M. SCHWARTZKOPFF, F. KOCH, *Phys. Rev. Lett.*, **1998**, *81*, 2803–2806.
- [Ko14] E. S. KOIJ, K. BUTTER, J. J. KELLY, *Electrochem. Solid-State Lett.*, **1999**, *2*, 178–180.
- [Ko15] D. KOVALEV, H. HECKLER, G. POLISSKI, F. KOCH, *Phys. Status Solidi*, **1999**, *215*, 871–932.

- [Ko16] P. A. KOHL, C. WOLOWODIUK, F. W. OSTERMAYER, *J. Electrochem. Soc.*, **1983**, *130*, 2288–2293.
- [Ko17] N. KOSHIDA, H. KOJAMA, *Mater. Res. Soc. Symp. Proc.*, **1993**, *283*, 337–342.
- [Ko18] F. KOZLOWSKI, W. WAGENSEIL, P. STEINER, W. LANG, *Mater. Res. Soc. Symp. Proc.*, **1995**, *358*, 677–682.
- [Ko19] D. KOVALEV, J. DIENER, H. HECKLER, G. POLISSKI, N. KÜNZNER, F. KOCH, *Phys. Rev. B*, **2000**, *61*, 4485–4487.
- [Ko20] N. KOSHIDA, T. OZAKI, X. SHENG, H. KOJAMA, *Jpn. J. Appl. Phys. Part 2*, **1995**, *34*, L705.
- [Ko21] T. KOMODA, X. SHENG, N. KOSHIDA, *J. Vac. Sci. Technol., B*, **1999**, *17*, 1076–1079.
- [Ko22] D. KOVALEV, G. POLISSKI, J. DIENER, H. HECKLER, N. KÜNZNER, V. YU, F. KOCH, *Appl. Phys. Lett.*, **2001**, *78*, 916–918.
- [Ko23] T. KOMODA, *Mater. Res. Soc. Symp. Proc.*, **2000**, F 4.1.1–F 4.1.12.
- [Ko24] D. KOVALEV, V. TIMOSHENKO, N. KÜNZNER, E. GROSS, F. KOCH, *Phys. Rev. Lett.*, **2001**, 068301–1.
- [Kr1] P. KRAUSE, E. OBERMEIER, *J. Micro-mech. Microeng.*, **1995**, *5*, 112–114.
- [Kr2] N. KRAMERE, M. NIESTEN, C. SCHÖNENBERGER, *Appl. Phys. Lett.*, **1995**, *67*, 2989–2991.
- [Kr3] M. KRÜGER, R. ARENS-FISCHER, M. THÖNISSEN, H. MÜNDER, M. G. BERGER, H. LÜTH, S. HILBRICH, W. THEISS, *Thin Solid Films*, **1996**, *276*, 257–260.
- [Ku1] R. KÜHN, K. BIRETT, *Merkblätter gefährliche Arbeitsstoffe*, Ecomed Fachverlag, Landsberg/Lech, **1987**.
- [Ku2] A. KUX, F. MÜLLER, F. KOCH, *Mater. Res. Soc. Symp. Proc.* **1993**, *283*, 311–16.
- [Ku3] A. KUX, D. I. KOVALEV, F. KOCH, *Thin Solid Films*, **1995**, *255*, 143–145.
- [Ku4] A. KUX, M. BEN-CHORIN, *Thin Solid Films*, **1996**, *276*, 272–275.
- [Ku5] M. KUHL, G. M. O'HALLORAN, P. T. J. GENNISSSEN, P. J. FRENCH, *J. Micro-mech. Microeng.*, **1998**, *8*, 317–322.
- [Ku6] A. KUX, M. BEN-CHORIN, *Phys. Rev. B*, **1995**, *51*, 17535–17541.
- [Ku7] M. S. KULKARNI, H. F. ERK, *J. Electrochem. Soc.*, **2000**, *147*, 176–188.
- [Kw1] T. A. KWA, R. F. WOLFFENBUTTEL, *J. Micromech. Microeng.*, **1995**, *5*, 95–97.
- [La1] I. LAMPERT, H. FUSSSTETTER, H. JACOB, *J. Electrochem. Soc.*, **1986**, *133*, 1472–1474.
- [La2] V. A. LABUNOV, V. P. BONDARENKO, L. K. GLINENKO, *Thin Solid Films*, **1986**, *137*, 123.
- [La3] D. LAPADATU, M. DE COOMAN, R. PUERS, *Sens. Actuators, A*, **1996**, *53*, 261–266.
- [La4] W. LANG, P. STEINER, *Sens. Mater.*, **1996**, *8*, 327–344.
- [La5] W. LANG, P. STEINER, H. SANDMAIER, *Sens. Actuators, A*, **1995**, *51*, 31–36.
- [La6] N. LALIC, J. LINNROS, *Thin Solid Films*, **1995**, *276*, 155–158.
- [La7] J. A. LAUERHAAS, G. M. CREDO, J. L. HEINRICH, M. J. SAILOR, *Mater. Res. Soc. Symp. Proc.* **1992**, *256*, 137–141.
- [La8] M. LANNOO, C. DELERUE, G. ALLAN, *Phys. Rev. Lett.*, **1995**, *74*, 3415–4318.
- [La9] G. LAMMEL, P. RENAUD, *Sens. Actuators*, **2000**, *85*, 356–360.
- [La10] S. LANGA, I. M. TIGINYANU, J. CASTENSEN, M. CHRISTOPHERSEN, H. FÖLL, *Electrochem. Solid-State Lett.*, **2000**, *3*, 514–516.
- [La11] G. LAMMEL, S. SCHWEITZER, P. RENAUD, in *Proceedings of the 14th IEEE International MEMS Conference*, Miyazaki, **2001**, pp. 578–581.
- [Le1] V. LEHMANN, U. GÖSELE, *Appl. Phys. Lett.*, **1991**, *58*, 856–858.
- [Le2] V. LEHMANN, K. MITANI, D. FEIJOO, U. GÖSELE, *J. Electrochem. Soc.*, **1991**, *138*, L3–4.
- [Le3] V. LEHMANN, U. GÖSELE, *Adv. Mater.*, **1992**, *4*, 114–116.
- [Le4] V. LEHMANN, *J. Electrochem. Soc.*, **1996**, *143*, 1313–1318.
- [Le5] V. LEHMANN, *Thin Solid Films*, **1995**, *255*, 1–4.
- [Le6] V. G. LEVICH, *Acta Phys. Chim. S.S.S.R.*, **1942**, *17*, 257.
- [Le7] L. LEBOUCHER, L. W. FISCHER, W. BILTZ, *Z. Anorg. Chem.*, **1932**, *207*, 61.
- [Le8] V. LEHMANN, H. FÖLL, *J. Electrochem. Soc.*, **1990**, *137*, 653–659.
- [Le9] V. LEHMANN, *J. Electrochem. Soc.*, **1993**, *140*, 2836–2843.
- [Le10] V. LEHMANN, B. JOBST, T. MUSCHIK, A. KUX, V. PETROVA-KOCH, *Jpn. J. Appl. Phys.*, **1993**, *32*, 2095–2099.
- [Le11] V. LEHMANN, H. FÖLL, *J. Electrochem. Soc.*, **1988**, *135*, 2831–2835.

- [Le12] H. J. LEWERENZ, *Electrochim. Acta*, **1992**, *37*, 847–864.
- [Le13] H. J. LEWERENZ, M. AGGOUR, *J. Electroanal. Chem.*, **1993**, *351*, 159–168.
- [Le14] V. LEHMANN, F. HOFMANN, F. MÖLLER, U. GRÜNING, *Thin Solid Films*, **1995**, *255*, 20–22.
- [Le15] V. LEHMANN, H. CERVA, U. GÖSELE, *Mater. Res. Soc. Symp. Proc.*, **1992**, *256*, 3–6.
- [Le16] G. LERONDEL, R. ROMESTAIN, S. BARRÉ, *J. Appl. Phys.*, **1997**, *81*, 6171–6178.
- [Le17] V. LEHMANN, U. GRÜNING, *Thin Solid Films*, **1997**, *297*, 13–17.
- [Le18] V. LEHMANN, *Thin Solid Films*, **1996**, *276*, 138–142.
- [Le19] V. LEHMANN, *Adv. Mater.*, **1992**, *4*, 762–764.
- [Le20] H.-D. LEE, H.-J. LEE, C.-K. KIM, C.-H. HAN, *Appl. Phys. Lett.*, **1995**, *66*, 3272–3274.
- [Le21] V. LEHMANN, S. RÖNNEBECK, *J. Electrochem. Soc.*, **1999**, *146*, 2968–2975.
- [Le22] V. LEHMANN, *Electrochem. Soc. Proc.*, **1996**, 96-18, 78–83.
- [Le23] V. LEHMANN, R. STENGL, A. LUIGART, *Mater. Sci. Eng., B*, **2000**, *69/70*, 11–22.
- [Le24] V. LEHMANN, U. GÖSELE, *Mater. Res. Soc. Symp. Proc.*, **1993**, *283*, 27–32.
- [Le25] E. J. LEE, J. S. HA, M. J. SAILOR, *Mater. Res. Soc. Symp. Proc.*, **1995**, *358*, 387–392.
- [Le26] S. E. LÉTANT, S. CONTENT, T. T. TAN, F. ZENHAUSERN, M. J. SAILOR, *Sens. Actuators*, **2000**, *85*, 193–198.
- [Le27] V. LEHMANN, R. STENGL, H. REISINGER, R. DETEMPLE, W. THEIS, *Appl. Phys. Lett.*, **2001**, *78*, 589–591.
- [Le28] S. W. LEONARD, H. M. VAN DRIEL, A. BIRNER, U. GÖSELE, P. R. VILLENEUVE, *Opt. Lett.*, **2000**, *25*, 1550–1552.
- [Le29] S. B. LEE, D. BABIC, *J. Electrochem Soc.*, **2000**, *147*, 4512–4518.
- [Le30] V. LEHMANN, S. RÖNNEBECK, in *Proceedings of the 14th IEEE International MEMS Conference*, Miyazaki, **2001**, pp. 84–85.
- [Le31] V. LEHMANN, in *Proceedings of the 8th International ECS Symposium on Passivity of Metals and Semiconductors*, **2000**, p. 410.
- [Li1] T. L. LIN, S. C. CHEN, Y. C. KAO, K. L. WANG, *J. Appl. Phys.*, **1986**, *48*, 1793–5.
- [Li2] H. LINDE, L. AUSTIN, *J. Electrochem. Soc.*, **1992**, *139*, 1170–1174.
- [Li3] T. LIN, M. E. SIXTA, J. N. COX, M. E. DELANEY, *Mater. Res. Soc. Symp. Proc.*, **1993**, *298*, 379–384.
- [Li4] K.-H. LI, C. TSAI, J. C. CAMPBELL, B. K. HANCE, J. M. WHITE, *Appl. Phys. Lett.*, **1993**, *62*, 3501–3503.
- [Li5] G. LI, X. HOU, S. YUAN, H. CHEN, F. ZHANG, H. FAN, X. WANG, *J. Appl. Phys.*, **1996**, *80*, 5967–5970.
- [Li6] K.-H. LI, C. TSAI, J. SARATHY, J. C. CAMPBELL, *Appl. Phys. Lett.*, **1993**, *62*, 3192.
- [Li7] K. A. LITTAU, P. J. SZAJOWSKI, A. J. MULLER, A. R. KORTAN, L. E. BRUS, *J. Phys. Chem.*, **1993**, *97*, 1224–1230.
- [Li8] M. LIGEON, F. MULLER, R. HERINO, F. GASPARD, *J. Appl. Phys.*, **1989**, *66*, 3814–3819.
- [Li9] F. LI, M. K. BALAZS, B. E. DEAL, *Solid State Technol.*, **2000**, *43*, 87–98.
- [Li10] X. LI, P. W. BOHN, *Appl. Phys. Lett.*, **2000**, *77*, 2572–2574.
- [Li11] M. LIEHR, C. M. GREENLIEF, S. R. KASI, M. OFFENBERG, *Appl. Phys. Lett.*, **1990**, *56*, 629–632.
- [Lo1] A. LONI, L. T. CANHAM, M. G. BERGER, R. ARENS-FISCHER, H. MÜNDER, H. LÜTH, H. F. ARRAND, T. M. BENSON, *Thin Solid Films*, **1996**, *276*, 143–146.
- [Lo2] H. A. LOPEZ, P. M. FAUCHET, *Appl. Phys. Lett.*, **1999**, *75*, 3989–3991.
- [Lo3] H. A. LOPEZ, P. M. FAUCHET, *Appl. Phys. Lett.*, **2000**, *77*, 3704–3706.
- [Lu1] M. H. LUDWIG, A. AUGUSTIN, R. E. HUMMEL, TH. GROSS, *J. Appl. Phys.*, **1996**, *80*, 5318–5324.
- [Lu2] Y. LUBIANIKER, I. BALBERG, *Phys. Rev. Lett.*, **1997**, *78*, 2433.
- [Ly1] V. LYSENKO, S. PERICHON, B. REMAKI, D. BARBIER, B. CHAMPAGNON, *J. Appl. Phys.*, **1999**, *86*, 6841–6846.
- [Ma1] M. MATSUMURA, S. R. MORRISON, *J. Electroanal. Chem.*, **1983**, *147*, 157–166.
- [Ma2] M. J. MADOU, W. P. GOMES, F. FRANSEN, F. CARDON, *J. Electrochem. Soc.*, **1982**, *129*, 2749.
- [Ma3] H. Z. MASSOUD, J. D. PLUMMER, E. A. IRENE, *J. Electrochem. Soc.*, **1985**, *132*, 1745–1753.

- [Ma4] W. D. MACKINTOSH, H. H. PLATTNER, *J. Electrochem. Soc.*, **1977**, *124*, 396–400.
- [Ma5] M. J. MADOU, S. R. MORRISON, V. P. BONDAENKO, *J. Electrochem. Soc.*, **1988**, *135*, 229–235.
- [Ma6] T. MARUYAMA, S. OHTANI, *Appl. Phys. Lett.*, **1994**, *65*, 1346–1348.
- [Ma7] E. MARTIN, C. DELERUE, G. ALLAN, M. LANNOO, *Phys. Rev. B*, **1994**, *50*, 18258–18267.
- [Ma8] J. J. MARES, J. KRISTOFIK, E. HULICIUS, *Thin Solid Films*, **1995**, *255*, 272–275.
- [Ma9] P. MALY, J. KUDRNA, F. TROJANEK, A. HOSPODKOVA, *Thin Solid Films*, **1996**, *273*, 84–87.
- [Ma10] T. MATSUMOTO, O. B. WRIGHT, T. FUTAGI, H. MIMURA, Y. KANEMITSU, *Mater. Res. Soc. Symp. Proc.*, **1993**, *298*, 199–203.
- [Ma11] T. MATSUMOTO, Y. MASUMOTO, S. NAKASHIMA, N. KOSHIDA, *Thin Solid Films*, **1997**, *297*, 31–34.
- [Ma12] M. MAJIMA, T. OTOGAWA, Y. KITAGAWARA, *Jpn. J. Appl. Phys.*, **1997**, *36*, 6195–6199.
- [Ma13] T. MATSUMOTO, M. DAIMON, H. MIMURA, Y. KANEMITSU, N. KOSHIDA, *J. Electrochem. Soc.*, **1995**, *142*, 3528–3533.
- [Ma14] G. MAUCKNER, K. THONKE, T. BAIER, T. WALTER, R. SAUER, *J. Appl. Phys.*, **1994**, *75*, 4167–4170.
- [Ma15] N. MATSUMOTO, *Jpn. J. Appl. Phys.*, **1998**, *37*, 5425–5436.
- [Ma16] H. MATSUMOTO, K. HIGUCHI, S. KYUSHIN, M. GOTO, *Angew. Chem. Int. Ed. Engl.*, **1992**, *31*, 1354.
- [Ma17] G. MAUCKNER, J. HAMANN, W. REBITZER, T. BAIER, K. THONKE, R. SAUER, *Mater. Res. Soc. Symp. Proc.*, **1995**, *358*, 489–494.
- [Mc1] P. MCTIGUE, T. A. O'DONNELL, B. VERITY, *Aust. J. Chem.*, **1985**, *38*, 1797.
- [Mc2] R. MCINTOSH, T.-S. KUAN, E. DEFRESART, *J. Electron. Mater.*, **1992**, *21*, 57–60.
- [Mc3] P. MCCORD, S. L. YAU, A. J. BARD, *Science* **1992**, *257*, 68–69.
- [Me1] M. MEHREGANY, S. D. SENTURIA, *Sens. Actuators*, **1988**, *13*, 375–390.
- [Me2] A. MERLOS, M. C. ACERO, M. H. BAO, J. BAUSELLS, J. ESTEVE, *Sens. Actuators, A*, **1993**, *37–38*, 737–743.
- [Me3] E. MENDEL, *Solid State Technol.*, **1967**, *10*, 27.
- [Me4] M. MEURIS, P. W. MERTENS, A. OPDEBEECK, H. F. SCHMIDT, M. DEPAS, S. VEREECKE, M. M. HEYNS, A. PHILIPPOSIAN, *Solid State Technol.*, **1967**, *38*, 109–113.
- [Me5] J. E. A. M. VAN DEN MEERAKKER, J. H. C. VAN VEGCHEL, *J. Electrochem. Soc.*, **1989**, *136*, 1949–1957.
- [Me6] G. MENDE, E. HENSEL, F. FENSKE, H. FLIETNER, *Thin Solid Films*, **1989**, *168*, 51–60.
- [Me7] G. MENDE, *J. Electrochem. Soc.*, **1980**, *127*, 2085.
- [Me8] P. MEAKIN, *Phys. Rev. A*, **1983**, *27*, 2616.
- [Me9] B. K. MEYER, V. PETROVA-KOCH, T. MUSCHIK, H. LINKE, P. OMEILING, V. LEHMANN, *Appl. Phys. Lett.*, **1993**, *63*, 1930–1932.
- [Me10] E. A. MEULENKAMP, L. M. PETER, D. J. RILEY, R. I. WIELGOSZ, *J. Electroanal. Chem.*, **1995**, *392*, 97.
- [Me11] R. MEMMING, G. SCHWANDT, *Surf. Sci.*, **1966**, *4*, 109.
- [Me12] G. MENDE, H. FLIETNER, M. DEUTSCHER, *J. Electrochem. Soc.*, **1993**, *140*, 188–194.
- [Me13] G. MENDE, in *Semiconductor Micromachining Vol. II* (Eds S. A. CAMPBELL, H. J. LEWERENZ), Wiley & Sons, New York, **1998**, pp. 263–312.
- [Me14] J. E. A. M. MEERAKKER, M. R. L. MELLIER, *J. Electrochem. Soc.*, **2001**, *148*, G166–171.
- [Mg1] R. M'GHAIETH, H. MAAREF, I. MIHALCESCU, J. C. VIAL, *Microelectron. J.*, **1999**, *30*, 695–698.
- [Mi1] I. MIHALCESCU, J. C. VIAL, A. BSIESY, F. MULLER, R. ROMESTAIN, E. MARTIN, C. DELERUE, M. LANNOO, G. ALLAN, *Phys. Rev. B*, **1995**, *51*, 17605–17613.
- [Mi2] S. MIYAZAKI, K. SAKAMOTO, K. SHIBA, M. HIROSE, *Thin Solid Films*, **1995**, *255*, 99–102.
- [Mi3] H. MIZUNO, H. KOYAMA, N. KOSHIDA, *Appl. Phys. Lett.*, **1996**, *69*, 3779–3781.
- [Mi4] I. MIHALCESCU, G. LERONDEL, R. ROMESTAIN, *Thin Solid Films*, **1997**, *297*, 245–249.
- [Mi5] P. DE MIERRY, A. ETCHEBERRY, M. AUCOUTURIER, *J. Appl. Phys.*, **1991**, *69*, 1099–1101.
- [Mi6] T. MILLS, *IEEE Reliability Phys. Symp. Proc.*, **1983**, 324–331.

- [Mi7] H. MIMURA, T. FUTAGI, T. MATSUMOTO, T. NAKAMURA, Y. KANEMITSU, *Jpn. J. Appl. Phys.*, **1994**, *33*, 586–589.
- [Mi8] MIKRAJUDDIN, F. G. SHI, K. OKUYAMA, *Microelectron. J.*, **2000**, *31*, 187–191.
- [MI1] R. MLCAK, H. L. TULLER, P. GREIFF, J. SOHN, L. NILES, *Sens. Actuators A*, **1994**, *40*, 49–54.
- [Mo1] M. MORITA, T. OHMI, E. HASEGAWA, M. KAWAKAMI, M. OHWADA, *J. Appl. Phys.*, **1990**, *68*, 1272–1281.
- [Mo2] S. R. MORRISON, *Electrochemistry at Semiconductor and Oxidized Metal Electrodes*, Plenum Press, New York, **1980**.
- [Mo3] P. MORFOULI, G. PANANAKAKIS, *Phys. Status Solidi*, **1989**, *111*, 529–539.
- [Mo4] A. MOLASSIOTI-DOHMS, U. DETTLAFF-WEGLIKOWSKA, S. FINKBEINER, W. HÖNLE, J. WEBER, *J. Electrochem. Soc.*, **1996**, *143*, 2674–2677.
- [Mo5] D. J. MONK, D. S. SOANE, R. T. HOWE, *J. Electrochem. Soc.*, **1994**, *141*, 264–269.
- [Mo6] D. J. MONK, D. S. SOANE, R. T. HOWE, *Thin Solid Films*, **1993**, *232*, 1–12.
- [Mo7] Y. MOCHIZUKI, M. MIZUTA, *Jpn. J. Appl. Phys.*, **1993**, *32*, L1387.
- [Mo8] T. MONGUCHI, H. FUJIOKA, K. ONO, Y. BABA, M. OSHIMA, *J. Electrochem. Soc.*, **2000**, *147*, 602.
- [Mo9] Y. MOROSHITA, S. KAWAI, J. SUNAGAWA, T. SUZUKI, *Electrochem. Solid-State Lett.*, **2001**, *4*, G4–6.
- [Mu1] H. MURAOKA, T. OHHASHI, Y. SUMITOMO, in *Semiconductor Silicon* (Eds H. R. HUFF, P. R. BURGESS), Electrochemical Society Symposium Series, Electrochemical Society, Princeton, NJ, **1973**, pp. 327–338.
- [Mu2] H. MÜNDER, C. ANDRZEJAK, M. G. BERGER, U. KLEMRADT, H. LÜTH, R. HERINO, M. LIGEON, *Thin Solid Films*, **1992**, *221*, 27–33.
- [Mu3] H. MÜNDER, M. G. BERGER, S. FROHNHOFF, M. THÖNISSEN, H. LÜTH, *J. Lumin.*, **1993**, *57*, 5–8.
- [Mu4] W. W. MULLINS, R. F. SEKERKA, *J. Appl. Phys.*, **1964**, *35*, 444.
- [Mu5] N. MÜLLER, R. TENNE, *Appl. Phys. Lett.*, **1981**, *39*, 283.
- [Mu6] F. MÜLLER, A. BIRNER, J. SCHILLING, U. GÖSELE, C. KETTNER, P. HÄNGGI, *Phys. Status Solidi A*, **2000**, *182*, 585.
- [My1] M. MYNBAEVA, A. TITKOV, A. KRYGANOVSII, V. RATINIKOV, K. MYNBAEV, H. HUHTINEN, R. LAIHO, V. DIMITRIEV, *Appl. Phys. Lett.*, **2000**, *76*, 1113–1115.
- [Na1] K. J. NASH, P. D. J. CALCOTT, L. T. CANHAM, R. J. NEEDS, *Phys. Rev. B*, **1995**, *51*, 17698–17707.
- [Na2] A. G. NASSIPOULOS, S. GRIGOROPOULOS, D. PAPADIMITRIOU, *Appl. Phys. Lett.*, **1996**, *69*, 2267–2269.
- [Na3] T. NAKAGAWA, H. KOYAMA, N. KOSHIDA, *Appl. Phys. Lett.*, **1996**, *69*, 3206–3208.
- [Na4] T. NAMMORI, T. NUNOI, Y. HAYASHI, *Jpn. J. Appl. Phys.*, **1990**, *29*, L166–168.
- [Na5] K. S. NAHM, Y. H. SEO, H. J. LEE, *J. Appl. Phys.*, **1997**, *81*, 2418–2424.
- [Na6] A. G. NASSIPOULOS, S. GRIGOROPOULOS, L. T. CANHAM, A. HALIMAOU, I. BERBEZIER, E. GOGOLIDES, D. PAPADIMITRIOU, *Thin Solid Films*, **1995**, *255*, 329–333.
- [Na7] A. NATARAJAN, G. OSKAM, P. C. SEARSON, *J. Appl. Phys.*, **1998**, *83*, 2112–2120.
- [Na8] T. NAKAGAWA, H. SUGIYAMA, N. KOSHIDA, *Jpn. J. Appl. Phys.*, **1998**, *37*, 7186–7189.
- [Ne1] S. S. NEOGI, D. VENABLES, Z. MA, D. M. MAHER, M. TAYLOR, S. CORCORAN, *J. Appl. Phys.*, **1997**, *82*, 5811–5815.
- [Ne2] R. J. REEDS, S. BHATTACHARJEE, K. J. NASH, A. QTEISH, A. J. READ, L. T. CANHAM, *Phys. Rev. B*, **1994**, *50*, 14223–14227.
- [Ni1] M. NIWANO, J. KAGEYAMA, K. KURITA, K. KINASHI, I. TAKAHASHI, N. MIYAMOTO, *J. Appl. Phys.*, **1994**, *76*, 2157–2163.
- [Ni2] A. NISHIDA, K. NAKAGAWA, H. KAKIBAYASHI, T. T. SHIMIDA, *Jpn. J. Appl. Phys.*, **1992**, *31*, L1219.
- [Ni3] M. NIWANO, T. MIURA, Y. KIMURA, R. TAJIMA, N. MIYAMOTO, *J. Appl. Phys.*, **1996**, *79*, 3708–3713.
- [Ni4] K. NISHIMURA, Y. NAGAO, N. IKEDA, *J. Appl. Phys.*, **1998**, *37*, L303–305.
- [Ni5] Y. NISHIMOTO, T. ISHIHARA, K. NAMBA, *J. Electrochem. Soc.*, **1999**, *146*, 457–461.
- [Ni6] A. J. NIJDAM, E. VAN VEENENDAAL, J. G. E. GARDENNIERS, A. P. M. KENTGENS, G. H. NACHTEGAAL, M. ELWENSPOEK, *J. Electrochem. Soc.*, **2000**, *147*, 2195–2198.

- [No1] R. A. NOULTY, D. G. LEAIST, *Electrochim. Acta*, **1985**, 30, 1095–1099.
- [No2] D. D. NOLTE, *Appl. Phys. Lett.*, **1997**, 25, 3401–3403.
- [Ob1] G. OBERMEIER, J. HAGE, D. HUBER, *J. Appl. Phys.*, **1997**, 82, 595–600.
- [Og1] H. OGAWA, K. ISHIKAWA, M. T. SUZUKI, Y. HAYAMI, S. FUJIMURA, *Jpn. J. Appl. Phys.*, **1995**, 34, 732–736.
- [Og2] A. OGURA, *Jpn. J. Appl. Phys.*, **1996**, 35, L71–73.
- [Og3] Y. H. OGATA, F. KATO, T. TSUBOI, T. SAKKA, *J. Electrochem. Soc.*, **1998**, 145, 2439–2444.
- [Oh1] T. OHMI, *J. Electrochem. Soc.*, **1996**, 143, 2957–2964.
- [Oh2] H. OHEDA, *Phys. Rev. B*, **1995**, 52, 16530–16541.
- [Oh3] T. OHWAKI, M. TAKEDA, Y. TAKAI, *Jpn. J. Appl. Phys. B*, **1997**, 36, 5507–5513.
- [Oh4] H. OHJI, P. J. FRENCH, *Sens. Actuators*, **1999**, 74, 109–112.
- [Oh5] H. OHJI, P. J. FRENCH, K. TSUTSUMI, *Sens. Actuators*, **2000**, 82, 254–258.
- [Ok1] P. O'KEEFFE, Y. AOYAGI, S. KOMURO, T. KATO, T. MORIKAWA, *Appl. Phys. Lett.*, **1995**, 66, 836–838.
- [Ok2] S. OKA, M. KATAYAMA, *Jpn. J. Appl. Phys.*, **1997**, 36, 1995–1998.
- [Ok3] T. OKU, K. SATO, M. OTSUBO, *Jpn. J. Appl. Phys.*, **1997**, 36, 1374–1379.
- [Oo1] N. OOKUBO, S. SAWADA, *Phys. Rev. B*, **1995**, 51, 17526–17534.
- [Or1] D. W. OSMOND, *IBM Techn. Disclosure Bull.*, **1982**, 24, 5150–5151.
- [Os1] H.-C. OSTENDORF, A. L. ENDRÖS, *Appl. Phys. Lett.*, **1997**, 71, 3275–3277.
- [Os2] S. OSSICINI, C. M. BERTONI, M. BIAGINI, A. LUGLI, G. ROMA, O. BISI, *Thin Solid Films*, **1997**, 297, 154–162.
- [Ot1] S. OTTOW, G. S. POPKIROV, H. FÖLL, *J. Electroanal. Chem.*, **1998**, 455, 29–37.
- [Ot2] S. OTTOW, V. LEHMANN, H. FÖLL, *J. Electrochem. Soc.*, **1996**, 143, 385.
- [Ow1] J. C. QWRUTSKY, J. K. RICE, S. GUHA, P. STEINER, W. LANG, *Appl. Phys. Lett.*, **1995**, 67, 1966–1968.
- [Oz1] F. OZANAM, J. N. CHAZALVIEL, A. RADI, M. ETMAN, *Ber. Bunsenges. Phys. Chem.*, **1991**, 95, 98.
- [Oz2] F. OZANAM, C. DA FONSECA, A. VENKATESWARA RAO, J.-N. CHAZALVIEL, *Appl. Spectrosc.*, **1997**, 51, 519.
- [Oz3] F. OZANAM, J. N. CHAZALVIEL, R. B. WEHRSPORN, *Thin Solid Films*, **1997**, 297, 53–60.
- [Oz4] F. OZANAM, J. N. CHAZALVIEL, *J. Electron Spectrosc. Relat. Phenom.*, **1993**, 64/65, 395–402.
- [Pa1] L. PAULING, *The Nature of the Chemical Bond*, 3rd edn, Cornell University Press, Ithaca, NY, **1960**.
- [Pa2] E. D. PALIK, V. M. BERMUDEZ, O. J. GLEMBOCKI, *J. Electrochem. Soc.*, **1985**, 132, 871–884.
- [Pa3] E. D. PALIK, O. J. GLEMBOCKI, I. HEARD, P. S. BRUNO, L. TENERZ, *J. Appl. Phys.*, **1991**, 70, 3291–3300.
- [Pa4] E. D. PALIK, H. F. GRAY, P. B. KLEIN, *J. Electrochem. Soc.*, **1983**, 130, 956–959.
- [Pa5] E. D. PALIK, O. J. GLEMBOCKI, J. D. RINKO, I. HEARD, *J. Electrochem. Soc.*, **1989**, 136, 1420–1425.
- [Pa6] E. D. PALIK, O. J. GLEMBOCKI, I. HEARD, *J. Electrochem. Soc.*, **1987**, 134, 404–409.
- [Pa7] E. D. PALIK, O. J. GLEMBOCKI, R. E. STAHLBUSH, *J. Electrochem. Soc.*, **1988**, 135, 3126.
- [Pa8] E. D. PALIK, J. W. FAUST, H. F. GRAY, R. F. GREENE, *J. Electrochem. Soc.*, **1982**, 129, 2051–2059.
- [Pa9] V. P. PARKHUTIK, *Electrochim. Acta*, **1991**, 36, 1611–1616.
- [Pa10] V. P. PARKHUTIK, L. K. GLINENKO, V. A. LABUNOV, *Surf. Technol.*, **1983**, 20, 1265–1277.
- [Pa11] V. P. PARKHUTIK, J. M. ALBELLA, J. M. MARTINEZ-DUART, J. M. GOMEZ-RODRIGUEZ, A. M. BARO, V. I. SHERSHULSKY, *Appl. Phys. Lett.*, **1992**, 62, 366–368.
- [Pa12] L. PAVESI, M. CESCHINI, *Phys. Rev. B*, **1993**, 49, 17625.
- [Pa13] D. PAPADIMITRIOU, Y. S. RAPTIS, A. G. NASSIOPOULOU, G. KALTSAS, *Phys. Status Solidi A*, **1998**, 43, 43–48.
- [Pa14] V. PAILLARD, P. PUECH, *Phys. Status Solidi A*, **1998**, 43, 43–48.
- [Pe1] V. PETROVA-KOCH, T. MUSCHIK, A. KUX, B. K. MEYER, F. KOCH, V. LEHMANN, *Appl. Phys. Lett.*, **1992**, 61, 943–945.
- [Pe2] V. PETROVA-KOCH, A. KUX, F. MÜLLER, T. MUSCHIK, F. KOCH, V. LEHMANN, *Mater. Res. Soc. Symp. Proc.*, **1992**, 256, 41–46.



- [Pe3] E. PEINER, A. SCHLACHETZKI, D. KRÜGER, *J. Electrochem. Soc.*, **1995**, *142*, 576–580.
- [Pe4] E. PEINER, A. SCHLACHETZKI, *J. Electrochem. Soc.*, **1992**, *139*, 552–557.
- [Pe5] V. PETROVA-KOCH, T. MUSCHIK, *Thin Solid Films*, **1995**, *255*, 246–249.
- [Pe6] K. E. PETERSEN, *Proc. IEEE*, **1982**, *70*, 420–454.
- [Pe7] L.-H. PENG, C.-W. CHUANG, J.-K. HO, C.-N. HUANG, C.-Y. CHEN, *Appl. Phys. Lett.*, **1998**, *72*, 939–941.
- [Pe8] J. PERRIERE, J. SIEJKA, R. P. H. CHANG, *Thin Solid Films*, **1982**, *95*, 309.
- [Pe9] S. PÉRICHON, V. LYSENKO, P. ROUSSEL, B. REMAKI, B. CHAMPAGNON, D. BARBIER, P. PINARD, *Sens. Actuators*, **2000**, *85*, 335–339.
- [Pe10] C. PENG, K. D. HIRSCHMAN, P. M. FAUCHET, *J. Appl. Phys.*, **1996**, *80*, 295–300.
- [Ph1] F. PHILLIP, K. URBAN, M. WILKENS, *Ultramicroscopy*, **1984**, *13*, 379–386.
- [Pi1] C. PICKERING, M. I. J. BEALE, D. J. ROBBINS, P. J. PEARSON, R. GREEF, *J. Phys. C: Solid State Phys.*, **1984**, *17*, 6535–6552.
- [Pi2] G. J. PIETSCH, *Appl. Phys. A*, **1995**, *60*, 347–363.
- [Pi3] G. J. PIETSCH, Y. J. CHABAL, G. S. HIGASHI, *J. Appl. Phys.*, **1995**, *78*, 1650–1658.
- [Pl1] Y. V. PLESKOV, *Dokl. Akad. Nauk*, **1959**, *126*, 111.
- [Po1] E. A. PONOMAREV, C. LEVY-CLEMENT, *Electrochem. Solid-State Lett.*, **1998**, *1*, 42–45.
- [Po2] G. POLISSKI, H. HECKLER, D. KOVALEV, M. SCHWARTZKOPFF, F. KOCH, *Appl. Phys. Lett.*, **1998**, *73*, 1107–1109.
- [Po3] G. S. POPKIROV, S. OTTOW, *J. Electroanal. Chem.*, **1997**, *429*, 47–54.
- [Pr1] J. B. PRICE, in *Semiconductor Silicon* (Eds H. R. HUFF, P. R. BURGESS), Electrochemical Society Symposium Series, Electrochemical Society, Princeton, NJ, **1973**, p. 339.
- [Pr2] H. PRIGGE, P. GERLACH, A. SCHNEGG, H. JACOB, *J. Electrochem. Soc.*, **1991**, *138*, 1385–1389.
- [Pr3] H. PROSCHKE, G. NAGORSEN, D. ROSS, *J. Electrochem. Soc.*, **1992**, *139*, 521–524.
- [Pr4] J. P. PROOT, C. DELERUE, G. ALLEN, *Appl. Phys. Lett.*, **1992**, *61*, 1948–1950.
- [Pr5] S. M. PROKES, O. J. GLEMBOCKI, *Phys. Rev. B*, **1994**, *49*, 2238.
- [Pr6] S. M. PROKES, W. E. CARLOS, V. M. BERMUDEZ, *Appl. Phys. Lett.*, **1992**, *61*, 1447–1449.
- [Pr7] E. K. PROBST, P. A. KOHL, *J. Electrochem. Soc.*, **1994**, *141*, 1006–1013.
- [Pr8] A. PRASAD, S. BALAKRISHNAN, S. K. JAIN, G. C. JAIN, *J. Electrochem. Soc.*, **1982**, *129*, 596–599.
- [Qu1] G. QUIEROLO, M. L. POLIGNANO, *J. Vac. Sci. Technol.*, **1992**, *10*, 408.
- [Ra1] S. I. RAIDER, R. FLITSCH, M. J. PALMER, *J. Electrochem. Soc.*, **1975**, *122*, 413.
- [Ra2] J. RAPPICH, V. Y. TIMOSHENKO, T. DITTRICH, *Ber. Bunsenges. Phys. Chem.*, **1997**, *101*, 139–142.
- [Ra3] S. RAUSCHER, TH. DITTRICH, M. AGGOUR, J. RAPPICH, H. FLIETNER, H. J. LEWERENZ, *Appl. Phys. Lett.*, **1995**, *66*, 3018–3020.
- [Re1] A. REISMAN, M. BERKENBIILT, S. A. CHAN, F. B. KAUFMANN, D. C. GREEN, *J. Electrochem. Soc.*, **1979**, *126*, 1406–1415.
- [Re2] A. J. READ, R. J. NEEDS, K. J. NASH, L. T. CANHAM, P. D. J. CALCOTT, A. QUEISH, *Phys. Rev. Lett.*, **1992**, *69*, 1232–1235.
- [Re3] S. H. REN, J. D. DOW, *Phys. Rev. B*, **1992**, *45*, 6492–6496.
- [Re4] C. F. REINHARDT, W. G. HUME, A. L. LINCH, J. M. WETHERHOLD, *J. Chem. Educ.*, **1969**, *46*, A171–179.
- [Re5] A. J. REDDY, J. MICHEL, B. PAREKH, J.-H. SHYU, L. C. KIMERLING, *J. Electrochem. Soc.*, **2000**, *147*, 2337–2339.
- [Ri1] M. M. RIEGER, P. A. KOHL, *J. Electrochem. Soc.*, **1995**, *142*, 1490–1495.
- [Ri2] A. RICHTER, P. STEINER, F. KOZŁOWSKI, W. LANG, *IEEE Electron Device Lett.*, **1991**, *12*, 691–692.
- [Ri3] M. M. RIEGER, J. C. FLAKE, P. A. KOHL, *J. Electrochem. Soc.*, **1999**, *146*, 4485–4489.
- [Ri4] M. H. AL RIFAI, M. CHRISTOPHERSON, S. OTTOW, J. CARSTENSEN, H. FÖLL, *J. Electrochem. Soc.*, **2000**, *147*, 627–635.
- [Ro1] H. ROBBINS, B. SCHWARTZ, *J. Electrochem. Soc.*, **1959**, *106*, 505.

- [Ro2] H. ROBBINS, B. SCHWARTZ, *J. Electrochem. Soc.*, **1960**, *107*, 108.
- [Ro3] I. RONGA, A. BSIESY, F. GASPARD, R. HERINO, M. LIGEON, F. MULLER, *J. Electrochem. Soc.*, **1991**, *138*, 1403–1407.
- [Ro4] M. ROSENBAUER, M. STUTZMANN, H. D. FUCHS, S. FINKENBEINER, J. WEBER, *J. Lumin.*, **1993**, *57*, 153–157.
- [Ro5] M. ROSENBAUER, S. FINKENBEINER, E. BUSTARRET, J. WEBER, M. STUTZMANN, *Phys. Rev.*, **1995**, *51*, 10539–10547.
- [Ro6] M. B. ROBINSON, A. C. DILLON, S. M. GEORGE, *Appl. Phys. Lett.*, **1993**, *62*, 1494–1496.
- [Ro7] F. C. RONG, J. F. HARVEY, E. H. POINDEXTER, G. J. GERARDI, *Appl. Phys. Lett.*, **1993**, *63*, 920–922.
- [Ro8] S. RÖNNEBECK, S. OTTOW, J. CARSTENSEN, H. FÖLL, *Electrochem. Solid-State Lett.*, **1999**, *2*, 126–128.
- [Ro9] W. J. ROYEA, D. J. MICHALAK, N. S. LEWIS, *Appl. Phys. Lett.*, **2000**, *77*, 2566–2568.
- [Ru1] W. R. RUNYAN, *Semiconductor Instrumentation and Measurements*, McGraw-Hill, New York, **1975**, Chapter 4.
- [Ru2] M. RÜCKSCHLOSS, O. AMBACHER, S. VEPREK, *J. Lumin.*, **1993**, *57*, 1–4.
- [Ru3] M. RUIKE, M. HOUZOUJI, A. MOTOHASHI, N. MURASE, A. KINOSHITA, K. KANEKO, *Langmuir*, **1996**, *12*, 4828–4831.
- [Sa1] S. G. DOS SANTOS FILHO, C. M. HASENACK, L. C. SALAY, P. MERTENS, *J. Electrochem. Soc.* **1995**, *142*, 902–907.
- [Sa2] K. SAITO, M. MATSUDA, M. YASUTAKE, T. HAITTORI, *Jpn. J. Appl. Phys.*, **1995**, *34*, L609–611.
- [Sa3] N. SATO, K. SAKAGUCHI, K. YAMAGATA, Y. FUJIYAMA, T. YONEHARA, *J. Electrochem. Soc.*, **1995**, *142*, 3116–3122.
- [Sa4] G. D. SANDERS, Y.-C. CHANG, *Phys. Rev. B*, **1992**, *45*, 9202–9213.
- [Sa5] S. SAWADA, N. HAMADA, N. OOKUBO, *Phys. Rev. B*, **1994**, *49*, 5236–5245.
- [Sa6] S. SATO, M. SHIKIDA, Y. MATSUSHIMA, T. YAMASHIRO, K. ASAUMI, Y. IRIYE, M. YAMAMOTO, *Sens. Actuators, A*, **1998**, *64*, 87–93.
- [Sa7] M. J. SAILOR, in *Properties of Porous Silicon* (Ed. L. CANHAM), EMIS Data Review Series No. 18, IEE, London, **1997**, pp. 364–370.
- [Sa8] K. SAKAGUCHI, T. YONEHARA, *Solid State Technol.*, **2000**, *43*, 88–92.
- [Sa9] G. D. SANDERS, C. J. STANTON, Y.-C. CHANG, *Phys. Rev. B*, **1993**, *48*, 11067–11076.
- [Sc1] P. F. SCHMIDT, W. MICHEL, *J. Electrochem. Soc.*, **1957**, *104*, 230–236.
- [Sc2] P. F. SCHMIDT, D. A. KEIPER, *J. Electrochem. Soc.*, **1959**, *106*, 592.
- [Sc3] P. F. SCHMIDT, J. ORASHNIK, C. C. HARDMAN, *Solid-State Electron.*, **1964**, *7*, 631.
- [Sc4] K. SCHULZE, M. HENZLER, *Surf. Sci.*, **1993**, *124*, 336.
- [Sc5] U. SCHNAKENBERG, W. BENECKE, B. LÖCHEL, *Sens. Actuators, A*, **1990**, *21–23*, 1031–1035.
- [Sc6] U. SCHNAKENBERG, W. BENECKE, B. LÖCHEL, S. ULLERICH, P. LANGE, *Sens. Actuators, A*, **1991**, *25–27*, 1–7.
- [Sc7] D. G. SCHIMMEL, *J. Electrochem. Soc.*, **1976**, *123*, 734.
- [Sc8] B. SCHWARTZ, H. ROBBINS, *J. Electrochem. Soc.*, **1961**, *108*, 365.
- [Sc9] B. SCHWARTZ, H. ROBBINS, *J. Electrochem. Soc.*, **1976**, *123*, 1903–1909.
- [Sc10] P. F. SCHMIDT, M. J. RAND, *Solid State Commun.* **1966**, *4*, 169–172.
- [Sc11] G. SCHLICHTHÖRL, E. A. PONOMAREV, L. M. PETER, *J. Electrochem. Soc.*, **1995**, *142*, 3062–3067.
- [Sc12] S. SCHUPPLER, S. L. FRIEDMAN, M. A. MARCUS, D. L. ADLER, X.-H. XIE, F. M. ROSS, T. D. HARRIS, W. L. BROWN, Y. J. CHABAL, L. E. BRUS, P. H. CITRIN, *Phys. Rev. Lett.*, **1994**, *72*, 2648–2651.
- [Sc13] R. SCHWARZ, F. WANG, M. BEN-CHORIN, S. GREBNER, A. NIKOLOV, F. KOCH, *Thin Solid Films*, **1995**, *255*, 23–26.
- [Sc14] M. SCHOISSWOHL, J. L. CANTIN, M. CHAMARRO, H. J. VON BARDELEBEN, T. MORGENSTERN, E. BUGIEL, W. KISSINGER, *Phys. Rev. B*, **1995**, *52*, 11898–11903.
- [Sc15] P. SCHMUKI, D. J. LOCKWOOD, H. J. LABBE, J. W. FRASER, *Appl. Phys. Lett.*, **1996**, *69*, 1620–1623.
- [Sc16] M. SCHOISSWOHL, J. L. CANTIN, H. J. VON BARDELEBEN, *Appl. Phys. Lett.*, **1995**, *66*, 3660–3662.
- [Sc17] D. K. SCHRODER, *IEEE Trans. Electron Devices*, **1997**, *44*, 160–170.

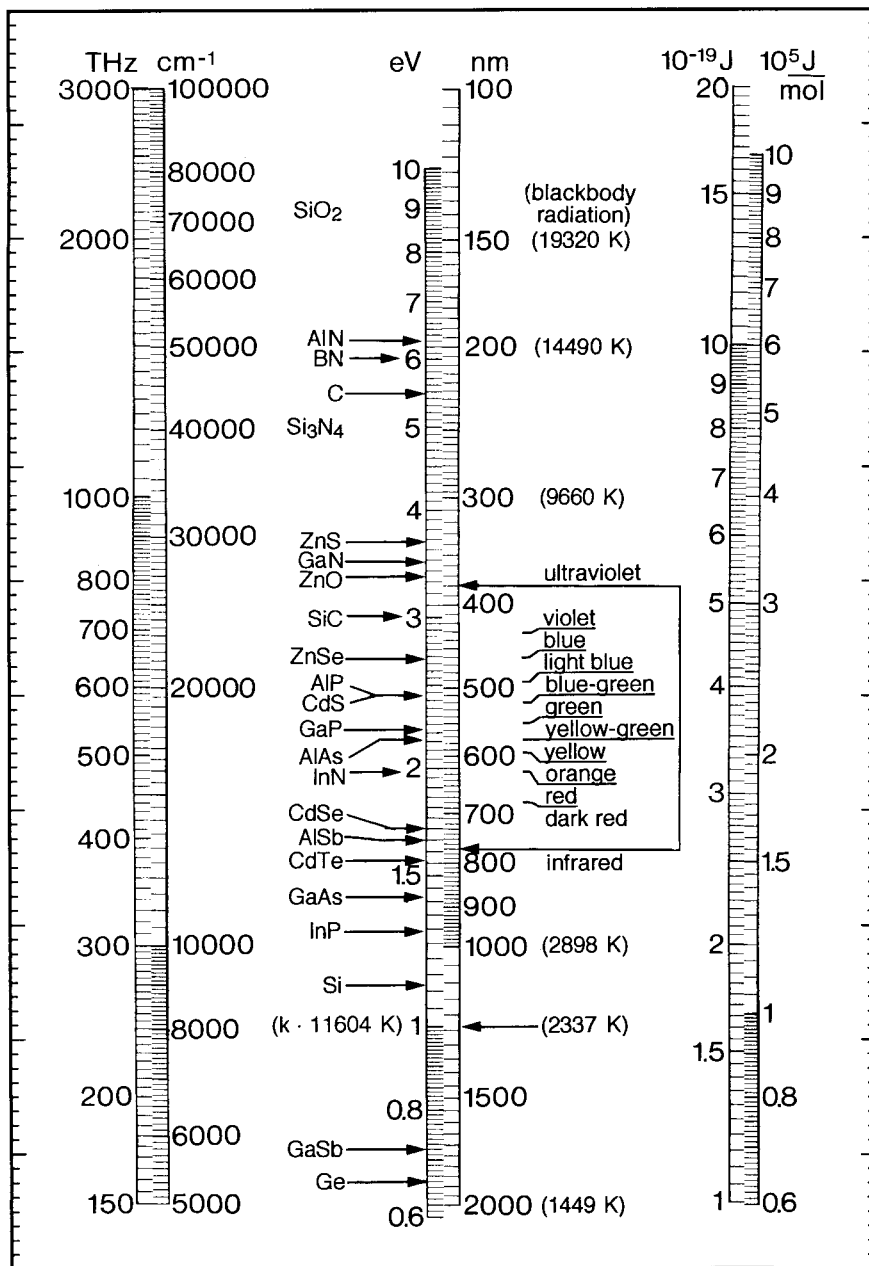
- [Sc18] L. SCHIRONE, G. SOTGIU, M. MONTECCHI, *J. Lumin.*, **1999**, *80*, 163–167.
- [Sc19] R. SCHUSTER, V. KIRCHNER, P. ALLONGUE, G. ERTL, *Science*, **2000**, *289*, 98–101.
- [Sc20] M. J. SCHÖNING, A. KUROWSKI, M. THUST, P. KORDOS, J. W. SCHULTZE, H. LÜTH, *Sens. Actuators, B*, **2000**, *64*, 59–64.
- [Se1] M. SEIPT, *Z. Naturforsch., A: Phys. Sci.*, **1959**, *14*, 926.
- [Se2] C. SERRE, S. BARRET, R. HÉRINO, *J. Electroanal. Chem.*, **1994**, *370*, 145.
- [Se3] H. SEIDEL, L. CSEPREGI, A. HEUBERGER, H. BAUMGÄRTEL, *J. Electrochem. Soc.*, **1990**, *137*, 3612–3626.
- [Se4] H. SEIDEL, L. CSEPREGI, A. HEUBERGER, H. BAUMGÄRTEL, *J. Electrochem. Soc.*, **1990**, *137*, 3626–3632.
- [Se5] F. SECCO D'ARGONA, *J. Electrochem. Soc.*, **1972**, *119*, 948–951.
- [Se6] Y. H. SEO, K. S. NAHM, K. B. LEE, *J. Electrochem. Soc.*, **1993**, *140*, 1453–1458.
- [Se7] P. C. SEARSON, X. G. ZHANG, *J. Electrochem. Soc.*, **1990**, *137*, 2539–2546.
- [Se8] P. C. SEARSON, J. M. MACAULAY, F. M. ROSS, *J. Appl. Phys.*, **1992**, *72*, 253–258.
- [Se9] C. SERRE, S. BARRET, R. HÉRINO, *J. Electrochem. Soc.*, **1994**, *141*, 2049–2053.
- [Se10] R. SEDLACIK, J. OSWALD, R. HÉRINO, *Thin Solid Films*, **1997**, *297*, 64–67.
- [Se11] B. SELL, C. GATZKE, J. M. FERNANDEZ, *Semicond. Sci. Technol.*, **1998**, *13*, 423–427.
- [Se12] S. SEN, J. KONTKIEWICZ, A. M. KONTKIEWICZ, G. NOWAK, J. SIEJKA, P. SAKTHIVEL, K. AHMED, P. MUKHERJEE, S. WITANACHCHI, A. M. HOFF, J. LAGOWSKI, *Mater. Res. Soc. Symp. Proc.*, **1995**, *358*, 369–374.
- [Se13] R. SEDLACIK, F. KAREL, J. OSWALD, A. FEJFAR, I. PELANT, J. KOCKA, *Thin Solid Films*, **1995**, *255*, 269–271.
- [Sh1] K. SHIBA, K. SAKAMOTO, S. MIYAZAKI, M. HIROSE, *Jpn. J. Appl. Phys.*, **1993**, *32*, 2722–2724.
- [Sh2] C. D. SHARPE, P. LILLEY, *J. Electrochem. Soc.*, **1980**, *127*, 1918–1922.
- [Sh3] T. K. SHAM, D. T. JIANG, I. COULTHARD, J. W. LORIMER, X. H. FENG, K. H. TAN, S. P. FRIGO, R. A. ROSENBERG, D. C. HOUGHTON, B. BRYSKIEWICZ, *Nature*, **1993**, *363*, 331–333.
- [Sh4] X. SHENG, H. KOYAMA, N. KOSHIDA, S. IWASAKI, N. NEGISHI, T. CHUMAN, T. YOSHIKAWA, K. OGASAWARA, *J. Vac. Sci. Technol., B*, **1997**, *15*, 1.
- [Sh5] J. S. SHOR, I. GRIMBERG, B.-Z. WEISS, A. D. KURTZ, *Appl. Phys. Lett.*, **1993**, *62*, 2836–2838.
- [Sh6] S. SHIH, K. H. JUNG, T. Y. HSIEH, J. SARATHY, J. C. CAMPBELL, D. L. KWONG, *Appl. Phys. Lett.*, **1992**, *60*, 1863–1865.
- [Si1] E. SIRTIL, A. ADLER, *Z. Metallkd.*, **1961**, *52*, 529–531.
- [Si2] A. J. SIMONS, T. I. COX, M. J. UREN, P. D. J. CALCOTT, *Thin Solid Films*, **1995**, *255*, 12–15.
- [Si3] A. J. SIMONS, in *Properties of Porous Silicon* (Ed. L. CANHAM), EMIS Data Review Series No. 18, IEE, London, **1997**, pp. 192–199.
- [Si4] A. J. SIMONS, T. I. COX, A. LONI, P. D. J. CALCOTT, M. J. UREN, L. T. CANHAM, *Mater. Res. Soc. Symp. Proc.*, **1997**, *452*, 693–698.
- [Si5] S. J. SILVERMAN, D. R. BENN, *J. Electrochem. Soc.*, **1958**, *105*, 150–152.
- [Si6] A. J. SIMONS, in *Properties of Porous Silicon* (Ed. L. CANHAM), EMIS Data Review Series No. 18, IEE, London, **1997**, pp. 176–184.
- [Sm1] R. L. SMITH, S. D. COLLINS, *Phys. Rev. A*, **1989**, *39*, 5409–5413.
- [Sm2] R. L. SMITH, S.-F. CHUANG, S. D. COLLINS, *J. Electron. Mater.*, **1988**, *17*, 533.
- [Sm3] R. L. SMITH, S. D. COLLINS, *J. Appl. Phys.*, **1992**, *71*, R1–22.
- [Sm4] R. L. SMITH, S. D. COLLINS, *Sens. Actuators, A*, **1990**, *21–23*, 830–834.
- [Sm5] L. SMITH, A. SODERBARG, *J. Electrochem. Soc.*, **1993**, *140*, 271.
- [Sm6] R. L. SMITH, B. KLOECK, N. DE ROOIJ, S. D. COLLINS, *J. Electroanal. Chem.*, **1987**, *238*, 103–113.
- [So1] C. J. SOFIELD, A. M. STONEHAM, *Semicond. Sci. Technol.*, **1995**, *10*, 215–244.
- [So2] A. SOMASHEKHAR, S. O'BRIEN, *J. Electrochem. Soc.*, **1996**, *143*, 2885–2891.
- [So3] G. SOTGUI, L. SCHIRONE, F. RALLO, *Thin Solid Films*, **1997**, *297*, 18–21.
- [Sp1] C. A. SPINDT, C. E. HOLLAND, A. ROSENGREEN, I. BRODIE, *J. Vac. Sci. Technol., B*, **1993**, *11*, 468.

- [St1] N. STEERE, *CRC Handbook of Laboratory Safety*, Chemical Rubber Company Press Inc., Florida, USA, 1978.
- [St2] J. STUMPER, R. GREEF, L. M. PETER, *J. Electroanal. Chem.*, **1991**, 310, 445–452.
- [St3] A. J. STECKL, J. XU, H. C. MOGUL, *J. Electrochem. Soc.*, **1994**, 141, 674–679.
- [St4] M. STUTZMANN, M. S. BRANDT, M. ROSENBAUER, H. D. FUCHS, S. FINKBEINER, J. WEBER, P. DEAK, *J. Lumin.*, **1993**, 57, 321–330.
- [St5] P. STEINER, F. KOZLOWSKI, H. SANDMAIER, W. LANG, *Mater. Res. Soc. Symp. Proc.*, **1993**, 283, 343–351.
- [St6] P. STEINER, W. LANG, *Thin Solid Films*, **1995**, 255, 52–58.
- [St7] A. J. STECKL, J. XU, H. C. MOGUL, S. MOGREN, *Appl. Phys. Lett.*, **1993**, 62, 1982–1984.
- [St8] M. STUTZMANN, J. WEBER, M. S. BRANDT, H. D. FUCHS, M. ROSENBAUER, P. DEAK, A. HÖPFNER, A. BREITSCHWERDT, *Adv. Solid State Phys.*, **1992**, 32, 179.
- [St9] A. J. STECKL, J. XU, H. C. MOGUL, *Appl. Phys. Lett.*, **1993**, 62, 2111–2113.
- [St10] S. STEHLKE, S. BASTIDE, J. GUILLET, C. LEVY-CLEMENT, *Mater. Sci. Eng., B*, **2000**, 69–70, 81–86.
- [St11] D. STIEVENARD, D. DERESMES, *Appl. Phys. Lett.*, **1995**, 67, 1570–1572.
- [St12] A. STEEL, M. TORRES, J. HARTWELL, Y.-Y. YU, N. TING, G. HOKE, H. YANG, in *Microarray Biochip Technology* (Ed. M. SCHENA), Bio Techniques Books, Natick, MA, **2000**, Chapter 5.
- [St13] M. P. STEWART, J. M. BURIK, *Adv. Mater.*, **2000**, 12, 859–869.
- [Su1] K. B. SUNDARAM, H.-W. CHANG, *J. Electrochem. Soc.*, **1993**, 140, 1592–1597.
- [Su2] T. SUZUKI, S. ADACHI, *Jpn. J. Appl. Phys.*, **1994**, 33, 2689.
- [Su3] Y. SUGITA, S. WATANABE, N. AWAJI, *Jpn. J. Appl. Phys.*, **1996**, 35, 5437–5443.
- [Su4] H. SUGIYAMA, O. NITTONO, *J. Cryst. Growth*, **1990**, 103, 156–163.
- [Su5] E. SUZUKI, Y. HAYASHI, *IEEE Trans. Electron Devices*, **1989**, ED-36, 1150–1154.
- [Su6] B. T. SULLIVAN, D. J. LOCKWOOD, H. J. LABBE, Z.-H. LU, *Appl. Phys. Lett.*, **1996**, 69, 3149–3151.
- [Su7] I. SUEMUNE, N. NOGUCHI, M. YAMANISHI, *Jpn. J. Appl. Phys.*, **1992**, 31, L494–497.
- [Ta1] M. TABE, *Appl. Phys. Lett.*, **1984**, 45, 1073.
- [Ta2] O. TABATA, R. ASAHI, H. FUNABASHI, K. SHIMAOKA, S. SUGIJAMA, *Sens. Actuators, A*, **1992**, 34, 51–57.
- [Ta3] T. TAKAGAHARA, K. TAKEDA, *Phys. Rev. B*, **1992**, 46, 15578–15581.
- [Ta4] K. TAKEDA, K. SHIRAIISHI, *Philos. Mag. B*, **1992**, 65, 535.
- [Ta5] H. TAMURA, M. RÜCKSCHLOSS, T. WIRSCHER, S. VEPREK, *Appl. Phys. Lett.*, **1994**, 65, 1537–1539.
- [Ta6] A. TAKAZAWA, T. TAMURA, M. YAMADA, *Appl. Phys. Lett.*, **1993**, 63, 940–942.
- [Ta7] H. TANINO, A. KUPRIN, H. DEAL, *Phys. Rev. B*, **1996**, 53, 1937–1947.
- [Ta8] H. TAKAGI, H. OGAWA, Y. YAMAZAKI, A. ISHIZAKI, T. NAKAGIRI, *Appl. Phys. Lett.*, **1990**, 56, 2379–2380.
- [Ta9] E. TANNENBAUM, *Solid-State Electron.*, **1961**, 2, 123.
- [Ta10] H. TAMURA, M. RÜCKSCHLOSS, T. WIRSCHER, S. VEPREK, *Thin Solid Films*, **1995**, 255, 92–95.
- [Ta11] Y. TAKAHASHI, T. FURUTA, Y. ONO, T. ISHIYAMA, M. TABE, *Jpn. J. Appl. Phys.*, **1995**, 34, 950–954.
- [Ta12] M. TAKAHASHI, M. ARAKI, N. KOSHIDA, *Jpn. J. Appl. Phys.*, **1998**, 37, L1017–1019.
- [Ta13] T. TAKIZAWA, S. ARAI, M. NAKAHARA, *Jpn. J. Appl. Phys.*, **1994**, 33, L643–645.
- [Ta14] S. TANAKA, H. KOYAMA, N. KOSHIDA, *Appl. Phys. Lett.*, **1998**, 73, 2334–2336.
- [Te1] R. TENNE, G. HODES, *Appl. Phys. Lett.*, **1980**, 37, 428.
- [Te2] R. TENNE, H. FLAISHER, R. TRIBOULET, *Phys. Rev. B*, **1984**, 29, 5799.
- [Th1] M. J. J. THEUNISSEN, J. A. APPELS, W. H. C. G. VERKUYLEN, *J. Electrochem. Soc.*, **1970**, 117, 959–965.
- [Th2] M. J. J. THEUNISSEN, *J. Electrochem. Soc.*, **1972**, 119, 351–360.
- [Th3] W. THEISS, S. HENKEL, M. ARNTZEN, *Thin Solid Films*, **1995**, 255, 177–180.
- [Th4] M. THÖNNISSEN, S. BILLAT, M. KRÜGER, H. LÜTH, M. G. BERGER, U. FROTSCHER, U. ROSSOW, *J. Appl. Phys.*, **1996**, 80, 2990–2993.

- [Th5] W. THEISS, M. ARNTZEN, S. HILBRICH, M. WERNKE, R. ARENS-FISCHER, M. G. BERGER, *Phys. Status Solidi B*, **1996**, *190*, 15–21.
- [Th6] W. THEISS, M. WERNKE, V. OFFERMANN, *Thin Solid Films*, **1995**, *255*, 181–184.
- [Th7] W. THEISS, *Surf. Sci. Rep.*, **1997**, *29*, 91–192.
- [Th8] S. M. THOMSEN, *J. Am. Chem. Soc.*, **1952**, *74*, 1690.
- [Th9] V. LE THANH, D. BOUCHIER, G. HINCELIN, *J. Appl. Phys.*, **2000**, *87*, 3700–3706.
- [Tj1] R. W. TJERKSTRA, J. G. E. GARDENIERS, J. J. KELLY, A. VAN DEN BERG, *IEEE J. Microelectromech. Syst.*, **2000**, *9*, 495–501.
- [To1] R. TOMASUNAS, I. PELANT, J. KOCKA, R. LEVY, P. GILLOT, J. B. GRUN, B. HÖNERLAGE, *J. Appl. Phys.*, **1996**, *79*, 2481–2483.
- [Tr1] G. W. TRUCKS, K. RAGHAVACHARI, G. S. HIGASHI, Y. J. CHABAL, *Phys. Rev.*, **1990**, *65*, 504–507.
- [Tr2] F. TROJANEK, P. MALY, I. PELANT, A. HOSPODKOVA, V. KOHLOVA, J. VALENTA, *Thin Solid Films*, **1995**, *255*, 77–79.
- [Ts1] R. TSU, D. BABIC, L. IOTRIATTI, *J. Appl. Phys.*, **1997**, *82*, 1327–1329.
- [Ts2] S. S. TSAO, T. R. GUILINGER, M. J. KELLY, H. J. STEIN, J. C. BARBOUR, J. A. KNAPP, *J. Appl. Phys.*, **1990**, *67*, 3842–3847.
- [Ts3] C. TSAI, K.-H. LI, J. SARATHY, S. SHIH, J. C. CAMPBELL, *Appl. Phys. Lett.*, **1991**, *59*, 2814–2816.
- [Ts4] L. TSYBESKOV, S. P. DUTTAGUPTA, K. D. HIRSCHMAN, P. M. FAUCHET, *Appl. Phys. Lett.*, **1996**, *68*, 2058.
- [Ts5] S. S. TSAO, D. R. MYERS, T. R. GUILINGER, M. J. KELLY, A.K. DATYE, *J. Appl. Phys.*, **1983**, *62*, 4182–4186.
- [Tu1] D. R. TURNER, *J. Electrochem. Soc.*, **1958**, *105*, 402–408.
- [Tu2] D.R. TURNER, in *The Electrochemistry of Semiconductors* (Ed. P. J. HOLMES), Academic Press, London, New York, **1962**, pp. 155–204.
- [Tu3] B. TUCK, *J. Mater. Sci.*, **1975**, *10*, 321–39.
- [Tu4] D. R. TURNER, *J. Electrochem. Soc.*, **1960**, *107*, 810–816.
- [Tu5] X.-Z. TU, *J. Electrochem. Soc.*, **1988**, *135*, 2105–2107.
- [Tu6] H. L. TULLER, R. MLCAK, *Sens. Actuators, B*, **1996**, *35–36*, 255–261.
- [Tu7] D. R. TURNER, *J. Electrochem. Soc.*, **1959**, *106*, 701–705.
- [Ub1] H. UBARA, T. IMURA, A. HIRAKI, *Solid State Commun.*, **1984**, *50*, 673.
- [Uc1] Y. UCHIDA, J. YUE, F. KAMASE, T. SUZUKI, T. HATTORI, M. MATSUMURA, *Jpn. J. Appl. Phys.*, **1986**, *25*, 1633–1639.
- [Uh1] A. UHLIR, *Bell System Tech. J.*, **1956**, *35*, 333–347.
- [Un1] T. UNAGAMI, *Jpn. J. Appl. Phys.*, **1980**, *2*, 231–241.
- [Un2] T. UNAGAMI, *J. Electrochem. Soc.*, **1980**, *127*, 476–483.
- [Un3] H. UNNO, K. IMAI, S. MURAMOTO, *J. Electrochem. Soc.*, **1987**, *134*, 645–648.
- [Us1] U.S. Department of Health, *Registry of Toxic Effects of Chemical Substances*, Rockville, MD, **1979**.
- [Va1] R. M. VADJIKAR, A. K. NATH, *J. Mater. Sci.*, **1995**, *30*, 5466–5472.
- [Va2] R. P. VASQUES, R. W. FATHAUER, T. GEORGE, A. KSENDZOV, *J. Appl. Phys.*, **1992**, *60*, 1004–1006.
- [Va3] A. VALANCE, *Phys. Rev. B*, **1997**, *55*, 9706.
- [Ve1] S. VERHAVERBEKE, I. TERLINCK, C. VINCKIER, G. STEVENS, R. CARTUYVELS, M. M. HEYNS, *J. Electrochem. Soc.*, **1994**, *141*, 2852.
- [Ve2] J. VAN DE VEN, H. J. P. NABBEN, *J. Electrochem. Soc.*, **1991**, *138*, 3401–3406.
- [Ve3] S. VERHAVERBEKE, H. BENDER, M. MEURIS, P. W. MERTENS, H. F. SCHMIDT, M. M. HEYNS, *Mater. Res. Soc. Symp. Proc.*, **1993**, *315*, 57.
- [Ve4] A. VENKATESWARA RAO, F. OZANAM, J.-N. CHAZALVIEL, *J. Electrochem. Soc.*, **1991**, *138*, 153–159.
- [Vi1] J. R. VIG, *J. Vac. Sci. Technol.*, **1985**, *3*, 1027.
- [Vi2] J. C. VIAL, A. BSIESY, F. GASPARD, R. HERINO, M. LIGEON, F. MULLER, R. ROMESTAIN, *Phys. Rev. B*, **1992**, *45*, 14171–14176.
- [Vo1] F. L. VOGEL, W. G. PFANN, H. E. COREY, E. E. THOMAS, *Phys. Rev.*, **1953**, *90*, 489–490.
- [Vo2] M. VOOS, PH. UZAN, C. DELALANDE, G. BASTARD, A. HALMAOUI, *Appl. Phys. Lett.*, **1992**, *61*, 1213–1215.

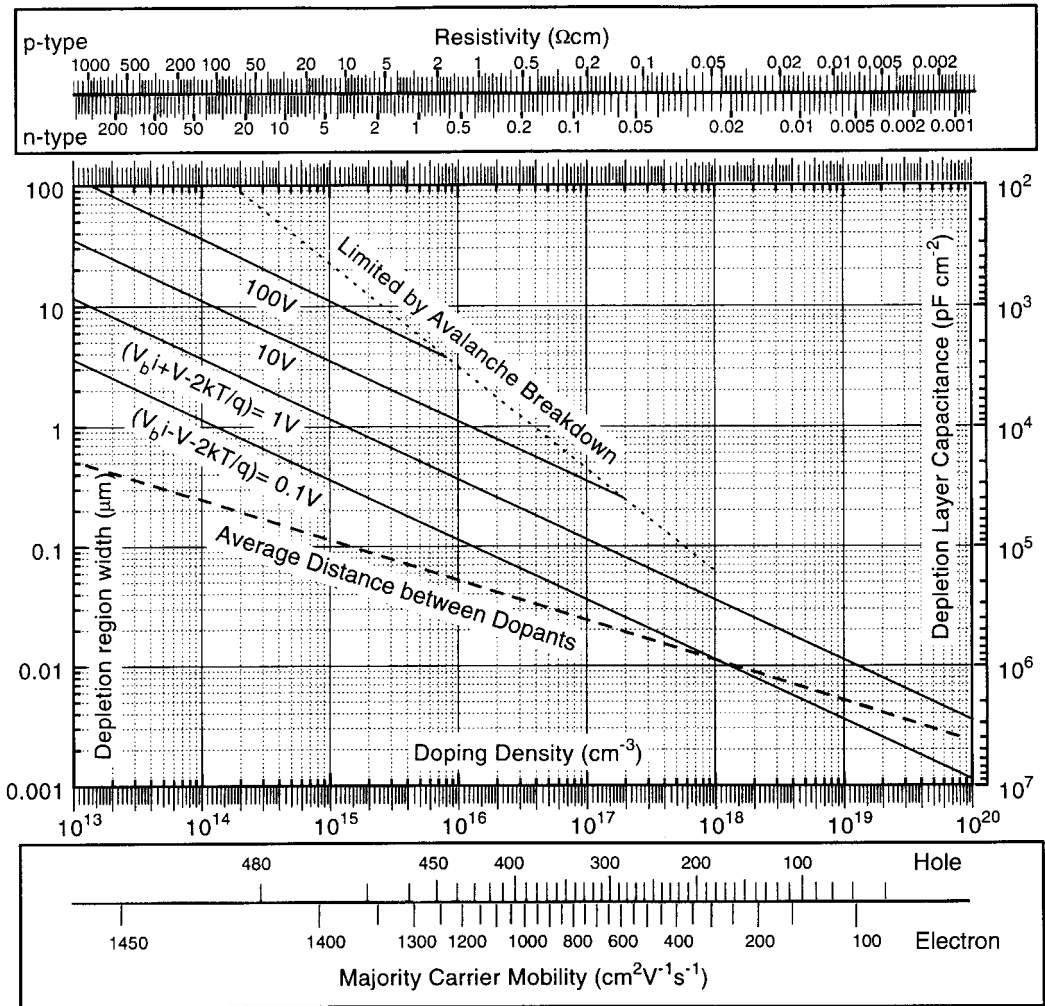
- [Wa1] L. J. WARREN, *Anal. Chim. Acta*, **1971**, 53, 199.
- [Wa2] S. WATANABE, Y. SUGITA, *Appl. Phys. Lett.*, **1995**, 66, 1797.
- [Wa3] T. WANG, S. SURVE, P. J. HESKETH, *J. Electrochem. Soc.*, **1994**, 141, 2493–2497.
- [Wa4] D. WALZ, J.-P. JOLY, R. FALSTER, G. KAMARINOS, *Jpn. J. Appl. Phys.*, **1995**, 34, 4091–4095.
- [Wa5] L.-W. WANG, A. ZUNGER, *Phys. Rev. Lett.*, **1994**, 73, 1039–1042.
- [Wa6] K. WATANABE, T. OKADA, I. CHOE, Y. SATO, *Sens. Actuators, B*, **1996**, 33, 194–197.
- [Wa7] Y. WATANABE, T. SAKAI, *Rev. Electron. Commun. Labs.*, **1971**, 19, 899.
- [Wa8] G. L. WALDBOTT, *Acta Med. Scand. Suppl.*, **1963**, 400, 1–44.
- [Wa9] J. WALZ, G. LE CARVAL, J. P. JOLY, G. KAMARINOS, *Semicond. Sci. Technol.*, **1995**, 10, 1022–1033.
- [Wa10] J. WANG, F. L. ZHANG, W. C. WANG, J. B. ZHENG, X. Y. HOU, X. WANG, *J. Appl. Phys.*, **1994**, 75, 1070–1073.
- [Wa11] L. J. WARREN, *Anal. Chim. Acta*, **1971**, 53, 199–202.
- [We1] H. WELLER, *Adv. Mater.*, **1993**, 5, 88–95.
- [We2] R. B. WEHRSPHORN, J.-N. CHAZALVIEL, F. OZANAM, I. SOLOMON, *Thin Solid Films*, **1997**, 297, 5–8.
- [We3] C. P. WEN, K. P. WELLER, *J. Electrochem. Soc.*, **1972**, 119, 547–548.
- [We4] H. WENDT, H. CERVA, V. LEHMANN, W. PAMLER, *J. Appl. Phys.*, **1989**, 65, 2402.
- [We5] R. B. WEHRSPHORN, J.-N. CHAZALVIEL, F. OZANAM, *J. Electrochem. Soc.*, **1998**, 145, 2958–2961.
- [We6] R. B. WEHRSPHORN, F. OZANAM, J.-N. CHAZALVIEL, *J. Electrochem. Soc.*, **1999**, 146, 3309–3314.
- [We7] A. WEISS, K. H. NOTHNAGEL, *Ber. Bunsenges. Phys. Chem.*, **1971**, 75, 216–229.
- [Wi1] M. J. WINTON, S. D. RUSSEL, R. GRONSKY, *J. Appl. Phys.*, **1997**, 82, 436–441.
- [Wi2] J. WITTMANN, W. BERGHOLZ, H. HOFFMANN, *J. Electrochem. Soc.*, **1999**, 146, 313–320.
- [Wi3] B. J. WIERSMA, Y. TAK, K. R. HEBERT, *J. Electrochem. Soc.*, **1991**, 138, 371–379.
- [Wo1] J. WOJTIWICZ, in *Modern Aspects of Electrochemistry*, Vol. 8 (Eds J. O'M. BOCKRIS and B. CONVAY), Plenum Press, New York, **1972**.
- [Wo2] M. V. WOLKIN, J. JORNE, P. M. FAUCHET, G. ALLAN, C. DELERUE, *Phys. Rev. Lett.*, **1999**, 82, 197–200.
- [Wu1] Z. Y. WU, S. HALL, J. M. KEEN, *J. Electrochem. Soc.*, **1996**, 143, 2972–2980.
- [Wu2] C. P. WU, E. C. DOUGLAS, C. W. MULLER, R. WILLIAMS, *J. Electrochem. Soc.*, **1979**, 126, 1982–1988.
- [Xi1] X. H. XIA, J. J. KELLY, *J. Electrochem. Soc.*, **2001**, 148, C348–352.
- [Xu1] Y. P. XU, R. S. HUANG, *J. Electrochem. Soc.*, **1990**, 137, 948–953.
- [Xu2] F. XUE, X. BAO, F. YAN, *J. Appl. Phys.*, **1997**, 81, 3175–3180.
- [Xu3] J. XU, A. J. STECKL, *IEEE Electron Device Lett.*, **1994**, 15, 507–509.
- [Ya1] E. YABLONOVITCH, D. L. ALLARA, C. C. CHANG, T. GMITTER, T. B. BRIGHT, *Phys. Rev. Lett.*, **1986**, 57, 249–252.
- [Ya2] J. D. I. YAM, J. J. SANTIAGO-AVILES, J. N. ZEMEL, *Sens. Actuators, A*, **1991**, 29, 121.
- [Ya3] S. YAO, P. J. HESKETH, *J. Electrochem. Soc.*, **1995**, 142, L23–25.
- [Ya4] K. H. YANG, *J. Electrochem. Soc.*, **1984**, 131, 1140–1145.
- [Ya5] H. YAN, X. HU, *J. Appl. Phys.*, **1993**, 73, 4324–4331.
- [Ya6] J. YAN, S. SIGH, K. H. JUNG, D. L. KWONG, M. KOVAR, J. M. WHITE, B. E. GNADE, L. MAGEL, *Appl. Phys. Lett.*, **1994**, 64, 1374–1376.
- [Ya7] M. YANG, D. HUANG, P. HAO, F. ZHANG, X. HOU, X. WANG, *J. Appl. Phys.*, **1994**, 75, 651.
- [Ya8] E. YABLONOVITCH, T. J. GMITTER, *Solid-State Electron.*, **1992**, 35, 261–267.
- [Ya9] N. YAMAMOTO, H. TAKAI, *Jpn. J. Appl. Phys.*, **1999**, 38, 5706–5709.
- [Ya10] Z. YAMANI, S. ASHHAB, A. NAYFEY, W. H. THOMPSON, M. NAYFEH, *Appl. Phys. Lett.*, **1998**, 83, 3929–3931.
- [Ya11] Z. YAMANI, W. H. THOMPSON, L. ABUHASSAN, M. H. NAYFEH, *Appl. Phys. Lett.*, **1997**, 70, 3404–3406.
- [Yo1] J. J. YON, K. BARLA, R. HERINO, G. BOMCHIL, *J. Electrochem. Soc.*, **1987**, 62, 1042–1048.
- [Yo2] I. M. YOUNG, M. I. J. BEALE, J. D. BENJAMIN, *Appl. Phys. Lett.*, **1985**, 46, 1133.

- [Yu1] T. YU, R. LAIHO, L. HEIKKILÄ, *J. Vac. Sci. Technol., B*, **1994**, *12*, 2437–2439.
- [Yu2] D. P. YU, Q. L. YANG, Y. DING, H. Z. ZHANG, Z. G. BAI, J. J. WANG, Y. H. ZOU, W. QIAN, G. C. XIONG, D. Q. FENG, *Appl. Phys. Lett.*, **1998**, *73*, 3076–3078.
- [Yu3] W. K. YUE, D. L. PARKER, M. H. WEICHHOLD, *Tech. Dig. IEEE (IEDM) Intl Electron Devices Meeting*, **1990**, 167–170.
- [Ze1] J. ZEMAN, M. ZIGONE, G. L. J. A. RIKKEN, G. MARTINEZ, *J. Phys. Chem. Solids*, **1995**, *56*, 655–661.
- [Zh1] G. ZHOU, Y. NAKANISHI, Y. HATANAKA, *J. Electrochem. Soc.*, **1993**, *140*, 1468.
- [Zh2] S. B. ZHANG, A. ZUNGER, *Appl. Phys. Lett.*, **1993**, *63*, 1399–1401.
- [Zh3] X. G. ZHANG, *J. Electrochem. Soc.*, **1991**, *138*, 3750–3756.
- [Zh4] S.-L. ZHANG, X. WANG, K. HO, J. LI, P. DIAO, S. CAI, *J. Appl. Phys.*, **1994**, *76*, 3016–3019.
- [Zh5] X. G. ZHANG, S. D. COLLINS, R. L. SMITH, *J. Electrochem. Soc.*, **1989**, *136*, 1561–1565.
- [Zh6] Y. ZHANG, P. A. SNOW, P. ST. J. RUSELL, *Appl. Phys. Lett.*, **2000**, *77*, 2440–2442.
- [Zo1] G. ZOTH, W. BERGHOLZ, *Electrochem. Soc. Extended Abstracts*, **1988**, *88-1*, 273–274.
- [Zu1] I. ZUBEL, I. BARYCKA, K. KOTOWSKA, M. KRAMKOWSKA, *Sens. Actuators, A*, **2001**, *87*, 163–171.



Energy conversion table. Values of photon (vacuum) wavelength (nm), wavenumber ( $\text{cm}^{-1}$ ), frequency (THz) and energy (eV, J), as well as the energy per mole ( $\text{J mol}^{-1}$ ) of a chemical reaction can be easily converted if a ruler is placed horizontally over the chart. The bandgaps of different semiconductors are also indicated, as well as the wavelength of the intensity peak of a blackbody radiation for different temperatures.





Silicon conversion table. For conversion of substrate doping density to resistivity, and vice versa, and to determine carrier mobility, position a ruler vertically over the chart. For a certain doping density (ordinate) and applied bias (solid lines) the depletion region width (left abscissa) and capacitance (right abscissa) are given. The distance between two dopant atoms is shown (broken line, left abscissa) idealizing the positions of the dopants to be in an fcc lattice.

CHF %wt	50%HF/H <sub>2</sub> O ml/l Eq.(1.12)	pH [Se2]	Density kg/l Eq.(1.10)	Resistivity Ohm cm Eq.(1.11)	J <sub>PS</sub> mA/cm <sup>2</sup> Eq.(4.9)	Γ <sub>p</sub> μm/min Eq.(9.5)	SiO <sub>2</sub> nm/min Eq.(2.3)	Si <sub>3</sub> N <sub>4</sub> nm/min Eq.(2.4)	CHF Mol/kg Eq.(1.7)	CHF Mol/l Eq.(1.9)
0.05	0.856	2.30	0.9972	1923	0.043	0.001	0.025	0.009	0.0250	0.0249
0.10	1.714	2.14	0.9973	961.5	0.121	0.003	0.300	0.018	0.0500	0.0499
0.15	2.573	2.04	0.9975	641.0	0.223	0.006	0.576	0.027	0.0750	0.0748
0.20	3.434	1.96	0.9977	480.8	0.343	0.010	0.852	0.036	0.1000	0.0998
0.25	4.297	1.90	0.9979	384.6	0.480	0.014	1.128	0.045	0.1250	0.1247
0.30	5.161	1.84	0.9980	320.5	0.631	0.018	1.404	0.054	0.1500	0.1497
0.35	6.028	1.80	0.9982	274.7	0.795	0.023	1.681	0.063	0.1749	0.1746
0.40	6.896	1.75	0.9984	240.4	0.971	0.028	1.958	0.072	0.1999	0.1996
0.45	7.765	1.72	0.9986	213.7	1.159	0.033	2.235	0.081	0.2249	0.2246
0.50	8.637	1.68	0.9987	192.3	1.357	0.039	2.513	0.09	0.2499	0.2496
0.60	10.39	1.62	0.9991	160.3	1.784	0.051	3.068	0.108	0.2999	0.2996
0.70	12.14	1.57	0.9994	137.4	2.248	0.065	3.625	0.127	0.3499	0.3497
0.80	13.90	1.52	0.9998	120.2	2.746	0.079	4.183	0.145	0.3999	0.3998
0.90	15.67	1.47	1.0001	106.8	3.277	0.094	4.743	0.163	0.4499	0.4499
1.0	17.45	1.44	1.0005	96.15	3.838	0.111	5.304	0.181	0.4998	0.5000
1.1	19.24	1.40	1.0008	87.41	4.428	0.128	5.866	0.200	0.5498	0.5502
1.2	21.03	1.37	1.0011	80.13	5.046	0.145	6.429	0.218	0.5998	0.6005
1.3	22.83	1.34	1.0015	73.96	5.689	0.164	6.994	0.236	0.6498	0.6508
1.4	24.63	1.31	1.0018	68.68	6.358	0.183	7.560	0.255	0.6998	0.7011
1.5	26.45	1.28	1.0022	64.10	7.051	0.203	8.128	0.273	0.7498	0.7514
1.6	28.27	1.26	1.0025	60.10	7.768	0.224	8.697	0.291	0.7997	0.8017
1.7	30.10	1.23	1.0029	56.56	8.508	0.245	9.268	0.310	0.8497	0.8522
1.8	31.93	1.21	1.0032	53.42	9.269	0.267	9.840	0.328	0.8997	0.9026
1.9	33.78	1.19	1.0036	50.61	10.05	0.290	10.41	0.347	0.9497	0.9531
2.0	35.63	1.17	1.0039	48.08	10.86	0.313	10.99	0.365	0.9997	1.0036
2.2	39.36	1.13	1.0046	43.71	12.53	0.361	12.15	0.402	1.0996	1.1047
2.4	43.11	1.09	1.0053	40.06	14.27	0.411	13.31	0.439	1.1996	1.2060
2.5	45.00	1.08	1.0056	38.46	15.17	0.437	13.90	0.458	1.2496	1.2566
2.6	46.90	1.06	1.0060	36.98	16.09	0.464	14.48	0.477	1.2996	1.3074
2.8	50.72	1.03	1.0067	34.34	17.98	0.518	15.66	0.514	1.3996	1.4090
3.0	54.58	1.00	1.0074	32.05	19.95	0.575	16.85	0.552	1.4995	1.5106
3.5	64.36	0.94	1.0091	27.47	25.13	0.724	19.85	0.646	1.7494	1.7653
4.0	74.35	0.88	1.0108	24.04	30.71	0.885	22.92	0.741	1.9994	2.0210
4.5	84.57	0.83	1.0125	21.37	36.64	1.056	26.04	0.836	2.2493	2.2774
5.0	95.01	0.79	1.0143	19.23	42.91	1.236	29.24	0.933	2.4992	2.5349
5.5	105.7	0.75	1.0160	17.48	49.51	1.426	32.50	1.029	2.7491	2.7931
6.0	116.6	0.71	1.0177	16.03	56.41	1.625	35.85	1.127	2.9990	3.0521
6.5	127.8	0.68	1.0194	14.79	63.61	1.833	39.27	1.225	3.2490	3.3120
7.0	139.2	0.65	1.0212	13.74	71.09	2.048	42.78	1.324	3.4989	3.5731
7.5	150.9	0.62	1.0229	12.82	78.84	2.271	46.39	1.423	3.7488	3.8346
8.0	162.9	0.59	1.0246	12.02	86.85	2.502	50.09	1.523	3.9987	4.0971
8.5	175.1	0.56	1.0263	11.31	95.12	2.740	53.89	1.624	4.2486	4.3603
9.0	187.7	0.54	1.0281	10.68	103.6	2.986	57.80	1.725	4.4986	4.6250
9.5	200.6	0.51	1.0298	10.12	112.4	3.238	61.82	1.827	4.7485	4.8900
10	213.8	0.49	1.0315	9.615	121.4	3.497	65.95	1.930	4.9984	5.1558
11	241.2	0.45	1.0350	8.741	140.0	4.034	74.59	2.137	5.4982	5.6906
12	270.0	0.41	1.0384	8.013	159.6	4.597	83.75	2.347	5.9981	6.2284
13	300.4	0.37	1.0419	7.396	179.9	5.183	93.47	2.560	6.4979	6.7702
14	332.5	0.34	1.0453	6.868	201.1	5.793	103.8	2.775	6.9978	7.3148
15	366.5	0.31	1.0488	6.410	223.0	6.424	114.8	2.993	7.4976	7.8635
16	402.4	0.28	1.0522	6.010	245.7	7.077	126.4	3.213	7.9975	8.4150
17	440.5	0.25	1.0557	5.656	269.0	7.751	138.8	3.436	8.4973	8.9706
18	481.0	0.23	1.0591	5.342	293.1	8.445	151.9	3.661	8.9971	9.5288
19	524.1	0.20	1.0626	5.061	317.9	9.158	165.8	3.889	9.4970	10.092
20	570.0	0.18	1.0660	4.808	343.3	9.891	180.6	4.120	9.9968	10.657
22	671.8	0.14	1.0729	4.371	396.1	11.41	212.7	4.589	10.997	11.798
24	789.3	0.10	1.0798	4.006	451.3	13.00	248.7	5.069	11.996	12.954
25	855.1	0.08	1.0833	3.846	479.8	13.82	268.2	5.313	12.496	13.537
26	926.3	0.06	1.0867	3.698	508.9	14.66	288.8	5.559	12.996	14.123
28	1088	0.03	1.0936	3.434	568.7	16.38	333.3	6.059	13.996	15.306
30	1283	-0.01	1.1005	3.205	630.7	18.17	382.6	6.570	14.995	16.502
35	1995	-0.08	1.1178	2.747	794.8	22.90	528.5	7.893	17.494	19.555
40	3420	-0.15	1.1350	2.404	971.0	27.98	711.0	9.280	19.994	22.693
45	7696	-0.20	1.1523	2.137	1159	33.38	934.7	10.73	22.493	25.919
50	-	-0.26	1.1695	1.923	1357	39.10	1205	12.25	24.992	29.228

Properties of aqueous hydrofluoric acid. Top row indicates unit and equation or reference used for calculation. Bold values are certified by experimental data.

